Neurochemical Monitoring in a Humanised Murine Model of Parkinson's Disease using Amperometry and Microdialysis

A thesis submitted by

Caroline H. Reid B.Sc. (Hons.)

to the National University of Ireland for the degree of

Doctor of Philosophy

Based on research carried out in the
Department of Chemistry, Faculty of Science and Engineering,
Maynooth University

October 2018

Under the supervision of Dr. Niall J. Finnerty and Dr. Karen English

Head of Department: Dr. Jennifer McManus

Table of Contents

Declaration

This thesis has not been submitted before, in whole or in part, to this or any University for any degree, and except where otherwise stated, is the original work of the author.

Signed: _____

Caroline H. Reid.

To my Mum and Dad,

Your continuous love and guidance made me who I am,

Therefore, I dedicate this thesis to you.

Life is not easy for any of us. But what of that? We must have perseverance and above all confidence in ourselves. We must believe that we are gifted for something and that this thing must be attained.

Marie Curie (1867 – 1934)

Acknowledgements

Firstly, I would like to extend a massive thank you to my supervisor, Dr. Niall Finnerty. I don't know even where to begin in thanking you for your guidance and support over the last four years. You have gone over and above the role of supervisor in terms of teaching me everything I know about the world of sensors whilst always remaining just a phone call away whenever I doubted myself. Your enthusiasm is something I greatly admire and it is truly infectious. Thank you for allowing me to be part of a such a special consortium, SysMedPD. I will always reflect on these years with great fondness.

I would like to take this opportunity to thank my co-supervisor, Dr. Karen English. Thank you for your critical review of my thesis while remaining a source of support whilst I was writing my thesis. It was much appreciated. To Prof. Dr. Jens Schwamborn, thank you for giving me the opportunity to come over to Luxembourg and work in your lab. I truly enjoyed my time spent learning a whole host of new scientific techniques amongst some great people I met there. Likewise, thank you for your support and advice during my writing of this thesis and throughout *in vivo* experimental work. To everyone in SysMedPD, thank you for being a great bunch to work alongside. This really is such a wonderful consortium and I feel I have developed greatly both as a person and as a researcher during my experience on this project. I would like to wish each and every one of you every success for future endeavours. Thank you to the EU Horizon 2020 funding program for providing my funding for the last three years.

Also, I would like to say a big thank you to the Developmental and Cellular Biology group in the University of Luxembourg. Thank you all for welcoming me with open arms and making me feel like I was part of the group. A special mention must be made to Dr. Kathrin Hemmer and Ms. Thea van Wüellen. Thank you for your constant help in teaching me new techniques while always being at the end of an email whenever I needed help. Additionally, thank you for providing the cells for the transplantations and performing IHC staining throughout this project. I will never forget your excellent tour guide skills in Luxembourg!

A further thanks must be extended to Dr. Javier Jarazo who overtook these tasks in the latter few months of this project. Additionally, thank you to our colleagues

in Leiden University; Prof. Thomas Hankemeier, Dr. Amy Harms and Cornelius Willacey for performing metabolomic analysis on microdialysis samples.

To my family, mum and dad, I am massively lucky to have you guys as my parents. Your love and unwavering support of me in everything I do is something I will always hold dear. The ability to always be able to turn to you for advice and help whenever it was needed is greatly comforting. In everything I have ever done you have always been there, even when I did wreck your heads at times. I will always appreciate the opportunity to come home to a hug when I needed it, even at 26! Thank you for always remaining a massive source of support during this PhD journey.

Ciarán, I think you need a special mention in this thesis. Your constant love, support and patience especially when I just needed to talk was something I will never be able to thank you enough for. You have been there since day one of this PhD so I kind of feel like you've been on this PhD journey as much as I have. Thank you for waiting for me on the weekends whilst I was doing 'the check' without so much as a complaint. Thank you for letting me be your guinea pig for all your new recipes which kept me sane during the writing process. Just remember, it's all about the enzymes!

To the best housemate I ever could have imagined. Dearbhlaith where do I even begin? From the first day I met you in undergrad I should have known you would be a bad influence. I will fondly remember our nightly chats, our snow expedition and constant giggles. I'm so glad you were always a pillar of sense in No. 172 (haha!). You will always BEE a massive part of my PhD journey.

I would like to extend my gratitude to the Chemistry Department. Firstly to Noel Williams, thank you for your technical support throughout my time as a post grad. You are truly invaluable to this Department and your knowledge of all things engineering is quite astounding. You are a true gentleman and you were always there whenever I had a computer query…which was a lot! To Donna and Carol, thank you for helping me in the printing of my thesis and whenever I needed help. To the technicians, thank you for your help whenever I needed advice or help. Each one of you were always readily available to lend a hand. Similarly, to Deirdre and Gillian in the BRU, thank you for your advice to one of my many questions. Also, for helping me escape from the BRU the day I got locked in…I'll never live that down.

To all the postgrads, thank you for the laughs along the way. I wish everyone of you the best of luck for the years ahead. A special mention must be extended to the

famous five; Jessica, Justine, Karen and Michelle. Thank you for the trips away, cinema nights and our other adventures. I have lovely memories from my time here and plus how could I forget to mention our PressExpress invention?!

To Deirdre and Rory, thank you for always taking an interest in how I was getting on during this PhD. I always looked forward to relaxing over a lovely dinner in your house at the weekend. Finally, to the Wicklow girls; Enya, Laura, Rachel, Sarah, Sinead and Siobhán thank you for always making me laugh. You are the greatest people to be around, and my sides constantly ache the minute we meet up. Thank you for always asking how I was getting on, it was nice to know you were always there. If I have forgotten anyone, I swear it wasn't on purpose but thesisitis is real! I will be sure to thank you in person.

Abbreviations & Definitions

Abbreviations:

AA	Ascorbic Acid
ATP	Adenosine Triphosphate
aCSF	Artificial Cerebrospinal Fluid
CBF	Cerebral Blood Flow
BT	Brain Tissue
$CaCl_2$	Calcium Chloride
Cat	Catalase
CPA	Constant Potential Amperometry
CPE	Carbon Paste Electrode
ECF	Extracellular Fluid
EDRF	Endothelium Derived Relaxing Factor
ESC	Embryonic Stem Cell
ETC	Electron Transport Chain
GA	Glutaraldehyde
GSH	Glutathione
H_2O_2	Hydrogen Peroxide
H_2SO_4	Sulfuric Acid
i.p.	Intraperitoneal Injection
iNSC	Induced Neural Stem Cell
iPSC	Induced Pluripotent Stem Cell
KCl	Potassium Chloride
KOH	Potassium Hydroxide
L-NAME	N^G-nitro-L-arginine
MSA	Mercaptosuccinic Acid
N_2	Nitrogen
NaCl	Sodium Chloride
$NaH_2PO_4.H_2O$	Sodium Phosphate Monobasic
$NaNO_2$	Sodium Nitrite
NaOH	Sodium Hydroxide

NEDD	N-1-Napthylethylenediamine
NMDA	N-Methyl-D-Aspartate
NO	Nitric Oxide
O_2	Oxygen
$O_2^{\cdot-}$	Superoxide
$ONOO^-$	Peroxynitrite
o-PD	*o*-Phenylenediamine
PD	Parkinson's Disease
PBS	Phosphate Buffer Saline
PINK1	PTEN-induced Kinase 1
PPD	Poly-*o*-Phenylenediamine
Pt	Platinum
SA	Sodium Azide
SCE	Saturated Calomel Electrode
SNpc	Substantia Nigra pars compacta
SULF	Sulfanilamide

Definitions:

Experimental Study Groups		
Nomenclature	**Definition of group**	**Test/Control**
NOD SCID mice	NSG (NOD.Cg-Prkdc^{scid} Il2rg^{tm1Wjl}/SzJ**)**	Non-Humanised Control (no cells)
WT mice	NSG + human dopaminergic neuron cell line derived from healthy control cohort	Humanised Cell Control
PINK1 mice	NSG + patient-derived PINK1 expressing dopaminergic neurons derived from iPSCs	Experimental test (Humanised mouse model of PD)
SHAM mice	NSG + Control Media	Surgical Control

Abstract

The main objective of this thesis was to elucidate an overall neurochemical signature of the progression of patient-specific Parkinson's disease (PD) through the amperometric monitoring of nitric oxide (NO), oxygen (O_2) and hydrogen peroxide (H_2O_2) coupled with microdialysis sampling. The development of a humanised mouse model of PD provides an invaluable tool in which to study PD in a physiological setting. By application of amperometric sensors and microdialysis sampling in these PD models, the functional neurochemical behaviour of the PD can be assessed *in vivo*.

Chapter 1 details an introduction into neurochemical monitoring, PD and the potentially altered role of NO, O_2 and H_2O_2 in contributing to the pathology of this disease. The theory and underlying principles associated with this project are examined in Chapter 2. Chapter 3 includes all of the experimental protocols used throughout the course of this thesis.

The validation of each amperometric sensor included in this project is presented in Chapter 4. Previously published performance criteria currently exists on the NO sensor, O_2 sensor and H_2O_2 biosensor. Therefore, it was paramount to ensure their optimum performance prior to application in a murine model. Chapter 5 details the characterisation of the aforementioned sensors in the striatum of NOD SCID mice. Characterisation of each of the amperometric sensors included the systemic and local administration of a variety of inducers and inhibitors of the analyte under investigation. Hence, allowing for the optimal performance of the sensor to be confirmed *in vivo*. Subsequently, the application of each of these sensors in a humanised model of PD is examined in Chapter 6. Dynamics of NO, O_2 and H_2O_2 levels in the striatum of humanised PINK1, Wild Type (WT) and SHAM mice are included to identify any alterations in the aforementioned analytes that may exist in PD.

Additionally, microdialysis sampling conducted in humanised PINK1 and WT mice (Chapter 7) was coupled with amperometric recordings to assess any potential biomarkers of PD. An overall conclusion of this thesis is made in Chapter 8 which aims to deliver a general overview into the main findings obtained throughout this body of work.

Chapter 1

Introduction

1.1 Introduction

The human brain is an incredibly complex organ which forms the central part of our nervous system. Every movement, feeling, memory and bodily function is processed and controlled by the brain in response to external stimuli. The complexity of the brain can be attributed to the 100 billion neurons and one trillion glia cells contained within the brain[1]. Neurons are nerve cells which facilitate electrical and chemical communication throughout the brain. The neuron is comprised of a cell body, commonly referred to as the soma. From the soma, branching filament projections known as dendrites extend out into the surrounding microenvironment. Neurons receive incoming excitatory or inhibitory signals at the dendrites allowing for an action potential to be fired or ceased. Following the initiation of an action potential, the axon of the neuron transports electrical signals to the axon terminals where it is communicated to adjacent neurons (Figure 1.1.1). Each neuron is thought to be connected to up to 10,000 other neurons which further supports the complexity exhibited by the brain. New neuronal connections are constantly being formed during our lifetime which shape our personalities, the memories we store and new skills we learn. These neurons work to connect with each other through the brain by means of structures referred to as synapses. It is at these synapses that neurochemical signalling is facilitated through the secretion of neurotransmitters (Section 1.2). Moreover, glial cells are known to support the structure of the neurons. However, they have also been observed to modulate neurochemical transmission by stimulating the post-synaptic neurons or by enhancing or depressing the further release of signalling molecules on the pre-synaptic neuron[2].

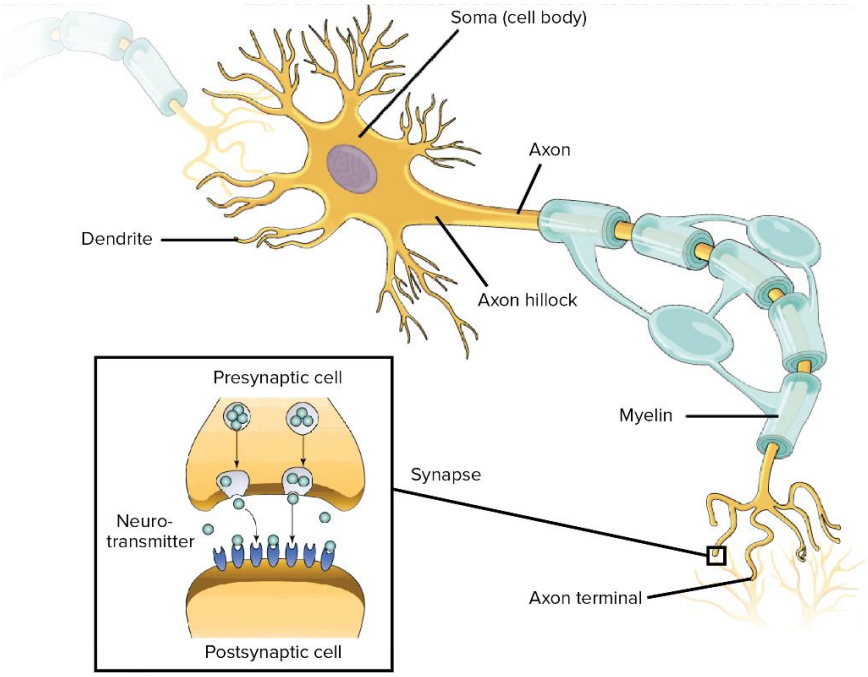

Figure 1.1.1: Schematic of the structure of a neuron incorporating an inset of the synapse. (Sourced: https://www.khanacademy.org/science/biology/human-biology/neuron-nervous-system/a/overview-of-neuron-structure-and-function).

1.2 Neurochemical Signalling

Neurons communicate with each other in a process referred to as neurochemical signalling. Neurochemical signalling involves the release of neurotransmitters or neuromodulators from the pre-synaptic neuron into the synaptic cleft. It is here that these aforementioned signalling molecules bind to receptors in the post-synaptic neuron resulting in transient changes in membrane potential or the activation of signalling cascades. The initiation of an action potential controls the release of signalling molecules from the pre-synaptic cleft. Neurons remain at rest due to the maintenance of a concentration gradient which is upheld between the inside of the neuron, where a negative concentration exists, and the surrounding extracellular fluid (ECF) which contains a greater proportion of positively charged ions. Although, ionic concentrations attempt to balance out inside and outside of the membrane by permitting ions to pass through the membrane through ions channels. K^+ ions pass freely through the membrane, while at rest Cl^- and Na^+ ions find difficulty in permeating the membrane. It is reported that the resting potential of the neurons is

approximately - 70 mV. Therefore, at rest, a greater concentration of K^+ ions exists inside the neuron while a high concentration of Na^+ ions resides outside the neuron.

By a temporary shift in the membrane potential of the neuron, an action potential is initiated. This change in the membrane potential is caused by depolarisation of the cell body resulting in the resting potential to move towards 0 mV. An action potential is instigated by a neighbouring neuron which causes voltage-gated Na^+ channels on the neuronal cell body to open. Thus, causing positively charged Na^+ ions to flow across the membrane. The influx of positively charged ions results in the neuron becoming more positive and depolarising. Depolarisation of the preceding neuron is ceased following the opening of K^+ ion channels allowing for K^+ to flow out of the cell body. Simultaneously, Na^+ channels begin to close leading to a repolarisation of the cell body. Thereafter, a resting potential of - 70 mV is reinstated.

The initiation of this action potential results in an electrical impulse travelling down the length of the axon to facilitate the opening of Na^+ ion channels resulting in the depolarisation of the axon terminal membrane. As a result of depolarisation, Ca^{2+} channels open leading to an influx of Ca^{2+} where it binds to vesicles contained in the axon terminal. This binding results in the Ca^{2+} dependent release of signalling molecules into the synaptic cleft. Following this release, repolarisation of the membrane occurs by the opening of K^+ channels. Signalling molecules that are released can either be excitatory or inhibitory meaning that the signal can continue to the next neuron or neurochemical signalling is ceased. Following activation or inhibition of the relevant post-synaptic receptor, neurotransmitters are either degraded in the synaptic cleft or taken-up by the pre-synaptic neuron. Additionally, these signalling molecules can also flow into the ECF, hence, allowing them to act as biomarkers of biochemical pathways and processes.

1.3 Neurochemical Analysis

As stated in Section 1.1, the brain is one of the most complex organs in the human body. It is due to this complexity that the ability to understand the mechanisms and biological pathways associated with feelings, thoughts and behaviour remains intrinsically difficult. The interaction between electrical and chemical processes remains the foundation of each neurochemical event managed in the brain. Thus, the measurement of real-time neurochemical events remains the gold standard in which to

gain a better understanding of underlying neuronal processes. Non-invasive neurochemical measurements include positron emission tomography (PET) and functional magnetic resonance imaging (fMRI). These techniques work by monitoring shifts in brain function and neuronal activity[3,4]. However, these techniques suffer from poor temporal resolution. In contrast, invasive techniques offer many advantages including greater temporal resolution in the measurement of neurochemical dynamics. Microdialysis sampling (Chapter 7) and *in vivo* amperometric recordings (Chapters 5 & 6) are invasive techniques involving the measurement of neurochemicals present in the ECF. Furthermore, *in vivo* amperometric techniques offer the ability to measure neurochemical events in real-time.

Microdialysis sampling is based on the technique refined by Delgado *et al.*[5] in 1972 whereby a 'dialytrode' was developed involving the perfusion of a solution through a dialysis bag after which it was carried to a site where it could be accessed. However, this technique was substantially improved by Ungerstedt *et al.*[6] who worked to increase the efficiency of the microdialysis probe by increasing the surface area of the dialysis membrane. Since this significant contribution made by Ungerstedt *et al.*, microdialysis has been successfully used to sample the ECF of neural tissue allowing for the analysis of numerous analytes and their associated metabolites. The theory underlying microdialysis is further discussed in Section 2.7. The increasing popularity in the use of microdialysis in neurochemical analysis can be attributed to the number of advantages that the microdialysis technique possesses. Firstly, the microdialysis membrane acts as physical barrier between the perfusate and the tissue allowing for the elimination of high molecular weight substances, such as bacteria, from being collected and contaminating the sample. In addition, the membrane helps to protect the surrounding tissue from the turbulent flow of the perfusate. Analyte depletion is also reduced due to the use of a lower perfusion flow rate in microdialysis sampling leading to a greater relative recovery rate (Section 2.7). Additionally, pharmacokinetic agents can be infused into the probe where they can be delivered to the surrounding local microenvironment in a technique referred to as retromicrodialysis. One of the major advantages of microdialysis when compared to *in vivo* amperometry is that it is not limited to the detection of one analyte as multiple analytes can be sampled simultaneously while sampling can also be conducted without fluid loss.

Like all techniques, disadvantages associated with the use of microdialysis do exist. Microdialysis probes are considerably larger than microelectrode sensors implanted for *in vivo* amperometry. Therefore, this larger construct can result in neural tissue damage which may interfere with the system under investigation. Moreover, microdialysis sampling is limited by slower temporal resolution when compared to *in vivo* amperometry. In addition, an area of analyte depletion may exist around the microdialysis probe during sampling as all analytes that demonstrate the ability to cross the membrane of the probe will be collected. In turn, this can affect basal levels of certain analytes under examination[7–9].

The use of voltammetric techniques for the detection of oxygen was reported by Clark *et al.*[10] in the 1950s. However, pioneering studies conducted by Adams *et al.*[11] can be associated with the application of voltammetric techniques allowing for the detection of analyte concentration changes in the brain ECF. Voltammetry involves the detection of an analyte as a function of the applied potential. The voltammetric technique used throughout this project is constant potential amperometry which is further discussed in Section 2.4. Many advantages of using voltammetry exist which include the excellent temporal and spatial resolution exhibited by microelectrodes *in vivo* which allows for real-time monitoring of the analyte of interest[12]. Moreover, microelectrodes are much smaller in diameter when compared to the diameter of a microdialysis probe resulting in less tissue damage surrounding the electrode which may alter concentrations of the target analyte[13]. In addition, microelectrodes do not require the use of expensive analytical techniques, such as HPLC, for detection of analytes[14]. However, limitations associated with the use of microelectrodes do exist. For example, microelectrodes are only able to monitor one analyte at a given time while they must also be sensitive and selective for the detection of a target analyte.

Taken together, the use of microdialysis and *in vivo* voltammetry can provide an insight into the behaviour of target analytes in various biological processes that underlie homeostatic conditions and conditions that are in flux during neurodegenerative states. The use of these valuable analytical techniques allows for potential biomarkers of disease states to be identified for the first time while allowing for tailored novel candidate neuroprotection agents to be developed.

1.3.1 Neurochemical NO Monitoring

NO is a gaseous free radical which is produced enzymatically from L-arginine. The type of NO produced is dependent on the site at which the NO was produced as three NO synthase (NOS) enzymes exist; endothelial NOS (eNOS), inducible NOS (iNOS) and neuronal NOS (nNOS)[15]. In the brain, nNOS is found at the greatest concentration allowing for the production of neuronal NO. Through the binding of L-arginine to the NOS enzyme and the presence of varying cofactors, NO is produced alongside L-citrulline (Equation 1.3.1.1). Guanidine nitrogen atoms of L-arginine provide the nitrogen for the formation of NO while the oxygen is derived from molecular O_2. Thereafter, L-citrulline can be recycled back to L-arginine allowing for NO production to continue[16].

L-arginine + 2NADPH + O_2 ⟶ L-citrulline + NO + $2NADP^+$ **(Equation 1.3.1.1)**

Due to the presence of varying types of NOS enzymes, NO possesses the ability to carry out a host of different biological functions. Such roles include functions in synaptic plasticity, neurosignalling and learning and memory[17]. NO was first identified as the endothelium derived relaxing factor (EDRF) in the 1980s[18]. It plays a vital role in the regulation of blood flow through vasodilatory and vasoconstrictive processes. Following NO production in the endothelium, it diffuses across into the lumen where it eventually crosses surrounding cell membranes into the cytosol. It is here that it meets the haem-containing protein, soluble guanylyl cyclase (sGC). The activity of sGC results in the formation of cyclic GMP leading to signal transduction in adjacent cells and relaxation in surrounding blood vessels[16]. As blood flow attributes to the functioning of many biological processes, NO is an important target species to monitor. Additionally, NO is a recognised neurotransmitter while eliciting an important role in immune responses against varying pathogens. Therefore, the measurement of NO in the brain can provide a valuable insight into neurological functions and mechanisms.

When present at elevated concentrations, NO can have a pathogenic role. Firstly, by means of a diffusion-limited reaction with superoxide ($O_2^{\cdot-}$), NO can form Peroxynitrite ($ONOO^-$). $ONOO^-$ is a highly toxic species formed following an increased accumulation of NO and $O_2^{\cdot-}$ in cells. Usually, both NO and $O_2^{\cdot-}$ are kept

under control during homeostatic conditions. However, during pathological conditions, the concentrations of the aforesaid substances are increased leading to an increased production of $ONOO^-$. $ONOO^-$ is a very strong oxidant which can cause extensive damage through the oxidation of multiple biological molecules[19]. Moreover, NO can also function pathologically by inflicting changes in enzymatic activity through nitrolysation and nitrosation of various proteins[16].

Due to the importance of NO in the various biological functions and the role of NO in pathophysiological diseases, it is paramount that a selective and sensitive detection technique is applied for the real-time monitoring of NO in biological systems. Measurements of NO have been previously conducted indirectly by monitoring levels of cGMP and through the application of NO-synthase inhibitors[20,21]. Other commonly used analytical methods of measuring NO have included the use of UV-visible spectrophotometry[22]. However, NO is a known free radical *in vivo* with a very short half-life (< 10 s) due to its reaction with a range of endogenous molecules[23], thus, making it very difficult to measure NO. Additionally, NO exists at very low concentrations (0.1 µM)[24] *in vivo* amongst a host of endogenous interfering species, including ascorbic acid (AA), which increases the difficulty in detecting NO successfully. For this reason, long-term *in vivo* NO recordings using microelectrochemical sensors have been used due to the excellent temporal and spatial resolution that they possess. Primarily, electrochemical sensors are developed to exhibit optimum selectivity and sensitivity following *in vivo* implantation making them suitable for NO detection.

An electrochemical NO sensor has been previously developed and characterised both *in vivo*[17] and *in vitro*[25]. The aforementioned sensor has been demonstrated to be highly selective against a host of interfering agents while remaining sensitive in the detection of NO[25,26] while retaining excellent temporal and spatial resolution. Moreover, the sensor has been demonstrated to remain stable following *in vivo* implantation[26] making it suitable for the *in vivo* detection of NO. Therefore, this NO sensor was included in *in vivo* NO investigations.

1.3.2 Neurochemical O_2 Monitoring

O_2 is vital to the homeostatic functioning of the brain. Brain tissue O_2 acts as a major substrate in energy production allowing for cellular demands to be maintained.

At rest, it is reported that the brain consumes 20 % of the total oxygen in the human body. In addition, O_2 demand is highly region specific resulting in O_2 concentrations varying greatly across the brain[27]. O_2 levels can be altered in the brain in response to neuronal stimulation and neuromodulator release[28,29]. Even though O_2 is under constant flux in the brain, O_2 concentrations are kept at homeostatic conditions under the tight regulation by cerebral blood flow (CBF). However, any substantial deviations in either O_2 utilisation or supply from the CBF can greatly affect biological functioning due to the low O_2 reserve present in tissues[30]. Therefore, highlighting the importance of O_2 monitoring especially in neurodegenerative and pathological conditions.

The measurement of brain tissue O_2 is determined as a net change between supply from CBF and utilisation by surrounding cells. However, O_2 measurements are dependent on the tissue composition and the depth of the implanted sensor in the biological tissue[31]. O_2 was one of the first substances to be detected voltammetrically *in vivo* by Clark *et al.* using a noble metal electrode[10]. This technique offered good spatial and temporal resolutions over previously used methods allowing for measurements to be made in freely-moving animals through the electrochemical reduction of O_2. Since this discovery, the development of various electrodes for electrochemical O_2 measurements has been made which includes manufacturing O_2 sensing electrodes from noble metals, such as Pt and Au, and from carbon-based substrates to form glassy carbon, carbon fibre (CFE) and carbon paste electrodes (CPE)[32]. Noble metal electrodes have been associated with the successful *in vivo* monitoring of O_2 using Constant Potential Amperometry (CPA, see Section 2.4). By application of a suitable potential, the production of an amperometric current results, which is proportional to the concentration of O_2 present. Although metal electrodes, especially Pt electrodes, exhibit an excellent ability in facilitating the reduction of molecular O_2 at the sensor surface[33], metal electrodes are susceptible to biofouling and surface poisoning following implantation in biological tissue[34].

However, carbon based electrodes have an added advantage over the use of noble metal electrodes in O_2 detection due to the excellent stability and biocompatibility properties they possess. Additionally, CFEs have a typical diameter of 10 µm resulting in minimal tissue damage to the surrounding area. Due to the small diameter that they possess, CFEs can be implanted *in vivo* both in, and around, metabolic cells resulting in the detection of fluctuating O_2 levels. While CPEs possess

a diameter that is larger than capillary zones (< 100 µm) meaning that an average tissue O_2 level can be measured from the surrounding area[35]. Another significant advantage of CPEs is the excellent long-term stability that they exhibit following *in vivo* implantation. Carbon based electrodes exhibit greater stability *in vivo*, as unlike metal based electrodes, they do not require any surface modifications. Previous work conducted by Bolger *et al.*[30] reported the excellent stability of CPEs following *in vivo* implantation while also demonstrating the efficient ability of this sensor to monitor varying levels of O_2 in the rat brain. For these reasons, CPEs based on the design by Bolger *et al.* were included into O_2 sensing investigations reported in this thesis.

1.3.3 Neurochemical H_2O_2 Monitoring

During cellular respiration, H_2O_2 is produced due to the leakage of electrons from the electron transport chain (ETC). However, H_2O_2 levels are tightly controlled by antioxidant mechanisms. Although high concentrations of H_2O_2 exhibit neurotoxic effects, H_2O_2 has been observed to play a vital role in homeostatic biological processes. For example, H_2O_2 has been observed to be an intracellular regulator of organelle function and growth, as well as, acting as a diffusible messenger allowing for the regulation of synaptic transmission and plasticity[36]. In recent times, endogenous H_2O_2 has been hypothesised to provide a neuromodulatory function in the release of certain neurotransmitters. Previous work undertaken by Rice *et al.* has identified H_2O_2 as having a role in the regulation of neuronal activity via K_{ATP} channels by inhibiting the release of dopamine from dopaminergic neurons in the substantia nigra[37].

Contrastingly, high concentrations of H_2O_2 are known to be toxic resulting in oxidative damage to the surrounding biological environment contributing to the overall pathology of various neurodegenerative diseases including PD[38]. However, under normal conditions, H_2O_2 remains relatively unreactive unless exposure to free metal ions occurs allowing for the formation of toxic free radicals by means of the Fenton reaction[39]. Tight regulation of H_2O_2 levels is maintained by antioxidants such as catalase and glutathione peroxidase, which facilitate the breakdown of H_2O_2 to water. Without this tight control, increased levels of H_2O_2 result in oxidative damage to surrounding cellular structures. Disturbances to this complex antioxidant network occur in neurodegenerative diseases, thus, leading to an overall increase in H_2O_2 levels

in vivo. Therefore, it is of utmost importance that levels of H_2O_2 are monitored to gain a better understanding into the mechanisms underlying neurodegenerative pathology.

In vivo amperometry is an excellent method of monitoring H_2O_2 in the brain ECF due to its excellent temporal resolution. To date, few reports exist which detail the *in vivo* recording of H_2O_2 in real-time. However, previous work by Kulagina *et al.* has detailed measurements of H_2O_2 conducted in the brain of anaesthetised rats. H_2O_2 recordings were performed using carbon fibre microelectrode crossed-linked with a horseradish peroxidase containing redox polymer[40]. Moreover, the selective detection of H_2O_2 was achieved using Prussian blue enzyme stabilised in polydopamine by Li *et al.*[41].

Previous research conducted by O'Brien *et al.* included the development of a highly selective and sensitive *in vitro* dual H_2O_2 biosensor[42]. This dual biosensor has the ability to simultaneously measured H_2O_2 and degrade H_2O_2. By subtraction of the degraded H_2O_2 amperometric current from the measured H_2O_2 amperometric current, the total level of H_2O_2 present in the *in vivo* environment can be obtained. Recently, additional work has reported the successful characterisation of this H_2O_2 biosensor both *in vitro*[43] and in the striatum of freely-moving rats[44]. Following the successful characterisation of this dual H_2O_2 biosensor *in vitro* and *in vivo*, it was decided to include this H_2O_2 biosensor design in all *in vivo* H_2O_2 experimentation throughout this thesis.

1.4 Parkinson's Disease

PD is the second most common progressive neurodegenerative disease after Alzheimer's disease. One of the main risk factors associated with PD is increasing age, as a close to exponential increase in incidences of PD is observed between 55 and 79 years[45]. With increasing life expectancies, PD threatens to pose a burden, both economically and socially. PD is associated with a deterioration of dopaminergic neurons along with the formation of α-synuclein aggregates, termed Lewy bodies, in the substantia nigra pars compacta (SNpc). The SNpc is an important source of dopamine for other basal ganglia nuclei which exhibit important roles in movement. Thus, a number of motor manifestations are observed in PD patients. PD is typically characterised by well-defined motor symptoms such as tremor, bradykinesia, rigidity and postural instability[46]. Diagnosis is difficult due to the heterogenous nature of PD

pathology. Following the appearance of clinical motor symptoms, a diagnosis can be made along with the patients' history and response to dopaminergic drugs. However, it has become apparent that PD also exhibits a prodromal period, during which neurodegeneration begins. Previous reports have indicated that the presence of non-motor symptoms are closely associated with the Lewy pathology[47]. Motor symptoms are not apparent during this stage. Hence, a range of under-recognised non-motor symptoms exist which include depression, fatigue, sleep disturbance, cognitive impairment and dementia[48]. The delay in recognising the non-motor symptoms contributes to the overall progression of PD resulting in an impaired quality of life and a reduction in life expectancy[49]. Although therapies of PD currently exist, these treatments do not prevent the progressive degenerative processes of this disease. An example of a therapy currently used in PD patients is deep brain stimulation. Deep brain stimulation has been shown to have many benefits in providing symptomatic relief to patients. However, these therapies do not provide neuroprotective benefits to slow progression[50].

Over the past two decades, PD pathology has been examined extensively. Nevertheless, the primary causes and underlying biological mechanisms still remain greatly unknown. For this reason, a suitable therapeutic treatment has not been established. The cause of PD appears to be multifactorial as the SNpc displays a vulnerability to genetic, cellular and environment factors which contribute to pathogenesis over time[51]. It appears that some forms of PD are familial while most cases are sporadic. In 3 - 5 % of sporadic cases and approximately 30 % of familial cases, monogenic mutations exist. Monogenic mutations involve a single mutation in either dominate or recessive genes[52]. These single point mutations affect PTEN (phosphatase and tensin homologue)-induced kinase 1 (PINK1), Parkin, DJ1, ATP13A2, SNCA and leucine-rich repeat kinase 2 (LRRK2) genes. Each of these genes are involved in a variety of biological pathways in humans, thus, further confirming the aetiopathogenic diversity observed in PD. Additionally, mutations account for approximately 50 % of all early-onset cases[53]. Further supporting the need to gain a better understanding into the underlying processes that result in the formation of PD.

Mutations in mitochondrial genes have been implicated as one of the causes of monogenic PD. Previous reports have highlighted mitochondrial dysfunction in the

SNpc in patients whereby complex I deficiency and impaired electron transfer were observed[54]. The mitochondria is the main source of cellular energy for eukaryotic cells as it generates adenosine triphosphate (ATP) by oxidative phosphorylation. Mitochondria are known to possess their own double stranded DNA (mtDNA) which is known to encode 37 mitochondrial genes. Out of these 37 genes, 13 are translated into subunits of the ETC. Moreover, 7 genes that are encoded by mtDNA are observed to code for complex I subunits[55]. Therefore, suggesting that the presence of even 1 point mutation or deletion in any one of these genes could alter the activity of complex I substantially[56]. This leads to dysfunction in the ETC resulting in free radicals production which causes further damage to mtDNA through the production of monogenic mutations resulting in the formation of negative-feedback loop.

1.4.1 Dysregulation of the Electron Transport Chain in PD

The ETC is the main power house of ATP production. ATP production is facilitated by the movement of electrons along this chain by means of electron transporters, at which a redox reaction occurs. Five transporters, alongside ATP-synthase, are observed to make up the ETC which resides on the inner membrane of the mitochondria. The ETC works to convert energy obtained from the oxidation of NADH and $FADH_2$ into the generation of ATP by oxidative phosphorylation. The process of oxidative phosphorylation is initiated following the donation of a pair of electrons to complex I and II by NADH and $FADH_2$. The transport of these electrons down the length of the chain results in the accumulation of protons within the matrix. A concentration gradient forms whereby protons diffuse out of the matrix and into the intermembrane space. Hence, generating a proton gradient which is used to generate ATP by ATP synthase[57].

Although electron transport is highly efficient, leakage of electrons can occur throughout the chain, in particular from complex I and complex III[58]. The ETC has been observed to be a major source of reactive oxygen and nitrogen species due to the leakage of electrons resulting in the formation of these aforementioned reactive species through a reaction with molecular oxygen. Such reaction results in the production of $O_2^{\cdot-}$, H_2O_2 and the hydroxyl free radical ($HO^{\cdot}$)[59]. Under homeostatic conditions, the production of reactive oxygen and nitrogen species remains low while remaining under the tight regulation of mitochondrial antioxidants. Antioxidants

include manganese superoxide dismutase (MnSOD) which works to breakdown $O_2^{\cdot-}$ to H_2O_2 followed by the conversion to H_2O by glutathione. However, cellular damage can be induced by oxidative stress following an imbalance in the production of reactive oxygen species and antioxidant activity[60].

Mitochondrial dysfunction has a major impact on neurons due to the large number of mitochondria they contain and their involvement in ATP production. Hence, one of the expected consequences of mitochondrial dysfunction is the failure to meet cellular energy demand[57]. An evident role of mitochondrial dysfunction was apparent following reports that Complex I was decreased in the SNpc of PD patients[61]. In addition, this deficiency was also present in frontal cortex and skeletal muscle suggesting an overall reduction in complex I in PD exists[62,63]. Similarly, complex III has been reported to have a reduced function in PD patients. Such reductions in complex I and III can lead to free radical leakage from the ETC leading to overall free radical damage of the mitochondria[58]. Moreover, reductions in complex III can result in a reduction in complex I which could further contribute to electron leakage overall[64].

1.4.2 Effects of Increased Oxidative Stress in PD

The underlying mechanisms of PD still remain largely unknown. However, numerous investigations have indicated a clear link between oxidative stress and mitochondrial dysfunction resulting in the degeneration of dopaminergic neurons, lipid peroxidation, protein modifications, DNA damage and decreased levels of glutathione (GSH)[28]. Within this thesis, levels of NO, O_2 and H_2O_2 were monitored in humanised PINK1 mice due to their association to pathophysiological processes in PD.

Numerous studies have highlighted a role of NO in increased excitotoxicity, protein modification and DNA damage[65]. Firstly, excitotoxicity is mediated following a decrease in the magnesium blockade of the N-methyl-D-aspartate (NMDA) receptor. Glutamate works to activate the NMDA receptor leading to an increased accumulation of Ca^{2+}. Ca^{2+} works to activate NOS leading to an increase in the production of NO[38]. Thereafter, increased levels of NO react with $O_2^{\cdot-}$, resulting in the formation of $ONOO^{-}$[19]. $ONOO^{-}$ contributes to cellular damage by causing DNA damage and activating caspase pathways leading to cell death[65,66]. Furthermore, NO has been

observed to inhibit mitochondrial function by causing oxidative damage to complex I and IV and the mitochondrial membrane[39].

Dawson *et al.* previously highlighted the involvement of NO in excitotoxicity whereby neuronal cultures obtained from nNOS knockout mice where shown to be resistant to NMDA mediated excitotoxicity[67]. Additionally, the accumulation of Ca^{2+} following NMDA receptor activation further amplifies toxicity in neurons by contributing to alterations in mitochondrial membrane potential and ATP synthesis. As a result, ROS production is increased leading to an increase in cellular toxicity and damage. Damage caused to complex I can lead to complete inhibition of the complex. Hence, a reduction in ATP levels is experienced. Reductions in ATP levels work to maintain Na^+/K^+-ATPase which functions to retain the resting potential of the cell. Any reductions in ATP levels will directly influence the resting potential of the cell leading to depolarisation of the neuron. Incidentally, an increase in the activation of the NMDA receptor is produced by this increase in excitotoxicity[58].

Protein modification is also thought to be associated with increased NO levels by nitrosylation and nitration. A range of cellular proteins that are closely connected with structural, survival and apoptotic processes can be modified by NO-mediated protein S-nitrosylation due to the presence of reactive cysteine thiols on these proteins. Such proteins include the NMDA receptor, caspase 3 and 9 and parkin[65]. In addition, protein nitration involves the addition of a nitro group. The latter process has been suggested to play a role in the selective nitration of α-synuclein, therefore, contributing to the pathogenesis of PD[68]. While, S-nitrosylation inhibits the activity of ubiquitin E3 ligase of Parkin leading to the loss of the neuroprotective properties of Parkin[69].

NO has an important mitochondrial function by acting as a regulator of electron transfer and ATP synthesis through the inhibition of cytochrome oxidase. Cytochrome complexes are known to contain iron-sulfur clusters. It is through the NO-mediated removal of iron that inhibition of these complexes is believed to occur. Therefore, it is postulated that respiratory chain complexes are inhibited by NO as the activity of cytochrome oxidase was noted to be reduced in PD patients. Additionally, it has been hypothesised that NO works to inhibit α-ketoglutarate dehydrogenase leading to the overall inhibition of complex I[70].

Furthermore, the level of mitochondrial ROS production can be assessed through the measurement of H_2O_2 in the ECF. The reason being that leakage of

electrons from the mitochondrial ETC results in the production of $O_2^{\cdot-}$. MnSOD works to rapidly convert $O_2^{\cdot-}$ to H_2O_2 under homeostatic conditions rendering it undetectable. Additionally, H_2O_2 is known to permeate cellular membranes allowing it act as a stoichiometric indicator of $O_2^{\cdot-}$ production[59]. It is due to this permeability that allows for H_2O_2 to be measured in the ECF by implanted electrochemical sensors. Also, glutathione (GSH) is a major antioxidant found in the brain which works to degrade potentially harmful H_2O_2. However, levels of this antioxidant have been reported to be reduced in the brains of PD patients[28]. GSH is synthesised by the neurons and glia cells while astrocytes have been noted to have an important involvement in the release of GSH into the ECF[56]. Reductions in GSH allows for impaired clearance of H_2O_2 and promotion of $O_2^{\cdot-}$ formation in the ECF[38], thus, measurement of increased H_2O_2 levels may suggest a decrease in GSH activity. Furthermore, monitoring the level of GSH may prove to be especially important in PD due to an association between reduced levels of GSH in early stages of this disease[72]. An increase in H_2O_2 levels can stimulate the generation of $O_2^{\cdot-}$. By means of the Fenton reaction, H_2O_2 can react with ferrous iron (Fe^{2+}) to produce highly reactive radical, $HO^{\cdot}$.[39]. Additionally, high levels of iron have been observed in the SNpc of PD patients which further contributes to the production of ROS species[73]. This increased production of these highly toxic species proves to be extremely damaging to dopaminergic neurons. The metabolism of dopamine contained in dopaminergic neurons by monoamine oxidase produces additional amounts of H_2O_2. Hence, the H_2O_2 produced can work to participate in Fenton reactions increasing the amount of H_2O_2 produced in the microenvironment while also furthering the pathological progression of PD[56].

Molecular O_2 has an intrinsic role in reactive oxygen species production following the leakage of electrons from the ETC. Reduction in O_2 tissue concentration in PD may be indicative of an increased demand in O_2 due to the increased production of oxidative stress species or altered cellular metabolism. For example, the availability of O_2 may be a limiting factor in NO production during pathological processes[70]. Therefore, increased NO production may lead to an increase in O_2 consumption. Also, due to the mitochondrial dysfunction observed in PD, a decrease in ATP production results. For this reason, O_2 levels may be observed to be altered in PD patients due to a mitochondrial switch in energy formation. Thus, measurements of O_2 serve as an important indicator in PD progression.

To conclude, the role of NO, O_2 and H_2O_2 appear to play a major role in contributing to the pathogenesis of PD. For this reason, it is important to monitor levels of these analytes in PD to gain a greater understanding of pathologic biological mechanism into how the disease progresses. Therefore, Chapter 6 details investigations conducted in humanised PINK1 mice which examines alterations in the aforementioned analytes.

1.5 PINK1 Mutations

Mutations in the PINK1 gene are thought to be a major cause in autosomal recessive PD[74]. PINK1 encodes a highly conserved serine/threonine kinase which contains a N-terminal mitochondrial targeting motif[75]. It has been demonstrated to be located primarily in the mitochondria with the kinase domain facing the cytoplasm and the N-terminal tail spanning the mitochondrial membrane[76]. The location of PINK1 highlights a potential involvement in mitochondrial function[77]. It has also been reported to have an important role in the regulation of mitochondrial fission and fusion[78]. Furthermore, as the kinase domain of this gene is found to be facing the cytoplasm allowing for the physical interaction with cytosolic Parkin to occur. PINK1 is thought to be an upstream activator of Parkin[79]. Additionally, this interaction between these genes has been demonstrated to exhibit neuroprotective functions such as the selective autophagy of depolarised mitochondria[80]. PINK1 is known to phosphorylate Parkin resulting in the activation of its E3 ligase activity. Thereafter, Parkin is recruited to damaged mitochondria resulting in the selective mitophagy of damaged mitochondria[81]. The neuroprotective role of PINK1 is further supported following studies involving PINK1-knockout drosophila flies whereby a significant reduction in mitochondrial respiration powered by the ETC was observed. This reduction stemmed from decreased enzymatic activity of complex I and IV leading to reduced ATP production[82].

PINK1 mutations are responsible for between 2 - 4 % of early onset PD in the Caucasian population with this figure rising to 4 - 9 % in Asian populations[83]. Due to its intrinsic involvement in recessive forms of PD, it was important to investigate neurochemical phenomena associated with PINK1 mutations which may result in a better understanding into the underlying processes of this disease. Therefore, the focus of this thesis involves humanised mouse models of PD which were transplanted with

induced pluripotent stem cell (iPSC) derived dopaminergic neurons containing a monogenic PINK1 mutation. These cells were supplied by collaborators at the University of Luxembourg.

1.6 Humanised Mouse Models

Until recently, the ability to study neurochemical mechanisms associated with PD could only be conducted in post-mortem samples, *ex vivo* investigations or in expensive clinical trials. However, the generation of 'humanised' mice has allowed for the engraftment of various human cell types in mouse models allowing them to function as they would in the human physiological environment. The generation of humanised mice models provides the ability to investigate human disease pathogenesis in a physiological environment that was previously inaccessible[84]. Highly immunodeficient mice are paramount to the success of a humanised model as they do not reject xenografts while supporting the growth and differentiation of cells *in vivo*[85,86]. The discovery of severe combined immunodeficiency (SCID) mice was key in the progression of developing immunodeficient mice that were suitable for xenotransplantation[85,87]. Their successful involvement in xenotransplantations can be attributed to the multiple immunodeficiencies they possess which includes a reduction in B, T and natural killer (NK) cells, as well as, a decreased macrophage and dendritic cell function[88]. As a result of this crucial development, a host of humanised mouse models currently exist including models of infectious disease[89], such as hepatitis C[90] and models of debilitating disease such as cancer[91].

Although animal models of PD currently exist, they do not capture the chronically diverse neurodegenerative pathology that is experienced in humans[92,93]. In turn, this can result in a failure to translate seemingly neuroprotective candidates in existing mouse models to a clinical setting. The development of human derived iPSCs has allowed for physiological investigations to be carried out into the mechanisms surrounding various human pathological conditions. Thus, allowing for interspecies variability to be overcome. Although many benefits are associated with xenotransplantation of human derived iPSCs, some disadvantages do exist. For example, the possibility that even a few undifferentiated cells can result in the formation of teratomas following xenotransplantation[94]. Previous work undertaken by Takahashi and Yamanaka[95] addressed many of these concerns by developing a method

for the generation of iPSCs from somatic cells. It was reported that skin fibroblasts were reprogrammed back to a pluripotent state by the induction of four defined factors; Oct3/4, Sox2, Klf4 and c-Myc. These reprogrammed cells were observed to capture the essential characteristics of embryonic stem cells (ESCs) by displaying similar morphology, gene expression and proliferation[96]. This crucial finding enables the generation of all somatic cells of the human body including multiple neural cells lineages such as dopaminergic neurons[97].

Induced neural stem cells (iNSCs) have been shown to exhibit long-term *in vivo* survival rates whilst demonstrating no predisposition to tumour formation. Moreover, transplanted iNSCs have been observed to functionally integrate into the host striatum due to the formation of synaptic connections with existing neuronal connections[98]. Therefore, it can be concluded that the transplantation of iNSCs into mouse brain is a safe and successful procedure which allows for the study of human derived neural stem cells in a physiological environment. Following the development of iPSC technology, the successful generation and characterisation of a humanised mouse model has been achieved involving the transplantation of human iPSC-derived neural stem cells into mouse brain by collaborators in the University of Luxembourg[98–100].

Chapter 6 & 7 incorporates the use of this humanised model of PD. This humanised model of PD involves the xenotransplantation of PD patient-derived iPSCs, supplied by collaborators in the University of Luxembourg, that have been differentiated into dopaminergic neurons. These differentiated dopaminergic neurons were assessed using Tyrosine Hydroxylase (TH) and quantified using Tuj1 (Neuron-specific class III β-tubulin) which is a neural stem cell marker. Following transplantation of these cells into the mouse striatum, the cells are allowed to integrate anatomically for a number of weeks. As the ability to access functional dopaminergic neurons human *in vivo* investigations proves to be incredibly difficult, this humanised mouse model allows for unprecedented access to examine the functional neurochemical behaviour of dopaminergic neurons *in situ*.

1.7 Overview of the Project

This thesis is associated with gaining an overall neurochemical signature of the progression of patient-specific PD through the amperometric monitoring of NO, O_2 and H_2O_2 coupled with microdialysis sampling. Chapter 2 details the theoretical background of each of the experimental techniques included throughout this project. Chapter 3 details all of the experimental protocols associated with manufacture of each electrochemical sensor and each experimental set-up. The results attained throughout the project are contained in Chapter 4 - 7. Chapter 4 outlines the validation of the previously published amperometric sensors to confirm replication of the performance criteria of each sensor prior to their application in an *in vivo* model. Characterisation of each of the sensors in the striatum of NOD SCID mice is contained in Chapter 5. In addition, Chapter 6 details the neurochemical monitoring of NO, O_2 and H_2O_2 in the striatum of humanised PINK1 mice, WT mice and SHAM mice. Microdialysis sampling was conducted thereafter in humanised PINK1 and WT mice (Chapter 7) to assess potential biomarkers of PD by means of metabolomic analysis that was conducted by collaborators in Leiden University. To conclude, Chapter 8 discusses the main findings of this project to allow for an overall conclusion of the work undertaken to be attained.

1.8 References

1. Herculano-Houzel, S. The human brain in numbers: a linearly scaled-up primate brain. *Front. Hum. Neurosci.* **3,** 1–11 (2009).
2. Newman, E. A. New roles for astrocytes: Regulation of synaptic transmission. *Trends Neurosci.* **26,** 536–542 (2003).
3. Shibasaki, H. Human brain mapping: Hemodynamic response and electrophysiology. *Clin. Neurophysiol.* **119,** 731–743 (2008).
4. Dopfel, D. & Zhang, N. Mapping stress networks using functional magnetic resonance imaging in awake animals. *Neurobiol. Stress* (2018).
5. Delgado, J. M., DeFeudis, F. V., Roth, R. H., Ryugo, D. K., & Mitruka, B. M. Dialytrode for long term intracerebral perfusion in awake monkeys. *Arch. Int. Pharmacodyn. Ther.* **198,** 9–21 (1972).
6. Ungerstedt, U. & Pycock, C. Functional correlates of dopamine neurotransmission. *Bull Schweiz Akad Med Wiss* **30,** 44–55 (1974).
7. Chefer, V. I., Thompson, A. C., Zapata, A. & Shippenberg, T. S. Overview of Brain Microdialysis. *Curr. Protoc. Neurosci.* **47,** 7–1 (2009).
8. De Lange, E. C. M., De Boer, A. G. & Breimer, D. D. Methodological issues in microdialysis sampling for pharmacokinetic studies. *Adv. Drug Deliv. Rev.* **45,** 125–148 (2000).
9. Altaf S. Darvesh, Richard T. Carroll, Werner J. Geldenhuys, Gary A. Gudelsky, J. & Klein, Charles K. Meshul, and C. J. V. der S. In vivo brain microdialysis: advances in brain neuropsychopharmacology and drug discovery. *Expert Opin. Drug Discov.* **6,** 109–127 (2011).
10. Clark, Jr., L.C., Misrahy, G., Fox, R. P. Chronically implanted polarographic electrodes. *J. Appl. Physiol.* **13,** 85–91 (1958).
11. Kissinger, P.T , Hart, J.B. & Adams, R. N. Voltammetry in brain tissue - a new neurophysiological measurement. *Brain Res.* **55,** 209–213 (1973).
12. van der Zeyden, M., Oldenziel, W. H., Rea, K., Cremers, T. I. & Westerink, B. H. Microdialysis of GABA and glutamate: Analysis, interpretation and comparison with microsensors. *Pharmacol. Biochem. Behav.* **90,** 135–147 (2008).
13. Khan, A. S. & Michael, A. C. Invasive consequences of using micro-electrodes and microdialysis probes in the brain. *TrAC - Trends Anal. Chem.* **22,** 503–508

(2003).

14. Bourne, J. A. Intracerebral microdialysis: 30 Years as a tool for the neuroscientist. *Clin. Exp. Pharmacol. Physiol.* **30,** 16–24 (2003).
15. Papapetropoulos, A., Rudic, R. D. & Sessa, W. C. Molecular control of nitric oxide synthases in the cardiovascular system. *Cardiovasc. Res.* **43,** 509–520 (1999).
16. Bruckdorfer, R. The basics about nitric oxide. *Mol. Aspects Med.* **26,** 3–31 (2005).
17. Finnerty, N. J., O'Riordan, S. L., Brown, F. O., Serra, P. A., O'Neill, R. D. & Lowry, J. P. In vivo characterisation of a Nafion®-modified Pt electrode for real-time nitric oxide monitoring in brain extracellular fluid. *Anal. Methods* **4,** 550 (2012).
18. Ignarro, L. J., Buga, G. M., Wood, K. S., Byrns, R. E. & Chaudhuri, G. Endothelium-derived relaxing factor produced and released from artery and vein is nitric oxide. *Proc. Natl. Acad. Sci.* **84,** 9265–9269 (1987).
19. Beckman, J. S. & Koppenol, W. H. Nitric oxide, superoxide, and peroxynitrite: the good, the bad, and ugly. *Am. J. Physiol. Physiol.* **271,** C1424–C1437 (1996).
20. Pålsson, E., Finnerty, N., Fejgin, K., Klamer, D., Wass, C., Svensson, L. & Lowry, J. Increased cortical nitric oxide release after phencyclidine administration. *Synapse* **63,** 1083–1088 (2009).
21. Klamer, D., Engel, J. A. & Svensson, L. The nitric oxide synthase inhibitor, L-NAME, blocks phencyclidine-induced disruption of prepulse inhibition in mice. *Psychopharmacology (Berl).* **156,** 182–186 (2001).
22. Ridnour, L. A., Sim, J. E., Hayward, M.A, Wink, D. A., Martin, S. M., Buettner, G. R., Spitz, D. R. A spectrophotometric method for the direct detection and quantitation of nitric oxide, nitrite, and nitrate in cell culture media. *Anal. Biochem.* **281,** 223–229 (2000).
23. Lancaster, J. R. A tutorial on the diffusibility and reactivity of free nitric oxide. *Nitric Oxide - Biol. Chem.* **1,** 18–30 (1997).
24. Hall, C. N. & Garthwaite, J. What is the real physiological NO concentration in vivo? *Nitric Oxide - Biol. Chem.* **21,** 92–103 (2009).
25. Brown, F. O., Finnerty, N. J. & Lowry, J. P. Nitric oxide monitoring in brain extracellular fluid: characterisation of Nafion®-modified Pt electrodes in vitro

and in vivo. *Analyst* **134,** 2012–20 (2009).

26. Wynne, A. M., Reid, C. H. & Finnerty, N. J. In vitro characterisation of ortho phenylenediamine and Nafion®-modified Pt electrodes for measuring brain nitric oxide. *J. Electroanal. Chem.* **732,** 110–116 (2014).
27. Rink, C. & Khanna, S. Significance of Brain Tissue Oxygenation and the Arachidonic Acid Cascade in Stroke. **14,** (2011).
28. Ances, B. M., Buerk, D. G., Greenberg, J. H. & Detre, J. A. Temporal dynamics of the partial pressure of brain tissue oxygen during functional forepaw stimulation in rats. *Neurosci. Lett.* **306,** 106–110 (2001).
29. Zimmerman, J. B. & Mark Wightman, R. Simultaneous Electrochemical Measurements of Oxygen and Dopamine in Vivo. *Anal. Chem.* **63,** 24–28 (1991).
30. Bolger, F. B., McHugh, S. B., Bennett, R., Li, J., Ishiwari, K., Francois, J., Conway, M. W., Gilmour, G., Bannerman, D. M., Fillenz, M. & Tricklebank, M. Characterisation of carbon paste electrodes for real-time amperometric monitoring of brain tissue oxygen. *J. Neurosci. Methods* **195,** 135–42 (2011).
31. Baumg, H., Heinrich, U. & Liibbers, D. W. of Physiology Oxygen supply of the blood-free perfused guinea-pig brain in normo- and hypothermia measured by the local distribution of oxygen pressure. 228–234 (1989).
32. Finnerty, N. J. & Bolger, F. B. In vitro development and in vivo application of a platinum-based electrochemical device for continuous measurements of peripheral tissue oxygen. *Bioelectrochemistry* **119,** 124–135 (2018).
33. Bolger, F., Bennett, R. & Lowry, J. An in vitro characterisation comparing carbon paste and Pt microelectrodes for real-time detection of brain tissue oxygen. *Analyst* **136,** 4028–35 (2011).
34. Wilson, G. S. & Gifford, R. Biosensors for real-time in vivo measurements. *Biosens. Bioelectron.* **20,** 2388–2403 (2005).
35. Bolger, F. B. & Lowry, J. P. Brain tissue oxygen: In vivo monitoring with carbon paste electrodes. *Sensors* **5,** 473–487 (2005).
36. Rice, M. E. H_2O_2: a dynamic neuromodulator. *Neuroscientist* **17,** 389–406 (2011).
37. Avshalumov, M. V. Endogenous Hydrogen Peroxide Regulates the Excitability of Midbrain Dopamine Neurons via ATP-Sensitive Potassium Channels. *J.*

Neurosci. **25,** 4222–4231 (2005).

38. Olanow, C. W. & Tatton, W. G. Etiology and Pathogenesis of Parkinson's Disease. **22,** 123–144 (1999).
39. Dias, V., Junn, E. & Mouradian, M. M. The role of oxidative stress in parkinson's disease. *J. Parkinsons. Dis.* **3,** 461–491 (2013).
40. Kulagina, N. V. & Michael, A. C. Monitoring hydrogen peroxide in the extracellular space of the brain with amperometric microsensors. *Anal. Chem.* **75,** 4875–4881 (2003).
41. Li, R., Liu, X., Qiu, W. & Zhang, M. In Vivo Monitoring of H_2O_2 with Polydopamine and Prussian Blue-coated Microelectrode. *Anal. Chem.* **88,** 7769–7776 (2016).
42. O'Brien, K. B., Killoran, S. J., O'Neill, R. D. & Lowry, J. P. Development and characterization in vitro of a catalase-based biosensor for hydrogen peroxide monitoring. *Biosens. Bioelectron.* **22,** 2994–3000 (2007).
43. O'Riordan, S. L., McLaughlin, K., Lowry, J. P. In vitro physiological performance factors of a catalase-based biosensor for real-time electrochemical detection of brain hydrogen peroxide in freely-moving animals. *Anal. Methods* **8,** 7614–7622 (2016).
44. O'Riordan, S.L., Lowry, J. P. In vivo characterisation of a catalase-based biosensor for real-time electrochemical monitoring of brain hydrogen peroxide in freely-moving animals. *Anal. Methods* **9,** 1253–1264 (2017).
45. Driver, J. Incidence and remaining lifetime risk of PD in advanced age. **48,** 1–6 (2010).
46. Lonneke M L de Lau, M. M. B. B. Epidemiology of Parkinson's disease. *J. Neural Transm.* **5,** 525–535 (2006).
47. Braak, H., Del Tredici, K., Rüb, U., De Vos, R. A., Steur, E. N. J. & Braak, E. Staging of brain pathology related to sporadic Parkinson's disease. *Neurobiol. Aging* **24,** 197–211 (2003).
48. Postuma, R. B., Aarsland, D., Barone, P., Burn, D. J., Hawkes, C. H., Oertel, W. & Ziemssen, T. Identifying prodromal Parkinson's disease: Pre-Motor disorders in Parkinson's disease. *Mov. Disord.* **27,** 617–626 (2012).
49. Chaudhuri, K. R. & Schapira, A. H. V. Non-motor symptoms of Parkinson's disease: dopaminergic pathophysiology and treatment. *Lancet Neurol.* **8,** 464–

74 (2009).

50. Burke, R. E. & Malley, K. O. Axon degeneration in Parkinson's disease. *Exp. Neurol.* **246,** 72–83 (2013).
51. Obeso, J. A., Rodriguez-Oroz, M. C., Goetz, C. G., Marin, C., Kordower, J. H., Rodriguez, M., Hirsch, E. C., Farrer, M., Schapira, A. H. & Halliday, G. Missing pieces in the Parkinson's disease puzzle. *Nat. Med.* **16,** 653–661 (2010).
52. Lill, C. M. Genetics of Parkinson's disease. *Mol. Cell. Probes* **30,** 386–396 (2016).
53. Farrer, M. J. Genetics of Parkinson disease: Paradigm shifts and future prospects. *Nat. Rev. Genet.* **7,** 306–318 (2006).
54. Keeney, P. M. Parkinson's Disease Brain Mitochondrial Complex I Has Oxidatively Damaged Subunits and Is Functionally Impaired and Misassembled. *J. Neurosci.* **26,** 5256–5264 (2006).
55. Schapira, A. H. Mitochondria in the aetiology and pathogenesis of Parkinson's disease. *Lancet Neurol.* **7,** 97–109 (2008).
56. Hauser, D. N. & Hastings, T. G. Mitochondrial dysfunction and oxidative stress in Parkinson's disease and monogenic parkinsonism. *Neurobiol. Dis.* **51,** 35–42 (2013).
57. Perier, C. & Vila, M. Mitochondrial Biology and Parkinson's Disease. 1–19 (2012).
58. Keane, P. C., Kurzawa, M., Blain, P. G. & Morris, C. M. Mitochondrial Dysfunction in Parkinson's Disease. *Parkinsons. Dis.* **2011,** 1–18 (2011).
59. Liu, Y., Fiskum, G. & Schubert, D. Generation of reactive oxygen species by the mitochondrial electron transport chain. *J Neurochem* **80,** 780–787 (2002).
60. Hwang, O. Role of Oxidative Stress in Parkinson's Disease. *Exp. Neurobiol.* **22,** 11 (2013).
61. Schapira, A. H. V. Mitochondrial dysfunction in Parkinson's disease. *Cell Death Differ.* **14,** 1261–1266 (2007).
62. Parker, W.D. Jr, Parks, J.K., Swerdlow, R. H. Complex I Deficiency in Parkinson's Disease Frontal Cortex. *Brain Res.* **1189,** 215–218 (2008).
63. Bindoff, L. A., Birch-Machin, M. A., Cartlidge, N. E. F., Parker Jr, W. D. & Turnbull, D. M. Respiratory chain abnormalities in skeletal muscle from

patients with Parkinson ' s disease. *J. Neurol. Sci.* **104,** 203–208 (1991).

64. Acín-Pérez, R., Bayona-Bafaluy, M.P., Fernández-Silva, P., Moreno-Loshuertos, R., Pérez-Martos, A., Bruno, C., Moraes, C.T. and Enríquez, J. A. Respiratory Complex III Is Required to Maintain Complex I in Mammalian Mitochondria. *Mol. Cell* **13,** 805–815 (2004).
65. Zhang, L., Dawson, V. L. & Dawson, T. M. Role of nitric oxide in Parkinson's disease. *Pharmacol. Ther.* **109,** 33–41 (2006).
66. Szabo, C., Zingarelli, B., O'Connor, M. & Salzman, A. L. DNA strand breakage, activation of poly (ADP-ribose) synthetase, and cellular energy depletion are involved in the cytotoxicity of macrophages and smooth muscle cells exposed to peroxynitrite. *Proc Natl Acad Sci U S A* **93,** 1753–1758 (1996).
67. Dawson, V. L., Kizushi, V. M., Huang, P. L., Snyder, S. H. & Dawson, T. M. Resistance to neurotoxicity in cortical cultures from neuronal nitric oxide synthase-deficient mice. *J Neurosci* **16,** 2479–2487 (1996).
68. Good, P.F., Hsu, A., Werner, P., Perl, D., P., Olanow, C. W. Protein Nitration in Parkinson's Disease. *J. Neuropathol. Experiemntal Neurol.* **57,** 338–342 (1998).
69. Chung, K. K. K., Thomas, B., Li, X., Pletnikova, O., Troncoso, J. C., Marsh, L., Dawson, V. L. & Dawson, T. M. S -Nitrosylation of Parkin Regulates Ubiquitination and Compromises Parkin's Protective Function. *Science.* **11624,** 1328–1332 (2003).
70. Kavya, R., Saluja, R., Singh, S. & Dikshit, M. Nitric oxide synthase regulation and diversity: Implications in Parkinson's disease. *Nitric Oxide - Biol. Chem.* **15,** 280–294 (2006).
71. Sofic, E., Lange, K. W., Jellinger, K. & Riederer, P. Reduced and oxidized glutathione in the substantia nigra of patients with Parkinson's disease. *Neurosci. Lett.* **142,** 128–130 (1992).
72. Jenner Peter. Oxidative stress in Parkinson's disease. *An. Neurol.* **53,** S26-38 (2003).
73. Wang, J. Y., Zhuang, Q. Q., Zhu, L. B., Zhu, H., Li, T., Li, R., Chen, S. F., Huang, C. P., Zhang, X. & Zhu, J. H. Meta-analysis of brain iron levels of Parkinson's disease patients determined by postmortem and MRI measurements. *Sci. Rep.* **6,** 1–13 (2016).

74. Valente, E. M., Abou-Sleiman, P. M., Caputo, V., Muqit, M. M., Harvey, K., Gispert, S., Ali, Z., Del Turco, D., Bentivoglio, A. R., Healy, D. G., & Albanese, A. Hereditary Early-Onset Parkinson's Disease Caused by Mutations in PINK1. *Science.* **304,** 1158–1161 (2004).

75. Heeman, B., Van den Haute, C., Aelvoet, S. A., Valsecchi, F., Rodenburg, R. J., Reumers, V., Debyser, Z., Callawaert, G., Koopman, W. J., Willems, P. H. & Baekelandt, V. Depletion of PINK1 affects mitochondrial metabolism, calcium homeostasis and energy maintenance. *J. Cell Sci.* **124,** 1115–1125 (2011).

76. Zhou, C., Huang, Y., Shao, Y., May, J., Prou, P., Perier, C., Dauer, W., Schon, E. A & Przedborski, S. The kinase domain of mitochondrial PINK1 faces the cytoplasm. *Proc. Natl. Acad. Sci. U. S. A.* **105,** 12022–7 (2008).

77. Weihofen, A., Thomas, K. J., Ostaszewski, B. L., Cookson, M. R. & Selkoe, D. J. Pink1 forms a multi-protein complex with Miro and Milton, linking Pink1 function to mitochondrial trafficking. **48,** 2045–2052 (2010).

78. Yu, W., Sun, Y., Guo, S. & Lu, B. The PINK1/Parkin pathway regulates mitochondrial dynamics and function in mammalian hippocampal and dopaminergic neurons. *Hum. Mol. Genet.* **20,** 3227–3240 (2011).

79. Clark, I. E., Dodson, M. W., Jiang, C., Cao, J. H., Huh, J. R., Seol, J. H., Yoo, S. J., Hay, B. A. & Guo, M. Drosophila pink1 is required for mitochondrial function and interacts genetically with parkin. *Nature* **441,** 1162–1166 (2006).

80. Seirafi, M., Kozlov, G. & Gehring, K. Parkin structure and function. *FEBS J.* **282,** 2076–2088 (2015).

81. Kalinderi, K., Bostantjopoulou, S. & Fidani, L. The genetic background of Parkinson's disease: current progress and future prospects. *Acta Neurol. Scand.* **134,** 314–326 (2016).

82. Liu, W., Acín-Peréz, R., Geghman, K.D., Manfredi, G., Lu, B. & Li, C. Pink1 regulates the oxidative phosphorylation machinery via mitochondrial fission. *Proceedings of the National Academy of Sciences* **108,** 12920–12924 (2011).

83. Schulte, C. & Gasser, T. Genetic basis of Parkinson's disease: Inheritance, penetrance, and expression. *Appl. Clin. Genet.* **4,** 67–80 (2011).

84. Ito, R., Takahashi, T., Katano, I. & Ito, M. Current advances in humanized mouse models. *Cell. Mol. Immunol.* **9,** 208–214 (2012).

85. Shultz, L. D., Ishikawa, F. & Greiner, D. L. Humanized mice in translational biomedical research. *Nat. Rev. Immunol.* **7,** 118–130 (2007).

86. Brehm, M., Shultz, L. & Greiner, D. Humanized Mouse Models to Study Human Diseases. *Curr. Opin. …* **17,** 120–125 (2010).

87. Bosma, G. C. A severe combined immunodeficiency mutation in the mouse. *Nature* **301,** 527–530 (1983).

88. Ito, M., Hiramatsu, H., Kobayashi, K., Suzue, K., Kawahata, M., Hioki, K., Ueyama, Y., Koyanagi, Y., Sugamura, K., Tsuji, K. & Heike, T. NOD/SCID/γcnull mouse: an excellent recipient mouse model for engraftment of human cells. *Bone* **100,** 3175–3182 (2002).

89. Davis, P. H. & Stanley, S. L. Breaking the species barrier: Use of SCID mouse-human chimeras for the study of human infectious diseases. *Cell. Microbiol.* **5,** 849–860 (2003).

90. Kneteman, N. M., Anti-H Weiner, A.J., O'connell, J., Collett, M., Gao, T., Aukerman, L., Kovelsky, R., Ni, Z.J., Hashash, A., Kline, J. & Hsi, B. CV therapies in chimeric scid-Alb/uPA mice parallel outcomes in human clinical application. *Hepatology* **43,** 1346–1353 (2006).

91. Nakamura, Y., Ito, M., Yamamoto, T., Yan, X.Y., Yagasaki, H., Kamachi, Y., Kudo, K. & Kojima, S. Engraftment of NOD/SCID/gammac(null) mice with multilineage neoplastic cells from patients with juvenile myelomonocytic leukaemia. *Br. J. Haematol.* **130,** 51–7 (2005).

92. Chesselet, M. F., Fleming, S., Mortazavi, F. & Meurers, B. Strengths and limitations of genetic mouse models of Parkinson's disease. *Park. Relat. Disord.* **14,** 84–87 (2008).

93. Jucker, M. The benefits and limitations of animal models for translational research in neurodegenerative diseases. *Nat. Med.* **16,** 1210–1214 (2010).

94. Yamanaka, S. A Fresh Look at iPS Cells. *Cell* **137,** 13–17 (2009).

95. Takahashi, K. & Yamanaka, S. Induction of Pluripotent Stem Cells from Mouse Embryonic and Adult Fibroblast Cultures by Defined Factors. *Cell* **126,** 663–676 (2006).

96. Takahashi, K., Tanabe, K., Ohnuki, M., Narita, M., Ichisaka, T., Tomoda, K. & Yamanaka, S. Induction of Pluripotent Stem Cells from Adult Human Fibroblasts by Defined Factors. *Cell* **131,** 861–872 (2007).

97. Zhang, P., Xia, N. & Reijo Pera, R. A. Directed Dopaminergic Neuron Differentiation from Human Pluripotent Stem Cells. *J. Vis. Exp.* 1–8 (2014).

98. Hemmer, K., Zhang, M., van Wüllen, T., Sakalem, M., Tapia, N., Baumuratov, A., Kaltschmidt, C., Kaltschmidt, B., Schöler, H.R., Zhang, W. & Schwamborn, J. C. Induced neural stem cells achieve long-term survival and functional integration in the adult mouse brain. *Stem Cell Reports* **3,** 423–431 (2014).

99. Reinhardt, P., Glatza, M., Hemmer, K., Tsytsyura, Y., Thiel, C.S., Höing, S., Moritz, S., Parga, J.A., Wagner, L., Bruder, J.M. & Wu, G. Derivation and Expansion Using Only Small Molecules of Human Neural Progenitors for Neurodegenerative Disease Modeling. *PLoS One* **8,** (2013).

100. Hargus, G., Ehrlich, M., Araúzo-Bravo, M.J., Hemmer, K., Hallmann, A.L., Reinhardt, P., Kim, K.P., Adachi, K., Santourlidis, S., Ghanjati, F. & Fauser, M. Origin-dependent neural cell identities in differentiated human iPSCs in vitro and after transplantation into the mouse brain. *Cell Rep.* **8,** 1697–1703 (2014).

Chapter 2

Theory

2.1 Introduction

The overall objective of this thesis is to gain a better understanding of the phenotypic progression of patient specific PD by coupling the use of microelectrodes to facilitate the neurochemical monitoring of NO, O_2 and H_2O_2 with microdialysis sampling of possible metabolic markers of PD. Chapter 2 is primarily concerned with further explaining the electrochemical principles and methodologies associated with each of these techniques which were utilised in both *in vitro* and *in vivo* investigations.

To facilitate the electrochemical detection of NO, O_2 and H_2O_2 *in vitro* and *in vivo*, CPA was utilised. CPA is the optimum technique for detection of the aforementioned species due to the high temporal resolution it possesses[1]. This is extremely important in the detection of NO especially due to its reactivity and short half-life it possesses *in vivo*[2]. CPA is discussed in detail in Section 2.4. The electrochemical detection of NO, O_2 and H_2O_2 by CPA *in vitro* and *in vivo* was enabled using a three-electrode set up. This electrochemical set-up consisted of a reference electrode, working electrodes and an auxiliary electrode (see Section 3.6.1). Firstly, the reference electrode was used to deliver a fixed potential to the electrochemical cell from which the potential of the working electrodes could be determined. For *in vitro* experimentation, a Saturated Calomel Electrode (SCE) was used. SCEs are based on the reaction between elemental mercury and mercury (I) chloride, thus, making SCEs very robust and stable in electrochemical experiments. For *in vivo* investigations, a pseudo-reference was used. The manufacture of the pseudo reference is detailed in Section 3.8.6. Pseudo reference electrodes were included in *in vivo* studies due to the smaller geometry they possess, making them more suitable for *in vivo* use while presenting no risk of contamination to the surrounding environment from solvent molecules or ions that would normally be contained in a SCE. The auxiliary electrode worked to complete the electrochemical circuit by acting as a source or sink of electrons. In addition, the working electrode surface is where all redox processes take place allowing for a continuous Faradaic current to be monitored.

Electrochemical processes are detailed in Section 2.2. Oxidative and reductive processes are facilitated by two principal mass transport methods which work to deliver electrochemical analytes to the electrode surface. These processes are further discussed in Section 2.3. Section 2.4 describes CPA and its role in the detection of NO, O_2 and H_2O_2. Nafion® and *o*-PD modifications were made to the NO sensor and

H_2O_2 biosensor to improve the overall sensitivity and selectivity of these electrochemical sensors are included in Sections 2.5 and 2.6.

Section 2.7 details the incorporation of microdialysis in this thesis as a sampling technique allowing for the detection of various biological species contained in the brain ECF[3]. Microdialysis sampling of humanised NOD SCID mice allows for variations that may exist in sampled metabolites to be examined (Chapter 7). Additionally, the microdialysis probe was implanted, in close alignment, with the H_2O_2 biosensor in non-humanised NOD SCID mice to investigate the effect of the local administration of inducers and inhibitors of H_2O_2 production *in vivo* (Chapter 5).

2.2 Electrochemical Reactions

Electrochemical monitoring of a particular analyte is dependent on the electrochemical reaction which occurs at the surface of the working electrode. Following the application of a suitable potential, a redox reaction of the target analyte occurs at the active surface of the electrode leading to the production of a Faradaic current which is proportional to the concentration of the analyte. Redox reactions involve the transfer of electrons from one species to another which results in the oxidation or reduction of electroactive species in the surrounding environment. Equation 2.2.1 describes the reaction equation, where *n* is the number of electrons and O and R represent the oxidised and reduced species.

$$\mathrm{O} + n\mathrm{e}^- \leftrightarrow \mathrm{R} \qquad \textbf{(2.2.1)}$$

The term, Fermi Level, refers to the highest energy state occupied by electrons in a material at absolute zero temperature. When the electrode and solution is at equilibrium (Figure 2.2.1), the highest occupied molecular orbital (HOMO) of the solution is observed to correspond to the Fermi level of the metal electrode. Therefore, no electron transfer can occur resulting in no current being produced.

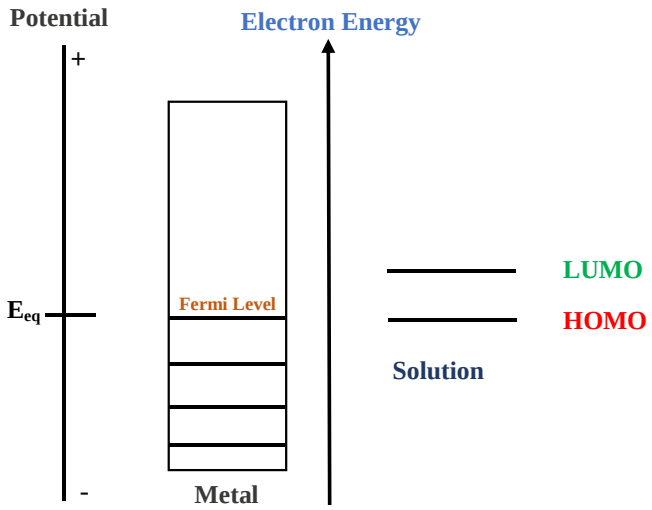

Figure 2.2.1: Schematic of the electrode and solution at equilibrium.

However, by application of a suitable potential (E_{app}), the energy of the Fermi level can be altered. As shown in Figure 2.2.2, application of a potential which is higher, or more positive, than equilibrium potential (E_{eq}) leads to a reduction in electron energy in the metal electrode. Hence, leading to a reduction in the Fermi level of the metal. Therefore, an oxidation reaction is produced as higher energy electrons from the solution HOMO level transfer into the lower energy Fermi level of the metal electrode. This transfer of electrons between the solution and the metal electrode allows for a Faradaic current to flow[4]. Both the NO sensor and the H_2O_2 biosensor function as a result of an oxidation reaction involving the transfer of electrons from the solution HOMO level into the Fermi level of the electrode.

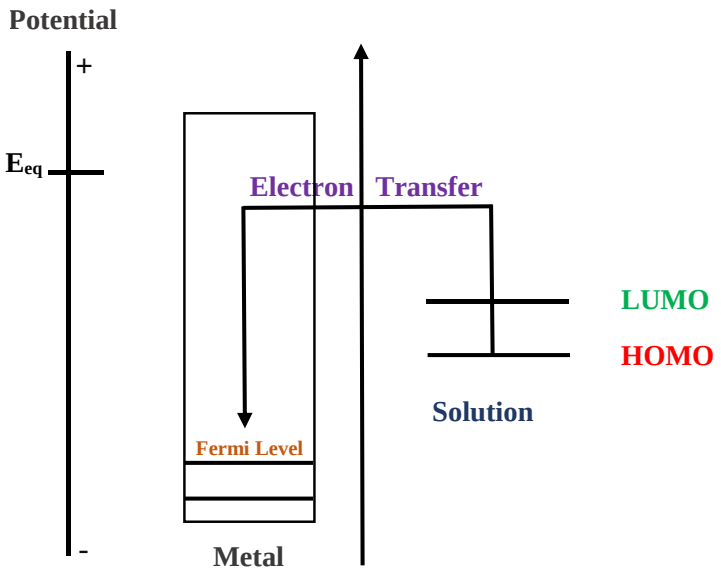

Figure 2.2.2: Schematic of an oxidation reaction between the electrode and surrounding solution.

In contrast, if a negative potential is applied, an increase in the Fermi level of the metal results. Due to the increased Fermi level, electrons transfer from an area of high energy to the lowest unoccupied molecular orbital (LUMO) of the solution to produce a reduction reaction. In this thesis, the O_2 sensor described undergoes a reduction reaction whereby high energy electrons transfer into the LUMO.

Transfer of electrons between the solution and the electrode are dependent on a number of factors. Such factors include mass transport which enable reactants to move to the electrode surface (see Section 2.3), the properties and applied potential of the electrode, the rate at which the product moves away from the electrode surface to allow reactant species to reach the electrode and the reactivity of the species in the surrounding solution. These factors vary between *in vitro* and *in vivo* environments. For example, *in vivo* environments contain biological tissues which continually generate analytes whilst simultaneously metabolising or uptaking species for cellular function. Therefore, affecting the concentration of a target species that reaches the electrode surface or the amount of the reactive species that is removed from the electrode surface by the surrounding tissue. Additionally, mass transport processes are much more complex *in vivo* due to the heterogeneity of the tissues. Analytes have to navigate a tortuous path to access the electrode surface. This tortuosity is further amplified by the presence of pathological conditions.

A capacitance current is produced if the potential is applied when the target analyte is not present. This is due to an accumulation of opposing charges at the electrode surface and the surrounding solution, known as the electrical double layer. The double layer is comprised of several charged layers. The inner layer closest to the electrode surface, which is commonly referred to as the Stern layer, is comprised of solvent molecules that are specifically adsorbed. The inner Helmholtz plane (IHP) refers to the spherical centres of these adsorbed ions. The outer Helmholtz plane (OHP) represents the layer of solvated ions which can only approach the metal at distance x_2. These solvated ions are held to the charged metal by long-range electrostatic forces. Moreover, these non-specifically adsorbed species are distributed in a three-dimensional direction under the influence of thermal motion and chemical attraction. This second layer is referred to as the diffuse layer. The diffuse layer begins at OHP and extends into the bulk solution[4] (Figure 2.2.3).

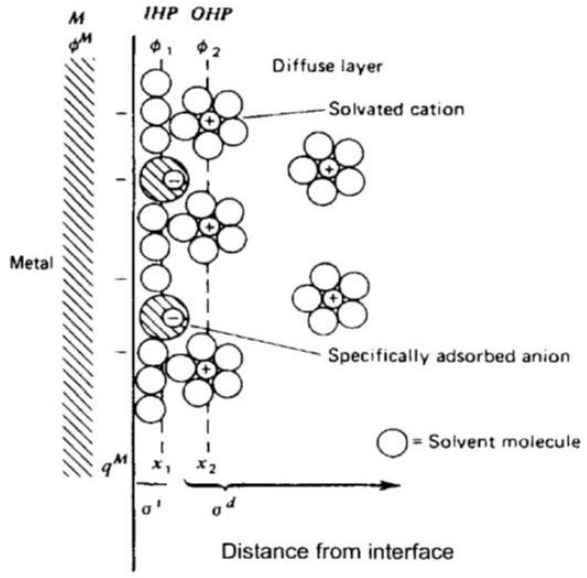

Figure 2.2.3: Schematic of the double layer structure. Sourced from Bard & Faulkner, 2001[4].

As capacitance current is not representative of target analyte species present, it has been subtracted from all *in vitro* data presented in this thesis. However, under physiological conditions, the baseline amperometric current is comprised of both a capacitance and Faradaic contribution due to the presence of tonic levels of the target analyte in the ECF.

2.3 Mass Transport

The rate at which an electrochemical reaction occurs at the electrode surface is dependent on mass transport. Mass transport refers to the rate at which electrons are transferred from the bulk solution to the electrode surface and the rate at which they can cross the electrode interface thereafter. The Faradaic current (I) obtained experimentally is a direct measurement of the redox reaction rate that exists at the electrode which is represented by Faraday's law (Equation 2.3.1):

$$I = nFAJ \qquad \textbf{(2.3.1)}$$

Where (I) is indicative of the measured current, *n* is the number of moles present, F is the Faraday constant (96,485 C mol^{-1}), A is the area of the electrode (m^2) and J is the flux of ions (mol m^{-2} s^{-1}).

Although the above equation relates to the process of mass transport both *in vitro* and *in vivo*, the brain is a complex environment whereby certain reactions and structures may influence mass transport processes which are not encountered during *in vitro* investigations. For this reason, it is imperative to consider chemical processes involved in the generation and removal of analytes in the brain microenvironment which will have an overall effect on mass transport processes. *In vitro* mass transport processes occur within an electrochemical cell of fixed geometry. However, *in vivo* analytes must demonstrate the ability to diffuse from the source of its production into the ECF to allow for its detection. During its diffusion, the analyte is susceptible to removal by various metabolic or uptake processes termed as sinks. Therefore, limiting the available analyte concentration for detection at an implanted microelectrode or microdialysis probe. For this reason, carefully consideration of *in vivo* mass transport must be made to ensure optimal detection of the target analyte under investigation.

All *in vitro* and *in vivo* investigations conducted throughout this thesis were governed by two mass transport processes; convection and diffusion.

2.3.1 Convection

Two forms of convection exist; natural convection and forced convection. Natural convection is present in any solution whereby the transport of species occurs due to small thermal or density differences that exist, resulting in the mixing of a

solution in a random and unpredictable fashion. However, by introduction of forced convection to the electrochemical experiment, natural convection is neglected. Forced convection increases the rate of the transport of species considerably. Therefore, due to effects of forced convection being multiple magnitudes greater than natural convection, the random parameter associated with natural convection is effectively removed. Forced convection was included in *in vitro* experiments via a magnetic stirrer following the introduction of aliquots of analytes into the electrochemical cell. However, the contribution of forced convection can be disregarded due to analysis of experimental data obtained from steady state currents in quiescent solutions.

Similarly, the transport of species to the electrode surface is under the influence of convective processes *in vivo*. For example, the delivery of O_2 to the electrode surface is achieved by blood flow which is under forced convection as the heart works to pump blood around the body.

2.3.2 Diffusion

Diffusion occurs in solutions whereby the movement of species is influenced by a concentration gradient resulting in species moving from an area of high concentration to an area of lower concentration. The movement in moles (or mass) of a species through a defined area per unit time is termed as flux[5]. In one dimension, the rate of diffusion is described by Fick's first law (Equation 2.3.2.1) which states that flux of species is directly proportional to the concentration gradient and the solute diffusion coefficient per unit distance:

$$\mathrm{J} = -\mathrm{D}\,\frac{\partial \mathrm{C}}{\partial \mathrm{x}} \qquad \textbf{(2.3.2.1)}$$

Where J is the flux of species, D is the diffusion coefficient with the negative sign representing the movement of species down the concentration gradient from an area of high concentration to an area of low concentration, $\partial C/\partial x$ denoted the concentration gradient in the x direction.

However, in environments which are more than one-dimension, a Laplace operator, ∇, is substituted into Equation 2.3.2.1 resulting in Equation 2.3.2.2. In *in vivo* environments, such as the brain, analytes diffuse through heterogenous tissues

where they encounter various removal processes, in three-dimensions, through a range of chemical reactions such as receptor binding and metabolic reactions.

$$J = -D\nabla^2 c \qquad \textbf{(2.3.2.2)}$$

Fick's second law (Equation 2.3.2.3) is used to describe changes in flux per unit time resulting in the concentration changes of electroactive species adjacent to the electrode surface as a function of time. These changes result from movement of electroactive species which is illustrated in Figure 2.3.2.1. The second law is derived from Fick's first law.

$$\frac{\partial C}{\partial t} = -\frac{\partial J}{\partial x} = D\frac{\partial^2 C}{\partial x^2} \qquad \textbf{(2.3.2.3)}$$

Concentration gradients may be produced during the progression of the reaction as a result of the electroactive species being consumed. Concentration gradients are assumed to be constant i.e. ($\partial C/\partial t$) = 0, no change in C with t, using microelectrodes. This is because of the small dimension of microelectrodes[6] resulting in the minimal removal of analyte from solution to produce a small steady-state current response.

For planar electrodes, the bulk solution is able to access the surface of the electrode uniformly. In this case, deviations of current with time can represented by the Cottrell equation (Equation 2.3.2.4) which is derived from Fick's second law:

$$I = nFAJ = \frac{nFAD^{1/2}C_\infty}{(\pi t)^{1/2}} \qquad \textbf{(2.3.2.4)}$$

Where I denotes the current measured at time, t, at the electrode surface of area, A, which is directly proportional to C_∞ being the bulk concentration of the electroactive species. J is the flux, *n* is the number of electrons, D is the diffusion coefficient and F is the Faraday constant.

However, the diffusional path of an analyte in *in vivo* environments is tortuous. Analytes encounter numerous chemical reactions through the brain including uptake

and subsequent degradation leading to an overall change in the flux of target analytes over time (Figure 2.3.2.1).

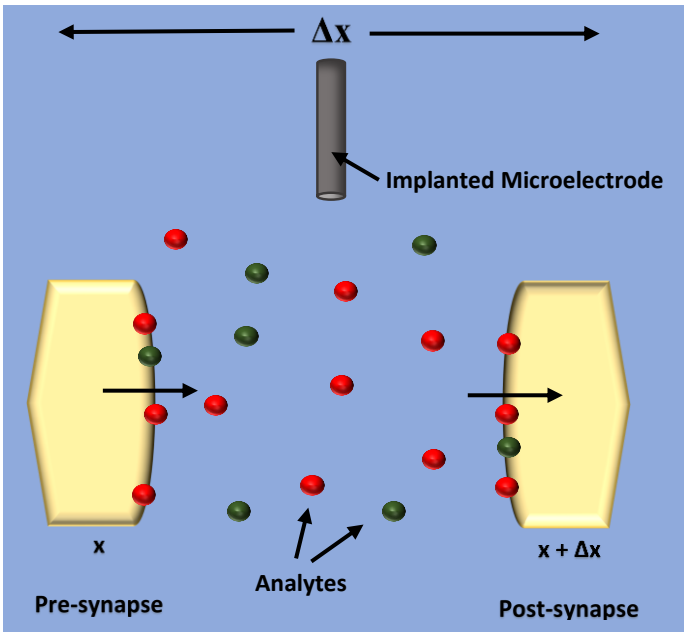

Figure 2.3.2.1: Three dimensional diffusion of analytes in the ECF from sources (pre-synaptic neuron) opposing a concentration gradient with an element of width (Δx) to reach analyte sinks (post-synaptic synapse).

The influence of chemical reactions on the flux of chemical species is taken into account by inclusion of specific reaction terms, R, into Equation 2.3.2.3 which represents the overall flux process *in vivo*. Inclusion of the term, R, produces Equation 2.3.2.5 which states that changes in analyte concentration ($\partial C/\partial t$) is a function of diffusional processes through biological tissue coupled with reactions, R, that might be encountered. Such reactions include generation of these analytes alongside uptake and degradative process.

$$\frac{\partial c}{\partial t} = D\frac{\partial^2 C}{\partial x^2} - R \qquad \textbf{(2.3.2.5)}$$

Implantation of microelectrodes in biological tissue acts to remove target analytes from the surrounding environment due to redox reactions which occur at the surface of these electrodes. Due to this process, Equation 2.3.2.5 can be rewritten as Equation 2.3.2.6. Equation 2.3.2.6 takes into account the generation of a target analyte,

diffusional processes, removal of the target analyte by reaction at the microelectrode, removal of the analyte by uptake and degradation in the biological environment resulting in obtainment of an overall observation in flux concentrations of a species. A steady-state is observed to be attained when the generation and removal of an analyte are equal. Therefore, concentration of the measured analyte by the implanted microelectrode would be constant over time.

$$\frac{\partial C}{\partial t} = D\frac{\partial^2 C}{\partial x^2} + G_{(Tissue)} - R_{(Tissue)} - R_{(Microelectrode)} \qquad \textbf{(2.3.2.6)}$$

Equation 2.3.2.6 describes flux processes in Cartesian coordinates. However, once microelectrodes and microdialysis probes are implanted in the brain, Cartesian coordinates are not applicable. Spherical diffusion is associated with microelectrode, while cylindrical coordinates are used to represent microdialysis sampling.

2.4 Constant Potential Amperometry

CPA was used throughout this project to record data during electrochemical experiments. CPA involves the application of a constant potential that is known to result in the oxidation or reduction of the analyte under investigation. Following electron transfer at the electrode surface, the generation of a Faradaic current results with respect to time. The production of the Faradaic current is influenced by the diffusion (Section 2.3.2) of electroactive species to the electrode surface which results in the attainment of a steady-state diffusion limited current (i_{ss}):

$$i_{SS} = \frac{nFACD}{r} \qquad \textbf{(2.4.1)}$$

Where *n* is the number of electrons, F is the Faraday constant, A is the surface area of the electrode, C is the concentration, D is the diffusion coefficient and r is the radius. However, the steady-state current is also influenced by additional factors including the geometry, insulation thickness of the electrodes and the geometric factor, G, which is included in Equation 2.4.2:

$$i_{SS} = \frac{GnFACD}{r} \quad \textbf{(2.4.2)}$$

Following the detection of an electroactive species at the electrode surface, the resulting Faradaic current is directly proportional to the diffusion coefficient and the substrate concentration as indicated in Equation 2.4.2. Due to the gaseous nature of analytes under investigation throughout this project, it was important to incorporate a voltammetric technique with good temporal resolution which is the reason why CPA was included in all *in vitro* and *in vivo* experimentation[1].

2.4.1 Nitric Oxide Detection

The detection of NO throughout this thesis was facilitated using the Nafion®-coated Pt electrode developed previously[2,7]. A potential profile was obtained using cyclic voltammetry by Brown *et al.*[2] which identified + 900 mV *vs.* SCE to be the most suitable potential to be applied for the oxidation of NO. Furthermore, the NO sensor incorporates a Nafion® membrane which is thermally annealed to the electrode surface. Nafion®, annealed to the surface of the Pt electrode, works to reject the contribution of interfering anionic and cationic species on the electrode surface due to the presence of negatively charged groups throughout the polymer structure while neutral species are permitted through the membrane[8]. Additionally, Nafion® works to enhance the detection of NO. Increased detection of NO is facilitated due to the presence of negatively charged sulfonate groups functioning to stabilise the presence of the nitrosonium ion (NO^+). NO^+ production results from the initial oxidation of NO at metal electrode surfaces as seen in Equation 2.4.1.1. However, by incorporation of Nafion® into the NO sensor design, the accumulation of NO^+ at the electrode surface is prevented. Therefore, eliminating further oxidation processes described in Equation 2.4.1.2 and 2.4.1.3 and allowing for the increased detection of NO[9].

$$NO \rightarrow NO^+ + e^- \quad \textbf{(2.4.1.1)}$$

$$NO^+ + OH^- \rightarrow HNO_2 \quad \textbf{(2.4.1.2)}$$

$$HNO_2 + H_2O \rightarrow NO_3^- + 2e^- + 3H^+ \quad \textbf{(2.4.1.3)}$$

2.4.2 Oxygen Detection

The electrochemical detection of O_2 at the surface of working electrodes manufactured from noble metals has been reported to occur in numerous ways. The first of which includes a four-electron transfer which occurs in a one-step reaction without intermediate formation[10] (Equations 2.4.2.1).

$$O_2 + 4H^+ + 4e^- \rightarrow 2H_2O \quad \textbf{(2.4.2.1)}$$

Additionally, a two-step reaction has also been proposed whereby hydrogen peroxide is formed as an intermediate[10] (Equations 2.4.2.2 & 2.4.2.3):

$$O_2 + 2H^+ + 2e^- \rightarrow H_2O_2 \quad \textbf{(2.4.2.2)}$$

$$H_2O_2 + 2H^+ + 2e^- \rightarrow 2H_2O \quad \textbf{(2.4.2.3)}$$

At a carbon surface, the reduction of O_2 is a two-electron reaction resulting in the production of H_2O_2, as described in Equation 2.4.2.2. However, at carbon surfaces, the direct reduction of H_2O_2 is observed to be impeded[11]. Therefore, the initial one-electron transfer is deemed to be rate-limiting prior to superoxide ion protonation followed by further reduction resulting in the electrochemical detection of O_2 by a four-electron pathway (Equation 2.4.2.4).

$$2H_2O_2 \rightarrow 2H_2O + O_2 \quad \textbf{(2.4.2.4)}$$

For the detection of O_2 by CPA, a potential of - 650 mV *vs.* SCE was applied. An applied potential of - 650 mV *vs.* SCE was deemed to be optimal for O_2 detection following a study carried out by Bolger *et al.*[10]. Cyclic voltammetry was utilised to identify a clear O_2 reaction peak at ca. - 600 mV. By obtaining the potential of maximum slope, $E_{s,max}$, the highest value of electron transfer kinetics could be identified along the wave. Following this, it was decided to use a potential of - 650 mV *vs.* SCE for all O_2 calibrations.

2.4.3 Hydrogen Peroxide Detection

The electrochemical measurement of H_2O_2 is widely conducted using first generation biosensors[12] constructed from Pt metal which allows for the oxidation of enzymatically produced H_2O_2. Equation 2.4.3.1 below represents the oxidation of H_2O_2 at the electrode surface that occurs following the application of a potential of + 700 mV *vs.* SCE. It is at this applied potential that H_2O_2 is oxidised on the electrode surface in a diffusion-controlled manner which gives rise to a linear current response which is dependent on the concentration of H_2O_2[13]. The oxidation of H_2O_2 is a two-electron reaction followed by the formation of an oxide on the surface of the electrode. Previous reports have highlighted that oxidation of H_2O_2 is favoured on oxidised Pt surfaces. Therefore, indicating oxidation is dependent on the initial formation of platinum oxide on the surface of the Pt electrode. A similar phenomenon has been reported to occur on Palladium electrodes[14].

$$H_2O_2 \rightarrow O_2 + 2H^+ + 2e^- \quad \textbf{(2.4.3.1)}$$

$$Pt(OH)_2 + H_2O_2 \rightarrow Pt + 2H_2O + O_2 \quad \textbf{(2.4.3.2)}$$

$$Pt + 2H_2O_2 \rightarrow Pt(OH)_2 + 2H^+ + 2e^- \quad \textbf{(2.4.3.3)}$$

During this thesis, the total sensitivity of the H_2O_2 biosensor design was found following subtraction of the current obtained on the catalase electrode from the current measured on the blank electrode as previously described by O'Brien *et al.*[13]. Once this sensor is implanted in the brain, the total currents measured at the blank (I_{blank}, Equation 2.4.3.4) and the catalase ($I_{catalase}$, Equation 2.4.3.5) electrodes will consist of the interference current (I_{INT} and I'_{INT} respectively) attributed from species present in the ECF and the endogenous H_2O_2 (I_{HP}) current:

$$I_{blank} = I_{INT} + I_{HP} \quad \textbf{(2.4.3.4)}$$

$$I_{catalase} = I'_{INT} + C_{HP}I_{HP} \quad \textbf{(2.4.3.5)}$$

$$\Delta I = I_{blank} - I_{catalase} \quad \textbf{(2.4.3.6)}$$

Where C_{HP} represents the proportion of measured undegraded H_2O_2 by the catalase electrode which is ideally zero. Hence, providing that a similar interference current is measured on both the blank and catalase electrode following *in vitro* calibrations, subtraction of the catalase current from the blank current will result in the current that is dependent on H_2O_2 only (Equation 2.4.3.6) in *in vivo* investigations.

2.5 Electropolymerisation of *o*-Phenylenediamine

Ascorbic acid, AA, is one of the most abundant antioxidants found *in vivo*, with particularly high levels found in the central nervous system[15,16]. AA is known to exist in biological fluids as a ubiquitous reducing agent[17] whilst exhibiting a very low redox potential[18]. In addition, AA has also been reported to be readily oxidised at metal electrodes between - 100 and + 400 mV vs. SCE[12]. Hence, making it the major electroactive interferent for electrochemical sensors in the brain. Figure 2.5.1 details the oxidation of AA leading to the formation of the intermediate, L-dehydroascorbic acid. This intermediate is further hydrated where it exists at equilibrium with the hydrated form. By means of hydrolysis, L-2,3-diketogulonic acid is formed which is electroinactive.

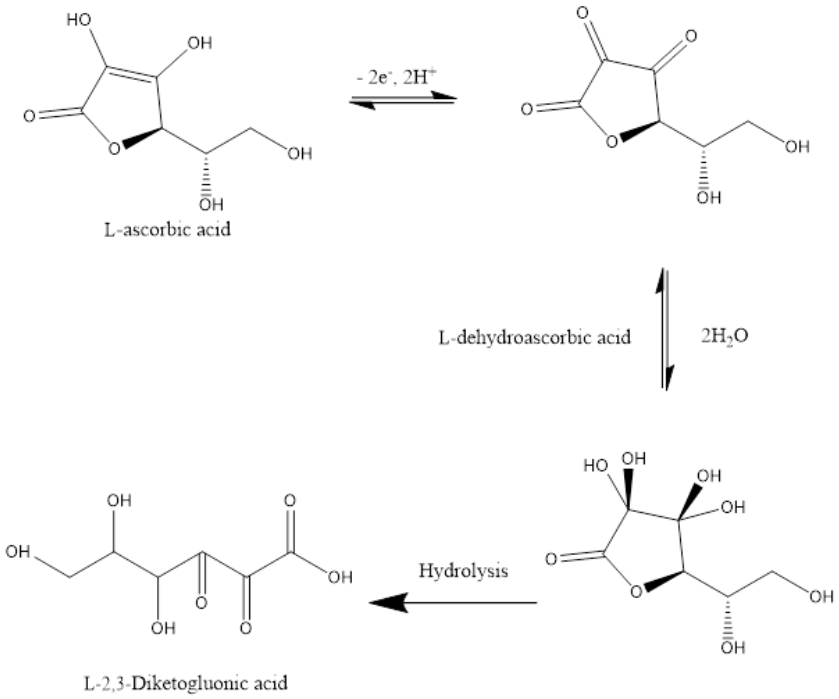

Figure 2.5.1: The oxidation of ascorbic acid.

Due to the high concentration of interfering species, such as AA in the brain ECF, it is of utmost importance that the sensor is selective to the measurement of the target analyte. To achieve this criteria, *o*-phenylenediamine (*o*-PD) is incorporated into the design of particular sensors, such as the H_2O_2 biosensor, to enable selective detection of the target analyte. For this reason, the previously characterised H_2O_2 biosensor[13,19,20] used throughout this project, incorporates a polyphenylenediamine polymer layer to eliminate the detection of unwanted species.

The electrosynthesis of polyphenylenediamines (PPD) can produce either a conducting or insulting polymer. However, insulating polymers have been demonstrated to display excellent permselective properties by impeding the detection of interfering species at the electrode surface while remaining highly permeable to H_2O_2[21]. Moreover, PPD also works to protect the sensor from biofouling following implantation making it advantageous in biosensor design for *in vivo* monitoring[22,23]. Previous reports have described two different structures of the insulating polymer (Figure 2.5.2). At present, it remains unknown as to which structure actually exists. The two structures that have been postulated include a 'ladder' structure where the amino groups are condensed within the benzene rings along the polymer chain[24]. The

second structure consists of an 'open' 1,4 - substituted benzenoid-quinoid structure[25]. However, suggestions by Losito *et al.*[26] indicate that the 'open' form of PPD is more dominant due to its ability to sterically hinder large molecules from the metal surface.

Electropolymerisation of PPD (Section 3.4.4.2) from *o*-PD is conducted at a neural pH to produce a self-sealing insulating polymer on the electrode surface[27]. This polymer is typically reported to have a thickness of approximately 10 - 35 nm [28]. It has been previously concluded that the polymer membrane formed from *o*-PD displays optimal interference rejection and permselective properties in *in vivo* monitoring. Previous studies have indicated that amperometry is the optimum electrochemical method for conducting electropolymerisation of *o*-PD as it was observed polymers generated using cyclic voltammetry were associated with an increased permeability to analytes such as AA[28]. Additionally, PPD polymer membranes generated using amperometry have been reported to exhibit a 'self-blocking' ability. This phenomenon was observed by Killoran *et al.*[28] whereby the permeability of AA was noted to decrease in a concentration dependent manner. It is postulated that the products formed by AA oxidation (Figure 2.5.1) block pores in the polymer further preventing AA from accessing the electrode surface[21]. This theory is supported by comparison of the electropolymerisation of *o*-PD in background electrolyte and in the absence of background analyte. AA calibrations carried out on PPD electrosynthesised in the absence of background analyte were noted to display a significantly better AA blocking ability when compared to PPD generated in the presence of background electrolyte. Thus, it was suggested that ions present in the electrolyte become trapped in the PPD layer generated before subsequently being released[29]. Hence, small gaps result in the polymer matrix. This theory supports the 'self-blocking' property of PPD during AA calibrations as AA oxidation products work to block these gaps and sterically hinder AA from accessing the electrode surface.

A

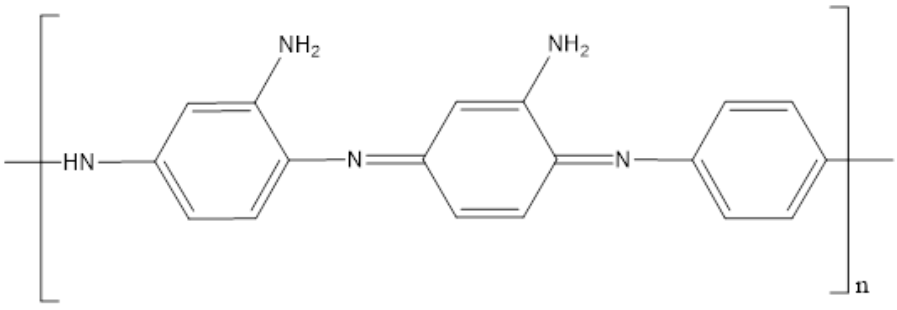

B

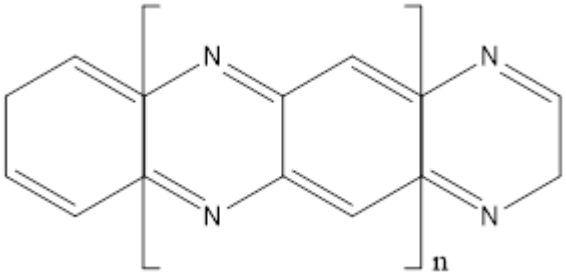

Figure 2.5.2: Proposed structures of *o*-phenylenediamine (A) Ladder structure, (B) open 1,4 - substituted benzenoid-quinoid structure.

2.6 Nafion®

Nafion® is a perfluorinated polymer membrane (Figure 2.6.1) consisting of a hydrophobic polytetrafluoroethylene (PTFE) backbone containing perfluorovinyl ether pendant side chains at regularly spaced intervals. Each of the aforementioned side chains are known to terminate in either sulfonic or carboxylic ionic functional groups[30]. Nafion® membranes have been reported to exhibit good durability while also displaying thermal and chemical stability due to the presence of the hydrophobic polytetrafluoroethylene backbone. Additionally, the hydrophilic sulfonic acid group positioned at the end of the perfluorinated side chains act as proton-conductive groups allowing Nafion® to demonstrate high ionic conductivity[31,32]. Moreover, small-angle X-ray studies have been observed to demonstrate that pendant side chains organise themselves into inverted micelles. Therefore, these inverted micelles form channels coated in the aforementioned sulfonic acid groups which allows for positively charged ions and neutral species to pass freely through the membrane. In contrast, negatively charged ions are repelled[33].

Nafion® coated Pt electrodes (Section 3.4.2) are utilised throughout this project to enable the electrochemical detection of NO. The inclusion of Nafion® annealed on the surface of Pt electrodes for NO detection has previously demonstrated excellent sensitivity to NO present in the surrounding environment while maintaining selective detection of NO over interfering electroactive species[2,7,34,35]. In addition, the H_2O_2 biosensor design (Section 3.4.4) also incorporated a Nafion® membrane which exhibited excellent selective properties in the detection of H_2O_2[19,28].

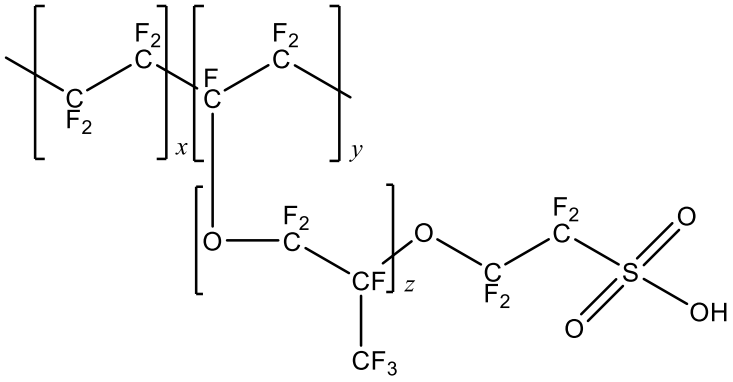

Figure 2.6.1: The structure of Nafion®

2.7 Microdialysis

Microdialysis is an important sampling technique which allows for the measurement of neurotransmitters, catecholamines, amino acids, in addition to, the metabolites of the aforementioned biological substances in the brain ECF from various different brain regions[36]. Microdialysis is an invasive procedure, involving the implantation of a sampling probe into the target tissue which is relatively large when compared to the dimension of individual cells and the intercellular space[37]. The microdialysis probe is perfused with a solution of similar ionic strength and pH as the surrounding microenvironment which is termed the perfusate. A semi-permeable membrane is contained at the bottom of the probe which when implanted allows analytes present in the ECF to diffuse across the membrane by means of a concentration gradient (Figure 2.7.1). The analytes flow into the perfusate where they are collected for further chemical analysis[38]. This process is controlled by Fick's law of diffusion which is the method of mass transport in the probe (Section 2.3). It is only when a concentration gradient is established, that the transport of analytes will be facilitated across this semi-permeable membrane[39]. The process of mass transport in microdialysis sampling was previously modelled by Bungay *et al.*[37,40] whereby a number of equations were derived under steady state conditions to highlight changes in microdialysis extraction efficiency (EE, Equation 2.7.1). Such changes in EE can be attributed to various factors associated with the resistance of analyte mass transport to the microdialysis probe. The parameters which contribute to this resistance include flow rate of the perfusate (Q), the dialysate (R_d), the tissue containing the microdialysis probe (R_{ECF}), the membrane geometry (R_m) and any trauma layers that may exist

following implantation of the probe[5,37]. Artificial cerebrospinal fluid (aCSF) was utilised in microdialysis sampling in this project. aCSF mimics the ionic concentration of the brain ECF. Analytes are collected from an area of higher analyte concentration to the lower concentration of the probe. However, the collection of analytes is a multifactorial process involving the diffusion coefficient of the analyte, the mass transport properties of target species, the length of the semi-permeable membrane of the microdialysis probe, the flow rate of the perfusate and the properties of the surrounding tissue[5].

$$EE = 1 - \exp\left[\frac{-1}{Q(R_d+R_m+R_{ECF})}\right] \quad \textbf{(2.7.1)}$$

One of the most important parameters underlying microdialysis is relative recovery. Relative recovery is defined as the ratio difference between the concentration of the dialysate and the concentration of the tissue in which the probe is implanted[41]. Knowledge of this factor is essential to calculate the actual metabolite concentration relative to the concentration of the analyte present in the dialysate. By knowing the relative recovery rate, parameters such as flow rate, membrane length and the collection period can be chosen that will allow dialysate samples containing a sufficient concentration of the target analyte for detection[42]. Equation 2.7.2 represents the relative recovery (RR) for steady-state conditions:

$$RR = \frac{C_{outlet} - C_{inlet}}{C_{sample,\infty} - C_{inlet}} \quad \textbf{(2.7.2)}$$

Where C_{inlet} is the analyte inlet concentration, C_{outlet} is the analyte outlet concentration and $C_{sample,\infty}$ is the undisturbed sample concentration at a distance far away from the probe[43]. The rates of relative recovery were not crucial to microdialysis sampling conducted within this project as the objective was not to calculate absolute concentrations of the analytes sampled. Rather, the relative trend in analyte concentration against a predefined baseline was obtained to enable biomarkers associated with neuronal activation to be identified (Chapter 7).

In addition, microdialysis experiments can be sub-divided into two groups: conventional microdialysis and zero-net-flux micordialysis. Firstly, conventional

microdialysis involved the infusion of aCSF allowing for metabolite diffusion into the probe where they are collected from the perfusate for additional analysis. This is the technique utilised in Chapter 7. Moreover, zero-net-flux involves the perfusion of aCSF containing different concentrations of an analyte under examination over the anticipated concentration of that analyte present in the ECF. By perfusion of varying concentrations of this analyte, the quantity of the analyte gained or lost can be established.

Microdialysis can also be used to deliver pharmacokinetic agents with a low molecular weight which usually do not cross the blood-brain barrier. This process is commonly referred to as retromicrodialysis. Retromicrodialysis was coupled with the co-implantation of the H_2O_2 biosensor in close proximity (See Section 5.3.3.2.1) which facilitated the local delivery of dose-dependent concentrations of H_2O_2 and H_2O_2 inducers to enable perturbation of H_2O_2 levels in the surrounding environment which could be measured amperometrically. Additionally, retromicrodialysis was used to deliver 100 mM K^+ and 100 µM Paraquat (Chapter 7) to enable perturbation of the neurochemical environment.

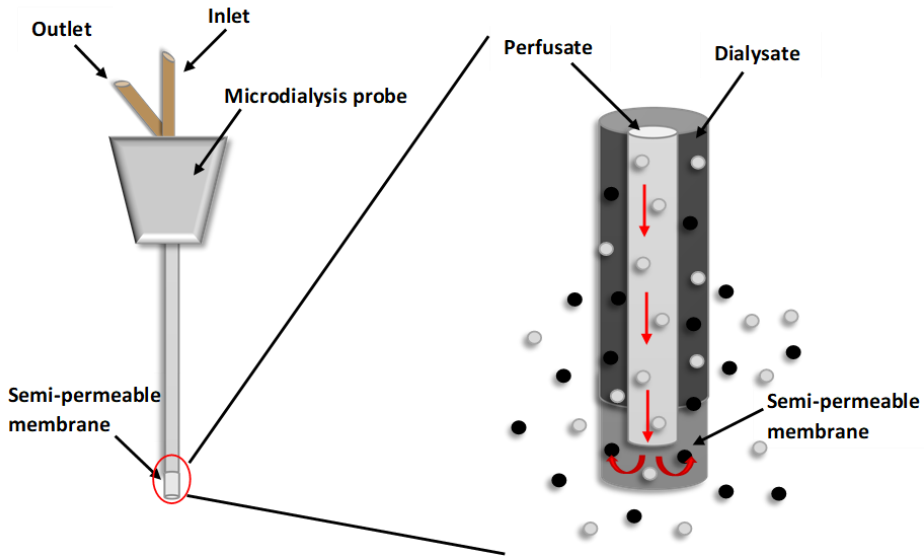

Figure 2.7.1: Schematic of the microdiaysis probe (left) with a detailed representation of the sampling membrane (right).

2.8 Data Analysis

Linear regression or non-linear regression was used to analyse data that was recorded using CPA. By obtaining the average steady state current, regression was applied allowing this value to be graphically plotted with the current response against analyte concentration. Where linear regression was applicable, r^2 values could be obtained. r^2 values indicate how well data points fit a fitted regression line where $0 < r^2 > 1$. The closer the r^2 value lies to 1 suggests that a linear relationship between the x values and y values exists, as 1 denotes that all points lie on the straight line.

2.8.1 Statistical Analysis

Statistical analysis was included to examine if obtained data was significantly different. To enable statistical differences to be identified, *t*-tests and one-way ANOVA were used. Both paired and unpaired *t*-tests were utilised with paired *t*-tests being used to compare data recorded from the same electrodes and unpaired *t*-tests being applied to data obtained from different electrodes for *in vitro* experiments. Comparatively, paired *t*-tests were used to compare the effect of the same compound in a number of animals *in vivo*. Unpaired *t*-tests compared the effect of two different compounds in various animals, for example the effect of saline *vs.* L-NAME. In addition, one-way ANOVA was used to analyse data between two or more independent groups. For example, one-way ANOVA analysis was included in *ex vivo* biocompatibility investigations to identify statistical differences over a 14-day study. Following conductance of one-way ANOVA analysis, Bonferroni *post hoc* analysis was performed to identify where the differences occurred in a group once an overall statistically significant difference had been identified in the overall group.

In a hypothesis test, a *p*-value was used to determine if data was significantly significant. Obtainment of a p-value < 0.05 indicated that the data was statistically significant and thus, rejects the null hypothesis. In contrast, if a p-value was > 0.05, the null hypothesis was accepted indicating that no statistically difference exists between two sets of data.

2.8.2 Current Densities

Electrodes of different geometries were constructed during this project. Hence, to compare data obtained from each of these electrodes, it was vital to compare current

densities as current values cannot be directly compared between electrodes of different geometries. Current densities can be attained using Equation 2.8.2.1 below:

$$J = \frac{I}{A} \quad \textbf{(2.8.2.1)}$$

Where J is the current density, I is the current and A is the area of the active surface of the electrode.

2.9 References

1. Borja-Cacho, D. & Matthews, J. Temporal Resolution in Electrochemical Imaging on Single PC12 cells using Amperometry and Voltammetry at Microelectrode Arrays. *Anal. Chem.* **83,** 571–577 (2011).
2. Brown, F. O., Finnerty, N. J. & Lowry, J. P. Nitric oxide monitoring in brain extracellular fluid: characterisation of Nafion®-modified Pt electrodes in vitro and in vivo. *Analyst* **134,** 2012–20 (2009).
3. Westerinkt, B. H. C. Brain microdialysis and its application for the study of animal behaviour *. **70,** 103–124 (1995).
4. Bard, A. J. & Faulkner, L. R. *Electrochemical Methods-Fundamentals and Applications*. (Wiley, 2001).
5. Paul, D.W., Stenken, J. A. A review of flux considerations for in vivo neurochemical measurements. *Analyst* **140,** 3709 (2015).
6. Forster, R. J. Microelectrodes : New Dimensions in Electrochemistry. *Chem. Soc. Rev.* 289–297 (1994).
7. Brown, F. O. & Lowry, J. P. Microelectrochemical sensors for in vivo brain analysis: an investigation of procedures for modifying Pt electrodes using Nafion®. *Analyst* **128,** 700 (2003).
8. Lehmani, A., Turq, P., Michelle, P., Jacques, P. & Simonin, J. Ion transport in Nation ® 117 membrane. *J. Electroanal. Chem.* **428,** 81–89 (1997).
9. Isik, S., Castillo, J., Blöchl, A., Csöregi, E. & Schuhmann, W. Simultaneous detection of l-glutamate and nitric oxide from adherently growing cells at known distance using disk shaped dual electrodes. *Bioelectrochemistry* **70,** 173–179 (2007).
10. Bolger, F., Bennett, R. & Lowry, J. An in vitro characterisation comparing carbon paste and Pt microelectrodes for real-time detection of brain tissue oxygen. *Analyst* **136,** 4028–35 (2011).
11. Martel, D. & Kuhn, A. Electrocatalytic reduction of H_2O_2 at $P_2Mo_{18}O_6^{26-}$ modified glassy carbon. *Electrochimica Acta* **45,** 1829–1836 (2000).
12. Lowry, J. P. & Neill, R. D. O. Neuroanalytical Chemistry In Vivo Using Electrochemical Sensors. *Am. Sci. Publ.* **10,** (2006).
13. O'Brien, K. B., Killoran, S. J., O'Neill, R. D. & Lowry, J. P. Development and characterization in vitro of a catalase-based biosensor for hydrogen peroxide

monitoring. *Biosens. Bioelectron.* **22,** 2994–3000 (2007).

14. Hall, S. B., Khudaish, E. A. & Hart, A. L. Electrochemical oxidation of hydrogen peroxide at platinum electrodes. Part 1. An adsorption-controlled mechanism. *Electrochim. Acta* **43,** 579–588 (1997).
15. Rice, M. E. Ascorbate compartmentalization in the CNS. *Neurotox Res* **1,** 81–90 (1999).
16. Miele, M. & Fillenz, M. In vivo determination of extracellular brain ascorbate. *J. Neurosci. Methods* **70,** 15–19 (1996).
17. Li, Y. & Schellhorn, H. E. New Developments and Novel Therapeutic Perspectives for Vitamin C. *J. Nutr.* **137,** 2171–2184 (2007).
18. Atrash, S. S. E. L. Characterisation In Vitro of a Naphthoquinone-Mediated Glucose Oxidase-Modified Carbon Paste Electrode Designed for Neurochemical Analysis In Vivo. **40,** 2791–2797 (1995).
19. O'Riordan, S. L., McLaughlin, K., Lowry, J. P. In vitro physiological performance factors of a catalase-based biosensor for real-time electrochemical detection of brain hydrogen peroxide in freely-moving animals. *Anal. Methods* **8,** 7614–7622 (2016).
20. O'Riordan, S.L., Lowry, J. P. In vivo characterisation of a catalase-based biosensor for real-time electrochemical monitoring of brain hydrogen peroxide in freely-moving animals. *Anal. Methods* **9,** 1253–1264 (2017).
21. Craig, J. D. & O'Neill, R. D. Comparison of simple aromatic amines for electrosynthesis of permselective polymers in biosensor fabrication. *Analyst* **128,** 905–911 (2003).
22. Lowry, J. P., O'Neill, R. D., Boutelle, M. G. & Fillenz, M. Continuous monitoring of extracellular glucose concentrations in the striatum of freely moving rats with an implanted glucose biosensor. *J. Neurochem.* **70,** 391–396 (1998).
23. Wynne, A. M., Reid, C. H. & Finnerty, N. J. In vitro characterisation of ortho phenylenediamine and Nafion®-modified Pt electrodes for measuring brain nitric oxide. *J. Electroanal. Chem.* **732,** 110–116 (2014).
24. Chiba, K., Ohsaka, T., Ohnuki, Y., & Oyama, N. Electrochemical preparation of a ladder polymer containing phenazine rings. *J. Electroanal. Chem. interfacial Electrochem.* **219,** 117–124 (1987).

25. Yano, J. Electrochemical and structural studies on soluble and conducting polymer from o-phenylenediamine. *ournal Polym. Sci. Part A Polym. Chem.* **33,** 2435–2441 (1995).
26. Losito, I., Palmisano, F. & Zambonin, P. G. O-Phenylenediamine Electropolymerization By Cyclic Voltammetry Combined With Electrospray Ionization-Ion Trap Mass Spectrometry. *Anal. Chem.* **75,** 4988–4995 (2003).
27. Malitesta, C., Palmisano, F., Torsi, L. & Zambonin, P. G. Glucose fast-response amperometric sensor based on glucose oxidase immobilized in an electropolymerized poly(o-phenylenediamine) film. *Anal. Chem.* **62,** 2735–40 (1990).
28. Killoran, S. J. & O'Neill, R. D. Characterization of permselective coatings electrosynthesized on Pt-Ir from the three phenylenediamine isomers for biosensor applications. *Electrochim. Acta* **53,** 7303–7312 (2008).
29. Rothwell, S. A., Killoran, S. J., Neville, E. M., Crotty, A. M. & O'Neill, R. D. Poly(o-phenylenediamine) electrosynthesized in the absence of added background electrolyte provides a new permselectivity benchmark for biosensor applications. *Electrochem. commun.* **10,** 1078–1081 (2008).
30. Zakil, F. A., Kamarudin, S. K. & Basri, S. Modified Nafion membranes for direct alcohol fuel cells: An overview. *Renew. Sustain. Energy Rev.* **65,** 841–852 (2016).
31. Neburchilov, V., Martin, J., Wang, H. & Zhang, J. A review of polymer electrolyte membranes for direct methanol fuel cells. *J. Power Sources* **169,** 221–238 (2007).
32. Zhang, L., Chae, S.-R., Hendren, Z., Park, J.-S. & Wiesner, M. R. Recent advances in proton exchange membranes for fuel cell applications. *Chem. Eng. J.* **204–206,** 87–97 (2012).
33. Mauritz, K. A. & Moore, R. B. State of understanding of Nafion®. *Chem. Rev.* **104,** 4535–4585 (2004).
34. Finnerty, N. J., O'Riordan, S. L., Brown, F. O., Serra, P. A., O'Neill, R. D., Lowry, J. P. In vivo characterisation of a Nafion®-modified Pt electrode for real-time nitric oxide monitoring in brain extracellular fluid. *Anal. Methods* **4,** 550 (2012).
35. Finnerty, N. J., O'Riordan, S. L., Pålsson, E. & Lowry, J. P. Brain nitric oxide:

regional characterisation of a real-time microelectrochemical sensor. *J. Neurosci. Methods* **209,** 13–21 (2012).

36. Altaf S. Darvesh, Richard T. Carroll, Werner J. Geldenhuys, Gary A. Gudelsky, J. & Klein, Charles K. Meshul, and C. J. V. der S. In vivo brain microdialysis: advances in brain neuropsychopharmacology and drug discovery. *Expert Opin. Drug Discov.* **6,** 109–127 (2011).
37. Bungay, P. M., Newton-Vinson, P., Isele, W., Garris, P. A. & Justice, J. B. Microdialysis of dopamine interpreted with quantitative model incorporating probe implantation trauma. *J. Neurochem.* **86,** 932–946 (2003).
38. Kennedy, R. T., Watson, C. J., Haskins, W. E., Powell, D. H. & Strecker, R. E. In vivo neurochemical monitoring by microdialysis and capillary separations. *Curr. Opin. Chem. Biol.* **6,** 659–665 (2002).
39. Weiss, D. J., Lunte, C. E. & Lunte, S. M. In vivo microdialysis as a tool for monitoring pharmacokinetics. *Trends Anal. Chem.* **19,** 606–616 (2000).
40. Bungay, P. M., Sumbria, R. K. & Bickel, U. Unifying the mathematical modeling of in vivo and in vitro microdialysis. *J. Pharm. Biomed. Anal.* **55,** 54–63 (2011).
41. Li, Z., Hughes, D., Urban, J. P. G. & Cui, Z. Effect of pumping methods on transmembrane pressure, fluid balance and relative recovery in microdialysis. *J. Memb. Sci.* **310,** 237–245 (2008).
42. Chefer, V. I., Thompson, A. C., Zapata, A. & Shippenberg, T. S. Overview of Brain Microdialysis. *Curr. Protoc. Neurosci.* **47,** 7–1 (2009).
43. Fletcher, H. J. & Stenken, J. A. An in vitro comparison of microdialysis relative recovery of Met- and Leu-enkephalin using cyclodextrins and antibodies as affinity agents. *Anal. Chim. Acta* **620,** 170–175 (2008).

Chapter 3

Experimental

3.1 Introduction

This chapter outlines the experimental procedures associated with the *in vitro* and *in vivo* characterisation of the NO and O_2 sensors, and the H_2O_2 biosensor. Each of these sensors have been characterised formerly whereby they have been shown to exhibit maximum sensitivity to the detection of the relevant analyte whilst also retaining selectivity against other endogenous electroactive species found within the brain[1–9].

A detailed description of the computer-based instrumentation used throughout these investigations is described in Section 3.2. Section 3.3 reports on the various chemicals and solutions employed throughout the course of this project. Electrode preparation is reported in Section 3.4, alongside the various electrode modifications associated with each relevant sensor type. The electrochemical cell set-up, experimental techniques and an outline of the different calibrations carried out on each sensor are contained within Section 3.5. Section 3.6 illustrates the *in vitro* investigations and various treatments carried out on the respective sensors.

The *in house* synthesis of NO, as developed by Brown et al.[10], is referred to in Section 3.7. The focus of Section 3.8 is on the *in vivo* procedures used within this project. A detailed description of the *in vivo* transplantation techniques, animals used and the experimental protocol will be reported. Section 3.9 gives a detailed account of the use of microdialysis and involvement of this technique in investigations in anaesthetised animals. In addition, *in* vivo injection administration will be depicted in Section 3.10.

Methods of fixation of the striatal tissue is discussed in Section 3.11 to enable analysis to be conducted at the University of Luxembourg. Immunohistochemical analysis and the use of FACS, including metabolomic and transcriptomic analysis, is also addressed in Section 3.11. Section 3.12 contains a report on all the supplementary equipment used throughout the course of this project.

3.2 Computer Based Instrumentation and Computer Programs

The attainment of data was achieved by three main components. These included the computer, the powerlab® and the potentiostat. The *in vitro* experimental set-up is depicted in Figure 3.2.1 below.

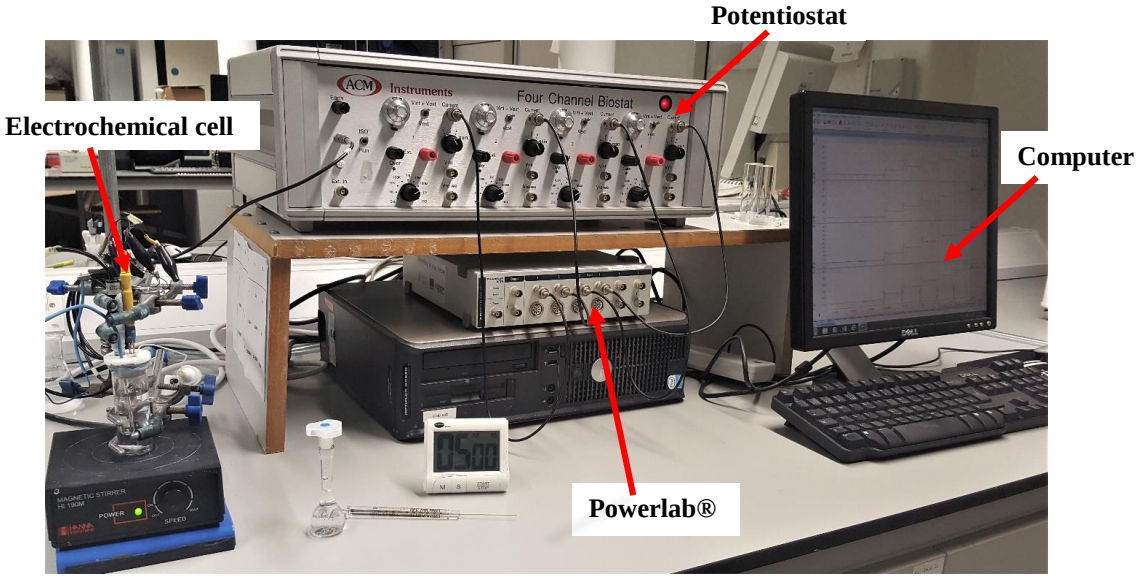

Figure 3.2.1: Electrochemical set-up consisting of an electrochemical cell housing working, reference and auxiliary electrodes, the potentiostat, powerlab® and the computer system.

3.2.1 Computer

The computer system on which data was recorded *in vitro* was a Dell Optiplex GX320 with an Intel Pentium D processor. *In vivo*, data was collected on a Dell Latitude E5540 with an Intel core i3 processor.

3.2.2 Potentiostat

In an electrochemical three-electrode setup, the potentiostat works by delivering a suitable known potential to the working electrodes. The potential being delivered during amperometry experiments is kept constant with respect to the reference electrode. Therefore, changes in current being measured within the cell can be monitored by the potentiostat. The recorded current can be manipulated by

employing various gain settings on the potentiostat to help amplify the signal to noise ratio, thus, resulting in a cleaner signal for analysis. For *in vitro* measurements, a four channel biostat was used (ACM instruments; Cumbria, UK). *In vivo* measurements were recorded using a software controlled four channel quadstat (Quadstat, eDAQ Ltd., Australia). The four channel biostat (a) and the four channel quadstat (b) can be observed below in Figure 3.2.2.1.

(a)

(b)

Figure 3.2.2.1: (a) Four channel biostat and (b) the four channel quadstat.

3.2.3 Data Acquisition

The acquisition of data was achieved by employing the powerlab® for *in vitro* experimentation whilst the eCorder system was utilised *in vivo*. The aforementioned systems are a crucial component of the computer based instrumentation for data acquisition. They comprise of a hardware and software unit which is designed to detect external analogue signals from the potentiostat before converting them to digital signals so it can be read by the computer system to which it is connected by USB connection. In addition, they work to amplify and eliminate any unwanted noise being

recorded in real-time. The hardware component of the system includes the processing unit and analog outputs for connection of external devices. Furthermore, the software is an application run on the computer to which the unit is connected. Throughout this project, LabChart and eChart programs have been employed (Section 3.2.4). Subsequently, the Powerlab® and eCorder work to act as an interface between the computer and external instrumentation to allow for analogue-to-digital and digital-to-analogue conversion. For *in vitro* recordings, an eight channel Powerlab® 8/35 (AD Instruments Ltd., Dunedin, New Zealand) was employed (Figure 3.2.3.1a). *In vivo*, an eCorder 821, from eCorder, eDAQ Ltd, Australia, was used (Figure 3.2.3.1b).

(a)

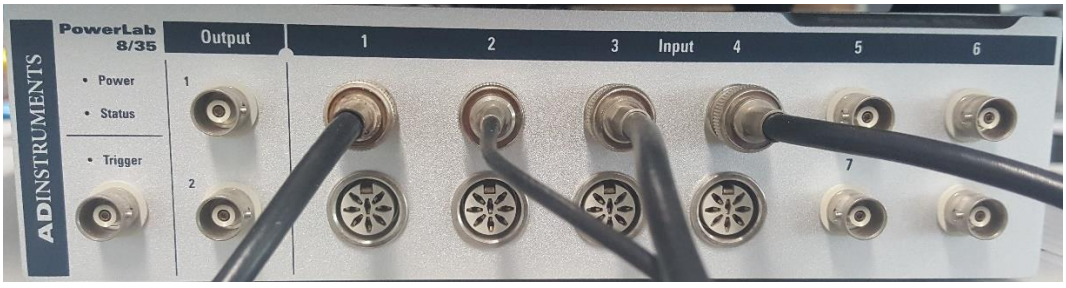

(b)

Figure 3.2.3.1: (a) An eight channel Powerlab® 8/35 and (b) the eCorder 821.

3.2.4 Computer Programs

The software packages used for data acquisition were LabChart® Pro version 8 (AD Instruments Ltd., Dunedin, New Zealand), eChart version 5.5 (eDAQ Ltd, Australia) and EChem version 2.1 (eDAQ Pty Ltd; Denistone East, Australia). Data was analysed statistically and graphically using GraphPad Prism® version 5.0 (GraphPad Prism® Software Inc., California, USA). Analysis methods employed in this project included statistical parameters such as Student's *t*-test for paired and unpaired parameters, where appropriate, and one-way ANOVA analysis. Statistical

analysis was employed to determine the level of significance of obtained results. Two-tailed levels of significance were used in this project whereby $p < 0.05$ was considered to be significant. Data was graphed using GraphPad Prism® version 5.0 (GraphPad Prism® Software Inc., California, USA) for raw data in *in vitro* and *in vivo* investigations.

3.3 Chemicals and Solutions

3.3.1 Chemicals

Listed below is a compiled list of all the *in vitro* and *in vivo* chemicals and the relevant suppliers utilised during this research project.

3.3.1.1 In Vitro Chemicals

L-Ascorbic Acid	Sigma Aldrich Co.
Calcium Chloride	Sigma Aldrich Co.
Catalase from bovine liver	Sigma Aldrich Co.
Graphite Powder	Sigma Aldrich Co.
Glutaraldehyde (grade 1, 25% in H_2O)	Sigma Aldrich Co.
Hydrogen Peroxide, 30 % w/w ACS reagent	Sigma Aldrich Co.
Magnesium Chloride	Sigma Aldrich Co.
N-1-Naphthyl-ethylenediamine (NEDD)	Sigma Aldrich Co.
Nafion® 5% in aliphatic alcohol	Sigma Aldrich Co.
Nitric Oxide gas	*In house* synthesis
Nitrogen gas	BOC Gases
Oxygen gas	BOC Gases
o-Phenylenediamine	Sigma Aldrich Co.
Potassium Chloride	Sigma Aldrich Co.
Potassium Hydroxide	Sigma Aldrich Co.
Pyrogallol	Sigma Aldrich Co.
Silicone Oil	Sigma Aldrich Co.
Sodium Chloride	Sigma Aldrich Co.
Sodium Phosphate Monobasic	Sigma Aldrich Co.
Sodium Hydroxide	Sigma Aldrich Co.

Sodium Nitrite	Sigma Aldrich Co.
Sulfanilamide	Sigma Aldrich Co.
Sulphuric Acid	AppliChem Panreac.

3.3.1.2 In Vivo Chemicals

Acetazolamine (Diamox)	Sigma Aldrich Co.
L-Arginine	Sigma Aldrich Co.
Buprenorphine Hydrochloride (Buprecare)	Animalcare, UK.
Carprofen (Carprieve 5 % w/v)	Norbrook, Ireland.
Chloral Hydrate	Sigma Aldrich Co.
Dentalon	Hereaus Kulzer GmbH.
Dormidor	Animalcare, UK.
Isoflurane	Sigma Aldrich Co.
Lidocaine (Norocaine)	Furry Park Vets, Dublin.
L-N^G-Nitroarginine methyl ester hydrochloride (L-NAME)	Sigma Aldrich Co.
Ketamine Hydrochloride (Vetalar)	Zoetis, Ireland.
Mercaptosuccinic Acid	Sigma Aldrich Co.
Paraquat (Methyl Viologen Dichloride Hydrate)	Sigma Aldrich Co.
Sodium Ascorbate	Sigma Aldrich Co.
Sodium Azide	Sigma Aldrich Co.

3.3.2 Solutions

All solutions were freshly made up on the day that the experiment was being carried out. The solutions utilised doubly distilled deionised water unless otherwise stated.

3.3.2.1 In Vitro Solutions

Ascorbic Acid (AA)

A 0.1 M AA solution was prepared by dissolving 0.176 g of AA in 10 mL of doubly distilled deionised water.

Carbon Paste

Carbon Paste was composed of a mixture of 0.71 g of graphite powder with 250 µL silicon oil. A pestle and mortar was used to ensure complete integration of the two substances. The mixture was ground for a period of approximately three hours.

Catalase-Glutaraldehyde (Cat-Ga (0.25%))

A 0.25 % solution of catalase-glutaraldehyde was made by dissolving 25 mg of catalase in 1 mL of 0.25 % glutaraldehyde. Catalase is 2000 - 5000 units/mg protein.

Glutaraldehyde (Ga (0.25%))

Glutaraldehyde solution (0.25 %) comprises of 0.25 mL of 25 % glutaraldehyde in 25 mL PBS.

Hydrogen Peroxide (H_2O_2)

A 0.1 M stock solution of H_2O_2 was produced by dissolving 56 µL H_2O_2 in 5 mL of doubly distilled deionised water.

Mercaptosuccinic Acid

A 100 mM solution of mercaptosuccinic acid was prepared by dissolving 0.0015 g in 10 mL of doubly distilled deionised water.

Neutral Griess Reagent

Neutral griess reagent comprises of 0.4 mM N-1-Naphthyl-ethylenediamine (NEDD) and 0.017 mM Sulfanilamide (SULF). This reagent was made up of 0.0104 g NEDD and 0.293 g SULF dissolved in 100 mL air saturated 100 µM PBS, pH 7.4.

Nitric Oxide (NO)

A stock solution of NO was made by use of an *in house* synthesis protocol[10]. This involved the reaction of $NaNO_2$ and H_2SO_4 to produce NO gas. The gas was purified by bubbling through solution of 4 M KOH. The concentration of the NO gas was then determined by use of UV spectroscopy.

***o*-Phenylenediamine**

A 300 mM of *o*-PD was prepared by dissolving 0.162 g of *o*-PD in 5 mL of N_2 saturated PBS.

Phosphate Buffered Saline (PBS)

PBS solution, with a pH 7.4, was made by dissolving 8.9 g NaCl, 1.76 g NaOH and 6.06 g $NaH_2PO_4.H_2O$ in 1 L of doubly distilled deionised water.

Potassium Hydroxide (KOH)

A 4 M KOH solution was prepared by dissolving 112 g of KOH in 500 mL of doubly distilled deionised water.

5 % alkaline Pyrogallol

A 5 % alkaline solution of pyrogallol was made up in 4 M KOH. This was achieved by addition of 5 g per 100 mL KOH.

Sodium Nitrite ($NaNO_2$)

A saturated solution of $NaNO_2$ was prepared in doubly distilled deionised water.

Sodium Azide

A 1 M solution of sodium azide was firstly prepared by dissolving 0.65 g in 10 mL of doubly distilled deionised water. An aliquot of 1 mL was taken from this solution and diluted to 10 mL using doubly distilled deionised water. This gave the required stock solution of 100 mM.

Sulfuric Acid (H_2SO_4)

A 6 M H_2SO_4 stock solution was prepared using 97 % H_2SO_4 commercial solution. 329 mL of H_2SO_4 was added to 1 L of doubly distilled deionised water.

3.3.2.2 In Vivo Solutions

Acetazolamide (Diamox)

A 50 mg/kg solution of was made up by dissolving Acetazolamide in 1 mL of 0.9% Saline. A 1 mL/kg administration of Acetazolamide was employed.

L-arginine

L-arginine was systemically administered by dissolving 200 mg/kg in 1 mL of 0.9 % Saline. L-arginine was administred as a 1 mL/kg dose.

Artificial cerebrospinal fluid (aCSF)

Preparation of aCSF involved dissolving 4.3 g NaCl (0.15 M), 0.149 g KCl (0.004 M), 0.088 g $CaCl_2$ (0.0016 M), 0.102 g $MgCl_2$ (0.0021 M) and 0.137 g $NaH_2PO_4.H_2O$ (0.0020 M) in 500 mL of doubly distilled deionised water. The pH of the solution was adjusted to pH 7.4

Buprenorphine hydrochloride (Buprecare)

Buprecare is a 0.3 g/mL stock solution of Buprenorphine hydrochloride which was administered 0.1 mg/kg post-surgery.

Carprofen (Carprieve)

Carprieve is a 50 mg/mL stock solution. Carprofen was administered as 10 mg/kg.

Chloral Hydrate

A 350 mg/kg solution was prepared by dissolving chloral hydrate in 1 mL of 0.9 % Saline. Administration of Chloral Hydrate was as a 1 mL/kg dose.

Hydrogen Peroxide (H_2O_2)

A stock solution of H_2O_2 (100 mM) was made up by dissolving 56 µL in 5 ml of aCSF. The following concentrations of H_2O_2 were made up as follows for local infusions/microdialysis of varying concentrations of H_2O_2:

20 µM: A 20 µM solution was made by dilution of 2 µL of stock solution in 10 mL aCSF.

50 µM: 5 µL of H_2O_2 stock solution was dissolved in 10 mL aCSF to achieve a 50 µM solution of H_2O_2.

100 µM: A 100 µM solution was achieved by dilution of 10 µL of stock solution in 10 mL aCSF.

500 µM: 50 µL of H_2O_2 stock solution was dissolved in 10 mL aCSF.

1 mM: A 1 mM solution of H_2O_2 was made up using 100 µL of H_2O_2 stock solution dissolved in 10 mL aCSF.

10 mM: 1 mL of H_2O_2 stock solution was dissolved in 10 mL aCSF to achieve a 10 mM solution of H_2O_2.

K^+ aCSF

K^+ aCSF (100 mM) solution was prepared by dissolving 2.98 g NaCl (0.051 M), 7.45 g KCl (0.100 M), 0.176 g $CaCl_2$ (0.0016 M), 0.204 g $MgCl_2$ (0.0021 M) and 0.274 g $NaH_2PO_4.H_2O$ (0.0020 M) in 500 mL of doubly distilled deionised water. The pH of the solution was adjusted to pH 7.4.

Lidocaine (Norocaine)

A stock solution of 20 mg/mL was used to administer a 5 mg/kg topical dose prior to surgical incision.

Mercaptosuccinic Acid

A 1 mM solution of Mercaptosuccinic Acid was made up by dissolving 1.5 g in 10 mL of aCSF.

L-N^G-Nitroarginine Methyl Ester Hydrochloride (L-NAME)

For systemic administrations of L-NAME, 30 mg/kg of L-NAME was dissolved in 1 mL of 0.9 % saline.

Paraquat (Methyl Viologen Dichloride Hydrate)

A stock solution of 100 mM paraquat was prepared by dissolving 0.0257 g in 10 mL of doubly distilled deionised water. An aliquot of 100 µL of the 100 mM solution was placed into a fresh 10 mL volumetric flask and made up with aCSF resulting in a 100 µM paraquat solution. 100 µM paraquat solution was employed in retromicrodialysis experiments.

Saline

A 0.9 % saline solution was prepared by dissolving 0.9 g of NaCl in 100 mL of doubly distilled deionised water.

Sodium Ascorbate

Sodium Ascorbate was prepared by dissolving 500 mg/kg in 1 mL 0.9 % Saline. Sodium Ascorbate is used as the main interferent to use in the animal as it is not necessary to alter the pH of the solution. Ascorbic acid is pH altered and thus can cause unnecessary discomfort to the animal. Sodium Ascorbate was administered to the animal as a 1 mL/kg dose.

Sodium Azide

A 100 mM concentration of Sodium Azide was made up using 0.65 g Sodium Azide in 10 mL of aCSF.

3.4 Working Electrode Preparation

Platinum (Pt) wire was used throughout this project for the manufacture of NO and H_2O_2 working electrodes. O_2 working electrodes were manufactured from silver (Ag) wire. NO and H_2O_2 sensors utilised Teflon®-coated Platinum/Iridium wire (90:10). This Pt wire had an outer diameter of 175 µm (5T) when coated and an inner diameter of 125 µm when bare.

For the manufacture of CPEs, silver (Ag) wire was used. The Ag wire consisted of an inner diameter of 200 µm and an outer diameter of 280 µm when coated with Teflon® insulation. A smaller Ag was applied for the manufacture of a number of *in vivo* O_2 sensors. This wire had an outer diameter of 177 µm and an inner diameter of 125 µm.

3.4.1 Disk and Cylinder Electrode Preparation

Disk electrodes were manufactured by cutting a length of Teflon®-coated Platinum/Iridium (Pt/Ir 90 %/10 %) wire (127 µm bare diameter, 175 µm coated diameter, 5T, Science Products GmbH, Hofheim, Germany) to approximately 4 cm. From one end of the wire, a length of approximately 3 mm of Teflon® was removed. This allowed for the wire to be soldered into a gold clip. The gold clip acts a connection to instrumentation whilst also providing rigidity to the sensor. At the opposite end of the wire, the wire was cut to allow for a fresh disk surface to be obtained. A schematic of a disk electrode can be seen below in Figure 3.4.1.1.

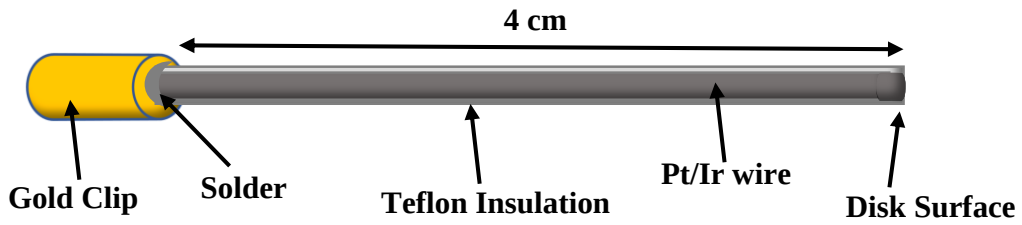

Figure 3.4.1.1: Schematic representation of a disk electrode.

For the manufacture of cylinder electrodes, the Pt/Ir (90 %/10 %) wire was soldered into a gold clip by removing a 2 mm length of Teflon® from one end of the wire. The other end of the wire was cut to a disk surface before a length of 2 mm of the Teflon® was removed before the Pt wire was cut back to reveal a fresh 1 mm cylinder surface. Figure 3.4.1.2 depicts a schematic diagram of a 1 mm cylinder electrode.

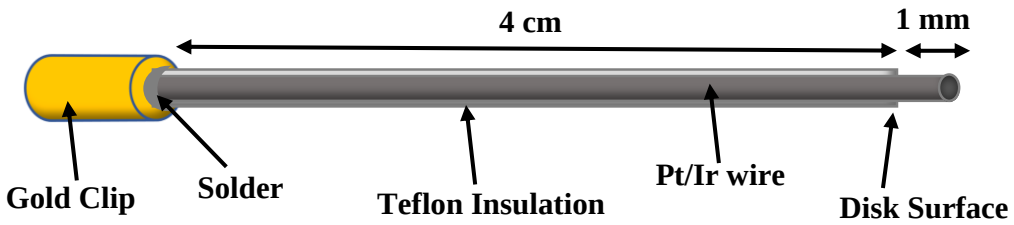

Figure 3.4.1.2: Schematic representation of a 1 mm Cylinder electrode.

3.4.2 Nitric Oxide Electrode Preparation

NO sensors were constructed from a disk electrode as previously described in Section 3.4.1. Disk electrodes were modified with Nafion® as previously developed by Brown *et al.*[11]. Firstly, the application of Nafion® to the disk surface involved annealing a concentrated Nafion® pre-coat to the fresh disk surface. The Nafion® pre-coat was achieved by placing a small volume of Nafion® on a clock glass using a syringe. The droplet was allowed to air dry for a period of approximately 10-minutes at room temperature. Once it was ensured that the droplet had evaporated, the next four layers of Nafion® were applied to the clock glass allowing sufficient drying time between the application of each subsequent layer. A local concentrated layer of Nafion® was then achieved. A further drop of Nafion® was then applied once the pre-coat Nafion® layer was completely dry to allow for adherence of the concentrated Nafion® layer to the electrode surface. The active disk surface was then dipped through the Nafion® pre-coat before removing the electrode and leaving it to dry at room temperature for 2-minutes. The electrodes were then placed in an oven at 210 ºC to anneal for a period of 5-minutes. Following annealing, the dip-bake procedure was repeated; the concentrated pre-coat of Nafion® was formed before dipping the electrodes in the pre-coat and annealing at 210 ºC for 5-minutes. This resulted in the manufacture of an NO sensor which can be seen in Figure 3.4.2.1 below.

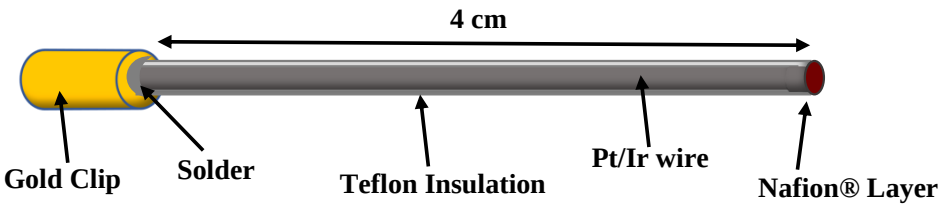

Figure 3.4.2.1: Schematic of a NO sensor.

3.4.3 Carbon Paste Electrode Preparation (CPE)

CPEs were manufactured using wire with two different geometries. Firstly, CPEs with a smaller geometry were constructed from a 4 cm length of Teflon®-insulated silver (Ag) wire (8T, 177 µm outer diameter, 125 µm bare diameter, Advent Research Materials; Oxford, UK). Additionally, CPEs were also manufactured using a larger diameter wire (8T, 280 µm outer diameter, 200 µm bare diameter, Science

Products GmbH; Hofheim, Germany). From one end of the wire, a length of approximately 2 mm of Teflon® was removed. This allowed for the wire to be soldered into a gold clip. The gold clip acts a connection to instrumentation whilst also providing rigidity to the sensor. At the opposite end of the wire, the wire was cut to allow for a fresh flat surface to be obtained. The Teflon® was carefully motioned up the wire to allow for a 1 mm or 0.5 mm cavity to be achieved. The cavity was packed with carbon paste (Section 3.3.2.1) by means of dipping the cavity into a small amount of carbon paste. Following this, the paste was packed into the cavity using a small length of bare Ag wire as previously detailed[1,12]. This procedure was repeatedly carried out until the cavity had been completely packed with carbon paste. Lastly, the electrode was tapped against the tip of a scalpel blade to ensure a flat surface was obtained. Figure 3.4.3.1 depicts a schematic of a CPE.

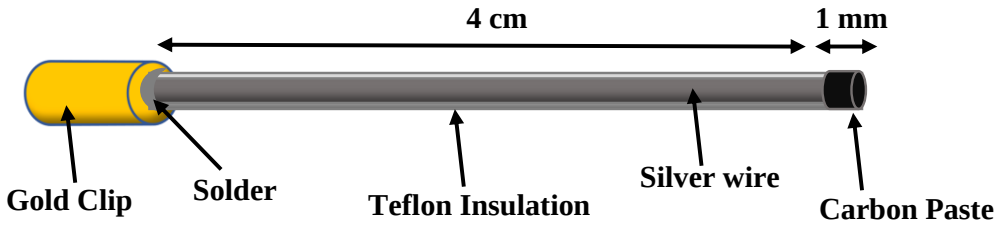

Figure 3.4.3.1: Schematic representation of a CPE sensor.

3.4.4 Hydrogen Peroxide Electrode Preparation

The H_2O_2 biosensor was manufactured based on the description previously detailed[7]. This biosensor is based on a dual sensor design which utilises 1 mm cylinder electrodes (Section 3.4.1) manufactured from Teflon®-insulated Pt/Ir wire. One electrode is used for the detection of H_2O_2 and incorporates a Nafion®-PPD coated 1 mm cylinder electrode. This electrode is denoted as the blank electrode. Whilst the other electrode is used for the degradation of H_2O_2 and is referred to as the catalase electrode. The catalase electrode incorporates Nafion®-PPD-Cat-Glu modifications on the surface of the 1 mm cylinder. Both electrodes are dip-coated with Nafion® initially. This involves dipping the tip of the electrode in Nafion® momentarily before allowing it to air dry for 5-minutes. This procedure is repeated to allow for 5 dips in total with 5-minutes drying time between each immersion. Such procedure is carried out before

electropolymerising *o*-PD onto the modified Nafion® surface (see Section 3.4.4.2 below).

3.4.4.1 Nafion® dip Modification

For the fabrication of H_2O_2 dual biosensor, Nafion® was applied to the cylinder surface of the electrode by means of a dip modification technique. The electrodes were dipped into a stock of Nafion® for ca. 1 second. Following dipping, the electrode was removed and allowed to air dry at room temperature for a period of 5-minutes. The electrodes were dried by placing them in a vertical position with the active surface facing downwards. The process of applying Nafion® by dipping was repeated using the same procedure a further 4 times to give a total of 5 Nafion® coats on the electrode surface. Once complete, the electrodes were allowed to dry at room temperature for at least 3-hours before further modification with *o*-PD was conducted (Section 3.4.4.2) .

3.4.4.2 Electropolymerisation of o-PD

The modification of electrode surfaces using *o*-PD has been extensively characterised[6]. The function of *o*-PD is to act as an interferent rejection layer on the electrode surface as previously discussed in Section 2.5. Hence, this allows for only the analyte of interest to be detected. Therefore, the *o*-PD layer ensures selectivity for the target analyte over other electroactive species in a hostile biological environment[13]. *o*-PD can be electropolymerised onto Nafion® modified electrode surfaces and onto bare Pt electrodes to form the non-conducting polymer polyphenylenediamine (PPD) on its surface. Prior to electropolymerisation, the electrochemical cell and PBS solution were purged with N_2. A solution of 300 mM *o*-PD was made up in N_2 saturated PBS (Section 3.3.2.1) and electropolymerisation was carried out at a constant potential of + 700 mV *vs.* SCE for 30-minutes. It was ensured that the solution was kept under a N_2 saturated atmosphere as the *o*-PD monomer rapidly oxidises in air. The modified electrodes were then allowed to dry overnight before further modification or calibration.

3.4.4.3 Cat-Glu(0.25%) modification

The catalase electrode was further modified with a Cat-Glu(0.25%) layer following incorporation of Nafion® and PPD on its surface. Such procedure involved

immersing the electrode in a solution of Cat-Glu$_{(0.25\%)}$, as described in Section 3.3.2.1, for a period of 5-minutes. The enzymatic solution was stored on ice throughout the modification procedure to conserve enzymatic activity. Following this, the electrode was allowed to air dry for 5-minutes. The catalase electrode was dipped a further 4 times momentarily within a time frame of 5-minutes in between each dip. Once the procedure was completed, it resulted in a Nafion®-PPD-Cat-Ga$_{(0.25\%)}$ electrode termed as the catalase electrode.

3.5 Electrode Treatments

It is of utmost importance to examine the effects of brain tissue on the properties of the sensor following implantation *in vivo*. Once a sensor is implanted in the mouse brain, it is exposed to a harsh biological environment containing multiple electrode poisons such as lipids and proteins. Such poisons work by attacking the modified electrode and thus, affecting the performance of the sensor *in vivo*. In addition, once implanted the surrounding tissue can react physiologically to the presence of the sensor leading to inhibition of the target analyte to reach the electrode surface and thus restricting mass transport[14]. Additionally, this phenomenon has been detailed previously for numerous *in vivo* electrochemical measurements and highlights the need to investigate such a matter further before the implantation of an electrode *in vivo*. The exact effect of the *in vivo* environment on electrode performance cannot be recreated *ex vivo*. However, a good representation of the harsh milieu is to expose the electrodes to a homogenate solution of brain tissue.

3.5.1 Brain Tissue Treatment

The electrodes to be treated with brain tissue were calibrated against their relevant analyte to ensure sensitivity prior to brain tissue exposure. Selectivity, against AA, was also tested for the NO and H_2O_2 sensors. AA was chosen to test the selectivity properties of the relevant sensors due to its extensive abundance *in vivo*[15,16]. Once the performance of each of the electrodes had been established, they were placed in a homogenate solution of *ex vivo* brain tissue for a selected period. The electrodes were kept in the fridge at 4 ºC for this period. The electrodes were recalibrated for sensitivity and selectivity following sufficient exposure to brain tissue on days 1, 3, 7 and 14.

The H_2O_2 catalase electrodes incorporates an adsorbed enzyme on the surface of the electrode. Therefore, it is important to consider the physical effect of implantation on the functionality of the enzyme. *Ex vivo* investigations were utilised to mimic the *in vivo* implantation due to the difficulties encountered in removing the H_2O_2 biosensor successfully from sacrificed mice. *In vivo* conditions were mirrored by carefully implanting the H_2O_2 catalase electrodes (n = 12) in a mouse brain using a micromanipulator. Following exposure of the H_2O_2 catalase electrode to brain tissue for 60-minutes, the electrodes were carefully removed. Thereafter, each of the sensors were recalibrated to compare their sensitivity and selectivity to pre-implantation values.

3.5.2 Post Implanted Sensors

Following implantation of the O_2 and NO sensors *in vivo*, the sensors were removed and recalibrated to compare their sensitivity and selectivity to pre-implantation values obtained. This was to investigate the long-term stability of the sensor following exposure to the harsh biological environment of the brain. H_2O_2 biosensors were not recalibrated following implantation due to the sensitive nature of the enzyme on the dual biosensor becoming damaged during removal *in vivo*. It was decided that recalibration of the dual biosensor would not be an accurate determination of the long-term stability of the biosensor due to the physical damage to the surface membrane during removal.

3.6 Electrochemical Experiments

3.6.1 Electrochemical Cell Set-up

Electrochemical *in vitro* experiments were carried out in an electrochemical cell at room temperature (~ 25 ºC). The electrochemical cell was a three-electrode set up and consisted of a reference electrode, an auxiliary electrode and four working electrodes. The electrochemical cell set up can be seen in Figure 3.6.1.1 below. All experiments were carried out in PBS, pH 7.4. The reference electrode utilised was a saturated calomel reference electrode (SCE). It acts by delivering a known and fixed potential to the electrochemical cell so individual potentials of the working electrodes can be measured accurately and relative to the reference point. The auxiliary electrode acts as source or sink of electrodes, allowing for the flow of current within the

electrochemical cell. The auxiliary electrode is made of a conducting Pt wire and it does not interfere in any electrochemical reactions taking place. Redox reactions of the analyte of interest which occur at the working electrode surface can then be investigated and further analysed. The electrochemical cell is encased in a glass cell which is covered with a Teflon® lid. The lid acts to allow for placement of electrodes within the cell whilst also allowing for the gas inlet and injection port. A magnetic stirring bead can also be found within the electrochemical cell which provides agitation to the bulk solution following addition of analyte aliquots to the cell.

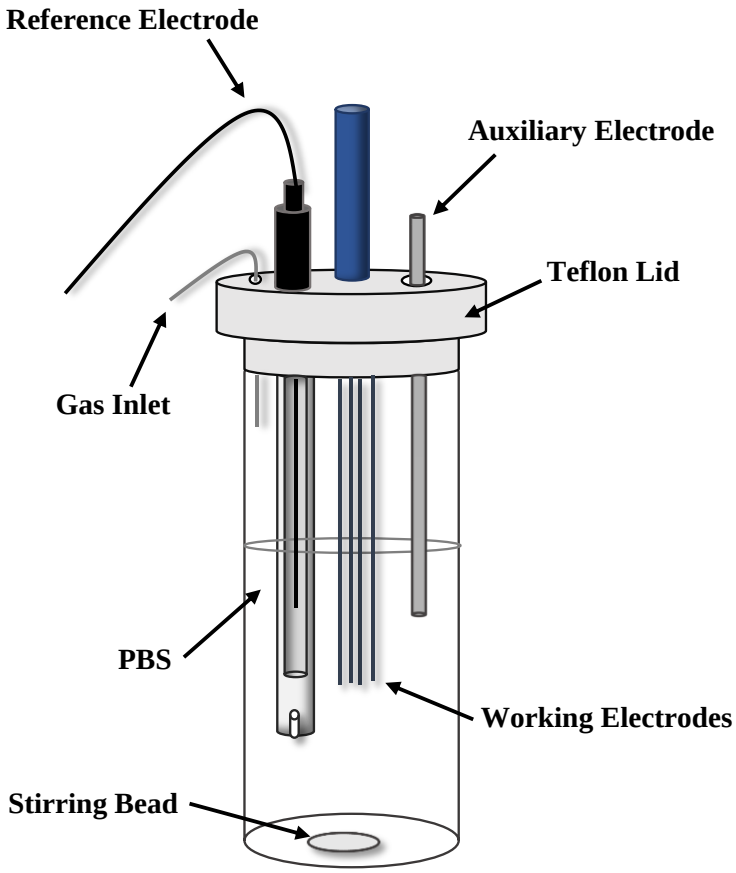

Figure 3.6.1.1: Schematic diagram of the electrochemical cell set-up.

3.6.2 Experimental Techniques

CPA was the main experimental technique used in electrochemical experiments. CPA (Section 2.4) is an electrochemical technique whereby a constant fixed potential is applied to the working electrodes. A redox reaction is instigated at the working electrode surface which results in the measurement of a steady state

current[17]. The potential applied is chosen based on its efficiency to adequately allow for oxidation/reduction of the analyte of interest i.e. NO, O_2 and H_2O_2 to occur. The amplitude of the measured current can be related to the relative concentration of the analyte of interest being investigated. CPA allows for a range of electroactive species to be detected in real-time and thus, gives rise to an array of chemical species with similar oxidation/reduction potentials to the applied potential, to be detected and thus, contribute to the overall recorded current. It is therefore crucial to design a sensor that will eliminate any unwanted species from being detected at its surface.

3.6.2.1 Ascorbic Acid Calibrations

Interference testing was achieved by carrying out AA calibrations on the working electrodes. A 0.1 M stock solution was used over the following concentration range (Table 3.6.2.1.1):

Table 3.6.2.1.1: Concentration range of an AA calibration.

Stock Solution: 0.1 M	**AA, µM**
Injection volume	
-	0
+ 40 µL	200
+ 40 µL	400
+ 40 µL	600
+ 40 µL	800
+ 40 µL	1000

To an electrochemical cell, 20 ml of PBS was added. The PBS was purged with N_2 for a period of 30-minutes until it was fully saturated. AA calibrations were carried out at room temperature under a N_2 atmosphere for the duration of the calibration. A potential of + 700 mV *vs*. SCE was utilised for the detection of AA. Following application of this potential, the current was allowed to reach a stable baseline before AA aliquots were added to the cell. Once a stable baseline had been achieved, aliquots of AA, as referred to in Table 3.6.2.1.1 above, were added to the cell by means of the injection port in the Teflon® lid (Figure 3.6.1.1). Agitation of the

bulk solution followed each injection for ca. 5-seconds. After each injection, the current was allowed to stabilise before adding another aliquot of AA ca. 5-minutes.

3.6.2.2 Nitric Oxide Calibrations

Prior to NO calibrations being carried out, 20 ml PBS was purged with N_2 for 30-minutes. The NO was synthesised according to Brown *et. al*[10]. A potential of + 900 mV *vs.* SCE was applied to the working electrodes. The electrodes were allowed to attain a stable baseline before any aliquots of NO were added to the cell. The following NO concentration range was used as listed below in Table 3.6.2.2.1:

Table 3.6.2.2.1: Concentration range of a NO calibration.

NO, µM
0
0.2
0.4
0.6
0.8
1.0

As the NO sensor had been previously extensively characterised[4,5,11], all *in vivo* NO sensors were tested for sensitivity and selectivity prior to implantation *in vivo*. Selectivity calibrations involved calibrating the sensors against AA, which is the most copious electroactive interferent in the brain. Interferent studies were carried out following NO calibrations using CPA with an applied potential of + 900 mV *vs.* SCE.

3.6.2.3 Oxygen Calibrations

O_2 calibrations were carried out *in vitro* at - 650 mV *vs.* SCE. Following the application of the potential, PBS was N_2 saturated for 30-minutes. After this, a N_2 environment was maintained for a further 10-minutes. This procedure was repeated using air followed by O_2 to complete the calibration. This three-point calibration gave rise to the concentrations of N_2, air and O_2 which can be seen in Table 3.6.2.3.1 below.

Table 3.6.2.3.1: Concentration range of an O_2 calibration.

Percentage O_2	O_2, µM
N_2 (0%)	0
Air (21%)	240
O_2 (100%)	1200

3.6.2.4 Hydrogen Peroxide Calibrations

H_2O_2 calibrations were performed in 20 mL of air saturated PBS. A 0.1 M stock solution of H_2O_2 was made, see Section 3.3.2.1. CPA was utilised for the detection of H_2O_2 with a potential of + 700 mV *vs*. SCE being applied. As with NO and O_2 sensors, the current was allowed to reach a stable baseline before the addition of H_2O_2 over the concentration range shown below in Table 3.6.2.4.1:

Table 3.6.2.4.1: Concentration range of an O_2 calibration.

Stock Solution: 0.1 M	H_2O_2, µM
Injection volume	
-	0
+ 4 µL	20
+ 4 µL	40
+ 4 µL	60
+ 4 µL	80
+ 4 µL	100

As the H_2O_2 biosensor had been previously characterised for the interference properties it possesses, it was sufficient to test the selective properties of the H_2O_2 biosensor using an AA calibration before being implanted *in vivo*.

3.7 NO Synthesis and UV Spectroscopy

The synthesis of NO was performed *in house* by means of a very reproducible method developed by Brown *et al.*[10]. This inexpensive method works by utilising concentrated H_2SO_4 to carry out a disproportionation reaction with $NaNO_2$. Thereafter, NO gas is produced and bubbled through KOH into distilled H_2O

contained in a round bottomed flask. UV spectroscopy was employed to obtain the concentration of the aqueous NO stock solution. Figure 3.7.1 portrays the experimental set-up of NO synthesis.

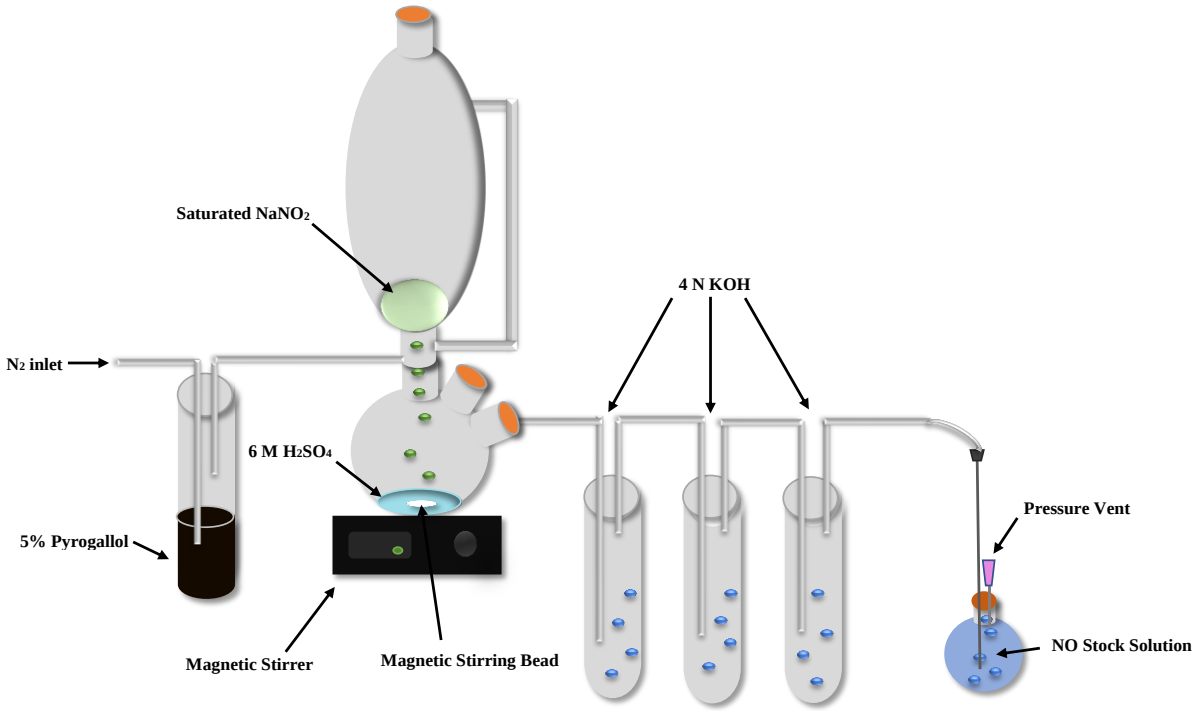

Figure 3.7.1: The experimental set-up of NO synthesis

3.8 *In Vivo* Experiments and Surgical Protocol

The following section details the procedures and materials utilised during the *in vivo* experiments carried out throughout this project. All experimental procedures were carried out under the license AE19124/P010 and AE19124/P015 in accordance with the European Communities Regulations 2002 (Irish Statutory Instrument 165/2013). All procedures were approved by the Maynooth University Ethics Committee (Animal Experimentation) in accordance with the Council of the European Parliament Directive 2010/63/EU. *In vivo* experiments involving freely-moving animals were monitored continuously over a 24-hour period. The health of such animals was carefully monitored in accordance with the published guidelines[18]. Following the recovery of the animal from anaesthesia and at the beginning of each day, the health of the animal was monitored and noted. It was of crucial importance to

minimise any suffering to the animal and the number of animals used throughout the course of this project.

3.8.1 Subjects

For all *in vivo* experiments, NOD SCID (NOD.Cg-*Prkdc*^{scid} *Il2rg*^{tm1Wjl}/SzJ**,** Jackson Labs, USA) mice were used. NOD SCID mice were obtained from Charles River (UK Ltd., Manstin Rd., Margate, Kent, CT9 4LT, UK). Animals typically weighed between 25 and 40 g prior to experimentation. In addition, animals used in transplantation experiments were typically between 7 and 10 weeks old at the time of transplantation. All NOD SCID mice were housed in individually ventilated cages with humidity and a temperature of 17 - 23 ºC being maintained. The environment was also light controlled (12-hour light, 12-hour dark cycle). A maximum of five animals per cage were housed together. Food and water were available *ad libitum*.

Prior to experimentation, all animal were housed for a period of approximately 5-days to allow for the animal to habituate to a new housing environment and prevent unnecessary weight loss. The freely-moving mice utilised for long term amperometric recordings were housed individually in an open top recording cage following surgery. This was to prevent damage to the headpiece containing the electrodes. Following a period of recovery post-surgery, the animal was connected to a potentiostat by means of a six-pin Teflon® socket and a bespoke screened four core cable which was manufactured *in house*. This cable was mounted through a swivel slip ring (CPC Farnell, Preston, UK) above the subject's head. Animals utilised for *in vivo* transplantation were individually housed following surgery. This was to allow the animal recover fully and for the surgical sutures to heal. Following this, the animals were group housed for a number of weeks to allow for integration of the transplant in the striatum of said mice.

Animals employed in experimentation involving microdialysis were housed individually in ventilated cages following surgery to allow for sufficient recovery. Once recovered, the animal was transferred daily to a bespoke microdialysis set-up to be connected to the microdialysis apparatus and swivel (Section 3.9). Following the procedure, the animal was returned to the ventilated cage for the night to rest.

3.8.2 Preparation of Small Molecule Neural Precursor Cells (smNPCs) for Transplantation into the Striatum of NOD SCID Mice.

smNPCs were cultured by Schwamborn *et al.* (LCSB, University of Luxembourg, Luxembourg)[19–21] before being sent to Maynooth University for transplantation into the striatum of NOD SCID mice. smNPCs (Passage 9 - 25) were housed under medium conditions before transplantation. Firstly, the smNPCs were split into single cells by digesting them with pre-warmed Accutase. An aliquot of 3 mL of Accutase was added to the cells before the cells were incubated at 37 ºC before being diluted in N2B27 medium. N2B27 medium consisted mainly of Dulbecco's modified Eagle's medium (DMEM)-F12 (Invitrogen)/Neurobasal (Invitrogen) 50:50 with 1:200 N2 supplement (Invitrogen), 1:100 B27 supplement lacking vitamin A (Invitrogen) with 1 % penicillin/streptomycin/glutamine (PAA). Cells were diluted in N2B27 medium and centrifuged at 2115 rpm for 3-minutes. The cells were resuspended in N2B27 and transplanted at a density between 50,000 and 150,000 cells/µL depending on the cells being transplanted. The cell suspension was kept on ice before 3 µL of the suspension was injected into each hemisphere of the mouse brain by 5 µL Hamilton syringe (Hamilton Robotics, Bonduz, GR, Switzerland). Individual cell preparations were used for each mouse undergoing striatal transplantation. The aforementioned cell preparation is based on the established protocol from Schwamborn *et al.*[21,22]. The coordinates used for the transplantation site are stated in Section 3.8.3.

3.8.3 Surgical Protocol – Transplantation of smNPCs into the Striatum.

All surgical procedures were carried out using aseptic techniques. All bench tops and surfaces were cleaned down using 70 % ethanol while all instruments were autoclaved prior to use. The anaesthetic used during all surgeries was Isoflurane which is a volatile anaesthetic. A Univentor 401 vaporiser (Univentor Ltd., Zejtun ZTN 3000, Malta) was used to deliver the anaesthetic to the animal. Animals were fully anaesthetised using 4 % Isoflurane in a perspex induction chamber for a period of approximately 5-minutes. The animal was then fixed in a Stoelting stereotaxic frame (Stoelting Co., Illinois, USA) in the laminar flow hood. The nose piece of the frame was moved to fit around the snout of the animal and anaesthesia was maintained

between 2.0 % and 2.5 % depending on the level of pain expected during the surgery. Table 3.8.3.1 details the levels of anaesthetic delivered to the animal in the induction chamber and via the nosepiece:

Table 3.8.3.1: The levels of anaesthetic and air delivered to the animal during surgery.

	Isoflurane %	Air, mL/min
Induction Chamber	4	400 - 500
Nosepiece	1.5 - 3	150 - 250

A heat pad (Stoelting Co., Illinois, USA) was utilised to keep the animal warm with the temperature of the animal being maintained at 37 ºC by means of a rectal temperature probe. Elma analgesic cream was placed on the earbars prior to insertion in the ear canal of the animal. It was ensured that the head of the animal was completely level between lambda and bregma before commencing the surgery. Once the animal was fixed in the stereotaxic frame, the head of the animal was disinfected using Povidone iodine solution and a pre-operative dose of the analgesic, Carprofen (10 mg/kg) was administered to the animal. The animal was then covered with a sterile surgical drape. The eyes were coated with a topical eye and nose ointment (Bepanthan) to ensure that they did not dry out or become irritated due to the laminar flow hood being activated during surgery.

On the dorsal side of the skull of the animal, an incision was made to a length of approximately 2 cm in the anterior-posterior direction. Once the periosteum was visible, an aliquot of Lidocaine (5 mg/kg) was administered to numb the site of the incision. Sterile cotton buds were used to push back any tissue and thus, reveal the skull. Clamps were used to hold back tissue around the incision site and reveal the skull of the animal. The identification of bregma was carried out by applying minimal pressure to the point at which the coronal and sagittal suture meet in the skull of the animal. Once identified, bregma was marked as a zero point. From bregma, lambda was found and it was ensured it was not more than - 3.8 ± 0.2 mm (A - P) and 0.0 ± 0.1 mm (D - V) from bregma. If it was found to be outside this threshold, the animal was levelled until it was within an acceptable range. Correction of the coordinates was

facilitated by multiplying all of the coordinates by a correction factor, y (y = x/3.8). The stereotaxic arm was then moved back to bregma before placing the arm at the relevant coordinates, as detailed in the Table 3.8.3.2 below:

Table 3.8.3.2: Stereotaxic coordinates for implantation of smNPCs in the striatum of a NOD SCID mouse.

Brain Region	(A - P)	(M - L)	(D - V)
Striatum	+ 0.6	± 1.5	- 4.0/ - 4.2

Coordinates are based on bregma being the zero point and the relevant coordinates being found in reference to bregma in accordance with Paxinos and Watson (2008)[23] as a guide for placement. The drill was moved to the relevant coordinate for the Hamilton syringe (Hamilton Robotics, Bonduz, GR, Switzerland) to be implanted into the striatum. The drill was lowered until it touched the skull and this was taken as a zero point for the dorsal/ventral axis. Anaesthesia was increased during the drilling process to minimise any discomfort felt by the animal. The hole was then drilled to a depth of approximately 0.3 mm. The cells being transplanted were taken up in a 5 µL Hamilton 7005KH Syringe (Hamilton Robotics, Bonduz, GR, Switzerland) that had been previously rinsed with EtOH and sterile water. The syringe was then connected to Model 5000 Microinjection Unit with Model 5000-G Course Adjustment Handle (both David Kopf Instruments). The syringe was lowered until it reached the skull beside the drill hole. The syringe was then moved into the opening of the drill hole before being lowered to the relevant D - V coordinate seen in Table 3.8.3.2 above. A pocket was created to allow for proliferation of the cells in the striatum by lowering the syringe down 0.2 mm more than what was needed. The Hamilton was then moved back into position before the cells were injected. Over a time period of 5-minutes, 3 µL of cell suspension was injected. The Hamilton syringe remained in position for a period of 3-minutes following injection to prevent backflow of the cells into the tip of the syringe. The Hamilton syringe was then brought back up very slowly before another 3 µL of the cell suspension was transplanted into the contralateral hemisphere in the same manner. Once the surgery was complete, the

clamps were removed and the skin around the incision was sutured up. The animal was sutured in a posterior direction to the incision site. Anaesthesia was ceased and the animal was removed from the ear bars and the stereotaxic frame. The animal was placed in a pre-warmed incubator (29 ºC) until it had recovered. A 1 mL/kg injection of 0.9 % saline was administered to the animal to provide rehydration and aid in recovery. The animal was closely monitored in the immediate few hours following surgery. This was to ensure that the animal was not experiencing any pain and was recovering well. If it was thought that the animal was experiencing any discomfort, they were administered with the opioid analgesic, buprenorphine (0.1 mg/kg) subcutaneously. Once it was deemed that the animal had recovered sufficiently, they were transferred to their IVC home cage where they remained for 6 weeks to allow for integration of the transplanted cells in the striatum of the NOD SCID mouse.

3.8.4 Surgical Protocol – Sensor Implantation.

Sensors were implanted into non-humanised and humanised mice transplanted with smNPCs. Sensor implantation in transplanted animals was carried out once the transplanted cells had been allowed to integrate for 6-weeks in the mouse brain. Surgery was carried out as per Section 3.8.2 until the drilling process. The coordinates used for the sensor implantation are as follows (See Table 3.8.4.1):

Table 3.8.4.1: Stereotaxic coordinates for electrode implantation in the striatum of a NOD SCID mouse from the skull.

Sensor Implanted	(A - P)	(M - L)	(D - V)
NO	+ 0.5	± 1.5	- 4.0
O_2	+ 0.5	± 1.5	- 4.0
H_2O_2	+ 0.5	± 1.5	- 4.5

Once the sensor hole had been formed, an additional hole for the auxiliary electrode, reference electrode and three anchor screws were drilled as illustrated in Figure 3.8.4.1 below:

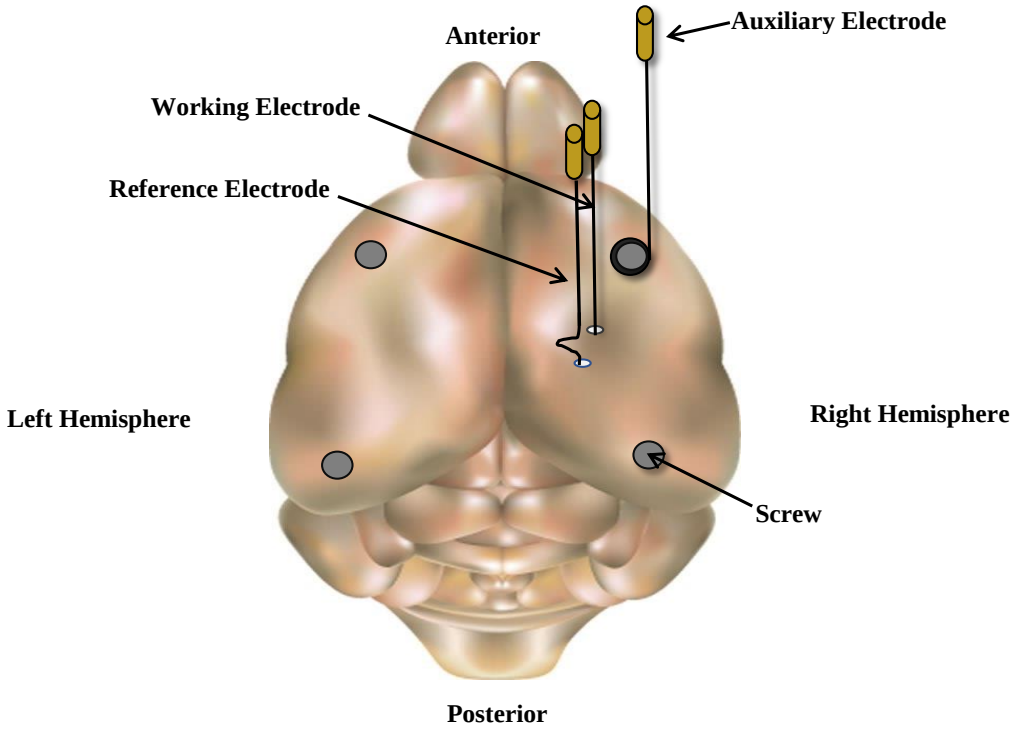

Figure 3.8.4.1: Schematic of a typical sensor placement in the striatum of a NOD SCID mouse.

Once the support screw holes were formed, each of the screws (Agnthos, Lidingö, Sweden) were implanted. The sensor was lowered until it reached the top of the skull and this was taken as a zero point on the dorsal/ventral axis. Thereafter, the sensor was lowered into position. A thin layer of loose cement (Dentalon, Heraeus GmbH.) was placed over the skull to hold the sensor in place. Once the cement was fully dry, the cement was built up to the height of the screws and allowed to fully dry once more. It was ensured that the electrodes were able to stand sufficiently before the sensor was released from the stereotaxic arm. The exposed wires were then orientated so that the gold clips of the electrodes could be manoeuvred easily into the Teflon® pedestal (Plastics One Inc., Virginia, USA.). The placement of the electrodes in the pedestal can be seen in Figure 3.8.4.2 below:

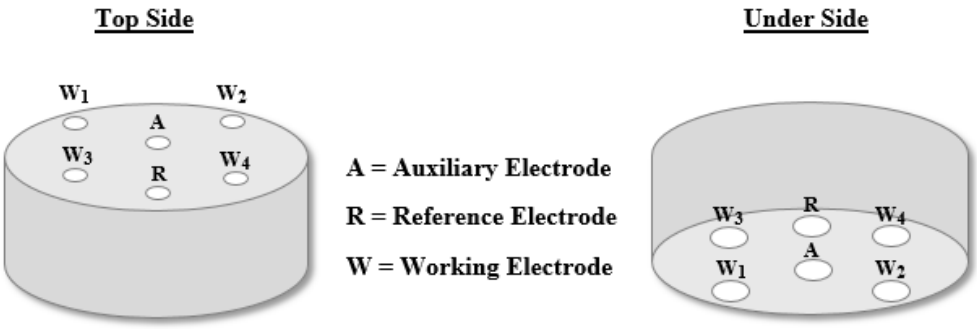

Figure 3.8.4.2: A schematic representation of electrode placement in the pedestal used to connect the electrodes to the potentiostat. The schematic details the holes for the specific electrodes and the hole size difference between the top side and under side of the pedestal.

After placement of the gold clips in the pedestal, cement was placed around the gold clips to anchor them and prevent any movement when the cable was connected to the pedestal. The exposed wires were then twisted and placed down on the skull to allow for the cement to be built up around the wires to protect the electrodes and provide good rigidity to the pedestal. The cement prevents the risk of moisture getting into the electrodes or the animal causing damage to the electrodes during experimentation. It is advised to avoid placing any cement on the bottom of the pedestal as it prevents connection of the cable to twist down onto the pedestal and thus, preventing the best connection to the instrumentation.

Once the surgery was complete, the clamps were removed and the skin around the incision was sutured up around the cement. A suture was placed posterior to the probe placement. Anaesthesia was ceased and the animal was removed from the ear bars and the stereotaxic frame. The animal was placed in a pre-warmed incubator (29 ^{o}C) until it had recovered. A 1 mL/kg injection of 0.9 % saline was administered to the animal to provide rehydration and aid in recovery. The animal was closely monitored in the immediate few hours following surgery. This was to ensure that the animal was not experiencing any pain and was recovering well. If it was thought that the animal was experiencing any discomfort they were administered the opioid analgesic, buprenorphine (0.1 mg/kg) subcutaneously. Once it was deemed that the animal had recovered sufficiently, they were transferred to their recording cage where they remained whilst *in vivo* experiments were being carried out. Once the animal was

well recovered and their weight had stabilised, the animal was connected up and the potential could be applied to the sensors. All sensors were allowed reach a stable baseline before any *in vivo* investigations were carried out.

3.8.5 Surgical Protocol – Microdialysis Implantation

For the implantation of the microdialysis guide cannula, the surgery was similar to the surgery for the transplantation of smNPCs and sensor implantations (Section 3.8.3 and 3.8.4). Microdialysis guide cannulas were implanted at the coordinates listed below (Table 3.8.5.1) in NOD SCID mice and transplanted animals.

Table 3.8.5.1: Stereotaxic coordinates for a microdialysis guide cannula in the striatum of a NOD SCID mouse.

	(A - P)	(M - L)	(D - V)
NOD SCID	+ 0.5	± 2.0	- 3.5
NOD SCID (graft)	+ 0.6	± 1.5	- 3.0

The microdialysis guide cannula was attached to the stereotaxic arm where it was lowered until it reached the skull. Thereafter, the guide cannula was lowered to the relevant D - V coordinate. Once the guide was lowered into position, a thin layer of cement was applied to the skull to ensure the position of the probe was held in place. Before the guide cannula was removed from the stereotaxic arm, the cement was built up to the height of the screws. Furthermore, a tethering system was employed during microdialysis experimentation. Hence, a peg for the tethering system was positioned in between the back screws prior to the cement hardening completely. Following this, the cement was built up around the peg and probe. The animal was sutured at a posterior position to the guide probe to allow the skin to heal around the cement. Once the surgery had concluded, animals were allowed to recover for a period of 3-days before the stylet within the microdialysis guide was replaced for the microdialysis probe (Section 3.9).

3.8.6 *In Vivo* Reference and Auxiliary Electrodes

The figures shown below illustrate the reference (Figure 3.8.6.1) and auxiliary (Figure 3.8.6.2) electrodes used in *in vivo* surgery. The reference and auxiliary electrodes form part of the three-electrode set up *in vivo* and work in the same manner as in *in vitro* experiments. Reference and auxiliary electrodes are manufactured from a Teflon® - insulated silver (Ag) wire (200 µm bare diameter, 200 µm coated diameter, 8T, Science Products GmbH, Hofheim, Germany) which is cut to a length of 4 cm. From one end of the wire, a length of approximately 2 mm of Teflon® was removed. Removal of the Teflon® from one end of this end of the wire allowed for the wire to be soldered into the gold clip. Moreover, the manufacture of the reference electrode involved removal of a 5 mm piece of Teflon® from the other end of the Ag wire. The bare wire was manipulated to form a loop that could rest flush on the skull with the ability for a vertical piece to fit inside the drilled hole and into the brain tissue below (Figure 3.8.6.1).

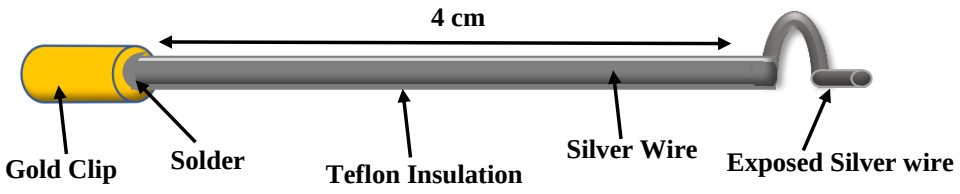

Figure 3.8.6.1: Schematic representation showing an *in vivo* reference electrode.

Furthermore, the auxiliary electrode was constructed by removal of 5 mm of Teflon® from the other end of the wire. This allowed for the wire to be curved around a surgical screw. The screw was soldered to the bare Ag wire to allow for fixation of the screw into position (Figure 3.8.6.2). In addition, both electrodes were strengthened at the meeting of the wire and the gold clip by means of epoxy being placed on top on the solder. This provided strength to the electrodes during handling in surgery.

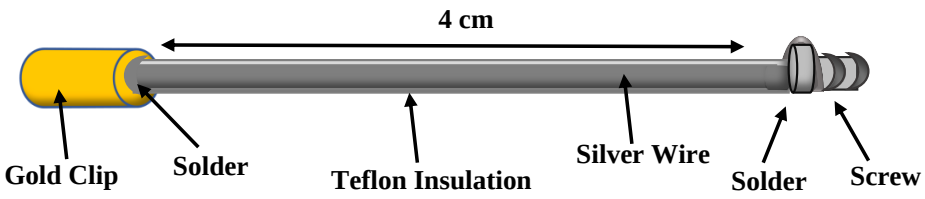

Figure 3.8.6.2: Schematic representation showing an *in vivo* auxiliary electrode.

3.8.7 Continuous Monitoring in Freely-Moving Animals

CPA was used for all *in vivo* investigations in freely-moving animals. All animals were housed in open top recording cages for the duration of the experimentation. In all, there was no more than 5-days continuous recording throughout this project. Following recovery from surgery, the animal was connected to the potentiostat by means of a light weight cable manufactured *in house*. This light weight cable was a bespoke screened four core cable with a six-pin Teflon® socket which was attached to the pedestal. The cable was mounted above the subject's head by means of a swivel slip ring (CPC Farnell, Preston, UK). Additionally, this allowed for free movement of the animal whilst also permitting for continuous recordings to take place. The optimum potential was then applied to the electrodes and currents were allowed to stabilise before any perturbations to the system under investigation were carried out. A settling period of typically 24-hours was chosen.

3.9 Microdialysis

Microdialysis is an efficient sampling technique which enables sampling and quantification of many small molecular weight substances such as neurotransmitters from the ECF of the brain. Microdialysis probes encompass a semi permeable membrane located at the tip. By means of a concentration gradient, analytes can diffuse across the membrane to be collected and analysed (Section 2.7). A major advantage of microdialysis is the ability to measure target analytes in awake and freely-moving animals. In addition, the use of a microdialysis probe allows for pharmacokinetic agents to be delivered to the surrounding ECF in a technique referred to as retromicrodialysis (Section 2.7).

Characterisation studies involving microdialysis sampling were conducted on freely-moving NOD SCID mice using a 0.5 mm sampling membrane. Prior to

connection of the subject to the microdialysis apparatus, it was ensured that all tubing to be used was flushed with Millipore H_2O and aCSF/AA (AA, 0.25 mM). Once complete, the system was flushed using the aCSF/AA solution at a flow rate of 2.0 µL/min using a 1 mL Hamilton syringe (Hamilton Robotics, Bonduz, GR, Switzerland) fixed in the microinfusion pump. Thereafter, the subject was connected to the tether whilst also connecting the inlet tubing and outlet tubing of the microdialysis probe to the apparatus. It was ensured to confirm the flow before returning the subject to the cage. Different flow rates were investigated throughout the characterisation studies, therefore, the flow rate was set at either 0.1 µL, 0.2 µL or 0.5 µL. Following this, collection of samples commenced whereby microdialysate was collected on ice every 60-minutes over 180-minutes. Samples were stored at - 40˚C before shipment to Leiden University for analysis.

Microdialysis sampling conducted in humanised NOD SCID mice involved a microdialysis probe with a 1 mm sampling membrane and connection of the subject to a tether (Instech Laboratories, Pennsylvania, USA), allowing for free movement of the animal throughout experimentation (see Figure 3.9.1). As described for characterisation studies, all tubing to be used was flushed with Millipore H_2O and aCSF/AA (AA, 0.25 mM) with dialysate which was collected for 10-minutes at 10.0 µL/min in a vial before being disposed of. The flow rate was then reduced to 0.5 µL/min and the dialysate was collected for 15-minutes prior to disposal. After this wash-out period, vial # 1 was collected on ice at a flow rate of 0.5 µL/min. Each vial was collected for 10-minute periods to enable a temporal profile to be constructed. The vial was placed in ice following collection before being transferred to the - 40 ºC freezer.

Retromicrodialysis was included in these studies whereby a desired compound was introduced into the Hamilton syringe and delivered to the semi permeable membrane of the microdialysis probe. This allowed for an effect of the introduced selected compound to be analysed accordingly. Changeover of the solutions in the Hamilton syringe had to be completed quickly. The flow was ceased following collection of vial #5 and the inlet tubing was disconnected at the swivel. The syringe was changed to the desired perfusate (100 mM K^+ or 100 µM paraquat) before reconnecting to the inlet tubing. Flow was confirmed by using a flow rate of 10.0 µL/min before reducing the flow to 0.5 µL/min or 2.0 µL/min. Once confirmed, the

tubing was reconnected to the swivel and flow was confirmed at the collection outlet. Sampling was re-established as before following this.

Samples of larger volumes were required for certain analysis procedures. This lead to a small deviation in protocol. Following disposal of the collection of perfusate at 10.0 µL/min for 10 mins, the flow rate was reduced to 2.0 µL/min. Perfusate was thereafter collected on ice for 55-minutes to allow for the collection of ca. 110 µL. Vials were changed every 55-minutes and stored on ice before being transferred to the freezer.

Sampling was usually completed over a 3-hour period. Following completion, the subject was disconnected from the tubing and tether and returned to its home IVC cage. Millipore H_2O was used to flush all tubing and swivels to eliminate any residual salts from blocking the apparatus.

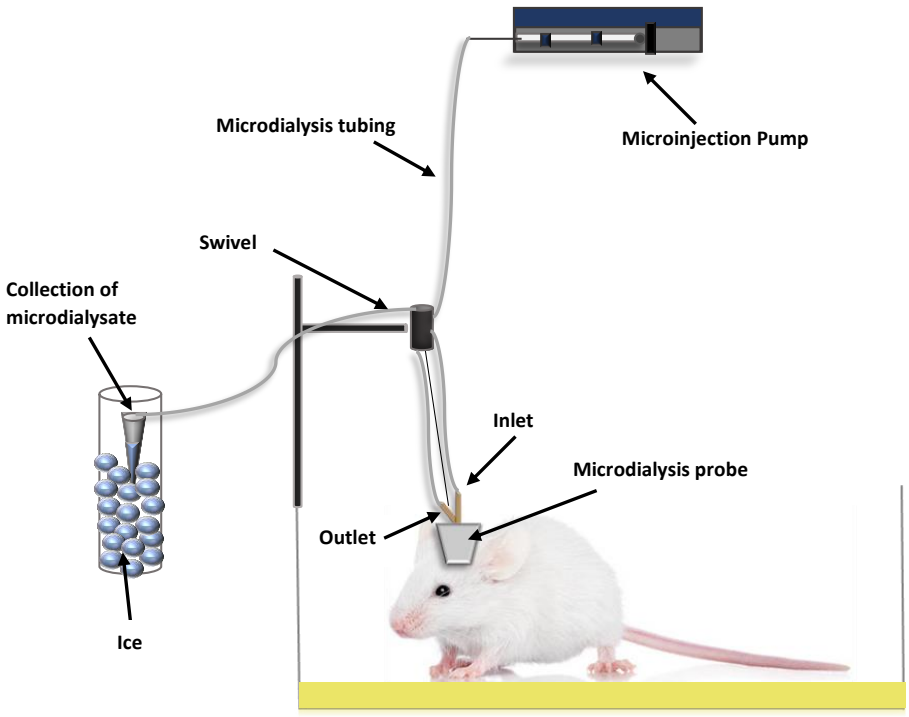

Figure 3.9: Schematic diagram representing the microdialysis sampling set-up.

3.9.1 Local Infusions/Perfusions in Anaesthetised Mice

3.9.1.1 Retroperfusion of H_2O_2

Retromicrodialysis works in a similar manner to microdialysis whereby molecules and analytes can permeate a semi-permeable membrane into the surrounding brain tissue. Microdialysis functions by collecting dialysate, which

contains molecules that have diffused into the microdialysis probe and thus, can be collected for analysis (Section 3.9). Retromicrodialysis differs in that the perfusate can be used to deliver substances to the brain microenvironment which might not otherwise be able to cross the blood brain barrier if administered systemically. Analytes of interest flow down the probe and diffuse across the semi-permeable membrane into the surrounding milieu[24]. Previously, retromicrodialysis has been employed to administer characterisation compounds and selected analytes to the surrounding tissue. The technique of retromicrodialysis has been coupled with an implanted amperometric sensor in freely-moving rats and anaesthetised mice[9,25].

The employment of retromicrodialysis with an implanted amperometric sensors allowed for the characterisation of the H_2O_2 biosensor in the brain of NOD SCID mice. Achievement of the retromicrodialysis construct with the attached amperometric biosensor resulted by aligning each of the electrodes in the H_2O_2 biosensor design to the microdialysis probe. The electrodes were fixed briefly to the probe by means of adhesive to allow for the modified electrode surfaces to be lined up with the sampling membrane of the microdialysis probe. Extreme care was taken not to damage the modified surfaces of each of the electrodes. Fixation of the electrodes to the probe was attained by application of a thin layer of epoxy along the length of the electrode/probe interface. Whilst the construct dried, the tips of the modified electrodes were motioned into the desired position at the sampling membrane (Figure 3.9.1.1.1). The construct was allowed dry before being stored at 4 ºC prior to surgical implantation.

Local perfusions of H_2O_2 (0, 100 µM, 500 µM, 1 mM and 10 mM) and Mercaptosuccinic Acid (MSA, 1 mM) were carried out using the construct following implantation *in vivo*. A syringe pump was used to deliver the perfusate at a flow rate of 1.0 µL/ min for a 20-minute period. It was ensured that there was perfusate exiting the outlet of the probe prior to each perfusion. Moreover, it was ensured currents returned to baseline prior to each administration. This was achieved by leaving an interlude of 15-minutes between each perfusion. Intervals were used to wash out the microdialysis tubing manually of previous concentrations of perfusate. For subsequent perfusions, flow was confirmed by passing the solution through the tubing at a flow rate of 1.0 µL/ min momentarily. Once this was achieved, the probe was reconnected to the inlet of the microdialysis probe. A semi-randomised order was implemented for H_2O_2 perfusions whilst MSA perfusion always followed H_2O_2. Prior to the start of

MSA perfusions, a wash out perfusion was performed for a 5-minute period. The purpose of clearing the microdialysis tubing was to alleviate any outstanding H_2O_2 present within the probe from affecting the result of the MSA administration thereafter.

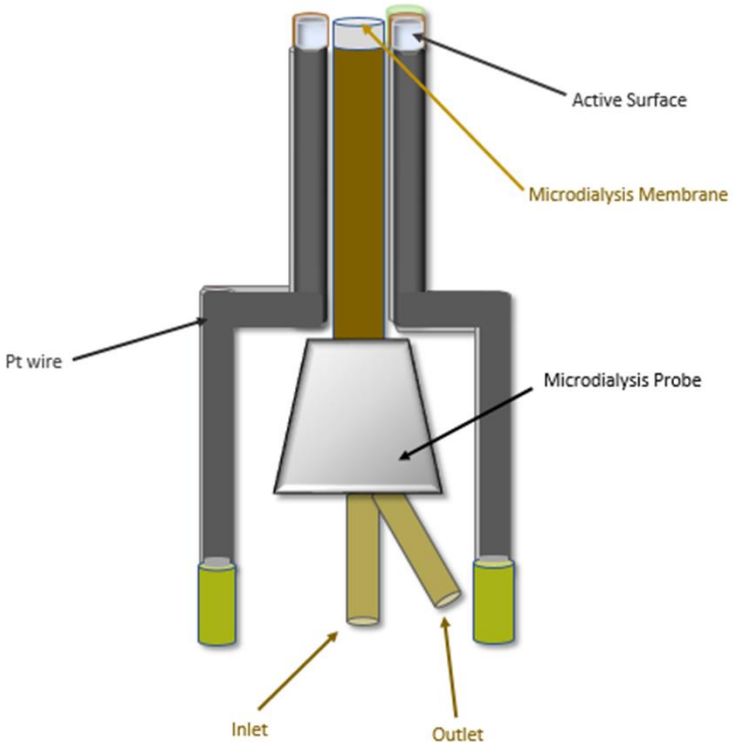

Figure 3.9.1.1.1: Schematic illustration of the H_2O_2 biosensor/microdialysis probe construct.

3.9.1.2 Microinfusion of H_2O_2

Further characterisation studies were carried out by implantation of the H_2O_2 biosensor with the inclusion of a microinfusion probe. The manufacture of a microinfusion probe *in house*, along with the H_2O_2 biosensor, allowed for the ability to evaluate the most proficient method of local delivery of H_2O_2 *in vivo*. The design consisted of a 23G hypodermic needle (Aquilant Analytical Sciences, Dublin, Ireland) which was cut to a length of 2 cm. The rough end of the cut needle was smoothed using a metal file. Through the needle, an 8 cm length of silica tubing (110 µm i.d, 170 µm o.d, Aquilant Analytical Sciences, Dublin, Ireland) was guided until approximately 1 cm and 5 cm lay outside the smoothed and bevelled ends of the needle, respectively. Epoxy was applied at either end of the needle allowing the tubing to be fixed in place. Thereafter, the silica tubing was cut flush to the smooth end of

the needle once the epoxy was firmly dry. At the other bevelled end, the silica tubing was decreased to a length of approximately 2 cm. Flow of aCSF was confirmed through the constructed probe before the probe was fixed to the H_2O_2 biosensor to be implanted. A microdialysis pump was utilised to deliver flow to the microinfusion probe at a flow rate of 0.2 µL/min until the flow was confirmed at the end of the microinfusion tubing. Thereafter, the electrodes of the H_2O_2 biosensor were aligned with the length of silica tubing ensuring that the modified ends of the electrodes were not disturbed. Once aligned, the electrodes were fixed in place by application of epoxy to the electrode/tubing interface. During the drying process, a forceps was employed to manipulate the modified tips of the electrodes in front of the exit point of the silica tubing. Furthermore, the tip of a 1 mL plastic syringe (Aquilant Scientific, Dublin, Ireland) was cut and motioned over the epoxied area until it covered the tip of the bevelled needle. Once it was in place, dental acrylate was deposited into the plastic syringe tip where it was allowed to harden (Figure 3.9.1.2.1). The utilisation of the dental acrylate provided efficient rigidity to the microinfusion construct throughout surgical recordings whereby the practice of attachment and removal of infusion tubing can cause movement of the construct.

Following surgical implantation of the construct, H_2O_2 was locally infused (0, 20 µM, 50 µM, 100 µM, 1 mM and 10 mM), Sodium Azide (SA, 1 mM) and MSA (1 mM). Infusions took place at a flow rate of 0.2 µL/min for a period of 150-seconds. Between each administration, a break of 10-minutes was given to allow currents to return to baseline before the succeeding infusion commenced. The microdialysis tubing was removed throughout this timeframe allowing for the solution to be changed before the next infusion. Additionally, the previous solution was manually flushed out of the tubing allowing for the next solution to be delivered immediately to the target area. The subsequent solution was allowed to flow at a rate of 0.2 µL/min through the tubing. Once the flow was confirmed, the tubing was reattached to the microinfusion probe. A semi-randomised order was incorporated in the microinfusion experimental protocol. In comparison to microdialysis experiments, all SA and MSA investigations were carried out following conclusion of H_2O_2 infusions. Preceding SA/MSA infusions, a wash out perfusion of aCSF was infused for a period of 150-seconds to eliminate any remaining H_2O_2 existing in the probe resulting from previous infusions.

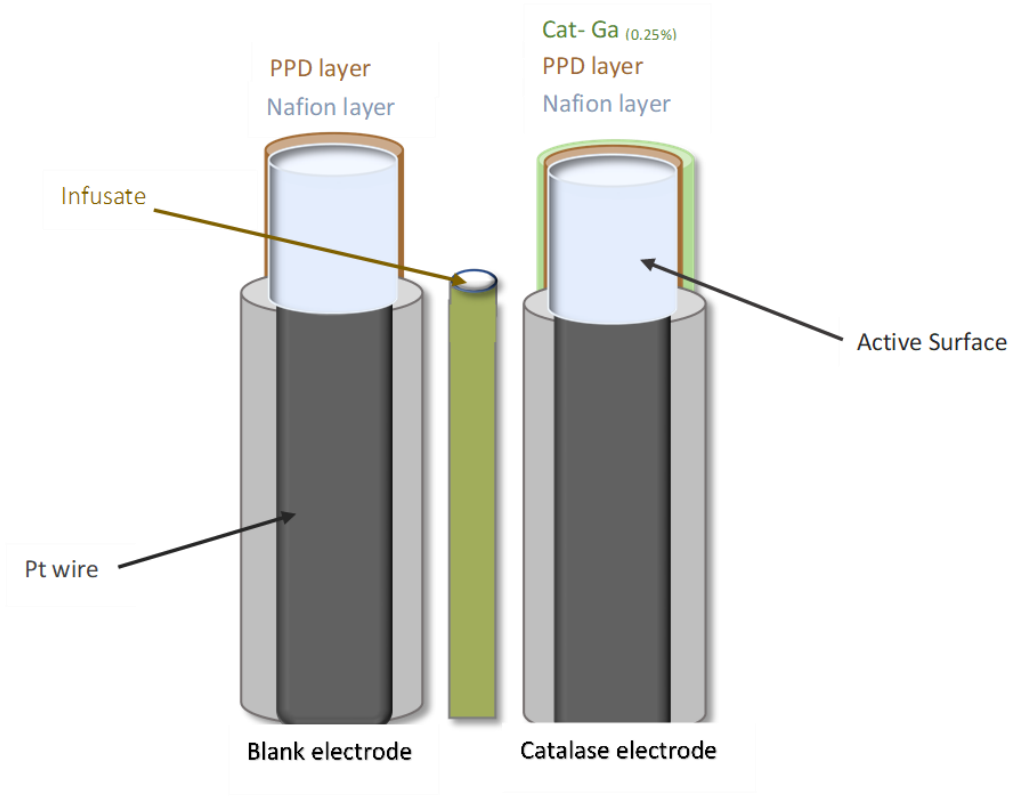

Figure 3.9.1.2.1: Schematic illustration of the H_2O_2 biosensor/microinfusion probe construct.

3.10 *In Vivo* Injections and Physiological Stimuli

3.10.1 Intraperitoneal Injections (i.p. injections)

Intraperitoneal injections were administered to the animal at a 45 º angle to the body, into the lower caudal right or left quadrant of the ventral abdomen. This ensured avoidance of all vital organs. Subjects were held on their back so it was securely supported. The needle was inserted into one of the lower quadrants to a depth of a few millimetres so to penetrate the body wall. The injection was given swiftly to reduce any stress to the animal and the absorption of the target substance is rapid[18].

3.10.2 Subcutaneous Injections (s.c. injections)

Subcutaneous injections were administered to the animal into the scruff of the neck by lifting a fold of skin and injecting the needle into the fold parallel to the body of the animal. This allows for the avoidance of the tissues beneath[18].

3.10.3 Restraint test

Restraint tests are used primarily as a psychological stressor in subjects. It works by restricting the free movement of the animal which induces neuronal activation in the animal during *in vivo* experiments[26]. The animal is held in position using one hand for a period of 2-minutes. As the movement of the animal has been restricted, an increase in stress and anxiety is observed. Whilst being restricted, the animal tries to free itself so a firm hold is required. However, great care is required to avoid injury to the animal during the restraint. Following the two minute period, the animal was released and behaviour returns to normal within a few minutes.

3.11 Fixation of Striatal Tissue for Quantitative Analysis

Euthanasia was carried out by cervical dislocation following completion of *in vivo* investigations on non-humanised NOD SCID mice. For humanised mice transplanted with non-GFP labelled cells, euthanasia was performed using transcardial perfusion which is further discussed in Section 3.11.1 below. For brains that were fixed by transcardial perfusion, the brain was removed and placed in 4 % paraformaldehyde overnight before being placed in PBS to facilitate histology studies in the University of Luxembourg. Humanised mice transplanted with GFP-labelled cell lines were euthanised by cervical dislocation followed by SNAP freezing of the brain (Section 3.11.2). SNAP frozen brains were stored in dry ice being transported to the University of Luxembourg for transcriptomic and metabolomic analysis.

3.11.1 Transcardial Perfusion

Humanised animals that required cranial IHC analysis were transcardially perfused to allow for fixation of the relevant brain region. Once experimentation was complete, animals were anaesthetised intraperitoneally with Ketamine (100 mg/kg) and Dormitor (5 mg/kg) at a dose of 10 mL/kg. Confirmation that the subject was deeply anaesthetised was observed by carrying out a paw reflex test and the presence of a corneal response. Subsequently, the animal was placed on the top of metal grid placed on top of an open Perspex container. The forelimbs and back limbs were fixed in placed to allow for the chest area of the animal to be outstretched. Following this, the mid chest area was cut open in a caudal rostral direction to the sternum and along the side of the rib cage. The sternum and front of the rib cage were secured using a

forceps to reveal the internal chest area. Once the heart was exposed, the left ventricle was pierced with a 21G microneedle (Sarstedt, Germany). The left atrium was perfused with PBS. The right atrium of the heart was then slit and PBS was perfused through the blood vessels at a steady rate until 50 mL of PBS had been perfused. Confirmation that the procedure was successful was determined by a loss of colour in the vessels in the chest wall followed by a discolouration of the organs in the chest cavity. Following the cessation of PBS perfusion, a 4 % paraformaldehyde fixative solution was perfused at a steady rate until 50 mL of fixative had been administered. The hardening of the limbs and a rise in the tail signalled success of the perfusion. After the perfusion, rapid removal of the brain took place. The brain was placed in 4 % paraformaldehyde overnight. The paraformaldehyde solution was changed for PBS solution the following day before the tissue was transported to Luxembourg for analysis.

3.11.2 SNAP Freezing

Transplanted grafts containing GFP-labelled cells were required for metabolomic and transcriptomic analysis. Following an *in vivo* integration period of seven weeks, transplanted brain tissue was SNAP frozen. Firstly, subjects were euthanised by cervical dislocation before the brain was quickly removed from the skull. Both brain hemispheres were separated using a sterile scalpel blade before dissecting the hemispheres further to allow for isolation of the area containing the transplanted cells. Following removal, the brain was placed in an Eppendorf tube and submerged in liquid nitrogen for 5-minutes. The Eppendorf tube was stored on dry ice thereafter before being transported to Luxembourg for subsequent analysis.

3.12 Immunofluorescent Imaging, Metabolomic and Transcriptomic Analysis of Striatal Transplants of Human Dopaminergic Neurons

Once the transplanted NOD SCID mouse brain tissue had been either fixed by transcardial perfusion or SNAP frozen, it was sent to the University of Luxembourg for immunofluorescence staining of transplanted tissue, coupled with, sorting of the transplanted cells by FACS with transcriptomics and metabolomics. Such analysis was

needed to examine any phenotypic differences associated with the cells transplanted from healthy individuals and PD patients.

3.13 Supplementary Equipment

3.13.1 *In Vitro* Equipment

Air pump

The air pump employed in O_2 calibrations was a Rena® 50 air pump (Rena®, France).

Electronic Balance

The electronic balance employed throughout this project was a three decimal MH 214 from Fisher Scientific, Ireland.

Electrode wire

Pt wire was acquired from Science Products (Hofheim, Germany). All Ag wire was obtained from Advent Research Materials (Oxford, UK).

Magnetic Stirrer

The Magnetic stirrer was a HI 190M obtained from Hanna Instruments, Farnell, Dublin 2, Ireland.

Microscope

The microscope used throughout the manufacture and design of the sensors was the stereomicroscope SZ51 from Olympus America Inc. The microscope for *in vivo* stereotaxic surgeries was an Olympus SZ61 from Olympus America Inc.

Oven

For the manufacture of NO sensors, Nafion® was annealed onto the surface of the electrode by using a Memmert UFE 400 from Memmert GmbH, Schwabach, Germany.

pH meter

A Jenway 350 pH meter was used in obtaining an accurate pH for the relevant solutions.

Sonicator

The sonication of solutions was facilitated by filling the sonicator up to the optimum level with deionised water before placing the round bottom flask or volumetric flask in the bath for the required time. The sonicator was a Fisher brand FB15048, Leicestershire, UK.

3.13.2 *In Vivo* Equipment

Anaesthesia System

The anaesthesia system used for all stereotaxic surgeries was a Univentor 400 Anaesthesia unit which comprised of a vaporiser for induction. A Rena® Air 50 (Rena® France) was the air pump utilised with the system. The induction chamber employed had a volume of 1.4 L. All apparatus was supplied from Agnthos, Lidingö, Sweden.

Incubator

An incubator was used following surgery to allow the animal to recover at 29 ºC until recovered. The incubator used was a Thermacage MK3 obtained from Datesand, UK.

Microdialysis Probes

Microdialysis Probes used for Microdialysis investigations had a 0.5 mm/1 mm semi-permeable membrane and were sourced from BASi, Indiana, USA.

Microdialysis Pump

The pump used for microdialysis experiments was a Univentor 801 microdialysis syringe pump obtained from Agnthos, Lidingö, Sweden.

Stereotaxic Frame

For all stereotaxic surgeries, a Stoelting stereotaxic frame (Illinois, USA) was used to fix animals in the correct position allowing for the accurate coordinates to be obtained for sensor implantation.

Water Bath

For incubation of N2B27 medium during smNPC transplantations, a Grant Sub Aqua 5 water bath was employed.

3.14 References

1. Bolger, F., Bennett, R. & Lowry, J. An in vitro characterisation comparing carbon paste and Pt microelectrodes for real-time detection of brain tissue oxygen. *Analyst* **136,** 4028–35 (2011).
2. Bolger, F. B. & Lowry, J. P. Brain tissue oxygen: In vivo monitoring with carbon paste electrodes. *Sensors* **5,** 473–487 (2005).
3. Bolger, F. B., McHugh, S. B., Bennett, R., Li, J., Ishiwari, K., Francois, J., Conway, M. W., Gilmour, G., Bannerman, D. M., Fillenz, M. & Tricklebank, M. Characterisation of carbon paste electrodes for real-time amperometric monitoring of brain tissue oxygen. *J. Neurosci. Methods* **195,** 135–42 (2011).
4. Finnerty, N. J., O'Riordan, S. L., Pålsson, E. & Lowry, J. P. Brain nitric oxide: Regional characterisation of a real-time microelectrochemical sensor. *J. Neurosci. Methods* **209,** 13–21 (2012).
5. Finnerty, N. J., O'Riordan, S. L., Brown, F. O., Serra, P. A., O'Neill, R. D., Lowry, J. P. In vivo characterisation of a Nafion®-modified Pt electrode for real-time nitric oxide monitoring in brain extracellular fluid. *Anal. Methods* **4,** 550 (2012).
6. Wynne, A. M., Reid, C. H. & Finnerty, N. J. In vitro characterisation of ortho phenylenediamine and Nafion®-modified Pt electrodes for measuring brain nitric oxide. *J. Electroanal. Chem.* **732,** 110–116 (2014).
7. O'Riordan, S. L., McLaughlin, K., Lowry, J. P. In vitro physiological performance factors of a catalase-based biosensor for real-time electrochemical detection of brain hydrogen peroxide in freely-moving animals. *Anal. Methods* **8,** 7614–7622 (2016).
8. O'Brien, K. B., Killoran, S. J., O'Neill, R. D. & Lowry, J. P. Development and characterization in vitro of a catalase-based biosensor for hydrogen peroxide monitoring. *Biosens. Bioelectron.* **22,** 2994–3000 (2007).
9. O'Riordan, S.L., Lowry, J. P. In vivo characterisation of a catalase-based biosensor for real-time electrochemical monitoring of brain hydrogen peroxide in freely-moving animals. *Anal. Methods* **9,** 1253–1264 (2017).
10. Brown, F. O., Finnerty, N. J., Bolger, F. B., Millar, J. & Lowry, J. P. Calibration of NO sensors for in-vivo voltammetry: laboratory synthesis of NO and the use of UV-visible spectroscopy for determining stock concentrations. *Anal.*

Bioanal. Chem. **381,** 964–971 (2005).

11. Brown, F. O., Finnerty, N. J. & Lowry, J. P. Nitric oxide monitoring in brain extracellular fluid: characterisation of Nafion®-modified Pt electrodes in vitro and in vivo. *Analyst* **134,** 2012–20 (2009).
12. Lowry, J. P., Boutelle, M. G. & Fillenz, M. Measurement of brain tissue oxygen at a carbon paste electrode can serve as an index of increases in regional cerebral blood flow. *J. Neurosci. Methods* **71,** 177–182 (1997).
13. Garjonyte, R. & Malinauskas, A. Amperometric glucose biosensor based on glucose oxidase immobilized in poly o -phenylenediamine / layer. *Sensors Actuators B Chem.* **56,** 85–92 (1999).
14. McConnell, G. C., Rees, H. D., Levey, A. I., Gutekunst, C. A., Gross, R.E. & Bellamkonda, R. V. Implanted neural electrodes cause chronic, local inflammation that is correlated with local neurodegeneration. *J. Neural Eng.* **6,** (2009).
15. Miele, M. & Fillenz, M. In vivo determination of extracellular brain ascorbate. *J. Neurosci. Methods* **70,** 15–19 (1996).
16. Rice, M. E. Ascorbate compartmentalization in the CNS. *Neurotox Res* **1,** 81–90 (1999).
17. Kotanen, C. N., Moussy, F. G., Carrara, S. & Guiseppi-Elie, A. Implantable enzyme amperometric biosensors. *Biosens. Bioelectron.* **35,** 14–26 (2012).
18. Wolfensohn, S., Lloyd, M. *Handbook of Laboratory Animal Management and Welfare.* (Wiley-Blackwell, 2013).
19. Reinhardt, P., Glatza, M., Hemmer, K., Tsytsyura, Y., Thiel, C.S., Höing, S., Moritz, S., Parga, J.A., Wagner, L., Bruder, J. M. & Wu, G. Derivation and Expansion Using Only Small Molecules of Human Neural Progenitors for Neurodegenerative Disease Modeling. *PLoS One* **8,** (2013).
20. Hemmer, K., Smits, L. M., Bolognin, S. & Schwamborn, J. C. In vivo phenotyping of Parkinson-specific stem cells reveals increased a-Synuclein levels but no spreading. (2017).
21. Han, D. W., Tapia, N., Hermann, A., Hemmer, K., Höing, S., Araúzo-Bravo, M.J., Zaehres, H., Wu, G., Frank, S., Moritz, S. & Greber, B. Direct reprogramming of fibroblasts into neural stem cells by defined factors. *Cell Stem Cell* **10,** 465–472 (2012).
22. Hemmer, K., Zhang, M., van Wüllen, T., Sakalem, M., Tapia, N., Baumuratov,

A., Kaltschmidt, C., Kaltschmidt, B., Schöler, H. R., Zhang, W. & Schwamborn, J. C. Induced neural stem cells achieve long-term survival and functional integration in the adult mouse brain. *Stem Cell Reports* **3,** 423–431 (2014).

23. Franklin, K., Paxinos, G. *The Mouse Brain in Stereotaxic Coordinates*. (Academic Press, 2008).
24. Höcht, C., Opezzo, J. A. W. & Taira, C. A. Applicability of reverse microdialysis in pharmacological and toxicological studies. *J. Pharmacol. Toxicol. Methods* **55,** 3–15 (2007).
25. Reid, C. H. & Finnerty, N. J. Real-time amperometric recording of extracellular H_2O_2 in the brain of immunocompromised mice: An in vitro, ex vivo and in vivo characterisation study. *Sensors (Switzerland)* **17,** (2017).
26. Cloutier, M., Bolger, F. B., Lowry, J. P. & Wellstead, P. An integrative dynamic model of brain energy metabolism using in vivo neurochemical measurements. *J. Comput. Neurosci.* **27,** 391–414 (2009).

Chapter 4

In Vitro Investigations

4.1 Introduction

Chapter 4 is associated with validating previously characterised amperometric sensors to ensure replication of previously published performance criteria prior to their ultimate application in the striatum of NOD SCID mice[1–10]. The sensors in question are the NO sensor, O_2 sensor and the H_2O_2 biosensor [1,6–8,11,12]. Each of these sensors have been previously characterised, however, it is of vital importance to demonstrate efficient sensitivity, selectivity and stability of each of the aforementioned sensors *in vitro* before being applied to *in vivo* studies.

Primarily, an electrochemical sensor must be sensitive enough to measure an analyte of interest. Sensor sensitivity can be optimised by modification of the electrode surface. Equally, if sensor sensitivity is enhanced, it is imperative to ensure the selectivity of the sensor is retained due to a vast abundance of electroactive interfering species present in the *in vivo* environment. For example, Nafion® is included in the NO sensor design. Nafion® is an ion exchange polymer consisting of a hydrophobic polytetrafluoroethylene (PTFE) backbone. Regularly spaced along the backbone are small portions of hydrophilic perfluorovinyl ether pendant side chains terminating in sulfonic or carboxylic ionic functional groups[13–15]. Sulfonate groups, that are negatively charged, work to eliminate the detection of negatively charged species but allow for the passage of neutral species, such as NO, to reach the electrode surface[16]. Thus, Nafion® works to eliminate the detection of electroactive interferents whilst improving the detection of NO.

Extensive characterisation of the NO sensor has been previously conducted for the amperometric detection of NO *in vitro*[6,10,11] and *in vivo*[4,5,10,17,18]. However, it was imperative to ensure validation of the *in vitro* properties of the NO sensor prior to deployment in NOD SCID mice. Previous investigations have confirmed the selectivity of the NO sensor. Negligible responses of a host of interfering species were recorded to be < 1 % including ascorbic acid (AA), uric acid, serotonin, DOPAC, 5-HIAA, dopamine, L-glutathione, homovanillic acid, nitrite and H_2O_2. More recently, gaseous transmitters, hydrogen sulfide and carbon monoxide, have been identified as potential interferents *in vivo*. Additional studies reported a < 1 % contribution of a physiological concentration of hydrogen sulfide recorded on the NO sensor. The detection of carbon monoxide (CO) was slightly higher. However, the contribution of CO resulted in only ca. 2 % of the overall NO signal[11].

Clark-type electrodes remain one of the most common techniques in the detection of O_2 *in vivo* since they were first employed in the voltammetric detection of molecular O_2 in the brain in the 1950s[19]. Pt electrodes are commonly employed in the manufacture of Clark-type electrodes. However, bare Pt electrodes are commonly subjected to biofouling *in vivo* making CPEs the electrode of choice for the amperometric detection of O_2 in the mammalian brain[1]. Previous works have included data based on the *in vitro* measurement of O_2 at bare Pt disk electrodes and CPEs with a 1 mm and 2 mm cavity packed with carbon paste followed by their subsequent implantation in wistar rats[1,3,12]. Additionally, negligible responses for a variety of endogenous interferents have been recorded previously for the CPEs[1,12]. CPEs demonstrated < 1 % contribution of AA, uric acid, homovanilic acid, DOPAC, dopamine, serotonin and 5-HIAA, as well as, other electroactive species including L-cysteine, L-glutathione, L-trytophan, L-tyrosine and dehydroascorbic acid. CPEs demonstrate excellent selectivity which can be attributed to the negative potential applied to the CPE during electrochemical measurements. Therefore, the detection of these species is not a major concern.

Presently, CPEs have never been utilised in immunocompromised mice. With this in mind, it was hypothesised if the size of the CPEs could be reduced. It would be beneficial to use a smaller CPE to reduce damage to surrounding tissue during implantation[20,21]. The design for a smaller CPE would consist of Ag wire with a reduced outer diameter of 177 µm containing a 0.5 mm cavity packed with carbon paste to increase the efficiency of electron transfer from the point of the redox reaction on the sensor surface to the metal transducer of the sensor. Thereafter, studies were conducted to confirm a suitable sensitivity range for O_2 detection (Section 3.6.2.3) as a sensor of these dimensions had not been previously characterised.

The purpose of *in vitro* investigations conducted on the previously characterised H_2O_2 biosensor design was to validate performance and reproducibility in *in vitro* amperometric recordings[7,22]. The H_2O_2 biosensor is a complex dual electrode design. The dual biosensor design consists of a H_2O_2 detection component (blank electrode) and a H_2O_2 removal component (catalase electrode) which acts as a sentinel electrode in this construct. Once the selectivity of the blank and catalase electrodes are matched, subtraction of the current measured at the catalase electrode from that recorded at the blank electrode allows for accurate detection of H_2O_2 to be accomplished by removal of any contribution from interfering species *in vivo.*

Previous studies conducted by O'Brien *et al.* have demonstrated a negligible response of the H_2O_2 biosensor to a host of interfering species at physiological concentrations. These inferences included AA, dopamine, DOPAC, uric acid, L-glutathione, L-trytophan, L-tyrosine, L-cysteine, serotonin, 5-HIAA and homovanillic acid[8]. Therefore as the overall biosensor design relies on the ability to efficiently reject contribution from interfering species, it is imperative to test each modification component *in vitro* to enable maximum performance of the dual biosensor design in terms of sensitivity and selectivity to allow for *in vivo* application. In addition, the stability of each of the electrodes in the dual electrode design must be investigated to ensure retention of sensitivity and selectivity parameters primarily to allow for reliable recording of fluctuations of H_2O_2 *in vivo*. Moreover, it is also important to examine if the immobilised enzyme contained on the surface of the catalase electrode will remain intact following *in vivo* implantation as the incorporation of catalase is a critical component of the overall dual biosensor design.

Additionally, sensocompatibility investigations were included to mimic the hostile biological milieu of the brain *ex vivo*. The brain is a complex network containing many proteins and lipids that act upon the sensor following implantation and thus, decrease the performance of the sensor[23]. Biological tissue surrounding the implanted sensor can react physiologically to this foreign body and adhere to it, leading to a reduction in the mass transport of the analyte of interest to the electrode surface[24,25]. Therefore, it is of crucial importance to study this phenomenon to ensure that the properties of the sensor can be maintained *in vivo*. Although an exact representation of the *in vivo* environment cannot be recreated *in vitro*, brain tissue homogenate can be used to mimic said environment.

In conclusion, the main objective of this chapter was to replicate the manufacture of each of the aforementioned sensor types. Succeeding examination of the sensitivity, selectivity and sensocompatibility of each of the sensors, validation of the most successful manufacture protocol for these sensors will be concluded to allow for the determination of the neurochemical monitoring of NO, O_2 and H_2O_2 in the striatum of immunocompromised NOD SCID mice.

4.2 Experimental

Section 3.2 highlights all of the instrumentation and software employed. The solutions and chemicals are described in Section 3.3. Section 3.4.2 - 3.4.4 details the manufacture of all the sensors utilised for *in vitro* investigations. *In vitro* recordings were all conducted in a standard three-electrode glass electrochemical cell containing 20 mL of phosphate buffer saline (PBS, pH 7.4).

For NO experiments, a working potential of + 900 mV *vs*. SCE was applied. Aliquots of NO, synthesised *in house* (Section 3.7), were added to the electrochemical cell to allow for NO calibrations to be conducted (Section 3.6.2.2). Subsequent AA calibrations were carried out on the sensor following NO calibrations to confirm selectivity (Section 3.6.2.1).

For O_2 calibrations, a working potential of - 650 mV *vs.* SCE was applied to the sensor. To ensure sensitivity of the CPE for O_2 detection, a three-point calibration was used. This involved introduction of various amounts of O_2 to the electrochemical cell (Section 3.6.2.3). Analysis involved measuring the current under quiescent conditions so regression analysis data could be achieved.

H_2O_2 investigations were conducted at a potential of + 700 mV *vs.* SCE. Aliquots of H_2O_2 (Section 3.6.2.4) were added to the electrochemical cell to confirm sensitivity of the electrode. Selectivity of the biosensor was tested by AA calibrations (Section 3.6.2.1) being conducted.

All data presented is as mean ± SEM, where *n* denoted the number of electrodes. Due to the linearity of the calibration plots obtained, the slopes (nA/µM) for O_2 and H_2O_2 and (pA/µM) for NO, are representative of the sensitivity of the relative sensor. The r^2 value represents the linearity of the calibration plot obtained. Statistical analysis involved carrying out paired and unpaired *t*-tests, in addition to, one-way ANOVA analysis. Statistical analysis tests were completed using GraphPad Prism® version 5.0 (GraphPad Prism® Software Inc., California, USA) which resulted in a *p*-value being obtained. *p*-values indicate the probability of the results being significantly different. The level of significance is denoted by the number of asterisks assigned to the value.

4.3 Results and Discussion

4.3.1 *In Vitro* Validation of the NO Sensor

4.3.1.1 NO Sensitivity Investigations

For NO *in vitro* calibrations, an excellent linear response was achieved (r^2 = 0.99, Figure 4.3.1.1.1 *inset*). Table 4.3.1.1.1 displays the results obtained for *in vitro* experiments. Furthermore, a sensitivity of 1331 ± 34 pA/µM (*n* = 53) was recorded over a physiological concentration range of 0 - 1 µM[26,27]. Hence, these results demonstrate excellent sensitivity of the NO sensor for the detection of NO. In addition, the obtained results are comparable to previous characterisation studies[6,10,11]. Furthermore, the excellent sensitivity of this NO sensor can be attributed to the high proton conductivity of the Nafion® membrane due to the presence of hydrophilic perfluorinated side chains in the polymer matrix[14–16]. Moreover, the presence of the negatively charged sulfonate groups act to stabilise the presence of the nitrosonium ion (NO^+) preventing the accumulation on the electrode surface following oxidation of NO and thus, working to increase the detection of NO[28].

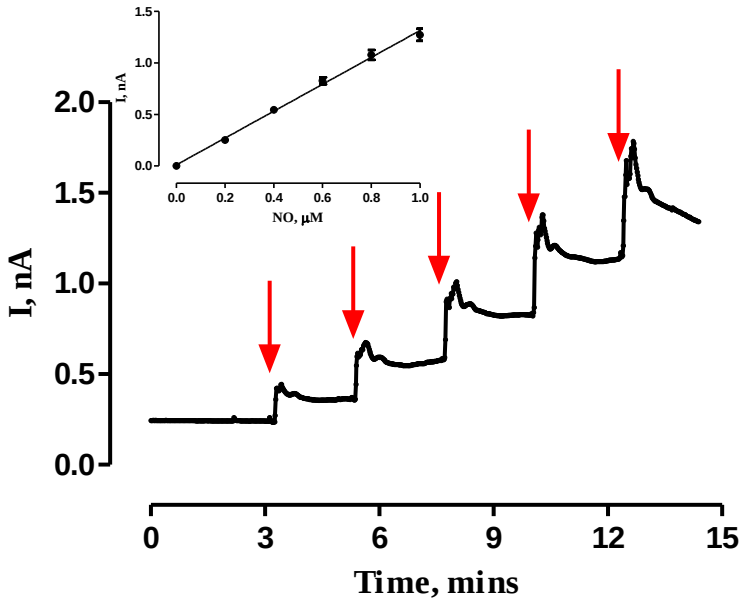

Figure 4.3.1.1.1: Typical *in vitro* data trace recorded using Nafion®-coated Pt disk sensors following addition of 0 to 1 µM NO. Red arrows indicate the addition of aliquots of 0.2 µM NO. *Inset*: Current concentration profile for NO calibration on Nafion®-coated Pt disk electrodes (*n* = 53), r^2 = 0.99.

Table 4.3.1.1.1: Average NO responses recorded over a 0 to 1 µM concentration range of NO using Nafion®-coated Pt disk electrodes, *n* = 53, carried out at + 900 mV *vs.* SCE. Background values are subtracted.

Nafion®-coated Pt disk sensor (*n* = 53)		
NO, µM	**Mean I, pA**	**SEM**
0.0	0	0
0.2	246	11
0.4	538	21
0.6	827	32
0.8	1095	43
1.0	1297	50

4.3.1.2 Selectivity Investigations on the NO sensor

Selectivity properties of the NO sensor were examined prior to *in vivo* implantation. Thus, the selectivity of the NO sensor was validated by observing the effect of 0 - 1000 µM AA on the recorded current (Figure 4.3.1.2.1). AA was chosen to determine the selectivity of the NO sensor due to the wide oxidation potential it possesses and the high abundance of AA present in the brain ECF[29,30]. As a result, it presents the greatest threat to implanted sensors in terms of interference amongst all the electroactive species present *in vivo*.

Following the addition of 1000 µM AA (*n* = 53), a mean current of 30 ± 11 pA was recorded (Table 4.3.1.2.1). Therefore, the efficiency of the Nafion® membrane to reject the most copious electroactive interferent present in the brain ECF has been achieved. Previous studies have documented that the presence of SO_3^- groups in the polymer matrix which work to exclude anions, e.g. AA, in the surrounding environment by electrostatic repulsion whilst allowing for neutral species to pass through the membrane[31].

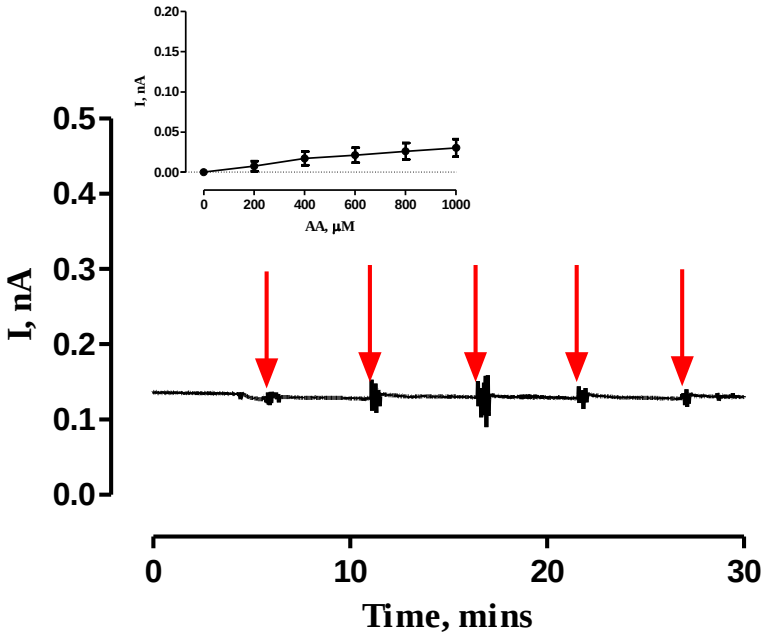

Figure 4.3.1.2.1: Typical *in vitro* data recorded on a Nafion® coated Pt electrode over a 0 - 1000 µM AA calibration. Red arrows indicate the addition of 200 µM aliquots of AA. *Inset*: Current concentration profile for AA calibration on Nafion® coated Pt disk sensors (*n* = 53) at + 900 mV *vs.* SCE.

Table 4.3.1.2.1: Average AA responses recorded over a 0 to 1000 µM concentration range using Nafion® coated Pt disk electrodes, *n* = 53, carried out at + 900 mV *vs.* SCE. Background values are subtracted.

Nafion® coated Pt disk sensor (*n* = 53)		
AA, µM	**Mean I, pA**	**SEM**
0	0	0
200	8	6
400	17	8
600	21	9
800	26	10
1000	30	11

For comparison, AA calibrations were conducted on bare Pt disk electrodes to highlight the efficiency of Nafion® in preventing the detection of interfering species.

Figure 4.3.1.2.2 illustrates the contribution of a 0 - 1000 µM AA calibration carried out on bare Pt disk electrodes with an excellent linear response achieved, r^2 = 0.99. The mean current recorded following the addition of 1000 µM AA was 26 ± 1 nA (*n* = 16, Table 4.3.1.2.2). As referred to previously, the mean current obtained following a 1000 µM AA on the Nafion®- coated Pt electrodes was 30 ± 11 pA (*n* = 53) indicating that a thousand-fold difference exists between $I_{1000\ \mu M}$ values obtained on bare Pt disk electrodes and Nafion®-coated Pt electrodes. Therefore, this clearly shows that the incorporation of Nafion® at the electrode surface effectively negates the detection of interfering species.

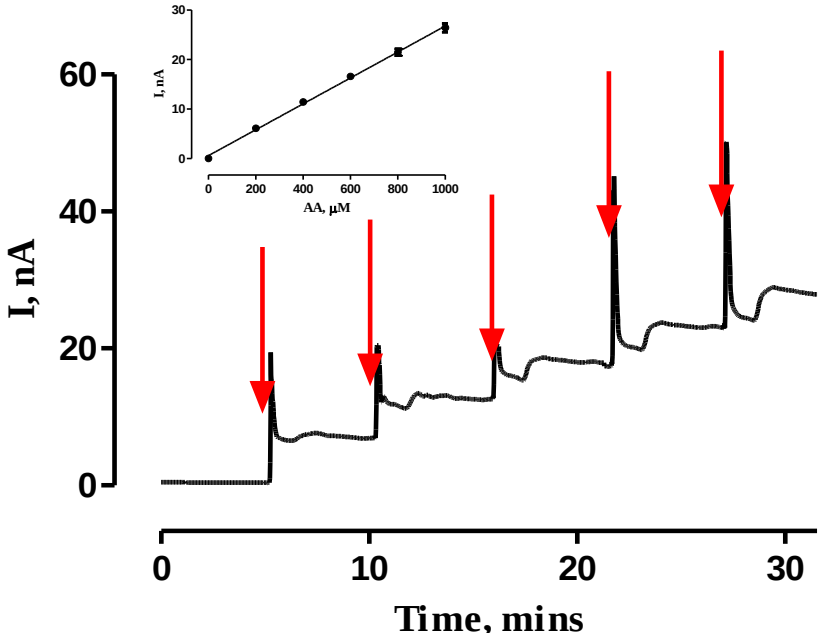

Figure 4.3.1.2.2: Typical *in vitro* data recorded on a bare Pt disk electrode over a 0 - 1000 µM AA calibration range. Red arrows indicate the addition of 200 µM aliquots of AA. *Inset*: Current concentration profile for 0 - 1000 µM AA calibration on bare Pt disk sensors (*n* = 16) at + 700 mV *vs.* SCE, r^2 = 0.99.

Table 4.3.1.2.2: Average AA responses recorded over a 0 to 1000 µM concentration range using bare Pt disk electrodes, *n* = 16, carried out at + 700 mV *vs.* SCE. Background values are subtracted.

Bare Pt disk sensor (*n* = 16)		
AA, µM	**Mean I, nA**	**SEM**
0	0	0.0
200	6	0.2
400	11	0.4
600	17	0.5
800	21	0.7
1000	26	0.9

4.3.1.3 Ex Vivo Sensocompatibility of the NO sensor

Ex vivo sensocompatibility studies were conducted to investigate the sensitivity and selectivity of the NO sensor following exposure to homogenised brain tissue. *Ex vivo* studies work to mimic the brain environment, therefore, giving an understanding of how the sensor will function following implantation. Figure 4.3.1.3.1 illustrates the sensitivities of the NO sensor that were obtained during *ex vivo* studies. The sensitivities on Day 0 are represented as 100 %. The sensitivities recorded on each subsequent day were taken as a percentage of Day 0. A significant difference in the sensitivity of the NO sensor was demonstrated ($p < 0.0001$, one-way ANOVA, $n = 4$) over Day 1 (121.0 ± 7.4 %), Day 3 (57.4 ± 5.8 %), Day 7 (59.7 ± 2.9 %) and Day 14 (56.6 ± 5.2 %). A drop in sensitivity of approximately 50 % was only observed following Day 3. This drop in sensitivity can be attributed to exposure of the NO sensor to brain tissue. However, it is normal to experience a 20 - 50 % loss in sensitivity following initial exposure of the sensor to biological tissue as a result of brain tissue adhering to the electrode surface limiting the amount of available active surface[32,33]. Moreover, by means of Bonferroni *post hoc* analysis, a significant difference was observed between Day 1 and Day 14 ($p < 0.0001$). However, sensitivity does not decrease significantly after Day 3 with no significant difference observed between Day 3 & 7 ($p = 0.33$) and Day 3 & 14 ($p = 0.12$).

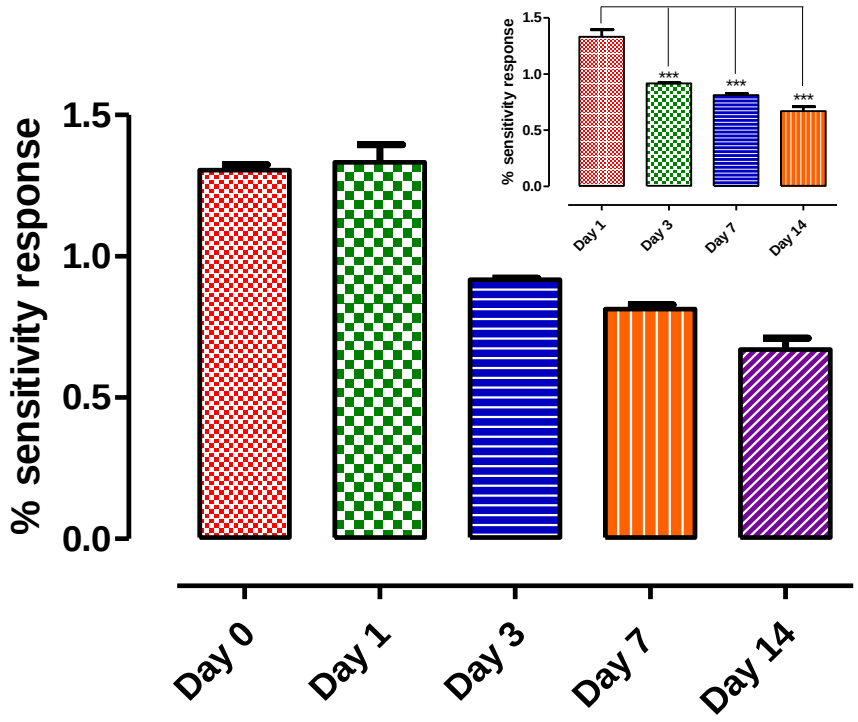

Figure 4.3.1.3.1: Comparison of the effect of *ex vivo* homogenised brain tissue exposure on NO sensor sensitivity calibrated on Day 0, 1, 3, 7 and 14 (one-way ANOVA, *n* = 4) PBS (pH 7.4) at + 900 mV vs. SCE. *Inset*: Bonferroni *post hoc* analysis. Data represented as mean ± SEM.

Following investigations into the effect of brain tissue on the sensitivity of the NO sensor, selectivity properties were subsequently examined. It is vital to ensure that the interference rejection layer is maintained to allow for reliable *in vivo* recordings to be undertaken. AA calibrations were performed on the NO sensor following brain tissue exposure to attain currents at 400 µM and 1000 µM AA. These values were presented as a percentage of the corresponding pre-implantation currents (Day 0). As with sensitivity studies, Day 0 is given as a 100 % with the subsequent days taken as a percentage of Day 0. No significant difference in the characteristics of the permselective rejection membrane at 400 µM AA ($p > 0.05$, one-way ANOVA, $n = 4$) is illustrated in Figure 4.3.1.3.2 over Day 1 (124.7 ± 40.2 %), Day 3 (166.1 ± 38.5 %), Day 7 (122.0 ± 18.1 %) and Day 14 (137.3 ± 62.7 %). Similarly, no significant difference ($p > 0.05$, one-way ANOVA, $n = 4$) was obtained following the addition of 1000 µM AA over Day 1 (191.1 ± 95.0 %), Day 3 (217.1 ± 82.7 %), Day 7 (116.6 ± 23.0 %) and Day 14 (148.3 ± 66.5 %). Additionally, no significant difference ($p > 0.05$) was reported by Bonferroni *post hoc* analysis between Day 1 and the subsequent 14 days at 400 µM (Figure 4.3.1.3.2 *inset*) and 1000 µM AA. Therefore, it can be

concluded that AA had a negligible response on the NO sensor. Thus, the NO sensor has been demonstrated to retain its selectivity properties for up to 14-days making it suitable for application in *in vivo* investigations.

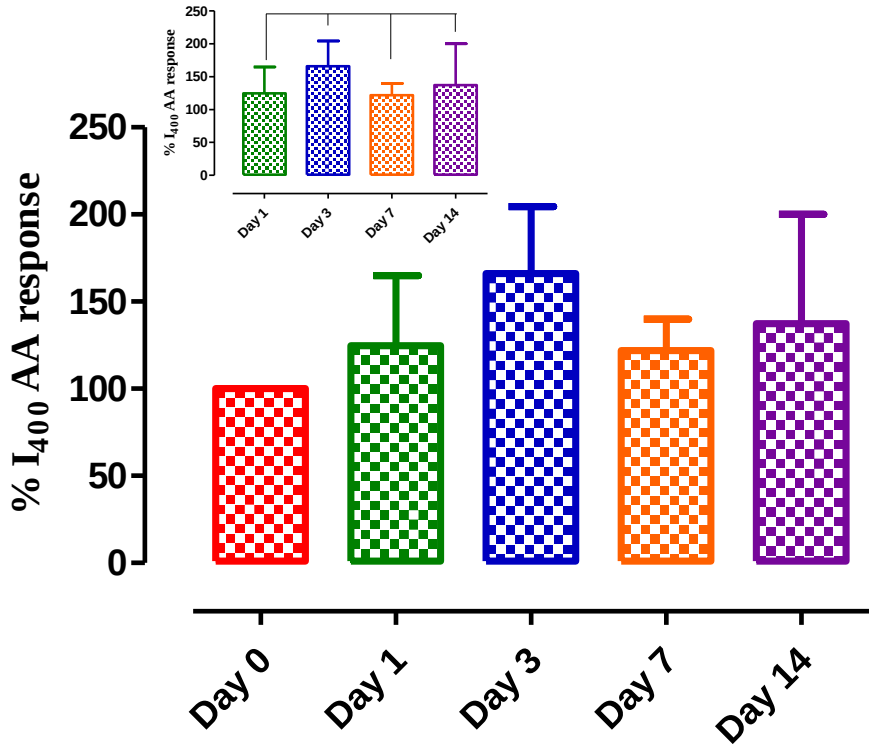

Figure 4.3.1.3.2: Comparison of the effect of *ex vivo* homogenised brain tissue exposure on NO sensor sensitivity calibrated on Day 0, 1, 3, 7 and 14 (one-way ANOVA, *n* = 4) PBS (pH 7.4) at + 900 mV vs. SCE. *Inset*: Bonferroni *post hoc* analysis. Data represented as mean ± SEM.

4.3.1.4 Post In Vivo NO Calibrations

Recalibration of the NO sensor following implantation was conducted. As mentioned previously, the microenvironment of the brain is a harsh biological environment which can affect the sensitivity and selectivity properties of the NO following exposure. Therefore, these aforementioned parameters were examined following implantation of the NO sensors for an average of 21 days (*n* = 8). The response of the pre-implanted and post-implanted NO sensors to a 0 - 1 µM concentration range of NO is illustrated in Figure 4.3.1.4.1 with the results tabulated in Table 4.3.1.4.1.

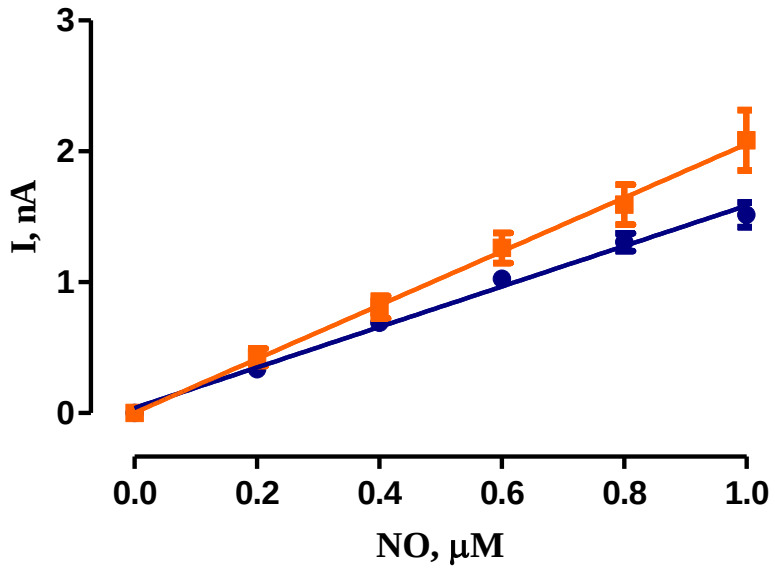

Figure 4.3.1.4.1: Current concentration profile for NO calibration on Nafion® coated Pt disk electrodes pre-implantation (*n* = 8, r^2 = 0.99, blue trace) and post-implantation (*n* = 8, r^2 = 0.99, orange trace).

Table 4.3.1.4.1: Average NO responses recorded over a 0 - 1 µM concentration range of NO on Nafion® coated Pt disk electrodes pre-implantation (*n* = 8, r^2 = 0.99, blue trace) and post-implantation (*n* = 8, r^2 = 0.99, orange trace).

	NO sensor (pre-implantation) (*n* = 8)		NO sensor (post-implantation) (*n* = 8)	
NO, µM	**Mean I, pA**	**SEM**	**Mean I, pA**	**SEM**
0	0	0	0	0
0.2	334	27	426	66
0.4	690	44	809	86
0.6	1025	52	1262	116
0.8	1306	68	1593	153
1.0	1515	94	2084	231

A significant difference (unpaired *t*-test, $p < 0.0001$) was observed between the sensitivity of the pre-implanted NO sensors (1547 ± 66 pA/µM, *n* = 8) and post-implanted NO sensors (2053 ± 41 pA/µM, *n* = 8). Additionally, linear responses (r^2 = 0.99) were obtained for both. However, the significant increase in sensitivity reported

by the NO sensors following *in vivo* implantation may be due to damage caused to the NO sensor during the removal of the sensor from sacrificed mice leading to an increase in sensitivity being experienced post-implantation. Each electrode is contained with a headpiece on the head of the euthanised subject. However, it is very difficult to remove this headpiece without causing some damage to the electrodes contained within it. Hence, it can be hypothesised that the increase in sensitivity has resulted from an increase in the active surface area of the sensor produced by a small tear in the Teflon® surrounding the disk surface of the Pt wire. Additionally, damage caused to the headpiece can allow for moisture to access the gold clips of the electrodes, thus, affecting the recorded amperometric signal. Figure 4.3.1.4.2 illustrates a raw trace from a NO calibration conducted on (A) pre-implanted electrodes and (B) post-implanted electrodes. Figure 4.3.1.4.2 highlights the unstable amperometric signal recorded from post-implanted electrodes compared to the stable signal recorded from pre-implanted electrodes. Furthermore, a much higher baseline was recorded on post-implanted electrodes due to moisture reaching the gold clips of the electrodes.

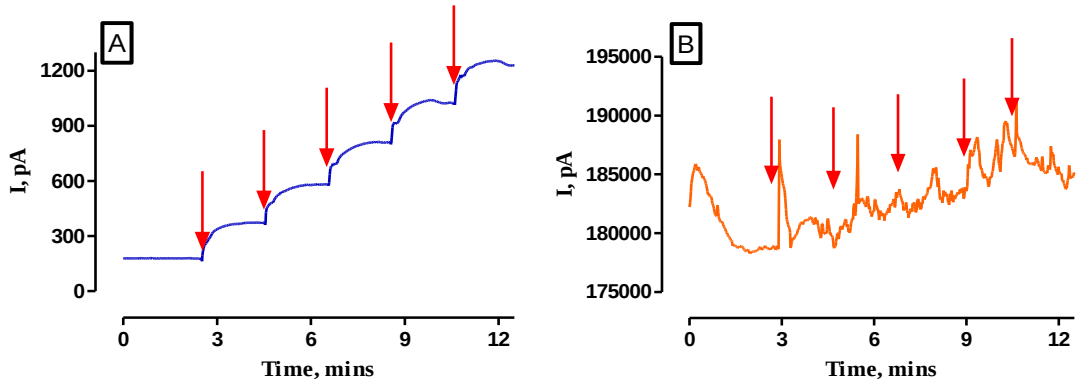

Figure 4.3.1.4.2: Typical *in vitro* data trace recorded using (A) pre-implanted Nafion®-coated Pt disk sensors (*n* = 8, blue trace) and (B) post-implanted Nafion®-coated Pt disk sensors (*n* = 8, orange trace) following the addition of 0 - 1 µM NO. Red arrows indicate addition of aliquots of 0.2 µM NO.

4.3.1.5 Post In Vivo AA Calibrations

Following post-implantation of the NO sensors, the selectivity parameters of the sensor were also investigated. A 0 - 1000 µM AA calibration was carried out on NO sensors that had been implanted *in vivo* for an average of 21 days (*n* = 8). The

inclusion of the Nafion® membrane works to increase the detection of NO detection but also works as an anionic rejection membrane preventing the detection of anionic interferents such as AA. Therefore, the selectivity of the NO sensor was investigated post-implantation. Figure 4.3.1.5.1 illustrates the response of a 0 - 1000 µM AA calibration conducted on pre- (n = 8) and post-implanted (n = 8) NO sensors. The recorded currents are displayed in Table 4.3.1.5.1.

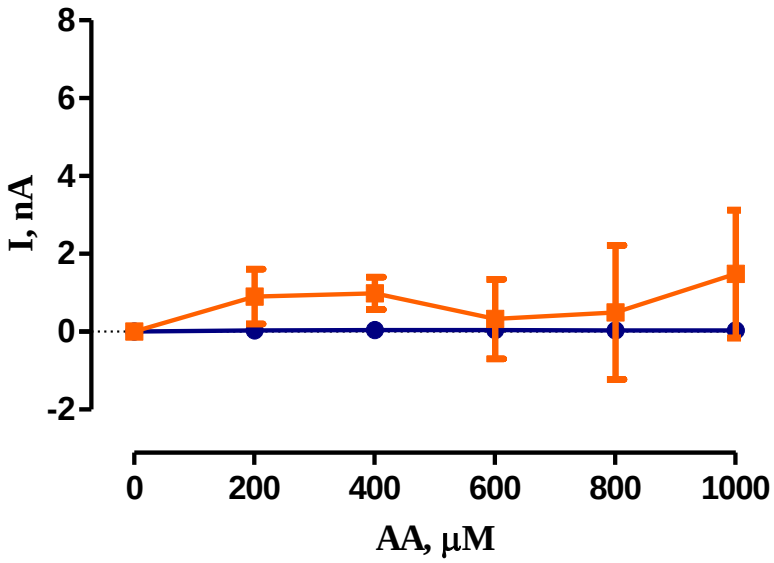

Figure 4.3.1.5.1: Current concentration profile for AA calibration on Nafion®-coated Pt disk electrodes pre- implantation (n = 8, r^2 = 0.99, blue trace) and post-implantation (n = 8, r^2 = 0.99, orange trace).

Table 4.3.1.5.1: Average AA responses recorded over a 0 - 1000 µM concentration range of AA on Nafion® coated Pt disk electrodes pre- implantation (*n* = 8, r^2 = 0.99, blue trace) and post-implantation (*n* = 8 , r^2 = 0.99, orange trace).

	NO sensor (pre-implantation) (*n* = 8)		NO sensor (post-implantation) (*n* = 8)	
AA, µM	**Mean I, pA**	**SEM**	**Mean, pA**	**SEM**
0	0	0	0	0
200	30	25	900	705
400	45	28	987	416
600	38	23	326	1022
800	33	19	498	1723
1000	30	18	1483	1645

It is evident from the results recorded in Table 4.3.1.5.1 that there is a significant increase ($p < 0.01$, unpaired *t*-test) in the detection of AA on post-implanted NO sensors. The recorded response of $I_{400\ \mu M}$ and $I_{1000\ \mu M}$ value for pre-implanted NO sensors was 45 ± 28 pA (*n* = 8) and 30 ± 18 pA (*n* = 8) respectively. Whereas, the recorded response of $I_{400\ \mu M}$ and $I_{1000\ \mu M}$ value for post-implanted NO sensors was 987 ± 416 pA (*n* = 8) and 1483 ± 1645 pA (*n* = 8) respectively. Hence, these results indicate that the Nafion® membrane has been compromised following exposure to striatal brain tissue leading to an increase in AA detection at the Pt surface. However, it is more plausible to attribute this increase in AA detection to damage caused to the Nafion® membrane during removal of the NO sensors from sacrificed subjects. This hypothesis can be supported by data obtained from *in vivo* stability investigations and *ex vivo* sensocompatibility studies, as discussed in Sections 5.3.1.6 and 4.3.1.3, whereby the selectivity of the NO sensor was retained following implantation *in vivo*.

Additionally, although removal of the NO sensors has caused damage to the Nafion® membrane, the majority of the Nafion® membrane was observed to remain intact. Table 4.3.1.2.2 highlighted the contribution of $I_{400\ \mu M}$ and $I_{1000\ \mu M}$ AA recorded on bare Pt disk electrodes as 11 ± 0.4 nA (*n* = 16) and 26 ± 0.9 nA (*n* = 16) respectively. This study highlights a much greater contribution of AA recorded following the addition of 400 µM and 1000 µM AA when compared to the values obtained in Table

4.3.1.5.1. Therefore, it can be suggested that the majority of the Nafion® remained on the Pt surface following removal from the subject.

4.3.2 *In Vitro* Validation of the O_2 Sensor

4.3.2.1 Sensitivity Investigation using Bare Pt Wire

Bare Pt wire demonstrated excellent linearity over an O_2 concentration range of 0 - 1200 µM, $r^2 = 0.99$ (Figure 4.3.2.1.1). In addition, a mean current of -1115 ± 30 nA, $n = 7$ was achieved (Table 4.3.2.1.1) The sensitivity recorded for the bare Pt wire was - 0.91 ± 0.06 nA/µM ($n = 7$).

Calibrations were conducted on bare Pt disk electrodes to investigate the ability to measure O_2 amperometrically *in vitro*. The inclusion of Pt wire in the manufacture of Clark-type electrodes has long been chosen as the transducer of choice for O_2 detection. However, bare Pt electrodes are extremely vulnerable to surface biofouling following implantation in brain tissue. Thus, the sensitivity of the O_2 sensing electrode can be compromised.

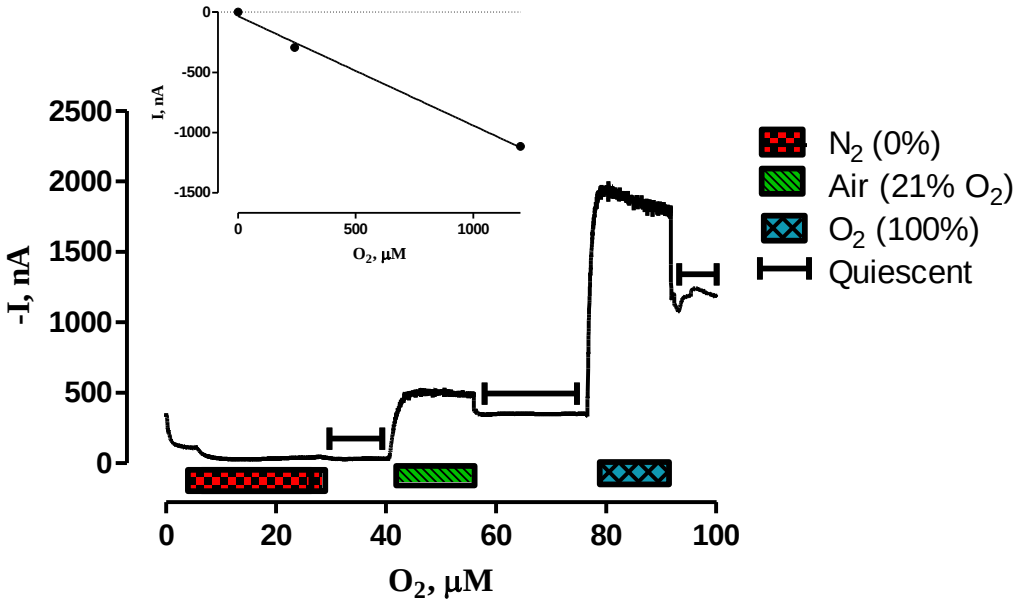

Figure 4.3.2.1.1: Typical *in vitro* data trace recorded using CPEs during an O_2 calibration over a concentration range of 0 - 1200 µM. *Inset*: Current concentration profile for O_2 calibration on CPEs ($n = 7$), $r^2 = 0.99$.

Table 4.3.2.1.1: Average O_2 responses recorded over a 0 - 1200 µM concentration range of O_2 using CPEs (*n* = 7) carried out at - 650 mV *vs*. SCE. Background values are subtracted.

	CPEs (*n* = 7)	
O_2, µM	**Mean I, nA**	**SEM**
0	0	0
240	- 292	13
1200	-1115	30

4.3.2.2 In Vitro Investigation of a 2 mm Cavity CPE

In vitro recordings using the 2 mm cavity CPE presented excellent linearity, r^2 = 0.99 (*n* = 8, Figure 4.3.2.2.1) over an O_2 concentration range of 0 - 1200 µM. Moreover, the sensitivity obtained was - 1.90 ± 0.01 nA/µM (*n* = 8). Table 4.3.2.2.1 highlights the mean current of - 2281 ± 226 nA (*n* = 8) obtained at 1200 µM O_2.

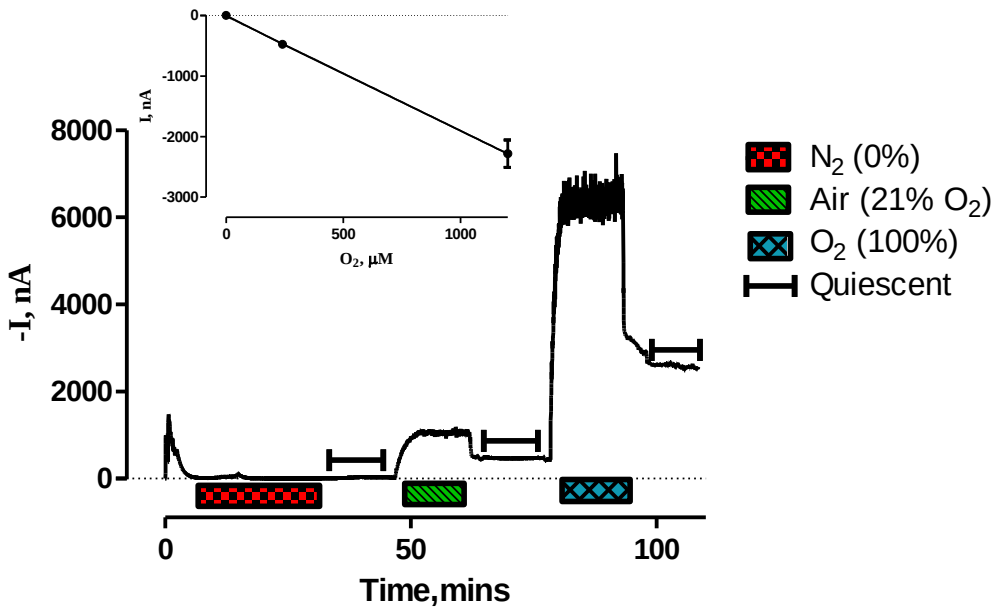

Figure 4.3.2.2.1: Typical *in vitro* data trace recorded using CPEs during an O_2 calibration over a concentration range of 0 - 1200 µM. *Inset*: Current concentration profile for O_2 calibration on CPEs (*n* = 8), r^2 = 0.99.

Table 4.3.2.2.1: Average O_2 responses recorded over a 0 - 1200 µM concentration range of O_2 using CPEs, *n* = 8, carried out at - 650 mV *vs.* SCE. Background values are subtracted.

	CPEs (*n* = 8)	
O_2, µM	**Mean I, nA**	**SEM**
0	0	0
240	-473	31
1200	-2281	226

4.3.2.3 In Vitro Investigation of a 1 mm Cavity CPE

Investigations *in vitro* carried out using CPEs with a 1 mm cavity for amperometric O_2 recordings exhibited excellent linearity, $r^2 = 0.99$ (*n* = 35, see Figure 4.3.2.3.1), over a concentration range of 0 - 1200 µM O_2. In addition, the recorded sensitivity was - 1.83 ± 0.04 nA/µM (*n* = 35). The sensitivity obtained is in agreement with previous studies which state a sensitivity value of - 1.49 ± 0.01 nA/µM^3. The average currents obtained for O_2 calibrations are displayed in Table 4.3.2.3.1.

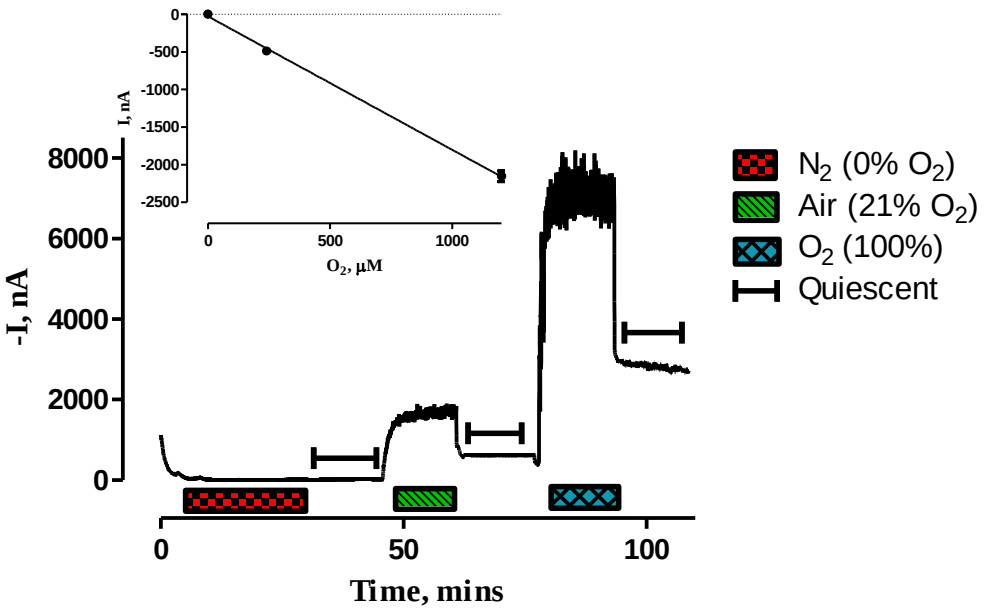

Figure 4.3.2.3.1: Typical *in vitro* data trace recorded using CPEs during an O_2 calibration over a concentration range of 0 - 1200 µM. *Inset*: Current concentration profile for O_2 calibration on CPEs (*n* = 35), $r^2 = 0.99$.

Table 4.3.2.3.1: Average O_2 responses recorded over a 0 - 1200 µM concentration range of O_2 using CPEs, *n* = 35, carried out at - 650 mV *vs*. SCE. Background values are subtracted.

	CPEs (*n* = 35)	
O_2, µM	**Mean I, nA**	**SEM**
0	0	0
240	-487	42
1200	-2207	48

4.3.2.4 Sensitivity Investigation of a Miniaturised CPE Incorporating a 0.5 mm Cavity

Excellent linearity was observed in recordings using the 0.5 mm cavity CPE over 0 - 1200 µM, $r^2 = 0.99$, $n = 37$ (Figure 4.3.2.4.1). A sensitivity of - 0.98 ± 0.01 nA/µM, $n = 37$, was achieved. The average current responses of the 0.5 mm cavity electrode can be seen in Table 4.3.2.4.1.

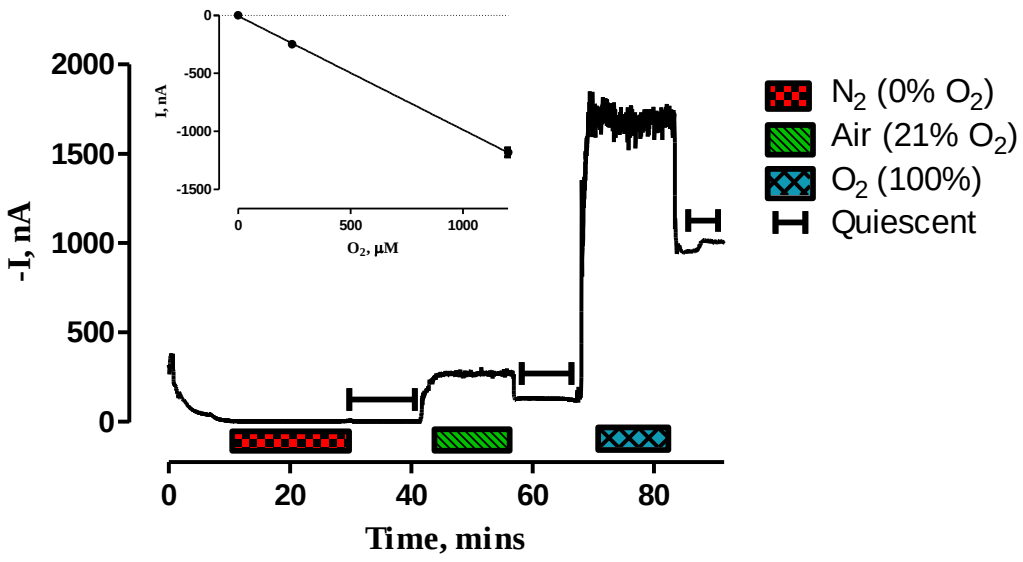

Figure 4.3.2.4.1: Typical *in vitro* data trace recorded using CPEs during an O_2 calibration over a concentration range of 0 - 1200 µM. *Inset*: Current concentration profile for O_2 calibration on CPEs (*n* = 37), $r^2 = 0.99$.

Table 4.3.2.4.1: Average O_2 responses recorded over a 0 - 1200 µM concentration range of O_2 using CPEs, *n* = 37, carried out at - 650 mV *vs*. SCE. Background values are subtracted.

	CPEs (*n* = 37)	
O_2, µM	**Mean I, nA**	**SEM**
0	0	0
240	-249	11
1200	-1181	38

4.3.2.5 Comparison of the O_2 CPE Sensitivity using Current Densities

To allow for an accurate comparison of the sensitivities of each of the aforementioned O_2 sensor designs, current densities were investigated. Current densities represents the current per unit area (Section 2.8.2). Current densities can be obtained using Equation 4.3.2.5.1 highlighted below.

$$J = \frac{I}{A} \qquad \textbf{(4.3.2.5.1)}$$

Where *J* is the current density, *I* is the current and *A* is the area of the active surface of the electrode. Employment of current density data in this analysis allows for a direct comparison to be made between electrodes of different sizes by normalisation of the obtained response to current density[34]. The current density obtained for the bare Pt electrodes was - 72 ± 5 nA/mm^2/µM. Additionally, the current densities of the O_2 sensors incorporating a 2.0 mm, 1.0 mm and 0.5 mm cavity were - 61 ± 0.3, - 47 ± 0.3 and - 80 ± 1 nA/mm^2/µM respectively. Significant differences were found between the current density obtained for the 0.5 mm cavity CPE when compared with the bare Pt electrode ($p < 0.0001$), 2.0 mm cavity CPE ($p < 0.0001$) and 1.0 mm cavity CPE ($p < 0.0001$). This result indicates that the sensitivity of this sensor design is optimum for the detection of O_2 whilst exhibiting excellent *in vitro* sensocompatibility making it suitable for long term amperometric recordings in freely-moving immunocompromised mice. Furthermore, this analysis displays that there is no compromise in sensitivity following a reduction in the size of the CPE. Reducing the size of the CPE increases its suitability to implantation in the striatum of mice by reducing damage to the surrounding endogenous neurochemical environment

following implantation. Hence, the application of the miniaturised O_2 sensor is the most suitable design for application in NOD SCID mice to enable accurate detection of tissue O_2.

4.3.2.6 Ex Vivo Sensocompatibility of the O_2 Sensor

The utilisation of CPEs in the detection of O_2 is desirable due to long-term stability that they possess *in vivo*. Biofouling can be a major problem *in vivo* resulting in reduced diffusion of target analytes to the electrode surface. However, CPEs are resistant to electrode biofouling due to the presence of the pasting oil which repels poisoning from the lipid-protein rich environment[35]. For this reason, the application of CPEs in amperometric O_2 investigations has increased substantially in recent years due to the advantageous long term stability attributes they possess. As the miniaturised O_2 sensor had never been previously studied, it was vital that the stability of the electrode was confirmed over a number of days. An array of protein and lipids found *in vivo* work to adhere to the surface of the CPE, thus, reducing sensitivity by limiting the amount of active surface available[32]. Therefore, it must be ensured that any sensor implanted *in vivo* will retain stability to allow for long term recordings to be conducted.

Exposure of CPEs to *ex vivo* brain tissue is an efficient method to mimic the *in vivo* environment experienced by the sensor following implantation. By carrying out such investigations, an understanding to how the sensor will behave *in vivo* was achieved. Figure 4.3.2.6.1 highlights the sensitivities of the 0.5 mm CPEs obtained following exposure of the CPEs to homogenised brain tissue obtained from NOD SCID mice. The sensitivities on Day 0 are represented as 100 %. The sensitivities recorded on each of the following days was taken as a percentage of Day 0. Figure 4.3.2.6.1 illustrates that there is no significant difference ($p = 0.05$, one-way ANOVA, $n = 4$) in the recorded sensitivity of each of the electrodes over Day 1 (71.4 ± 5.6 %), Day 3 (96.5 ± 13.5 %), Day 7 (109.3 ± 4.3 %) and Day 14 (100.6 ± 9.8 %). Initially, a small decrease in sensitivity of approximately 25 % was observed. This decrease is within normal parameters whereby previous reports have highlighted that a decrease in sensitivity of between 20 - 50 % is normally accepted[36]. However, no significant difference was observed between Day 0 and 14. Furthermore, no significant difference, by means of Bonferroni *post hoc* analysis, was observed between Day 1 and Days 3 and 14 in the recorded sensitivity (Figure 4.3.2.6.1 *inset*) following

exposure to *ex vivo* brain tissue. However, a significant difference ($p < 0.05$, one-way ANOVA, $n = 4$) was reported between Day 1 (71.4 ± 5.6 %) and Day 7 (109.3 ± 4.3 %).

Moreover, it must be noted that although it appears that an improvement in the sensitivity of the CPE is recorded following Day 1, this could be attributed to the presence of pasting oil contained within the carbon paste. The pasting oil has been previously reported to leach out whilst in contact with biological tissue to prevent biofouling of the implanted electrode[35]. Therefore, protein and lipid adhesion is greatly reduced allowing for an improvement in diffusion of O_2 to the sensor surface. Such phenomenon allows for the long term stability of the CPE over long periods. Hence, the stability of the CPE has been verified over 14 days *ex vivo* which is in agreement with previous findings whereby the long term stability of CPEs has been reported in freely-moving rats[3]. Therefore, the sensor is now suitable for implantation in immunocompromised mice.

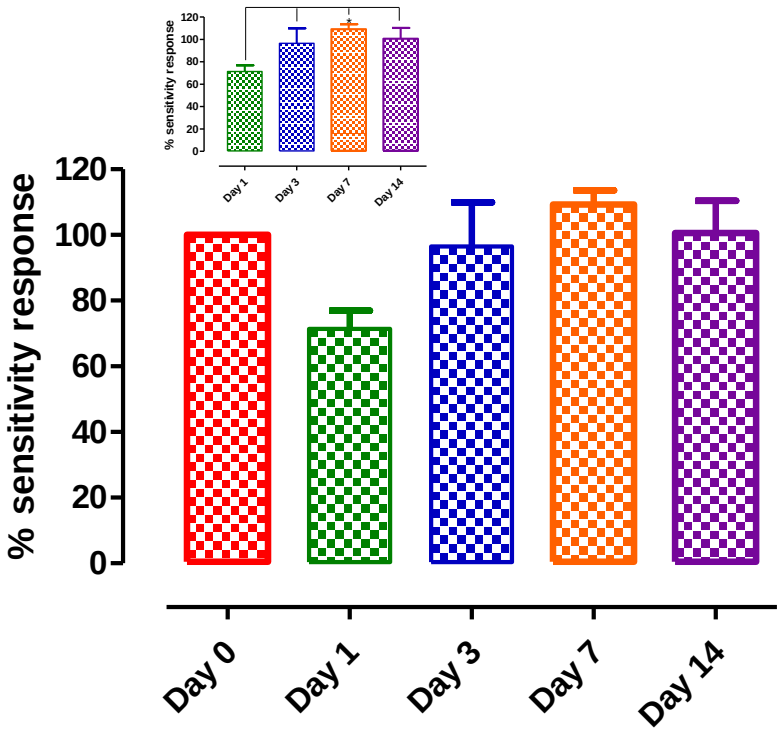

Figure 4.3.2.6.1: Comparison of the effect of *ex vivo* homogenised brain tissue exposure on CPE sensitivity calibrated on Day 0, 1, 3, 7 and 14 (one-way ANOVA, *n* = 4) in PBS (pH 7.4) at - 650 mV *vs.* SCE. *Inset*: Bonferroni *post hoc* analysis. Data represented as mean ± SEM.

Table 4.3.2.6.1: Tabulated results for O_2 calibrations conducted on CPEs (n = 4) in PBS (pH 7.4) on Day 0 and Day 14 following exposure to *ex vivo* brain tissue at - 650 mV *vs*. SCE.

	CPEs Day 0 (n = 4)		CPEs Day 14 (n = 4)	
O_2, µM	**Mean I, nA**	**SEM**	**Mean I, nA**	**SEM**
0	0	0	0	0
240	-311	9	-236	13
1200	-1048	33	-1021	69

4.3.2.7 Post In Vivo Investigations on the O_2 Sensor

Following implantation of the O_2 sensor (miniaturised design, 0.5 mm cavity), for an average of 8 days (n = 8), the sensitivity of the sensor was investigated. The purpose of this study was to examine if there was any effect of brain tissue on the sensitivity of the sensor following exposure to a harsh biological environment. Figure 4.3.2.7.1 illustrates the response of the O_2 sensor to a 0 - 1200 µM O_2 calibration pre- and post-implantation. Table 4.3.2.7.1 presents the recorded sensitivities pre- and post-implantation.

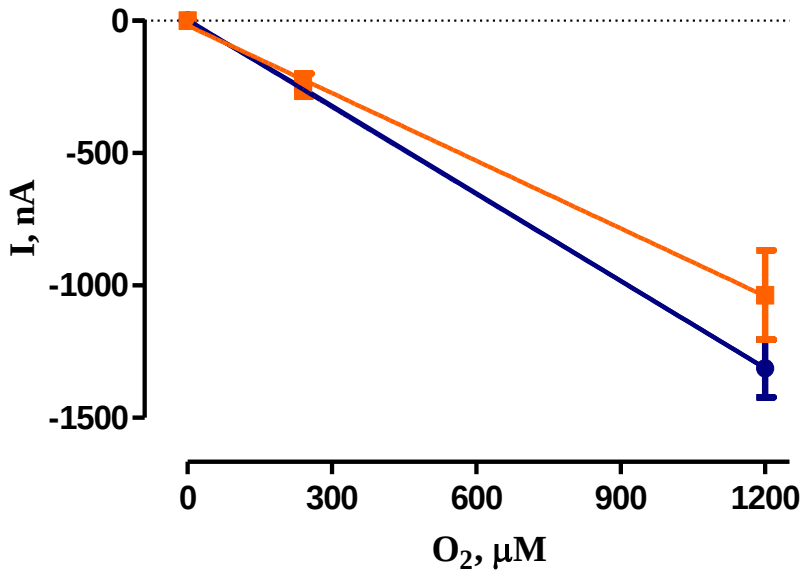

Figure 4.3.2.7.1: Current concentration profile for O_2 calibration carried out on CPEs pre-implantation (n = 8, r^2 = 0.99, blue trace) and post-implantation (n = 8 , r^2 = 0.99, orange trace).

Table 4.3.2.7.1: Average O_2 responses recorded over a 0 - 1200 µM concentration range of O_2 on CPEs pre-implantation (n = 8, r^2 = 0.99, blue trace) and post-implantation (n = 8, r^2 = 0.99, orange trace).

	O_2 sensor (pre-implantation) (n = 8)		O_2 sensor (post-implantation) (n = 8)	
O_2, µM	**Mean I, nA**	**SEM**	**Mean, nA**	**SEM**
0	0	0	0	0
240	-255	22	-243	43
1200	-1314	110	-1036	169

Comparison of the sensitivities of the 0.5 mm CPE was made pre-implantation (- 0.98 ± 0.01 nA/µM, n = 37) and post-implantation (- 0.85 ± 0.03 nA/µM, n = 8). A significant decrease ($p < 0.0001$, unpaired t-test) in sensitivity was observed following *in vivo* implantation. Moreover, a linear response was observed for both (r^2 = 0.99). As stated previously, all implanted sensors undergo an acceptable 20 - 50 % drop in sensitivity post-implantation[36]. For this reason, a slight drop (~12 %) in the sensitivity of the post-implanted CPEs was exhibited. However, this drop in sensitivity is minimal and highlights the excellent retention of the ability of the sensor to respond to changes in O_2. Therefore, the most viable reason for this slight drop in sensitivity is damage caused to the sensor during removal from sacrificed animals. As a result, caution must be taken when making direct comparisons between the obtained pre-implantation sensitivity and the sensitivity observed post-implantation.

4.3.3 *In Vitro* Validation of the H_2O_2 Biosensor

4.3.3.1 Selectivity Investigation of AA Calibrations on Bare Pt Wire

Firstly, a control had to be determined to quantify the contribution of AA on a bare 1 mm cylinder Pt electrode. The $I_{400\ \mu M}$ value, which is the mean current obtained after 400 µM addition of AA, was deemed to be 201 ± 6 nA (n = 21). Moreover, the addition of 1000 µM resulted in a mean current of 485 ± 10 nA (n = 21, Table 4.3.3.1.1) which indicates that the change in amperometric current is a direct result of the increasing concentration of AA present. A sensitivity of 490 ± 10 pA/µM was obtained and it yielded an excellent linear response of r^2 = 0.99 (n = 21, Figure 4.3.3.1.1).

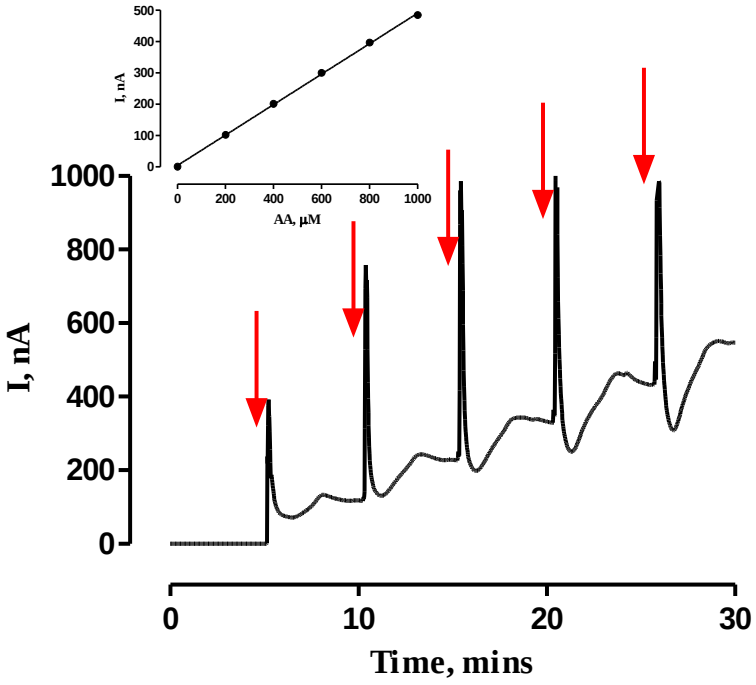

Figure 4.3.3.1.1: Amperometric calibration plot for AA measured in pH 7.4, at + 700 mV *vs.* SCE on bare 1 mm cylinder Pt electrodes (*n* = 21). *Inset*: Current concentration profile for H_2O_2 calibration on bare 1 mm cylinder Pt electrodes (*n* = 21), $r^2 = 0.99$. Red arrows indicate the point of injection. Data is presented as mean ± SEM.

Table 4.3.3.1.1: Tabulated results of the mean current response, standard error of mean values (SEM) and the number of electrodes calibrated (*n* = 21) following addition of 1000 µM AA .

	Bare 1 mm Cylinder Pt Electrodes (*n* = 21)	
AA, µM	**Mean I, nA**	**SEM**
0	0	0
200	102	3
400	201	6
600	300	8
800	397	9
1000	485	10

4.3.3.2 AA Calibrations on Pt-PPD Electrodes

From Section 4.3.3.1, it is clear that the AA detection on bare 1 mm cylinder Pt electrodes is substantial at + 700 mV *vs.* SCE. Therefore, it would be impossible to accurately measure H_2O_2 *in vivo* without modification to the electrodes to eliminate unwanted electroactive interferent detection. PPD is a size exclusion polymer (Section 2.5) that has been extensively studied[37–39].

AA calibrations performed on Pt-PPD electrodes (Figure 4.3.3.2.1) indicated that a negligible contribution of AA was measured on Pt-PPD electrodes in comparison to the linear response of AA measured on bare 1 mm cylinder Pt electrodes seen in Figure 4.3.3.1.1. AA calibrations carried out over a concentration range of 0 - 1000 µM produced a mean current of 328 ± 111 pA (n = 8) and 276 ± 88 pA (n = 8) following the addition of 400 µM and 1000 µM AA respectively. This current was negligible and indicated the AA contribution previously seen in Section 4.3.3.1 had been significantly reduced following incorporation of PPD on the electrode surface. Comparison of the $I_{400\mu M}$ and $I_{1000\ \mu M}$ values displayed for the AA calibration conducted on bare 1 mm cylinder Pt electrodes indicates that the modification of the Pt wire with PPD has prevented the detection of AA at its surface. Briefly, PPD is electropolymerised onto the surface of the electrode and works to prevent the detection of interfering species, including small organic molecules, whilst permitting H_2O_2 to pass freely through the semi-permeable membrane to reach the surface of the electrode[40].

Additionally from the recorded results, a characteristic self-blocking effect is evident. Previous works have highlighted the biphasic nature of AA calibrations conducted on Pt electrodes modified with a PPD membrane. The term self-blocking refers to the collection of AA or dehydroascorbic acid, which is an oxidation product of AA in the pores of the polymer matrix[41]. Therefore, further blocking access of interfering species from access the surface of the electrode. As a result, a decrease in the AA current is observed following addition of 400 µM AA due to the occurrence of this phenomenon. Moreover, an $I_{1000\ \mu M}$ value of 359 ± 111 pA (n = 8) is also in line with the $I_{1000\ \mu M}$ value previously reported, 240 ± 80 pA (n = 8)[42] further validating the ability of PPD in blocking the detection of interfering species at the Pt surface.

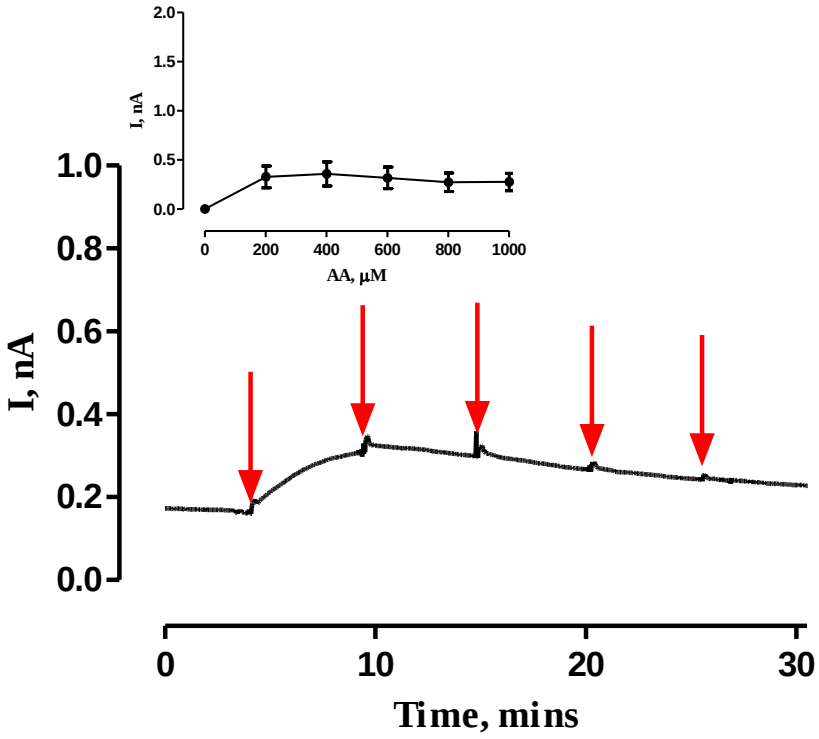

Figure 4.3.3.2.1: Amperometric calibration plot for AA measured in pH 7.4, at + 700 mV *vs.* SCE on Pt-PPD electrodes (*n* = 8). *Inset*: Current concentration profile for AA calibration on Pt-PPD (*n* = 8). Red arrows indicate the point of injection. Data is presented as mean ± SEM.

Table 4.3.3.2.1: Tabulated results of the mean current response, standard error of mean values (SEM) and the number of electrodes calibrated (*n* = 8) following addition of 1000 µM AA .

	Pt-PPD Electrodes (*n* = 8)	
AA, µM	**Mean I, pA**	**SEM**
0	0	0
200	328	111
400	359	123
600	318	110
800	273	95
1000	276	88

Figure 4.3.3.2.1 is a clear illustration of the importance of incorporating PPD into the biosensor design. Following addition of 1000 µM AA, there is a linear response of AA measured on bare Pt electrodes indicating that the concentration of

AA present is proportional to the AA being measured at the Pt surface. In comparison, there is a negligible response measured at Pt-PPD electrodes using the same concentration range. The AA contribution measured at the Pt-PPD electrodes is significantly different from the AA signal detected at the bare Pt electrodes (p < 0.0001, Figure 4.3.3.2.2). Additionally, the effectiveness of the PPD layer is further supported by the reduction in the mean current from 485 ± 10 nA (n = 21) on bare Pt to 276 ± 88 pA (n = 8, Table 4.3.3.2.2) on Pt-PPD electrodes. Therefore, this 1000-fold difference in $I_{1000\ \mu M}$ values indicates the efficient ability of the PPD layer to rejection the interfering species successfully.

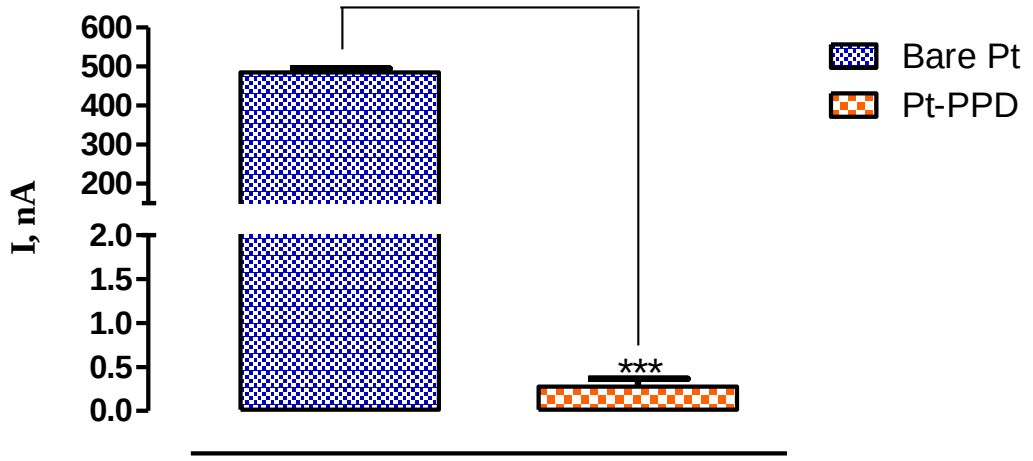

Figure 4.3.3.2.2: Comparison of the $I_{1000\ \mu M}$ recorded on bare Pt and Pt-PPD electrodes (p < 0.0001). Data represented as mean response ± SEM over an AA concentration range of 0 - 1000 µM calibrated in PBS (pH 7.4) at + 700 mV *vs.* SCE.

Table 4.3.3.2.2: Tabulated results of the mean current response, SEM and the number of electrodes calibrated for bare Pt (n = 21) and Pt-PPD electrodes (n = 8) following addition of 1000 µM AA .

AA, µM	Bare Pt (n = 21)			Pt-PPD (n = 8)		
	Mean, nA	SEM	n	Mean, pA	SEM	n
400	201	6	21	359	123	8
1000	485	10	21	276	88	8

4.3.3.3 AA Calibration on Pt-Nafion®-PPD Electrodes

Data below in Table 4.3.3.3.1 shows a mean current of 98 ± 16 pA (n = 97) and 46 ± 17 pA (n = 97) being detected following the addition of 400 µM and 1000 µM AA respectively. This negligible contribution displays the ability of PPD and Nafion® to efficiently block out the detection of interfering analytes at the electrode surface. Similarly, as seen in Section 4.3.3.2, the characteristic self-blocking of the PPD layer is apparent in the results obtained (Figure 4.3.3.2.1). The mean current reported in Section 4.3.3.2, using Pt-PPD electrodes was 276 ± 88 pA (n = 8) following the addition of 1000 µM AA, whilst the mean current reported using Pt-Nafion®-PPD electrodes was 46 ± 17 pA (n = 97). Therefore, Nafion® has been shown to work alongside PPD to efficiently eliminate the contribution of interfering species. Additionally, it is evident from the obtained results that the inclusion of the Nafion® layer, in addition to PPD, has increased the ability of the sensor in preventing detection of interfering analytes at the Pt surface in comparison to Pt-PPD electrodes. O'Riordan *et al.* previously reported an $I_{400\ \mu M}$ value of 150 ± 30 pA (n = 28) and an $I_{1000\ \mu M}$ value of 160 ± 20 pA (n = 28)[9], which indicates a similar response exhibited by the Pt-Nafion®-PPD electrodes, whereby a decrease in the amperometric response following AA calibrations was observed following application of Nafion® and PPD rather than PPD alone. Furthermore, the previously reported data is in complete agreement with the results obtained in this body of work indicating that the selectivity properties of the Pt-Nafion®-PPD electrode have been validated.

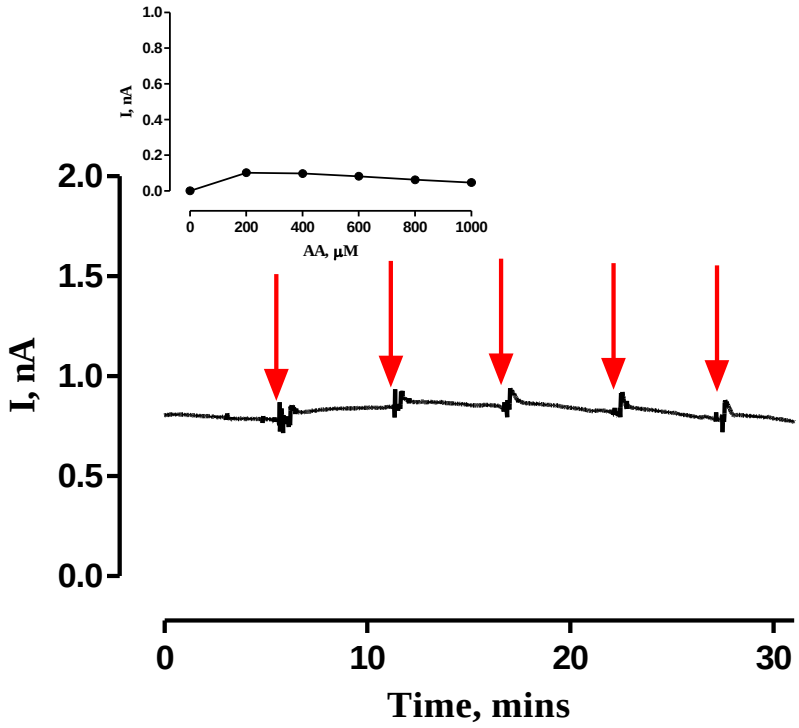

Figure 4.3.3.3.1: Amperometric calibration plot for AA measured in pH 7.4, at + 700 mV *vs.* SCE on Pt-Nafion®-PPD electrodes (*n* = 97). *Inset*: Current concentration profile for AA calibration on Pt-Nafion®-PPD electrodes (*n* = 97), r^2 = 0.99. Red arrows indicate the point of injection. Data is presented as mean ± SEM.

Table 4.3.3.3.1: Tabulated results of the mean current response, SEM and the number of electrodes calibrated (*n* = 97) following addition of 1000 µM AA .

	Pt-Nafion®-PPD Electrodes (*n* = 97)	
AA, µM	**Mean I, pA**	**SEM**
0	0	0
200	103	13
400	98	16
600	82	17
800	62	17
1000	46	17

Figure 4.3.3.3.2 illustrates that modifications with Nafion® and PPD work to eliminate the detection of interfering species *in vitro*. Furthermore, Table 4.3.3.3.2 details the $I_{400\ \mu M}$ and $I_{1000\ \mu M}$ values obtained for bare Pt electrodes and Pt-Nafion®-

PPD electrodes. Comparisons of 1000 µM AA on bare Pt and Pt-Nafion®-PPD indicate a significant difference ($p < 0.0001$) in the reduction of AA being detected at the electrode surface. These investigations have concluded that the Pt-Nafion®-PPD modified electrodes would be selective for measurement of the analyte of interest as has been previously shown by O'Riordan *et al.*[9,42].

Thus, once it was clear that the contribution from inferring species could be efficiently mitigated, the ability of the H_2O_2 biosensor to detect H_2O_2 accurately could now be investigated.

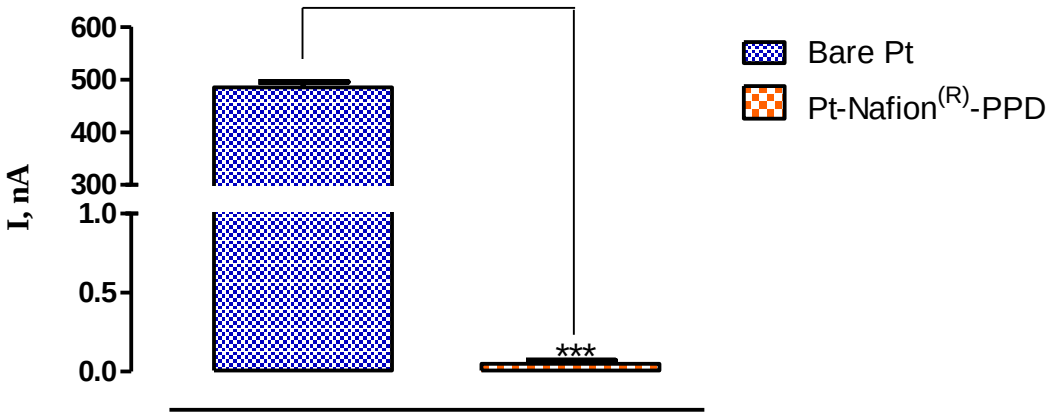

Figure 4.3.3.3.2: Comparison of the $I_{1000\ \mu M}$ recorded on bare Pt and Pt-Nafion®-PPD electrodes ($p < 0.0001$). Data represented as mean response ± SEM over an AA concentration range of 0 - 1000 µM calibrated in PBS (pH 7.4) at + 700 mV *vs.* SCE.

Table 4.3.3.3.2: Tabulated results of the mean current response, SEM and the number of electrodes calibrated for bare Pt (n = 21) and Pt-Nafion®-PPD electrodes (n = 97) following addition of 1000 µM AA .

AA, µM	Bare Pt (n = 21)			Pt-Nafion®-PPD (n = 97)		
	Mean, nA	SEM	*n*	Mean, pA	SEM	*n*
400	201	6	21	98	16	97
1000	485	10	21	46	17	97

4.3.3.4 H_2O_2 Calibration on Bare Pt Electrodes

Following the validation of the selectivity characteristics of the H_2O_2 biosensor design in the rejection of interfering species, it is imperative to ensure that the ability of the biosensor to detect H_2O_2 efficiently has not been compromised. The ECF concentration measured following the implantation of the H_2O_2 biosensor in the striatum of freely moving rats was reported to be 3.1 µM. *In vitro* H_2O_2 calibrations were carried out over a concentration range of 0 - 100 µM which is a much greater range than the concentration experienced in *in vivo* environments.

In vitro calibrations conducted on bare Pt electrodes displayed excellent linearity $r^2 = 0.99$ ($n = 68$, Figure 4.3.3.4.1) over 0 - 100 µM H_2O_2 concentration range with a sensitivity of 1.03 ± 0.01 nA/µM reported ($n = 68$). Furthermore, the mean current recorded following addition of 100 µM H_2O_2 was 102 ± 3 nA ($n = 68$, Table 4.3.3.4.1). The above obtained results highlight a much higher H_2O_2 contribution recorded when compared to H_2O_2 calibrations carried out on bare Pt electrodes previously which report a sensitivity of 0.54 ± 0.01 nA/µM ($n = 5$) and an $I_{100\ \mu M}$ value of 57 ± 7 nA ($n = 5$) being achieved[42]. By carrying out 0 - 100 µM H_2O_2 calibrations on bare Pt, an understanding of the magnitude of H_2O_2 current measured is attained.

Table 4.3.3.4.1: Tabulated results of the mean current response, SEM and the number of electrodes calibrated ($n = 68$) following addition of 100 µM H_2O_2.

	Bare Pt Electrodes ($n = 68$)	
H_2O_2, µM	**Mean I, nA**	**SEM**
0	0	0
20	21	1
40	43	1
60	64	2
80	83	2
100	102	3

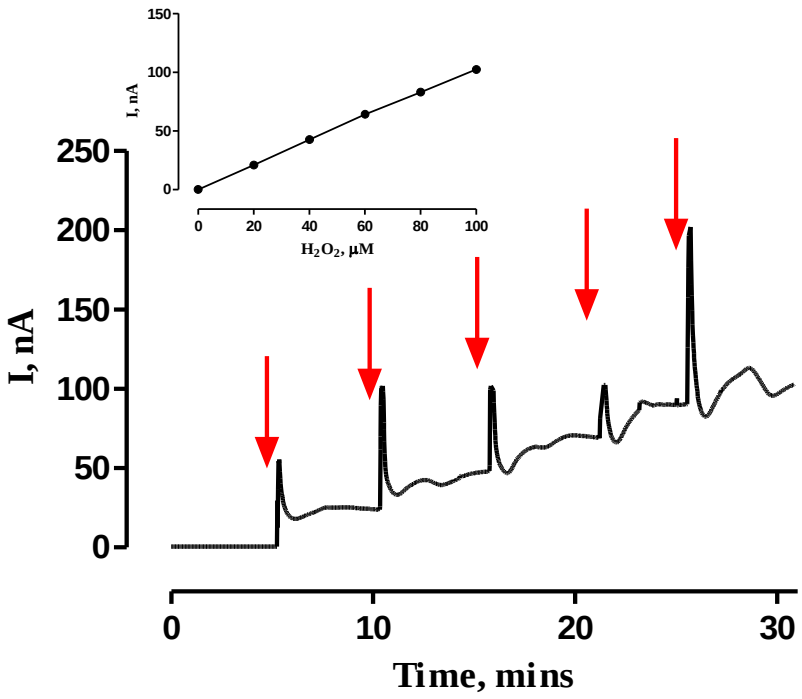

Figure 4.3.3.4.1: Amperometric calibration plot for H_2O_2 measured in pH 7.4, at + 700 mV *vs.* SCE on bare Pt electrodes (*n* = 68). *Inset*: Current concentration profile for H_2O_2 calibration on H_2O_2 biosensor (*n* = 68), r^2 = 0.99. Red arrows indicate the point of injection. Data is presented as mean ± SEM.

4.3.3.5 H_2O_2 Calibration on Blank (Pt-Nafion®-PPD) Electrodes

Firstly, H_2O_2 calibrations were performed on blank electrodes to confirm efficient sensitivity of the blank electrode. As demonstrated in Section 4.3.3.4, the contribution of H_2O_2 on unmodified Pt electrodes was investigated. With a mean contribution of H_2O_2 detection on bare Pt electrode now established, it was important to carry out H_2O_2 calibrations on the blank sensor to ensure efficient H_2O_2 detection following modification with Nafion® and PPD polymers.

Excellent linearity (r^2 = 0.99, *n* = 92, Figure 4.3.3.5.1) was determined over a H_2O_2 concentration range of 0 - 100 µM. The recorded sensitivity was 420 ± 2 pA/µM (*n* = 92) which was comparable to sensitivity values obtained by other research groups[8,9]. Table 4.3.3.5.1 displays the mean current values obtained over the H_2O_2 calibration range. Additionally, the $I_{100\ \mu M}$ value of 42 ± 1 nA (*n* = 92) is comparable to that obtained by others which reported 49 ± 1 nA (*n* = 24) following the addition of 100 µM H_2O_2.

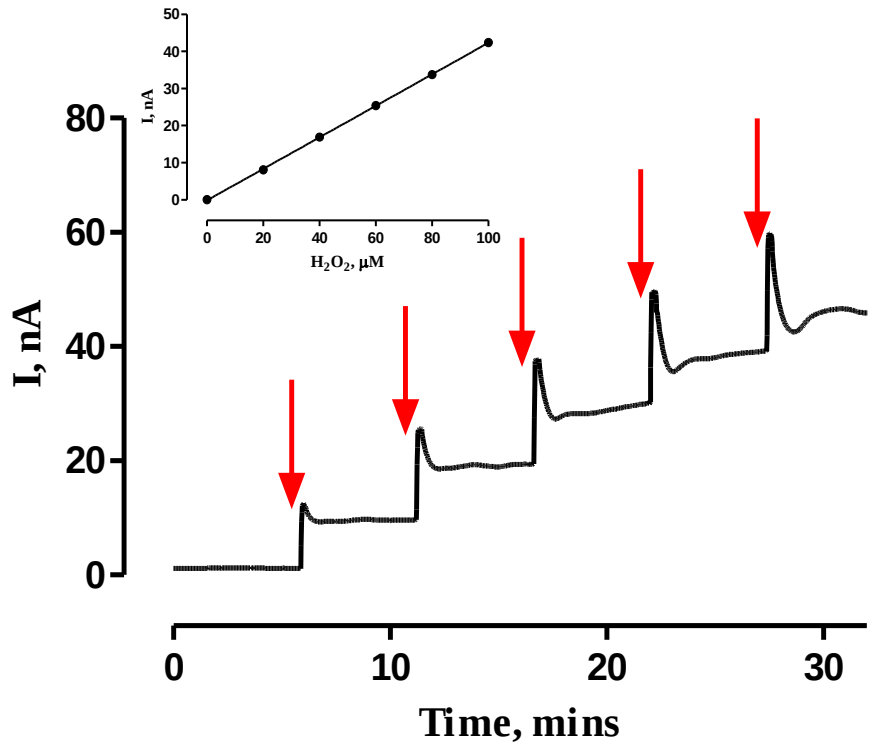

Figure 4.3.3.5.1: Amperometric calibration plot for H_2O_2 measured in pH 7.4, at + 700 mV *vs.* SCE on Pt-Nafion®-PPD electrodes. *Inset*: Current concentration profile for H_2O_2 calibration on H_2O_2 blank electrodes (n = 92), r^2 = 0.99. Red arrows indicate the point of injection. Data is presented as mean ± SEM.

Table 4.3.3.5.1: Tabulated results of the mean current response, SEM and the number of electrodes calibrated (n = 92) following addition of 100 µM H_2O_2.

	Pt-Nafion®-PPD Electrodes (n = 92)	
H_2O_2, µM	**Mean I, nA**	**SEM**
0	0.0	0.0
20	8.1	0.2
40	16.9	0.3
60	25.4	0.4
80	33.8	0.6
100	42.4	0.7

4.3.3.6 H_2O_2 Calibration on Catalase (Pt-Nafion®-PPD-Cat-Ga(0.25%)) Electrodes

Sensitivity values were examined for the catalase electrode using a H_2O_2 calibration range of 0 - 100 µM. A sensitivity value of 10 ± 0.3 pA/µM (n = 61) was obtained for the catalase electrode, as well as an excellent linearity value, r^2 = 0.99 (n = 61, Figure 4.3.3.6.1), being exhibited. Likewise, the sensitivity values achieved were in comparison to values obtained from other researchers[8,9].

Whilst the blank electrode gave a mean current of 42 ± 1 nA (n = 92), a significantly lower mean current of 979 ± 77 pA (n = 61) was measured on the catalase electrode. The presence of catalase on the sentinel electrode allows for the breakdown of H_2O_2 at the surface of the electrode and thus, a much lower current of approximately 40-fold difference, was measured. Moreover, as no interfering species were present during *in vitro* experiments, the mean recorded current of 979 ± 77 pA (n = 61) can be attributed to H_2O_2 (Table 4.3.3.6.1).

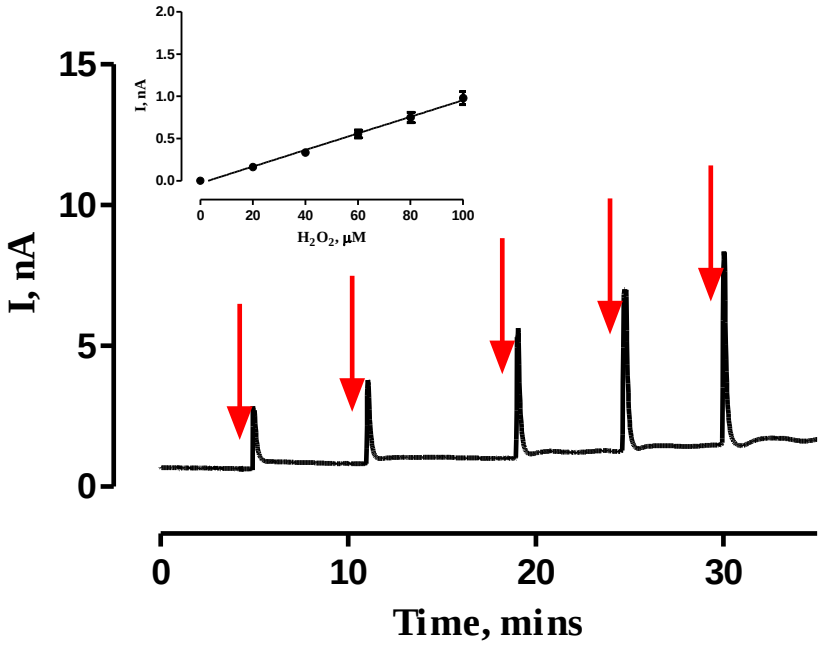

Figure 4.3.3.6.1: Amperometric calibration plot for H_2O_2 measured in pH 7.4, at + 700 mV *vs.* SCE on Pt-Nafion®-PPD-Cat-Ga(0.25 %) electrodes. *Inset*: Current concentration profile for H_2O_2 calibration on H_2O_2 blank electrodes (n = 61), r^2 = 0.99. Red arrows indicate the point of injection. Data is presented as mean ± SEM.

Table 4.3.3.6.1: Tabulated results of the mean current response, SEM and the number of electrodes calibrated (*n* = 61) following addition of 100 µM H_2O_2.

	Pt-Nafion®-PPD-Cat-Ga(0.25 %) Electrodes (*n* = 61)	
H_2O_2, µM	**Mean I, pA**	**SEM**
0	0	0
20	162	17
40	335	31
60	554	47
80	750	61
100	979	77

Additionally, it is evident that there is a significant decrease ($p < 0.0001$) in the detection of H_2O_2 was recorded on the catalase electrode which can be attributed to the incorporation of catalase at the electrode surface, see Figure 4.3.3.6.2. Therefore, it can be concluded that sentinel electrode is able to breakdown H_2O_2 at the electrode surface efficiently. By subtraction of the measured current on the catalase electrode from the blank electrode current, the total current which is attributed to H_2O_2 can now be measured as any contribution by electroactive interferents can be removed successfully.

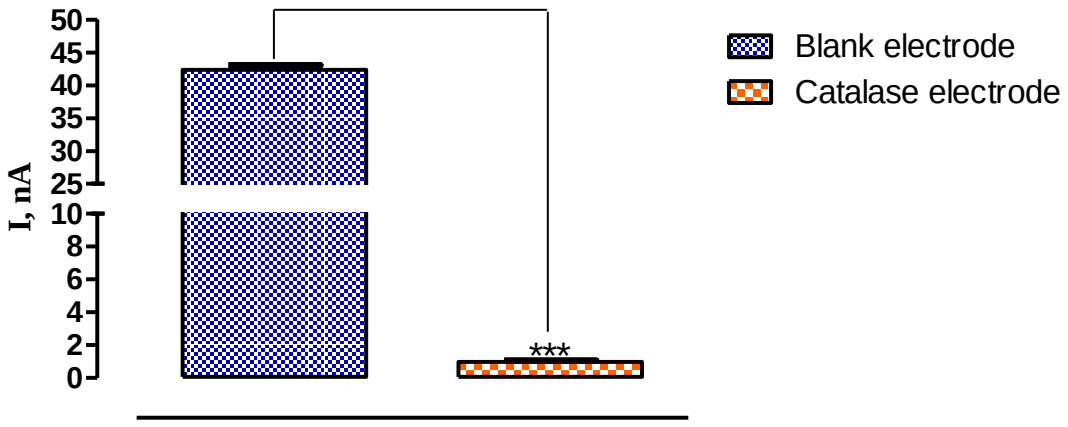

Figure 4.3.3.6.2: Comparison of $I_{100\ \mu M}$ H_2O_2 on Pt-Nafion®-PPD and Pt-Nafion®-PPD-Cat-Ga(0.25 %) electrodes ($p < 0.0001$). Data represented as mean response ± SEM over a H_2O_2 concentration range of 0 - 100 µM calibrated in PBS (pH 7.4) at + 700 mV *vs.* SCE.

Table 4.3.3.6.2: Tabulated results of the mean current response, SEM and the number of electrodes calibrated for Pt-Nafion®-PPD (*n* = 92) and Pt-Nafion®-PPD-Cat-Ga$_{(0.25\ \%)}$ electrodes (*n* = 61) following addition of 100 µM H_2O_2 .

H_2O_2, µM	Pt-Nafion®-PPD			Pt-Nafion®-PPD-Cat-Ga$_{(0.25\ \%)}$		
	Mean, nA	SEM	*n*	Mean, pA	SEM	*n*
100	42	1	92	979	77	61

4.3.3.7 AA Calibration on Pt-Nafion®-PPD-Cat-Ga$_{(0.25\ \%)}$ Electrodes

Previously, Section 2.4.3 detailed that if similar interference currents are recorded at the blank and catalase electrodes during *in vitro* calibrations, subtraction of the current measured at the catalase electrode from the blank electrode *in vivo* will result in the current that is solely dependent on H_2O_2. However, with the addition of a new component to the H_2O_2 biosensor design, it is of vital importance to confirm that the solution of Cat-Ga$_{(0.25\ \%)}$ has not affected the interference rejection layers of PPD and Nafion® beneath on the surface of the catalase electrode. AA calibrations were therefore carried out on the Pt-Nafion®-PPD-Cat-Ga$_{(0.25\ \%)}$ electrodes. A mean current of 71 ± 19 pA (*n* = 36) and 86 ± 32 pA (*n* = 36) was achieved after the addition of 400 µM and 1000 µM AA respectively (Table 4.3.3.7.1). The mean current achieved shows a negligible contribution from AA and indicated that the layers of PPD and Nafion® are working efficiently to block out interfering species following the addition of Cat-Ga$_{(0.25\ \%)}$ on the surface of the catalase electrode. Moreover, no significant difference was identified between the currents recorded on the Pt-Nafion®-PPD-Cat-Ga$_{(0.25\ \%)}$ electrodes at 400 µM (p = 0.58, unpaired t-test) and 1000 µM (p = 0.58, unpaired t-test). Previous results indicated a mean current of 140 ± 20 pA (*n* = 28) and 220 ± 30 pA (*n* = 28) after 400 µM and 1000 µM addition of AA[9]. This shows that the values obtained here are in line with previous results with a negligible detection being observed.

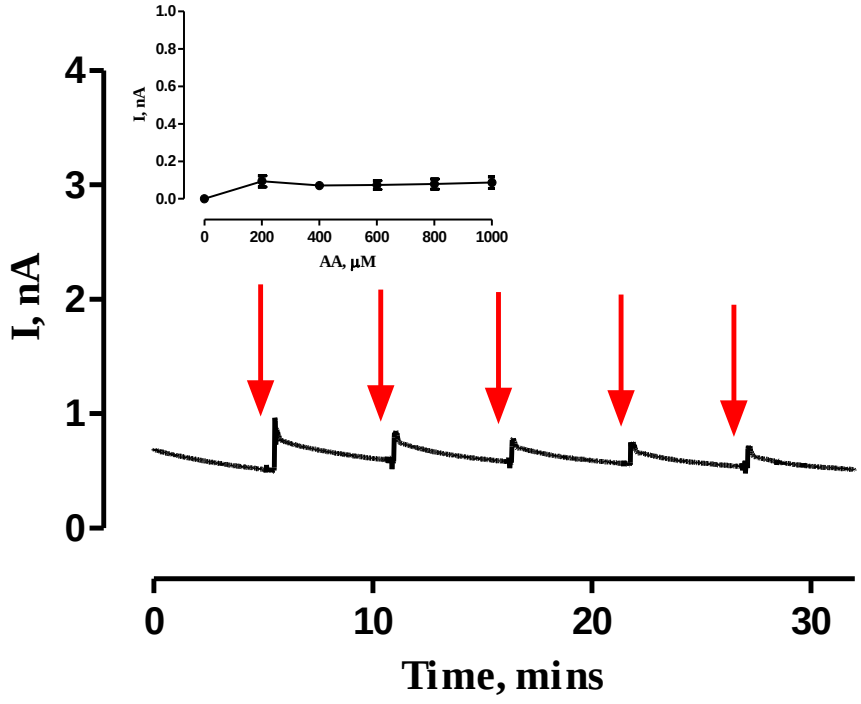

Figure 4.3.3.7.1: Amperometric calibration plot for AA measured in pH 7.4, at + 700 mV *vs.* SCE on Pt-Nafion®-PPD-Cat-Ga$_{(0.25\ \%)}$ electrodes (*n* = 36). Red arrows indicate the point of injection. Data is presented as mean ± SEM.

Table 4.3.3.7.1: Tabulated results of the mean current response, SEM and the number of electrodes calibrated (*n* = 36) following addition of 1000 µM AA.

	Pt-Nafion®-PPD-Cat-Ga$_{(0.25\ \%)}$ Electrodes (*n* = 36)	
AA, µM	**Mean I, nA**	**SEM**
0	0	0
200	94	30
400	71	19
600	73	23
800	79	27
1000	86	32

4.3.3.8 Interference Investigations on the H_2O_2 Biosensor Design using Mercaptosuccinic Acid (MSA) & Sodium Azide (SA)

In vivo acute studies are detailed in Section 3.9.1. Acute studies were undertaken to verify the ability of the H_2O_2 biosensor to measure endogenous striatal H_2O_2. In the striatum, H_2O_2 levels are kept under tight regulation by a host of antioxidants such as glutathione peroxidase and catalase. Glutathione peroxidase exhibits highly neuroprotective properties as its action ensures homeostatic levels of H_2O_2 are maintained[43]. Glutathione peroxidase works by enzymatically degrading H_2O_2 into H_2O and molecular O_2[44]. Local infusions of the GSH inhibitor, MSA, were performed to investigate the performance of the H_2O_2 biosensor to measure endogenous levels of H_2O_2.

The presence of infused MSA in the endogenous environment presents itself as a potential interferent to the electrochemical sensor *in vivo*. Hence, it is crucial to ensure rejection of MSA detection by inclusion of Nafion® and PPD polymers at the electrode surface. Foresaid polymers work efficiently in blocking the detection of the major interferent in the ECF, AA, as referred to in Section 4.3.3.3.

A concentration range of 0 -1000 µM MSA was calibrated on bare Pt (green line) and blank H_2O_2 electrodes (red line, Figure 4.3.3.8.1) *in vitro*. The current response of the bare Pt electrodes and the blank H_2O_2 electrodes to 1000 µM was 5 ± 0.2 nA (n = 8) and 129 ± 8 pA (n = 8) respectively, highlighting a 40-fold decrease in the detection of MSA on blank H_2O_2 electrodes. Furthermore, a significant difference ($p < 0.001$) between the detection of MSA on bare Pt and blank H_2O_2 electrodes exists indicating that the detection of MSA has been sufficiently blocked on the blank H_2O_2 electrodes. Therefore, it is clear from these aforementioned results that the interference rejection characteristics of the selective polymer have been confirmed *in vitro*.

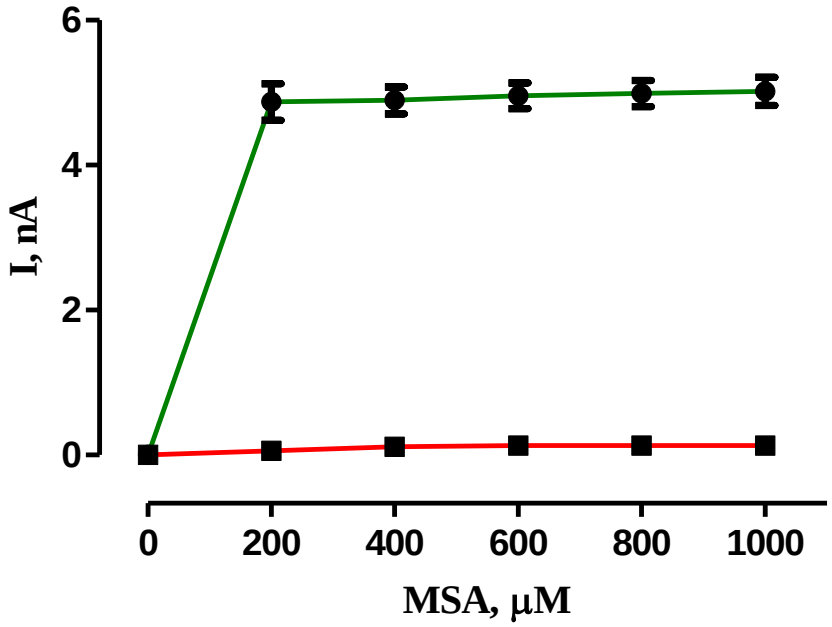

Figure 4.3.3.8.1: Current concentration profile for 0 - 1000 µM MSA calibrations on bare Pt electrodes (*n* = 8, green line) and H_2O_2 blank electrodes (*n* = 8, red line). Data is represented as mean ± SEM.

Similarly, SA acute investigations were carried out *in vivo* (Section 3.9.1.2). SA studies enabled the investigation of the performance of the H_2O_2 biosensor to measure endogenous levels of H_2O_2 due to the ability of SA to inhibit the action of catalase. Catalase works alongside glutathione peroxidase to elicit a highly efficient antioxidant system[45]. Striatal H_2O_2 levels are maintained due to the breakdown of H_2O_2 into H_2O by catalase[46].

As with MSA experiments, it was imperative to confirm that the H_2O_2 biosensor was measuring endogenous H_2O_2 levels and not SA. Therefore, the selectivity of the blank H_2O_2 electrodes was tested against 0 -1000 µM SA *in vitro*. The mean current response obtained on the bare Pt electrodes and the blank H_2O_2 electrodes was 305 ± 40 pA, (n = 8) and 118 ± 15 pA, (n = 8) respectively. Figure 4.3.3.8.2 highlights the negligible contribution of SA measured by the blank H_2O_2 electrodes (red line) in comparison to the detection of SA measured by bare Pt electrodes (green line). A significant difference (p < 0.0001) was determined following SA calibration on bare Pt (n = 8) and blank H_2O_2 electrodes (n = 8). These results confirm the ability of the blank H_2O_2 electrodes to measure endogenous H_2O_2 without detecting SA in the local area *in vivo*.

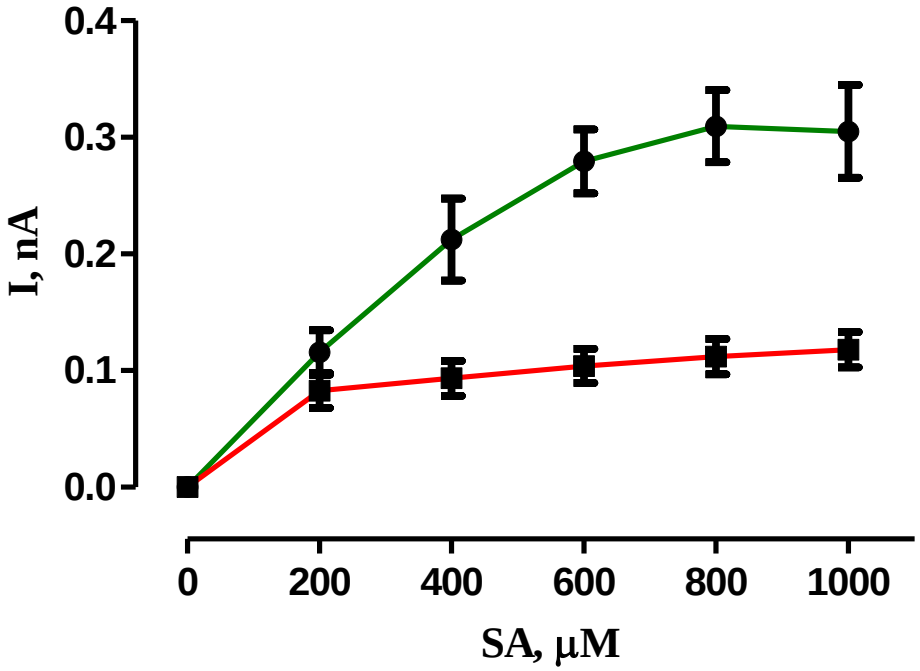

Figure 4.3.3.8.2: Current concentration profile for 0 - 1000 µM SA calibrations on bare Pt electrodes (*n* = 8, green line) and H_2O_2 blank electrodes (*n* = 8, red line). Data is represented as mean ± SEM.

In addition, the blank H_2O_2 electrodes are subjected to high concentrations of H_2O_2 infusions during *in vivo* microinfusion investigations. As alluded to in Section 3.9.1.2, a 150-second washout period using aCSF was employed to diminish the effect of any residual H_2O_2 still present in the microinfusion probe before the administration of MSA/SA commenced. However, the blank H_2O_2 electrodes are exposed to high concentrations of H_2O_2. Therefore, it must be confirmed that the interference rejection membrane have not been compromised from exposure to these high concentrations. *In vitro* studies were utilised to expose the blank H_2O_2 electrodes to 0 - 10 mM H_2O_2 followed by a 0 - 1000 µM MSA calibration to validate the retention of the rejection characteristics. Figure 4.3.3.8.3 illustrates that no compromise in the rejection properties has been experienced following a 0 - 10 mM H_2O_2 calibration. A negligible mean current of - 97± 14 pA (*n* = 4) was measured on blank H_2O_2 electrodes following 0 - 1000 µM MSA calibration. The negative value is a result of baseline drift *in vitro*. In contrast, the same electrodes were able to efficiently measure H_2O_2 which resulted in a mean current of 410 ± 21 nA (*n* = 4) following addition of 10 mM H_2O_2. *In vitro*,

these results strongly corroborate the ability of the blank H_2O_2 electrodes to efficiently block the detection of electroactive interferents whilst measuring H_2O_2.

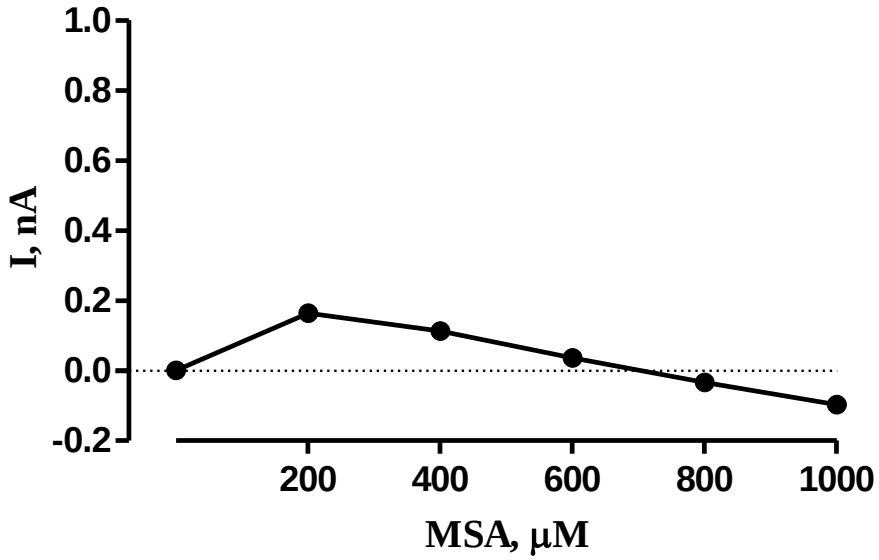

Figure 4.3.3.8.3: The MSA rejection characteristics of blank H_2O_2 electrodes (n = 4) following a 0 - 10 mM H_2O_2 calibration. Data is presented as mean ± SEM.

4.3.3.9 Ex Vivo Sensocompatibility of the H_2O_2 biosensor

Investigations into the sensitivities of the blank and catalase H_2O_2 electrodes following exposure to homogenised brain tissue are demonstrated in Figure 4.3.3.9.1. The sensitivities on Day 0 are denoted as 100 %. The sensitivities recorded on each subsequent day was taken as a percentage of Day 0. Figure 4.3.3.9.1A highlights the significant difference in sensitivity demonstrated by the H_2O_2 blank electrode (p < 0.0001, one-way ANOVA, n = 4) over Day 1 (84.6 ± 5.1 %), Day 3 (75.2 ± 2.5 %), Day 7 (73.4 ± 5.1 %) and Day 14 (60.0 ± 4.5 %). An initial drop in sensitivity was experienced which is in agreement with previous work which highlights a drop in sensitivity upon contact with biological tissue[36]. In addition, a significant difference was observed, by means of Bonferroni *post hoc* analysis, between Day 1 and Day 14 (p < 0.01). Conversely, Day 1, Day 3 and Day 7 showed no significant difference in sensitivity (Figure 4.3.3.9.1A *inset*).

Figure 4.3.3.9.1B highlights the sensitivities of the H_2O_2 catalase electrodes recorded over a 14-day period. Correspondingly, a significant difference (p < 0.01, one-way ANOVA, n = 4) was observed over Day 1 (84.6 ± 20.8 %), Day 3 (43.7 ± 9.1 %), Day 7 (115.3 ± 9.2 %), and Day 14 (139.8 ± 24.2 %). No significant difference (p

> 0.05) was noted between Day 1, 3, 7 and 14 according to Bonferroni *post hoc* analysis (Figure 4.3.3.9.1B *inset*).

From Figure 4.3.3.9.1B, it appears that there is a decrease in the sensitivity of the H_2O_2 catalase electrodes. However, it is important to remember that the H_2O_2 catalase electrode functions by degrading surrounding H_2O_2 due to the presence of catalase on the electrode surface. Therefore, Day 1 and Day 3 highlight an increase in the performance of the electrode following implantation due to a decrease in the detection of H_2O_2. Albeit, as previously described, once a foreign body is implanted in biological tissue, it is subjected to adherence from surrounding proteins and lipids. Said species work to help reduce analyte detection due to inhibition of diffusion across the electrode membrane being experienced. Therefore, it is important to highlight that this is not due to an improvement in biosensor performance.

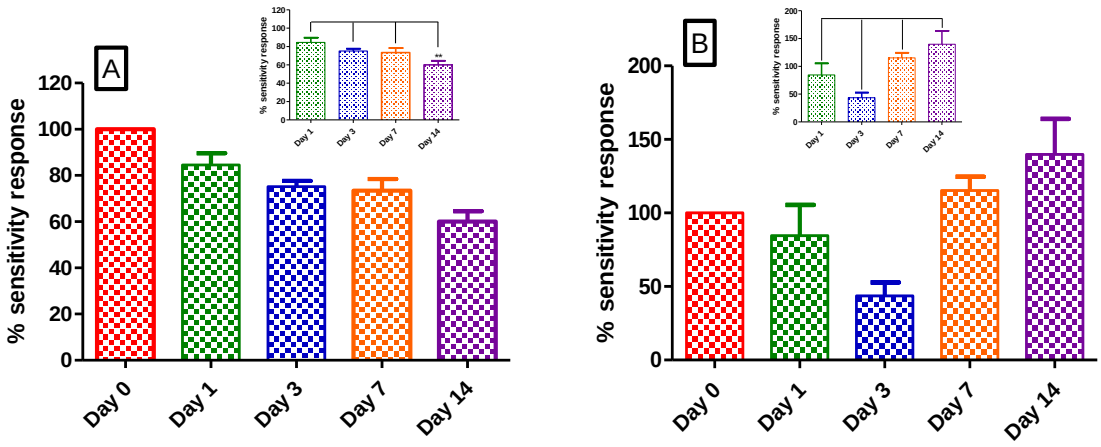

Figure 4.3.3.9.1: Sensitivities of blank (A) and Catalase (B) electrodes following *ex vivo* studies in homogenised brain tissue (0 - 14 days, *n* = 4). *Inset*: Day 1 - 14 Bonferroni *post hoc* analysis. Data represented as mean ± SEM.

Additionally, it was vital to ensure the integrity of the interference rejection properties following placement in brain tissue. Retention of the AA rejection properties of the permselective membrane are crucial to allow for *in vivo* recording to occur. Post-implantation AA calibrations were conducted to obtain currents at 400 µM and 1000 µM AA which were expressed as a percentage of the corresponding pre-implantation currents (Day 0). As with the sensitivity investigations, Day 0 was expressed as a 100 % and the succeeding days were taken as a percentage of Day 0.

Figure 4.3.3.9.2A highlights the significant difference ($p < 0.01$, one-way ANOVA, $n = 4$) in the characteristics of the permselective membrane for H_2O_2 blank electrodes on Day 1 (177.9 ± 22.8 %), Day 3 (256.7 ± 79.9 %), Day 7 (126.7 ± 27.0 %), Day 14 (350.2 ± 43.9 %) at 400 µM AA. Equally, Figure 4.3.3.9.2B displays a significant difference was observed on H_2O_2 catalase electrodes ($p < 0.05$, one-way ANOVA, $n = 4$) following addition of 400 µM AA over Day 1 (224.4 ± 31.8 %), Day 3 (383.5 ± 142.8 %), Day 7 (149.8 ± 45.8 %) and Day 14 (469.3 ± 78.9 %). In addition, no significant difference ($p > 0.05$) was observed using Bonferroni *post hoc* analysis between Day 1 and the subsequent 14 days at 400 µM AA (*Inset* Figure 4.3.3.9.2B). The inset in Figure 4.3.3.9.2B illustrates a slight increase in AA detection. This normally signifies that the permselective membrane has been compromised by the harsh surrounding environment leading to an increase in interferent detection. However, such results are expected following exposure to proteins and lipids as previously referred.

Nevertheless, it must be highlighted that the recorded currents of AA are < 1% of the total recorded currents of AA calibrations conducted on bare Pt as discussed in Section 4.3.3.1. Additionally, the interference rejection membrane has been known to display self-blocking characteristics. The concentration range of AA in the ECF has been stated to be between 200 - 500 µM[29]. It is within this concentration range, that self-blocking occurs. The self-blocking properties have been reported previously in *in vitro* studies (Section 4.3.3.2). During *in vitro* investigations, a very small proportion of AA crosses the semi-permeable PPD membrane. Upon further additions of AA aliquots, self-blocking occurs. This is where the porous membrane traps AA and dehydroascorbic acid within the polymer matrix and thus, incoming AA is sterically hindered from reaching the electrode surface. Previously, it has been hypothesised that a similar trend occurs *in vivo*[6]. Therefore, following initial exposure to endogenous AA concentrations the polymer will become sterically blocked. Once sterically hindered, the polymer will prevent any AA detection for the remainder of the *in vivo* investigation and thus, prevent the detection of interfering species.

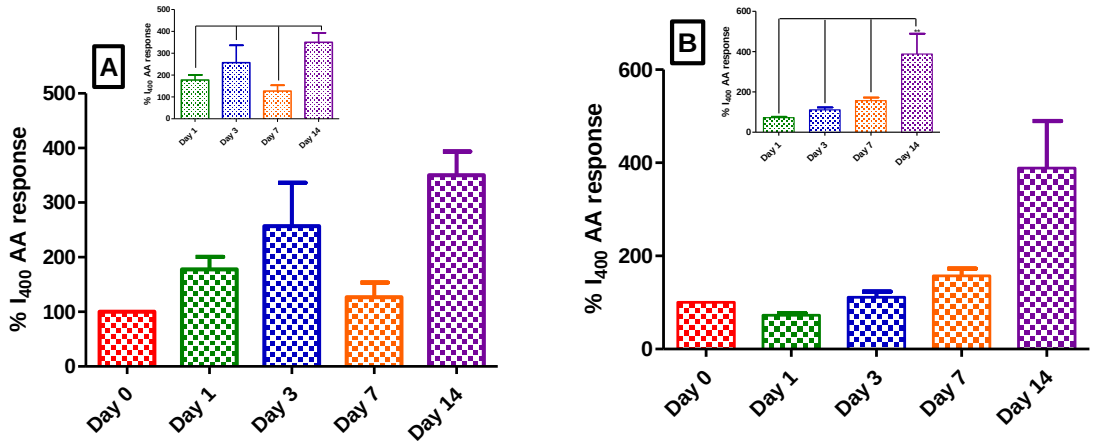

Figure 4.3.3.9.2: Selectivities of Blank (A) and Catalase (B) electrodes following *ex vivo* studies in homogenised brain tissue (0 - 14 days, *n* = 4). *Inset*: Day 1 - 14 Bonferroni *post hoc* analysis. Data represented as mean ± SEM.

4.3.3.10 Physical Effect of Implantation on the Enzymatic Activity of Catalase

Comparatively, the physical effect of implantation on the adsorbed enzyme on the surface of the electrode must be investigated before being applied to *in vivo* studies. Studying the physical effect on the enzyme was examined using an *ex vivo* set-up as damage was incurred to the H_2O_2 catalase electrode following removal from sacrificed subjects. As a result, it was not possible to obtain data from *in vivo* electrodes.

The *ex vivo* set-up was mirrored to mimic the *in vivo* environment whereby the physical effect of implanting the electrode was recreated by slowly inserting the pre-calibrated H_2O_2 catalase electrodes (n = 12) into mouse brains using a micromanipulator. Following exposure of the electrodes for a period of 60-minutes, the electrodes were removed from the brain tissue carefully. Post-calibrations of each of the electrodes were conducted thereafter, which allowed for comparison of pre- and post-insertion sensitivities of the electrodes. Analysis performed following the physical effect of insertion of the H_2O_2 catalase electrode in brain tissue, resulted in a significant difference ($p < 0.01$, unpaired t-test) in sensitivity being experienced. Figure 4.3.3.10.1 displays the sensitivities obtained pre- and post-insertion of the H_2O_2 catalase electrodes. A slight reduction in the sensitivity recorded for post-implanted H_2O_2 catalase electrodes (7.48 ± 0.2 pA/µM, n = 12) compared to pre-implanted H_2O_2 catalase electrodes (6.89 ± 0.5 pA/µM, n = 12) was observed. As alluded to previously, the brain is a complex biological environment rich in protein and lipids. The presence

of such biological components adsorb to the electrode following implantation. Therefore, diffusion of H_2O_2 across the membrane of the biosensor is hypothesised to be reduced slightly following contact with the brain tissue. It must be stated that such reductions in sensitivity are not as a result of the improvement of enzymatic activity. Similar occurrence was noted whereby a decrease in H_2O_2 sensitivity was observed in the first 72 hours post-implantation. Notwithstanding, retention of the adsorbed enzyme can be confirmed due to no compromise in the sensitivity being exhibited post-implantation (Figure 4.3.3.10.1). As a result, the H_2O_2 catalase electrode is suitable for *in vivo* application.

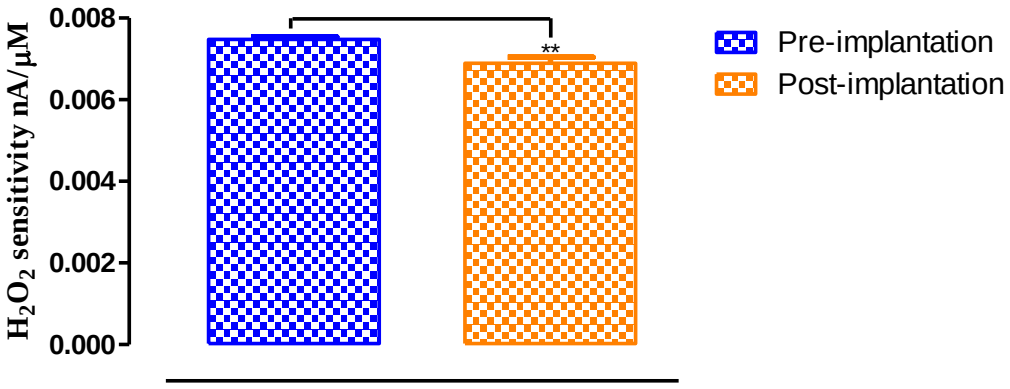

Figure 4.3.3.10.1: Catalase electrode sensitivity pre-insertion (blue) vs. catalase electrode sensitivity post-insertion (orange). Sensitivity represented as mean ± SEM.

4.3.3.11 Post In Vivo Investigations on the H_2O_2 Biosensor

It was not possible to conduct post *in vivo* implantation studies on the H_2O_2 biosensor due to the difficulty in removing the H_2O_2 biosensor from sacrificed mice without causing extensive damage to the enzymatic biosensor.

4.4 Conclusion

In summary, this chapter was associated with validating the sensitivity and selectivity parameters of the previously characterised NO and O_2 sensor and the H_2O_2 biosensor. The NO sensor displayed an excellent sensitivity of 1331 ± 34.1 pA/µM (*n* = 53) towards the detection of NO which is in good agreement with the sensitivity previously reported of 1670 ± 80.0 pA/µM[11]. Figure 4.3.1.2.1 clearly displays the excellent selectivity exhibited by the NO sensor with negligible interference from the interferent, AA, being measured. Whilst, sensocompatibility studies indicated that the sensitivity and selective properties of the NO sensor were retained for up to 14-days. Furthermore, post *vivo* investigations highlighted significant increases in NO sensitivity and AA detection following implantation. However, it was suggested that this increase can be attributed to damage caused to the sensor during removal of the headpiece from the euthanised subject as discussed in Section 4.3.1.4 and 4.3.1.5. In brief, the selectivity and sensitivity of the NO has been validated along with good operational stability of the sensor being observed. Additionally, the obtained results are in good agreement with previously reported characterisation studies[6,11]. Therefore, this sensor has now been deemed suitable for *in vivo* application.

Furthermore, the sensitivities of various O_2 sensors were compared to ensure that the sensor design with the greatest sensitivity was incorporated into *in vivo* studies. CPEs fabricated with a 2.0 mm cavity, 1.0 mm cavity and a 0.5 mm cavity all exhibited excellent sensitivity whilst Pt electrodes illustrated reliable recording of O_2 at - 650 mV *vs.* SCE. Moreover, the current densities calculated for the Pt sensor, 2.0 mm cavity CPE, 1.0 mm cavity CPE and 0.5 mm cavity CPE were compared to identify the optimal O_2 sensor design for *in vivo* application. The CPE incorporating the miniaturised design was recognised as exhibiting the maximum sensitivity (- 79.87 ± 0.82 nA/mm^2/µM) compared to the sensitivities attained for the Pt electrode (- 71.88 ± 4.74 nA/mm^2/µM), 2.0 mm cavity CPE (- 60.51 ± 0.32 nA/mm^2/µM) and 1.0 mm cavity (- 47.45 ± 0.32 nA/mm^2/µM). Additionally, the 0.5 mm cavity CPE was shown to remain stable over 14-days during *ex vivo* studies whilst also exhibiting retention of the excellent sensitivity parameters during post *vivo* investigations. Therefore, with the excellent sensitivity, selectivity and stability properties displayed by the 0.5 mm cavity CPE throughout *in vitro* investigations, this miniaturised design is now suitable to be included in *in vivo* experimentation.

Finally, the H_2O_2 dual biosensor was determined to exhibit excellent sensitivity and selectivity parameters when compared to previous studies involving this previously characterised biosensor[8,9]. The sensitivity of the blank H_2O_2 electrode achieved was 420.0 ± 2.0 pA/µM (n = 92) which is in good agreement to the sensitivity of the biosensor previously reported of 470 ± 3.0 pA/µM (n = 24)[42]. Likewise, the catalase H_2O_2 electrode exhibited high sensitivity (10 ± 0.3 pA/µM) to the addition of 1000 µM H_2O_2. Additionally, the blank H_2O_2 electrode and the catalase H_2O_2 electrode were shown to exhibit high selectivity when tested against physiologically relevant concentrations of AA. The recorded AA response on the blank electrode for the $I_{400\ \mu M}$ and $I_{1000\ \mu M}$ value was 98 ± 16 pA (n = 97) and 46 ± 17 pA (n = 97) respectively. Similarly, the $I_{400\ \mu M}$ and $I_{1000\ \mu M}$ value was 71 ± 19 pA (n = 36) and 86 ± 32 pA (n = 36) respectively for the catalase electrodes. These values demonstrate the ability of the blank and catalase electrodes in blocking the detection of AA making them suitable for *in vivo* studies. *Ex vivo* studies highlighted that no significant difference in the sensitivity and selectivity of the blank and catalase electrodes was recorded following exposure to homogenised brain tissue over 7 days. The selectivity of the blank electrode illustrated that no significant difference was recorded between Day 1 and the subsequent 14 days at 400 µM and 1000 µM AA. However, the selectivity of the catalase electrode was seen to be slightly compromised with a significant difference ($p < 0.05$) recorded between Day 1 and Day 14. However, it must be noted that the amount of AA detected contributed to < 1 % of the total recorded currents of AA calibrations conducted on bare Pt electrodes. Similarly, the physical effect of implanting the catalase electrode in *ex vivo* mouse brain tissue reported a slight compromise on the immobilisation of the adsorbed enzyme on the electrode surface. Therefore, the above obtained results validated that excellent sensitivity, selectivity and stability of both the blank H_2O_2 electrode and the catalase H_2O_2 electrode have been achieved, which remain in good agreement with previously reported data. Hence, the above obtained results indicate that this biosensor is now suitable for application in *in vivo* investigations.

4.5 References

1. Bolger, F., Bennett, R. & Lowry, J. An in vitro characterisation comparing carbon paste and Pt microelectrodes for real-time detection of brain tissue oxygen. *Analyst* **136,** 4028–35 (2011).
2. Bolger, F. B. & Lowry, J. P. Brain tissue oxygen: In vivo monitoring with carbon paste electrodes. *Sensors* **5,** 473–487 (2005).
3. Bolger, F. B., McHugh, S. B., Bennett, R., Li, J., Ishiwari, K., Francois, J., Conway, M. W., Gilmour, G., Bannerman, D. M., Fillenz, M. & Tricklebank, M. Characterisation of carbon paste electrodes for real-time amperometric monitoring of brain tissue oxygen. *J. Neurosci. Methods* **195,** 135–42 (2011).
4. Finnerty, N. J., O'Riordan, S. L., Pålsson, E. & Lowry, J. P. Brain nitric oxide: regional characterisation of a real-time microelectrochemical sensor. *J. Neurosci. Methods* **209,** 13–21 (2012).
5. Finnerty, N. J., O'Riordan, S. L., Brown, F. O., Serra, P. A., O'Neill, R. D., Lowry, J. P. In vivo characterisation of a Nafion®-modified Pt electrode for real-time nitric oxide monitoring in brain extracellular fluid. *Anal. Methods* **4,** 550 (2012).
6. Wynne, A. M., Reid, C. H. & Finnerty, N. J. In vitro characterisation of ortho phenylenediamine and Nafion®-modified Pt electrodes for measuring brain nitric oxide. *J. Electroanal. Chem.* **732,** 110–116 (2014).
7. O'Riordan, S. L., McLaughlin, K., Lowry, J. P. In vitro physiological performance factors of a catalase-based biosensor for real-time electrochemical detection of brain hydrogen peroxide in freely-moving animals. *Anal. Methods* **8,** 7614–7622 (2016).
8. O'Brien, K. B., Killoran, S. J., O'Neill, R. D. & Lowry, J. P. Development and characterization in vitro of a catalase-based biosensor for hydrogen peroxide monitoring. *Biosens. Bioelectron.* **22,** 2994–3000 (2007).
9. O'Riordan, S.L., Lowry, J. P. In vivo characterisation of a catalase-based biosensor for real-time electrochemical monitoring of brain hydrogen peroxide in freely-moving animals. *Anal. Methods* **9,** 1253–1264 (2017).
10. Brown, F. O. & Lowry, J. P. Microelectrochemical sensors for in vivo brain analysis: an investigation of procedures for modifying Pt electrodes using Nafion®. *Analyst* **128,** 700 (2003).

11. Brown, F. O., Finnerty, N. J. & Lowry, J. P. Nitric oxide monitoring in brain extracellular fluid: characterisation of Nafion®-modified Pt electrodes in vitro and in vivo. *Analyst* **134,** 2012–20 (2009).
12. Lowry, J. P., Boutelle, M. G., O'Neill, R. D. & Fillenz, M. Characterization of carbon paste electrodes in vitro for simultaneous amperometric measurement of changes in oxygen and ascorbic acid concentrations in vivo. *Analyst* **121,** 761–6 (1996).
13. Yin, C., Wang, Z., Luo, Y., Li, J., Zhou, Y., Zhang, X., Zhang, H., Fang, P. & He, C. Thermal annealing on free volumes, crystallinity and proton conductivity of Nafion membranes. *J. Phys. Chem. Solids* (2018).
14. Neburchilov, V., Martin, J., Wang, H. & Zhang, J. A review of polymer electrolyte membranes for direct methanol fuel cells. *J. Power Sources* **169,** 221–238 (2007).
15. Zakil, F. A., Kamarudin, S. K. & Basri, S. Modified Nafion membranes for direct alcohol fuel cells: An overview. *Renew. Sustain. Energy Rev.* **65,** 841–852 (2016).
16. Wang, H. S., Li, T. H., Jia, W. L. & Xu, H. Y. Highly selective and sensitive determination of dopamine using a Nafion®/carbon nanotubes coated poly(3-methylthiophene) modified electrode. *Biosens. Bioelectron.* **22,** 664–669 (2006).
17. Finnerty, N. J., Bolger, F. B., Pålsson, E. & Lowry, J. P. An investigation of hypofrontality in an animal model of schizophrenia using real-time microelectrochemical sensors for glucose, oxygen, and nitric oxide. *ACS Chem. Neurosci.* **4,** 825–831 (2013).
18. Finnerty, N., O'Riordan, S. L., Klamer, D., Lowry, J. & Pålsson, E. Increased brain nitric oxide levels following ethanol administration. *Nitric Oxide - Biol. Chem.* **47,** 52–57 (2015).
19. Clark, Jr., L.C., Misrahy, G., Fox, R. P. Chronically implanted polarographic electrodes. *J. Appl. Physiol.* **13,** 85–91 (1958).
20. Kozai, T. D. Y., Jaquins-Gerstl, A. S., Vazquez, A. L., Michael, A. C. & Cui, X. T. Brain tissue responses to neural implants impact signal sensitivity and intervention strategies. *ACS Chem. Neurosci.* **6,** 48–67 (2015).
21. Potter-Baker, K. A., K. A., Ravikumar, M., Burke, A. A., Meador, W. D., Householder, K. T., Buck, A. C., Sunil, S., Stewart, W. G., Anna, J. P.,

Tomaszewski, W. H. & Capadona, J.R. A comparison of neuroinflammation to implanted microelectrodes in rat and mouse models. *Biomaterials* **35,** 5637–5646 (2014).

22. Killoran, S. J. & O'Neill, R. D. Characterization of permselective coatings electrosynthesized on Pt-Ir from the three phenylenediamine isomers for biosensor applications. *Electrochim. Acta* **53,** 7303–7312 (2008).
23. Frost, M. & Meyerhoff, M. E. In vivo chemical sensors: Tackling biocompatibility. *Anal. Chem.* **78,** 7370–7377 (2006).
24. Sommakia, S., Rickus, J. L. & Otto, K. J. Effects of adsorbed proteins, an antifouling agent and long-duration DC voltage pulses on the impedance of silicon-based neural microelectrodes. *Proc. 31st Annu. Int. Conf. IEEE Eng. Med. Biol. Soc. Eng. Futur. Biomed. EMBC 2009* 7139–7142 (2009).
25. Trouillon, R., Cheung, C., Patel, B. A. & O'Hare, D. Comparative study of poly(styrene-sulfonate)/poly(L-lysine) and fibronectin as biofouling-preventing layers in dissolved oxygen electrochemical measurements. *Analyst* **134,** 784–793 (2009).
26. Malinski, T., Bailey, F., Zhang, Z. G. & Chopp, M. Nitric oxide measured by a porphyrinic microsensor in rat brain after transient middle cerebral artery occlusion. *J Cereb Blood Flow Metab* **13,** 355–358 (1993).
27. Brown, G. Nitric oxide regulates mitochondrial respiration and cell functions by inhibiting cytochrome oxidase. *FEBS Lett.* **369,** 136–139 (1995).
28. Isik, S., Castillo, J., Blöchl, A., Csöregi, E. & Schuhmann, W. Simultaneous detection of l-glutamate and nitric oxide from adherently growing cells at known distance using disk shaped dual electrodes. *Bioelectrochemistry* **70,** 173–179 (2007).
29. Miele, M. & Fillenz, M. In vivo determination of extracellular brain ascorbate. *J. Neurosci. Methods* **70,** 15–19 (1996).
30. Rice, M. E. Ascorbate compartmentalization in the CNS. *Neurotox Res* **1,** 81–90 (1999).
31. Lehmani, A., Turq, P., Michelle, P., Jacques, P. & Simonin, J. Ion transport in Nafion® 117 membrane. *J. Electroanal. Chem.* **428,** 81–89 (1997).
32. McConnell, G. C., Rees, H. D., Levey, A. I., Gutekunst, C. A., Gross, R.E. & Bellamkonda, R.V. Implanted neural electrodes cause chronic, local inflammation that is correlated with local neurodegeneration. *J. Neural Eng.* **6,**

(2009).

33. Khan, A. S. & Michael, A. C. Invasive consequences of using micro-electrodes and microdialysis probes in the brain. *TrAC - Trends Anal. Chem.* **22,** 503–508 (2003).
34. O'Neill, R. D., Rocchitta, G., McMahon, C. P., Serra, P. A. & Lowry, J. P. Designing sensitive and selective polymer/enzyme composite biosensors for brain monitoring in vivo. *TrAC - Trends Anal. Chem.* **27,** 78–88 (2008).
35. Kane, D. A. & O'Neill, R. D. Major differences in the behaviour of carbon paste and carbon fibre electrodes in a protein-lipid matrix: implications for voltammetry in vivo. *Analyst* **123,** 2899–2903 (1998).
36. Garguilo, M. G. & Michael, A. C. Quantitation of choline in the extracellular fluid of brain tissue with amperometric microsensors. *Anal. Chem.* **66,** 2621–2629 (1994).
37. Rothwell, S. A., Killoran, S. J., Neville, E. M., Crotty, A. M. & O'Neill, R. D. Poly(o-phenylenediamine) electrosynthesized in the absence of added background electrolyte provides a new permselectivity benchmark for biosensor applications. *Electrochem. commun.* **10,** 1078–1081 (2008).
38. Rothwell, S. A., Kinsella, M. E., Zain, Z. M., Serra, P. A., Rocchitta, G., Lowry, J. P. & O'Neill, R. D. Contributions by a novel edge effect to the permselectivity of an electrosynthesized polymer for microbiosensor applications. *Anal. Chem.* **81,** 3911–3918 (2009).
39. Rothwell, S. A., McMahon, C. P. & O'Neill, R. D. Effects of polymerization potential on the permselectivity of poly(o-phenylenediamine) coatings deposited on Pt-Ir electrodes for biosensor applications. *Electrochim. Acta* **55,** 1051–1060 (2010).
40. Ryan, M. R., Lowry, J. P. & O'Neill, R. D. Biosensor for neurotransmitter L-glutamic acid designed for efficient use of L-glutamate oxidase and effective rejection of interference. *Analyst* **122,** 1419–1424 (1997).
41. Craig, J. D. & O'Neill, R. D. Comparison of simple aromatic amines for electrosynthesis of permselective polymers in biosensor fabrication. *Analyst* **128,** 905–911 (2003).
42. O'Riordan, S. L. Oxidative stress markers in neurological diseases and disorders: electrochemical detection of hydrogen peroxide and nitric oxide. **1,** PhD Thesis (National University of Ireland Maynooth (NUIM), 2013).

43. Johan Forshammar, Block, L., Lundborg, C., Biber, B. & Hansson, E. Metabolism and functions of glutathione in brain. *J. Biol. Chem.* **286,** 649–671 (2011).
44. Ighodaro, O. M. & Akinloye, O. A. First line defence antioxidants-superoxide dismutase (SOD), catalase (CAT) and glutathione peroxidase (GPX): Their fundamental role in the entire antioxidant defence grid. *Alexandria J. Med.* 1–7 (2017).
45. Gaetani, G. F., Galiano, S., Canepa, L., Ferraris, A. M. & Kirkman, H. N. Catalase and Glutathione Peroxidase Are Equally Active Erythrocytes. *Blood* **73,** 334–339 (1989).
46. Sepasi Tehrani, H. & Moosavi-Movahedi, A. A. Catalase and its mysteries. *Prog. Biophys. Mol. Biol.* (2018).

Chapter 5

In Vivo Characterisation of Amperometric Sensors in the Striatum of NOD SCID Mice

5.1 Introduction

Extensive characterisation of the NO, O_2 sensors and the H_2O_2 biosensor has been conducted previously both *in vitro* and *in vivo*[1–10]. However, to date, none of the aforementioned sensors have been characterised in NOD SCID mice as any previous *in vivo* studies have involved the use of wistar rats. Therefore, it was imperative to conduct an *in vivo* characterisation of these sensors in the striatum of NOD SCID mice since their utilisation are pivotal to this project.

NOD SCID mice do not reject xenografts allowing for the growth and integration of human cells and tissues which allows for analysis of mechanisms of disease pathogenesis that would otherwise be challenging to carry out in the human population[11,12]. Within this project, patient-derived iPSCs are differentiated into dopaminergic neurons which are further transplanted into the striatum of NOD SCID mice allowing for a humanised model of PD to be achieved. Due to the ultimate application of each of the sensors in the humanised mouse model of PD, it was crucial to conduct an *in vivo* characterisation in this mouse strain. Therefore, Chapter 5 details the implantation of each of the sensors in immunocompromised NOD SCID mice to ensure maintenance of the sensitivity, selectivity and stability of the NO, O_2 sensors and the H_2O_2 biosensor *in vivo*.

The amperometric response of each of the aforementioned sensors was investigated by means of physiological stimulation and administration of varying characterisation compounds. Firstly, saline and restraint tests are known to induce neuronal activation by subjecting the animal to mild stress. The administration of saline and the action of the restraint test on the amperometric response was investigated due to the fluctuations in analyte levels associated with each of these physiological stressors. Restraint tests were carried out as described in Section 3.10.3 whereby the movement of the animal was restricted resulting in an increase in neuronal activation and CBF. Consequently, any changes in analyte concentration associated with the increased neuronal activation and cerebral blood supply would be recorded by the implanted sensor.

Additionally, the use of characterisation compounds, such as L-NAME and Diamox, were utilised to characterise the response of each sensor to fluctuations of endogenous analyte concentrations influenced by their systemic administration. The ability of the sensors to monitor changes caused by administration of such compounds

confirms the ability of the sensor to function efficiently *in vivo*. Furthermore, the selectivity of each of the sensors was investigated following the administration of sodium ascorbate. Ascorbate is the main interfering species in the brain due to existing at high concentrations and its ease of oxidation *in vivo*[13,14]. Thus, sodium ascorbate was included in *in vivo* investigations to determine the selectivity of the sensor following implantation.

Moreover, one of the most crucial criteria for successful continuous amperometric recordings is the ability for the sensor to demonstrate excellent sensocompatibility following *in vivo* implantation. Sensocompatibility accurately describes the impact of the surrounding tissue on the performance of the sensor following implantation *in vivo*[15]. The brain is rich in lipids and proteins which, accompanied by the immune response of the brain to implanted neural electrodes, can negatively affect the efficient functioning of the sensor. It has been widely reported that the implantation of microelectrodes can cause local tissue damage leading to an infiltration of plasma protein inflammatory cells which can adsorb to the electrode surface[16,17]. Adhesion of these biological constituents to the electrode surface can lead to impedance of analyte detection due to the difficulty in analyte diffusion across to the surface of the electrode[18]. A loss in sensitivity of up to 50 % *in vivo* has been reported in comparison to *in vitro* sensitivity values obtained[19]. Additionally, the selectivity of the sensor can be negatively affected by the harsh biological milieu in which the sensor is implanted allowing for the interference rejection layer of the sensor to become compromised. Therefore, it is crucial to ensure stability of the sensor is retained *in vivo* to allow for continuous long-term recordings to be conducted.

With these parameters in mind, the overall objective of this chapter was to characterise the NO, O_2 sensors and the H_2O_2 biosensor in the striatum of NOD SCID mice following the validation of the amperometric technology *in vitro*. By characterisation of each individual amperometric sensor signal through validation of the sensor response to the analyte of interest and stability of the sensor being exhibited over a number of days, it allowed for continuous long-term recordings to be undertaken in NOD SCID mice.

5.2 Experimental

All the experiments were undertaken using instrumentation and software discussed in Section 3.2. Solutions and chemicals employed are listed in Section 3.3. The manufacture of the NO and O_2 sensors, and the H_2O_2 biosensor are detailed in Section 3.4.2 - 3.4.4. Investigations involving the NO and O_2 sensors were carried out in the striatum of freely-moving animals. Correspondingly, H_2O_2 studies involved implantation in the striatum of freely-moving and anaesthetised animals. Surgical procedures associated with each of the aforementioned sensors are detailed in Section 3.8.4. Following surgical recovery, a potential of + 700 mV *vs*. SCE and + 900 mV *vs*. SCE was applied to the H_2O_2 biosensor and the NO sensor respectively. Comparatively, a potential of - 650 mV *vs.* SCE was applied to the O_2 sensor.

All data is presented as mean ± SEM, where *n* denoted the number of animals. In 24-hour recordings, *n* represents the number of days or nights/number of animals with one sensor implanted per animal. Statistical analysis involved paired and unpaired *t*-tests, in addition to, one-way ANOVA analysis. Elimination of inter electrode and inter animal variability was achieved by normalisation of baseline currents to 100 %, allowing for the global change in current to be represented as a percentage of the pre-perturbation baseline current. Statistical analysis tests were completed using GraphPad Prism which resulted in a *p*-value being obtained. *p*-values indicate the probability of the results being significantly different ($p < 0.05$). The level of significance is denoted by the number of asterisks assigned to the value.

Section 2.4.3 detailed that H_2O_2 is selectively monitored following subtraction of the catalase current from the blank current once the interference current of the blank and catalase electrodes is similar following *in vitro* calibrations. Accuracy of this subtraction method is further guaranteed by normalisation of all baseline currents to 100 % which results in the overall subtraction in the recorded current as a percentage of the pre-perturbation baseline current. Therefore, removal of any inconsistencies can be achieved amongst *in vivo* baseline levels due to normalisation to the current changes to the specific sensor.

5.3 Results and Discussion

5.3.1 Characterisation of the NO Sensor in the Striatum of NOD SCID Mice

5.3.1.1 Saline Administration

Characterisation compounds employed in Section 5.3.1 were all formulated in a 0.9 % saline solution prior to being intraperitoneally injected in volumes of 1 mL/kg to the subject. Therefore, characterisation of the response of the NO sensor to administration of the control saline injection must be established. Figure 5.3.1.1.1 illustrates the averaged raw data current response following administration of saline (n = 8). Upon administration of saline, a maximum current change (ΔI) of - 5 ± 2 pA (n = 8) was recorded after 1 ± 0.1 mins (n = 8) in the striatum which resulted in a - 2 ± 1 % (n = 8) change in current. Additionally, a concentration change of 4 ± 2 nM was achieved following the systemic administration. The ΔI was not significantly different (p = 0.05) from the pre-perturbation baseline of 417 ± 71 pA (n = 8). A post-perturbation baseline of 416 ± 72 pA (n = 8) was achieved after 3 ± 1 mins (n = 8). Furthermore, it was perceived that there was no significant difference (p = 0.52) between the post-perturbation baseline and the pre-perturbation baseline.

Previous findings have highlighted the ability of injection stress to provoke an increase in neuronal activation in the subject which is coupled with an increase in CBF[20,21]. Administration of an i.p. injection to the subject results in activation of the main excitatory neurotransmitter, glutamate. Following this, an increase in the production of NO results from the activation of neuronal NOS in response to the excitatory glutamate which requires Ca^{2+} alongside calmodulin for NO production[22]. However, basal levels return momentarily after systemic administration of saline which allows for characterisation of the stress response of the animal to an i.p. injection. Transient changes in the recorded baseline following saline administration are presented in previous studies undertaken in wistar rats whereby an increase in the NO amperometric current was demonstrated following saline administration[4,5].

However, Figure 5.3.1.1.1. highlights a clear decrease in the amperometric response recorded following saline administration in NOD SCID mice. This decrease in current obtained is in complete contrast to the increase in amperometric current previously obtained in wistar rats following systemic saline administration. It can be postulated that this reported difference may be attributed to investigations being

conducted in NOD SCID mice instead of wistar rats that were previously utilised. Therefore, the decrease in amperometric signal obtained may be strain specific, thus, further supporting the need to carry out characterisation studies in NOD SCID mice before further experimentation can be performed in immunocompromised mice. Similarly, the recorded current is observed to quickly return to post-perturbation baseline levels (Table 5.3.1.1.1) following saline administration.

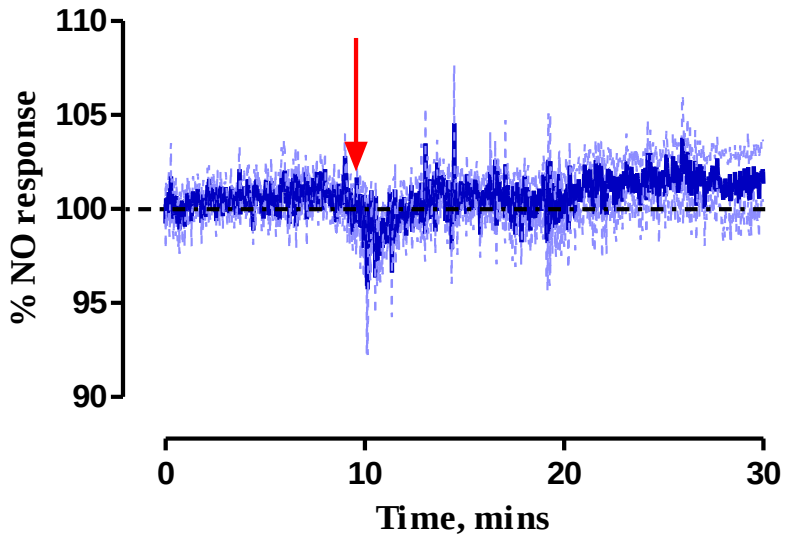

Figure 5.3.1.1.1: Averaged percentage raw data current response of NO sensors implanted in the striatum of NOD SCID mice to a 1 mL/kg i.p. injection of 0.9 % saline. Point of injection is represented by the red arrow. The blue trace indicates the mean percentage current response with the percentage error represented by the light blue trace.

Table 5.3.1.1.1: Summary of results of the NO sensors implanted in the striatum of NOD SCID mice following i.p. administration of 0.9 % saline (*n* = 8).

Saline Injection						
Pre-Perturbation Baseline (pA)	**Max Current (pA)**	**Current Change ΔI (pA)**	**Current Change (%)**	**Max Response Time (mins)**	**Post-Perturbation Baseline (pA)**	**Return to Baseline Time (mins)**
417 ± 71	412 ± 71	-5 ± 2	-2 ± 1	1 ± 0.1	416 ± 72	3 ± 1

5.3.1.2 L-NAME Administration

L-NAME was utilised in characterisation investigations to examine the response of the NO sensor to endogenous levels of NO following i.p. administration. L-NAME is non-selective NOS inhibitor[23,24] which elicits direct competition with L-arginine for binding on the NOS enzyme resulting in the inhibition of NO production[25]. Illustration of the averaged raw data trace following administration of 30 mg/kg L-NAME (n = 5) is depicted in Figure 5.3.1.2.1. Following systemic administration, a significant decrease ($p < 0.01$) in the recorded amperometric current of 31 ± 8 pA (n = 5) was observed from pre-perturbation baseline levels of 436 ± 86 pA (n = 5). This decrease equates to a percentage decrease of 7 ± 1 % (n = 5) and a concentration change of 23 ± 6 nM (n = 5) which occurred 41 ± 18 mins (n = 5) after L-NAME administration (Table 5.3.1.2.1). A new post-perturbation baseline current was measured (430 ± 84 pA, n = 5) after 103 ± 93 mins (n = 5) which was not significantly different (p = 0.17) from pre-perturbation baseline currents. Furthermore, the reported results corroborate with previous studies which highlighted a decrease in NO levels following L-NAME administration in wistar rats[4,5].

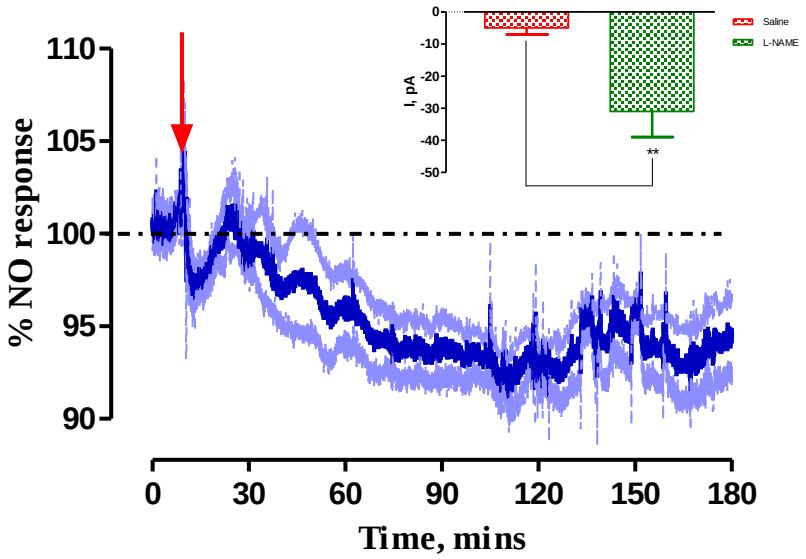

Figure 5.3.1.2.1: Averaged percentage raw data current response of NO sensors implanted in the striatum of NOD SCID mice to 30 mg/kg i.p. injection of L-NAME. Point of injection is represented by the red arrow. The blue trace indicates the mean percentage current response with the percentage error represented by the light blue trace. *Inset*: Comparison of saline (n = 8) *vs.* L-NAME (n = 5, unpaired t-test, $p < 0.05$). Data represented as mean current ± SEM.

Table 5.3.1.2.1: Summary of results of the NO sensors implanted in the striatum of NOD SCID mice following the i.p. administration of 30 mg/kg L-NAME (*n* = 5).

L-NAME Injection						
Pre-Perturbation Baseline (pA)	**Max Current (pA)**	**Current Change ΔI (pA)**	**Current Change (%)**	**Max Response Time (mins)**	**Post-Perturbation Baseline (pA)**	**Return to Baseline Time (mins)**
436 ± 86	405 ± 79	-31 ± 8	-7 ± 1	41 ± 18	430 ± 84	103 ± 93

Furthermore, the saline response was short-lived (3 ± 1 mins, *n* = 8) as opposed to L-NAME whereby a new post-perturbation baseline was only achieved after 103 ± 93 mins (*n* = 8). Hence, these results indicate the decrease in NO levels recorded in the striatum of the NOD SCID mice is much longer lasting which can be attributed to the action of the NOS inhibitor, L-NAME, following systemic administration.

5.3.1.3 L-arginine Administration

L-arginine is directly involved in the synthesis of NO through its binding to the NOS enzyme. It is through this binding, whilst in the presence of various co-factors and molecular O_2, that the production of NO and L-citrulline results[26]. Supplementation with L-arginine in previous studies has showed that acute or chronic administration of L-arginine improved vascular responsiveness via enhanced NO production[27,28].

The average raw data trace of amperometric recordings of NO following i.p. injection of 200 mg/kg L-arginine is presented in Figure 5.3.1.3.1. A maximum NO response was observed following administration of 200 mg/kg L-arginine which resulted in a significant increase ($p < 0.001$) in the recorded NO current from pre-perturbation baseline levels (545 ± 100 pA, *n* = 5). In addition, this increase in NO levels (23 ± 4 pA, *n* = 5) corresponded to a 5 ± 1 % (*n* = 5) difference which was obtained after 48 ± 9 mins (*n* = 5). Moreover, a concentration change of 18 ± 3 nM (*n* = 5) was attained following the administration of saline. New post-perturbation baseline levels (545 ± 99, *n* = 5) were reached after 128 ± 18 mins (*n* = 5, Table 5.3.1.3.1). However, the new baseline current recorded was not significantly different ($p = 0.95$) from pre-perturbation baseline levels. Furthermore, these results highlight

the ability of the NO sensor to respond to endogenous production of NO *in vivo*. Additionally, this work corroborates previous findings where significant increases in NO levels were also reported in previous studies involving wistar rats following administration of L-arginine to the subject[4,29].

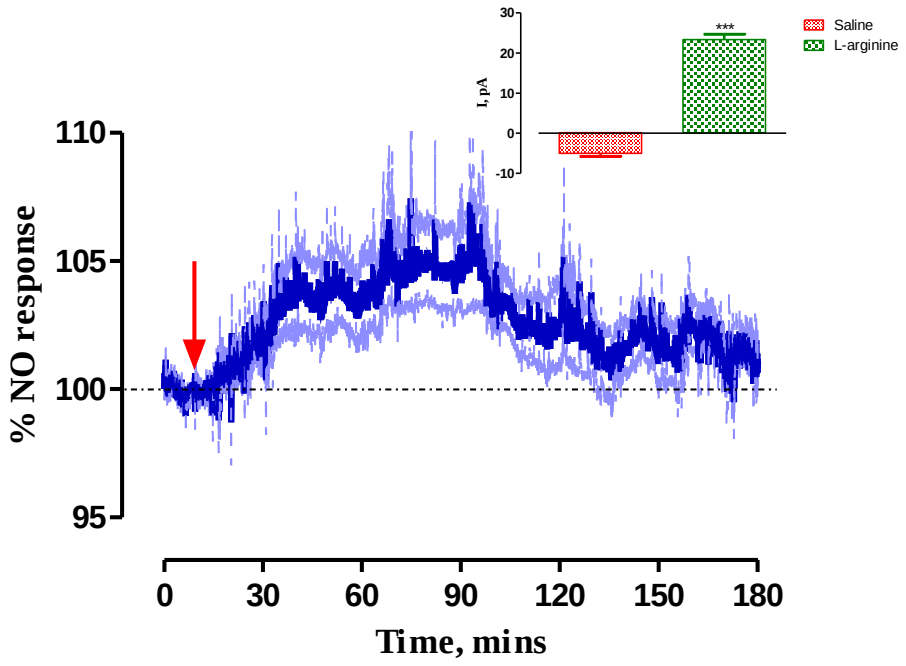

Figure 5.3.1.3.1: Averaged percentage raw data current response of NO sensors implanted in the striatum of NOD SCID mice to 200 mg/kg i.p. injection of L-arginine. Point of injection is represented by the red arrow. The blue trace indicates the mean percentage current response with the percentage error represented by the light blue trace. *Inset*: Comparison of saline (*n* = 8) *vs.* L-arginine (*n* = 5, unpaired *t*-test, $p < 0.001$). Data represented as mean current ± SEM.

Table 5.3.1.3.1: Summary of results of the NO sensors implanted in the striatum of NOD SCID mice following i.p. administration of 200 mg/kg L-arginine (*n* = 5).

L-arginine Injection						
Pre-Perturbation Baseline (pA)	**Max Current (pA)**	**Current Change ΔI (pA)**	**Current Change (%)**	**Max Response Time (mins)**	**Post-Perturbation Baseline (pA)**	**Return to Baseline Time (mins)**
545 ± 100	569 ± 100	23 ± 4	5 ± 1	48 ± 9	545 ± 99	128 ± 18

A significant difference ($p < 0.0001$, Figure 5.3.1.3.1 *inset*) in the ΔI was measured in the NO response following saline and L-arginine administration. Thus, verifying the increase in NO levels following systemic L-arginine administration is a direct result of the action L-arginine working to increase endogenous NO levels in the striatum.

5.3.1.4 Selectivity Investigation on the NO Sensor

The integrity of the Nafion® membrane on the NO sensor to eliminate contribution of interfering species was investigated following implantation. Figure 5.3.1.4.1 depicts the mean percentage current response recorded following systemic administration of a 500 mg/kg sodium ascorbate i.p. injection. Previous selectivity investigations conducted in wistar rats have demonstrated no deviation in the amperometric response from baseline levels following administration of sodium ascorbate suggesting retention of the interference rejection layer following implantation[4,5].

Following the systemic administration of sodium ascorbate, a ΔI of - 32 ± 6 pA ($n = 4$) was reached after 38 ± 17 mins ($n = 4$) which corresponded to a percentage change of - 14 ± 5 % ($n = 4$) and a concentration change of 24 ± 5 nM ($n = 4$). A significant difference ($p < 0.01$) was reported between ΔI and pre-perturbation baseline levels (301 ± 94 pA, $n = 4$). After 91 ± 27 mins ($n = 4$), a new post-perturbation was reached (288 ± 94, $n = 4$). Additionally, a close to significant difference ($p = 0.06$) existed between post-perturbation baseline and pre-perturbation baseline currents. Figure 5.3.1.4.1 revealed a decrease in the recorded NO current following systemic administration of sodium ascorbate. Although this response indicates that the integrity of the Nafion® membrane has been maintained following *in vivo* implantation, the response recorded in NOD SCID mice does not corroborate the amperometric response recorded in wistar rats following sodium ascorbate administration. This disparity may be strain specific due to sodium ascorbate having a different mode of action in immunocompromised mice when compared to wistar rats.

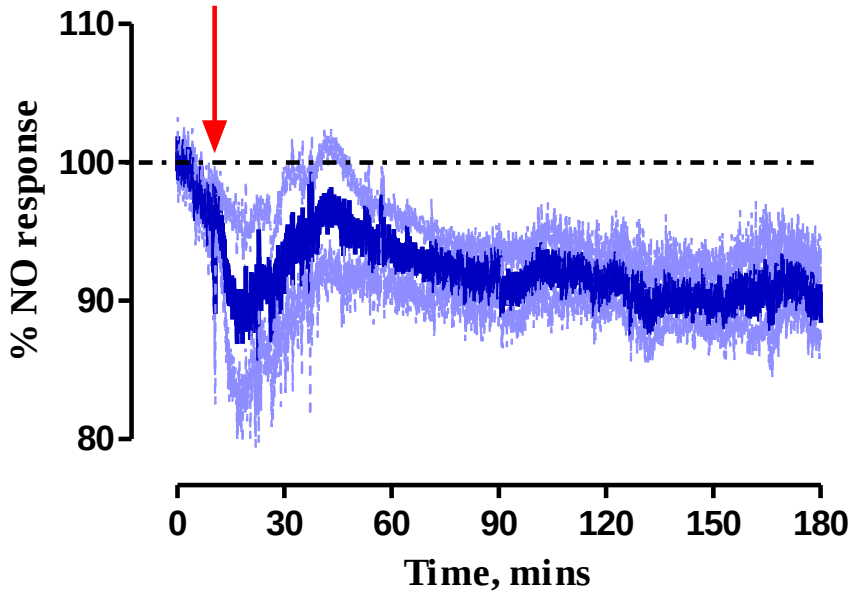

Figure 5.3.1.4.1: Average percentage baseline currents for NO sensors (*n* = 4) following 500 mg/kg sodium ascorbate i.p. injection recorded in the striatum of NOD SCID mice. Mean percentage current is represented by the blue trace. The light blue trace highlights the percentage error. Data represented as mean current ± SEM.

Table 5.3.1.4.1: Summary of results of the NO sensors implanted in the striatum of NOD SCID mice following i.p. administration of 500 mg/kg sodium ascorbate (*n* = 4).

Sodium Ascorbate Injection						
Pre-Perturbation Baseline (pA)	**Max Current (pA)**	**Current Change ΔI (pA)**	**Current Change (%)**	**Max Response Time (mins)**	**Post-Perturbation Baseline (pA)**	**Return to Baseline Time (mins)**
301 ± 94	269 ± 91	-32 ± 6	-14 ± 5	38 ± 17	288 ± 94	91 ± 27

Moreover, when compared to the obtained saline response in Section 5.3.1.1, the sodium ascorbate response highlights a much greater decrease (ΔI, - 32 ± 6 pA, *n* = 4) whereas the ΔI obtained for the saline response was only - 5 ± 2 pA (*n* = 8).

5.3.1.5 Restraint Test

The amperometric NO current obtained following a 2-minute restraint test is displayed in Figure 5.3.1.5.1. This response was seen to exhibit a dual effect whereby a decrease in the amperometric response was observed followed by an increase.

Firstly, a decrease in the recorded NO response was observed after 3 ± 1 mins (n = 4) which was shown to be significantly different (p = 0.01) from pre-perturbation baseline levels (251 ± 41 pA, n = 4). This ΔI of - 15 ± 5 pA (n = 4) corresponded to a - 7 ± 3 % (n = 4) decrease in the NO response and a concentration change of 13 ± 4 nM (n = 4). Following this decrease in the amperometric response, an increase was observed after 23 ± 4 mins (n = 4). This increase corresponded to a ΔI of 14 ± 5 pA (n = 4), a percentage change of 6 ± 2 % (n = 4) and a concentration change of 10 ± 3 nM (n = 4). Additionally, this increase was reported to be significantly different (p = 0.02) from pre-perturbation baseline levels. A post-perturbation baseline current (250 ± 42 pA, n = 4, Table 5.3.1.5.1) was reached after 64 ± 9 mins (n = 4). No significant difference (p = 0.62) was observed to exist between the pre-perturbation baseline current and the post-perturbation baseline current.

Restraint tests are known inducers of neuronal activation. Therefore, by restricting the movement of the animal, neuronal activation is triggered as the animal tries to free itself leading to an increase in CBF and NO. Thus, it can also be hypothesised that the initial decrease in NO recorded following initiation of the restraint test can be attributed to neuronal activation as a similar trend was observed in Figure 5.3.1.1.1 whereby a decrease in the amperometric signal was obtained following administration of an i.p. injection of saline. Figure 5.3.1.5.1 highlights an initial decrease in the amperometric NO response followed by an overshoot of current. Other groups have reported similar responses following the initiation of restraint tests whereby an increase in NO was noted upon initiation of a restraint test but no initial decrease was noted[30]. Conductance of restraint tests on NOD SCID mice to allow for real-time monitoring of NO has not been previously carried out. Therefore, this initial decrease may be a strain specific difference in the recorded NO amperometric response.

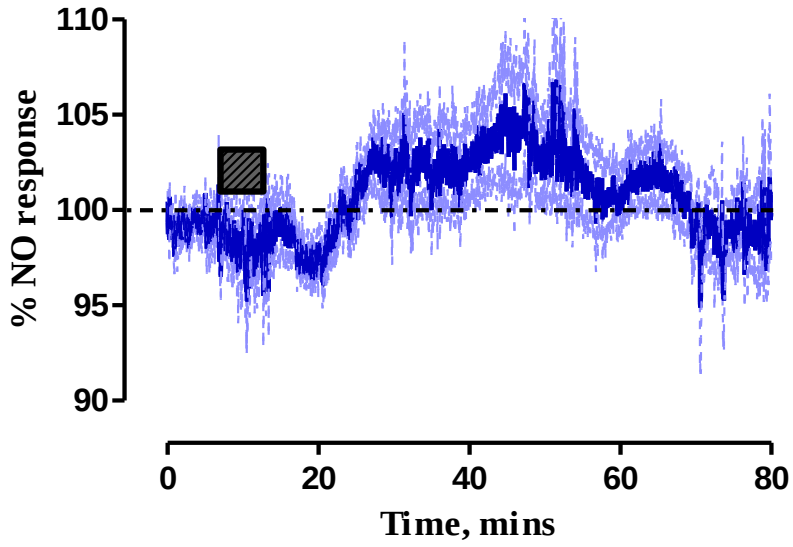

Figure 5.3.1.5.1: Averaged percentage raw data current response of NO sensors implanted in the striatum of NOD SCID mice to a 2-minute restraint test. Duration of restraint is represented by the dark grey box. The blue trace indicates the mean percentage current response with the percentage error represented by the light blue trace.

Table 5.3.1.5.1: Summary of results of the NO sensors implanted in the striatum of NOD SCID mice following 2-minute restraint test (*n* = 4).

Restraint Test							
Response No.	**Pre-Perturbation Baseline (pA)**	**Max Current (pA)**	**Current Change ΔI (pA)**	**Current Change (%)**	**Max Response Time (mins)**	**Post-Perturbation Baseline (pA)**	**Return to Baseline Time (mins)**
1	251 ± 41	236 ± 41	-15 ± 5	-7 ± 3	3 ± 1	-	-
2	-	265 ± 42	14 ± 5	6 ± 2	23 ± 4	250 ± 42	64 ± 9

A direct comparison can be made between the NO response obtained following saline administration and a 2-minute restraint test due to their ability to act as a physiological stressor. Similarly, an initial decrease in the recorded amperometric response was reported following saline administration and initiation of the restraint test. Therefore, suggesting that this decrease may be attributed to neuronal activation. However, the saline response is transient (3 ± 1 mins, *n* = 8) whereas the effect of the

restraint test is much longer (64 ± 9 mins, n = 4). Additionally, an increase in NO is exhibited following the initial decrease which is absent in the NO response recorded following saline administration. Therefore, it can be suggested that the restraint test elicits a greater effect on neuronal activation thus, causing a long-lasting effect on NO levels detected in the striatum of NOD SCID mice.

5.3.1.6 Baseline Stability of the NO Sensor in the Striatum of NOD SCID Mice

Figure 5.3.1.6.1 illustrates the average percentage baseline current recorded in the striatum of NOD SCID mice over 8-days. The baseline of Day 1 recordings were normalised to 100 % and baseline recordings of the succeeding days were normalised as a percentage of Day 1 recordings. It is important to note that the same time point was taken over each day over the 8-days to allow for a direct comparison of the recorded baselines to be made. Day 2 recordings showed a drop in current of ca. 20 % for the NO sensor. The initial drop in sensitivity observed by the NO sensor is in good agreement with previous studies which highlight a decrease of between 20 % and 50 % following initial exposure of the sensor to brain tissue[31]. Additionally, there was no significant difference in the recorded NO (p = 0.62, one-way ANOVA, n = 6) over this 8-day period. The obtained result is in close agreement with previous findings which highlighted no significant difference in baseline currents of NO for a continuous period following implantation in the brain of wistar rats[5]. Furthermore, these results corroborate with *ex vivo* compatibility studies whereby an initial drop in sensitivity was observed due to the initial exposure of the NO sensor to brain tissue. However, this was followed by no significant reduction in sensitivity for up to 14-days (Section 4.3.1.3). Therefore, these results suggest excellent stability of the NO sensor for continuous recordings over 8-days in NOD SCID mice.

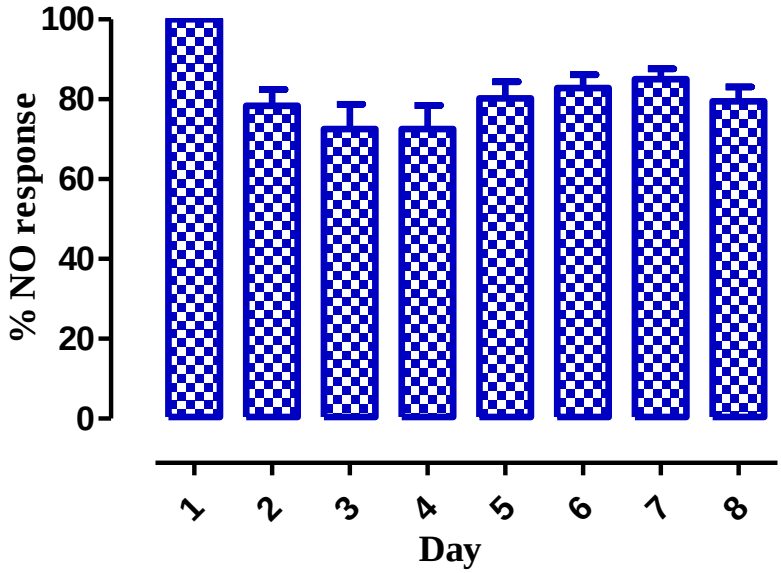

Figure 5.3.1.6.1: Average percentage baseline currents for NO sensors (*n* = 6) recorded in the striatum of NOD SCID mice.

5.3.1.7 24-Hour Amperometric Recordings in the Striatum of NOD SCID Mice

Amperometric recordings were conducted over a 24-hour period to investigate the changes in analyte concentration throughout this period. Recordings were conducted from 07:00 - 19:00 which was associated with the light cycle and from 19:00 - 07:00 which was representative of the night cycle. The hours of the foresaid phases were laid out by the light timer in the animal housing facility. As mice are nocturnal animals, it was expected that an increase in motor activity would be experienced during the night cycle.

Continuous recordings identified analyte concentration changes obtained using *in vitro* calibration curves as displayed in Figure 5.3.1.7.1. Changes in recorded amperometric signal were divided by the average sensitivity of the NO sensors resulting from *in vitro* investigations, allowing for concentration changes to be attained. During the light cycle, it can be seen in the concentration of NO (*n* = 11/5) remains within basal levels which can be attributed to a decrease in motor activity and neuronal activation during the light phase. However, it must be stated that compulsory health and welfare checks must be conducted during the light cycle which may have an influence on the sleeping pattern of the animal throughout this period. In contrast, the concentration of NO increases substantially following initiation of the night cycle (*n* = 12/5). This substantial increase in analyte concentration is associated with

increased motor activity of the animal which induces an increase in neuronal activation. Therefore, it can be concluded that there is an evident involvement of NO in the increased motor activity exhibited during this period. Endo *et al.* has previously reported that CBF exhibits diurnal variation measured using the hydrogen clearance technique[32]. It was found that an increase in the CBF was associated with the night cycle while a lower CBF rate was observed during the light cycle. Neurovascular coupling has been observed to be crucial to sustain neuronal function by increasing CBF in response to increased neuronal activity[33]. Thus, it can be hypothesised that an increase in NO observed during the night cycle is associated with an increase in CBF and neuronal activation which corresponds to the increased activity of the animal during this cycle.

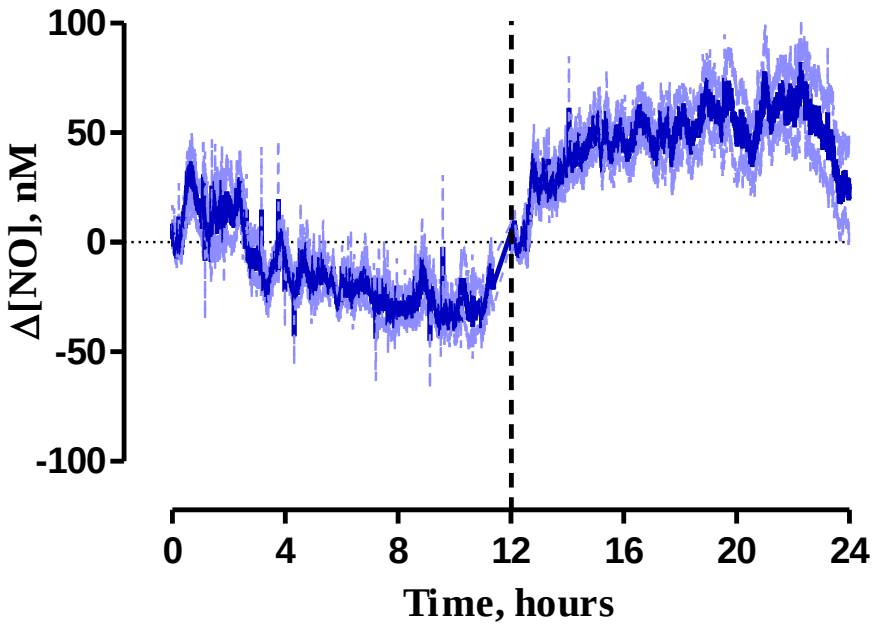

Figure 5.3.1.7.1: Averaged 24-hour Δ[NO] measured by NO sensors (*n* = 5). Mean Δ[NO] is represented by the blue trace. The light blue trace highlights the percentage error. The light phase (07:00 - 19:00, *n* = 11/5) relates to 0-12 hour with the dark phase (19:00 – 07:00, *n* = 12/5) from 12-24 hour. The dashed line at hour 12 represents the end of the light phase/start of the dark phase. Data represented as mean current ± SEM.

5.3.2 Characterisation of the O_2 Sensor in the Striatum of NOD SCID Mice.

5.3.2.1 Saline Administration

Firstly, the characterisation of the O_2 response was recorded using the O_2 sensor manufactured from CPE wire with an outer diameter of 280 µm as detailed in Section 3.4.3. Figure 5.3.2.1.1A highlights a ΔI of 1 ± 2 nA (n = 7) which was not significantly different (p = 0.64) from pre-perturbation baseline currents (200 ± 14 nA, n = 7) that were obtained following the i.p. administration of 1 mL/kg saline. The percentage current change of - 0.6 ± 1 % (n = 7) occurred 1 ± 0.2 mins (n = 7) following administration and equated to a concentration change of 1 ± 3 µM (n = 7). A post-perturbation baseline of 201 ± 14 nA (n = 7) was achieved 4 ± 1 mins (n = 7) after the i.p. injection (Table 5.3.2.1.1). It was deemed that there was no significant difference (p = 0.49) between the post-perturbation baseline and the pre-perturbation baseline currents.

It was decided to manufacture the O_2 sensor from Ag wire of a smaller geometry (Section 3.4.3) for conductance of *in vivo* investigations in NOD SCID mice, which is further discussed in Section 6.3.2. Therefore, the response of O_2 to the administration of saline was investigated using this wire. The observed O_2 response is detailed in Figure 5.3.2.1.1B. From a pre-perturbation baseline of 81 ± 9 nA (n = 6), a ΔI of 7 ± 1 nA (n = 6) was attained. This decrease in amperometric current was found to be significantly different (p < 0.01) from pre-perturbation baseline levels. Moreover, this increase occurred after 1 ± 0.1 mins (n = 6) and corresponded to a 10 ± 2 % (n = 6) and a concentration change of 8 ± 1 µM (n = 6). A new post-perturbation baseline (83 ± 8 nA, n = 6) was achieved after 7 ± 1 mins (n = 6) which was not significantly different from pre-perturbation baseline levels (p = 0.46).

Previous studies have illustrated a transient increase in tissue O_2 measured in wistar rats following administration of saline[2]. It has been reported that this transient change in O_2 detection following an i.p. injection of saline is thought to result from an increase in neuronal activation and CBF brought upon by a stress response associated with the i.p. injection[20,21]. This increase in CBF results in a transient increase in O_2 detection due to supply of O_2 exceeding utilisation by cells. Nonetheless, this response is momentary before O_2 currents return to baseline levels quickly.

However, a clear transient change in tissue O_2 wasn't as evident following measurements conducted in the striatum of NOD SCID mice measured using the O_2 sensor constructed from CPEs with an outer diameter of 280 µm. It can be hypothesised that the absence of a significant transient increase in O_2 following saline administration in NOD SCID mice may have been attributed to the conductance of measurements in NOD SCID mice using the larger CPE. CPEs manufactured with this geometry usually have a greater dimension to the scale of the capillary zone (< 100 µm) from which they are measuring. As a result, an average tissue O_2 level is measured[1]. Hence, it can be suggested that this CPE geometry might inflict tissue trauma resulting in fleeting changes in tissue oxygenation to be missed in a much smaller strain of animal. The larger wire is much more suitable for use in wistar rats due to a more suitable size ratio, thus, allowing for the larger wire to pick up these short-lived amperometric changes.

This was overcome by implanting CPEs manufactured with a smaller diameter wire (125 µm outer diameter). Figure 5.3.2.1.1B displays the average percentage raw data trace obtained using CPEs, manufactured with the smaller wire, following an i.p. injection of saline. It is clear from the below figure that an increase in the amperometric signal was observed following systemic administration of saline once the wire of smaller diameter was included in the manufacture of the CPE. Additionally, this stereotypic O_2 response was short-lived in immunocompromised mice similar to the O_2 response seen previously in wistar rats[2]. Also, as the O_2 sensor would ultimately be utilised to perform analysis either in or within close proximity of humanised transplanted grafts in the striatum of NOD SCID mice, it was much more favourable to manufacture O_2 sensors from a smaller wire.

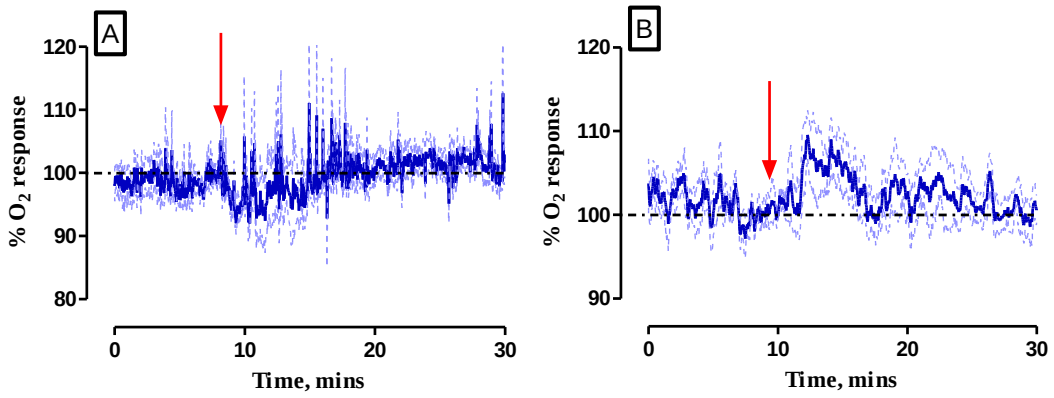

Figure 5.3.2.1.1: Averaged percentage raw data current response of (A) O_2 sensors (280 µm o.d.) and (B) O_2 sensors (125 µm o.d.) implanted in the striatum of NOD SCID mice to 1 mL/kg i.p. injection of 0.9 % saline. Point of injection is represented by the red arrow. The blue trace indicates the mean percentage current response with the percentage error represented by the light blue trace.

Table 5.3.2.1.1: Summary of results of the O_2 sensors (280 µm o.d., *n* = 8) and (125 µm o.d., *n* = 6) implanted in the striatum of NOD SCID mice following i.p. administration of 0.9 % saline.

Saline Injection							
CPE Diameter (µm)	**Pre-Perturbation Baseline (nA)**	**Max Current (nA)**	**Current Change ΔI (nA)**	**Current Change (%)**	**Max Response Time (mins)**	**Post-Perturbation Baseline (nA)**	**Return to Baseline Time (mins)**
280	200 ± 14	199 ± 14	-1 ± 2	-1 ± 1	1 ± 0.2	201 ± 14	4 ± 1
125	81 ± 9	89 ± 8	7 ± 1	10 ± 2	1 ± 0.1	83 ± 8	7 ± 1

5.3.2.2 L-NAME Administration

As detailed in Section 5.3.1.3, L-NAME is a non-selective inhibitor of the NOS enzyme[34]. L-NAME acts competitively with L-arginine for binding to the NOS enzyme. NOS inhibition has been found to induce vasoconstriction on cerebral blood vessels resulting in a decrease in supply of O_2 by CBF[35]. As utilisation of O_2 by the cells remains constant during this period, an overall decrease in O_2 should be observed as amperometric O_2 detection is a balance between the O_2 supply from the blood flow and consumption of O_2 by the cells.

Figure 5.3.2.2.1 illustrates a decrease in the O_2 currents following systemic i.p. administration of 30 mg/kg L-NAME. The ΔI of - 44 ± 4 nA (n = 5) following L-NAME administration was observed to be significantly different ($p < 0.001$) from pre-perturbation baseline levels (199 ± 12 nA, n = 5). This current change lead to a percentage change of - 19 ± 3 % (n = 5) and concentration change of 48 ± 4 µM (n = 5) after 28 ± 6 mins (n = 5). A new post-perturbation baseline current (181 ± 12 nA, n = 5) was achieved following 131 ± 35 mins (n = 5, Table 5.3.2.2.1) which was not significantly different ($p < 0.01$) from pre-perturbation baseline levels.

The above data suggests that a significant decrease in the O_2 response measured following L-NAME administration was a direct result of L-NAME instigating vasoconstriction in cerebral blood vessels and thus, reducing O_2 supply from reduced CBF whilst O_2 utilisation remaining constant. Previous studies have not included the application of L-NAME in O_2 characterisation studies. Therefore, this is the first time such a response has been detailed using O_2 sensors.

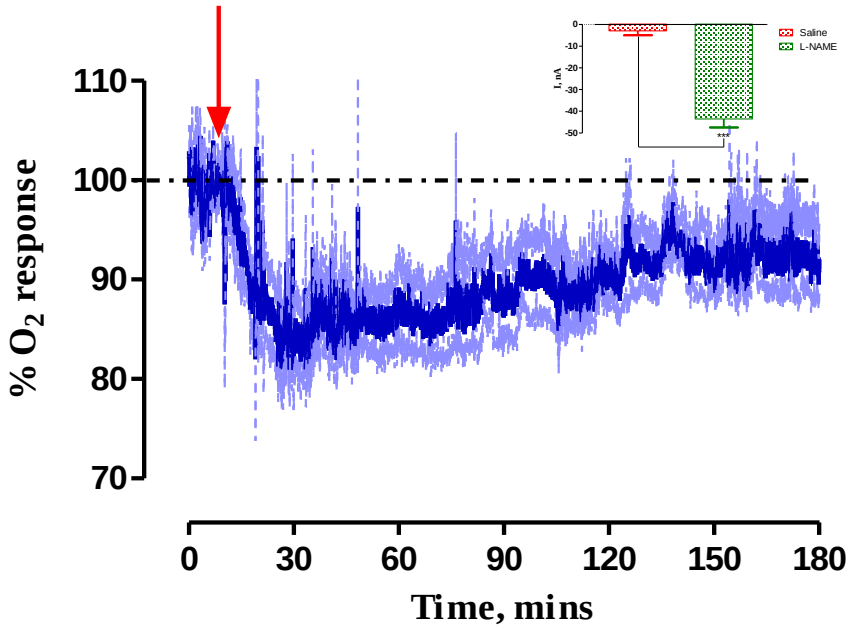

Figure 5.3.2.2.1: Averaged percentage raw data current response of O_2 sensors implanted in the striatum of NOD SCID mice to 1 mL/kg i.p. injection of 30 mg/kg L-NAME. Point of injection is represented by the red arrow. The blue trace indicates the mean percentage current response with the percentage error represented by the light blue trace. Data represented as mean current ± SEM.

Table 5.3.2.2.1: Summary of results of the O_2 sensors implanted in the striatum of NOD SCID mice following i.p. administration of 30 mg/kg L-NAME (*n* = 5).

L-NAME Injection						
Pre-Perturbation Baseline (nA)	**Max Current (nA)**	**Current Change ΔI (nA)**	**Current Change (%)**	**Max Response Time (mins)**	**Post-Perturbation Baseline (nA)**	**Return to Baseline Time (mins)**
199 ± 12	155 ± 10	-44 ± 4	-19 ± 3	28 ± 6	181 ± 12	131 ± 35

A significant difference ($p < 0.0001$) was observed between the ΔI obtained following saline and L-NAME administration indicating that the O_2 response following L-NAME is a direct result of the action of L-NAME to inhibit the production of NO due to the significant decrease in current (ΔI = - 44 ± 4 nA, $n = 5$) obtained.

5.3.2.3 Choral Hydrate Administration

Chloral hydrate is a known non-volatile anaesthetic that previously was widely employed in stereotaxic surgery involving laboratory rodents. Chloral hydrate is metabolised into trichloroethanol and trichloroacetic acid, with trichloroethanol acting as the active metabolite[36]. Suppression of the central nervous system by the action of chloral hydrate has been highlighted previously whereby the active metabolite, trichloroethanol, works to inhibit neurotransmitter receptors such as the NMDA receptors resulting in decreased synaptic firing[37,38]. In addition, the activity of GABA receptor function is heightened due to the presence of trichloroethanol, therefore, resulting in reduced neuronal excitation throughout the central nervous system[39]. Therefore, it is to be expected that following administration of chloral hydrate suppression of the central nervous system will result. Therefore, any decrease in the utilisation of O_2 by the suppressed central nervous system will lead to an increase in O_2 detection due to the supply of O_2 from CBF remaining constant.

The average percentage raw data trace can be observed in Figure 5.3.2.3.1. Following i.p. administration of 350 mg/kg chloral hydrate, a ΔI of 87 ± 22 nA (n = 5) from a pre-perturbation baseline of 201 ± 10 nA (n = 5) was reported. Moreover, this change in current resulted in a percentage current change of 40 ± 15 % (n = 5) and a concentration change of 103 ± 30 µM (n = 5) which occurred 13 ± 2 mins (n = 5)

after administration. In addition, a significant difference ($p < 0.05$) was observed between the maximum current change and the pre-perturbation baseline current. A new post-perturbation current of 195 ± 13 nA ($n = 5$) occurred after 97 ± 9 mins ($n = 5$, Table 5.3.2.3.1) after chloral hydrate administration. No significant difference ($p = 0.33$) was observed between the new post-perturbation baseline and pre-perturbation currents recorded. Previous findings following administration of chloral hydrate in wistar rats corroborate the aforementioned results[2].

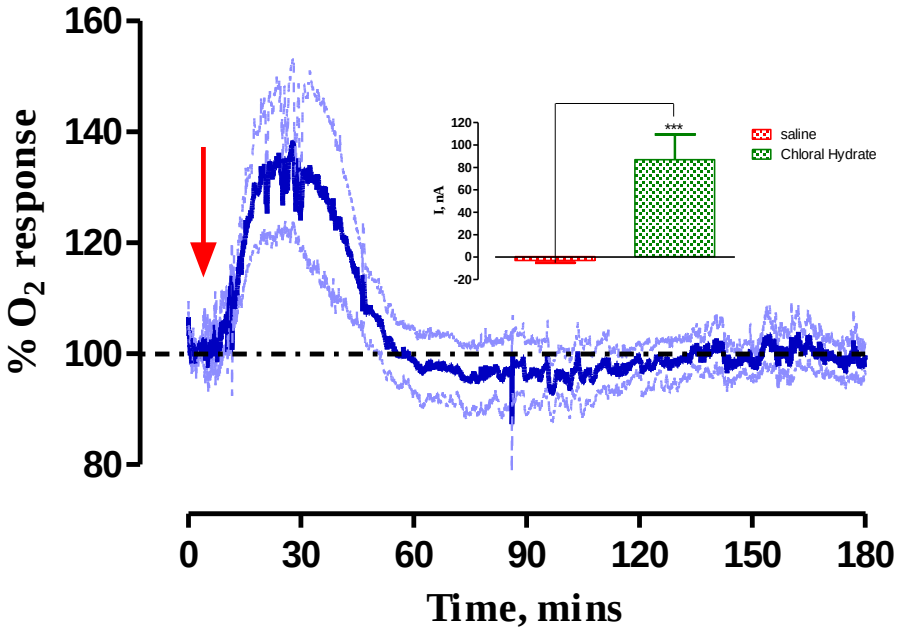

Figure 5.3.2.3.1: Averaged percentage raw data current response of O_2 sensors implanted in the striatum of NOD SCID mice to 1 mL/kg i.p. injection of 350 mg/kg Chloral Hydrate. Point of injection is represented by the red arrow. The blue trace indicates the mean percentage current response with the percentage error represented by the light blue trace. Data represented as mean current ± SEM.

Table 5.3.2.3.1: Summary of results of the O_2 sensors implanted in the striatum of NOD SCID mice following i.p. administration of 350 mg/kg Chloral Hydrate (*n* = 5).

Chloral Hydrate Injection						
Pre-Perturbation Baseline (nA)	**Max Current (nA)**	**Current Change ΔI (nA)**	**Current Change (%)**	**Max Response Time (mins)**	**Post-Perturbation Baseline (nA)**	**Return to Baseline Time (mins)**
201 ± 10	295 ± 27	87 ± 22	40 ± 15	13 ± 2	195 ± 13	97 ± 9

Comparison of chloral hydrate administrations against saline injections identified a much larger increase (ΔI, 87 ± 22 pA, *n* = 5) in the O_2 amperometric response measured following 350 mg/kg chloral hydrate administration when compared to saline administrations (ΔI, - 3 ± 2 pA, *n* = 8).

5.3.2.4 Azetazolamide (Diamox) Administration

Rapid shifts in extracellular pH are thought to accompany neuronal activation by causing modulations in ion gated channels[40]. The buffering capacity of the ECF is achieved through the reversible conversion of CO_2 to HCO_3^- which is catalysed by the metalloenzyme, carbonic anhydrase[41,42]. Diamox is a known carbonic anhydrase inhibitor which prevents the catalysis of the reversible CO_2: HCO_3^- reaction. As a result, metabolic acidosis results along with a promotion of renal elimination of HCO_3^- [43]. Such decreases in pH have been shown to modify the activity of ion-gated channels and ligand receptors. A study carried out by Tang *et al.*[44] highlighted this phenomenon whereby the activation of the NMDA receptor was strongly inhibited by a marked decrease in pH. Therefore, CBF works to counteract this change in homeostatic conditions by increasing the rate of CBF. As a result, the supply of O_2 greatly increases whilst utilisation of O_2 by the cells remains constant.

Figure 5.3.2.4.1 details the average raw data current response recorded involving the i.p. administration of Diamox. A ΔI of 21 ± 5 nA (*n* = 5) was recorded following Diamox administration which corresponded a percentage change of 8 ± 2 % (*n* = 5) from pre-perturbation baseline levels of 221 ± 23 nA (*n* = 5). Moreover, a concentration change of 23 ± 5 µM (*n* = 5) was observed following Diamox administration. Additionally, the current change that resulted following Diamox

administration was significantly different ($p < 0.05$) from the pre-perturbation baseline current. The maximum response was obtained 15 ± 3 mins (n = 5) after Diamox administration. Moreover, a new post-perturbation baseline current (220 ± 23 nA, n = 5) was reached after 97 ± 28 mins (n = 5, Table 5.3.2.4.1) which was not significantly different (p = 0.80) from the pre-perturbation baseline.

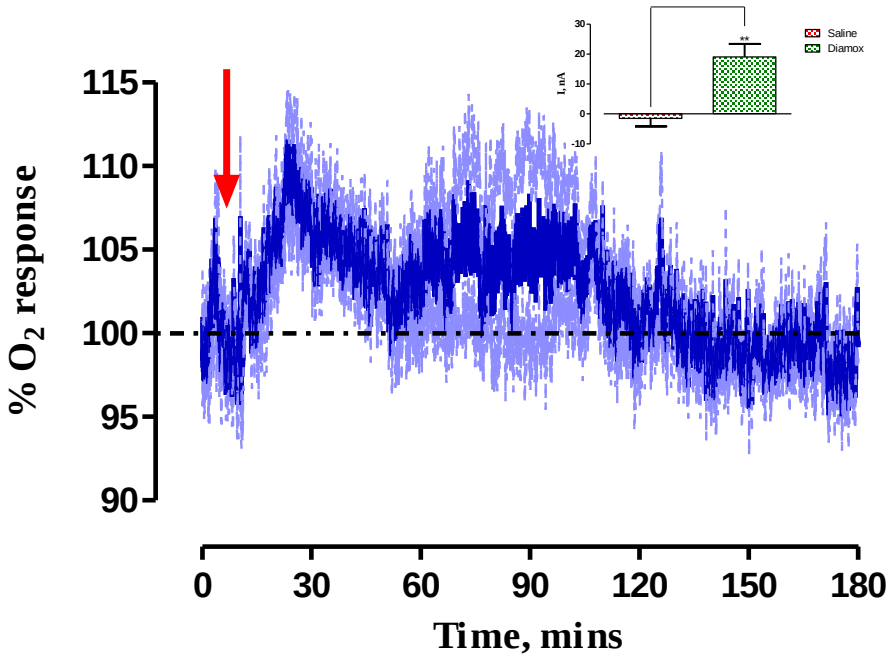

Figure 5.3.2.4.1: Averaged percentage raw data current response of O_2 sensors implanted in the striatum of NOD SCID mice to 1 mL/kg i.p. injection of 50 mg/kg Diamox. Point of injection is represented by the red arrow. The blue trace indicates the mean percentage current response with the percentage error represented by the light blue trace. Data represented as mean current ± SEM.

Table 5.3.2.4.1: Summary of results of the O_2 sensors implanted in the striatum of NOD SCID mice following i.p. administration of 50 mg/kg Diamox (n = 5).

Diamox Injection						
Pre-Perturbation Baseline (nA)	**Max Current (nA)**	**Current Change ΔI (nA)**	**Current Change (%)**	**Max Response Time (mins)**	**Post-Perturbation Baseline (nA)**	**Return to Baseline Time (mins)**
221 ± 23	242 ± 25	21 ± 5	8 ± 2	15 ± 3	220 ± 23	97 ± 28

Moreover, it can be postulated that the change in O_2 current detected in the striatum resulted from Diamox administration initiating an increase in CBF to the brain microenvironment. Such suggestions can be made due to the significant difference ($p < 0.0001$, Figure 5.3.2.4.1 *inset*) that was observed between the recorded maximum ΔI following saline and Diamox administration.

5.3.2.5 Restraint Test

As alluded to previously, restraint tests are used as a mild stressor causing an increase in neuronal activation and tissue O_2. Figure 5.3.2.5.1 displays the recorded amperometric O_2 current collected following a 2-minute restraint test. After 3 ± 1 mins ($n = 4$), a ΔI of 21 ± 4 nA ($n = 4$) was obtained from pre-perturbation baseline levels (83 ± 6 nA, $n = 4$). Additionally, this current change equated to a 24 ± 3 % ($n = 4$) change and a concentration change of 23 ± 4 µM ($n = 4$). It was noted that there was a significant difference ($p < 0.001$) between the maximum current response and the pre-perturbation baseline current. A new post-perturbation baseline (84 ± 6 nA, $n = 4$) was achieved after 59 ± 11 mins ($n = 4$, Table 5.3.2.5.1). Likewise, there was no significant difference ($p = 0.34$) between pre-perturbation baseline currents and post-perturbation baseline currents. The initiation of a restraint test is known to induce neuronal activation as the animal attempts to free itself[45]. Whilst the movement of the subject is restricted, an increase in tissue O_2 occurs as a direct result of increase neuronal activation. Following cessation of the restraint test, tissue O_2 are observed to return to baseline levels as the animal returns to a homeostatic state. A similar O_2 response was reported in wistar rats following a 5-minute restraint test. It was noted that a significant increase in tissue O_2 was recorded. However, the O_2 response in wistar rats was shorter in duration that the O_2 response recorded in NOD SCID mice[46] which may be attributed to O_2 monitoring being conducted in a different rodent strain.

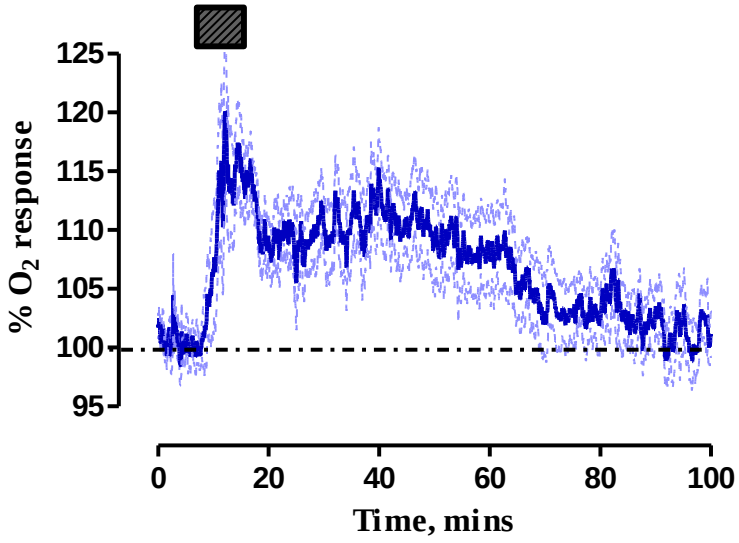

Figure 5.3.2.5.1: Averaged percentage raw data current response of O_2 sensors implanted in the striatum of NOD SCID mice to a 2-minute restraint test. Duration of restraint is represented by the dark grey box. The blue trace indicates the mean percentage current response with the percentage error represented by the light blue trace. Data represented as mean current ± SEM.

Table 5.3.2.5.1: Summary of results of the O_2 sensors implanted in the striatum of NOD SCID mice following 2-minute restraint test (*n* = 4).

Restraint Test						
Pre-Perturbation Baseline (nA)	**Max Current (nA)**	**Current Change ΔI (nA)**	**Current Change (%)**	**Max Response Time (mins)**	**Post-Perturbation Baseline (nA)**	**Return to Baseline Time (mins)**
83 ± 6	104 ± 9	21 ± 4	24 ± 3	3 ± 1	84 ± 6	59 ± 11

Upon initiation of the restraint test, a large spike in O_2 can be observed. A similar phenomenon was measured following administration of saline as seen in Figure 5.3.2.1.1B. Therefore, it can be suggested that this initial large increase in O_2 may be associated an increase in neuronal activation coupled with an increase in CBF. However, the elevated O_2 response occurs over a much longer time period compared to the short-lived response experienced following saline administration. Similarly, the NO response (Figure 5.3.1.5.1) obtained following a 2-minute restraint test occurs over a comparable timeframe to that observed in Figure 5.3.2.5.1.

5.3.2.6 Baseline Stability of the O_2 Sensor in the Striatum of NOD SCID Mice

As previously discussed, the adhesion of proteins and lipids to the electrode surface can negatively affect the performance of the sensor *in vivo*. Thus, leading to a loss in the sensitivity of the sensor. Figure 5.3.2.6.1 displays the average baseline current response of the O_2 sensor following implantation in the striatum of immunocompromised mice. The same time point was taken each day over a period of 8-days. Subsequently, the baseline of Day 1 recordings were normalised to 100 % with the baseline recordings of the following days normalised as a percentage of Day 1 recordings.

In contrast to the NO baseline stability investigations discussed in Section 5.3.1.5, the initial drop in sensitivity in the recorded O_2 currents following implantation is not as prevalent due to the O_2 sensor being extremely stable. The O_2 sensor has been deemed to be stable for up to three months[3]. The stability of the O_2 current can be attributed to the presence of the silicon oil in the design of the sensor (Section 3.3.2.1). Silicon oil leeches out slowly from the carbon paste cavity, thus, preventing, adhesion of proteins and lipids to the sensor surface resulting in excellent stability of the O_2 sensor. As a result, no significant difference was recorded in the O_2 currents over an 8-day period (p = 0.74, one-way ANOVA, n = 5). This result corroborates previous work reported whereby no significant difference was recorded in O_2 currents following implantation in the brain of wistar rats over a 21-day period[3]. Additionally, the above obtained results are in agreement with *ex vivo* compatibility studies (Section 4.3.2.6) whereby no significant difference observed over 14-days. Therefore, this stability investigation suggests that O_2 sensor maintains excellent stability allowing for continuous amperometric recordings in immunocompromised mice.

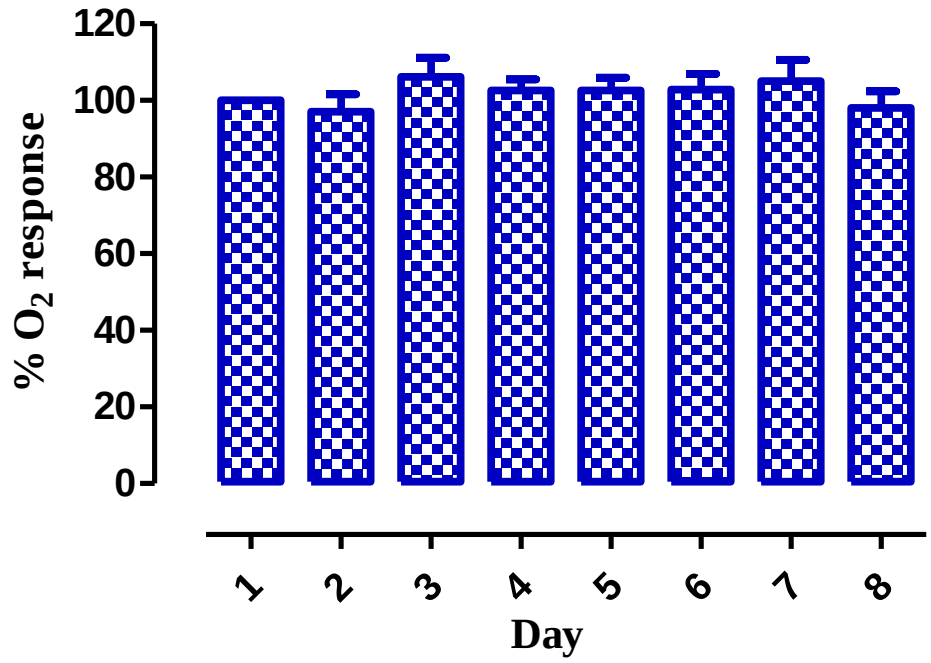

Figure 5.3.2.6.1: Average percentage baseline currents for O_2 sensors (*n* = 5) recorded in the striatum of NOD SCID mice.

5.3.2.7 24-Hour Amperometric Recordings in the Striatum of NOD SCID Mice

Changes in the concentration of O_2 were assessed over a 24-hour period. Continuous recordings were conducted over the light cycle (07:00 - 19:00) and the night cycle (19:00 - 07:00) which coincided with the light timer of the animal facility as previously discussed in Section 5.3.1.7. Figure 5.3.2.7.1 illustrates the concentration changes of O_2 over this 24-hour period. Analyte concentration changes were obtained from *in vitro* calibration curves.

Due to the nocturnal nature of the mice, it was expected that O_2 levels would remain close to basal levels to the decreased motor activity and neuronal activation exhibited by the animal during this phase which was observed in O_2 recordings (*n* = 10/5) performed in NOD SCID mice obtained in Figure 5.3.2.7.1. However, it is important to note that general husbandry and welfare checks were performed during this cycle meaning that the animal was not completely inactive during this phase. In contrast, a considerable increase in O_2 currents was exhibited during the night cycle (*n* = 16/5) which was associated with an increase in motor activity and thus, increased neuronal activation. Hence, it is clear that O_2 has a direct involvement in the increased activity of the animal during the night cycle.

Similar to 24-hour NO recordings conducted in the striatum of NOD SCID mice, O_2 levels increase during the dark phase whilst remaining at baseline concentrations during the light phase (Section 5.3.1.7). It was suggested that the increase in NO concentrations during the night cycle was associated with elevated neuronal activation and a corresponding increase in CBF. Therefore, with the increased demand for O_2 required during the night to meet demands of the surrounding cells, an increase in supply by CBF is required. Moreover, supply increases exceeding the level of utilisation leading to an increase in O_2 detection during the night cycle.

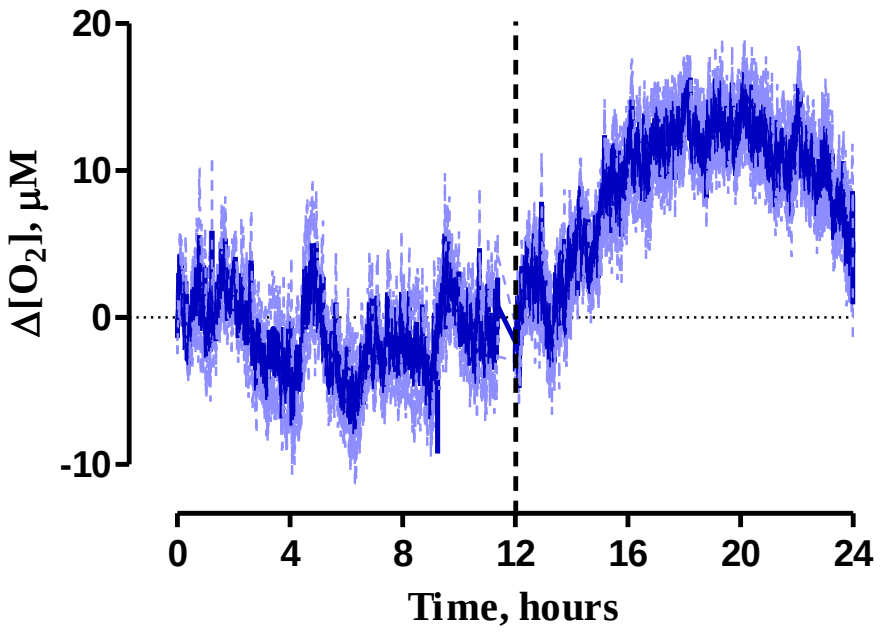

Figure 5.3.2.7.1: Averaged 24-hour Δ[O_2] measured by O_2 sensors. Mean Δ[O_2] is represented by the blue trace. The light blue trace highlights the percentage error. The light phase (07:00 - 19:00, *n* = 10/5) relates to 0-12 hour with the dark phase (19:00 - 07:00, *n* = 16/5) from 12-24 hour. The dashed line at hour 12 represents the end of the light phase/start of the dark phase. Data represented as mean current ± SEM.

5.3.3 Characterisation of the H_2O_2 Sensor in NOD SCID Mice

5.3.3.1 Chronic Recordings in Freely Moving NOD SCID Mice

5.3.3.1.1 Saline Administrations

Figure 5.3.3.1.1.1 highlights the average raw data response of the H_2O_2 biosensor following systemic administration of saline. As the measurement of H_2O_2 *in vivo* by the dual biosensor is conducted by means of a subtraction method (Section 2.4.3), the subtracted values are detailed. However, it must be stated that subtracted percentage changes were obtained by subtraction of the percentage change of the catalase electrode from the percentage change of the blank electrode relative to each particular electrode. Thus, the percentage current change is not attained from the ΔI divided by the subtracted baseline current. For brevity, subtracted data is only presented for all H_2O_2 investigations with blank and catalase data described in the relevant figures.

The subtracted ΔI of 35 ± 17 pA (n = 5) was recorded 4 ± 1 mins (n = 5) after systemic administration. This slight deviation in current corresponded to a 1 ± 2 % (n = 5) change in the recorded response from pre-perturbation levels (593 ± 151 pA, n = 5). Changes in the amperometric signal corresponded to a 1.0 ± 0.04 µM (n = 5) concentration change. This slight fluctuation in the amperometric current was brief, before returning to baseline levels (613 ± 154 pA, n = 5) after 9 ± 2 mins (n = 5, Table 5.3.3.1.1.1). However, Figure 5.3.3.1.1B illustrates that no overall change in H_2O_2 resulted following the systemic administration of saline. Furthermore, although slight increases are present in the average data response of the blank and catalase electrodes (Figures 5.3.3.1.1.1A & B), there is a clear absence of the apparent increase in the subtracted average current response which is representative of the H_2O_2 levels as alluded to in *in vitro* investigations. Additionally, the absence of any changes in the subtracted signal further supports the importance of inclusion of the subtraction method in the measurement of *in vivo* H_2O_2.

Previous studies have indicated similar recorded H_2O_2 responses following saline i.p. injections in wistar rats[7]. However, this is the first time that H_2O_2 levels have been monitored in the striatum of NOD SCID mice.

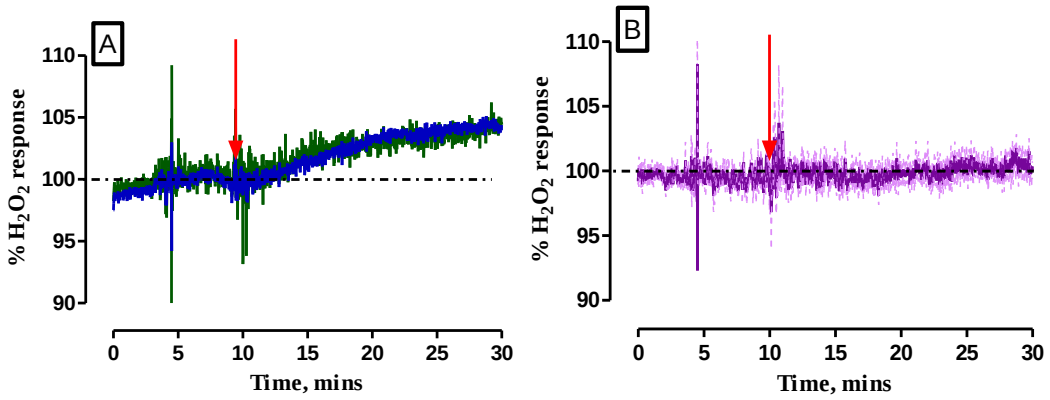

Figure 5.3.3.1.1.1: Averaged percentage raw data current response of H_2O_2 sensors implanted in the striatum of NOD SCID mice to 1 mL/kg i.p. injection of 0.9 % saline, (A) H_2O_2 blank electrode (*n* = 5, blue) & H_2O_2 catalase electrode (*n* = 5, green), (B) subtracted H_2O_2 current response (*n* = 5). The purple trace indicates the mean percentage current response with the percentage error represented by the light purple trace. Data represented as mean current ± SEM. Point of injection is represented by the red arrow.

Table 5.3.3.1.1.1: Summary of results of the H_2O_2 sensors implanted in the striatum of NOD SCID mice following i.p. administration of 0.9 % saline (*n* = 5).

Saline Injection							
	Pre-Perturbation Baseline (pA)	**Max Current (pA)**	**Current Change ΔI (pA)**	**Current Change (%)**	**Max Response Time (mins)**	**Post-Perturbation Baseline (pA)**	**Return to Baseline Time (mins)**
Blank	1580 ± 316	1654 ± 340	74 ± 26	5 ± 1	9 ± 2	1607 ± 314	24 ± 3
Catalase	987 ± 180	1026 ± 192	39 ± 12	4 ± 1	9 ± 2	995 ± 173	24 ± 3
Sub.	593 ± 151	628 ± 161	35 ± 17	1 ± 2	4 ± 1	613 ± 154	9 ± 2

5.3.3.1.2 Selectivity Investigation of the H_2O_2 Biosensor

Figure 5.3.3.1.2.2A illustrates the average percentage current response recorded following systemic administration of 500 mg/kg sodium ascorbate by i.p. injection. Detection of sodium ascorbate by a bare 1 mm cylinder Pt electrode (Figure 5.3.3.1.2.1B *inset*) reached a maximum after approximately 15-minutes following

administration. The maximum current response obtained was approximately 800 % which highlights the substantial contribution that ascorbate delivers to an unmodified electrode. However, administration of sodium ascorbate on the modified electrodes highlights the ability of the H_2O_2 biosensor to efficiently block the detection of the interferent as demonstrated in Figure 5.3.3.1.2.1B.

Following administration of sodium ascorbate, a subtracted current change of - 40 ± 43 pA (*n* = 5) was achieved. A maximum subtracted percentage response of 1 ± 3 % (*n* = 5) and a concentration change of - 1 ± 0.1 µM (*n* = 5) was obtained by subtraction of the percentage catalase current from the percentage blank current. This change occurred after 25 ± 13 mins (*n* = 5) before returning to baseline levels after 67 ± 23 mins (*n* = 5). Therefore, by subtraction of the contribution recorded on the blank electrode from the catalase electrode current, a negligible response from sodium ascorbate was measured. To conclude, this investigative study demonstrates the efficient selectivity properties obtained *in vitro* have been retained by the H_2O_2 biosensor *in vivo*.

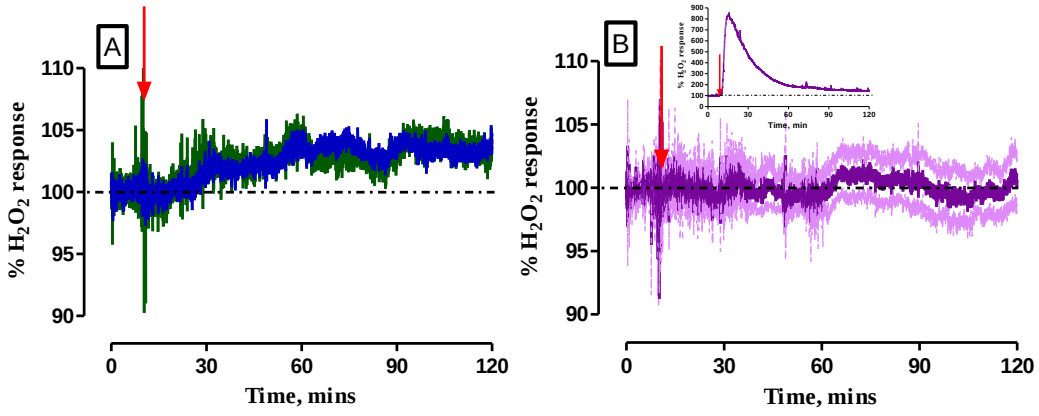

Figure 5.3.3.1.2.1: Averaged percentage raw data current response of H_2O_2 sensors implanted in the striatum of NOD SCID mice to a 1 mL/kg i.p. injection of 500 mg/kg sodium ascorbate, (A) H_2O_2 blank electrode (*n* = 5, blue) & H_2O_2 catalase electrode (*n* = 5, green) (B) subtracted H_2O_2 current response. The purple trace indicates the mean percentage current response with the percentage error represented by the light purple trace. Data represented as mean current ± SEM. Point of injection is represented by the red arrow. *Inset*: Typical example of a raw data percentage response of a bare 1 mm cylinder Pt electrode implanted in the striatum of NOD SCID mice to 500 mg/kg sodium ascorbate i.p. injection. Point of injection is represented by the red arrow. The purple trace indicates the mean percentage current response.

Table 5.3.3.1.2.1: Summary of results of the H_2O_2 sensors implanted in the striatum of NOD SCID mice following i.p. administration of 500 mg/kg sodium ascorbate (n = 5).

	Sodium Ascorbate Injection						
	Pre-Perturbation Baseline (pA)	**Max Current (pA)**	**Current Change ΔI (nA)**	**Current Change (%)**	**Max Response Time (mins)**	**Post-Perturbation Baseline (pA)**	**Return to Baseline Time (mins)**
Blank	1182 ± 663	1141 ± 610	-40 ± 57	0.2 ± 3	8 ± 3	1174 ± 636	54 ± 13
Catalase	660 ± 257	660 ± 246	0.2 ± 18	1 ± 4	8 ± 2	646 ± 268	55 ± 14
Sub.	526 ± 408	481 ± 364	-40 ± 43	1 ± 3	25 ± 13	528 ± 370	67 ± 23

5.3.3.2 Acute Investigations of H_2O_2 Dynamics in the Striatum of NOD SCID Mice.

5.3.3.2.1 Amperometric Measurement of H_2O_2 Utilising Retromicrodialysis

Due to concerns for animal welfare involving the perturbation of endogenous H_2O_2 levels, it was decided that further characterisation studies would performed in anaesthetised animals. Therefore, the main objective of Section 5.3.3.2.1 was to investigate the effect of perfusion of varying doses of H_2O_2 on the dual H_2O_2 biosensor implanted in the striatum of anaesthetised mice. By co-implantation of the microdialysis probe with the H_2O_2 biosensor, local concentrations of the target analyte and characterisation compounds can be delivered to the area surrounding the implanted sensor.

The administration of varying doses of H_2O_2 and characterisation compounds was carried out using aCSF as the vehicle. Consequently, the effect of aCSF perfusion on the amperometric signal was examined. Figure 5.3.3.2.1.1A illustrates the mean percentage current response of perfusion of aCSF over a 20-minute period. An evident decrease in the amperometric signal from baseline levels is observed following the start of aCSF perfusion. This decrease can be attributed to the diffusion of the endogenous analytes across the semi-permeable membrane on the microdialysis probe to the dialysate. After cessation of perfusion of the aCSF, the decrease in amperometric signal diminishes. However, the overall subtracted percentage current change (- 73 ± 80 pA, n = 4, Figure 5.3.3.2.1.1B) indicated only a slight deviation from pre-perfusion

baseline levels which occurred 13 ± 4 mins (n = 4) after the start of aCSF perfusion. This change in current corresponded to a percentage change of - 2 ± 2 % (n = 4) and no significant difference (p = 0.49) from pre-perturbation baseline levels was exhibited. A negligible effect of the control administration of aCSF perfusion on the H_2O_2 biosensor is therefore demonstrated.

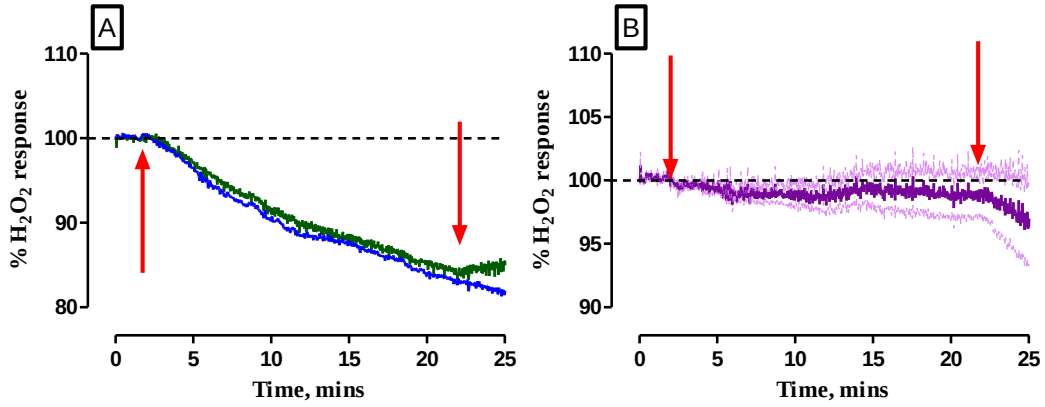

Figure 5.3.3.2.1.1: Averaged percentage raw data current response of H_2O_2 sensors co-implanted with a microdialysis probe, 20-minute aCSF perfusion (A) H_2O_2 blank electrode (blue) & H_2O_2 catalase electrode (green) implanted in the striatum of NOD SCID mice (n = 4), (B) H_2O_2 subtracted current response (n = 4) Start/end of perfusion is represented by the red arrows. The purple trace indicates the mean subtracted percentage current response with the percentage error represented by the light purple trace on graph B. Graph A are the mean percentage current responses.

Following on from control investigations, increasing H_2O_2 concentrations were perfused into the striatum of the anaesthetised animal using aCSF as a vehicle. A 10-minute washout period was included between perfusions to ensure a new baseline level was achieved before each perfusion. Figures 5.3.3.2.1.2A & C highlights a minor increase in the recorded current on the blank electrode following perfusion of 100 µM and 500 µM H_2O_2/aCSF. However, this effect was short lived as the current was observed to decrease quickly below baseline for the remainder of the perfusion. Concomitant, the amperometric signal of the catalase electrode decreased over the 20-minute perfusion. By examination of the subtracted signal, an overall increase in signal was noted over the course of the perfusion (Figure 5.3.3.2.1.2B & D). The resulting current was seen to exhibit a dose response effect between addition of 100 µM and 500 µM H_2O_2/aCSF. The decreases seen at both the blank and catalase electrodes

results from the use of retromicrodialysis in these studies. Although, endogenous concentrations of H_2O_2 are delivered to the vicinity of the microelectrodes, counter flow of the surrounding analytes across the semi-permeable membrane of the microdialysis probe will also occur. This results in an overall decrease in current being measured at both the blank and catalase electrodes. It is also important to remember that the current measured on the blank electrode will be higher than that measured by the catalase electrode due to the ability of the blank electrode being able to measure basal levels of H_2O_2 *in vivo*.

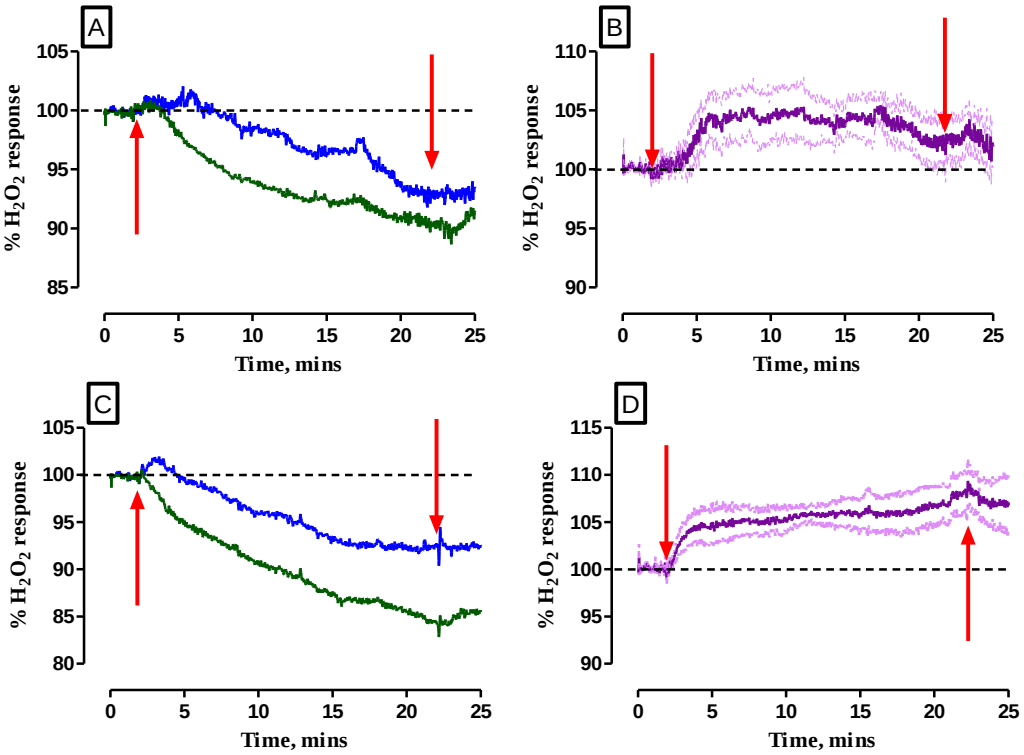

Figure 5.3.3.2.1.2: Averaged percentage raw data current response of H_2O_2 sensors co-implanted with a microdialysis probe, 20-minute 100 µM H_2O_2/aCSF perfusion (A) H_2O_2 blank electrode (blue) & H_2O_2 catalase electrode (green), (B) H_2O_2 subtracted current response (*n* = 3), and 20-minute 500 µM H_2O_2/aCSF perfusion (C) H_2O_2 blank electrode (blue) & H_2O_2 catalase electrode (green), (D) H_2O_2 subtracted current response (*n* = 3) implanted in the striatum of NOD SCID mice. Start/end of perfusion is represented by the red arrows. The purple trace indicates the mean percentage current response with the percentage error represented by the light purple trace on graph B and D. Graph A and C are the mean percentage current responses.

The dose response effect on the H_2O_2 biosensor was further displayed by perfusion of higher concentration of H_2O_2 to the local microenvironment in the

striatum. Figure 5.3.3.2.1.3 demonstrates the effect of 1 mM, 10 mM and 100 mM H_2O_2/aCSF on the H_2O_2 biosensor. A significant difference ($p < 0.05$) in the recorded signal was obtained with a 9 ± 2 % (n = 4) current change in amperometric signal. This increase which occurred 14 ± 3 mins (n = 4) after the start of the perfusion corresponded to a ΔI of 90 ± 34 pA (n = 4) from pre-perfusion levels. The current change that resulted from perfusion of 10 mM was 47 ± 9 pA (n = 3) which occurred 8 ± 2 mins (n = 3) after the start of the perfusion. A percentage current change of 23 ± 8 % (n = 3) resulted. Similarly, a percentage increase of 106 ± 80 % (n = 3) resulted following perfusion of 100 mM H_2O_2. This corresponded to a current change of 90 ± 115 pA (n = 3) which resulted 10 ± 5 mins (n = 3) after the start of the perfusion.

Additionally, there was a significant difference in each of the amperometric signals following perfusion of 1 mM, 10 mM and 100 mM H_2O_2/aCSF on the H_2O_2 biosensor when compared to the control perfusion of aCSF (Table 5.3.3.2.1.1). Moreover, it is important to note that large errors exist due to the large variability that exist between the H_2O_2 signal response recorded from different animals. This is due to the difficulty in measuring H_2O_2 *in vivo* even though the subtraction method is implemented to try and reduce this variability that exists between measurements conducted in different animals.

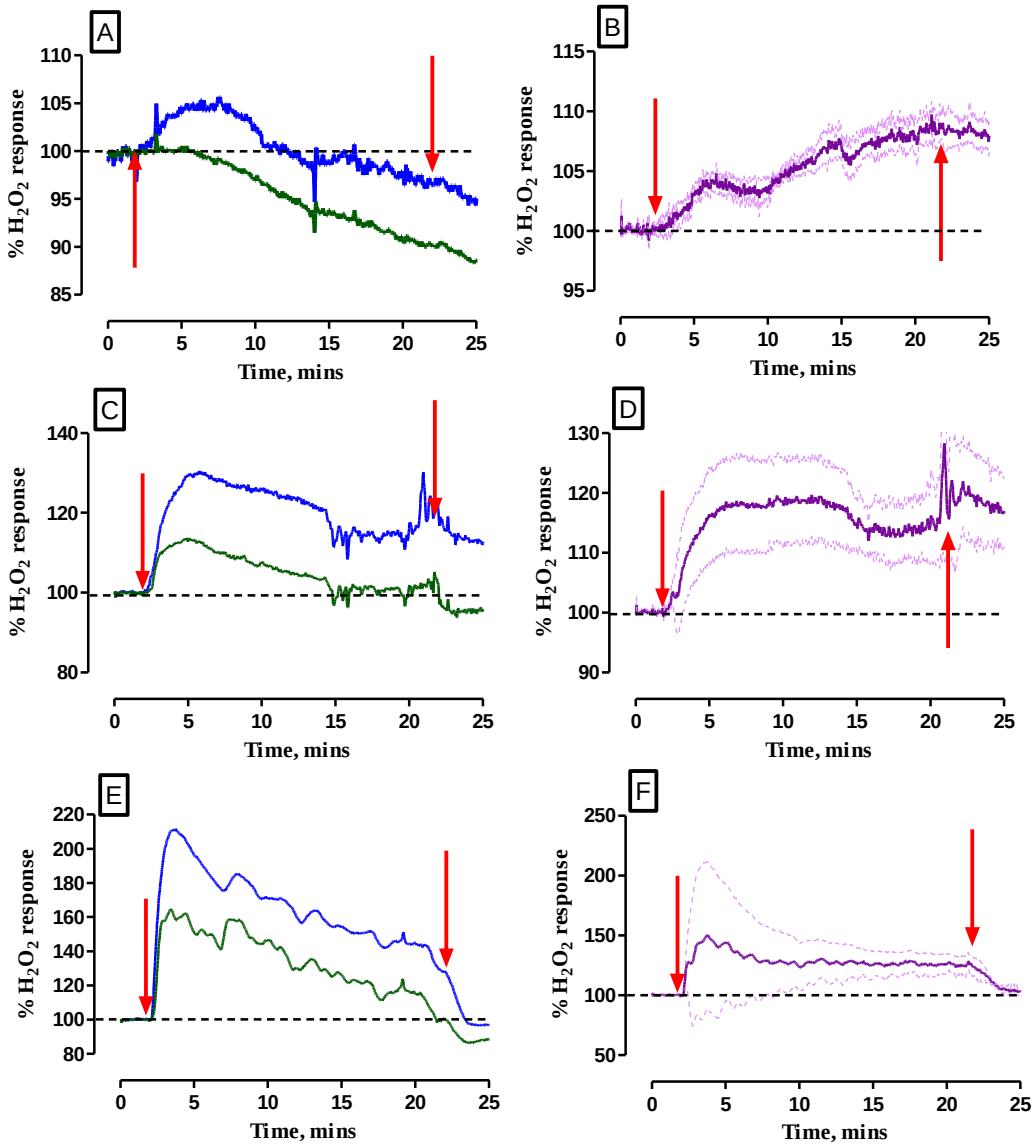

Figure 5.3.3.2.1.3: Averaged percentage raw data current response of H_2O_2 sensors co-implanted with a microdialysis probe implanted in the striatum of NOD SCID mice, 20 minute 1 mM H_2O_2/aCSF perfusion (*n* = 4), (A) H_2O_2 blank electrode (blue) & H_2O_2 catalase electrode (green), (B) Corresponding H_2O_2 subtracted current response, 20 minute 10 mM H_2O_2/aCSF perfusion (*n* = 3), (C) H_2O_2 blank electrode (blue) & H_2O_2 catalase electrode (green), (D) Corresponding H_2O_2 subtracted current response, and 20 minute 100 mM H_2O_2/aCSF perfusion (*n* = 3), (E) H_2O_2 blank electrode (blue) & H_2O_2 catalase electrode (green), (F) H_2O_2 subtracted current response. Start/end of perfusion is represented by the red arrows. The purple trace indicates the mean percentage current response with the percentage error represented by the light purple trace on graph B, D & F. Graph A, C & E are the mean percentage current responses.

Table 5.3.3.2.1.1: Summary of the acute *in vivo* data following co-implantation of a microdialysis probe with the H_2O_2 biosensor in response to increasing concentrations of H_2O_2.

H_2O_2, µM	Current Change ΔI (nA)	Max. % Current Change	Max. % Current Change *vs.* Baseline	Max. % Current Change *vs.* aCSF (unpaired *t*-test)
aCSF	-73 ± 80	-2 ± 2	P = 0.49	-
100 µM	45 ± 40	6 ± 2	P < 0.05	P < 0.05
500 µM	131 ± 74	9 ± 2	P < 0.05	P < 0.01
1 mM	90 ± 34	9 ± 2	P < 0.05	P < 0.01
10 mM	47 ± 9	23 ± 8	P = 0.06	P < 0.05
100 mM	90 ± 116	106 ± 80	P = 0.09	P < 0.05

Conversely, the recorded signals are much lower than those recorded in the *in vitro* setting. Moreover, an increase in H_2O_2 detection at the blank electrode only occurs following administration of a 1 mM concentration of H_2O_2 which does not corroborate with *in vitro* results. Figure 5.3.3.2.1.5. displays *in vitro* data for an extended H_2O_2 calibration conducted on H_2O_2 blank electrodes. This data resulted in a current change of 213 ± 20 nA (n = 4) at the same concentration range of 1 mM H_2O_2. Comparison of the data obtained *in vivo* and *in vitro* at the same concentration range indicates discrepancies in the correlation between the recorded amperometric signal recorded using the retromicrodialysis with the H_2O_2 biosensor against using the H_2O_2 biosensor *in vitro*.

A possible explanation for this may be that the sensor/probe interface is surrounded by a complex tissue matrix which tightly regulates H_2O_2 by antioxidant action in the surrounding areas. Major antioxidants such as catalase, glutathione peroxidase and thioredoxin peroxidase work to catalytically breakdown peroxidases. These enzymes can be found in various cellular locations such as the mitochondria and cytosol[47]. Therefore, due to the high regulation of H_2O_2 concentrations *in vivo*, it is difficult to draw comparisons to H_2O_2 calibrations carried out *in vitro*. It is also important to consider the proximity of the microelectrodes to the microdialysis probe. Although every care is taken to ensure the proximity of the biosensor is as near as possible to the probe, any discrepancies in the distance of the biosensor from the probe

will result in a drop in analyte detection at the relevant sensor due to the efficient regulation of H_2O_2 species endogenously. Furthermore, the use of the biosensor/probe construct is quite large in comparison to the scale of the mouse brain. Therefore, it must be noted that some damage will result from implantation of the construct. In turn, necrotic tissue may result around the microdialysis probe impeding the diffusion of H_2O_2 to the biosensor. Borland *et al*. previous highlighted this phenomenon whereby numerical models incorporating diffusion and active transport processes demonstrated that dopamine recovery was strongly affected in the tissue nearest the implanted probe as a direct result of the tissue being disrupted during implantation[48]. Nevertheless, a dose dependent response of the H_2O_2 biosensor is evident to increasing concentrations of H_2O_2 which conforms the ability of the biosensor to detect endogenous concentrations of the analyte of interest (Figure 5.3.3.2.1.4).

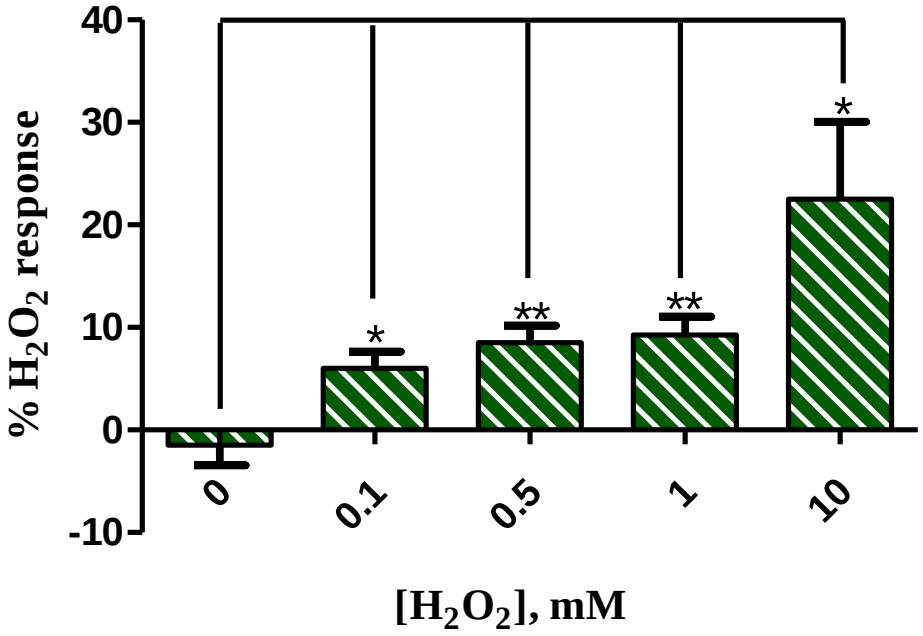

Figure 5.3.3.2.1.4: Dose response on the subtracted H_2O_2 current to 0 - 10 mM H_2O_2/aCSF (*n* = 4).

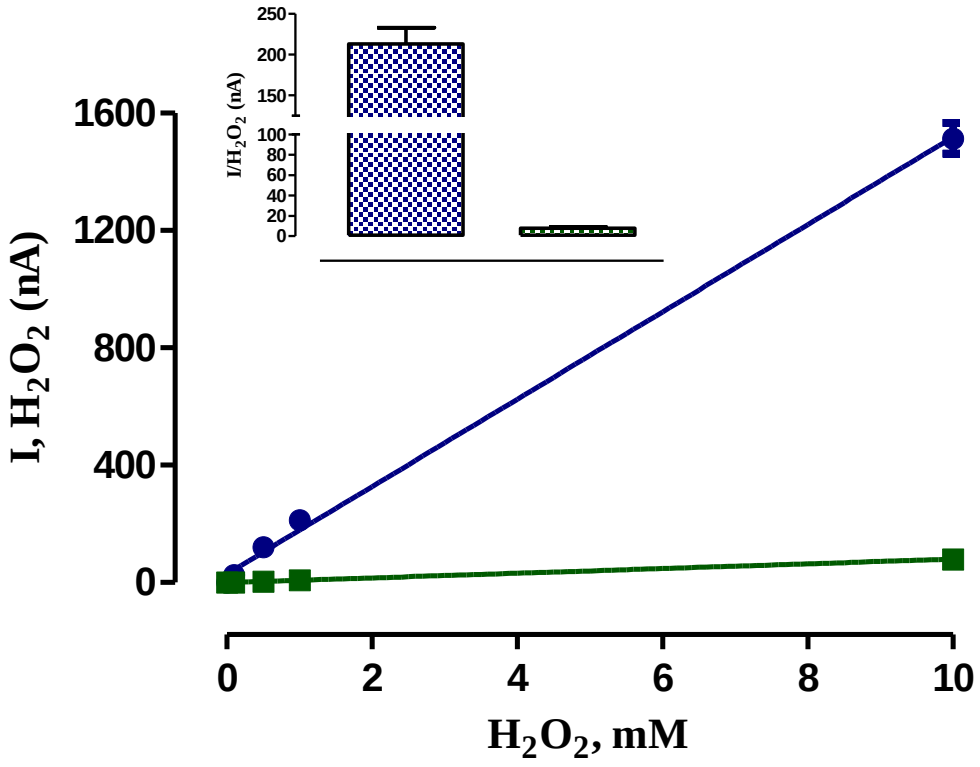

Figure 5.3.3.2.1.5: Current concentration profile for an extended calibration of H_2O_2 (0 - 10 mM) on H_2O_2 blank electrodes (*n* = 4, r^2 = 0.99, blue trace) and catalase electrodes (*n* = 3, r^2 = 0.99, green trace). *Inset*: Comparison of the average currents at 1 mM H_2O_2 for the blank and catalase electrodes.

5.3.3.2.2 Amperometric Measurement of H_2O_2 Utilising Microinfusion Techniques

Microinfusion probes were manufactured *in house* to be co-implanted with the H_2O_2 biosensor. Inclusion of microinfusion probes reduced concerns surrounding size and relative delivery that was encountered during retromicrodialysis investigations. Furthermore, the size of the microinfusion construct with the H_2O_2 biosensor is a lot smaller than the aforementioned construct (see Section 3.9.1.2). This allows for a closer proximity of the blank and catalase electrodes to microinfusion probe. With the reduced distance between the probe and the biosensor, it was hypothesised that less damage would be inflicted on the surrounding tissue by the construct whilst diffusion of H_2O_2 would be more efficient to the electrodes. During these experiments, it had to be ensured that large volumes of infusate would not pool in the striatum at any one time. Therefore, infusion time was reduced to ca. 150-seconds at a flow rate of 0.2 µL/min.

Firstly, a control administration of aCSF was conducted as aCSF was the vehicle used for all experimentation involving the microinfusion probe. Figure

5.3.3.2.2.1 illustrates the amperometric signal that resulted following perfusion of aCSF over a 150-second period. The subtracted current resulted in current change of - 5 ± 24 pA (n = 5) leading to a - 7 ± 4 % (n = 5) change in the current response following the start of perfusion. Furthermore, there was no significant difference (p = 0.18) between the recorded current following the start of infusion and pre-infusion current levels. Therefore, a decrease in the recorded current response is evident resulting from the start of the infusion of aCSF. It must be noted that the recorded decrease may result from baseline drift caused by the short settling periods associated with acute experiments. However, this decrease indicates that there is no change in current from aCSF infusion.

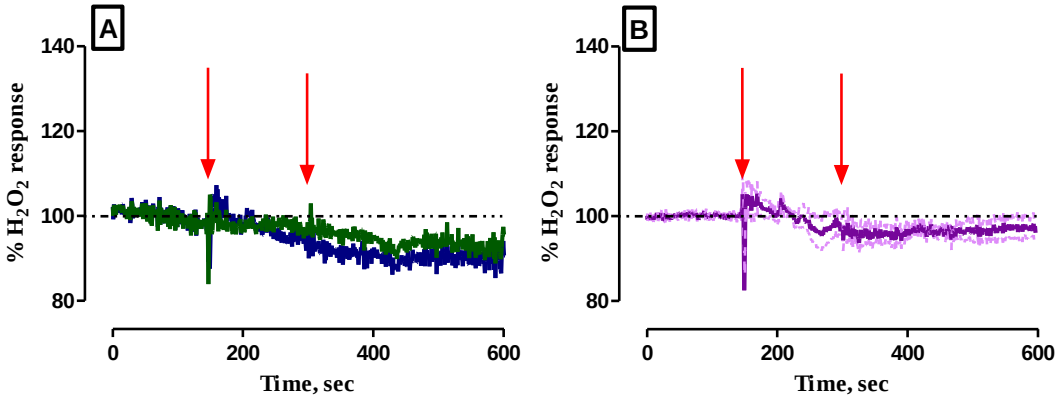

Figure 5.3.3.2.2.1: Averaged percentage raw data current response of the dual H_2O_2 biosensor co-implanted with a microinfusion probe following: (A) infusion of aCSF - H_2O_2 blank electrode (blue trace) & H_2O_2 catalase electrode (green trace), (B) infusion of aCSF - subtracted H_2O_2 current response. Start/end of infusion is represented by the red arrows. The purple trace indicates the mean percentage current response with the percentage error represented by the light purple trace.

Figure 5.3.3.2.2.2 displays the amperometric response following infusion of 20 µM, 50 µM and 100 µM H_2O_2/aCSF. The subtracted current response is represented by Figures 5.3.3.2.2.2B, D & F whilst the response of the individual electrodes is highlighted in Figures 5.3.3.2.2.2 A, C & E. The maximum subtracted currents obtained were 555 ± 252 pA (20 µM, n = 5), 818 ± 441 pA (50 µM, n = 5) and 1941 ± 675 pA (100 µM, n = 5). A percentage change of 184 ± 56 % (20 µM, n = 5), 359 ± 107 % (50 µM, n = 5) and 1008 ± 377 % (100 µM, n = 5) resulted from the maximum current recorded when compared to pre-infusion baseline levels.

Furthermore, significant differences ($p < 0.01$, $p < 0.01$ and $p < 0.05$, unpaired *t*-test) resulted from comparison of the maximum current response and pre-infusion baseline currents.

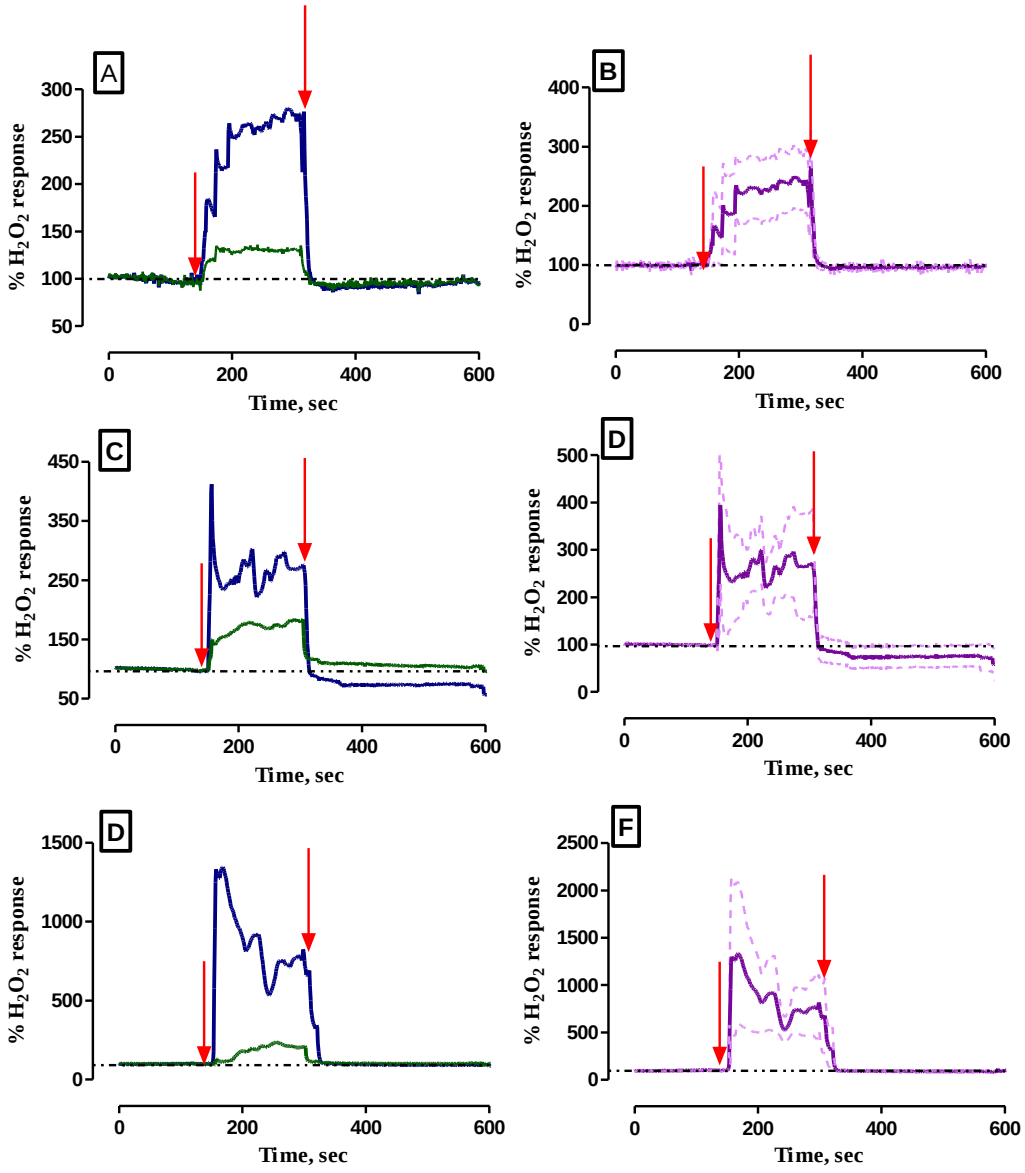

Figure 5.3.3.2.2.2: Averaged percentage raw data current response of the dual H_2O_2 biosensor co-implanted with a microinfusion probe following: (A) infusion of 20 µM H_2O_2/aCSF over 150-seconds on the H_2O_2 blank electrode (blue trace) & H_2O_2 catalase electrode (green trace), (B) Corresponding subtracted H_2O_2 current, (C) infusion of 50 µM H_2O_2/aCSF over 150-seconds on H_2O_2 blank electrode (blue trace) & H_2O_2 catalase electrode (green trace), (D) Corresponding subtracted H_2O_2 current, (E) infusion of 100 µM H_2O_2/aCSF over 150-seconds on the H_2O_2 blank electrode (blue trace) & H_2O_2 catalase electrode (green trace), (F) Corresponding subtracted H_2O_2 current. Start/end of infusion is represented by the red arrows. The purple trace indicates the mean percentage current response with the percentage error represented by the light purple trace.

An evident dose response recorded by the H_2O_2 biosensor was emphasised in Figure 5.3.3.2.2.2 with increases in the amperometric response being obtained following infusion of increasing concentrations of H_2O_2. Larger concentrations of H_2O_2 were also infused into the striatum of the anaesthetised subject to further confirm the dose response being exhibited. Infusion of 1 mM and 10 mM H_2O_2 was conducted and Figure 5.3.3.2.2.3 illustrates the subsequent results. Following infusion of 1 mM and 10 mM H_2O_2, the maximum subtracted current was 27 ± 8 nA (n = 5) and 140 ± 29 nA (n = 5) for blank and catalase electrodes respectively. The percentage change in current that resulted was 9262 ± 2814 % (1 mM, n = 5) and 39506 ± 7365 % (10 mM, n = 5).

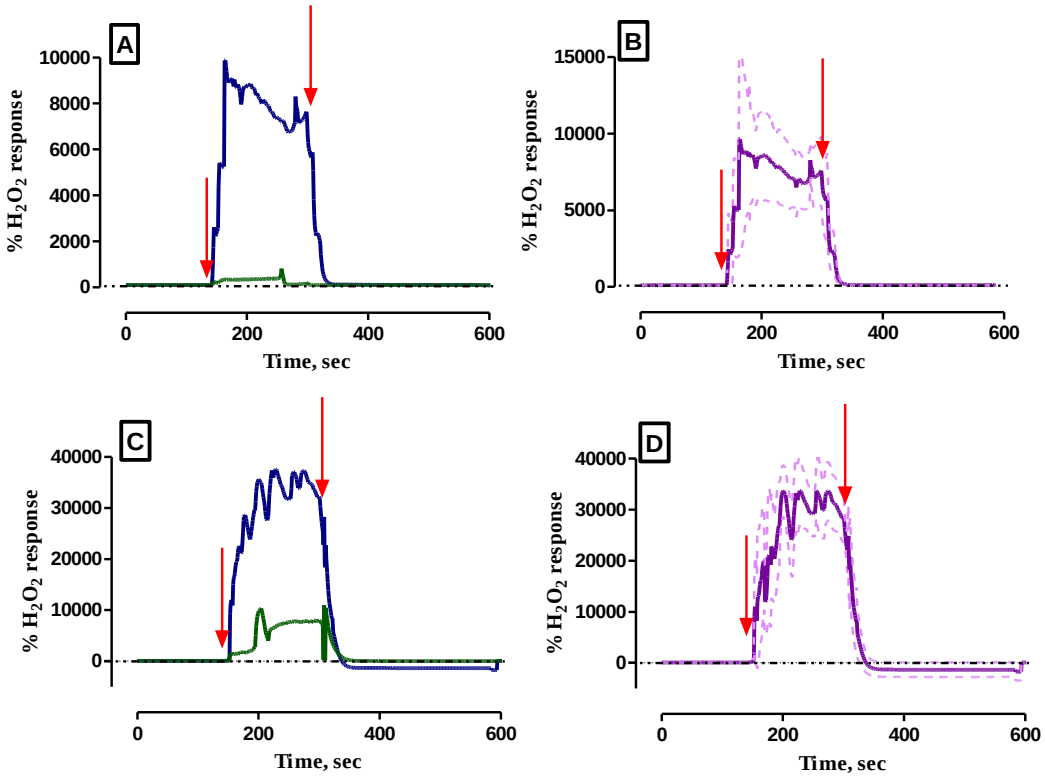

Figure 5.3.3.2.2.3: Averaged percentage raw data current response of the dual H_2O_2 biosensor co-implanted with a microinfusion probe following: (A) infusion of 1 mM H_2O_2/aCSF over 150-seconds on the H_2O_2 blank electrode (blue trace) & H_2O_2 catalase electrode (green trace), (B) Corresponding on the subtracted H_2O_2 current, (C) infusion of 10 mM H_2O_2/aCSF over 150-seconds on the H_2O_2 blank electrode (blue trace) & H_2O_2 catalase electrode (green trace), (D) Corresponding on the subtracted H_2O_2 current. Start/end of infusion is represented by the red arrows. The purple trace indicates the mean percentage current response with the percentage error represented by the light purple trace.

In summary, increasing concentrations result in a dose response effect at the H_2O_2 biosensor highlighting the ability of the biosensor to detect H_2O_2 delivered by the microinfusion construct (Table 5.3.3.2.2.1). Although, retromicrodialysis studies showed increases in the subtracted H_2O_2 response measured over all concentrations of H_2O_2, it is important to note that an actual increase measured at the blank electrode was only seen following perfusion of 1 mM H_2O_2 or higher. Therefore, it can be hypothesised that replacement of the larger microdialysis probe with a much smaller microinfusion probe works to overcome many of the problems experienced whilst trying to detect H_2O_2 in the anaesthetised animal in Section 5.3.3.2.1. Section 5.3.3.2.1 discussed the inability of the H_2O_2 blank sensor to detect H_2O_2 concentration below 1 mM. The results presented here are in complete contrast whereby a steady increase in the amperometric response is achieved following infusion of concentrations of H_2O_2 as low as 20 µM.

Similarly, the added benefit of incorporating the microinfusion probe into acute experimentation was the ability to detect the varying concentrations of H_2O_2 instantaneously. Previously, the use of the microdialysis probe had resulted in a delayed increase in H_2O_2 detection by the H_2O_2 biosensor. However, replacement of the microdialysis probe for the smaller microinfusion probe lead to an instantaneous response being exhibited by the H_2O_2 biosensor in the detection of H_2O_2. The improved results may be due to a number of factors associated with the incorporation of the smaller microinfusion probe. Firstly, the distance between the H_2O_2 biosensor and the microinfusion probe is greatly reduced in this design meaning that H_2O_2 reaches the H_2O_2 biosensor much faster and at a greater total concentration. The H_2O_2 levels are at a reduced risk of being diminished by the tightly regulated endogenous antioxidant system, as well as, diffusing off into the surrounding tissue away from the H_2O_2 biosensor. The elimination of the microdialysis probe results in the removal of the consideration for probe recovery rates which can delay the efficiency of the probe to deliver H_2O_2 to the H_2O_2 biosensor. To conclude, the H_2O_2 biosensor is able to efficiently respond to varying concentrations of H_2O_2 delivered using microinfusion probes in acute investigations (Figure 5.3.3.2.2.4).

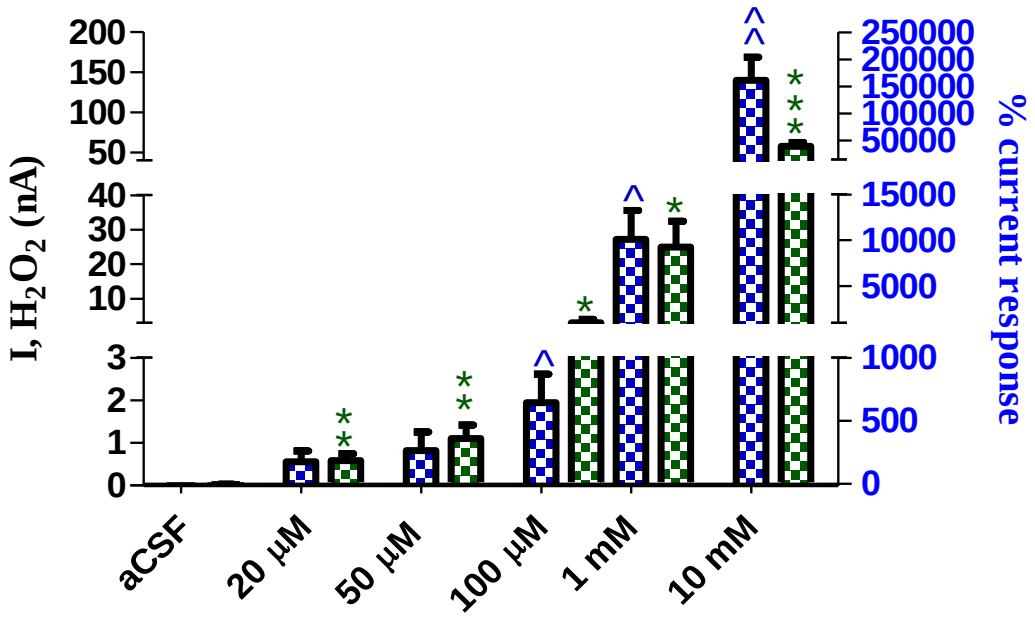

Figure 5.3.3.2.2.4: Dose response of infusion of 0 - 10 mM H_2O_2/aCSF (*n* = 5) on the H_2O_2 biosensor.

Table 5.3.3.2.2.1: Summary of the acute *in vivo* data following co-implantation of a microinfusion probe with the H_2O_2 biosensor in response to increasing concentrations of H_2O_2.

H_2O_2, µM	Current Change ΔI (nA)	Max. % Current Change	Max. % Current Change *vs.* Baseline	Max. % Current Change *vs.* aCSF (unpaired *t*-test)
aCSF	-5 ± 24 (pA)	-7 ± 4	P = 0.18	-
20 µM	1 ± 0.2	184 ± 56	P < 0.05	P < 0.01
50 µM	1 ± 0.4	359 ± 107	P = 0.06	P < 0.01
100 µM	2 ± 1	1008 ± 377	P < 0.05	P < 0.05
1 mM	27 ± 8	9262 ± 2814	P < 0.01	P < 0.05
10 mM	140 ± 29	39507 ± 7365	P < 0.05	P < 0.001

5.3.3.2.3 Local Administration of Antioxidant Inhibitors by Retromicrodialysis and Microinfusion Techniques

Section 5.3.3.2.2 discussed in detail the ability of the H_2O_2 biosensor to detect concentrations of H_2O_2 that were perfused into the locality of the biosensor. However, it was still crucial to confirm the ability of the H_2O_2 biosensor to detect endogenous levels of H_2O_2. To facilitate this, two modulators of H_2O_2 were included in acute investigations, MSA and SA. Reactive oxygen species, such as H_2O_2, are kept under tight control in normal conditions by the action of various enzymatic antioxidants including glutathione peroxidase and catalase. Firstly, glutathione peroxidase is part of the first line antioxidant defence system that works to breakdown H_2O_2 to water through the oxidation of the reduced form of GSH. MSA works to inhibit the action of glutathione peroxidase and thus, increase levels of endogenous H_2O_2. Consequently, the local delivery of a 1 mM concentration of MSA enables the inhibition of glutathione peroxidase and allow for the endogenous measurement of H_2O_2. Initially, local perfusions of MSA were conducted using the retromicrodialysis technique.

Figure 5.3.3.2.3.1 demonstrates the percentage current response resulting from the perfusion of MSA into the striatum. Upon perfusion of MSA into the striatum, a steady increase in H_2O_2 levels is observed on the recorded amperometric signal. A significant increase ($p < 0.05$) was detected in the subtracted percentage current response when compared against the response of aCSF retroperfusion. The ΔI obtained was 19 ± 2 pA ($n = 3$) which resulted in a percentage change of 10 ± 4 % *(*$n = 3$) occurring after 11 ± 5 mins ($n = 3$). Furthermore, this gradual increase in the recorded amperometric signal as a result of MSA perfusion corroborates previous studies involving the perfusion of MSA into the striatum of freely moving rats[7].

Figure 5.3.3.2.3.2 highlights the similarity in the recorded response following the retroperfusion of 1 mM H_2O_2 and 1 mM MSA. A significant difference in the recorded current response was observed for the perfusion of 1 mM H_2O_2 ($p < 0.01$) and 1 mM MSA ($p < 0.05$) when compared to the levels achieved for aCSF perfusion. Hence, it is evident that the H_2O_2 biosensor has now been validated to efficiently detect H_2O_2 species both by local perfusion and endogenous perturbations.

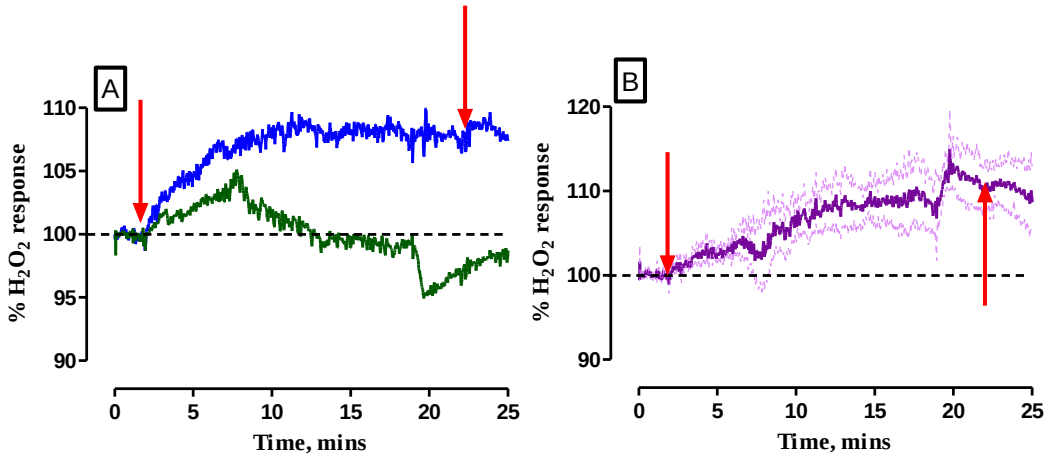

Figure 5.3.3.2.3.1: Averaged percentage raw data current response of the dual H_2O_2 biosensor co-implanted with a microdialysis probe following: (A) perfusion of 1 mM MSA over 20-minutes on the H_2O_2 blank electrode (blue trace) & H_2O_2 catalase electrode (green trace), (B) Corresponding subtracted H_2O_2 current. Start/end of perfusion is represented by the red arrows. The purple trace indicates the mean percentage current response with the percentage error represented by the light purple trace. Data is represented as mean ± SEM.

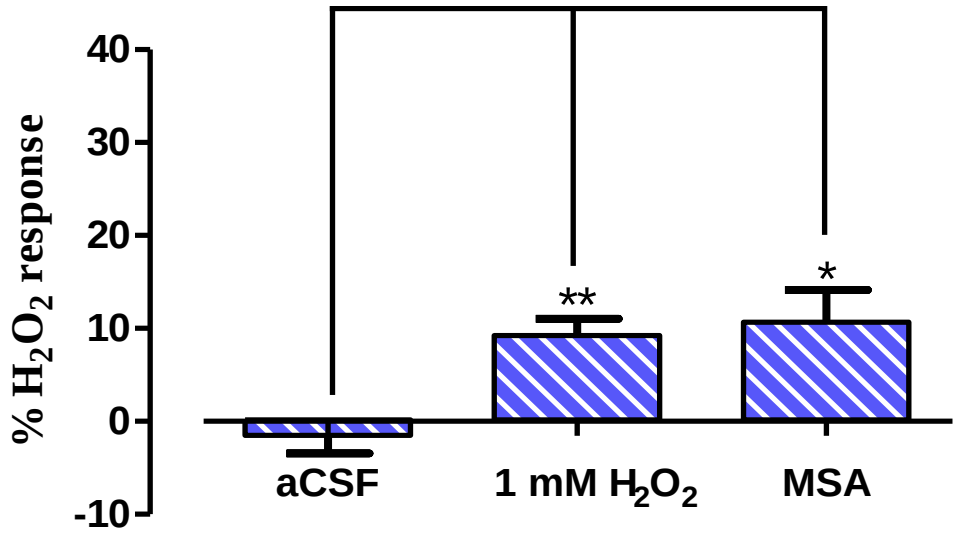

Figure 5.3.3.2.3.2: Averaged raw data percentage response of the subtracted response of the H_2O_2 biosensor to aCSF (n = 4), 1 mM H_2O_2/aCSF (n = 4). and 1 mM MSA (n = 3). The percentage current response is represented as mean ± SEM.

The effect of MSA on the H_2O_2 response was investigated using the microinfusion construct. A 1 mM concentration of MSA was infused and a significant increase ($p < 0.01$, Figure 5.3.3.2.3.3A) in the maximal subtracted current (7 ± 3 nA,

n = 3) was achieved. This change in current corresponded to a 1782 ± 422 % (*n* = 3) change from pre-infusion baseline levels.

The ability of the H_2O_2 biosensor to detect endogenous levels was also confirmed by infusion of the catalase inhibitor, SA. When levels of reactive oxygen species, like H_2O_2, become too high in mammalian systems, the complex antioxidant system works to breakdown these species to prevent damage to surrounding cells and tissue. One such antioxidant is catalase which is present primarily in the peroxisomes in living tissues which utilise oxygen. Catalase is a highly efficient enzyme that works to degrade H_2O_2 to water or molecular oxygen by using iron or manganese as a cofactor[49]. SA was administered to inflict inhibition of enzymatic catalase action, thus, causing an increase in endogenous H_2O_2 concentrations. A significant increase ($p < 0.001$) in the subtracted recorded amperometric current (11 ± 6 nA, *n* = 3, Figure 5.3.3.2.3.3B) resulted following infusion of 1 mM SA. This equated to a subtracted percentage change of 2439 ± 559 % (*n* = 3).

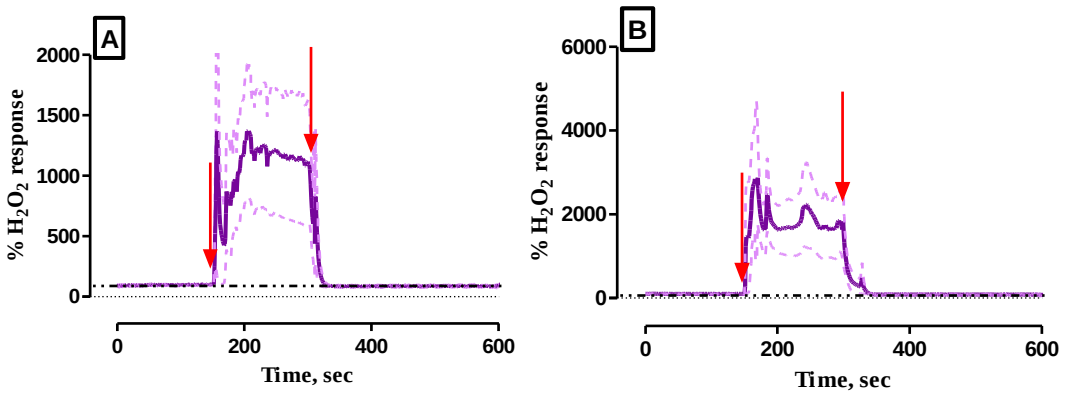

Figure 5.3.3.2.3.3: Averaged percentage raw data current response of the dual H_2O_2 biosensor co-implanted with a microinfusion probe following: (A) infusion of 1 mM MSA over 150-seconds on the subtracted current (*n* = 3), (B) infusion of 1 mM SA over 150-seconds on the subtracted current (*n* = 3). Point of injection is represented by the red arrow. The purple trace indicates the mean percentage current response with the percentage error represented by the light purple trace.

The results obtained in Section 5.3.3.2.3.3 further confirm that the inclusion of the microinfusion probe mitigates any of the limitations previously encountered when the microdialysis probe was included in previous acute investigations.

The below figure, Figure 5.3.3.2.3.4 illustrates the subtracted response of the H_2O_2 biosensor to endogenously produced H_2O_2 following administration of MSA and SA. A clear increase in H_2O_2 detection is evident when compared to administration of aCSF indicating that the H_2O_2 biosensor has now been validated to detect endogenous levels of H_2O_2. Additionally, Section 4.3.3.8 discussed the incorporation of an interference rejection layer on the H_2O_2 biosensor efficiently blocked the detection of MSA and SA on the electrode surface. Therefore, it can be confirmed that endogenously produced H_2O_2 was being measured at the electrode surface as illustrated in Figure 5.3.3.2.3.4 and MSA and SA were not contributing to the overall amperometric current measured.

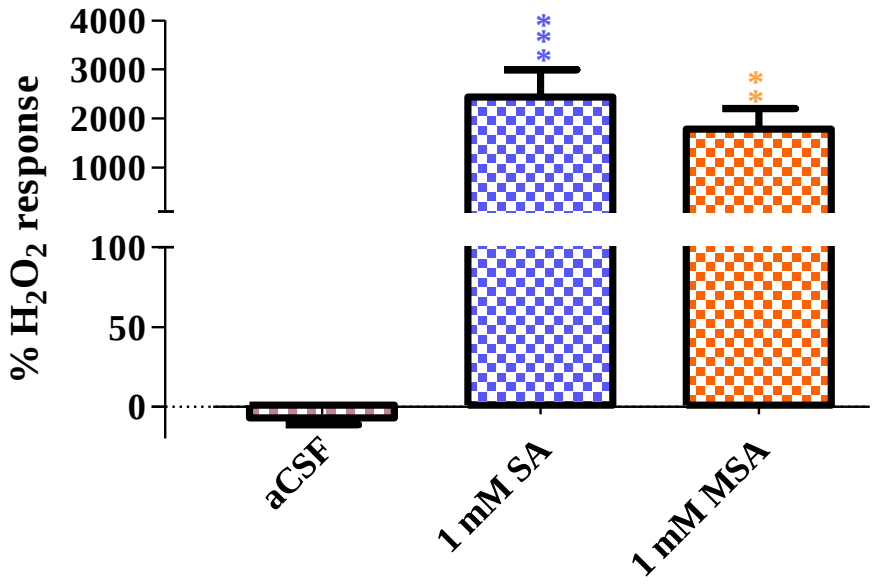

Figure 5.3.3.2.3.4: Averaged raw data percentage response of the subtracted response of the H_2O_2 biosensor to aCSF (*n* = 4), 1 mM MSA (*n* = 3) and 1 mM SA (*n* = 3). The percentage current response is represented as mean ± SEM.

5.3.3.3 Baseline Stability of the H_2O_2 Biosensor in the Striatum of NOD SCID Mice

The H_2O_2 biosensor contains an enzyme modification on the electrode surface as detailed in Section 3.4.4.3. For this reason, it was hypothesised to exhibit reduced *in vivo* stability in comparison with the aforementioned sensors. Examination of amperometric current demonstrated that the dual biosensor was stable for up to 5-days of continuous amperometric recording. Figure 5.3.3.3.1 displays the stable subtracted baseline that was obtained over 5-days of *in vivo* recording. The illustrated data was

normalised whereby the baseline recorded on Day 1 was normalised to 100 %. Subsequently, the baselines recording on Days 2-5 were reported as a percentage of the baseline recorded on Day 1. Figure 5.3.3.3.1 highlights a small decrease in the percentage baseline current reported on Day 2. Previous studies have reported that upon exposure of a microelectrode to the brain microenvironment, a decrease of 20 - 50 % in the sensitivity can be expected[31]. The work presented here corroborates such findings as the sensitivity decreases on Day 2 (77.8 ± 3.6 %) to fall within this range. Additionally, the stability of the biosensor was confirmed for 5-days following implantation as no significant decrease (p = 0.89, one-way ANOVA, n = 6) in the recorded sensitivity was observed. Furthermore, the recorded sensitivities were recorded as follows; Day 3: 71.5 ± 5.7 %, Day 4: 74.0 ± 9.3 %, Day 5: 70.0 ± 10.0 %.

Moreover, confirmation of the stability of the biosensor continuously for 5-days can be supported by a similar response demonstrated by the biosensor in *ex vivo* studies carried out previously (Section 4.3.3.9). Comparatively, following immersion of the biosensor in homogenous brain tissue *ex vivo*, a decrease of 15.4 ± 12.9 % was highlighted on Day 1 but no significant difference was reported in the 7 days following. Therefore, both the blank electrode and the catalase electrode were demonstrated to be stable for at least 7-days *ex vivo*. Although, 7-days stability was verified *ex vivo*, a period of only 5-days was confirmed for *in vivo* studies. However, a longer stability range could be investigated in future work to examine the stability of the biosensor post 5-days if deemed necessary.

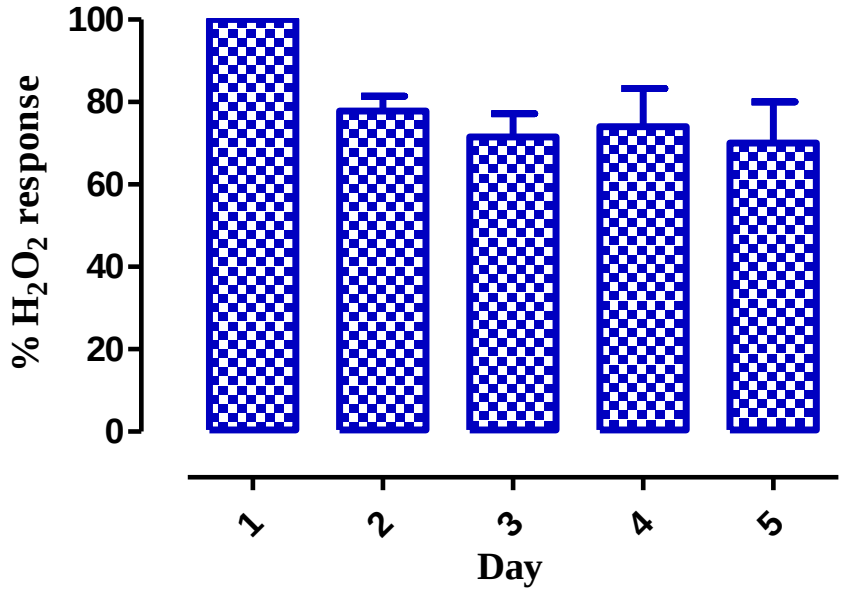

Figure 5.3.3.3.1: Average percentage baseline currents for H_2O_2 sensors (n = 6) recorded in the striatum of NOD SCID mice.

5.3.3.4 24-Hour Amperometric Recordings in the Striatum of NOD SCID Mice

Figure 5.3.3.4.1 illustrates H_2O_2 dynamics recorded over a 24-hour period. The purpose of this study was to examine any fluctuations in H_2O_2 currents which may be associated with an increase or decrease in motor activity of the subject. Figure 5.3.3.4.1 demonstrates the average currents recorded during the light (n = 14/7) and night cycle (n = 17/7). It was decided to report qualitative changes of H_2O_2 during this 24-hour period rather than quantitative changes due to the difficulty associated with obtaining accurate quantitative concentration values of H_2O_2 *in vivo*. Therefore, the average percentage currents presented are normalised to 100 %. From Figure 5.3.3.4.1, it is evident that there is a notable absence of a sustained increase in analyte detection during the night cycle as observed in NO and O_2 investigations (Sections 5.3.1.7 and 5.3.2.7). The amperometric current of H_2O_2 remains at basal levels throughout the 24-hour period with no significant variation in H_2O_2 levels experienced. It can be hypothesised that the levels of H_2O_2 remain at basal levels due to the tight regulation of the antioxidant network. Melatonin is a component of the antioxidant defence system which works to enhance glutathione peroxidase activity in the detoxification of H_2O_2. Pablos *et al.* previously reported that constant exposure of animals to light abolishes the night time increase of melatonin resulting in a decrease in glutathione peroxidase activity throughout this night cycle[50]. Additionally, the levels of

glutathione peroxidase and catalase activity were observed to increase both during the night cycle and during different time points throughout the day highlighting that H_2O_2 levels are under constant regulation by the antioxidant network throughout the 24-hour cycle[51,52].

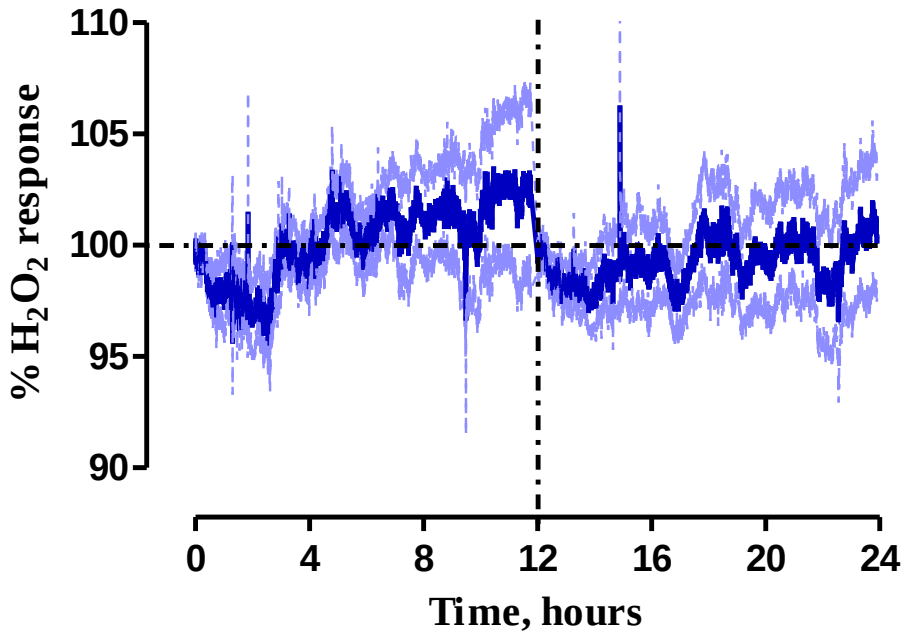

Figure 5.3.3.4.1: Averaged 24-hour percentage current response measured by H_2O_2 sensors (*n* = 7). Mean percentage current is represented by the blue trace. The light blue trace highlights the percentage error. The light phase (07:00 – 19:00, *n* = 14/7) relates to 0-12 hours with the dark phase (19:00 – 07:00, *n* = 17/7) from 12-24 hours. The dashed line at hour 12 represents the end of the light phase/start of the dark phase.

5.4 Conclusion

The main objective of this chapter was associated with characterising the NO, O_2 sensors and the H_2O_2 biosensor in the striatum of NOD SCID mice. Extensive characterisation of these aforementioned sensors has previously been conducted *in vitro* and in wistar rats confirming the excellent sensitivity, selectivity and stability of each of the relevant sensors. However, it was imperative to confirm efficient functionality of the performance of each of these sensors in NOD SCID mice.

Firstly, characterisation studies involving the NO and the O_2 sensor have demonstrated excellent sensitivity and selectivity *in vivo*. Each of these sensors demonstrated current changes in response to modulators and inhibitors of NO and O_2 with significant differences in the NO current being recorded following L-NAME and L-arginine administration, and in the O_2 current in response to L-NAME, chloral hydrate and Diamox when compared to baseline and control saline investigations. Additionally, the stability of these sensors was confirmed for up to 8-days allowing for reliable continuous recordings to be conducted *in vivo*. Moreover, the ability of both sensors to detect variations in recorded circadian rhythms of NO and O_2 further confirms the ability of these sensors to be employed in long-term amperometric recordings.

H_2O_2 recordings conducted in freely-moving animals confirmed excellent selectivity of the biosensor following administration of sodium ascorbate to the subject following subtraction of the percentage current. Likewise, a negligible response of H_2O_2 to administration of saline was also observed. Furthermore, the selectivity of the blank and catalase electrodes was demonstrated following administration of sodium ascorbate. As the interference rejection ability of both electrodes must be matched *in vitro* for the subtraction method to work, it is imperative that these selectivity parameters are retained following implantation in the harsh biological environment of the brain. By use of the subtraction method, a current dependent on H_2O_2 only can be attained. Hence, following confirmation that the selectivity of the blank and catalase electrodes has been maintained *in vivo*, it can be said that the subtracted current results from fluctuations in H_2O_2 only.

Further studies were carried out in anaesthetised animals using the H_2O_2 biosensor to avoid any concerns associated with toxicity to the animal using high concentrations of exogenous H_2O_2, as well as, inhibitors of the antioxidant system

systemically. Therefore, acute investigations included the use of microdialysis and microinfusion probes combined with the H_2O_2 biosensor to allow for local administration of exogenous H_2O_2 and antioxidant inhibitors in anaesthetised animals. However, the inclusion of the microinfusion probe was most successful allowing for confirmation that the H_2O_2 biosensor can measure varying concentrations of infused H_2O_2 and endogenously produced H_2O_2.

As seen with the studies involving the NO and O_2 sensors, the H_2O_2 biosensor was able to efficient detect variations in H_2O_2 dynamics over a 24-hour period whilst retaining stability for at least 5-days following implantation. It can therefore be deduced that the above obtained results validate the ability of each of these sensors to successfully monitor NO, O_2 and H_2O_2 in the striatum of immunocompromised NOD SCID mice. Hence, the aforementioned sensors are now ready to be deployed in a humanised mouse model of PD.

5.5 References

1. Bolger, F., Bennett, R. & Lowry, J. An in vitro characterisation comparing carbon paste and Pt microelectrodes for real-time detection of brain tissue oxygen. *Analyst* **136,** 4028–35 (2011).
2. Bolger, F. B. & Lowry, J. P. Brain tissue oxygen: In vivo monitoring with carbon paste electrodes. *Sensors* **5,** 473–487 (2005).
3. Bolger, F. B., McHugh, S. B., Bennett, R., Li, J., Ishiwari, K., Francois, J., Conway, M. W., Gilmour, G., Bannerman, D. M., Fillenz, M. & Tricklebank, M. Characterisation of carbon paste electrodes for real-time amperometric monitoring of brain tissue oxygen. *J. Neurosci. Methods* **195,** 135–42 (2011).
4. Finnerty, N. J., O'Riordan, S. L., Pålsson, E. & Lowry, J. P. Brain nitric oxide: Regional characterisation of a real-time microelectrochemical sensor. *J. Neurosci. Methods* **209,** 13–21 (2012).
5. Finnerty, N. J., O'Riordan, S. L., Brown, F. O., Serra, P. A., O'Neill, R. D., Lowry, J. P. In vivo characterisation of a Nafion®-modified Pt electrode for real-time nitric oxide monitoring in brain extracellular fluid. *Anal. Methods* **4,** 550 (2012).
6. Wynne, A. M., Reid, C. H. & Finnerty, N. J. In vitro characterisation of ortho phenylenediamine and Nafion®-modified Pt electrodes for measuring brain nitric oxide. *J. Electroanal. Chem.* **732,** 110–116 (2014).
7. O'Riordan, S. L., McLaughlin, K., Lowry, J. P. In vitro physiological performance factors of a catalase-based biosensor for real-time electrochemical detection of brain hydrogen peroxide in freely-moving animals. *Anal. Methods* **8,** 7614–7622 (2016).
8. O'Brien, K. B., Killoran, S. J., O'Neill, R. D. & Lowry, J. P. Development and characterization in vitro of a catalase-based biosensor for hydrogen peroxide monitoring. *Biosens. Bioelectron.* **22,** 2994–3000 (2007).
9. O'Riordan, S.L., Lowry, J. P. In vivo characterisation of a catalase-based biosensor for real-time electrochemical monitoring of brain hydrogen peroxide in freely-moving animals. *Anal. Methods* **9,** 1253–1264 (2017).
10. Brown, F. O. & Lowry, J. P. Microelectrochemical sensors for in vivo brain analysis: an investigation of procedures for modifying Pt electrodes using Nafion. *Analyst* **128,** 700–705 (2003).

11. Shultz, L. D., Ishikawa, F. & Greiner, D. L. Humanized mice in translational biomedical research. *Nat. Rev. Immunol.* **7,** 118–130 (2007).
12. Ito, R., Takahashi, T., Katano, I. & Ito, M. Current advances in humanized mouse models. *Cell. Mol. Immunol.* **9,** 208–214 (2012).
13. Rice, M. E. Ascorbate compartmentalization in the CNS. *Neurotox Res* **1,** 81–90 (1999).
14. Miele, M. & Fillenz, M. In vivo determination of extracellular brain ascorbate. *J. Neurosci. Methods* **70,** 15–19 (1996).
15. Reichert, W.M., Sharkawy, A. A. *In: von Recum AF (ed) Handbook of biomaterials evaluation.* (Taylor and Francis, 1999).
16. Kozai, T. D. Y., Jaquins-Gerstl, A. S., Vazquez, A. L., Michael, A. C. & Cui, X. T. Brain tissue responses to neural implants impact signal sensitivity and intervention strategies. *ACS Chem. Neurosci.* **6,** 48–67 (2015).
17. Ravikumar, M., Sunil, S., Black, J., Barkauskas, D. S., Haung, A. Y., Miller, R. H., Selkirk, S. M. & Capadona, J. R. The roles of blood-derived macrophages and resident microglia in the neuroinflammatory response to implanted Intracortical microelectrodes. *Biomaterials* **35,** 8049–8064 (2014).
18. Wisniewski, N., Moussy, F. & Reichert, W. M. Characterization of implantable biosensor membrane biofouling. *Fresenius. J. Anal. Chem.* **366,** 611–21 (2000).
19. Khan, A. S. & Michael, A. C. Invasive consequences of using micro-electrodes and microdialysis probes in the brain. *TrAC - Trends Anal. Chem.* **22,** 503–508 (2003).
20. Fillenz, M. & Lowry, J. P. The relation between local cerebral blood flow and extracellular glucose concentration in rat striatum. *Exp. Physiol.* **83,** 233–238 (1998).
21. Vahabzadeh, A., & Fillenz, M. Comparison of Stress-induced Changes in Noradrenergic and Serotonergic Neurons in the Rat Hippocampus Using Microdialysis. *Eur. J. Neurosci.* **6,** 1205–1212 (1994).
22. Garthwaite, J. & Boulton, C. L. Nitric Oxide Signaling in the Central Nervous System. *Annu. Rev. Physiol.* **57,** 683–706 (1995).
23. Mukherjee, P., Cinelli, M. A., Kang, S. & Silverman, R. B. Development of nitric oxide synthase inhibitors for neurodegeneration and neuropathic pain. *Chem. Soc. Rev.* **43,** 6814–6838 (2014).
24. Takei, Y., Takashima, S., Ohyu, J., Matsuura, K., Katoh, N., Takami, T.,

Miyajima, T. & Hoshika, A. Different effects between 7-nitroindazole and L-NAME on cerebral hemodynamics and hippocampal lesions during kainic acid-induced seizures in newborn rabbits. *Brain Dev.* **23,** 406–413 (2001).

25. Alderton, W. K., Cooper, C. E. & Knowles, R. G. Nitric oxide synthases: structure, function and inhibition. *Biochem. J.* **357,** 593–615 (2001).
26. Bruckdorfer, R. The basics about nitric oxide. *Mol. Aspects Med.* **26,** 3–31 (2005).
27. Hayashi, T., Juliet, P. A., Matsui-Hirai, H., Miyazaki, A., Fukatsu, A., Funami, J., Iguchi, A. & Ignarro, L. J. l-Citrulline and l-arginine supplementation retards the progression of high-cholesterol-diet-induced atherosclerosis in rabbits. *Proc. Natl. Acad. Sci. U. S. A.* **102,** 13681–13686. (2005).
28. Tsao, P. S., McEvoy, L. M., Drexler, H., Butcher, E. C. & Cooke, J. P. Enhanced endothelial adhesiveness in hypercholesterolemia is attenuated by L-arginine. *Circulation* **89,** 2176–2182 (1994).
29. Brown, F. O., Finnerty, N. J. & Lowry, J. P. Nitric oxide monitoring in brain extracellular fluid: characterisation of Nafion®-modified Pt electrodes in vitro and in vivo. *Analyst* **134,** 2012–20 (2009).
30. Leza, J. C., Salas, E., Sawicki, G., Russell, J. C. & Radomski, M. W. The effects of stress on homeostasis in JCR-LA-cp rats: the role of nitric oxide. *J. Pharmacol. Exp. Ther.* **286,** 1397–1403 (1998).
31. Kulagina, N. V., Shankar, L. & Michael, A. C. Monitoring glutamate and ascorbate in the extracellular space of brain tissue with electrochemical microsensors. *Anal. Chem.* **71,** 5093–5100 (1999).
32. Endo, Y., Jinnai, K., Endo, M., Fujita, K. & Kimura, F. Diurnal variation of cerebral blood flow in rat hippocampus. *Stroke* **21,** 1464–1469 (1990).
33. Attwell, D. *et al.* Glial and neuronal control of brain blood flow. *Nature* **468,** 232–243 (2010).
34. Pramila, B., Kalaivani, P., Anita, A. & Saravana Babu, C. L-NAME combats excitotoxicity and recuperates neurological deficits in MCAO/R rats. *Pharmacol. Biochem. Behav.* **135,** 246–253 (2015).
35. Gardiner, S. M., Compton, A. M., Bennett, T., Palmer, R. M. J. & Moncada, S. Regional haemodynamic changes during oral ingestion of N(G)-monomethyl-L-arginine or N(G)-nitro-L-arginine methyl ester in conscious Brattleboro rats. *Br. J. Pharmacol.* **101,** 10–12 (1990).

36. Fischer, W., Allgaier, C. & Illes, P. Inhibition by chloral hydrate and trichloroethanol of AMPA-induced $Ca2^{+}$ influx in rat cultured cortical neurones. *Eur. J. Pharmacol.* **394,** 41–45 (2000).
37. Peoples, R. W. & Weight, F. F. Inhibition of excitatory amino acid-activated currents by trichloroethanol and trifluoroethanol in mouse hippocampal neurones. *Br. J. Pharmacol.* **124,** 1159–1164 (1998).
38. Scheibler, P., Kronfeld, A., Illes, P. & Allgaier, C. Trichloroethanol impairs NMDA receptor function in rat mesencephalic and cortical neurones. *Eur. J. Pharmacol.* **366,** 99–100 (1999).
39. Peoples, R. W. & Weight, F. F. Trichloroethanol potentiation of y-aminobutyric acid-activated chloride current in mouse hippocampal neurones. 555–563 (1994).
40. Viitanen, T., Ruusuvuori, E., Kaila, K. & Voipio, J. The K+-Cl- cotransporter KCC2 promotes GABAergic excitation in the mature rat hippocampus. *Journal of Physiology* **588,** 1527–1540 (2010).
41. Shah, G. N., Ulmasov, B., Waheed, A., Becker, T., Makani, S., Svichar, N., Chesler, M. & Sly, W. S. Carbonic anhydrase IV and XIV knockout mice: Roles of the respective carbonic anhydrases in buffering the extracellular space in brain. *Proc. Natl. Acad. Sci.* **102,** 16771–16776 (2005).
42. Supuran, C. T. Carbonic anhydrase inhibitors. *Bioorganic Med. Chem. Lett.* **20,** 3467–3474 (2010).
43. Wang, C., Wang, R., Xie, H., Sun, Y., Tao, R., Liu, W., Li, W., Lu, H. & Jia, Z. Effect of acetazolamide on cytokines in rats exposed to high altitude. *Cytokine* **83,** 110–117 (2016).
44. Tang, C. M., Dichter, M. & Morad, M. Modulation of the N-methyl-D-aspartate channel by extracellular H^{+}. *Proc. Natl. Acad. Sci.* **87,** 6445–6449 (1990).
45. Cloutier, M., Bolger, F. B., Lowry, J. P. & Wellstead, P. An integrative dynamic model of brain energy metabolism using in vivo neurochemical measurements. *J. Comput. Neurosci.* **27,** 391–414 (2009).
46. Kealy, J., Bennett, R. & Lowry, J. P. Simultaneous recording of hippocampal oxygen and glucose in real time using constant potential amperometry in the freely-moving rat. *J. Neurosci. Methods* **215,** 110–120 (2013).
47. Veal, E. A., Day, A. M. & Morgan, B. A. Hydrogen Peroxide Sensing and Signaling. *Mol. Cell* **26,** 1–14 (2007).

48. Borland, L. M., Shi, G., Yang, H. & Michael, A. C. Voltammetric study of extracellular dopamine near microdialysis probes acutely implanted in the striatum of the anesthetized rat. *J. Neurosci. Methods* **146,** 149–158 (2005).
49. Ighodaro, O. M. & Akinloye, O. A. First line defence antioxidants-superoxide dismutase (SOD), catalase (CAT) and glutathione peroxidase (GPX): Their fundamental role in the entire antioxidant defence grid. *Alexandria J. Med.* 1–7 (2017).
50. Pablos, M. I., Reiter, R. J., Ortiz, G. G., Guerrero, J. M., Agapito, M. T., Chuang, J. I. & Sewerynek, E. Rhythms of glutathione peroxidase and glutathione reductase in brain of chick and their inhibition by light. *Neurochem. Int.* **32,** 69–75 (1998).
51. Sani, M., Sebaï, H., Gadacha, W., Boughattas, N. A., Reinberg, A. & Mossadok, B. A. Catalase activity and rhythmic patterns in mouse brain, kidney and liver. *Comp. Biochem. Physiol. - B Biochem. Mol. Biol.* **145,** 331–337 (2006).
52. Baydas, G., Gursu, M. F., Yilmaz, S. & Canpolat, S. Daily rhythm of glutathione peroxidase activity , lipid peroxidation and glutathione levels in tissues of pinealectomized rats. **323,** 195–198 (2002).

Chapter 6

In Vivo Amperometry Investigations in Humanised Mice

6.1 Introduction

The main objective of Chapter 6 was to assess neurochemical fluctuations during the progression of patient specific PD in humanised mice. This objective was achieved following the successful integration of human functional dopaminergic neurons into the striatum of NOD SCID mice. Hence, this humanised mouse model allowed for analysis of human derived dopaminergic neurons, originating from PD patients, to be conducted in a physiological environment. Examination into the neurochemical events exhibited by the integrated humanised dopaminergic neurons was conducted by applying amperometric technology to three different mice cohorts; Wild Type (WT) mice, PINK1 mice and SHAM mice. NOD SCID mice were transplanted with a healthy dopaminergic neural cell line derived from a healthy control cohort. These animals were denoted as WT mice and allowed for a humanised mouse control to be achieved. PINK1 mice involved the transplantation of patient-derived PINK1 expressing dopaminergic neurons derived from iPSCs[1] (by colleagues in the University of Luxembourg) into the striatum allowing for a humanised mouse model of PD to be achieved. Additionally, SHAM mice were included in NO and O_2 (see Sections 6.3.3 and 6.3.6) investigations to act as a scientific control. SHAM mice are NOD SCID mice that underwent surgeries that mirrored transplantation surgery protocol but transplantation of dopaminergic neurons derived from iPSCs was omitted. Instead, differentiation medium which was used in all cellular preparations in humanised cell transplantations, was stereotaxically injected. It was decided to inject differentiation medium instead of PBS as this was the medium used throughout all the cellular transplantations conducted in NOD SCID mice.

By application of the NO, O_2 sensors and the H_2O_2 biosensor in each of these cohorts, successful amperometric recordings of neurochemical dynamics could be achieved. Real-time amperometric recordings were utilised to assess neurochemical changes in the transplanted striatum in response to physiological stimulation following saline administration and restraint tests. Furthermore, the functionality of each of the sensors was validated in the humanised mouse striatum by administration of characterisation compounds, such as L-NAME and Diamox, that were previously described in Chapter 5. Thereafter, immunohistochemical staining conducted by colleagues in the University of Luxembourg, allowed for the placement of the implanted sensors in relation to the humanised graft to be confirmed. By correlation

of fluctuations in amperometric recordings in the aforementioned cohorts with other neurochemical analytical techniques, such as microdialysis (Chapter 7), the phenotypic progression of this disease can be assessed in order to gain an insight into an overall neurochemical signature of PD.

6.2 Experimental

All instrumentation and software utilised in Chapter 6 is detailed in Section 3.2. Details on the solutions and chemicals are stated in Section 3.3. Section 3.4.2 - 3.4.4 describes the manufacture of all the sensors included in *in vivo* investigations. A working potential of + 900 mV *vs.* SCE, - 650 mV *vs.* SCE and + 700mV *vs.* SCE was applied to NO, O_2 sensors and H_2O_2 biosensors respectively during *in vivo* experimentation. Surgical protocols involving the transplantation of PINK1 and WT cells are detailed in Section 3.8.3. SHAM surgeries were conducted in the same manner as transplantation surgeries. However, instead of implanting humanised cells, differentiation medium was stereotaxically injected. Section 3.8.4 discusses the surgical protocol associated with sensor implantation. Descriptions of *in vivo* investigations undertaken in freely-moving and anaesthetised animals are as described in Section 3.8.7 - 3.10.3. All i.p. injections were formulated in saline unless otherwise stated.

All data reported is as mean ± SEM, where n = number of animals except for 24-hour analysis where n/n = number of days or nights/number of animals. All statistical analysis was conducted using GraphPad Prism 5.0 (GraphPad Software Inc., CA., USA). Figures included in this chapter comparing humanised and non-humanised mice data had baseline currents normalised to 100 % and any current change was taken as a percentage of pre-perturbation baselines. Estimated concentration changes from pre-perturbation baselines are reported within this chapter and were determined from the *in vitro* sensitivity values obtained for the relevant sensors. Time bin analysis was conducted by taking the average concentration change of the relevant analyte over 10-minute intervals from raw data with differences in each time bin being compared to the obtained baseline level. For 24-hour recordings, the average concentration change was taken over 1-hour intervals. Significant differences were calculated using paired and unpaired student's *t*-tests resulting in *p*-values being

obtained. *p*-values indicated the probability of the results being significantly different with $p < 0.05$ considered significant.

6.3 Results and Discussion

6.3.1 Amperometric NO Investigations in the Humanised Mouse Transplanted with PINK1 Cells

6.3.1.1. Saline Administration

Previously, Section 5.3.1.1.1 discussed the response of systemic i.p. administration of saline on the amperometric NO response recorded in the striatum of NOD SCID mice. The effect of saline administration on the NO response in humanised PINK1 mice is illustrated in Figure 6.3.1.1.1A. The (ΔI) was achieved (11 ± 4 pA, $n = 8$) after 4 ± 2 mins ($n = 8$) from pre-injection baseline levels of 352 ± 27 pA ($n = 8$). This increase in current equated to a concentration change of 9 ± 3 nM ($n = 8$) and a 3 ± 1 % ($n = 8$) current change which was found to be significantly different ($p = 0.01$) from pre-injection baseline levels. A return to new baseline levels (346 ± 25 pA, $n = 8$) was achieved after 37 ± 7 mins ($n = 8$, Table 6.3.1.1.1). The new baseline level was found to not be significantly different ($p = 0.09$) from pre-injection baseline currents. The amperometric response of NO in the striatum of humanised PINK1 mice was comparable to that previously obtained in non-humanised mice. Figure 6.3.1.1.1B & C clearly illustrates the comparable NO response exhibited following systemic administration of saline in the striatum of both cohorts.

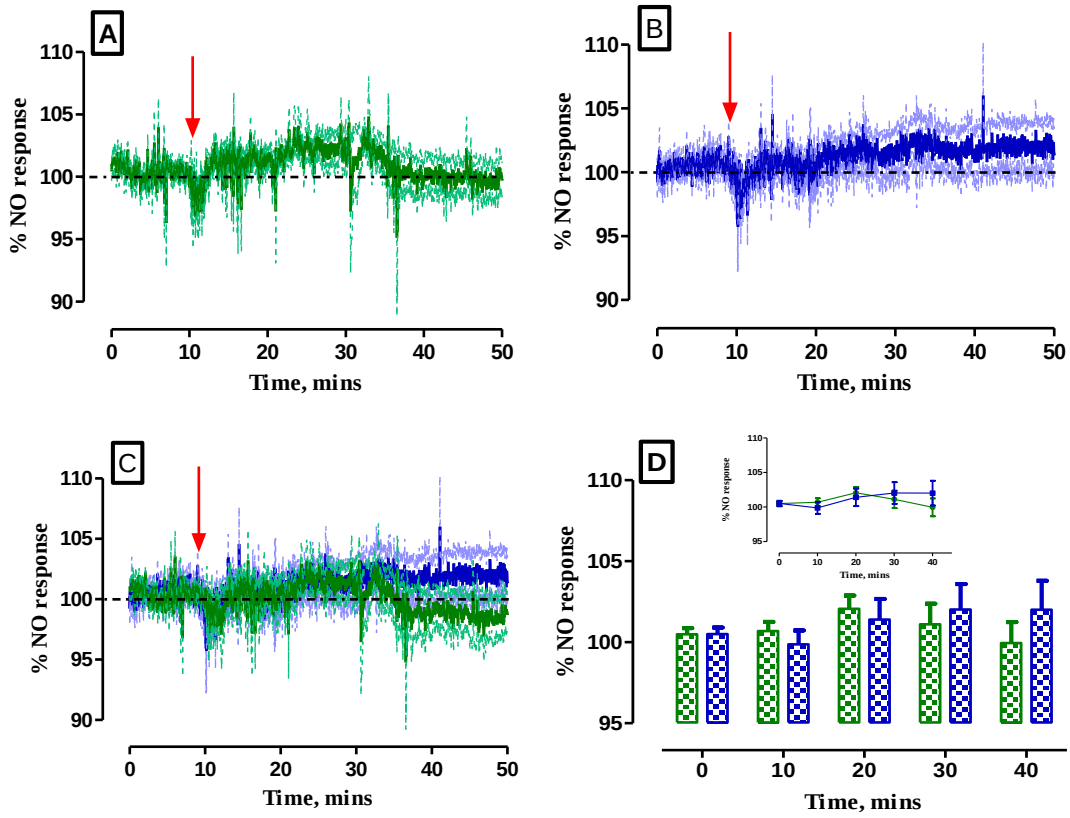

Figure 6.3.1.1.1: Averaged percentage raw data current response of the NO sensors implanted in the striatum of: (A) PINK1 humanised mice (*n* = 8, green trace), (B) NOD SCID mice (*n* = 8, blue trace), (C) overlay of humanised (green trace) vs. NOD SCID (blue trace) percentage current response following 1 mL/kg saline i.p. injection. Point of injection is represented by the red arrow. The green trace indicates the mean percentage PINK1 current response with the percentage error represented by the light green trace. The blue trace indicates the mean percentage NOD SCID current response with the percentage error represented by the light blue trace. (D) Bar graph comparing 10-minute time bins of percentage current responses. *Inset*: Time bin analysis of 50-minute raw percentage data current responses. Data represented as mean percentage current ± SEM.

Table 6.3.1.1.1: Summary of results of the NO sensors implanted in the striatum of humanised PINK1 mice following i.p. administration of 0.9 % saline (*n* = 8).

Saline						
Pre-Perturbation Baseline (pA)	**Max Current (pA)**	**Current Change (pA)**	**Current Change (%)**	**Max Response Time (mins)**	**Post-Perturbation Baseline (pA)**	**Return to Baseline Time (mins)**
352 ± 27	364 ± 28	11 ± 4	3 ± 1	4 ± 2	346 ± 25	37 ± 7

Additionally, time bin analysis was conducted to further support that a comparable response was obtained in PINK1 and NOD SCID mice (Figure 6.3.1.1.1D). Time bin analysis consisted of averaging 10-minute time periods from both humanised PINK1 mice and non-humanised NOD SCID mice over 40-minutes as the response from NOD SCID mice had returned to basal levels within this period. Comparatively, no significant difference was exhibited between the response recorded in humanised and non-humanised responses (Table 6.3.1.1.2).

Table 6.3.1.1.2: Statistical analysis of NO recordings obtained from the striatum of humanised PINK1 mice (*n* = 8) and non-humanised NOD SCID mice (*n* = 8) following 1 mL/kg saline i.p. administration.

Saline					
	PINK1 (*n* = 8)		**NOD SCID (*n* = 8)**		
Time, mins	**Mean, %**	**SEM**	**Mean, %**	**SEM**	***p***
0	100.5	0.4	100.5	0.4	0.98
10	100.7	0.6	99.9	0.9	0.44
20	102.1	0.8	101.4	1.3	0.66
30	101.1	1.3	102.0	1.6	0.66
40	99.9	1.3	102.0	1.8	0.37

As discussed in Section 5.3.1.1, the administration of systemic i.p. injections are known to provoke a stress response in the subject leading to an increase in neuronal activation and CBF. Such a response is brought about by the neurotransmitter-mediated signalling elicited by glutamate. Glutamate exhibits a major role in the

regulation of CBF due to its involvement in NO release from neurons and astrocytes. Therefore, resulting in an increase in CBF due to the vasodilatory properties associated with NO^2. Thus, transient increases in NO result (Figure 6.3.1.1.1A - C), occurring at similar timeframes in each cohort before returning to basal levels. Furthermore, no significant difference in the NO response was recorded following systemic administration of saline in PINK1 or NOD SCID mice. These results indicate that comparable responses are demonstrated in each animal group in response to an i.p. injection of saline. Further to this, IHC images contained in Section 6.3.1.6 indicate that the NO sensor was contained within, or was in close proximity, to the transplanted xenograft throughout these studies. Therefore, the NO sensor had the ability to measure from the humanised cells directly or was under the direct influence of the nearby graft due to anatomical integration of the graft in the host striatal tissue.

6.3.1.2 Restraint Test

Throughout this project, it was believed that the optimal method to measure alterations from the humanised graft was to initiate neuronal activation to try to elicit a response from the transplanted cells that could be differentiated from the host striatum. Humanised grafts were known to anatomically integrate into the host striatum[3]. Confirmation of anatomical integration was achieved by IHC staining of the transplanted striatum (Section 6.3.1.6) followed by further immunohistochemical analysis conducted by colleagues in the University of Luxembourg. Therefore, restraint tests were performed on humanised PINK1 mice to elicit neuronal activation in the transplanted graft by subjecting the animal to a mild stressor[4]. Restraint tests were conducted as detailed in Section 3.10.3. Briefly, restraint tests involved restricting the movement of the animal allowing any attempt by the animal to free itself to be associated with neuronal activation[5]. Hence, such changes in neuronal activation can be recorded by the implanted sensor.

Figure 6.3.1.2.1A illustrates the effect of a 2-minute restraint on the NO response recorded in humanised PINK1 mice. It must be stated that the restraint test caused a dual NO response to occur in the striatum of the animal. Firstly, a (ΔI) of - 14 ± 4 pA (n = 8) was recorded from baseline levels (307 ± 23 pA, n = 8). This decrease in the recorded current occurred after 5 ± 1 mins (n = 8) and corresponded to a - 4 ± 1 % (n = 8, Table 6.3.1.2.1) current change. In addition, this decrease in current

corresponded to a decrease in the concentration of NO of 10 ± 3 nM (n = 8). A significant difference (p < 0.01) was reported between the maximum decrease in current and pre-perturbation baseline levels.

Following this dip in the recorded current, an overshoot of current was experienced which has previously been seen by other groups following initiation of a restraint test[5]. An increase in current resulted in a (ΔI) of 15 ± 4 pA (n = 8) being obtained after 15 ± 4 mins (n = 8). Moreover, a significant difference (p < 0.01) was noted between the maximum current response and pre-perturbation baseline currents (307 ± 23 pA, n = 8). This increase in amperometric current resulted in a percentage current change of 5 ± 1 % (n = 8) and a concentration change of 11 ± 3 nM (n = 8). A return to baseline currents (300 ± 22 pA, n = 8) occurred after 64 ± 6 mins (n = 8). Moreover, the post-perturbation baseline current was found to not be significantly different (p = 0.65) from pre-perturbation baseline currents.

Table 6.3.1.2.1: Summary of results of the NO sensors implanted in the striatum of PINK1 humanised mice following administration of 2-minute restraint test (n = 8).

Restraint							
Response No.	**Pre-Perturbation Baseline (pA)**	**Max Current (pA)**	**Current Change (pA)**	**Current Change (%)**	**Max Response Time (mins)**	**Post-Perturbation Baseline (pA)**	**Return to Baseline Time (mins)**
1	307 ± 23	296 ± 21	-14 ± 4	-4 ± 1	5 ± 1	-	
2	-	326 ± 26	15 ± 4	5 ± 1	19 ± 3	300 ± 22	64 ± 6

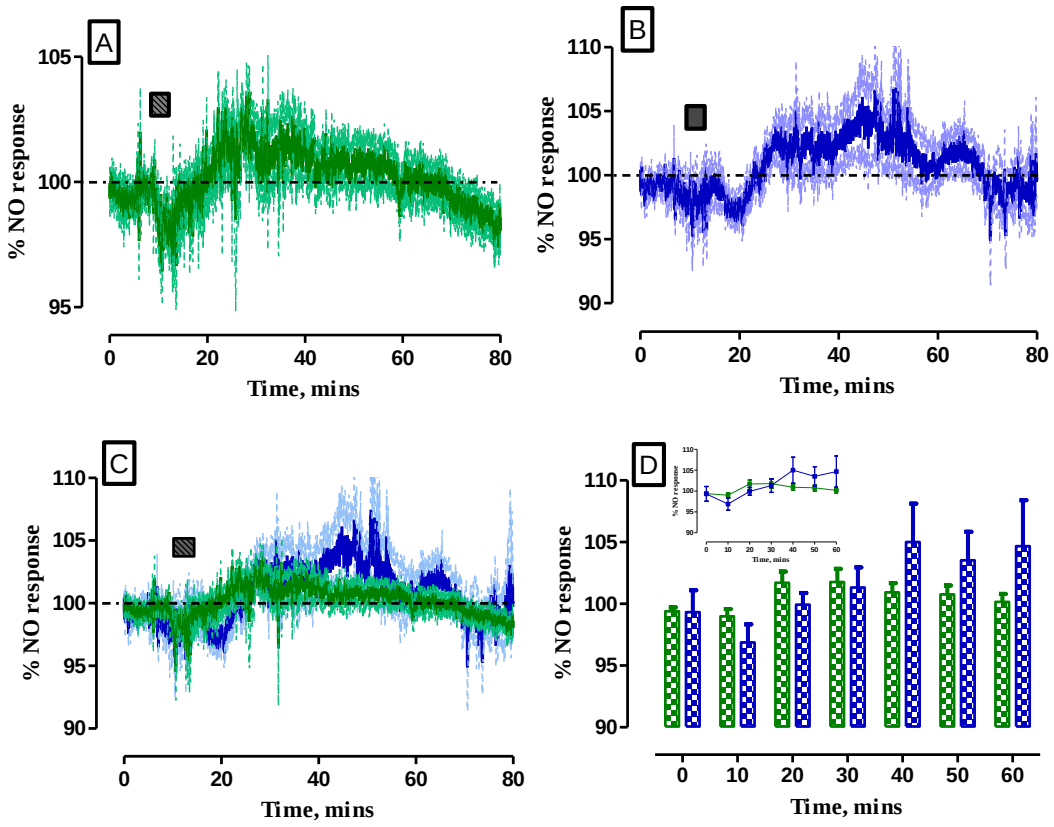

Figure 6.3.1.2.1: Averaged percentage raw data current response of the NO sensors implanted in the striatum of: (A) PINK1 humanised mice (*n* = 8, green trace), (B) NOD SCID mice (*n* = 4, blue trace), (C) overlay of humanised (green trace) vs. NOD SCID (blue trace) percentage current response following 2-minute restraint test. Duration of restraint is represented by the dark grey box. The green trace indicates the mean percentage PINK1 current response with the percentage error represented by the light green trace. The blue trace indicates the mean percentage NOD SCID current response with the percentage error represented by the light blue trace. (D) Bar graph comparing 10-min time bins of percentage current responses. *Inset*: Time bin analysis of 70-minute raw percentage data current responses. Data represented as mean percentage current ± SEM.

In addition, the amperometric response of NO recorded in PINK1 cell lines was similar to the NO response obtained from non-humanised NOD SCID mice (Figure 6.3.1.2.1 B & C). Due to this comparable response being recorded in both cohorts, time bin analysis was conducted to further analyse the NO response following a 2-minute restraint. Following this, no significant difference was determined between the responses recorded in the two animal groups (Table 6.3.1.2.2).

Table 6.3.1.2.2: Statistical analysis of NO recordings obtained from the striatum of humanised PINK1 mice (*n* = 8) and non-humanised NOD SCID mice (*n* = 4) following a 2-minute restraint.

Restraint					
	PINK1 (*n* = 8)		NOD SCID (*n* = 4)		
Time, mins	**Mean, %**	**SEM**	**Mean, %**	**SEM**	***p***
0	99.4	0.3	99.3	1.8	0.96
10	99.0	0.6	96.9	1.5	0.14
20	101.7	0.1	99.9	1.0	0.21
30	101.8	1.1	101.3	1.6	0.81
40	100.9	0.7	105.0	3.1	0.13
50	100.8	0.8	103.5	2.3	0.18
60	100.2	0.7	104.7	3.7	0.14

Restraint tests are known to induce a stress response in NOD SCID mice, as discussed in Section 5.3.1.5. This stress response initiates neuronal activation, and thus, alterations in the measured NO response. Following the performance of restraint tests on both animal groups, a comparable dual response in NO was observed with no significant difference being exhibited between the two cohorts. Additionally, NO levels were seen to return to baseline levels over a similar timeframe (Figure 6.3.1.2.1A - C). However, it is interesting to note that a larger decrease in the NO response was seen at t = 10 mins which appears to be absent in the PINK1 cohort. It is at this time that the restraint test was performed. Furthermore, a larger and more sustained overshoot in the NO current was observed in the NOD SCID group. Collectively, these findings suggest a reduced NO response in humanised PINK1 mice when compared to NO recordings obtained from non-humanised mice. Therefore, although no significant differences exist between the NO responses, it is interesting to note the difference in the NO trend between the two groups following neuronal activation. It would be of interest to increase *n* numbers in the NOD SCID cohort to examine if the observed differences in the NO trend would be significant between the two groups.

6.3.1.3 Validation of the NO Signal Using L-NAME

Figure 6.3.1.3.1A illustrates the NO sensor response to changes in NO following administration of an i.p. injection of L-NAME to the subject. Following L-NAME administration, the characteristic decrease in NO levels is detected by the NO sensor implanted in the striatum of humanised PINK1 mice. A current decrease of -20 ± 4 pA (n = 8) was recorded from baseline current levels (282 ± 27 pA, n = 8) after 76 ± 8 mins (n = 8). This significant decrease ($p < 0.001$) in current corresponded to an 8 ± 2 % (n = 8, Table 6.3.1.3.1) decrease in the amperometric signal and a concentration change of 15 ± 3 nA (n = 8). Additionally, a new baseline current of 271 ± 27 pA (n = 8) was achieved after 138 ± 11 mins (n = 8). This new baseline was significantly different ($p < 0.001$) from the pre-administration baseline. Moreover, this response is comparable to that recorded in the NOD SCID mice (Section 5.3.1.2) which is displayed in Figures 6.3.1.3.1B and 6.3.1.3.1C. Hence, it is evident that following administration of L-NAME, the production of NO is inhibited leading to a reduction in NO detection at the sensor surface. Thus, the NO sensor clearly displays the ability to respond to changes in NO levels in the striatum of xenotransplanted PINK1 mice and so, confirming that the sensor is performing as expected.

It is important to state that no time bin analysis was carried out on the amperometric response obtained following L-NAME administrations. The reason being that the administration of L-NAME was only to confirm functionality of the sensor in the humanised striatum. It was suggested that following anatomical integration of the graft into the host striatum, physiological stimulation would induce an effect on the transplanted graft. As a result, leading to alterations in NO that could be measured from inside the graft and in close proximity to the graft. Furthermore, chemical compounds would confirm the performance of the sensor ensuring it was not compromised by the transplanted graft.

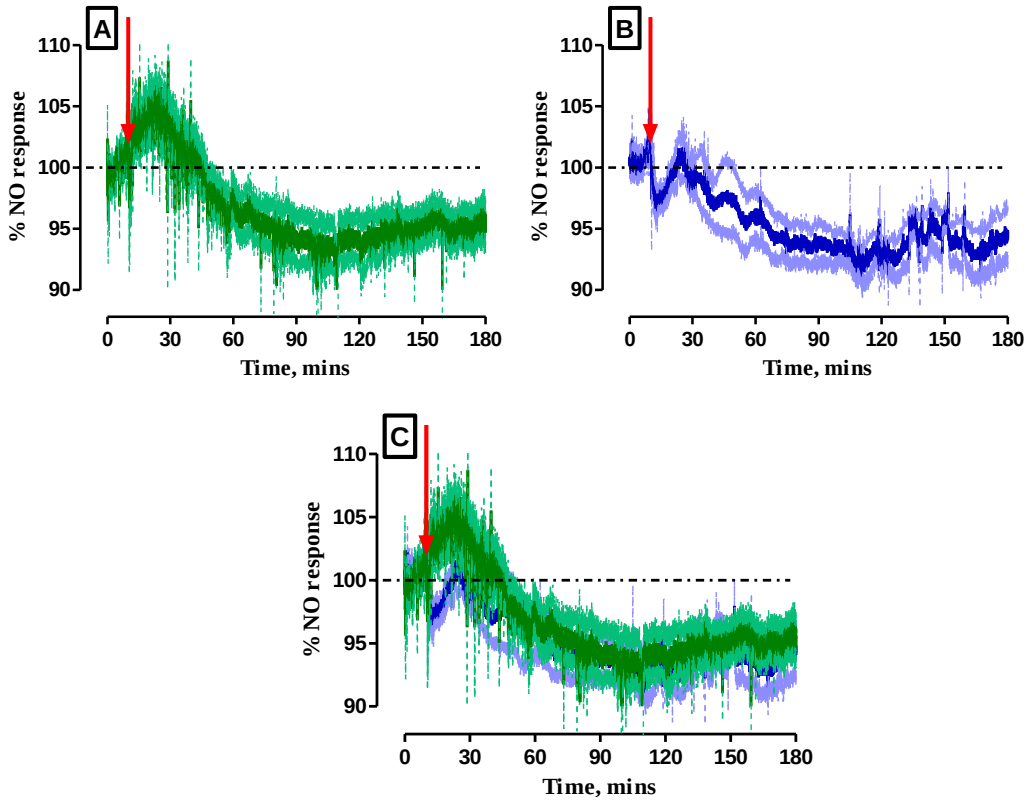

Figure 6.3.1.3.1: Averaged percentage raw data current response of the NO sensors implanted in the striatum of: (A) PINK1 humanised mice (*n* = 8, green trace), (B) NOD SCID mice (*n* = 5, blue trace), (C) overlay of humanised (green trace) vs. NOD SCID (blue trace) percentage current response following 30 mg/kg L-NAME i.p. injection. Point of injection is represented by the red arrow. The green trace indicates the mean percentage PINK1 current response with the percentage error represented by the light green trace. The blue trace indicates the mean percentage NOD SCID current response with the percentage error represented by the light blue trace. Data represented as mean percentage current ± SEM.

Table 6.3.1.3.1: Summary of results of the NO sensors implanted in the striatum of PINK1 humanised mice following i.p. administration of 30 mg/kg L-NAME (*n* = 8).

L-NAME Injection						
Pre-Perturbation Baseline (pA)	**Max Current (pA)**	**Current Change (pA)**	**Current Change (%)**	**Max Response Time (mins)**	**Post-Perturbation Baseline (pA)**	**Return to Baseline Time (mins)**
282 ± 27	262 ± 27	-20 ± 4	-8 ± 2	76 ± 8	271 ± 27	138 ± 11

6.3.1.4 Validation of the Selective Properties of the NO Sensor

Figure 6.3.1.4.1A displays the amperometric response of the NO sensor to 500 mg/kg sodium ascorbate whereby an evident decrease (- 37 ± 12 pA, n = 8) in the recorded current was experienced. Importantly, no detection of sodium ascorbate was seen, indicating that there is no compromise in the selectivity of the sensor following implantation *in vivo*. This observed decrease was significantly different (p = 0.02) from baseline current (292 ± 32 pA, n = 8) and corresponded to a concentration change of 28 ± 9 nM (n = 8). A maximum current of 255 ± 29 pA (n = 8) recorded equated to a - 12 ± 3 % (n = 8) decrease in current which occurred after 11 ± 3 mins (n = 8). After 62 ± 14 mins (n = 8), a new baseline current of 287 ± 31 pA (n = 8, Table 6.3.1.4.1) was observed which was not significantly different (p = 0.34) from pre-injection baseline levels.

Previous studies conducted in the striatum of NOD SCID mice involving sodium ascorbate indicated a decrease in the amperometric signal following administration (Section 5.4.1.4, Figure 6.3.1.4.1B). Similarly, a comparable decrease in NO was observed in humanised PINK1 mice following systemic administration of sodium ascorbate (Figure 6.3.1.4.1A - C). Additionally, the decrease in NO occurs at a similar timeframe in both cohorts. It is also interesting to note that the post-perturbation baseline never returns to pre-perturbation levels over a 100-minute period. Such decreases were never seen in studies involving freely-moving rats previously[6,7]. Therefore, indicating that this decrease is an immunocompromised mouse effect and it can be attributed to administering sodium ascorbate in a different rodent species.

Table 6.3.1.4.1: Summary of results of the NO sensors implanted in the striatum of PINK1 humanised mice following i.p. administration of 500 mg/kg sodium ascorbate (n = 8).

Sodium Ascorbate						
Pre-Perturbation Baseline (pA)	**Max Current (pA)**	**Current Change (pA)**	**Current Change (%)**	**Max Response Time (mins)**	**Post-Perturbation Baseline (pA)**	**Return to Baseline Time (mins)**
292 ± 32	255 ± 29	-37 ± 12	-12 ± 3	11 ± 3	287 ± 31	62 ± 14

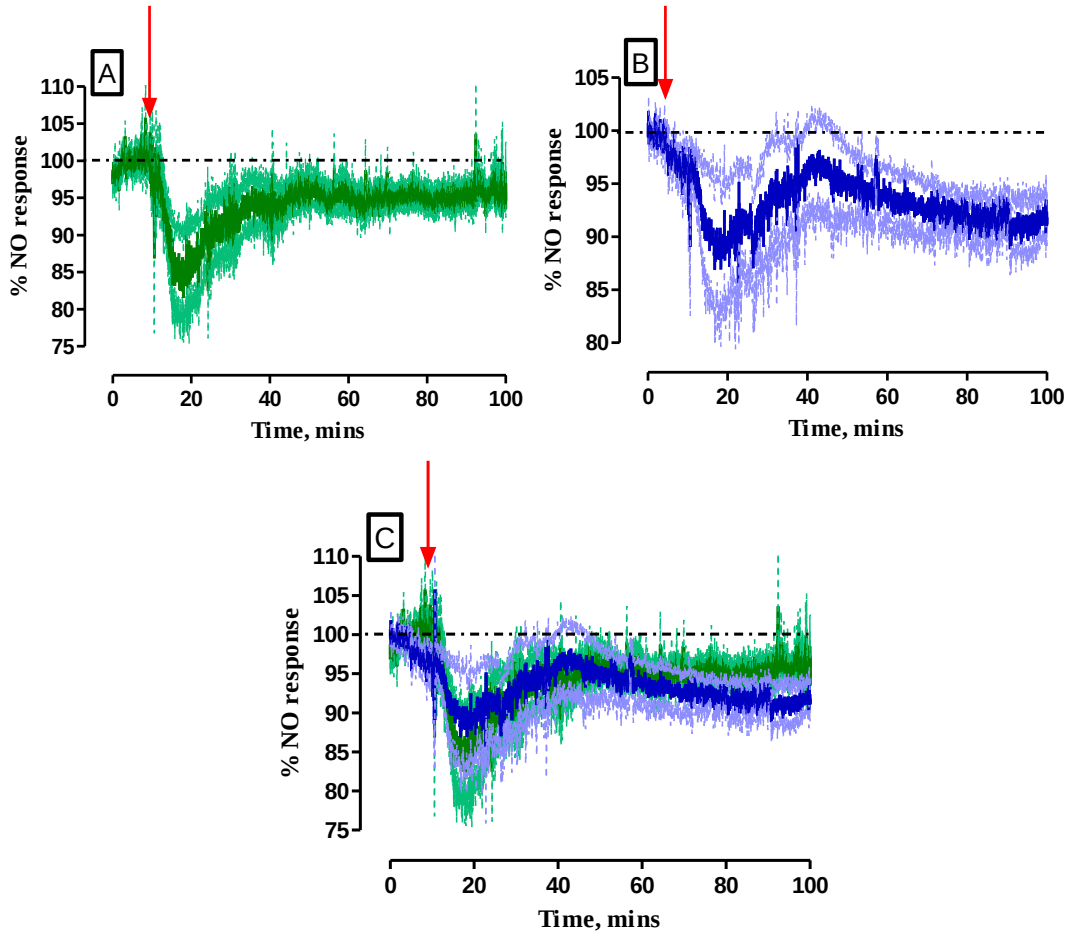

Figure 6.3.1.4.1: Averaged percentage raw data current response of the NO sensors implanted in the striatum of: (A) PINK1 humanised mice (*n* = 8, green trace), (B) NOD SCID mice (*n* = 4, blue trace), (C) overlay of humanised (green trace) vs. NOD SCID (blue trace) percentage current response following 500 mg/kg sodium ascorbate i.p. injection. Point of injection is represented by the red arrow. The green trace indicates the mean percentage PINK1 current response with the percentage error represented by the light green trace. The blue trace indicates the mean percentage NOD SCID current response with the percentage error represented by the light blue trace. Data represented as mean percentage current ± SEM.

6.3.1.5 24-hour Amperometric Recordings of NO

Previously, Section 5.3.1.7 discussed fluctuations associated with NO levels over a 24-hour period obtained from amperometric recordings conducted in the striatum of NOD SCID mice. Briefly, it was reported that NO levels remained at basal levels during the light cycle in NOD SCID mice (*n* = 14/5) due to a decrease in activity being exhibited by the animal (Figure 6.3.1.5.1 B). However, following initiation of

the dark cycle (*n* = 20/5), NO levels increased substantially which corresponded to an increase in the activity of the animal.

Similarly, 24-hour recordings were performed in the striatum of PINK1 transplanted mice. Figure 6.3.1.5.1A highlights a contrast in the NO current measured in humanised PINK1 mice during the night cycle when compared to levels measured in NOD SCID mice. As previously stated, an increase in NO levels was observed in NOD SCID mice which coincided with increased motor activity and neuronal activation. However, this increase in NO levels during the night cycle is absent in humanised PINK1 mice. Over the 12-hour night cycle, NO levels remain at basal levels and little deviation is seen in the recorded amperometric current from humanised PINK1 mice. Additionally, light cycle recordings taken from both cohorts express similar NO amperometric responses throughout this 12-hour period. Thus, it can be hypothesised that there is a clear difference in NO levels in humanised PINK1 mice and non-humanised NOD SCID mice during the night cycle that suggest reduced NO activity following neuronal activation.

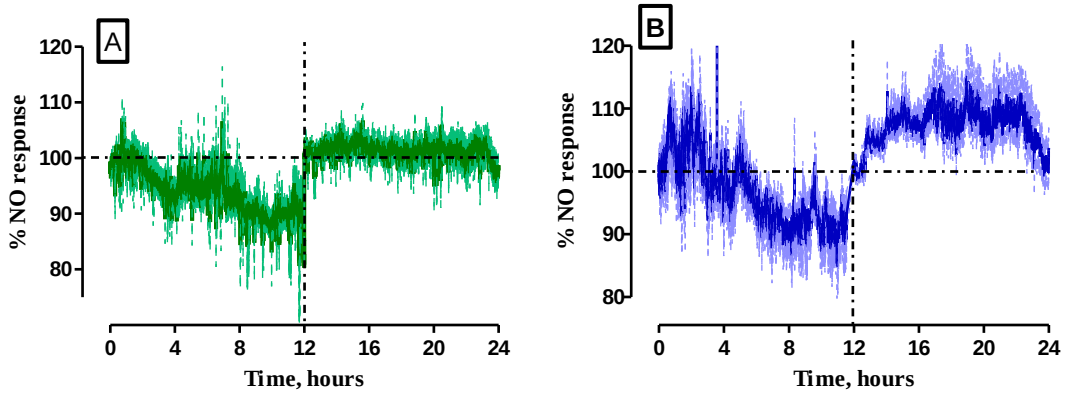

Figure 6.3.1.5.1: Averaged 24-hour percentage current response measured by NO sensors implanted in the striatum of (A) humanised PINK1 mice (green trace) during the light phase (*n* = 19/8, 0 - 12 hours) and the dark phase (*n* = 31/8, 13 - 24 hours) and of (B) NOD SCID mice (blue trace) during the light phase (*n* = 14/5, 0 - 12 hours) and the dark phase (*n* = 20/5, 13 - 24 hours). The green trace indicates the mean percentage mean PINK1 NO current response with the percentage error represented by the light green trace. The blue trace indicates the mean percentage mean NOD SCID NO current response with the percentage error represented by the light blue trace. Data represented as mean percentage current ± SEM.

6.3.1.6 IHC Staining of the Transplanted Striatum

IHC analysis was carried out on humanised PINK1 mouse brains that had been implanted with NO sensors allowing for the placement of the sensor to be confirmed. Each IHC image allowed for observation of the sensor placement in relation to the transplanted xenograft of PINK1 cells in the striatum. Following completion of *in vivo* experiments, transcardial perfusions (Section 3.11.1) were carried out on the relevant animals. Transcardial perfusion allowed for fixation of the brain to occur before manual removal of the sensors was conducted. As the sensors were contained in a headpiece on the animal, light force sometimes had to be applied to allow for removal. Thus, some sensor channels appear bigger in some IHC images. From IHC images, it appears that neurite extension occurs in three dimensions from the site of transplantation. Hence, anatomical integration of the PINK1 cells is evident in the host striatal tissue.

Figure 6.3.1.6.1 illustrates typical examples of the PINK1 graft stained in green with the sensor channel beside the channel. The size of the surviving graft measures approximately 200 µm in diameter with integration by neurite outgrowth clearly seen. A small discrepancy in sensor placement in an anterior-posterior direction is visible. However, this discrepancy is minimal and due to neurite outgrowth, it can be concluded that the sensor is measuring from an area under the influence of the humanised graft.

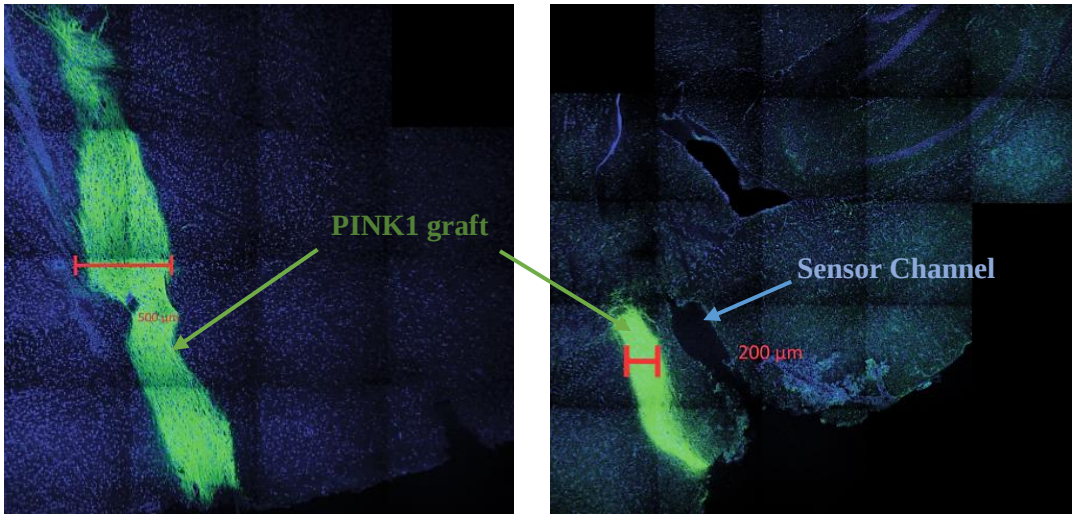

Figure 6.3.1.6.1: Typical examples of IHC images conducted highlighting the sensor placement in the striatum of humanised PINK1 mice.

Further examples of the PINK1 graft integrated into the host striatum are displayed in Figure 6.3.1.6.2. These grafts measured a diameter of 1000 µm and 500 µm indicating good survival and integration into the host striatal tissue. The sensor channel, which is indicated by the blue arrows, runs right down the centre of the graft indicating that the sensor was accurately implanted into the humanised graft.

It is clear that a discrepancy between graft sizes exists from the images contained in Section 6.3.1.6.1. A number of factors affect the size of the integrated graft *in vivo*. Some of these factors include the survival of the cells during transportation to Ireland. It was noted that some t-flasks contained higher levels of surviving cells compared to others. During transportation, these cells are away from their optimal storage conditions. Although, transport is usually fast and the cells are transported on heated pads, there is some level of cell death before they arrive in Ireland from Luxembourg. Additionally, during cell preparation, the level of cell detachment from the t-flask can vary resulting in an impact on the amount of cells that can be transplanted. Another factor affecting the size of the graft is their success at integrating once implanted *in vivo*. The cells need space to integrate in the striatum and this is dependent on the amount of space made available during transplantation which affects the size of the humanised graft.

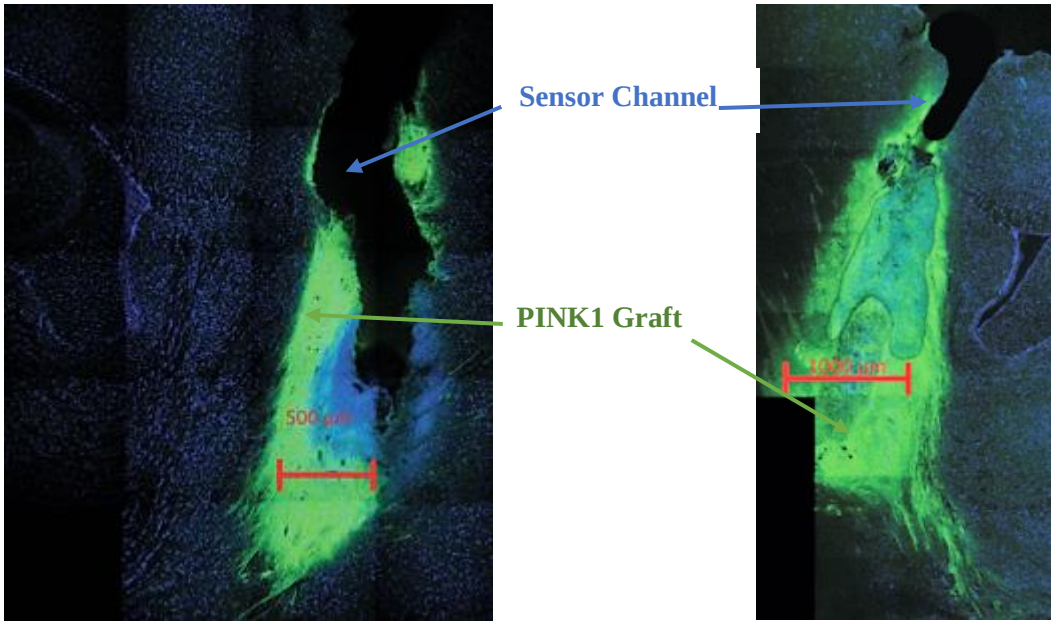

Figure 6.3.1.6.2: Typical examples of IHC images conducted highlighting the sensor placement in the striatum of humanised PINK1 mice. Blue arrows indicate the sensor channel.

The above images illustrate sensor channels both inside and outside of the humanised graft. Therefore, it is important to state that no difference was observed in the obtained amperometric measurements obtained from sensor placed both close to and in the graft. The reason being that the graft is well integrated into the host striatum with neurite outgrowth occurring in a three-dimensional direction. Therefore, even if the sensor was implanted in close proximity to the sensor, measurements obtained would still be under the direct influence of the transplanted humanised graft.

6.3.2 NO Measurements in Humanised Mice Transplanted with WT Cells

6.3.2.1 Saline Administration

Similar to Section 6.3.1.1.1, control saline administrations were carried out in humanised mice transplanted with WT control cells. Following administration of a 1 mL/kg i.p. injection of saline, a (ΔI) of 10 ± 3 pA (n = 10) was observed from recorded baseline currents (293 ± 44 pA, n = 10). A significant increase (p = 0.01) was noted between the (ΔI) from baseline levels. This increase corresponded to a 4 ± 1 % (n = 10) change and a concentration change of 7 ± 3 nM (n = 10) occurring after 11 ± 4 mins (n = 10) post administration. After 53 ± 10 mins (n = 10), a return to baseline was observed (292 ± 42 nA, n = 10, Table 6.3.2.1.1) whereby no significant difference (p = 0.78) was noted when compared to pre-injection baseline levels.

Saline administrations previously carried out in NOD SCID mice indicate a decrease in NO following saline administration (Section 5.3.1.1), however, these results are not directly comparable which is observed in Figure 6.3.2.1.1C. The decrease in amperometric signal following saline administration in non-humanised NOD SCID mice is seen to be transient and baseline levels return within 3 ± 1 mins (n = 8). However, a contrasting temporal response is apparent in the NO response recorded in humanised WT mice. The amperometric current is observed to remain elevated for a longer timeframe than that noted in non-humanised subjects. A return to baseline levels is exhibited after 53 ± 10 mins (n = 10) which highlights that a much greater timeframe is required by humanised WT animals to return to basal NO levels than demonstrated in NOD SCID animals.

Table 6.3.2.1.1: Summary of results of the NO sensors implanted in the striatum of WT humanised mice following i.p. administration of 0.9 % saline (*n* = 10).

Saline Injection						
Pre-Perturbation Baseline (pA)	**Max Current (pA)**	**Current Change (pA)**	**Current Change (%)**	**Max Response Time (mins)**	**Post-Perturbation Baseline (pA)**	**Return to Baseline Time (mins)**
293 ± 44	305 ± 44	10 ± 3	4 ± 1	11 ± 4	292 ± 42	53 ± 10

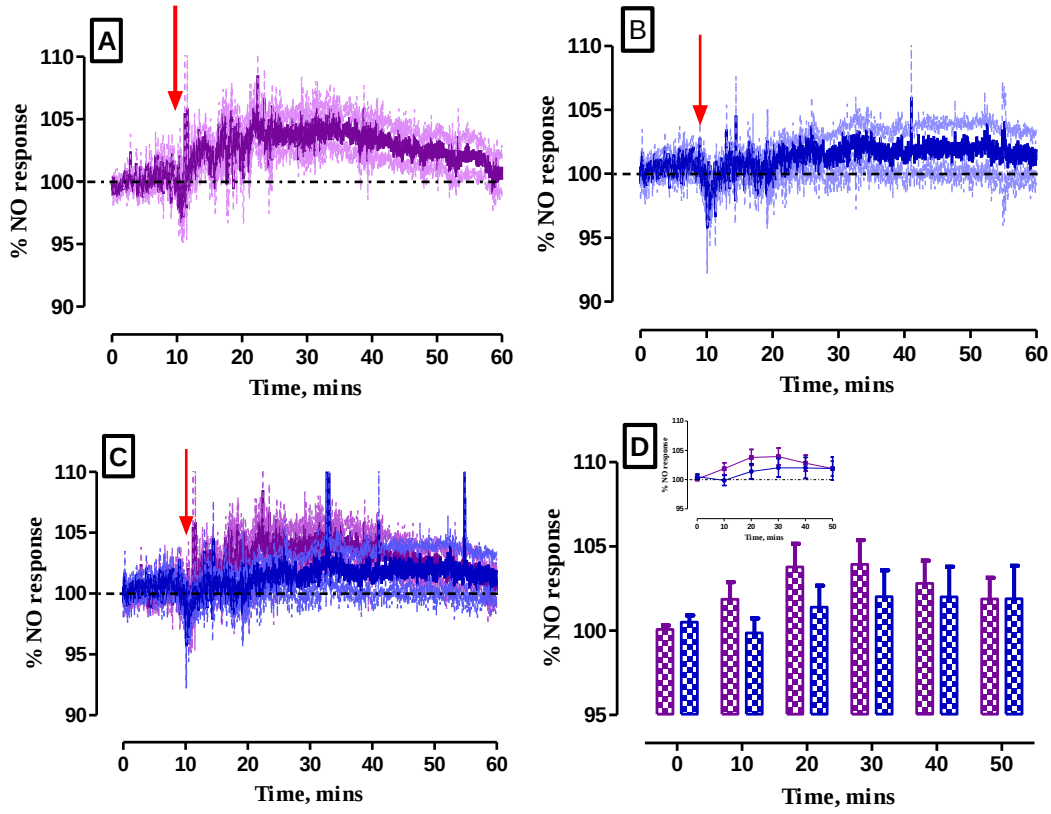

Figure 6.3.2.1.1: Averaged percentage raw data current response of the NO sensors implanted in the striatum of: (A) WT humanised mice (*n* = 10, purple trace), (B) NOD SCID mice (*n* = 8, blue trace), (C) overlay of WT (purple trace) vs. NOD SCID (blue trace) percentage current response following 1 mL/kg saline i.p. injection. Point of injection is represented by the red arrow. The purple trace indicates the mean percentage WT current response with the percentage error represented by the light purple trace. The blue trace indicates the mean percentage NOD SCID current response with the percentage error represented by the light blue trace. (D) Bar graph comparing 10-min time bins of percentage current responses. *Inset*: Time bin analysis of 60-minute raw percentage data current responses. Data represented as mean percentage current ± SEM.

Figure 6.3.2.1.1D illustrates the time bin analysis conducted to further investigate any discrepancies in the NO response between WT and NOD SCID mice. It was found that no significant difference existed between the NO response recorded in each cohort (Table 6.3.2.1.2).

Table 6.3.2.1.2: Statistical analysis of NO recordings obtained in the striatum of humanised WT mice (*n* = 10) and non-humanised NOD SCID mice (*n* = 8) following 1 mL/kg saline administration.

Saline					
	WT (*n* = 10)		NOD SCID (*n* = 8)		
Time, mins	Mean, %	SEM	Mean, %	SEM	*p*
0	100.1	0.2	100.5	0.4	0.35
10	101.9	1.0	99.9	0.9	0.17
20	103.8	1.4	101.4	1.3	0.23
30	104.0	1.5	102.0	1.6	0.39
40	102.8	1.4	102.0	1.8	0.72
50	101.9	1.3	101.9	1.9	0.99

However, it is clear that the recorded signal fails to return to baseline levels at similar times in both cohorts. In particular, Table 6.3.1.2.1 highlights a higher magnitude increase at t = 20 mins and t = 30 mins in WT mice. Therefore, it can be assumed that NO concentrations remain elevated over a longer time period than was previously seen in NOD SCID mice.

6.3.2.2 Restraint Test

Similar to Section 6.3.1.2, restraint tests were conducted on humanised WT mice to investigate any possible differences that may exist when comparing the NO response recorded in WT mice and NOD SCID mice. Figure 6.3.2.2.1C demonstrates the NO response recorded in both cohorts. A dual NO response was observed in WT mice which is comparable to the dual NO response recorded in PINK1 transplanted animals. Firstly, a (ΔI) of - 6 ± 2 pA (*n* = 7) was reported after 1 ± 0.4 mins (*n* = 7) which corresponded to an - 1 ± 3 % (*n* = 7) change from baseline currents (281 ± 28 pA, *n* = 7). This change in the amperometric current was associated with a concentration change of 5 ± 1 nM (*n* = 7). This maximum change in current was not

significantly different ($p = 0.79$) from baseline currents. Thereafter, an increase in NO current was exhibited with a (ΔI) of 14 ± 5 pA ($n = 7$) being attained after 23 ± 4 mins ($n = 7$). This increase corresponded to a 5 ± 2 % ($n = 7$) change in the amperometric current and a concentration change of 11 ± 4 nM ($n = 7$). Additionally, a significant difference ($p < 0.05$) existed between this increase in current and the pre-perturbation baseline. It took 67 ± 3 mins ($n = 7$) to reach a new baseline current of 276 ± 28 pA ($n = 7$, Table 6.3.2.2.1). Pre-perturbation and post-perturbation baseline currents were found to not be significantly different ($p < 0.05$) from each other.

Table 6.3.2.2.1: Summary of results of the NO sensors implanted in the striatum of humanised WT mice following administration of 2-minute restraint test ($n = 7$).

Restraint							
Response No.	**Pre-Perturbation Baseline (pA)**	**Max Current (pA)**	**Current Change (pA)**	**Current Change (%)**	**Max Response Time (mins)**	**Post-Perturbation Baseline (pA)**	**Return to Baseline Time (mins)**
1	281 ± 28	276 ± 30	-6 ± 2	-1 ± 3	1 ± 0.4	-	
2	-	272 ± 50	14 ± 4	5 ± 2	23 ± 4	276 ± 28	67 ± 3

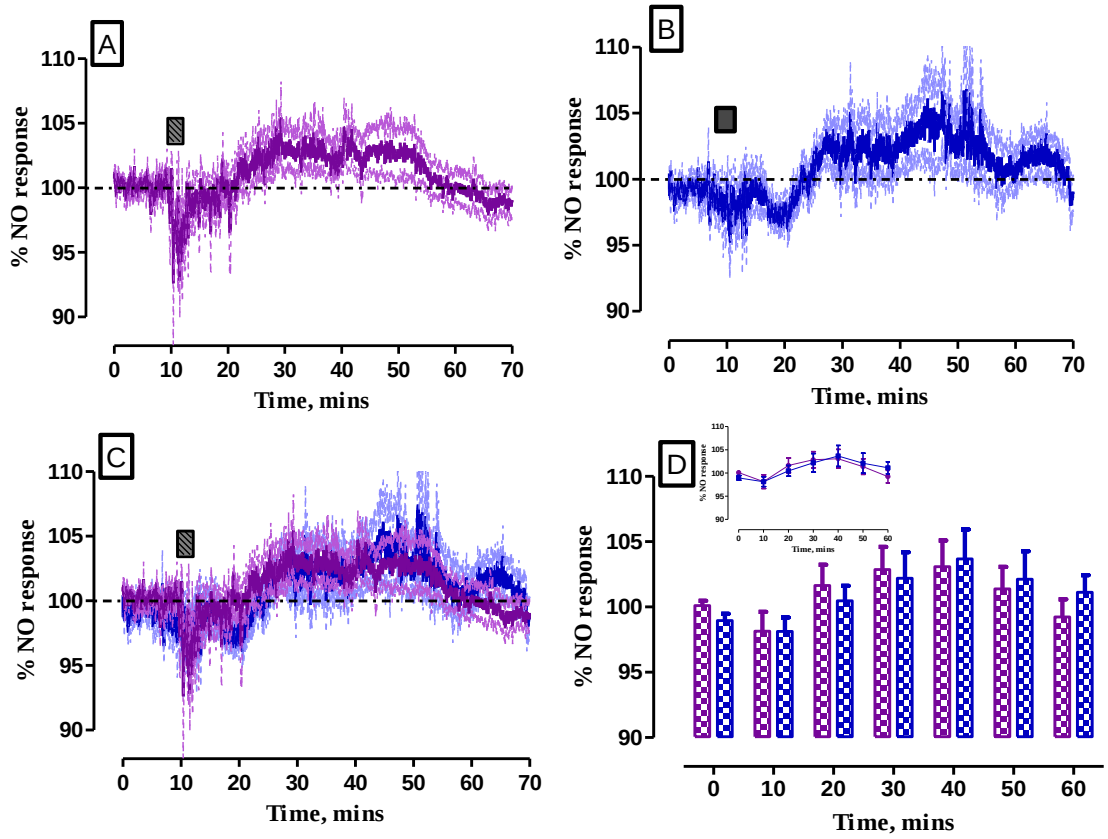

Figure 6.3.2.2.1: Averaged percentage raw data current response of the NO sensors implanted in the striatum of: (A) WT humanised mice (*n* = 7, purple trace), (B) NOD SCID mice (*n* = 4, blue trace), (C) overlay of humanised (purple trace) vs. NOD SCID percentage (blue trace) current response following 2-minute restraint test. Duration of restraint is represented by the dark grey box. The purple trace indicates the mean percentage WT current response with the percentage error represented by the light purple trace. The blue trace indicates the mean percentage NOD SCID current response with the percentage error represented by the light blue trace. (D) Bar graph comparing 10-min time bins of percentage current responses. *Inset*: Time bin analysis of 70-minute raw percentage data current responses. Data represented as mean percentage current ± SEM.

Figures 6.3.2.2.1A - C illustrate clearly that a similar NO response was recorded in each animal group following the performance of a 2-minute restraint test. Furthermore, Figure 6.3.2.2.1D illustrates a comparable NO response exhibited in WT mice and non-humanised mice as no significant differences were determined by time bin analysis conducted on the two responses (Table 6.3.2.2.2). Therefore, this comparable data indicates that following physiological stimulation of humanised mice, a similar NO response is exhibited in both cohorts. It is interesting to note that a near identical response was observed between WT and NOD SCID animals in

contrast to a reduced response in PINK1 mice. This further supports the reduced NO activity in PINK1 grafts.

Table 6.3.2.1.2: Statistical analysis of NO recordings obtained in the striatum of humanised WT mice (*n* = 7) and non-humanised NOD SCID mice (*n* = 4) following a 2-minute restraint.

Restraint					
	WT (*n* = 7)		NOD SCID (*n* = 4)		
Time, mins	**Mean, %**	**SEM**	**Mean, %**	**SEM**	***p***
0	100.1	0.4	99.0	0.5	0.10
10	98.1	1.5	98.1	1.1	0.99
20	101.6	1.6	100.5	1.1	0.61
30	102.9	1.7	102.2	2.0	0.81
40	103.1	2.0	103.7	2.2	0.85
50	101.4	1.7	102.1	2.1	0.79
60	99.2	1.3	101.1	1.3	0.36

6.3.2.3 Validation of the NO Signal Using L-NAME

Systemic administration of L-NAME to WT animals demonstrated a decrease in NO of - 61 ± 18 pA (*n* = 6, Figure 6.3.2.3.1A) from baseline levels (486 ± 86 pA, *n* = 6). This significant decrease ($p < 0.05$) corresponded to a - 14 ± 4 % (*n* = 6) and a concentration change of 49 ± 12 nM (*n* = 6) after 90 ± 11 mins (*n* = 6). Baseline currents did not return over the course of amperometric recordings conducted following L-NAME administration (Table 6.3.2.3.1). Figure 6.3.2.3.1C illustrates the comparable response of L-NAME in decreasing NO levels measured in humanised WT and NOD SCID mice. Hence, the ability of the NO sensor to detect fluctuating NO levels in transplanted WT mice has been demonstrated.

Table 6.3.2.3.1: Summary of results of the NO sensors implanted in the striatum of WT humanised mice following i.p. administration of 30 mg/kg L-NAME (*n* = 6).

L-NAME Injection						
Pre-Perturbation Baseline (pA)	**Max Current (pA)**	**Current Change (pA)**	**Current Change (%)**	**Max Response Time (mins)**	**Post-Perturbation Baseline (pA)**	**Return to Baseline Time (mins)**
486 ± 86	425 ± 80	-61 ± 18	-14 ± 4	90 ± 11	-	-

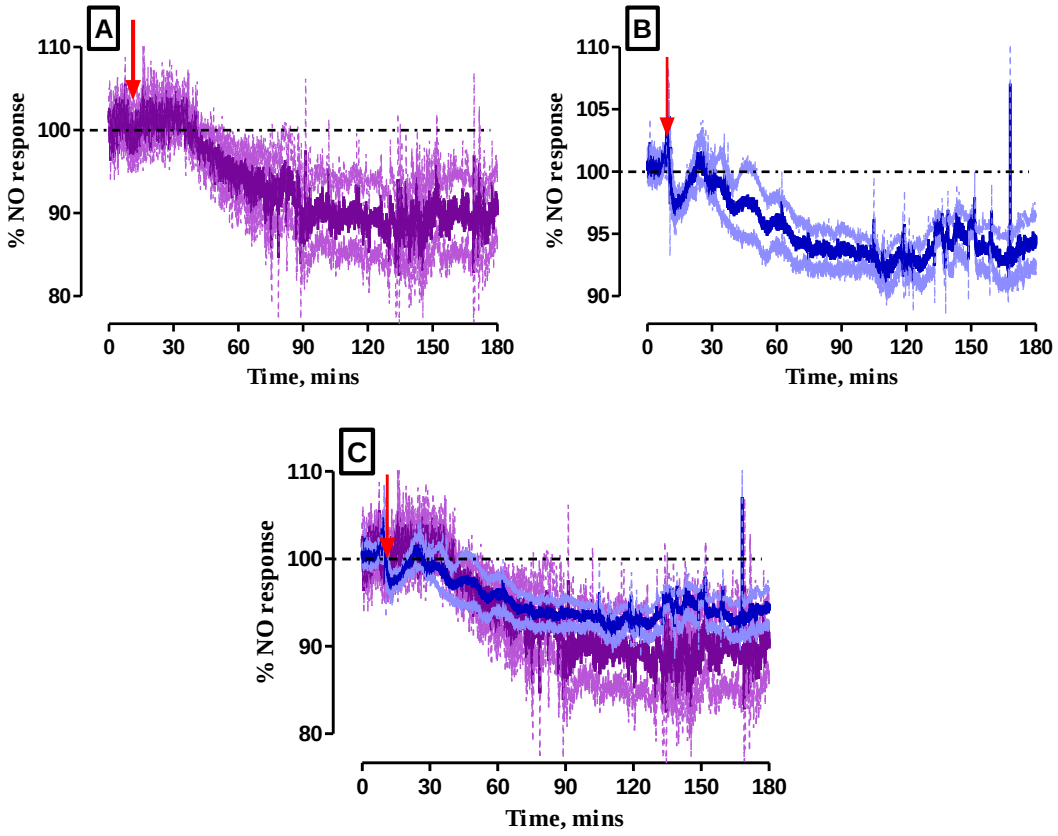

Figure 6.3.2.3.1: Averaged percentage raw data current response of the NO sensors implanted in the striatum of: (A) WT humanised mice (*n* = 6, purple trace), (B) NOD SCID mice (*n* = 5, blue trace), (C) overlay of WT (purple trace) vs. NOD SCID (blue trace) percentage current response following 30 mg/kg i.p. injection of L-NAME. Point of injection is represented by the red arrow. The purple trace indicates the mean percentage WT current response with the percentage error represented by the light purple trace. The blue trace indicates the mean percentage NOD SCID current response with the percentage error represented by the light blue trace. Data represented as mean percentage current ± SEM.

6.3.2.4 Validation of the Selective Properties of the NO Sensor

Figure 6.3.2.4.1A illustrates the effect of sodium ascorbate on the recorded signal. The (ΔI) obtained of - 21 ± 5 pA (n = 7) equated to a - 10 ± 2 % (n = 7) decrease in current. This decrease in NO corresponded to a concentration change of 16 ± 3 nM (n = 7). In addition, this decrease in current occurred 6 ± 1 mins (n = 7) following the systemic administration of sodium ascorbate. No significant difference (p = 0.06) was observed between the baseline current (265 ± 38 pA, n = 7) and the increase in the amperometric signal attained following sodium ascorbate administration. A new post-perturbation baseline current (262 ± 37 pA, n = 7) was obtained after 37 ± 4 mins (n = 7, Table 6.3.2.4.1) and was noted to not be significantly different (p = 0.41) from pre-injection baseline levels.

A comparable NO response is exhibited in transplanted mice and non-humanised NOD SCID mice (Figure 6.3.2.4.1A - C). Although the NO response obtained in both cohorts is comparable, the amperometric current is never seen to return to baseline levels following sodium ascorbate administration in NOD SCID mice whereas in WT mice, the baseline returns after 37 ± 4 mins (n = 7). From these results obtained, it can therefore be postulated that sodium ascorbate plays a role in reducing NO levels in the environment surrounding the sensor. However, this appears to be an immunocompromised mouse effect as opposed to a graft effect.

Table 6.3.2.4.1: Summary of results of the NO sensors implanted in the striatum of humanised WT mice following i.p administration of 500 mg/kg sodium ascorbate (n = 7).

Sodium Ascorbate Injection						
Pre-Perturbation Baseline (pA)	**Max Current (pA)**	**Current Change (pA)**	**Current Change (%)**	**Max Response Time (mins)**	**Post-Perturbation Baseline (pA)**	**Return to Baseline Time (mins)**
265 ± 38	250 ± 41	-21 ± 5	-10 ± 2	6 ± 1	262 ± 37	37 ± 4

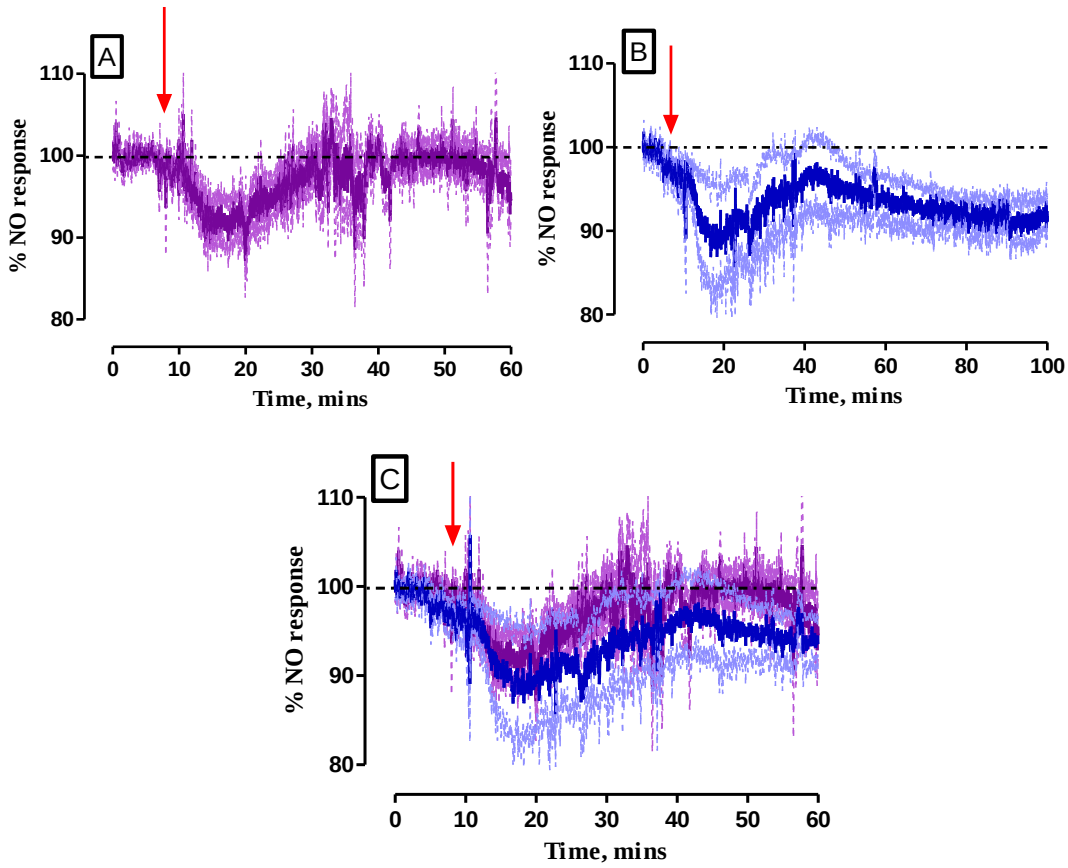

Figure 6.3.2.4.1: Averaged percentage raw data current response of the NO sensors implanted in the striatum of: (A) WT humanised mice (*n* = 7, purple trace), (B) NOD SCID mice (*n* = 4, blue trace), (C) overlay of WT (purple trace) vs. NOD SCID (blue trace) percentage current response following 500 mg/kg i.p. injection of sodium ascorbate. Point of injection is represented by the red arrow. The purple trace indicates the mean percentage WT current response with the percentage error represented by the light purple trace. The blue trace indicates the mean percentage NOD SCID current response with the percentage error represented by the light blue trace. Data represented as mean percentage current ± SEM.

6.3.2.5 24-hour Amperometric Recordings of NO

Figure 6.3.2.5.1A illustrates the NO response recorded over 24-hours which indicated that an increase in NO is experienced upon initiation of the night cycle in the WT cohort. A similar increase in NO was present in night cycle recordings obtained from non-humanised (Figure 6.3.1.5.1A & B). This sustained increase in NO exhibited through the night cycle can be attributed to the increased activity of the animal, thus, leading to an increase in neuronal activation. In humanised WT mice, light cycle recordings fluctuated around basal levels which is to be expected due to a decrease in motor activity and neuronal activation during this time period. These

findings suggest that a comparable NO response is observed in NOD SCID and WT mice over a 24-hour period.

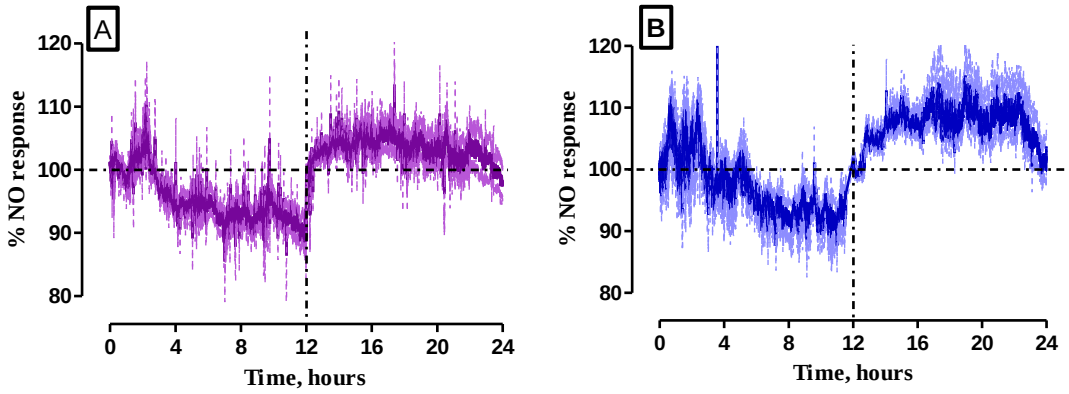

Figure 6.3.2.5.1: Averaged 24-hour percentage current response measured by NO sensors implanted in the striatum of (A) humanised WT mice (purple trace) during the light phase (*n* = 22/6, 0 - 12 hours) and the dark phase (*n* = 38/6, 13 - 24 hours) and of (B) NOD SCID mice (blue trace) during the light phase (*n* = 14/5, 0 - 12 hours) and the dark phase (*n* = 20/5, 13 - 24 hours). The purple trace indicates the mean percentage WT NO current response with the percentage error represented by the light purple trace. The blue trace indicates the mean NOD SCID percentage current response with the percentage error represented by the light blue trace. Data represented as mean percentage current ± SEM.

6.3.2.6 IHC Staining of the Transplanted Striatum

Imaging of the integrated graft, with the subsequent sensor implantation, was conducted by IHC staining of the transplanted striatal tissue. The below images in Figure 6.3.2.6.1 indicate the imaged xenotransplanted graft. IHC staining confirmed sensor placement in proximity to the transplanted graft following NO measurements in WT mice. Grafts in the below images are smaller compared to the grafts pictured in Section 6.3.1.6. However, the sensor channel is clearly located in close proximity to the transplanted cells. It is important to note that the graft still achieved good integration in the host striatum as seen by the neural outgrowth from the transplantation site.

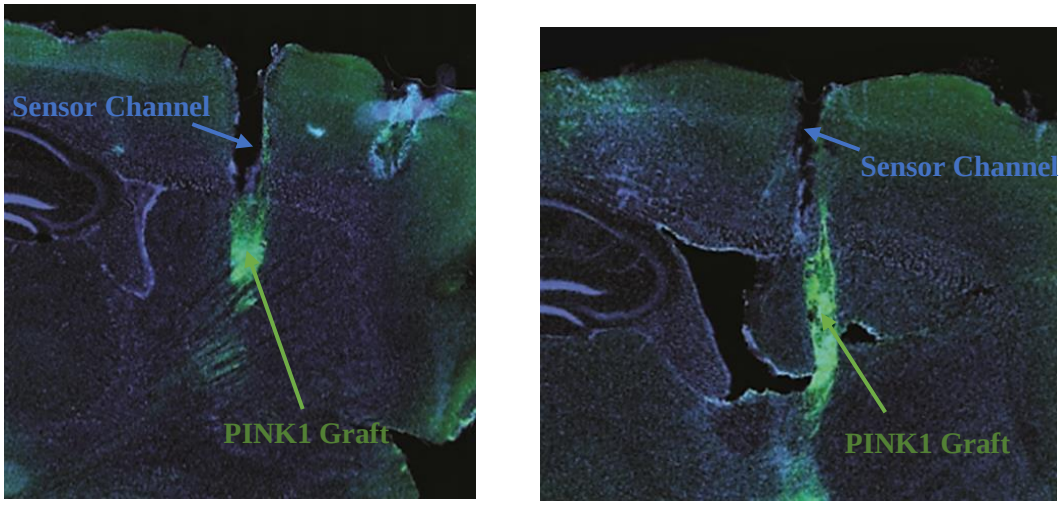

Figure 6.3.2.6.1: Typical examples of IHC images conducted highlighting the sensor placement in the striatum of humanised WT mice.

6.3.3 Comparison of NO Measurements in PINK1, WT and SHAM Mice

6.3.3.1 Saline Administrations

Figure 6.3.3.1.1A illustrates the effect of systemic saline administration on the recorded amperometric signal in 3 different animal groups; humanised PINK1 and WT mice and SHAM mice. SHAM mice were included to act as an experimental control group. SHAM surgeries involved repeating the same transplantation surgical protocol as used for humanised subjects but without transplanting any humanised cells. Therefore, any changes in NO measured within the SHAM group can be attributed to an effect of the surgery. In addition, any similar trends in NO changes exhibited in humanised animals can be identified to result as an effect of the surgical procedure rather than resulting from the humanised cells. The average Δ[NO] is represented below in Figure 6.3.3.1.1A which was obtained using *in vitro* sensitivity values. A comparable NO response was determined in each of the animal cohorts following saline administration. Further quantification of the NO response recorded was examined using time bin analysis to allow for any significant differences in the NO responses to be identified as represented in Figure 6.3.3.1.1B. Time bin analysis gave a quantitative insight into the observed response by averaging the raw current over 10-minute timeframes. It was found that no significant difference in Δ[NO] existed

following saline administration in humanised mice and SHAM animals (Table 6.3.3.1.1).

Table 6.3.3.1.1: Statistical analysis of NO recordings obtained in the striatum of PINK1 (*n* = 8), WT mice (*n* = 10) and SHAM mice (*n* = 6) following 1 mL/kg saline i.p. administration.

Saline									
	PINK1 (*n* = 8)		WT (*n* = 10)		SHAM (*n* = 6)		WT *vs.* PINK1	WT *vs.* SHAM	PINK1 *vs.* SHAM
Time (mins)	Mean (nM)	SEM	Mean (nM)	SEM	Mean (nM)	SEM	*p*	*p*	*p*
0	2.0	1.1	0.1	0.8	-2.2	2.3	0.18	0.28	0.10
10	2.1	1.6	2.6	2.7	1.3	1.1	0.88	0.71	0.69
20	6.0	2.1	8.9	3.8	5.3	1.9	0.53	0.48	0.82
30	2.8	3.8	9.9	4.6	4.4	1.6	0.26	0.37	0.72
40	-0.1	3.7	6.5	4.8	6.2	1.9	0.30	0.96	0.23

Firstly, no significant differences were found between the NO response recorded in humanised PINK1 and WT mice. However, it was observed that a larger Δ[NO] occurs in WT animals when compared to PINK1 mice suggesting a reduced NO activity in the PD cell lines. Additionally, it appeared that humanised WT mice demonstrated a higher NO concentration change than that observed in SHAMs, however, no significant differences were recorded (Table 6.3.3.1.1). Therefore, it can be postulated that a larger increase in NO production occurs in the WT graft. Similarly, the NO response monitored in humanised PINK1 and SHAM mice was examined and time bin analysis identified no significant differences (Table 6.3.3.1.1). Therefore, these results suggest similar Δ[NO] occurs in the striatum of each animal group following an i.p. injection of saline.

Although the Δ[NO] appears to be higher in WT mice when compared to levels recorded in PINK1 and SHAM animals, there is a clear lack of significance between these groups. However, it can be suggested that this lack of significance may be attributed to the low levels of NO that exist *in vivo* meaning that a much larger sample size may be required. Notwithstanding this, it is of great interest that a tendency

towards reduced NO levels in PD patient cells lines seems to be apparent. The PINK1 results recorded share similarities to the response obtained in SHAM mice which suggests an influence on NO levels from the surgical procedure. The fact that WT animals illustrated a higher NO response following mild neuronal activation infers that an effect can be measured from the transplanted grafts.

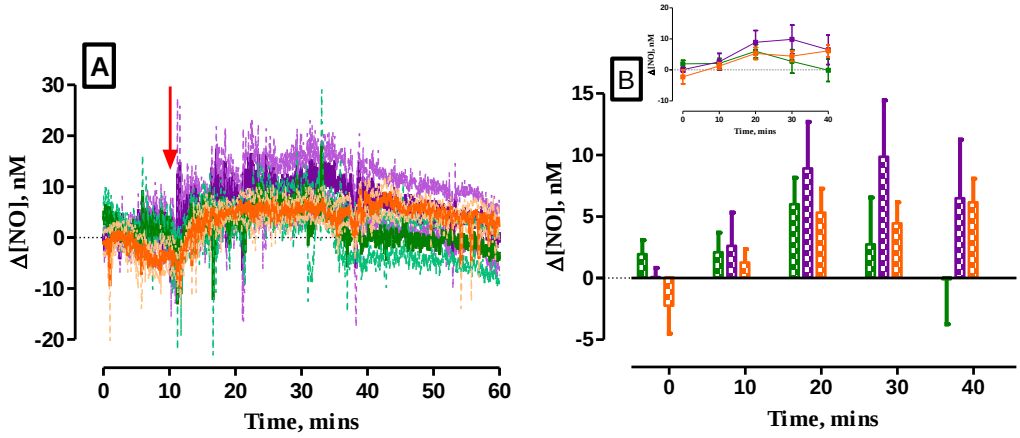

Figure 6.3.3.1.1: (A) Overlay of the average Δ[NO] recorded using NO sensors implanted in the striatum of humanised PINK1 (*n* = 8) and WT (*n* = 10) and SHAM (*n* = 6) mice following a 1 mL/kg saline i.p injection. Red arrow indicates the point of injection. The mean PINK1 Δ[NO] is represented by the green trace and the percentage error is represented by the light green trace. The mean WT Δ[NO] is represented by the purple trace and the percentage error is represented by the light purple trace. The mean SHAM Δ[NO] is represented by the orange trace and the percentage error is represented by the light orange trace. (B) Bar graph comparing 10-minute time bin analysis of Δ[NO] following a 1 mL/kg saline i.p. injection. Data represented as mean Δ [NO] ± SEM.

6.3.3.2 Restraint Test

Similarly, a comparable change in the concentration of NO was reported in humanised PINK1, WT and SHAM mice following a 2-minute restraint test (Figure 6.3.3.2.1A). Firstly, a dual response was observed in the recorded NO response in each of the three animal groups following a 2-minute restraint. Therefore, highlighting the similarity of the NO responses measured in each of the cohorts. Conductance of time bin analysis indicated no significant difference between the PINK1, WT and SHAM mice in response to the restraint test (Figure 6.3.3.2.1B, Table 6.3.3.2.1). Similarly, it was noticed that a slightly larger increase in NO was measured in WT animals following the administration of the restraint test. However, the magnitude of the

increase between WT mice and the other two experimental groups is not as evident as that that was previously seen in Section 6.3.3.1. Nevertheless, there is a clear tendency towards reduced NO levels in response to neuronal activation in PD patient cell lines.

Table 6.3.3.2.1: Statistical analysis of NO recordings obtained in the striatum of PINK1 (*n* = 8), WT mice (*n* = 7) and SHAM mice (*n* = 6) following a 2-minute restraint.

Restraint									
	PINK1 (*n* = 8)		WT (*n* = 7)		SHAM (*n* = 6)		WT *vs.* PINK1	WT *vs.* SHAM	PINK1 *vs.* SHAM
Time (mins)	Mean (nM)	SEM	Mean (nM)	SEM	Mean (nM)	SEM	*p*	*p*	*p*
0	-1.5	0.7	-0.4	0.6	0.1	1.4	0.22	0.72	0.26
10	-4.2	1.7	-6.0	4.1	-2.3	0.9	0.66	0.42	0.39
20	2.5	2.8	2.0	3.6	3.8	1.7	0.91	0.68	0.73
30	3.7	3.3	5.7	3.4	1.2	3.4	0.69	0.36	0.61
40	2.3	2.1	6.2	3.8	1.7	3.7	0.36	0.40	0.87
50	2.0	1.7	1.0	3.9	1.4	3.6	0.80	0.94	0.86
60	0.6	1.4	-4.4	3.3	-0.3	3.8	0.16	0.43	0.80

The similarity between the NO responses obtained in PINK1 and WT mice is clearly evident and it is illustrated in Figure 6.3.3.2.1A. By performance of time bin analysis, no significant difference was found between the NO amperometric signal in humanised animals between t = 10 mins and t = 60 mins. Additionally, both responses appear to return to baseline over a similar timeframe. However, it must be stated that it appears that NO levels are higher in humanised WT mice (Figure 6.3.3.2.1B) which infers higher NO production in the WT cohort.

In addition, Table 6.3.3.2.1 demonstrates that no significant difference exists between NO levels in humanised WT and SHAM mice. Both cohorts exhibited comparable NO response recorded over similar duration. The lack of significance is clear between the two animal groups, however, the NO response in humanised WT mice is higher following the initiation of neuronal activation. This further supports that elevated NO activity exists in WT mice.

Furthermore, the NO signal measured from humanised PINK1 and SHAM mice was examined. Both cohorts displayed similar dual responses in NO following a

2-minute restraint test. Following the performance of time bin analysis, no significant differences were observed between the NO amperometric response recorded in humanised PINK1 and SHAM mice (Table 6.3.3.2.1). The NO responses recorded in each of the aforementioned cohorts demonstrated a much greater similarity when compared to the amperometric response obtained in WT mice.

From the results discussed, it has been noted that larger changes in NO concentrations occur in humanised WT mice when compared to levels recorded in humanised PINK1 and SHAM mice. Although no significant difference exists between the cohorts, it can be suggested that a higher NO concentration is reached in WT subjects following performance of a 2-minute restraint test. Therefore, these findings suggest that there is a reduced NO activity in PINK1 transplanted mice.

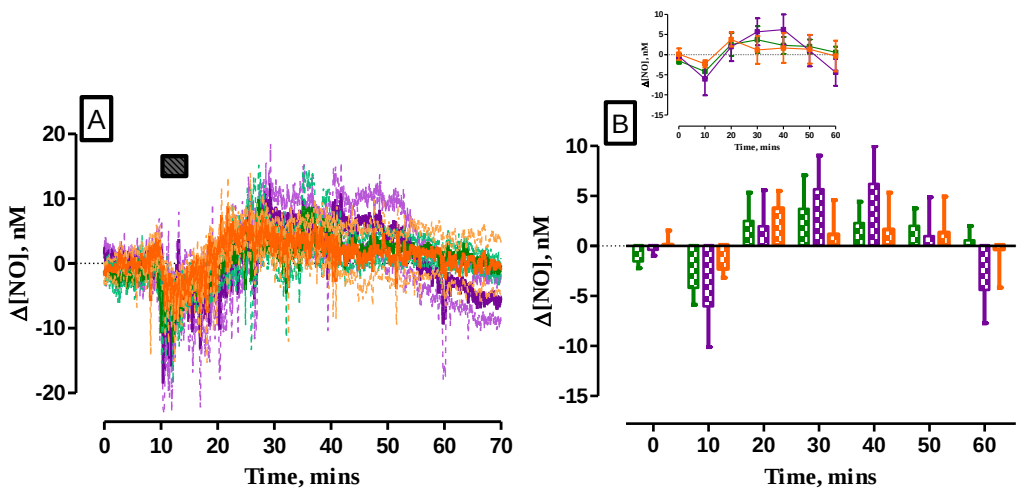

Figure 6.3.3.2.1: (A) Overlay of the average Δ[NO] recorded using NO sensors implanted in the striatum of humanised PINK1 (*n* = 8) and WT (*n* = 7) and SHAM (*n* = 6) mice following a 2-minute restraint. Duration of the restraint is represented by the dark grey box. The mean PINK1 Δ[NO] is represented by the green trace and the percentage error is represented by the light green trace. The mean WT Δ[NO] is represented by the purple trace and the percentage error is represented by the light purple trace. The mean SHAM Δ[NO] is represented by the orange trace and the percentage error is represented by the light orange trace. (B) Bar graph comparing 10-minute time bin analysis of Δ[NO] following a 2-minute restraint. Data represented as mean Δ [NO] ± SEM.

6.3.3.3 Characterisation Compounds

The effect of the characterisation compounds, L-NAME and ascorbate, on the amperometric NO signal in humanised mice and in SHAM mice is highlighted in

Figure 6.3.3.3.1. Results acquired from each of the cohorts have demonstrated a decrease in the NO response being exhibited following sodium ascorbate administration. Figure 6.3.3.3.1 highlights this decrease in NO concentration recorded following an i.p. injection of sodium ascorbate. From the Figure below, it is clear that no significant difference ($p = 0.28$) exists between the NO concentrations measured in humanised PINK1 and WT animals following exposure to sodium ascorbate. Similarly, no significant difference exists between the NO response recorded in humanised WT mice and SHAM mice ($p = 0.76$) or between humanised PINK1 and SHAM subjects ($p = 0.57$). Moreover, this decrease in the recorded NO concentration confirms the integrity of the selective membrane *in vivo*. In addition, this decrease in NO response was previously seen in Section 6.3.1.4 and 6.3.2.4 following the administration of sodium ascorbate. It can be hypothesised that this decrease is a result of the action of sodium ascorbate on NO levels in immunocompromised mice. Previous studies carried out by Finnerty *et al.*[6,7] have involved the administration of sodium ascorbate in freely-moving rats. These investigations have demonstrated no decrease in NO levels following administration. Thus, it can be hypothesised that the aforementioned decrease in NO in immunocompromised mice may be due to a mouse effect as the action of this compound in mice has never been previously reported.

Likewise, L-NAME was administered to the subjects to ensure the sensor was able to perform efficiently under physiological conditions. Figure 6.3.3.3.1 illustrates a decrease in NO concentrations measured following L-NAME administration. This suggests that the NO sensor demonstrates the ability to measure changes in NO efficiently in xenotransplanted striatal tissue. In contrast, a significant difference ($p = 0.01$) was reported between the magnitude of the decrease in NO concentration recorded in PINK1 and WT mice. Further experimentation was conducted to examine any significant differences in NO measurements obtained following L-NAME administration in humanised and SHAM mice. It was found that a significant decrease ($p = 0.04$) existed between the decrease in NO measured in WT and SHAM mice. In contrast, no significant difference ($p = 0.95$) was determined between humanised PINK1 and SHAM mice. At present, it is difficult to attribute this disparity in NO measurements to a recorded difference in transplanted cells. However, it is important to acknowledge that a greater decrease in NO levels exists in the WT cohort following L-NAME administration when compared to PINK1 and SHAM mice.

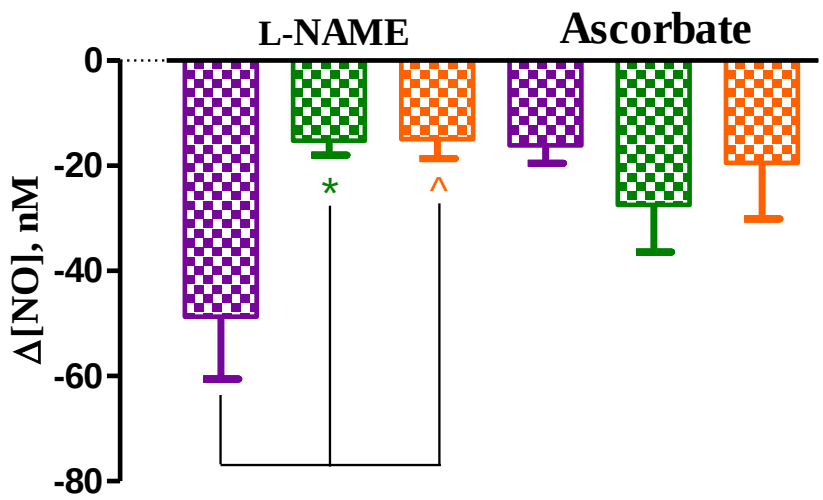

Figure 6.3.3.3.1: Bar chart of the average Δ[NO] recorded using NO sensors implanted in the striatum of humanised PINK1 (green, *n* = 8), WT (purple, *n* = 7) and SHAM (orange, *n* = 5) mice following a 30 mg/kg L-NAME i.p. injection and a 500 mg/kg sodium ascorbate i.p. injection. * denotes the level of significance between WT and PINK mice. ^ denotes the level of significance between WT and SHAM mice. Data represented as mean Δ [NO] ± SEM.

6.3.3.4 24-hour Recordings

Quantitative changes in NO concentration were examined over a 24-hour period in all 3 animal cohorts. Figure 6.3.3.4.1A highlights the concentration changes in NO over the light cycle. It is apparent that a comparable NO response was recorded in both humanised and SHAM animals (Figure 6.3.3.4.1A). Time bin analysis was conducted to allow for any significant differences in the NO concentration over this 12-hour period to be established (Figure 6.3.3.4.1B). Time bin analysis was performed by averaging 1-hour time intervals from the raw data trace over 24-hours. Significant differences were identified at t = 2 hours, t = 9 hours and t = 10 hours following comparison of PINK1 and WT cohorts. Additionally, a significant difference was observed between the PINK1 and SHAM NO responses at t = 2 hours with a close to significant difference being noted at t = 8 hours. In contrast, no significant differences were seen between the amperometric response recorded in WT and SHAM animals. Usually, the light cycle is associated with periods of inactivity and a decrease in neuronal activation. Hence, it was hypothesised that NO levels were comparable in each of the animal cohorts over the light cycle, but a tendency towards a larger NO decrease in PINK1 animals appeared to exist.

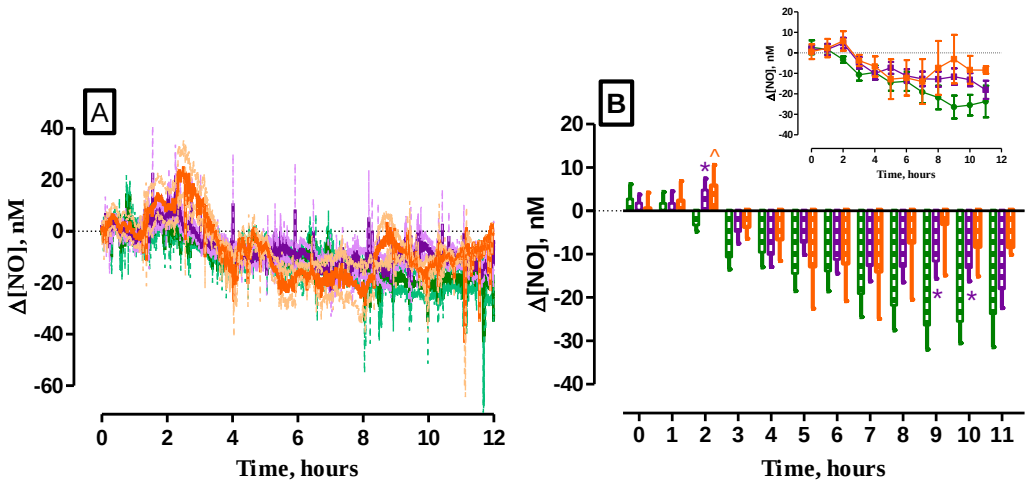

Figure 6.3.3.4.1: (A) Overlay of the averaged 12-hour Δ[NO] measured by NO sensors implanted in the striatum of humanised PINK1 (green trace, *n* = 19/8), WT mice (purple trace, *n* = 20/10) and SHAM mice (orange trace, *n* = 10/6) during the light phase (0 -12 hours). The mean PINK1 Δ[NO] is represented by the green trace and the percentage error is represented by the light green trace. The mean WT Δ[NO] is represented by the purple trace and the percentage error is represented by the light purple trace. The mean SHAM Δ[NO] is represented by the orange trace and the percentage error is represented by the light orange trace. (B) Bar graph comparing 1-hour time bin analysis of Δ[NO] over 12-hours. * denotes the level of significance between PINK1 and WT mice. ^ denotes the level of significance between PINK1 and SHAM mice. Data represented as mean Δ [NO] ± SEM.

Table 6.3.3.4.1: Statistical analysis of NO recordings obtained in the striatum of PINK1 (*n* = 8), WT mice (*n* = 10) and SHAM mice (*n* = 6) during the light cycle.

Light Cycle Recordings									
	PINK1 (*n* = 8)		WT (*n* = 10)		SHAM (*n* = 6)		WT *vs.* PINK1	WT *vs.* SHAM	PINK1 *vs.* SHAM
Time (mins)	Mean (nM)	SEM	Mean (nM)	SEM	Mean (nM)	SEM	*p*	*p*	*p*
0	2.8	3.4	1.8	2.0	0.6	3.6	0.80	0.75	0.68
1	1.8	2.6	1.7	2.8	2.4	4.5	0.99	0.90	0.90
2	-3.3	1.5	4.8	2.6	5.9	4.7	0.02	0.83	0.03
3	-10.7	2.8	-4.8	2.7	-3.7	2.7	0.15	0.87	0.24
4	-9.5	3.5	-10.0	2.9	-6.6	4.9	0.92	0.56	0.66
5	-14.4	4.1	-7.3	2.9	-12.8	9.7	0.15	0.46	0.86
6	-13.9	4.7	-11.2	3.2	-12.2	8.7	0.63	0.90	0.85
7	-19.1	5.4	-12.7	3.6	-14.0	10.9	0.31	0.88	0.64
8	-21.8	5.8	-12.8	3.7	-7.3	13.2	0.18	0.57	0.26
9	-26.4	5.6	-11.6	4.1	-3.0	11.8	0.04	0.44	0.08
10	-25.5	5.1	-13.1	3.2	-8.3	6.8	0.04	0.56	0.12
11	-23.7	7.7	-18.0	4.4	-8.3	1.7	0.50	0.38	0.29

Additionally, the NO concentration dynamics were assessed over the course of the night cycle. Figure 6.3.3.4.2A demonstrates the NO concentration monitored in each animal group over this 12-hour period. The below graph highlights a lower concentration of NO recorded during the night cycle in PINK1 cell lines. A comparable, higher NO concentration was measured in WT and SHAM cohorts. Moreover, no significant difference was reported between either WT and SHAM mice or PINK1 and WT subjects, following conductance of time bin analysis (Figure 6.3.3.4.2B, Table 6.3.3.4.2) over this 12-hour period. However, a significant difference was noted at t = 1 hours between PINK1 and SHAM animal groups. Although, this was the only significant difference identified, it is important to note that a reduction in NO dynamics was measured in PINK1 transplanted mice in response to neuronal activation during the night cycle. Again, these findings support the hypothesis that reduced NO dynamics exist in patient-derived PD cells which is an interesting finding.

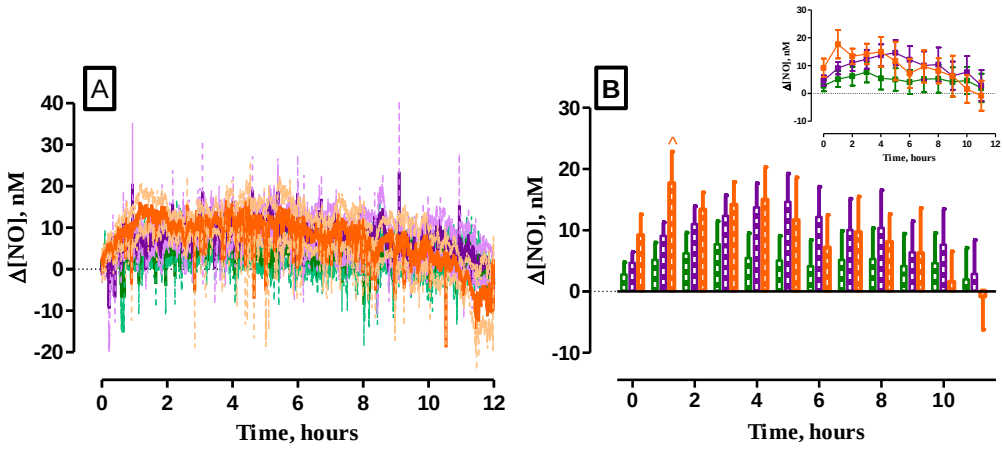

Figure 6.3.3.4.2: (A) Overlay of the averaged 12-hour Δ[NO] measured by NO sensors implanted in the striatum of humanised PINK1 (green trace, *n* = 30/8), WT (purple trace, *n* = 33/10) and SHAM mice (orange trace, *n* = 10/6) during the night phase (13 - 24 hours). The mean PINK1 Δ[NO] is represented by the green trace and the percentage error is represented by the light green trace. The mean WT Δ[NO] is represented by the purple trace and the percentage error is represented by the light purple trace. The mean SHAM Δ[NO] is represented by the orange trace and the percentage error is represented by the light orange trace. (B) Bar graph comparing 1-hour time bin analysis of Δ[NO] over 12-hours. Data represented as mean Δ [NO] ± SEM. ^ denotes the level of significance between PINK1 and SHAM mice.

Table 6.3.3.4.2: Statistical analysis of NO recordings obtained in the striatum of PINK1 (*n* = 8), WT mice (*n* = 10) and SHAM mice (*n* = 6) during the night cycle.

Night Cycle Recordings									
	PINK1 (*n* = 8)		WT (*n* = 10)		SHAM (*n* = 6)		WT *vs.* PINK1	WT *vs.* SHAM	PINK1 *vs.* SHAM
Time (mins)	Mean (nM)	SEM	Mean (nM)	SEM	Mean (nM)	SEM	*p*	*p*	*p*
0	2.8	2.0	4.7	1.8	9.3	3.3	0.48	0.23	0.11
1	5.2	2.8	9.1	2.2	17.7	5.1	0.27	0.08	0.03
2	6.3	3.4	11.0	2.9	13.4	2.8	0.29	0.67	0.23
3	7.7	3.7	12.3	3.4	14.2	3.7	0.36	0.78	0.33
4	5.5	4.0	13.7	3.9	15.0	5.3	0.15	0.87	0.20
5	5.0	4.0	14.7	4.6	11.7	6.9	0.13	0.75	0.41
6	4.1	4.3	12.2	4.9	7.2	5.3	0.23	0.60	0.69
7	5.2	4.7	10.1	5.1	9.7	5.8	0.49	0.97	0.61
8	5.3	5.0	10.4	6.1	8.1	4.5	0.53	0.85	0.76
9	4.2	5.3	6.4	5.1	6.3	7.3	0.76	0.99	0.83
10	4.7	4.9	7.6	5.8	1.6	4.9	0.70	0.60	0.73
11	2.0	5.1	2.9	5.6	-0.8	5.4	0.91	0.77	0.79

6.3.4 O_2 Measurements in Humanised Mice Transplanted with PINK1 Cells

6.3.4.1 Saline Administrations

The tissue O_2 response to systemic administrations of saline has previously been characterised in the striatum of NOD SCID mice (Section 5.3.2.1). Figure 6.3.4.1.1A displays the average raw data response attained following administration of saline in PINK1 cohorts. A (ΔI) of 17 ± 3 nA (n = 8) which corresponded to a percentage change of 19 ± 3 % (n = 8) was achieved. The change in O_2 obtained equated to a 21 ± 3 µM (n = 8) concentration change. Moreover, this increase in current was obtained after 2 ± 1 mins (n = 8) and it was noted to be significantly different (p < 0.01) from baseline currents (75 ± 5 nA, n = 8). A return to baseline currents (76 ± 5 nA, n = 8) was observed after 36 ± 6 mins (n = 8) following saline administration. No significant difference (p = 0.81) was reported between post-injection baseline levels and pre-injection baseline levels.

Conversely, data recorded from non-humanised mice following saline administration indicates a clear contrast in the temporal response of the effect of saline administration when compared to PINK1 mice. In comparison, Section 5.3.2.1 details a transient increase (7 ± 1 nA, n = 6) in the recorded O_2 signal in NOD SCID mice (10 ± 2 %, n = 6) which was reached after 1 ± 0.1 mins (n = 6) following saline administration before returning quickly to basal levels after 7 ± 1 mins (n = 6). A significant difference (p < 0.01) was noted between the increased amperometric current and pre-injection baseline levels. Additionally, no significant difference (p = 0.46) was found between post-injection baselines (83 ± 8 nA, n = 6) and pre-injection baseline levels (81 ± 9 nA, n = 6, Table 6.3.4.1.1).

Table 6.3.4.1.1: Summary of results of the O_2 sensors implanted in the striatum of PINK1 humanised mice following i.p. administration of 0.9 % saline (n = 8).

Saline Injection						
Pre-Perturbation Baseline (nA)	**Max Current (nA)**	**Current Change (nA)**	**Current Change (%)**	**Max Response Time (mins)**	**Post-Perturbation Baseline (nA)**	**Return to Baseline Time (mins)**
75 ± 5	91 ± 8	17 ± 3	19 ± 3	2 ± 1	76 ± 5	36 ± 6

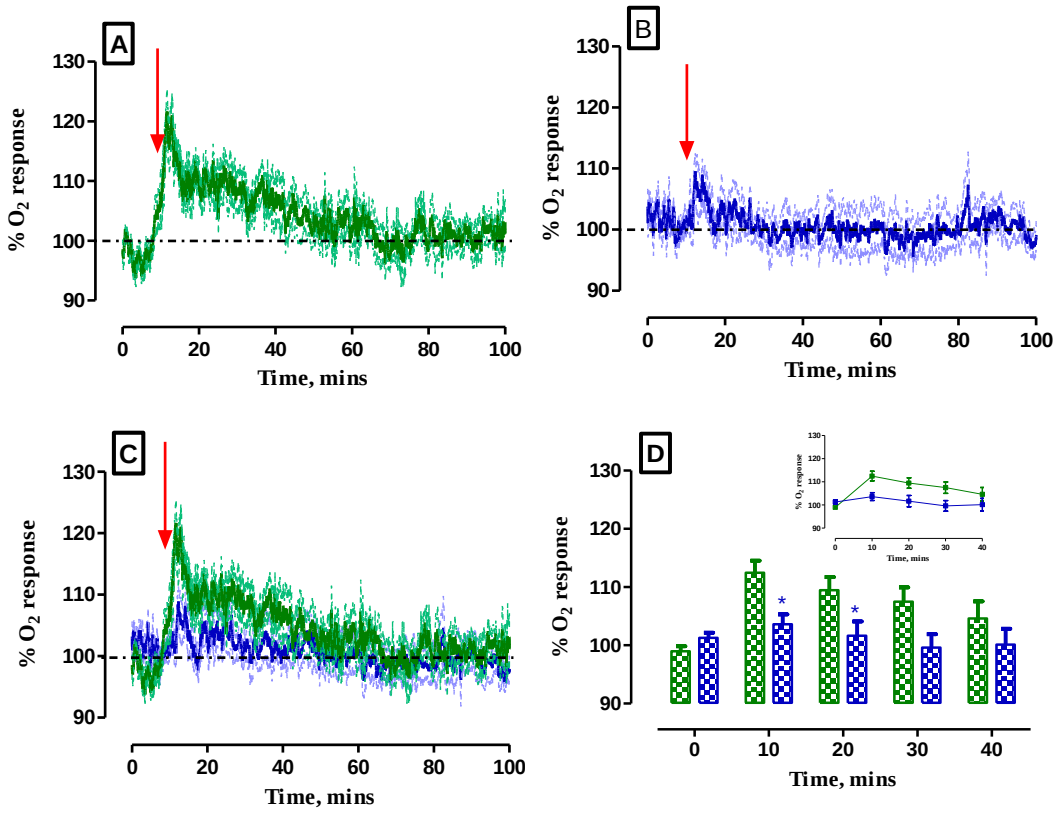

Figure 6.3.4.1.1: Averaged percentage raw data current response of the O_2 sensors implanted in the striatum of: (A) PINK1 humanised mice (*n* = 8, green trace), (B) NOD SCID mice (*n* = 6, blue trace), (C) overlay of humanised (green trace) vs. NOD SCID percentage (blue trace) current response following 1 mL/kg saline i.p. injection. Point of injection is represented by the red arrow. The green trace indicates the mean percentage PINK1 current response with the percentage error represented by the light green trace. The blue trace indicates the mean percentage NOD SCID current response with the percentage error represented by the light blue trace. (D) Bar graph comparing 10-minute time bins of percentage current responses. *Inset*: Time bin analysis of 50-minute raw percentage data current responses. Data represented as mean percentage current ± SEM. * denotes the level of significance.

This data illustrates that although a similar increase in O_2 detection is experienced, the temporal responses recorded in non-humanised and humanised mice differ greatly. The temporal disparities can be clearly seen in Figure 6.3.4.1.1C whilst being further supported by time bin analysis (Figure 6.3.4.1.1D). The recorded responses had returned to new baseline levels after 36 ± 6 mins (*n* = 8) for PINK1 transplanted animals allowing for time bin analysis to be conducted up to 40-minutes post-perturbation. Time bin analysis indicated a significant difference at t = 10 mins and t = 20 mins between the two cohorts. However, t = 30 mins and t = 40 mins showed

no significant difference between PINK1 and NOD SCID mice, but it must be noted that t = 30 mins is close to significance (Table 6.3.4.1.2).

Table 6.3.4.1.2: Statistical analysis of NO recordings obtained in the striatum of humanised PINK1 mice (*n* = 8) and non-humanised NOD SCID mice (*n* = 6) following 1 mL/kg saline i.p. administration.

Saline					
	PINK1 (*n* = 8)		NOD SCID (*n* = 6)		
Time, mins	**Mean, %**	**SEM**	**Mean, %**	**SEM**	***p***
0	99.0	0.8	101.3	0.9	0.10
10	112.5	2.1	103.6	1.7	0.01
20	109.5	2.2	101.7	2.4	0.04
30	107.5	2.5	99.6	2.3	0.05
40	104.6	2.9	100.1	2.7	0.32

As previously discussed in Chapter 2, the amperometric measurement of tissue O_2 is a fine balance between supply of O_2 from CBF (source) and utilisation of O_2 by cells (sink). Previously, saline i.p. administrations have been used to elicit a stress response, therefore, leading to an increase in neuronal activation and CBF. Brain tissue O_2 is very tightly regulated meaning that upon an increase in cellular O_2 demand, CBF increases. Thus, an increase in O_2 is detected at the sensor surface. Following mild neuronal activation, cellular demand for O_2 reduces allowing for the rate of CBF to return to homeostatic levels. Therefore, this increase in O_2 is usually transient before amperometric baseline levels quickly return as seen in NOD SCID mice (see Section 5.3.2.1). In contrast, the results recorded in humanised PINK1 animals show that the increased O_2 response is not transient and remains elevated over 36 ± 6 mins (n = 8). Hence, a difference in either cellular utilisation of O_2 or an increased supply of O_2 by the humanised mice may exist when compared to recordings conducted in non-humanised subjects. It is imperative to note that the xenograft does not contain its own vasculature supply. Therefore, the graft is dependent on oxygenation to occur from the surrounding host tissue. Good integration of the graft has been confirmed by IHC staining (Section 6.3.4.5) which highlights good neurite outgrowth into the surrounding area. With this in mind, increased O_2 measurements can be attributed to either an increase in O_2 being supplied to the area surrounding the graft whilst

utilisation of the O_2 by the transplanted cells is elevated or the utilisation of O_2 by cells has been reduced whilst O_2 is continually supplied to the area surrounding the grafted tissue.

6.3.4.2 Restraint Test

Due to the intriguing results recorded in PINK1 cell lines following saline administration, it was decided to examine the effects of a brief stress test on the amperometric O_2 signal. Figure 6.3.4.2.1A illustrates the recorded response of the animal to a 2-minute restraint test in PINK1 mice. Moreover, following a 2-minute restraint test, the (ΔI) recorded was 26 ± 4 nA (n = 8). This change in amperometric current was found to be significantly different (p < 0.001) from recorded baseline levels (80 ± 4 nA, n = 8). Additionally, this current change corresponded to a percentage current change of 32 ± 4 % (n = 8) and a concentration change of 29 ± 5 µM (n = 8). This maximum change in current occurred after 3 ± 1 mins (n = 8) before baseline levels (77 ± 5 nA, n = 8) were reached after 91 ± 11 mins (n = 8, Table 6.3.4.2.1). It was noted that there was no significant difference (p = 0.32) between baseline levels recorded pre- and post-restraint.

Table 6.3.4.2.1: Summary of results of the O_2 sensors implanted in the striatum of humanised PINK1 mice following 2-minute restraint test (n = 8).

Restraint						
Pre-Perturbation Baseline (nA)	**Max Current (nA)**	**Current Change (nA)**	**Current Change (%)**	**Max Response Time (mins)**	**Post-Perturbation Baseline (nA)**	**Return to Baseline Time (mins)**
80 ± 4	106 ± 7	26 ± 4	32 ± 4	3 ± 0.5	77 ± 5	91 ± 11

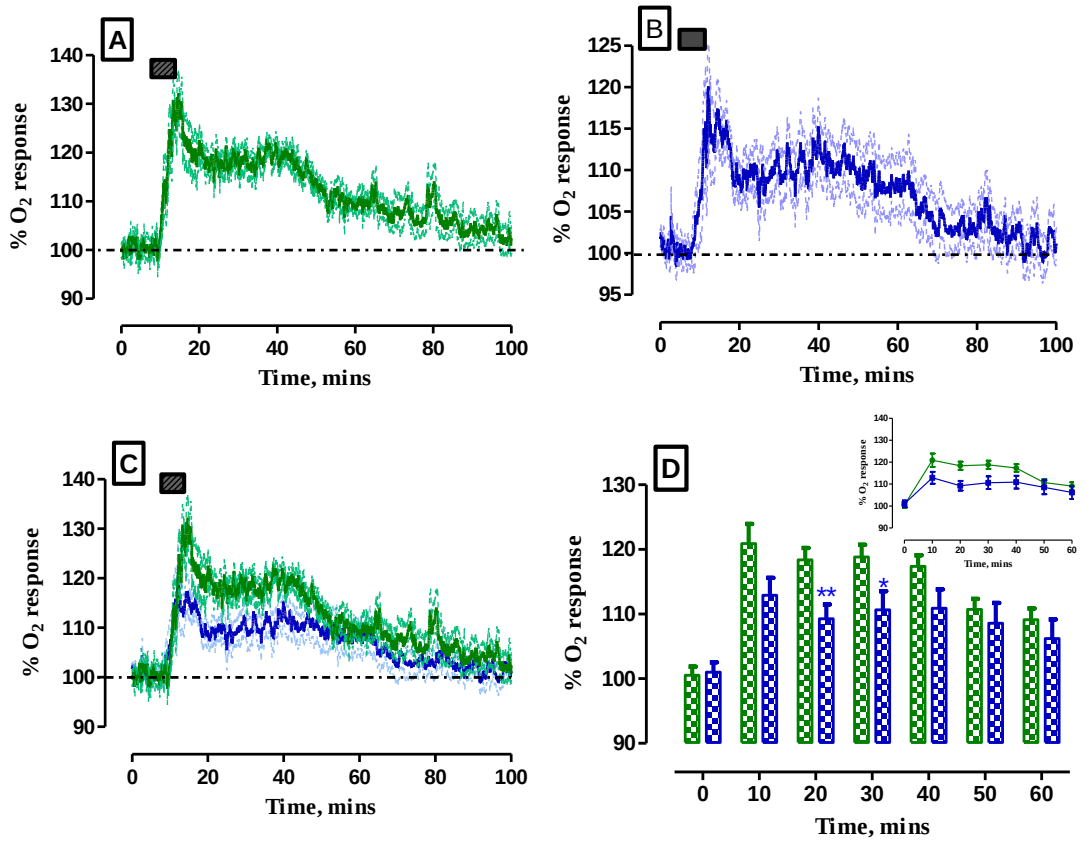

Figure 6.3.4.2.1: Averaged percentage raw data current response of the O_2 sensors implanted in the striatum of: (A) PINK1 humanised mice (*n* = 8, green trace), (B) NOD SCID mice (*n* = 4, blue trace), (C) overlay of humanised PINK1 (green trace) vs. NOD SCID (blue trace) percentage current response following 2-minute restraint test. Duration of the 2-minute restraint is represented by the dark grey box. The green trace indicates the mean percentage PINK1 current response with the percentage error represented by the light green trace. The blue trace indicates the mean percentage NOD SCID current response with the percentage error represented by the light blue trace. (D) Bar graph comparing 10-minute time bins of percentage current responses. *Inset*: Time bin analysis of 70-minute raw percentage data current responses. Data represented as mean percentage current ± SEM. * denotes the level of significance.

Time bin analysis resulted in the significant differences existing at t = 20 mins and t = 30 mins when comparing the O_2 amperometric response recorded in both cohorts (Table 6.3.4.2.2). Additionally, it was observed that time bins, t = 10 mins and t = 40 mins, are close to significance. Therefore, these results indicate that O_2 levels are significantly higher 10 and 20 minutes after the performance of a 2-minute restraint in PINK1 transplanted mice. In addition, from Figure 6.3.4.2.1C, O_2 remains higher in humanised PINK1 mice than in non-humanised mice over the course of 100-minutes following a restraint test.

This observed increase in tissue O_2 levels recorded in PD patient-derived PINK1 cells may be due to an increased rate in CBF to the transplanted graft. This graft contains cells that require O_2 to maintain homeostatic function in the absence of vasculature supply. Therefore, due to its anatomical integration into the host striatum, it may signal a demand for O_2 resulting in an increased in CBF to the surrounding area. Additionally, it could be postulated that utilisation of O_2 by the PINK1 cells is reduced. As these processes occurs concurrently, it would result in the presence of an increased level of tissue O_2. Also, it can also be inferred that PINK1 cells exhibit a higher rate of O_2 utilisation which would require a higher rate of O_2 supply to the adjacent area resulting in this elevated amperometric detection of brain tissue O_2. Nonetheless, it can be hypothesised that an altered rate of O_2 utilisation or demand exists in PINK1 mice.

Table 6.3.4.2.2: Statistical analysis of O_2 recordings obtained in the striatum of humanised PINK1 mice (n = 8) and non-humanised NOD SCID mice (n = 4) following a 2-minute restraint test.

Restraint					
	PINK1 (n = 8)		NOD SCID (n = 4)		
Time, mins	**Mean, %**	**SEM**	**Mean, %**	**SEM**	***p***
0	100.5	1.3	101.0	1.5	0.81
10	120.9	3.0	112.9	2.7	0.07
20	118.4	1.8	109.3	2.2	0.006
30	118.8	1.9	110.6	2.9	0.03
40	117.4	1.7	110.9	2.9	0.07
50	110.7	1.6	108.6	3.2	0.54
60	109.1	1.7	106.2	2.9	0.39

6.3.4.3 Validation of the O_2 Sensor using L-NAME and Diamox

Following the systemic administration of L-NAME, a clear decrease in O_2 current was detected as illustrated in Figure 6.3.4.3.1A. It was reported that 48 ± 9 mins (n = 7) after the administration of L-NAME, a (ΔI) of 18 ± 2 nA (n = 7) was observed. Additionally, this decrease was significantly different (p < 0.001) from baseline levels (81 ± 5 nA, n = 7). Overall, a 15 ± 7 % (n = 7) decrease in current was recorded before the current returned to a new baseline level (76 ± 4 nA, n = 7) after 241 ± 51 mins (n = 7, Table 6.3.4.3.1). In addition, no significant difference (p = 0.13)

was found between pre- and post-perturbation baseline levels. Comparatively, the recorded response was similar to the observed decrease in the amperometric O_2 signal recorded in the striatum of NOD SCID mice following L-NAME administration (Section 5.3.2.2). Moreover, this comparable decrease in O_2 concentration in both PINK1 mice and NOD SCID mice is clearly depicted in Figure 6.3.4.3.1A - C. Therefore, the ability of the O_2 sensor to detect fluctuations of endogenous O_2 have now been verified in humanised PINK1 transplanted animals.

Table 6.3.4.3.1: Summary of results of the O_2 sensors implanted in the striatum of PINK1 humanised mice following a 1 mL/kg i.p. injection of 30 mg/kg L-NAME (*n* = 7).

L-NAME Injection						
Pre-Perturbation Baseline (nA)	**Max Current (nA)**	**Current Change (nA)**	**Current Change (%)**	**Max Response Time (mins)**	**Post-Perturbation Baseline (nA)**	**Return to Baseline Time (mins)**
81 ± 5	63 ± 3	-18 ± 2	-15 ± 7	48 ± 9	76 ± 4	241 ± 51

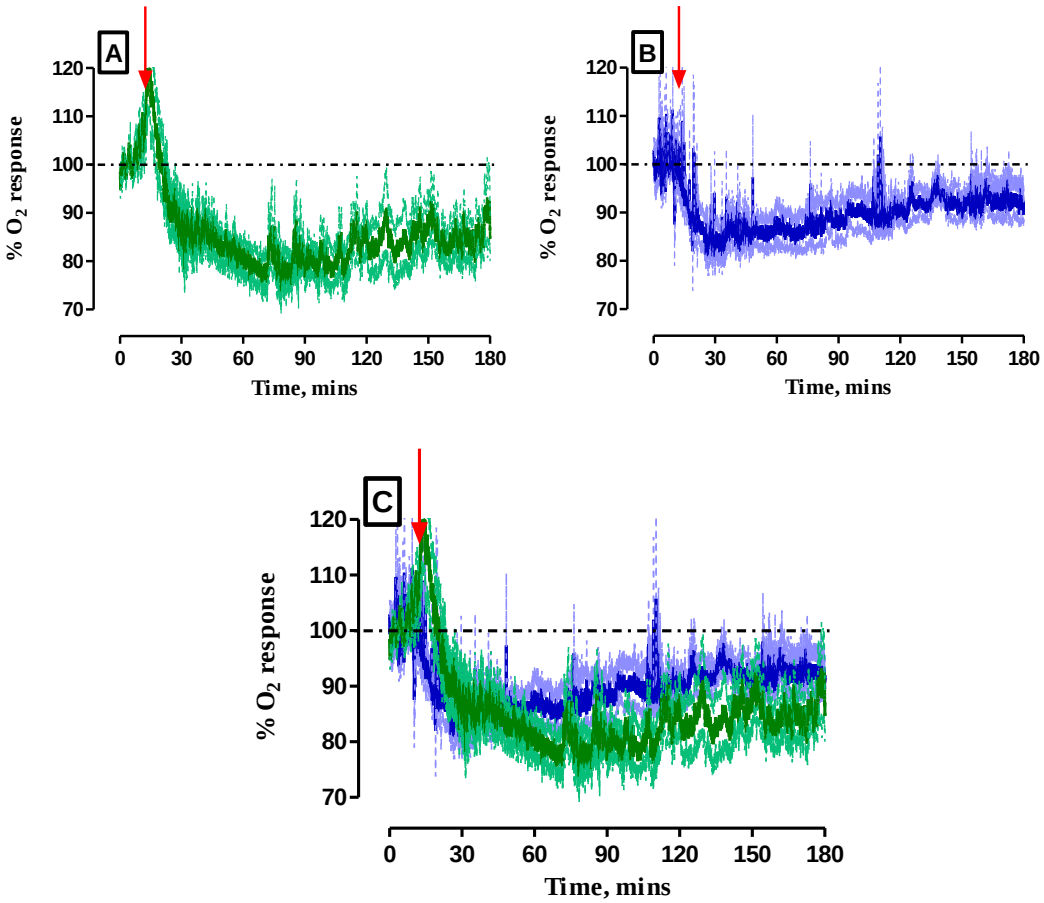

Figure 6.3.4.3.1: Averaged percentage raw data current response of the O_2 sensors implanted in the striatum of: (A) PINK1 humanised mice (*n* = 7, green trace), (B) NOD SCID mice (*n* = 5, blue trace), (C) overlay of humanised (green trace) vs. NOD SCID (blue trace) percentage current response following a 30 mg/kg L-NAME i.p. injection. Point of injection is represented by the red arrow. The green trace indicates the mean percentage humanised PINK1 current response with the percentage error represented by the light green trace. The blue trace indicates the mean percentage non-humanised NOD SCID current response with the percentage error represented by the light blue trace. Data represented as mean percentage current ± SEM.

Further validation of the O_2 sensor *in vivo* was conducted by administering 50 mg/kg Diamox to the subject. Figure 6.3.4.3.2A illustrates an increase in the recorded amperometric signal following systemic administration of Diamox. A (ΔI) of 14 ± 2 nA (n = 3) was recorded which corresponded to a 16 ± 4 % (n = 3) change in current from baseline levels (88 ± 8 nA, n = 3). A significant difference ($p < 0.05$) was noted between baseline levels and the maximum change in current which was achieved after 11 ± 5 mins (n = 3). Following 78 ± 14 mins (n = 3), a new baseline current of 86 ± 8 nA (n = 3) was achieved. This new baseline current was not found to be significantly

different (p = 0.40) from pre-injection baseline levels. Additionally, Figures 6.3.4.3.2A - C illustrates the comparable increases in O_2 current recorded in each cohort. In particular, Figure 6.3.4.3.2C displays the similar responses recorded in both groups confirming that the O_2 sensor possesses the ability to efficiently detect changes in O_2 concentrations in transplanted and non-transplanted animals.

Furthermore, the O_2 amperometric response recorded in humanised PINK1 humanised mice (Figure 6.3.4.3.2A) bears a resemblance to the O_2 response recorded following saline administration (Figure 6.3.4.1.1A). Thus, this similarity supports an increase in O_2 delivery in humanised mice following saline administration due to the initiation of neuronal activation brought about by i.p. administration.

Table 6.3.4.3.2: Summary of results of the O_2 sensors implanted in the striatum of PINK1 humanised mice following a 1 mL/kg i.p. injection of 50 mg/kg Diamox (n = 3).

Diamox Injection						
Pre-Perturbation Baseline (nA)	**Max Current (nA)**	**Current Change (nA)**	**Current Change (%)**	**Max Response Time (mins)**	**Post-Perturbation Baseline (nA)**	**Return to Baseline Time (mins)**
88 ± 8	101 ± 6	14 ± 2	16 ± 4	11 ± 5	86 ± 8	78 ± 14

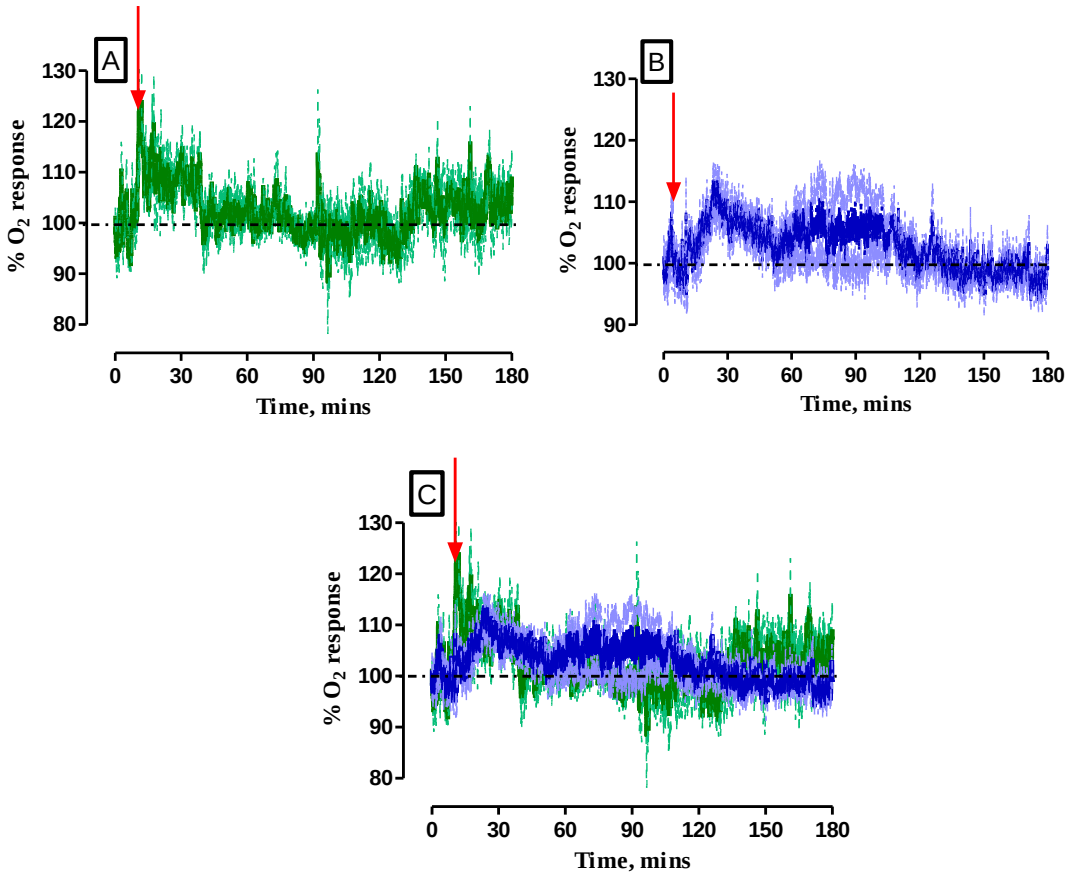

Figure 6.3.4.3.2: Averaged percentage raw data current response of the O_2 sensors implanted in the striatum of: (A) PINK1 humanised mice (*n* = 3, green trace), (B) NOD SCID mice (*n* = 5, blue trace), (C) overlay of humanised (green trace) vs. NOD SCID (blue trace) percentage current response following a 50 mg/kg Diamox i.p. injection. Point of injection is represented by the red arrow. The green trace indicates the mean percentage PINK1 current response with the percentage error represented by the light green trace. The blue trace indicates the mean percentage NOD SCID current response with the percentage error represented by the light blue trace. Data represented as mean percentage current ± SEM.

6.3.4.4 24-hour Amperometric Recordings of O_2

Figure 6.3.4.4.1A illustrates how a variation in O_2 levels was exhibited in PINK1 mice when compared to their non-humanised counterparts (see Section 5.3.2.7) during a 24-hour cycle. Throughout the light cycle, O_2 levels are increased slightly above baseline levels. It is important to note that these levels never returned to baseline concentration levels before the start of the night cycle as seen in the non-humanised group. It is important to note that PINK1 graft do not contain their own vasculature. However, the cells contained within this humanised graft are still

functioning normally throughout a 24-hour period. This homeostatic functioning is maintained by the delivery of O_2 from the surrounding host tissue to the graft which allows for cellular demands by the graft to be met. Therefore, it could be postulated that O_2 levels deviate above baseline throughout the light cycle due to the increased demand for O_2 driven by the transplanted graft, in addition to, the demand by the host tissue for O_2 supply. Additionally, it could also be suggested that if there is decreased utilisation of O_2 by PINK1 cells, it would further attribute to the higher level of O_2 experienced during the light cycle in humanised animals. However, it also cannot be ruled that the animals displayed increased motor activity during these recordings which lead to this increased current but usually they are inactive during this light period.

Furthermore, PINK1 O_2 concentrations recorded throughout the night cycle exhibit a similar trend to O_2 levels measured in non-humanised mice whereby an increase in O_2 is exhibited (see Section 5.3.2.7). Any increases in tissue O_2 seen during the light cycle may be masked during the night cycle due to the increased activity of the animal. With this increased activity comes a large increase in CBF and O_2 utilisation by cells, both in the graft and in the host, resulting in any small variations in O_2 utilisation or supply to be disguised. Nevertheless, the above results indicate that an evident difference exists between O_2 levels measured in the striatum of PINK1 and non-humanised mice over the light cycle.

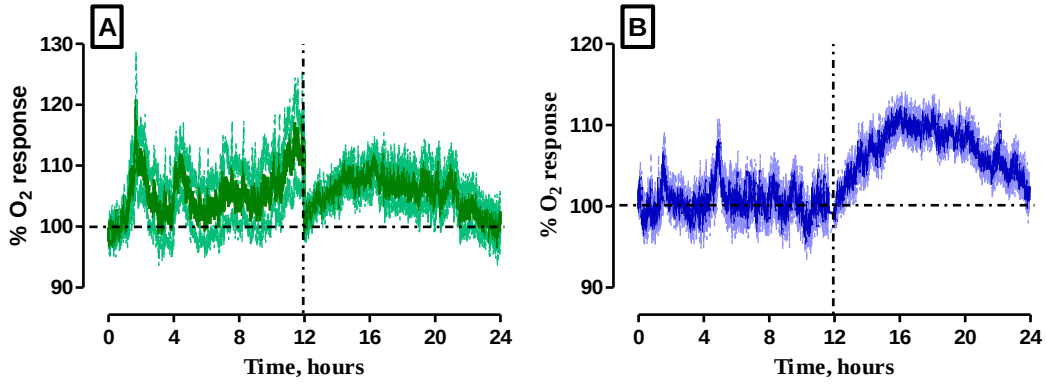

Figure 6.3.4.4.1: Averaged 24-hour percentage current response measured by O_2 sensors implanted in the striatum of (A) humanised PINK1 mice (green trace) during the light phase (*n* = 19/8, 0 - 12 hours) and the dark phase (*n* = 31/8, 13 - 24 hours) and of (B) NOD SCID mice (blue trace) during the light phase (*n* = 14/5, 0 - 12 hours) and the dark phase (*n* = 20/5, 13 - 24 hours). The green trace indicates the mean percentage PINK1 O_2 current response with the percentage error represented by the light green trace. The blue trace indicates the mean percentage mean NOD SCID O_2 current response with the percentage error represented by the light blue trace. Data represented as mean percentage current ± SEM.

6.3.4.5 IHC Staining of the Transplanted Striatum

The below images display the channel of the implanted sensors and the integrated PINK1 graft in the mouse striatum. The diameter of the surviving graft is also visible by the red scale bar. Moreover, the diameter of the surviving humanised PINK1 grafts obtained was between 200 µm and 500 µm. Each graft showed excellent three-dimensional integration in the host striatum which is indicated by the neurite outgrowth visible in Figure 6.3.4.5.1. The image below illustrates the implantation of the sensor in the graft, therefore, confirming that measurements are being taken from inside an area surrounded by transplanted patient-derived PD cells.

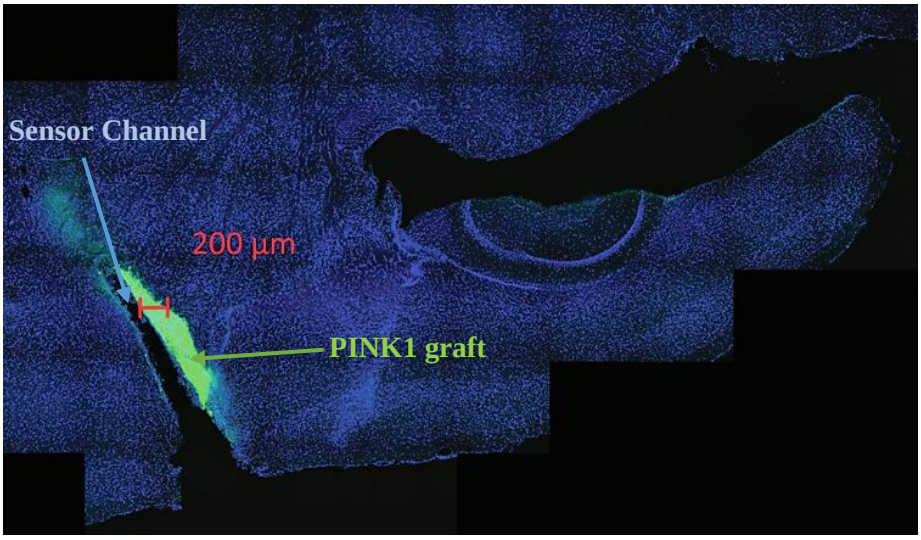

Figure 6.3.4.5.1: Typical examples of IHC images highlighting placement of the implanted sensor in relation to the transplanted graft in the striatum of humanised PINK1 mice. Red scale bar indicates the diameter of the graft.

Furthermore, the images below highlight the PINK1 graft which has integrated into the host striatum as indicated by the neurite outgrowth. The sensor channel appears larger in the next image on the right hand side, than it actually was due to difficulties experienced during the removal of the amperometric headpiece, which houses the sensors, following completion of O_2 amperometric recordings. The removal of the headpieces following transcardial perfusion is a complex manual task. Although great care was take to prevent any damage to the fixed brains, some sensor channels did appear bigger than they were during amperometric investigations.

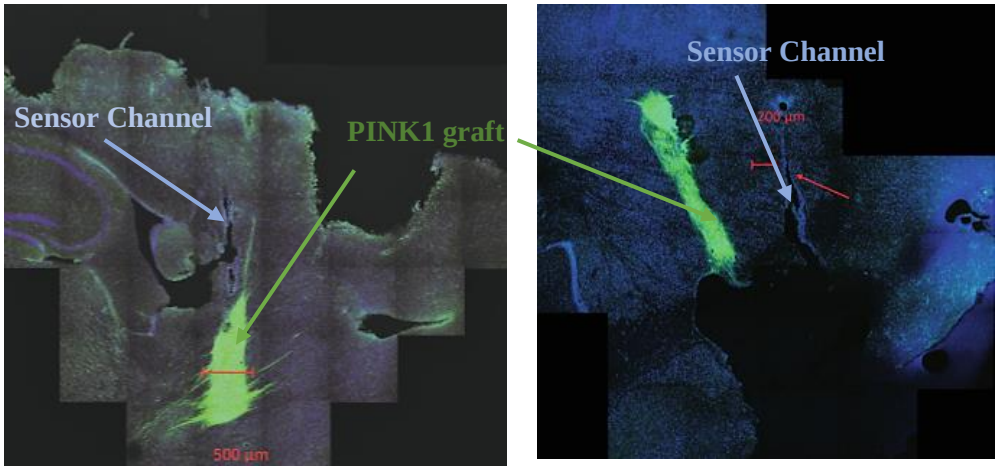

Figure 6.3.4.5.2: Typical examples of IHC images highlighting placement of the implanted sensor in relation to the transplanted graft in the striatum of humanised PINK1 mice. Red scale bar indicates the diameter of the graft.

6.3.5 O_2 Measurements in Humanised Mice Transplanted with WT Cells

6.3.5.1 Saline Administration

WT cells were transplanted into the striatum of NOD SCID animals allowing for a control group to be established. Thus, this allowed for a direct comparison between the humanised cohorts (Section 6.3.1.6). Saline was administered as a control i.p. injection to WT animals similar to that previously described in Section 6.3.4.1. Figure 6.3.5.1.1A details the average raw data current response obtained following saline administration. The systemic administration of 1 mL/kg saline resulted in a (ΔI) of 12 ± 1 nA (n = 8) from baseline levels of 81 ± 6 nA (n = 8). This change occurred 1 ± 0.2 mins (n = 8) following administration with a significant difference ($p < 0.001$) being observed between the change in the amperometric current and baseline currents. The resulting change in the amperometric signal following saline administration corresponded to a 17 ± 3 % (n = 8) change in current and a concentration change of 14 ± 2 µM (n = 8) before a return to baseline currents (82 ± 5 nA, n = 8) after 77 ± 4 mins (n = 8). Moreover, no significant difference (p = 0.46) in pre- and post-perturbation baseline currents was recorded.

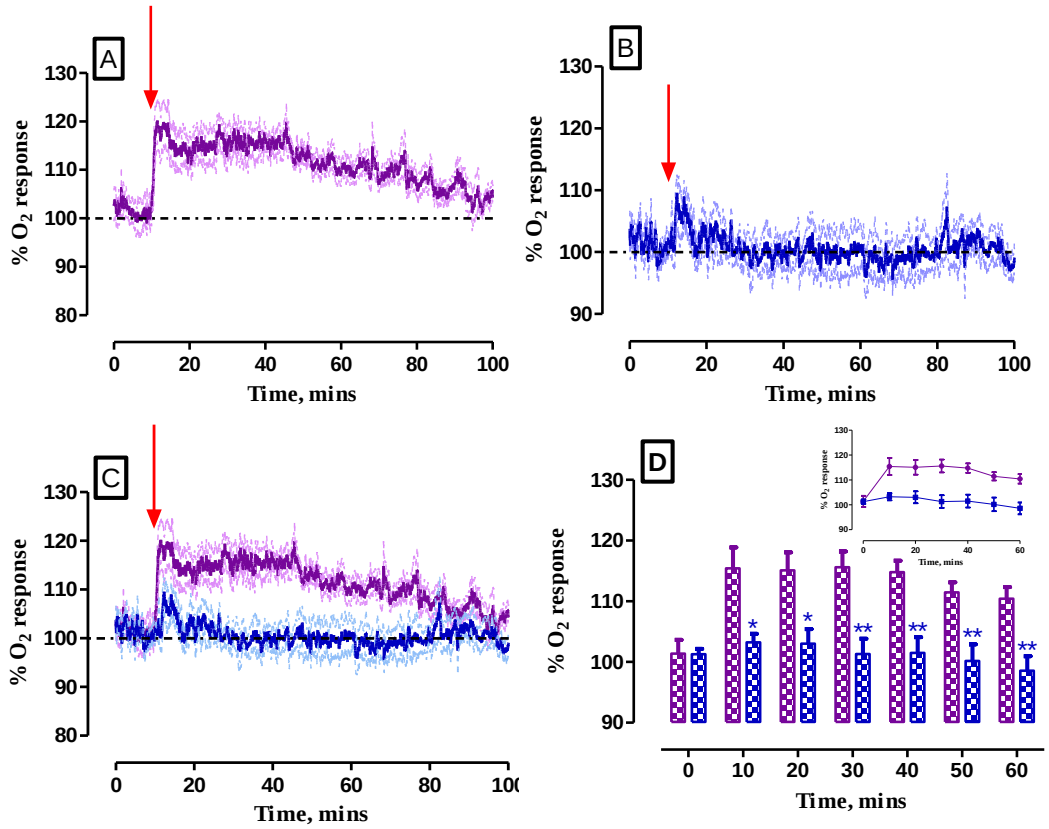

Figure 6.3.5.1.1: Averaged percentage raw data current response of the O_2 sensors implanted in the striatum of: (A) WT humanised mice (*n* = 8, purple trace), (B) NOD SCID mice (*n* = 6, blue trace), (C) overlay of humanised (purple trace) vs. NOD SCID (blue trace) percentage current response following 1 mL/kg saline i.p. injection. Point of injection is represented by the red arrow. The purple trace indicates the mean percentage WT current response with the percentage error represented by the light purple trace. The blue trace indicates the mean percentage NOD SCID current response with the percentage error represented by the light blue trace. (D) Bar graph comparing 10-minute time bins of percentage current responses. *Inset*: Time bin analysis of 70-minute raw percentage data current responses. Data represented as mean percentage current ± SEM. * denotes the level of significance.

Table 6.3.5.1.1: Summary of results of the O_2 sensors implanted in the striatum of humanised WT mice following i.p. administration of 0.9 % saline (*n* = 8).

Saline Injection						
Pre-Perturbation Baseline (nA)	**Max Current (nA)**	**Current Change (nA)**	**Current Change (%)**	**Max Response Time (mins)**	**Post-Perturbation Baseline (nA)**	**Return to Baseline Time (mins)**
81 ± 6	94 ± 5	12 ± 1	17 ± 3	1 ± 0.2	82 ± 5	77 ± 4

Section 6.3.2.1 discussed a disparity in the temporal response of saline administration recorded in NOD SCID mice and PINK1 transplanted mice. Post-perturbation baseline currents returned after a much longer period in humanised PD mice. Likewise, a similar difference in temporal responses was recorded in NOD SCID and WT mice following an i.p. injection of saline. Figure 6.3.5.1.1C displays the responses from both cohorts of animals overlaid which clearly highlights this temporal discrepancy. To further elucidate this disparity, time bin analysis was conducted to quantify this response (Figures 6.3.5.1.1D, Table 6.3.5.1.2). Time bin analysis was performed over a 60-minute time frame to allow for a direct comparison of the response of non-humanised and humanised WT mice to be made. Notably, significant differences were found between the NO responses obtained from the two cohorts between t = 10 mins and t = 60 mins.

Table 6.3.5.1.2: Statistical analysis of NO recording obtained in the striatum of humanised WT mice (*n* = 8) and non-humanised NOD SCID mice (*n* = 6) following 1 mL/kg saline administration.

Saline					
	WT (*n* = 8)		NOD SCID (*n* = 6)		
Time, mins	**Mean, %**	**SEM**	**Mean, %**	**SEM**	***p***
0	101.4	2.3	101.3	0.9	0.97
10	115.4	3.4	103.2	1.4	0.01
20	115.1	3.0	103.0	2.4	0.01
30	115.6	2.6	101.3	2.5	0.002
40	114.8	1.9	101.5	2.6	0.001
50	111.5	1.7	100.2	2.7	0.003
60	110.4	1.9	98.6	2.4	0.002

Therefore, it is apparent that a clear temporal difference exists between the saline response recorded in NOD SCID and WT animals. The response in WT mice remains elevated for a much longer time frame, as verified by time bin analysis. A similar phenomenon was previously discussed in Section 6.3.1.4.1, whereby a temporal disparity in O_2 levels was observed in humanised PINK1 animals when compared to non-humanised animals following saline administration. Due to the measurement of tissue O_2 existing as a balance between supply of O_2 from vasculature and utilisation by surrounding cells, it can be postulated that humanised mice may have an increased rate of O_2 utilisation or there is an increase in the supply of O_2 following saline administration.

The humanised graft requires O_2 to survive *in vivo*. However, the transplanted graft must obtain O_2 from the surrounding host striatum due to the lack of vasculature present in the humanised graft. Therefore, to meet the additional O_2 demand of the transplant, the rate of CBF may increase while utilisation remains constant leading to this elevated level of O_2. Likewise, this increased O_2 level in WT mice may be due to an increase in O_2 utilisation by WT cell lines coupled with increased rate in CBF to meet cellular O_2 demand. Hence, leading to this measured elevation in O_2 over a prolonged period. As the amperometric returns to baseline steadily after a 100-minute period, it appears the most plausible reasoning for the elevated levels of O_2 exhibited is that humanised WT cells display a higher rate of O_2 utilisation coupled with an increased rate in the supply of O_2 to the humanised graft. The reason being that O_2

remains tightly regulated in the brain with a return to baseline levels only being exhibited when O_2 supply returns to a homeostatic state and utilisation by the cells remains constant. This is clearly portrayed in the case of chloral hydrate administration in Section 5.3.2.3. It was observed following chloral hydrate administration that O_2 utilisation was significantly decreased as the animal was anaesthetised. As O_2 supply remained constant, an increase in O_2 amperometric response was observed. However, as O_2 is tightly regulated in the brain, the rate of O_2 supply was reduced prior to utilisation increasing as the animal began to wake up, leading to a return of the amperometric signal to baseline. It is also worth mentioning that this trend in O_2 signal is similar to restraint tests (Section 5.3.2.5) and Diamox administration (Section 5.3.2.4) performed in non-humanised NOD SCID mice.

6.3.5.2 Restraint Test

Similar to Section 6.3.5.1, a comparison was made between humanised WT mice and non-humanised NOD SCID mice following a 2-minute restraint. Figure 6.3.5.2.1A - C illustrates the average raw data current response obtained in both cohorts following the conductance of a restraint test. It was found that a (ΔI) of 26 ± 4 nA (n = 4) was attained from pre-perturbation baseline (89 ± 2 nA, n = 4) after 2 ± 0.3 mins (n = 4) in WT mice. This change in current corresponded to a 29 ± 4 % (n = 4) and a concentration change of 29 ± 4 µM (n = 4). In addition, a significant difference (p < 0.001) was noted between the change in the amperometric current and pre-perturbation baseline levels. A post-perturbation baseline (88 ± 2 nA, n = 4) was reached after 71 ± 4 mins (n = 4). This new post-perturbation baseline was found to not be significantly different (p = 0.22) from pre-perturbation levels.

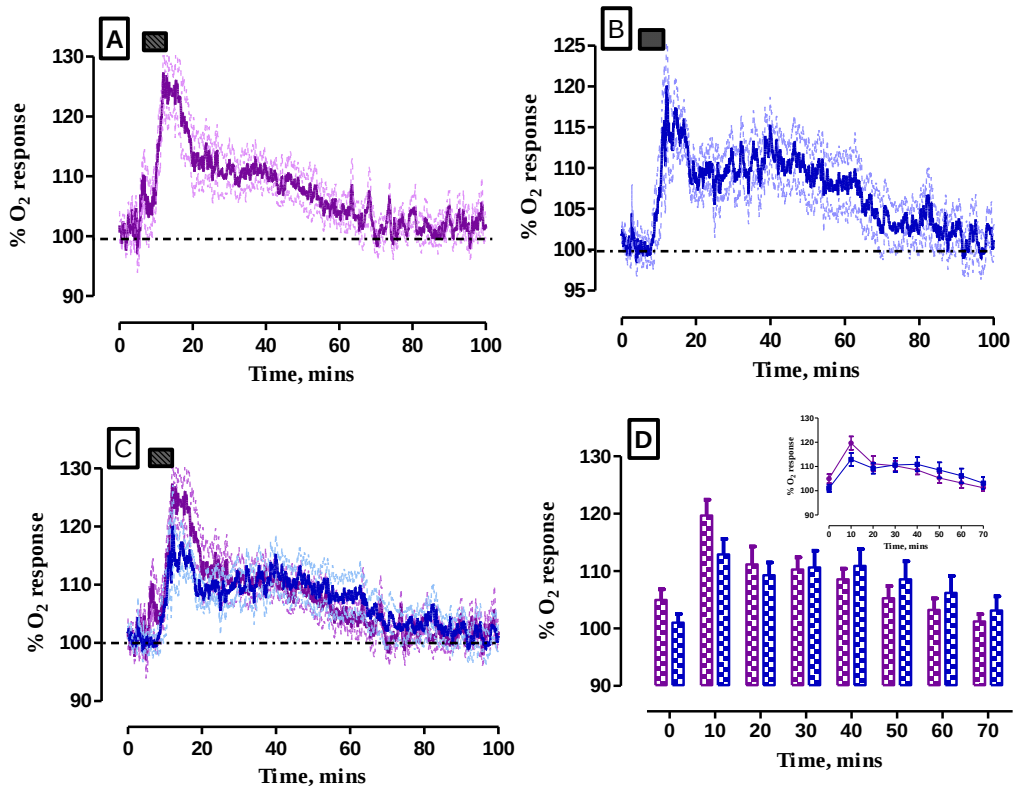

Figure 6.3.5.2.1: Averaged percentage raw data current response of the O_2 sensors implanted in the striatum of: (A) WT humanised mice (*n* = 4, purple trace), (B) NOD SCID mice (*n* = 4, blue trace), (C) overlay of humanised WT (purple trace) vs. NOD SCID (blue trace) percentage current response following 2-minute restraint test. Duration of the 2-minute restraint is represented by the dark grey box. The purple trace indicates the mean percentage WT current response with the percentage error represented by the light purple trace. The blue trace indicates the mean percentage NOD SCID current response with the percentage error represented by the light blue trace. (D) Bar graph comparing 10-minute time bins of percentage current responses. *Inset*: Time bin analysis of 80-minute raw percentage data current responses. Data represented as mean percentage current ± SEM.

Table 6.3.5.2.1: Summary of results of the O_2 sensors implanted in the striatum of humanised WT mice following 2-minute restraint test (*n* = 4).

Restraint						
Pre-Perturbation Baseline (nA)	**Max Current (nA)**	**Current Change (nA)**	**Current Change (%)**	**Max Response Time (mins)**	**Post-Perturbation Baseline (nA)**	**Return to Baseline Time (mins)**
89 ± 2	116 ± 4	26 ± 4	29 ± 4	2 ± 0.3	88 ± 2	71 ± 4

Unlike Section 6.3.5.1, no temporal disparity seemed to exist between the O_2 amperometric response recorded in both cohorts. From Figure 6.3.5.2.1C, a comparable trend can be observed with each of the responses returning within an 80-minute timeframe. Time bin analysis was performed on the data attained from each animal group to further quantify this O_2 response. Performance of time bin analysis indicated that no significant differences existed between the O_2 response in humanised WT and non-humanised animals. There was a large increase in O_2 recorded at t = 10 mins which is representative of an increase in O_2 being supplied to the graft.

Table 6.3.5.1.2: Statistical analysis of NO recordings obtained in the striatum of humanised WT mice (*n* = 4) and non-humanised NOD SCID mice (*n* = 4) following a 2-minute restraint test.

Restraint					
	WT (*n* = 4)		NOD SCID (*n* = 4)		
Time, mins	**Mean, %**	**SEM**	**Mean, %**	**SEM**	***p***
0	105.0	1.8	101.0	1.5	0.11
10	119.7	2.8	112.9	2.7	0.10
20	111.2	3.1	109.3	2.2	0.62
30	110.3	2.1	110.6	2.9	0.92
40	108.6	1.8	110.9	2.9	0.52
50	105.3	2.1	108.6	3.2	0.41
60	103.2	2.0	106.2	2.9	0.43
70	101.2	1.3	103.1	2.5	0.53

These results are in contrast to the results presented in Section 6.3.4.2 whereby a significant difference was reported in O_2 levels following a restraint test between PINK1 and non-humanised NOD SCID mice at t = 20 mins and t = 30 mins. Therefore, it can be confirmed that that restraint tests sustain neuronal activation over a more prolonged period of time. In contrast, saline administration would only induce neuronal activation transiently in the mouse tissue. However, neuronal activation is prolonged in a restraint test. It is obvious from Figure 6.3.5.2.1B that an elevated increase in O_2 is experienced in the host striatum during this period. Therefore, any effects of the graft in humanised mice are masked by the substantial O_2 increase by the host mouse tissue. Due to the lack of vasculature in the humanised graft, this overall increase in O_2 may be so great in the whole mouse brain that it overrides the

detection of any changes in utilisation by the transplanted cells. Moreover, any increase in O_2 delivery to the graft would be utilised by the murine tissue concurrently. The transplanted graft is small in comparison to the brain so therefore any substantial increases in O_2 supply or utilisation in the host brain will mask any changes in O_2 utilisation by the transplanted graft. Therefore, this may be a reason for the comparable O_2 response recorded in humanised WT and in non-humanised NOD SCID mice following a 2-minute restraint test.

Additionally, it is important to highlight the close resemblance in the temporal profiles recorded following saline administration and restraint tests in the WT cell lines which would support the saline response being indicative of increased O_2 supply and utilisation by the humanised graft. The time duration over which O_2 levels remain elevated is quite striking.

6.3.5.3 Signal Validation – L-NAME and Diamox

A clear decrease in the recorded O_2 signal following L-NAME administration is shown in Figure 6.3.5.3.1A. This decrease in current (ΔI, 21 ± 4 nA, n = 7) led to a percentage current decrease of 21 ± 2 % (n = 7) being obtained after 57 ± 22 mins (n = 7). This decrease in amperometric signal was found to be significantly different (p < 0.01) from baseline currents (98 ± 14 nA, n = 7). Additionally, this decrease corresponded to a concentration change of 23 ± 4 µM (n = 7) before baseline current levels (88 ± 12 nA, n = 7) resumed after 238 ± 55 mins (n = 7). Moreover, Figure 6.3.5.3.1C highlights that the response recorded in WT animals is comparable to the response obtained in NOD SCID mice following systemic L-NAME administration. Therefore, confirmation that the O_2 sensor responds to varying changes in O_2 in the striatum of transplanted WT subjects has now been confirmed.

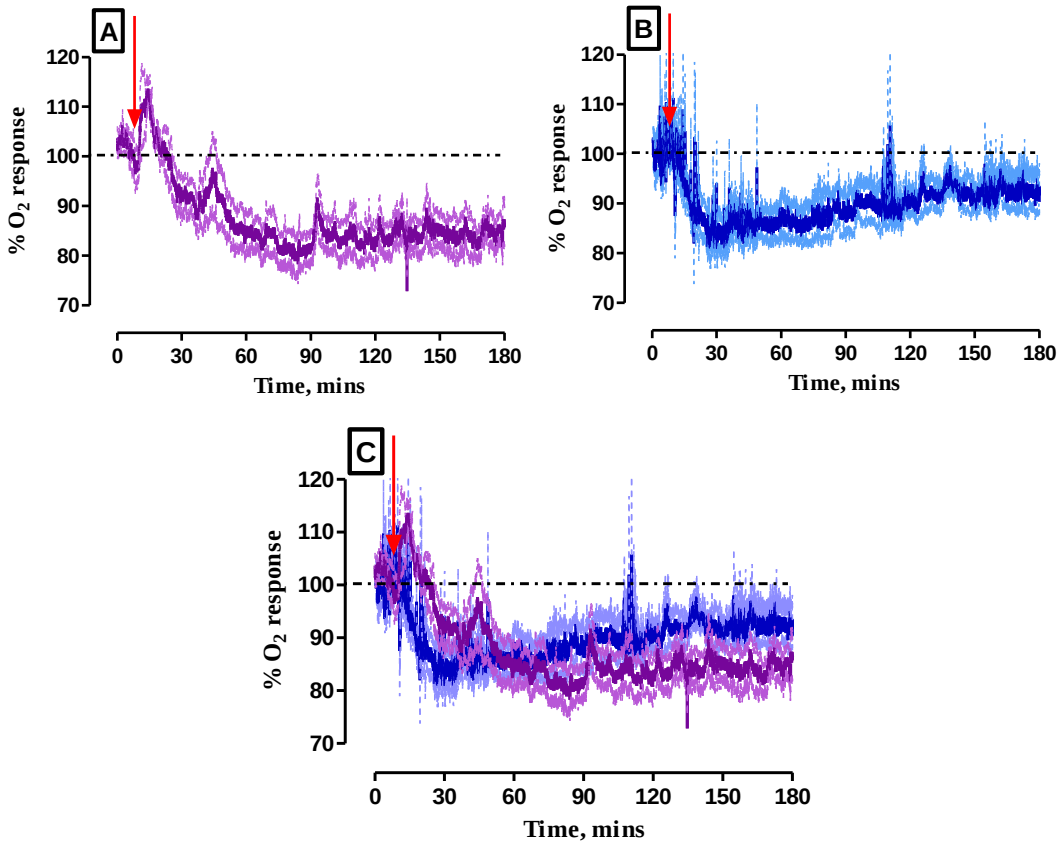

Figure 6.3.5.3.1: Averaged percentage raw data current response of the O_2 sensors implanted in the striatum of: (A) WT humanised mice (*n* = 7, purple trace), (B) NOD SCID mice (*n* = 5, blue trace), (C) overlay of humanised (purple trace) vs. NOD SCID (blue trace) percentage current response following 1 mL/kg i.p. injection of 30 mg/kg L-NAME. Point of injection is represented by the red arrow. The purple trace indicates the mean percentage WT current response with the percentage error represented by the light purple trace. The blue trace indicates the mean percentage NOD SCID current response with the percentage error represented by the light blue trace. Data represented as mean percentage current ± SEM.

Table 6.3.5.3.1: Summary of results of the O_2 sensors implanted in the striatum of WT humanised mice following a 1 mL/kg i.p. injection of 30 mg/kg L-NAME (*n* = 7).

L-NAME Injection						
Pre-Perturbation Baseline (nA)	**Max Current (nA)**	**Current Change (nA)**	**Current Change (%)**	**Max Response Time (mins)**	**Post-Perturbation Baseline (nA)**	**Return to Baseline Time (mins)**
98 ± 14	78 ± 12	-21 ± 4	-22 ± 2	57 ± 22	88 ± 12	238 ± 55

The response of the O_2 sensor to systemic administrations of Diamox in WT cell lines is illustrated in Figure 6.3.5.3.2A, whereby a characteristic increase is displayed. Following administration of Diamox, a (ΔI) of 21 ± 6 nA (n = 7) was obtained from a baseline current of 103 ± 17 nA (n = 7). Furthermore, this current change occurred after 19 ± 6 mins (n = 7) and equated to a percentage change of 20 ± 3 % (n = 7). A significant difference (p < 0.01) was found between pre-injection baseline currents and the maximum current change resulting from Diamox administration. A new post-injection baseline (105 ± 18 nA, n = 7) resulted after 68 ± 14 mins (n = 7) which was not significantly different (p = 0.30) from pre-injection baseline levels. Additionally, a comparable response is seen following Diamox administration in NOD SCID mice (Figure 6.3.5.3.2B) which is further discussed in Section 5.3.2.4. By overlaying the responses from both animal groups, it is clearly evident that comparable responses were obtained from both animal cohorts indicating that the O_2 sensor is able to efficiently detect changes in tissue O_2 in the WT cohort. Therefore, efficient functioning of the O_2 sensor has now been confirmed in the striatum of WT transplanted mice.

Furthermore, it is interesting to note that the Diamox response obtained bears a striking similarities to the saline and restraint responses in the WT cohort. Collectively, these findings support an increase in O_2 supply to the humanised graft during period of neuronal activation to address an increased cellular energy demand.

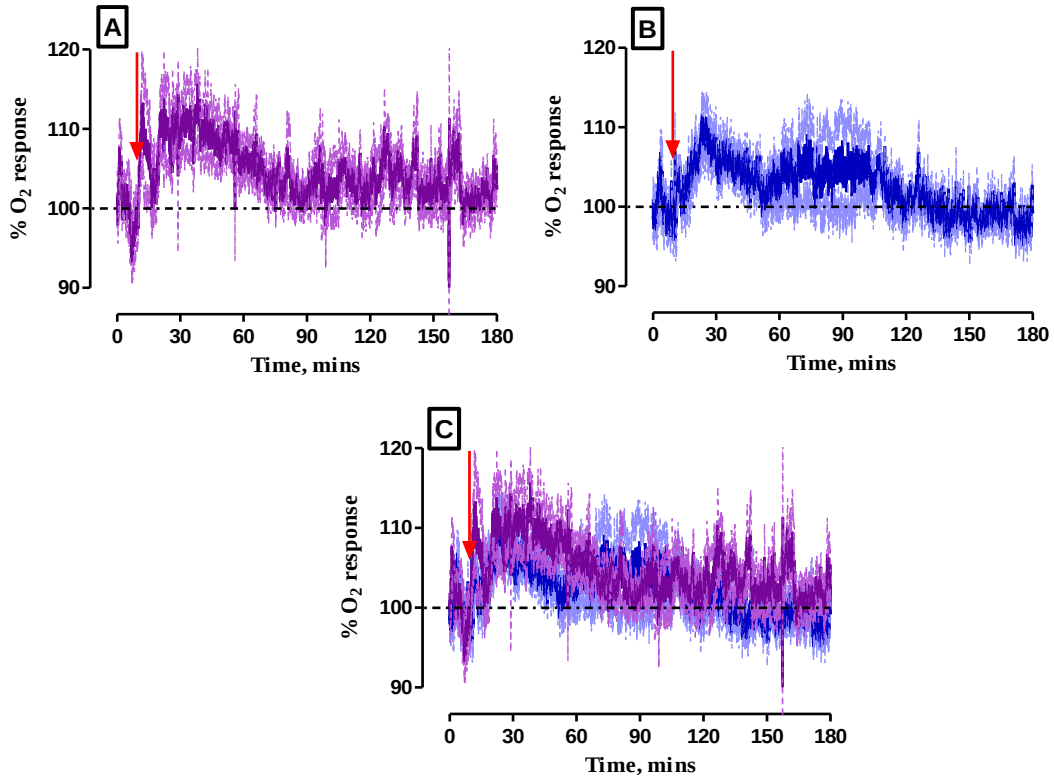

Figure 6.3.5.3.2: Averaged percentage raw data current response of the O_2 sensors implanted in the striatum of: (A) WT humanised mice (*n* = 7, purple trace), (B) NOD SCID mice (*n* = 6, blue trace), (C) overlay of humanised (purple trace) vs. NOD SCID (blue trace) percentage current response following 1 mL/kg i.p. injection of 50 mg/kg Diamox. Point of injection is represented by the red arrow. The purple trace indicates the mean percentage WT current response with the percentage error represented by the light purple trace. The blue trace indicates the mean percentage NOD SCID current response with the percentage error represented by the light blue trace. Data represented as mean percentage current ± SEM.

Table 6.3.5.3.2: Summary of results of the O_2 sensors implanted in the striatum of WT humanised mice following a 1 mL/kg i.p. injection of 50 mg/kg Diamox (*n* = 7).

Diamox Injection						
Pre-Perturbation Baseline (nA)	**Max Current (nA)**	**Current Change (nA)**	**Current Change (%)**	**Max Response Time (mins)**	**Post-Perturbation Baseline (nA)**	**Return to Baseline Time (mins)**
103 ± 17	125 ± 22	21 ± 6	20 ± 3	19 ± 6	105 ± 18	68 ± 14

6.3.5.4 24-hour Amperometric Recordings of O_2

Figure 6.3.5.4.1A illustrates a similar trend in the amperometric O_2 response recorded in WT and NOD SCID mice. During the light cycle, a comparable O_2 response can be seen in the two cohorts whereby O_2 levels remain at basal levels. This is not surprising as the light cycle is usually associated with decreased motor activity of the animal resulting in reduced neuronal activation during this 12-hour period. In addition, O_2 levels recorded during the night cycle showed comparable levels of O_2 being detected in WT transplanted mice and NOD SCID subjects. Both of these experimental groups displayed an increase in O_2 levels throughout the night cycle. This increase can be attributed to increased neuronal activation resulting from the increased movement of the animal. Therefore, the above results indicate that a comparable trend in O_2 levels exists in each cohort throughout a 24-hour period. It is important to state that the detection of any alterations in O_2 dynamics in the transplanted graft may be difficult as any overall alterations in O_2 in the mouse brain may mask any O_2 increases or decreases that may exist in the mouse brain. This is similar to the phenomenon discussed in Section 6.3.5.2 whereby a comparable O_2 response was detected in WT and NOD SCID animals following a 2-minute restraint.

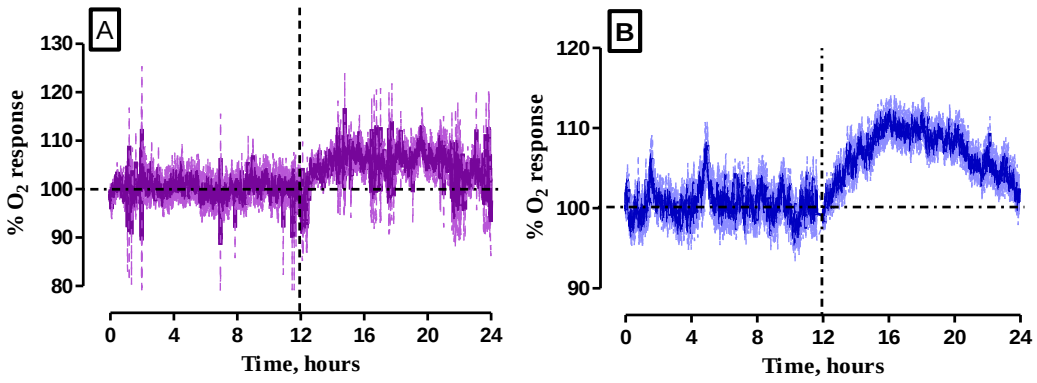

Figure 6.3.5.4.1: Averaged 24-hour percentage current response measured by O_2 sensors implanted in the striatum of (A) humanised WT mice (purple trace) during the light phase (*n* = 19/7, 0 - 12 hours) and the dark phase (*n* = 20/7, 13 - 24 hours) and of (B) NOD SCID mice (blue trace) during the light phase (*n* = 14/5, 0 - 12 hours) and the dark phase (*n* = 20/5, 13 - 24 hours). The purple trace indicates the mean percentage WT O_2 current response with the percentage error represented by the light purple trace. The blue trace indicates the mean percentage mean NOD SCID O_2 current response with the percentage error represented by the light blue trace. Data represented as mean percentage current ± SEM.

6.3.5.5 IHC Staining of the Transplanted Striatum

Typical images of immunohistochemical staining of the striatum of NOD SCID mice transplanted with humanised WT cell is illustrated in Figure 6.3.5.5.1. The below images indicate that the sensor was implanted into the middle of the humanised graft allowing for amperometric measurements to be directly influenced by the surrounding humanised cells. Additionally, the size of the graft shows good survival following *in vivo* transplantation. Survival of the graft is ensured by good neurite outgrowth exhibited into the host striatal tissue. The integration of the xenotransplanted graft is vital to its survival as it allows for the supply of substances such as O_2 and other vital nutrients to the grafted cells. This ensures that the cellular demands humanised tissue are met and so, maintaining homeostatic functioning.

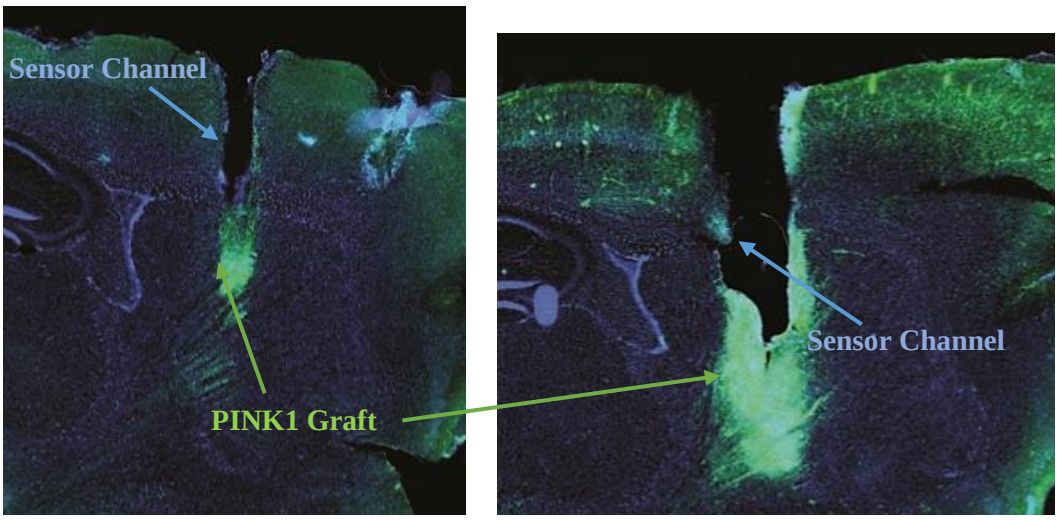

Figure 6.3.5.5.1: Typical examples of IHC images highlighting placement of the implanted sensor in relation to the transplanted graft in the striatum of humanised WT mice.

6.3.6 Comparison of O_2 Measurements Conducted in PINK1, WT and SHAM Mice.

6.3.6.1 Saline Administrations

Figure 6.3.6.1.1A illustrates the recorded O_2 concentration changes recorded in humanised and SHAM mice following an i.p. injection of saline. From Figure 6.3.6.1.1A, it is clear that following the systemic administration of saline, tissue O_2 levels increase substantially in all three cohorts. This increase can be attribute to increased neuronal activation coupled with an increase in CBF. However, disparities

in the amperometric O_2 response between the three animal groups begin to arise following this initial increase. Measurements conducted in WT mice display a higher O_2 concentration which remained elevated over a 90-minute period while tissue O_2 concentrations in PINK1 and SHAM mice are reported to slowly return to baseline over a shorter timeframe. However, it is important to note that the magnitude of the O_2 responses measured in PINK1 and SHAM mice is much smaller than what was observed in WT cell lines. Therefore, highlighting an obvious disparity in the O_2 amperometric response recorded between the animal groups.

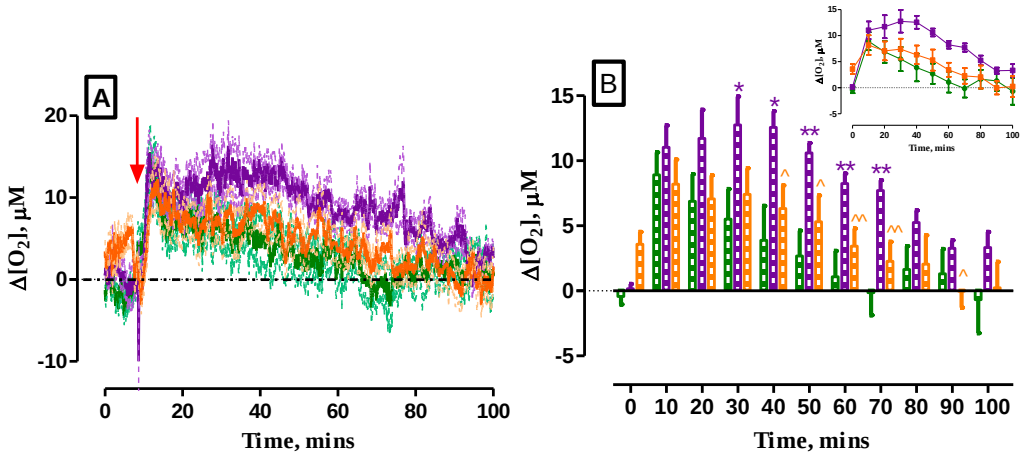

Figure 6.3.6.1.1: (A) Overlay of the average Δ[O_2] recorded using O_2 sensors implanted in the striatum of humanised PINK1 (*n* = 8), WT (*n* = 8) and SHAM (*n* = 7) mice following a 1 mL/kg saline i.p. injection. Red arrow indicates the point of injection. The mean PINK1 Δ[O_2] is represented by the green trace and the percentage error is represented by the light green trace. The mean WT Δ[O_2] is represented by the purple trace and the percentage error is represented by the light purple trace. The mean SHAM Δ[O_2] is represented by the orange trace and the percentage error is represented by the light orange trace. (B) Bar graph comparing 10-minute time bin analysis of Δ[O_2] following a 1 mL/kg saline i.p. injection. * denotes the level of significance between PINK1 and WT mice. ^ denotes the level of significance between WT and SHAM mice. Data represented as mean Δ [O_2] ± SEM.

Time bin analysis was conducted on the amperometric signals obtained from humanised and SHAM mice to closely examine and quantify any disparities that may exist between the three cohorts (Table 6.3.6.1.1). Figure 6.3.6.1.1B highlights the time bin analysis conducted by averaging 10-minute intervals from the raw trace data. As new baseline levels were reached within a 90-minute window in the three animal groups, statistical analysis was included in this section up until t = 90 mins.

Table 6.3.6.1.1: Statistical analysis of O_2 results implanted in the striatum of PINK1 (*n* = 8), WT mice (*n* = 8) and SHAM mice (*n* = 7) following 1 mL/kg saline i.p. administration.

Saline									
	PINK1 (*n* = 8)		WT (*n* = 8)		SHAM (*n* = 7)		WT *vs.* PINK1	WT *vs.* SHAM	PINK1 *vs.* SHAM
Time (mins)	Mean (µM)	SEM	Mean (µM)	SEM	Mean (µM)	SEM	*p*	*p*	*p*
0	-0.5	0.6	0.1	0.4	3.6	0.9	0.42	0.005	0.004
10	8.9	1.7	11.0	1.7	8.2	1.9	0.40	0.29	0.78
20	6.9	2.1	11.7	2.2	7.1	1.8	0.14	0.13	0.95
30	5.5	2.3	12.8	2.2	7.4	2.0	0.04	0.09	0.54
40	3.9	2.7	12.6	1.2	6.3	1.8	0.01	0.01	0.46
50	2.7	1.9	10.6	0.7	5.3	2.0	0.002	0.03	0.37
60	1.1	2.0	8.3	0.8	3.4	1.3	0.006	0.009	0.36
70	-0.1	1.7	7.7	0.8	2.3	1.5	0.001	0.007	0.32
80	1.6	1.8	5.3	0.9	2.1	2.0	0.10	0.21	0.86
90	1.3	1.9	3.3	0.6	-0.03	1.3	0.34	0.04	0.58

Following increased neuronal activation associated with i.p. administration, an increase in CBF is experienced to meet the increased cellular demand of the surrounding cells. However, this response is typically transient in non-humanised NOD SCID mice due to the tight regulation of O_2 by the brain. Thus, once neuronal activation is reduced, the brain signals for the rate of CBF to be decreased to a homeostatic state resulting in the return of the amperometric signal to baseline. The humanised grafts lack vasculature following transplantation resulting in the need for O_2 delivery from the surrounding host striatum to allow for graft survival. Therefore, following the initiation of mild neuronal activation, the graft signals to increase CBF to the adjacent areas. As a result, an increase in amperometric O_2 levels was noted in Figure 6.3.6.1.1A in all three cohorts. Additionally, no significant difference was observed between each of the animal groups at t = 10 mins and t = 20 mins.

As previously observed in Section 5.3.2.1, as neuronal activation reduces, the brain signals to lower the rate of CBF. Simultaneously, cellular utilisation of O_2 is ongoing resulting in the amperometric signal returning to baseline. Firstly, by examining the comparable responses recorded in PINK1 and SHAM mice, it appears that the surgical procedure is having some effect on tissue O_2 levels following mild neuronal activation. This effect can be possibly attributed to the development of a glial scar around the area. In addition, it could be inferred that an increased O_2 demand occurs in PINK1 transplanted and SHAM mice in contrast to non-humanised NOD SCID mice. As stated previously, the xenografted tissue does not contain its own vasculature. As the graft is lacking vasculature, it can be suggested that the graft is signalling for the increased delivery of O_2 to the surrounding area. Coupled with this, a slower rate of O_2 utilisation may exist in PINK1 cells which may contribute to the elevated levels of O_2 being observed. However, this increase in O_2 does not appear over a sustained period as levels are seen to return to baseline. This would suggest that a reduced rate of O_2 utilisation exists when compared to the WT cohort as levels return quicker due to a lesser requirement for O_2 by the PINK1 graft. In contrast, the WT grafts appear to exhibit an increased rate in O_2 supply and utilisation resulting in an elevated O_2 level being observed.

By referring to Section 5.3.2.4, Diamox administration illustrated a similar trend in the O_2 amperometric response to the response seen in WT animals. However, the duration of the response was much shorter suggesting that following a reduction in O_2 delivery, O_2 utilisation remained constant leading to a return of the amperometric signal to baseline. This further supports the hypothesis that O_2 utilisation appears to be altered in PINK1 cell lines. Additionally, no significant differences were reported between the SHAM mice and humanised PINK1 mice suggesting that a reduction in O_2 utilisation exists in PD patient-derived cells.

The O_2 amperometric response recorded in WT animals was observed to remain at a much higher level following saline administration when compared to the levels attained in PINK1 and SHAM mice. Moreover, significant differences were reported to exist at t = 30 mins, t = 40 mins, t = 50 mins, t = 60 mins and t = 70 mins between WT measurements and the other 2 cohorts. A similar phenomenon may exist in humanised WT mice whereby increased cellular activity in the humanised graft following neuronal stimulation resulting in an increased cellular O_2 demand. The level

of O_2 concentrations remain elevated following neuronal activation before baseline levels slowly return over time. It could be inferred that WT cell lines demonstrate an increased rate of O_2 utilisation coupled with an increased delivery of O_2 to sustain this increased cellular functioning. Over time, the rate of CBF reduces as neuronal activation returns to a normal state coupled with a reduction in O_2 utilisation by the grafted cells. As a result, the O_2 amperometric signal returns to baseline steadily over a longer period.

Therefore, it can be postulated that a higher concentration of O_2 exists in humanised WT cells following mild neuronal stimulation when compared with PINK1 and SHAM measurements. Additionally, the comparable responses obtained in PINK1 cell line and SHAM animals suggest an alteration in O_2 utilisation. Such changes in O_2 utilisation in PD cells may be due to a phenotypic alteration which may affect energy metabolism within the respective grafts. This will be discussed in more detail in Chapter 8.

6.3.6.2 Restraint Test

Following observation of interesting results in the recorded O_2 amperometric response following saline administration, it was decided to examine the effect of a 2-minute restraint test in humanised and SHAM mice. As saline i.p. injections act as a physiological stressor, a similar O_2 response is to be expected by restraint tests, which are known to instigate neurochemical changes as previously discussed. Tests conducted on humanised animals highlighted a comparable O_2 response to that obtained in SHAM mice (Figure 6.3.6.2.1A). As seen in Sections 6.3.4.2 and 6.3.5.2, restraint tests initiate neuronal activation, thus, causing an increase in CBF. Therefore, an increase in amperometric O_2 current in all three animal cohorts can be observed. In contrast to Section 6.3.6.1, the amperometric O_2 signal is comparable thereafter but it must be noted that PINK1 O_2 levels appear to be higher at t = 40 mins when compared to the other O_2 signals obtained.

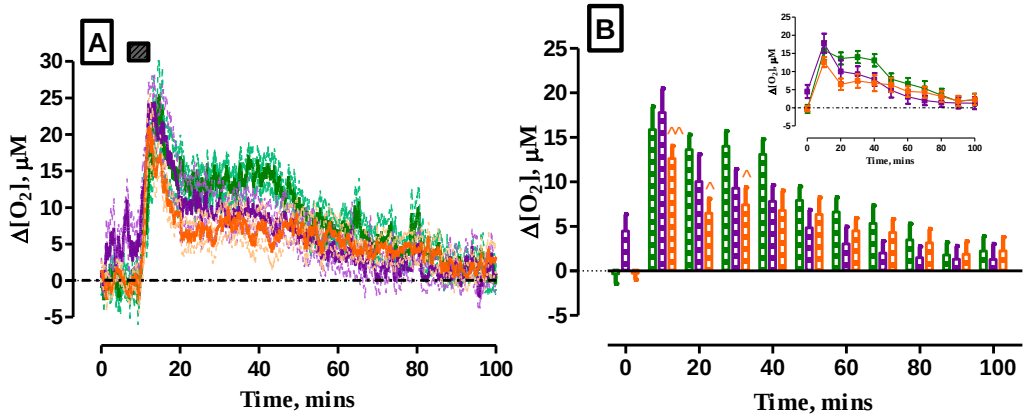

Figure 6.3.6.2.1: (A) Overlay of the average Δ[O_2] recorded using O_2 sensors implanted in the striatum of humanised PINK1 (*n* = 8), WT (*n* = 4) and SHAM (*n* = 7) mice following a 2-minute restraint. Duration of the restraint is represented by the dark grey box. The mean PINK1 Δ[O_2] is represented by the green trace and the percentage error is represented by the light green trace. The mean WT Δ[O_2] is represented by the purple trace and the percentage error is represented by the light purple trace. The mean SHAM Δ[O_2] is represented by the orange trace and the percentage error is represented by the light orange trace. (B) Bar graph comparing 10-minute time bin analysis of Δ[O_2] following a 2-minute restraint. ^ denotes the level of significance between WT and SHAM mice. Data represented as mean Δ [O_2] ± SEM.

Time bin analysis was performed on the amperometric signal obtained from humanised and SHAM mice to compare and quantify the measured O_2 response (Figure 6.3.6.2.1B, Table 6.3.6.2.1). Following this, a comparable O_2 response was measured between humanised WT animals and SHAMs due to no significant difference existing between them. Comparatively, no significant differences were obtained between the comparable O_2 response recorded in PINK1 and WT animal groups. However, it is worth mentioning that a close to significant difference exists at t = 30 mins and t = 40 mins when comparing the humanised cohorts. This may be attributed to higher levels of O_2 existing in PINK1 cohorts at these time points. Furthermore, significant differences were found at t = 20 mins, t = 30 mins and t = 40 mins when comparing O_2 measurements from PINK1 cell lines to SHAM mice even though a similar O_2 trend was exhibited in both animal groups. This suggests that altered O_2 dynamics exist in the PD patient cell line following neuronal activation.

Table 6.3.6.2.1: Statistical analysis of O_2 recordings obtained in the striatum of PINK1 (*n* = 8), WT mice (*n* = 4) and SHAM mice (*n* = 7) following a 2-minute restraint.

Restraint									
	PINK1 (*n* = 8)		WT (*n* = 4)		SHAM (*n* = 7)		WT *vs.* PINK1	WT *vs.* SHAM	PINK1 *vs.* SHAM
Time (mins)	Mean (µM)	SEM	Mean (µM)	SEM	Mean (µM)	SEM	*p*	*p*	*p*
0	-0.4	1.1	4.5	1.9	-0.3	0.7	0.03	0.01	0.97
10	15.9	2.6	17.8	2.7	12.6	1.4	0.62	0.08	0.26
20	13.6	1.7	10.0	3.1	6.5	1.6	0.29	0.28	0.006
30	14.0	1.7	9.3	2.1	7.4	1.9	0.10	0.53	0.02
40	13.1	1.7	7.8	1.8	6.8	2.2	0.05	0.74	0.04
50	7.9	1.5	4.8	2.0	6.4	1.9	0.23	0.60	0.54
60	6.6	1.6	3.0	1.9	4.5	1.4	0.17	0.54	0.33
70	5.3	2.0	2.0	1.3	4.3	1.5	0.21	0.30	0.69
80	3.5	1.8	1.5	1.2	3.1	1.6	0.41	0.46	0.89
90	1.8	1.4	1.3	1.5	1.9	1.4	0.82	0.80	0.97
100	2.2	1.7	1.3	1.7	2.3	1.5	0.70	0.69	0.99

Saline administrations also act as a physiological stressor. However, the administration of saline is a transient process whereas a restraint test is performed over a 2-minute period. Therefore, neuronal activation is induced over a longer timeframe. Additionally, the transplanted graft lacks vasculature and so delivery of O_2 is only maintained through diffusion from the surrounding host striatum. As the restraint test results in a greater level of tissue oxygenation in the mouse brain when compared to saline administration (see Section 5.3.2.5), it can be postulated that a greater influence from the murine tissue will be observed in humanised cohorts. With this elevated level of global O_2 in the mouse brain, it may mask an small deviations in O_2 demand and utilisation that may be observed in the humanised graft.

Notwithstanding this, a significant increase in PINK1 O_2 levels was observed when compared against SHAM and NOD SCID mice (see Section 6.3.4.1). This finding could be interpreted as a decrease in O_2 utilisation within the PINK1 graft

when considering the effect that was recorded in PINK1 mice following saline administration. In contrast, the other cohorts display normal O_2 utilisation resulting in lower O_2 amperometric responses. Collectively, these findings suggest that a reduced O_2 consumption may be occurring in PINK1 cell lines.

6.3.6.3 Signal Validation – L-NAME and Diamox

The influence of the characterisation compounds, Diamox and L-NAME, on O_2 concentrations was investigated in humanised cohorts (Figure 6.3.6.3.1). The effect of Diamox on O_2 levels was first compared in PINK1 and WT cell lines. It was found that no significant difference (p = 0.41) existed between the humanised animals. Therefore, these results conclude the efficiency of the O_2 sensor to detect changes in O_2 concentrations in xenotransplanted tissue.

Comparatively, no significant difference (p = 0.59) was reported in O_2 concentrations obtained between humanised animal groups following systemic administration of L-NAME. Thus, the O_2 sensor has been determined to respond to changing concentrations of O_2 in transplanted striatal tissue. To conclude, characterisation compounds have been utilised to illustrate that no significant differences exist in the ability of the O_2 sensor to detect endogenous fluctuations of O_2 in humanised PINK1 and WT mice.

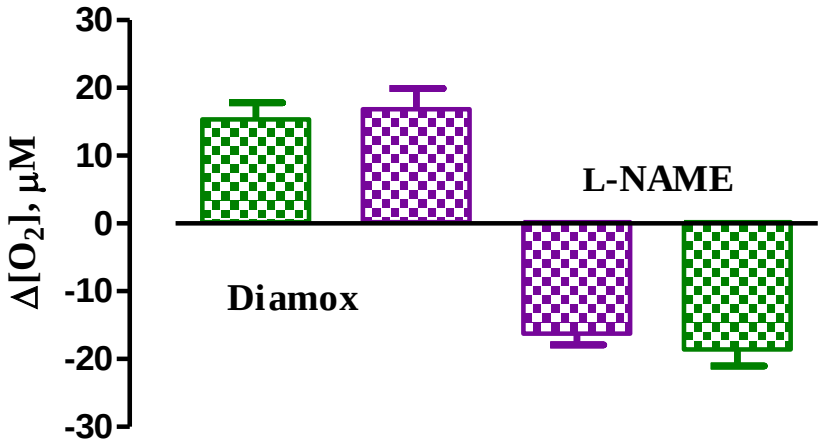

Figure 6.3.6.3.1: Bar chart of the average Δ[O_2] recorded using O_2 sensors implanted in the striatum of humanised PINK1 (green) and WT (purple) mice following a 50 mg/kg Diamox and 30 mg/kg L-NAME i.p. injection. Data represented as mean Δ [O_2] ± SEM.

6.3.6.4 24-hour Amperometric Recordings of O_2

Figure 6.3.6.4.1A displays the O_2 current recorded over the light cycle in humanised mice. A comparable trend in O_2 was detected over this 12-hour period in between PINK1, WT and SHAM mice whereby O_2 concentrations remained at basal levels. Quantification of the O_2 response over the course of the light phase was performed using time bin analysis. By means of time bin analysis (Figure 6.3.6.4.1B, Table 6.3.6.4.1), comparable O_2 concentration dynamics were detected, with no significant differences in O_2 detected between t = 1 hour and t = 10 hours in humanised transplanted mice and SHAM animals. However, it must be noted that O_2 concentrations appear to be significantly higher in WT transplanted mice at t = 0 hour which suggests that a higher O_2 concentration exists at this time point. It must also be emphasised that routine welfare checks occur during this time point which may cause the increase in O_2. Additionally, O_2 levels recorded in PINK1 cell lines appear to increase towards the end of the light cycle. It is at t = 11 hours that a significant difference was identified between PINK1 subjects and the other two cohorts. This may indicate that a difference may exist in O_2 dynamics in PINK1 cell lines prior to the beginning of the dark cycle.

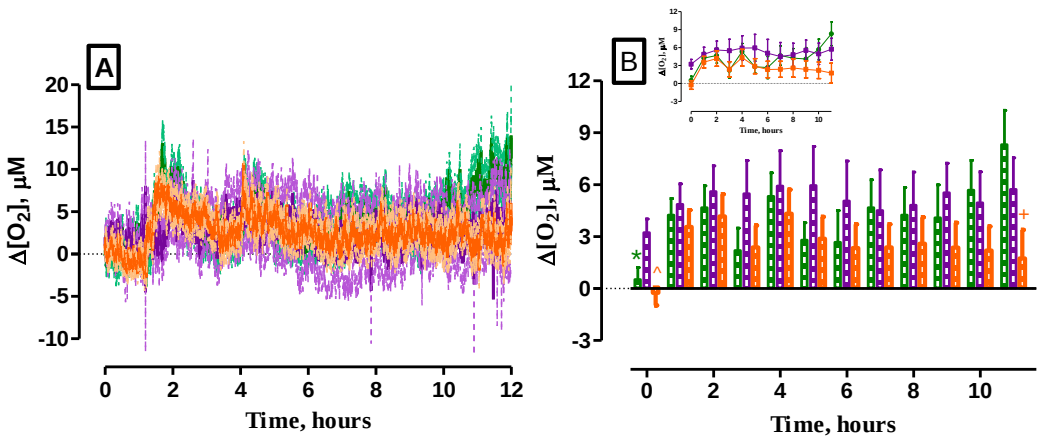

Figure 6.3.6.4.1: (A) Overlay of the averaged 12-hour Δ[O_2] measured by O_2 sensors implanted in the striatum of humanised PINK1 (green trace, *n* = 15/8), WT mice (purple trace, *n* = 20/7) and SHAM mice (orange trace, *n* = 19/7) during the light phase (0 - 12 hours). The mean PINK1 Δ[O_2] is represented by the green trace and the percentage error is represented by the light green trace. The mean WT Δ[O_2] is represented by the purple trace and the percentage error is represented by the light purple trace. The mean SHAM Δ[O_2] is represented by the orange trace and the percentage error is represented by the light orange trace. (B) Bar graph comparing 10-minute time bin analysis of Δ[O_2] over 12-hours. * denotes the level of significance between PINK1 and WT mice, ^ denotes the level of significance between WT and SHAM mice and $^+$ denotes the level of significance between PINK1 and SHAM mice. Data represented as mean Δ [O_2] ± SEM.

Table 6.3.6.4.1: Statistical analysis of O_2 results implanted in the striatum of PINK1 (*n* = 8), WT mice (*n* = 7) and SHAM mice (*n* = 7) during the light cycle.

Light Cycle Recordings									
	PINK1 (*n* = 8)		WT (*n* = 7)		SHAM (*n* = 7)		WT *vs.* PINK1	WT *vs.* SHAM	PINK1 *vs.* SHAM
Time (mins)	Mean (µM)	SEM	Mean (µM)	SEM	Mean (µM)	SEM	*p*	*p*	*p*
0	0.5	0.7	3.2	0.8	-0.2	0.7	0.02	0.003	0.47
1	4.2	1.0	4.9	1.2	3.6	1.0	0.56	0.39	0.63
2	4.7	1.3	5.6	1.5	4.2	1.3	0.65	0.47	0.79
3	2.2	1.3	5.5	1.9	2.4	1.3	0.20	0.18	0.93
4	5.3	1.4	5.9	2.0	4.3	1.4	0.83	0.52	0.63
5	2.8	1.0	6.0	2.3	2.9	1.3	0.28	0.24	0.96
6	2.7	1.8	5.1	2.3	2.3	1.4	0.46	0.31	0.88
7	4.7	1.6	4.5	2.3	2.4	1.3	0.96	0.43	0.29
8	4.2	1.6	4.8	1.9	2.6	1.5	0.83	0.37	0.48
9	4.1	1.9	5.5	1.7	2.4	1.4	0.58	0.16	0.47
10	5.7	1.7	5.0	1.8	2.2	1.4	0.78	0.23	0.13
11	8.3	2.0	5.7	1.8	1.7	1.7	0.36	0.12	0.02

The O_2 responses recorded during the night cycle highlighted a similar trend in O_2 in each of the three animal groups (Figure 6.3.6.4.2A). Concentrations of O_2 were observed to increase over the night cycle which coincides with the increased activity of the animal during this time. Furthermore, it appears that O_2 concentrations recorded in PINK1 transplanted mice decreased slightly after t = 5 hours which may suggest an alteration in O_2 dynamics during the night cycle. Time bin analysis allowed for quantitative changes in the O_2 response to be monitored (Figure 6.3.6.4.2B, Table 6.3.6.4.2). It was found that significant differences were identified at t = 0 hours and t = 1 hour between WT and PINK1 animals. Similarly, a significant difference was observed at t = 1 hour when comparing humanised WT mice and the SHAM O_2 response. This may suggest that a higher concentration of O_2 may exist in WT animals at the beginning of the night cycle. However, no significant differences existed between t = 2 hours and t = 11 hours in humanised and SHAM mice. These findings suggest that similar O_2 neurochemical dynamics exist between the three cohorts.

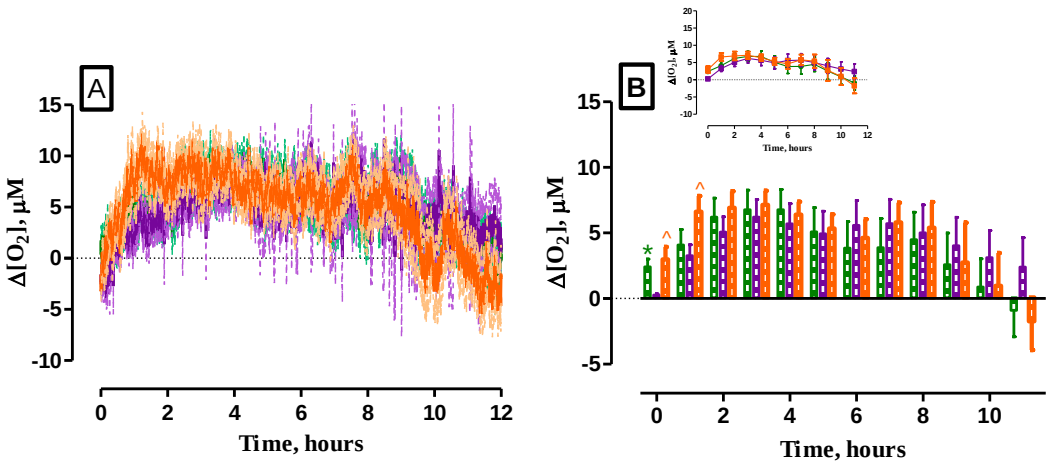

Figure 6.3.6.4.2: (A) Overlay of the averaged 12-hour Δ[O_2] measured by O_2 sensors implanted in the striatum of humanised PINK1 (green trace, *n* = 26/8), WT mice (purple trace, *n* = 25/7) and SHAM mice (orange trace, *n* = 14/7) during the night phase (13 – 24 hours). The mean PINK1 Δ[O_2] is represented by the green trace and the percentage error is represented by the light green trace. The mean WT Δ[O_2] is represented by the purple trace and the percentage error is represented by the light purple trace. The mean SHAM Δ[O_2] is represented by the orange trace and the percentage error is represented by the light orange trace. (B) Bar graph comparing 10-minute time bin analysis of Δ[O_2] over 12-hours. * denotes the level of significance between PINK1 and WT mice. ^ denotes the level of significance between WT and SHAM mice. Data represented as mean Δ [O_2] ± SEM.

Table 6.3.6.4.2: Statistical analysis of O_2 results implanted in the striatum of PINK1 (*n* = 8), WT mice (*n* = 7) and SHAM mice (*n* = 7) during the night cycle.

Night Cycle Recordings									
	PINK1 (*n* = 8)		WT (*n* = 7)		SHAM (*n* = 7)		WT *vs.* PINK1	WT *vs.* SHAM	PINK1 *vs.* SHAM
Time (mins)	Mean (µM)	SEM	Mean (µM)	SEM	Mean (µM)	SEM	*p*	*p*	*p*
0	2.1	0.5	0.3	0.1	4.8	1.0	0.002	0.0005	0.59
1	3.5	1.1	3.3	0.8	9.5	1.1	0.58	0.03	0.22
2	5.6	1.3	5.1	1.2	10.0	0.9	0.54	0.35	0.77
3	6.0	1.3	6.2	1.3	10.0	1.0	0.79	0.66	0.88
4	5.7	1.2	5.7	1.5	8.7	1.0	0.63	0.76	0.88
5	4.0	1.5	4.9	1.7	8.9	1.3	0.95	0.87	0.93
6	2.7	1.7	5.6	1.9	8.5	1.5	0.54	0.74	0.81
7	2.5	1.8	5.7	1.8	8.5	1.4	0.53	0.97	0.57
8	3.5	1.9	5.0	2.1	8.6	1.7	0.86	0.91	0.78
9	1.5	2.3	4.0	2.2	5.6	2.1	0.43	0.61	0.20
10	-0.1	2.0	3.1	2.1	4.5	1.8	0.45	0.55	0.98
11	-1.7	1.9	2.4	2.2	1.3	1.8	0.28	0.27	0.81

6.3.7 H_2O_2 Measurements in Humanised Mice Transplanted with PINK1 Cells

6.3.7.1 Saline Administration

Figure 6.3.7.1.1A illustrates the subtracted H_2O_2 response to a 1 mL/kg i.p. injection of saline. As alluded to in Section 5.3.3.1.1, subtracted values were obtained by subtraction of the current obtained on the catalase electrode from the current recorded on the blank electrode. The subtracted (ΔI) was 87 ± 70 pA (n = 4) which occurred after 10 ± 1 mins (n = 4) and equated to a percentage change of 1 ± 4 % (n = 4) and a concentration change of 0.2 ± 0.2 µM (n = 4). This slight fluctuation in current was found to not be significantly different (p = 0.30) from baseline current (2108 ± 1750 pA, n = 4). Moreover, a post-perturbation baseline of 2150 ± 1746 pA (n = 4) was obtained after 8 ± 6 mins (n = 4, Table 6.3.7.1.1). This post-perturbation was not significantly different (p = 0.31) from the pre-perturbation baseline current.

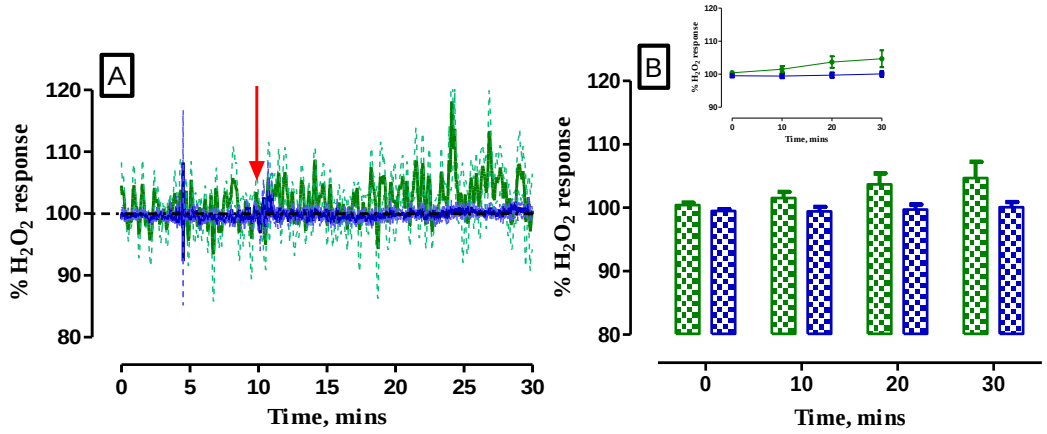

Figure 6.3.7.1.1: (A) Overlay of averaged percentage raw data current response of the H_2O_2 biosensors implanted in the striatum of humanised PINK1 (n = 4, green trace) *vs.* NOD SCID mice (n = 5, blue trace) following 1 mL/kg saline i.p. injection. Point of injection is represented by the red arrow. The green trace indicates the mean percentage PINK1 current response. The blue trace indicates the mean percentage NOD SCID current response. (B) Bar graph comparing 10-minute time bins of percentage current responses. *Inset*: Time bin analysis of 30-minute raw percentage data current responses. Data represented as mean percentage current ± SEM.

Table 6.3.7.1.1: Summary of results of the H_2O_2 sensors implanted in the striatum of humanised PINK1 mice following i.p. administration of 0.9 % saline (*n* = 4).

Saline Injection							
	Pre-Perturbation Baseline (pA)	**Max Current (pA)**	**Current Change (pA)**	**Current Change (%)**	**Max Response Time (mins)**	**Post-Perturbation Baseline (pA)**	**Return to Baseline Time (mins)**
Blank	2629 ± 1660	2756 ± 1661	127 ± 79	9 ± 4	17 ± 3	2670 ± 1659	65 ± 6
Cat.	521 ± 181	561 ± 196	40 ± 16	7 ± 1	14 ± 2	520 ± 182	57 ± 6
Sub.	2108 ± 1750	2196 ± 1755	87 ± 70	1 ± 4	10 ± 1	2150 ± 1746	8 ± 6

It is obvious from Figure 6.3.7.1.1A that following the systemic administration of saline, there is absence of any change in H_2O_2 levels following saline administration which suggests that saline administration does not cause any increase in H_2O_2 levels. Furthermore, time bin analysis was conducted to quantitatively compare the saline response recorded in PINK1 mice and NOD SCID mice. Time bin analysis was conducted by averaging the raw data current at 10-minute intervals (Figure 6.3.7.1.1D).

Table 6.3.7.1.2: Statistical analysis of H_2O_2 recordings obtained in the striatum of humanised PINK1 mice (*n* = 4) and non-humanised NOD SCID mice (*n* = 5) following 1 mL/kg saline i.p. administration.

Saline					
	PINK1 (*n* = 4)		**NOD SCID (*n* = 5)**		
Time, mins	**Mean, %**	**SEM**	**Mean, %**	**SEM**	***p***
0	100.4	0.4	99.5	0.3	0.07
10	101.5	1.0	99.4	0.7	0.11
20	103.7	1.7	99.7	0.8	0.06
30	104.7	2.6	100.1	0.8	0.10

Hence, it was found that no significant differences existed between responses recorded in humanised and non-humanised cohorts (Table 6.3.7.1.2). However, it must be noted that close to significant differences exist between the H_2O_2 response recorded in each cohort between t = 0 mins and t = 30 mins. This may suggest that there is an increase in H_2O_2 activity in PINK1 cell lines although no significant difference exists.

6.3.7.2 Restraint Test

The subtracted (ΔI) of 55 ± 51 pA (n = 4) corresponded to a 1 ± 5 % (n = 4) change that occurred 2 ± 9 mins (n = 4) after the restraint test. This change in current was not significant difference (p = 0.25) from baseline currents recorded (2743 ± 1202 pA, n = 4). Additionally, this change in the recorded amperometric current corresponds to a concentration change of 0.1 ± 0.1 µM (n = 4). A post-perturbation baseline (2703 ± 1207 pA, n = 4) was reached after 8 ± 12 mins (n = 4, Table 6.3.7.2.1) and it was found to not be significantly different (p = 0.16) from pre-perturbation baseline levels.

Figure 6.3.7.2.1 illustrates the effect of a 2-minute restraint test on levels of H_2O_2 measured in the striatum of humanised PINK1 mice. The subtracted response illustrates an absence of any changes in H_2O_2 associated with the performance of a 2-minute restraint test. As seen in Table 6.3.7.2.1, a 1 ± 5 % (n = 4) increase in the amperometric signal was obtained following the performance of a 2-minute restraint test. This recorded increase was reported to be short-lived before a return to baseline was attained. These findings are comparable to those recorded for saline in that no sustained change in H_2O_2 amperometric current was observed in PINK1 humanised mice following neuronal activation. There were no restraint tests performed in NOD SCID mice for comparison.

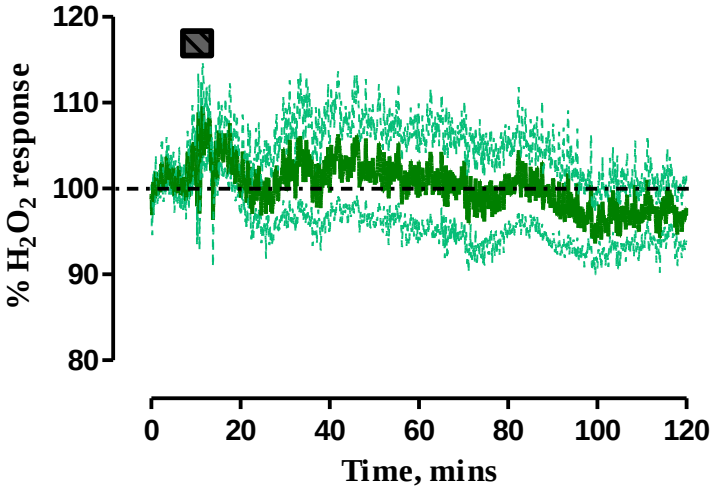

Figure 6.3.7.2.1: Averaged percentage subtracted raw data current response of the H_2O_2 biosensors implanted in the striatum of PINK1 humanised mice (*n* = 4) following 2-minute restraint test. Duration of restraint is represented by the dark grey box. The green trace indicates the mean percentage PINK1 current response with the percentage error represented by the light green trace. Data represented as mean percentage current ± SEM.

Table 6.3.7.2.1: Summary of results of the H_2O_2 sensors implanted in the striatum of humanised PINK1 mice following administration of 2-minute restraint test (*n* = 4).

	Restraint						
	Pre-Perturbation Baseline (pA)	**Max Current (pA)**	**Current Change (pA)**	**Current Change (%)**	**Max Response Time (mins)**	**Post-Perturbation Baseline (pA)**	**Return to Baseline Time (mins)**
Blank	3406 ± 1148	3555 ± 1123	126 ± 51	11 ± 4	30 ± 6	3376 ± 1149	124 ± 20
Cat.	663 ± 157	734 ± 177	71 ± 27	10 ± 3	28 ± 7	673 ± 164	116 ± 23
Sub.	2743 ± 1202	2821 ± 1179	55 ± 51	1 ± 5	2 ± 9	2703 ± 1207	8 ± 12

6.3.7.3 Selectivity Validation of the H_2O_2 Biosensor

The effect of sodium ascorbate was examined on H_2O_2 levels in PINK1 transplanted mice (Figure 6.3.7.3.1). A 2 ± 4 % (*n* = 4) change from the subtracted baseline current (2800 ± 1927 pA , *n* = 4) was observed after 10 ± 4 mins (*n* = 4, Table 6.3.7.3.1). This (ΔI) of 80 ± 26 pA (*n* = 4) corresponded to a concentration change of

0.2 ± 0.1 µM (n = 4). No significant difference (p = 0.74) existed between the change in the subtracted current and the subtracted baseline level. A new post-perturbation subtracted baseline current (2242 ± 2129 pA, n = 4) occurred after 20 ± 20 mins (n = 4) and no significant difference (p = 0.44) was found between the new post-perturbation baseline level and the pre-perturbation baseline level.

Figure 6.3.7.3.1A illustrates the H_2O_2 response recorded following the administration of sodium ascorbate. It is clear from the graph below that a comparable response was recorded in both humanised and non-humanised cohorts. The amperometric signal showed little deviation from baseline levels over the course of 120-minutes. Therefore, this demonstrates that the selective properties of the biosensor have been retained in the humanised striatum and it supports the selective characteristics of the H_2O_2 signal.

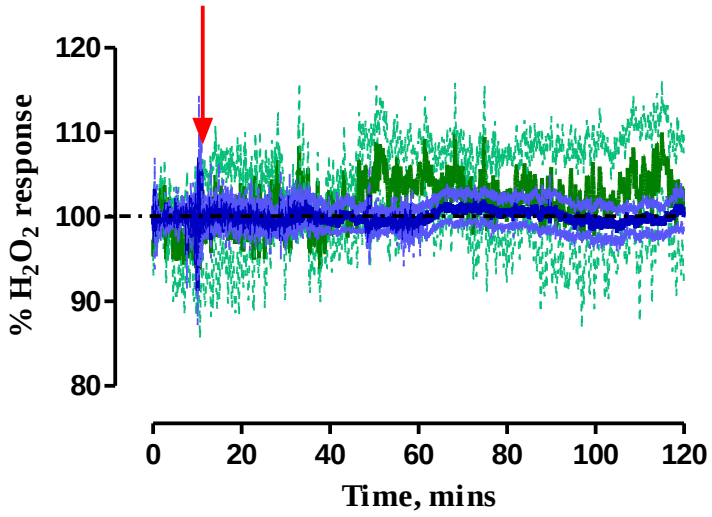

Figure 6.3.7.3.1: Overlay of averaged percentage raw data current response of the H_2O_2 biosensors implanted in the striatum of humanised PINK1 (n = 4, green trace) *vs.* NOD SCID mice (n = 5, blue trace) following 500 mg/kg sodium ascorbate i.p. injection. Point of injection is represented by the red arrow. The green trace indicates the mean percentage PINK1 current response with the percentage error represented by the light green trace. The blue trace indicates the mean percentage NOD SCID current response with the percentage error represented by the light blue trace. Data represented as mean percentage current ± SEM.

Table 6.3.7.3.1: Summary of results of the H_2O_2 sensors implanted in the striatum of humanised PINK1 mice following i.p. administration of 500 mg/kg sodium ascorbate (*n* = 4).

Sodium Ascorbate							
	Pre-Perturbation Baseline (pA)	**Max Current (pA)**	**Current Change (pA)**	**Current Change (%)**	**Max Response Time (mins)**	**Post-Perturbation Baseline (pA)**	**Return to Baseline Time (mins)**
Blank	3436 ± 1857	3372 ± 1871	110 ± 21	1 ± 4	17 ± 6	2858 ± 2045	55 ± 19
Cat.	636 ± 196	619 ± 187	-17 ± 49	-1 ± 5	7 ± 3	616 ± 184	35 ± 3
Sub.	2800 ± 1927	2754 ± 1941	80 ± 26	-3 ± 5	14 ± 6	2242 ± 2129	20 ± 20

6.3.7.4 24-hour Amperometric Recordings of H_2O_2

Neurochemical fluctuations in the concentration of H_2O_2 were qualitatively examined over a 24-hour period. Figure 6.3.7.4.1A & B illustrates the recorded amperometric signal over this 24-hour period. Referring to Sections 6.3.1.5 and 6.3.4.4, it was previously reported that the light cycle is usually associated with extended periods of inactivity. Whereas, a strong correlation between increased locomotor activity and neuronal activation is evident during the night cycle. However, this phenomenon was not apparent during 24-hour recordings recorded in the striatum of non-humanised NOD SCID mice. Figure 6.3.7.4.1B displays little deviation in the amperometric current from baseline levels in non-humanised NOD SCID mice over the course of 24-hours. However, it was hypothesised in Section 5.3.3.4 that H_2O_2 remain at basal levels due to the tight regulation of H_2O_2 by the complex antioxidant system present *in vivo*. In contrast, Figure 6.3.7.4.1A highlights an increase in H_2O_2 levels during the light cycle whilst H_2O_2 levels remain at basal levels throughout the night cycle which is a slight deviation from the H_2O_2 dynamics recorded over a 24-hour period in non-humanised mice. These results suggest a difference in diurnal current recorded in humanised PINK1 grafts when compared to NOD SCID recordings with a tendency towards increased H_2O_2 levels being recorded in the former.

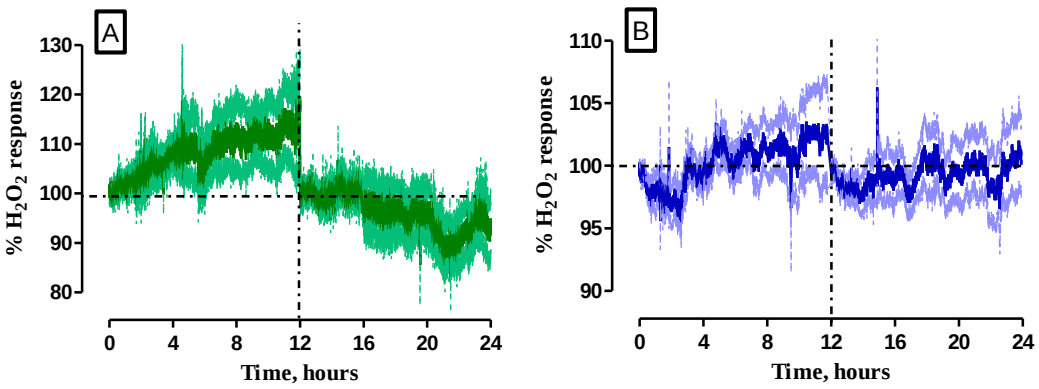

Figure 6.3.7.4.1: Averaged 24-hour percentage current response measured by H_2O_2 sensors implanted in the striatum of (A) humanised PINK1 mice (green trace) during the light phase (*n* = 16/4, 0 - 12 hours) and the dark phase (*n* = 16/4, 13 - 24 hours) and of (B) NOD SCID mice (blue trace) during the light phase (*n* = 14/7, 0 - 12 hours) and the dark phase (*n* = 17/7, 13 - 24 hours). The green trace indicates the mean percentage mean PINK1 H_2O_2 current response with the percentage error represented by the light green trace. The blue trace indicates the mean percentage mean NOD SCID H_2O_2 current response with the percentage error represented by the light blue trace. Data represented as mean percentage current ± SEM.

6.3.7.5 IHC Staining of the Transplanted Striatum

Figure 6.3.7.5.1A & B highlights the IHC images obtained indicating placement of the biosensor in relation to the transplanted PINK1 graft in the transplanted striatum. From Figure 6.3.7.5.1A & B, it was obvious that the humanised PINK1 graft had a diameter of approximately 500 µm in diameter. The sensor channel, with a diameter of approximately 200 µm, can be found directly in the middle of the graft. Therefore, the sensor has been accurately implanted in the middle of the transplanted graft. Moreover, amperometric H_2O_2 recordings were collected directly from the transplanted cells surrounding the tip of the sensor. Additionally, good integration of the transplanted PINK1 cells was evident in the subject. The humanised graft showed excellent survival following transplantation into the host whilst good integration of the cells into the host striatal tissue was clear by the neurite outgrowth into the surrounding tissue being present in the IHC image.

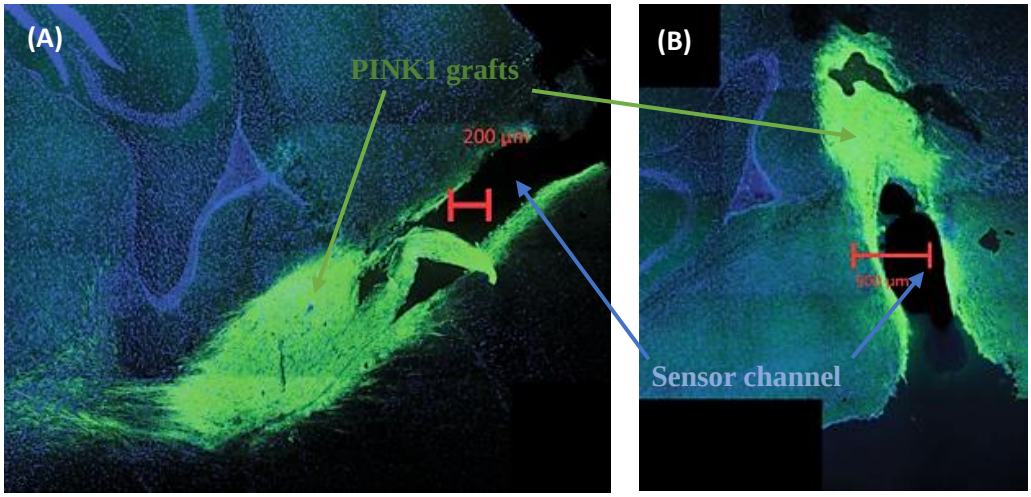

Figure 6.3.7.5.1: Typical examples of IHC images highlighting placement of the implanted biosensor in relation to the transplanted graft in the striatum of humanised PINK1 mice. Red scale bar indicates the diameter of the graft and the sensor channel.

6.3.8 H_2O_2 Measurements in Humanised Mice Transplanted with WT Cells

6.3.8.1 Saline Administration

Figure 6.3.8.1.1A illustrates the H_2O_2 response recorded in WT subjects following saline administration. Following administration of saline, the subtracted (ΔI) was 29 ± 42 pA (n = 4) from pre-perturbation baseline currents (1754 ± 760 pA, n = 4). This 4 ± 3 % (n = 4) change in current corresponded to a 0.1 ± 0.1 µM (n = 4) which was obtained after 1 ± 2 mins (n = 4) and it was found to not be significantly different (p = 0.53) from baseline currents. After 12 ± 1 mins (n = 4), a new post-perturbation baseline current (1732 ± 771 pA, n = 4, Table 6.3.8.1.1) was achieved and it found not to be significantly different (p = 0.60) from pre-perturbation levels. It can be seen that the systemic administration of saline does not result in any changes in the recorded amperometric signal in either WT or non-humanised cohorts (Figure 6.3.8.1.1A).

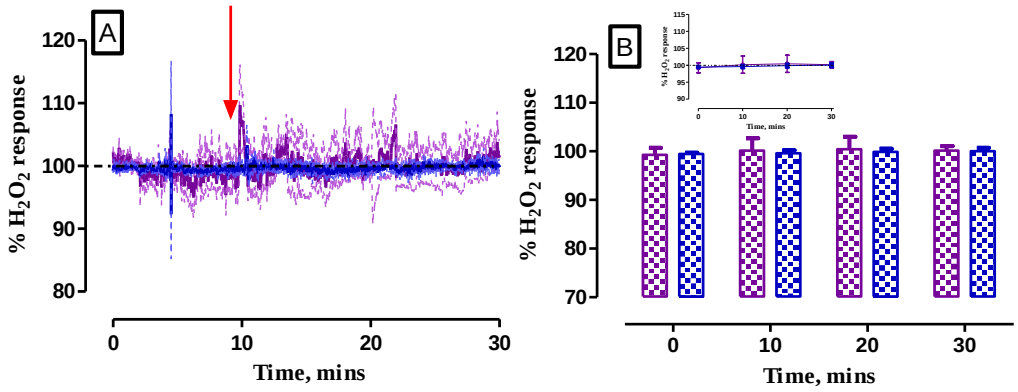

Figure 6.3.8.1.1: (A) Overlay of the averaged percentage raw data current response of the H_2O_2 biosensors implanted in the striatum of humanised WT mice (*n* = 4, purple trace) and NOD SCID mice (*n* = 5, blue trace) following 1 mL/kg saline i.p. injection. Point of injection is represented by the red arrow. The purple trace indicates the mean percentage WT current response with the percentage error represented by the light purple trace. The blue trace indicates the mean percentage NOD SCID current response with the percentage error represented by the light blue trace. (B) Bar graph comparing 10-minute time bins of percentage current responses. *Inset*: Time bin analysis of 30-minute raw percentage data current responses. Data represented as mean percentage current ± SEM.

Table 6.3.8.1.1: Summary of results of the H_2O_2 sensors implanted in the striatum of humanised WT mice following i.p. administration of 0.9 % saline (*n* = 4).

Saline Injection							
	Pre-Perturbation Baseline (pA)	**Max Current (pA)**	**Current Change (pA)**	**Current Change (%)**	**Max Response Time (mins)**	**Post-Perturbation Baseline (pA)**	**Return to Baseline Time (mins)**
Blank	3673 ± 1361	3741 ± 1344	67 ± 85	3 ± 2	4 ± 2	3611 ± 1358	13 ± 1
Cat.	1919 ± 685	1958 ± 671	39 ± 45	3 ± 2	3 ± 1	1879 ± 667	11 ± 2
Sub.	1754 ± 760	1783 ± 758	29 ± 42	4 ± 3	1 ± 2	1732 ± 771	12 ± 1

To further investigate the comparable response obtained in each animal group, time bin analysis was conducted (Table 6.3.8.1.2). Time bin analysis identified no significant differences between the saline responses obtained in WT and NOD SCID subjects. Therefore, it can be postulated that no change in H_2O_2 occurs as a result of

saline administration which could be associated with WT cells following mild neuronal activation.

Table 6.3.8.1.2: Statistical analysis of H_2O_2 recordings obtained in the striatum of humanised WT mice (*n* = 4) and non-humanised NOD SCID mice (*n* = 5) following 1 mL/kg saline i.p. administration.

Saline					
	WT (*n* = 4)		NOD SCID (*n* = 5)		
Time, mins	**Mean, %**	**SEM**	**Mean, %**	**SEM**	***p***
0	99.3	1.5	99.5	0.2	0.87
10	100.2	2.5	99.6	0.6	0.82
20	100.4	2.5	99.9	0.7	0.82
30	103.1	3.0	100.0	0.7	0.31

6.3.8.2 Restraint Test

Following a 2-minute restraint test, a (ΔI) of 350 ± 47 pA (n = 4) was achieved from a pre-perturbation baseline of 3794 ± 795 pA (n = 4). Moreover, this change in current was associated with a percentage change of - 8 ± 3 % (n = 4) and a concentration change of 0.9 ± 0.1 µM (n = 4). A significant difference ($p < 0.001$) was found to exist between the subtracted maximum current and the subtracted pre-perturbation baseline currents. Also, this current change occurred after 34 ± 3 mins (n = 4). It took 89 ± 4 mins (n = 4) for a new subtracted post-perturbation baseline to be reached (3686 ± 825 pA, n = 4, Table 6.3.8.2.1) which was not significantly different (p = 0.29) from pre-perturbation baseline levels.

The response of H_2O_2 to a 2-minute restraint test is displayed in Figure 6.3.8.2.1A measured in the striatum of humanised WT mice. A decrease in H_2O_2 was measured following a 2-minute restraint which is evident in the subtracted amperometric signal (Figure 6.3.8.2.1A). Therefore, it appears that a reduction in the amperometric H_2O_2 response occurs following neuronal activation.

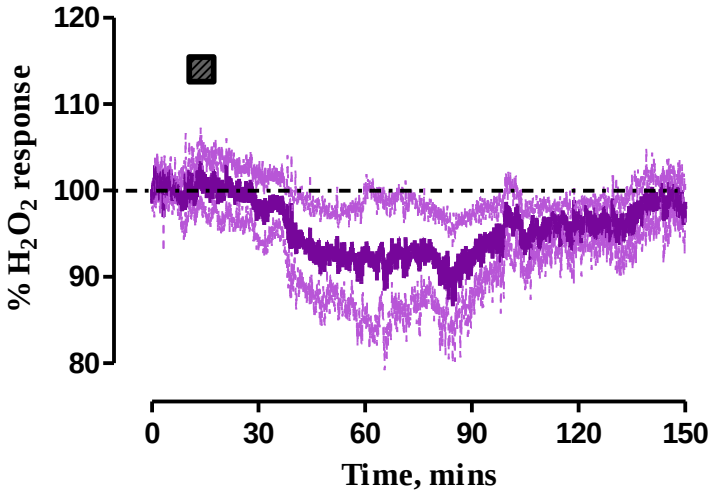

Figure 6.3.8.2.1: Averaged percentage subtracted raw data current response of the H_2O_2 biosensors implanted in the striatum of WT humanised mice (n = 4) following 2-minute restraint test. Duration of restraint is represented by the dark grey box. The purple trace indicates the mean percentage WT current response with the percentage error represented by the light purple trace. Data represented as mean percentage current ± SEM.

Table 6.3.8.2.1: Summary of results of the H_2O_2 sensors implanted in the striatum of humanised WT mice following administration of 2-minute restraint test (n = 4).

	Restraint						
	Pre-Perturbation Baseline (pA)	**Max Current (pA)**	**Current Change (pA)**	**Current Change (%)**	**Max Response Time (mins)**	**Post-Perturbation Baseline (pA)**	**Return to Baseline Time (mins)**
Blank	4477 ± 980	4875 ± 1004	397 ± 39	10 ± 1	8 ± 2	4358 ± 1023	93 ± 18
Cat.	683 ± 249	730 ± 251	47 ± 20	10 ± 3	18 ± 5	671 ± 251	91 ± 13
Sub.	3794 ± 795	4144 ± 830	350 ± 47	-8 ± 3	34 ± 3	3686 ± 825	89 ± 4

6.3.8.3 Selectivity Validation of the H_2O_2 Biosensor

A subtracted percentage change of - 4 ± 2 % (n = 4) was attained after 12 ± 4 mins (n = 4). This subtracted percentage change corresponded to a subtracted (ΔI) of 16 ± 58 pA (n = 4), which corresponded to a concentration change of 0.4 ± 0.1 µM (n = 4), being obtained from subtracted baseline currents of 2150 ± 779 pA (n = 4). No significant difference (p = 0.80) was found between the change in the

amperometric current and the subtracted baseline current. A new subtracted post-perturbation baseline current (2136 ± 839 pA, n = 4) was noted after 63 ± 16 mins (n = 4, Table 6.3.8.3.1), however, no significant difference (p = 0.93) was found between the subtracted post-perturbation baseline currents and pre-perturbation baseline currents.

Figure 6.3.8.3.1A displays the subtracted H_2O_2 amperometric response recorded in humanised WT mice following sodium ascorbate administration. It is clear from the below graph that the amperometric response decreases slightly from baseline levels. Overall, a comparable H_2O_2 response appears to be measured in the striatum of WT and NOD SCID mice. Moreover, the integrity of the permselective membrane has been retained *in vivo* supporting the selectivity of the H_2O_2 biosensor recordings.

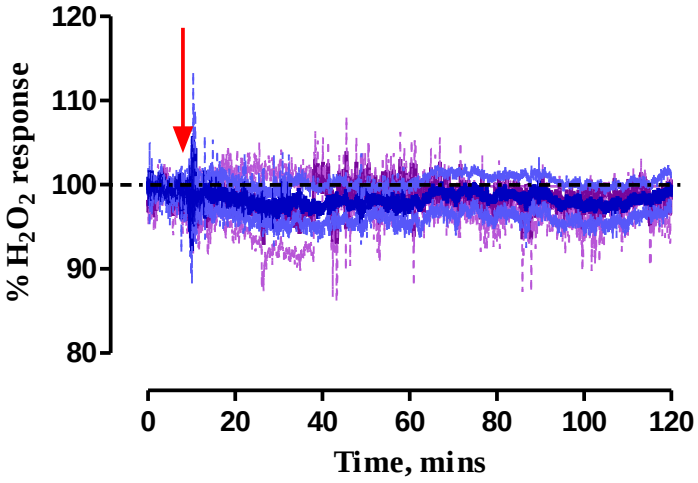

Figure 6.3.8.3.1: Overlay of the averaged percentage raw data current response of the H_2O_2 biosensors implanted in the striatum of humanised WT mice (n = 4, purple trace) and NOD SCID mice (n = 5, blue trace) following 500 mg/kg sodium ascorbate i.p. injection. Point of injection is represented by the red arrow. The purple trace indicates the mean percentage WT current response with the percentage error represented by the light purple trace. The blue trace indicates the mean percentage NOD SCID current response with the percentage error represented by the light blue trace.

Table 6.3.8.3.1: Summary of results of the H_2O_2 sensors implanted in the striatum of humanised WT mice following i.p. administration of 500 mg/kg sodium ascorbate (*n* = 4).

Sodium Ascorbate							
	Pre-Perturbation Baseline (pA)	**Max Current (pA)**	**Current Change (pA)**	**Current Change (%)**	**Max Response Time (mins)**	**Post-Perturbation Baseline (pA)**	**Return to Baseline Time (mins)**
Blank	2972 ± 600	2948 ± 648	-24 ± 88	-2 ± 3	10 ± 3	2839 ± 577	95 ± 27
Cat.	822 ± 230	782 ± 200	-17 ± 28	-3 ± 3	6 ± 2	703 ± 303	65 ± 28
Sub.	2150 ± 779	2166 ± 814	16 ± 58	-4 ± 2	12 ± 4	2839 ± 577	63 ± 16

6.3.8.4 24-hour Amperometric Recordings of H_2O_2

It was important to assess H_2O_2 dynamics over a 24-hour period as usually an increase in analyte detection occurs during periods of increased neuronal activation experienced during the night cycle. However, recordings in non-humanised NOD SCID mice exhibited no such increases as a result of the tight regulation of H_2O_2 by the complex antioxidant network experienced *in vivo*. Similarly, 24-hour amperometric recordings conducted in humanised WT mice illustrated no increase in H_2O_2 concentrations during the night cycle (Figure 6.3.8.4.1A). The absence of any substantial increases in H_2O_2 detection during the night cycle suggests that the efficient antioxidant system exists in the surrounding tissue which keeps H_2O_2 levels at homeostatic levels. Likewise, the amperometric H_2O_2 response recorded during the light cycle fluctuated around baseline levels. A comparable trend in H_2O_2 recordings was observed in NOD SCID mice (Figure 6.3.8.4.1B) whereby little deviation in H_2O_2 levels was reported. To conclude, it can be stated that comparable H_2O_2 responses were recorded in WT and non-humanised cohorts.

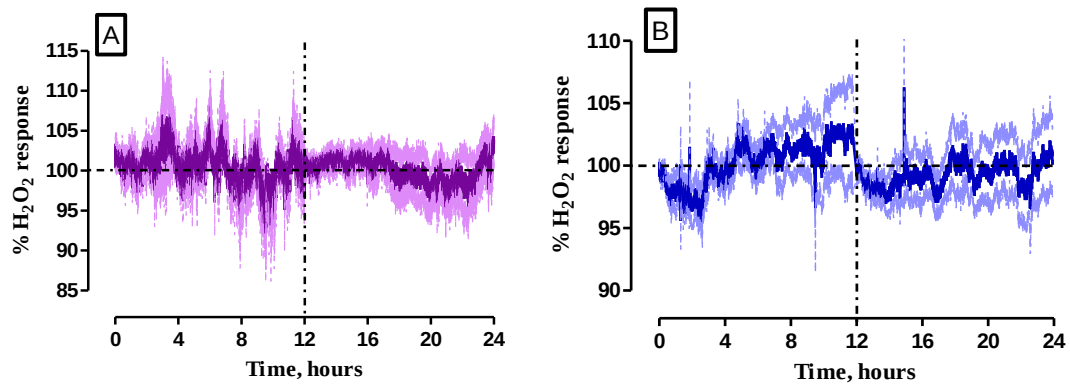

Figure 6.3.8.4.1: Averaged 24-hour percentage current response measured by H_2O_2 sensors implanted in the striatum of (A) humanised WT mice (purple trace) during the light phase (*n* = 9/4, 0 - 12 hours) and the dark phase (*n* = 9/4, 13 - 24 hours) and of (B) NOD SCID mice (blue trace) during the light phase (*n* = 14/7, 0 - 12 hours) and the dark phase (*n* = 17/7, 13 - 24 hours). The purple trace indicates the mean percentage mean WT H_2O_2 current response with the percentage error represented by the light purple trace. The blue trace indicates the mean percentage mean NOD SCID H_2O_2 current response with the percentage error represented by the light blue trace. Data represented as mean percentage current ± SEM.

6.3.8.5 IHC Staining of the Transplanted Striatum

The placement of the H_2O_2 biosensor in relation to the humanised xenograft was confirmed by IHC staining of the xenotransplanted striatum. Figure 6.3.8.5.1 details typical IHC images of striatal tissue that has been transplanted with humanised WT grafts. The grafts show good integration into the host tissue, with a diameter of 200 µm being obtained. Additionally, clear neurite outgrowth is evident into the host striatal tissue. The sensor channel is illustrated by the blue arrow. This channel is in close proximity to the humanised graft and so the sensor is able to reliably detect any neurochemical changes associated with the humanised cells. However, the diameter of the sensor channel is 500 µm which is substantially larger than the diameter of the electrodes of the H_2O_2 biosensor. Thus, this channel has become wider during the removal of the sensors from the euthanised animal due to the difficulty associated with removal of the headpiece.

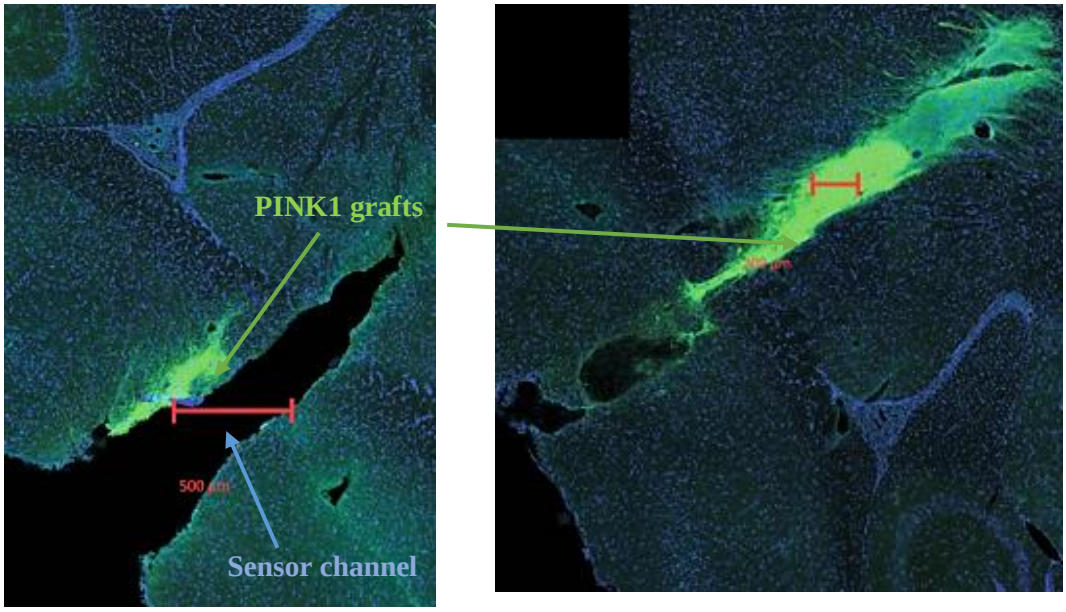

Figure 6.3.8.5.1: Typical examples of IHC images highlighting placement of the implanted biosensor in relation to the transplanted graft in the striatum of humanised WT mice. Red scale bar indicates the diameter of the graft.

6.3.9 Comparison of H_2O_2 Measurements Conducted in Humanised Mice Transplanted with PINK1 and WT Cells

6.3.9.1 Saline Administrations

Following on from the discussion comparing humanised PINK1 and WT mice with non-humanised mice, it was decided that data from humanised cohorts would be compared directly with each other. Comparisons were made between the average percentage subtracted current from humanised PINK1 and WT mice due to the difficulty in obtaining *in vivo* concentrations using the subtraction method associated with the H_2O_2 biosensor. Figure 6.3.9.1.1A illustrates the similar H_2O_2 response recorded in humanised cohorts following the systemic administration of saline. In addition, time bin analysis was conducted on all humanised recordings to investigate if any significant differences existed between the two animal groups (Table 6.3.9.1.1). No significant differences were found between the H_2O_2 response recorded following saline administration. Although a comparable amperometric trend is seen to exist between the H_2O_2 levels measured it both cohorts, there appears to be a tendency towards an increase in H_2O_2 in PINK1 animals. Therefore, it can be postulated that an

increased H_2O_2 activity results in PINK1 mice following increased neuronal activation associated with the administration of saline i.p. injections.

Table 6.3.9.1.1: Statistical analysis of H_2O_2 recordings obtained in the striatum of humanised PINK mice (*n* = 4) and WT mice (*n* = 4) following 1 mL/kg saline i.p. administration.

Saline					
	PINK1 (*n* = 4)		WT (*n* = 4)		
Time, mins	Mean, %	SEM	Mean, %	SEM	*p*
0	100.4	0.4	99.3	1.5	0.51
10	101.5	1.0	100.2	2.5	0.67
20	103.7	1.7	100.4	2.5	0.35
30	104.7	2.6	100.2	0.9	0.15

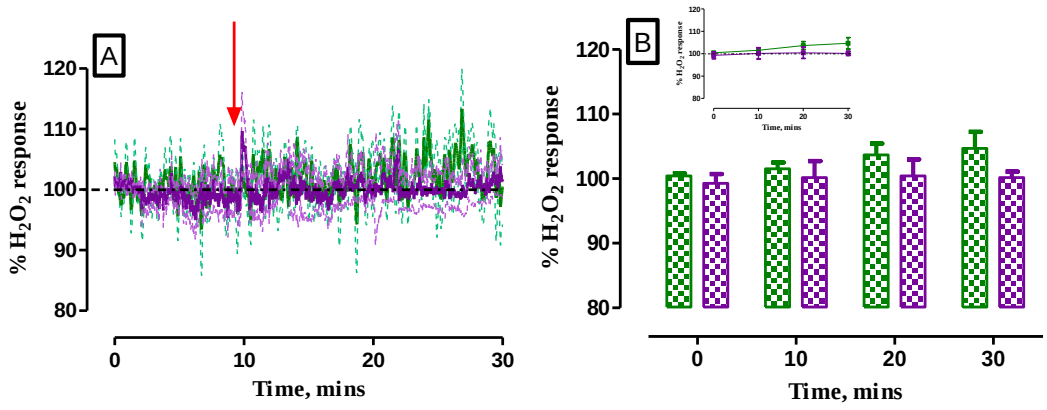

Figure 6.3.9.1.1: (A) Overlay of the average percentage current recorded using H_2O_2 biosensors implanted in the striatum of PINK1 and WT humanised mice following a 1 mL/kg saline i.p. injection. Red arrow indicates the point of injection. The mean PINK1 percentage current is represented by the green trace and the percentage error is represented by the light green trace. The mean WT percentage current is represented by the purple trace and the percentage error is represented by the light purple trace. (B) Bar graph comparing 10-minute time bin analysis of percentage current following a 1 mL/kg saline i.p. injection. Data represented as mean percentage current ± SEM.

6.3.9.2 Restraint Tests

Physiological stimulation was used to instigate neuronal activation in the within the humanised grafts using a 2-minute restraint test. The average H_2O_2

subtracted percentage change for PINK1 and WT mice is displayed in Figure 6.3.9.2.1A. It is evident that H_2O_2 levels decrease in WT transplanted mice following neuronal activation. This decrease is not apparent in PINK1 cell lines as the amperometric response is observed to fluctuate around baseline levels. Further quantitative investigations of the H_2O_2 responses were made using time bin analysis (Table 6.3.9.2.1). It was noted that no significant difference existed between the H_2O_2 levels recorded in humanised PINK1 and WT mice following a 2-minute restraint test. Time bin analysis was conducted over the course of 90-minutes. Although no significant differences were found between the two animal groups, it is clear that H_2O_2 appears to be reduced in WT transplanted mice following increased neuronal activation brought about by 2-minute restraint tests in humanised mice.

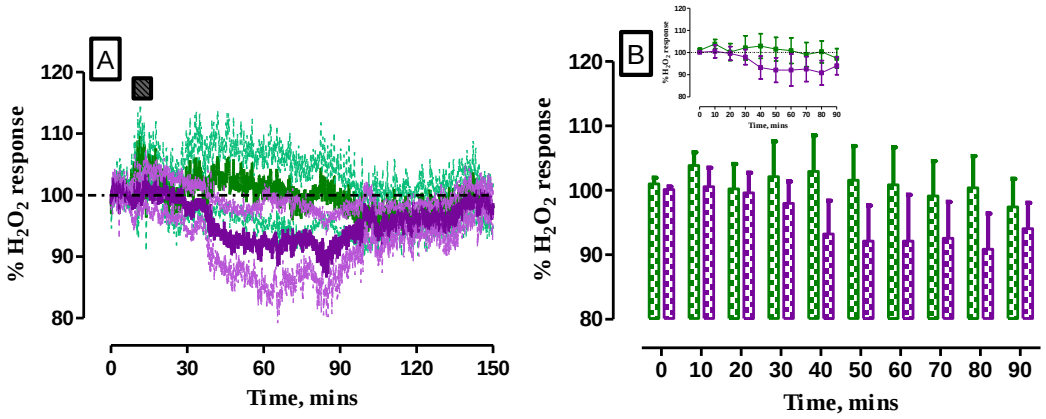

Figure 6.3.9.2.1: (A) Overlay of the average percentage current recorded using H_2O_2 biosensors implanted in the striatum of PINK1 and WT humanised mice following 2-minute restraint test. Duration of the 2-minute restraint test is indicated by the dark grey box. The mean PINK1 percentage current is represented by the green trace and the percentage error is represented by the light green trace. The mean WT percentage current is represented by the purple trace and the percentage error is represented by the light purple trace. (B) Bar graph comparing 10-minute time bin analysis of percentage current following a 2-minute test. Data represented as mean percentage current ± SEM.

Table 6.3.9.2.1: Statistical analysis of H_2O_2 recordings obtained in the striatum of humanised PINK1 mice (*n* = 4) and WT mice (*n* = 4) following a 2-minute restraint.

Restraint					
	PINK1 (*n* = 4)		WT (*n* = 4)		
Time, mins	**Mean, %**	**SEM**	**Mean, %**	**SEM**	***p***
0	101.0	0.9	100.1	0.4	0.45
10	103.9	2.1	100.6	2.9	0.37
20	100.2	3.9	99.6	3.1	0.91
30	102.1	5.5	98.0	3.4	0.58
40	103.0	5.6	93.3	5.1	0.33
50	101.6	5.3	92.1	5.5	0.33
60	100.9	5.8	92.1	7.2	0.41
70	99.1	5.4	92.6	5.6	0.50
80	100.4	5.0	90.9	5.5	0.30
90	97.4	4.4	94.1	4.0	0.66

6.3.9.3 Selectivity Validation of the H_2O_2 Biosensor

The effect of sodium ascorbate on the H_2O_2 response was assessed in humanised cohorts. Moreover, the H_2O_2 percentage current change in PINK1 and WT mice is displayed in Figure 6.3.9.3.1. In the humanised mouse striatum, a very comparable decrease in H_2O_2 currents existed in PINK1 animals and WT animals. The variance in the change recorded in each animal group failed to correspond to a significant difference (p = 0.86) between the two cohorts. Hence, this data highlights the efficient ability of the H_2O_2 biosensor to measure fluctuations in H_2O_2 selectively in xenotransplanted mice. Furthermore, the use of sodium ascorbate is widely utilised in *in vivo* experimentation to ensure that the membrane of the biosensor has remained intact following implantation. Thus, confirmation has been attained that the membrane of the biosensor has been maintained *in vivo*.

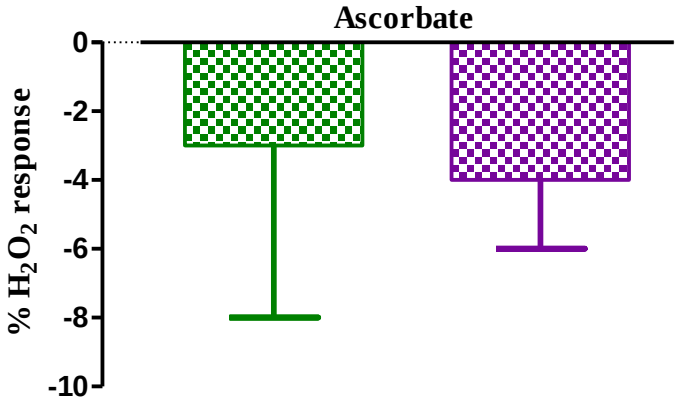

Figure 6.3.9.3.1: Bar chart of the average percentage change recorded using H_2O_2 biosensors implanted in the striatum of humanised PINK1 (green) and WT (purple) mice following a 500 mg/kg sodium ascorbate i.p. injection. Data represented as mean percentage current ± SEM.

6.3.9.4 24-hour Amperometric Recordings of H_2O_2

Furthermore, 24-hour analysis was performed to examine any differences in H_2O_2 neurochemical dynamics in data collected from humanised mice. The H_2O_2 response recorded during the light cycle is portrayed in Figure 6.3.9.4.1A. Subsequently, the H_2O_2 response was recorded in PINK1 mice appeared to increase during the light cycle. In contrast, the amperometric current obtained from WT subjects deviated slightly around basal levels throughout the course of the light cycle. Thus, levels of H_2O_2 measured in PINK1 animals appears to be higher than levels recorded in WT animals during this 12-hour period. Time bin analysis (Table 6.3.9.4.1) was conducted on the two animal groups and it was found that significant differences existed at t = 9 hours and t = 11 hours. These findings suggest a tendency for increased H_2O_2 levels in PINK1 mice but a larger sample size would be required to confirm significance between the humanised cohorts.

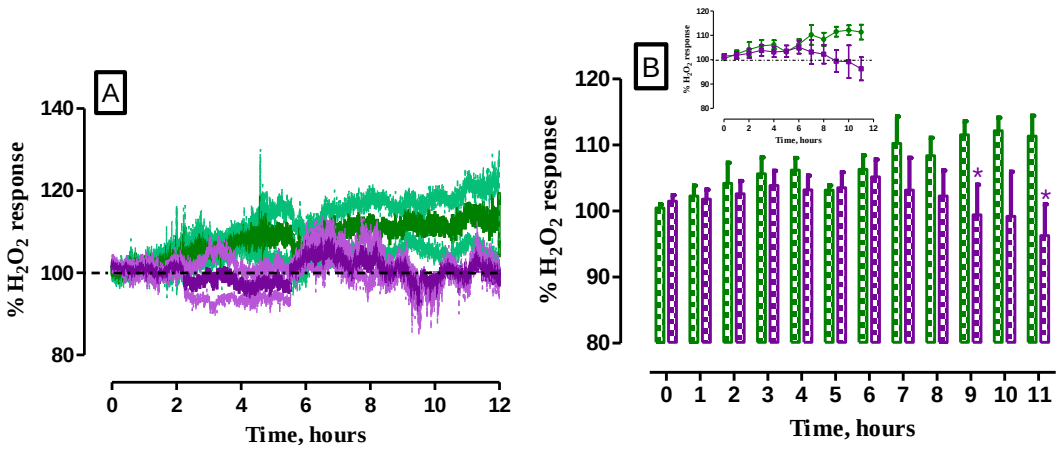

Figure 6.3.9.4.1: (A) Overlay of the averaged 12-hour percentage current measured by H_2O_2 biosensors implanted in the striatum of humanised PINK1 (*n* = 16/4, green trace) and WT mice (*n* = 9/4, purple trace) during the light phase (0 - 12 hours). The mean PINK1 percentage current is represented by the green trace and the percentage error is represented by the light green trace. The mean WT percentage current is represented by the purple trace and the percentage error is represented by the light purple trace. (B) Bar graph comparing 1-hour time bin analysis of percentage current over 12-hours. * denotes the level of significance. Data represented as mean percentage current] ± SEM.

Table 6.3.9.4.1: Statistical analysis of H_2O_2 recordings obtained in the striatum of PINK1 (*n* = 4) and WT mice (*n* = 4) during the light cycle.

Light Cycle Recordings					
	PINK1 (*n* = 4)		WT (*n* = 4)		WT *vs.* PINK1
Time (hours)	Mean, %	SEM	Mean, %	SEM	*p*
0	100.4	0.6	101.5	0.9	0.32
1	102.3	1.6	101.8	1.4	0.83
2	104.2	3.1	102.6	2.0	0.67
3	105.6	2.5	103.9	2.2	0.69
4	106.2	1.8	103.2	2.1	0.29
5	103.2	0.7	103.5	2.3	0.89
6	106.3	2.1	105.2	2.6	0.75
7	110.3	4.0	103.2	4.9	0.29
8	108.4	2.7	102.3	3.8	0.22
9	111.6	2.0	99.4	4.5	0.04
10	112.2	2.0.	99.2	6.7	0.08
11	111.4	3.1	96.3	4.8	0.03

Fluctuations in H_2O_2 levels during the night cycle were also examined (Figure 6.3.9.4.2A). Overall, a comparable H_2O_2 response was measured in both cohorts over this 12-hour period. Usually, the night cycle can be associated with heightened activity of the animal and thus, increased neuronal activation. Conversely, the H_2O_2 amperometric response decreases over the course of the night cycle suggesting that the humanised mice exhibited decreased H_2O_2 levels over this period. By means of time bin analysis (Table 6.3.9.4.2), no significant difference was reported between the PINK1 H_2O_2 response and WT H_2O_2 response. Therefore, it can be postulated that H_2O_2 decreases during the night cycle in humanised animals. This is interesting as it is during this period that the animal is supposed to be most active.

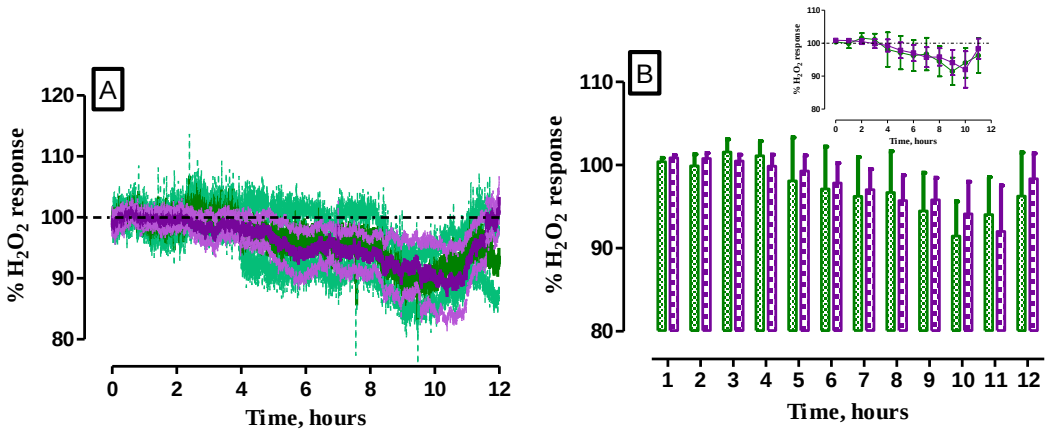

Figure 6.3.9.4.2: (A) Overlay of the averaged 12-hour percentage current measured by H_2O_2 biosensors implanted in the striatum of humanised PINK1 (*n* = 16/4, green trace) and WT mice (*n* = 9/4, purple trace) during the night phase (13 - 24 hours). The mean PINK1 percentage current is represented by the green trace and the percentage error is represented by the light green trace. The mean WT percentage current is represented by the purple trace and the percentage error is represented by the light purple trace. (B) Bar graph comparing 1-hour time bin analysis of percentage current over 12-hours. Data represented as mean percentage current ± SEM.

Table 6.3.9.4.2: Statistical analysis of H_2O_2 recordings obtained in the striatum of PINK1 (*n* = 4) and WT mice (*n* = 4) during the night cycle.

Night Cycle Recordings					
	PINK1 (*n* = 4)		WT (*n* = 4)		WT *vs.* PINK1
Time (hours)	**Mean, %**	**SEM**	**Mean, %**	**SEM**	***p***
0	100.4	0.4	100.9	0.3	0.42
1	99.9	1.4	100.8	0.6	0.57
2	101.6	1.5	100.5	0.8	0.52
3	101.1	1.8	99.9	1.4	0.58
4	98.1	5.2	99.3	1.8	0.83
5	97.1	5.1	97.8	2.4	0.90
6	96.2	4.7	97.0	2.5	0.88
7	96.7	4.9	95.7	3.0	0.87
8	94.5	4.6	95.8	2.6	0.80
9	91.5	4.2	94.1	3.8	0.64
10	94.0	4.5	92.0	5.5	0.78
11	96.3	5.3	98.3	3.1	0.74

6.4 Conclusion

The prime objective of Chapter 6 was to examine neurochemical deviations that may exist during the progression of patient specific PD in humanised mice. This objective was achieved through the integration of transplanted humanised PINK1 and WT cells in the striatum of NOD SCID mice followed by subsequent amperometric recordings.

Firstly, amperometric NO measurements conducted in humanised PINK1 and WT mice highlighted a comparable trend in the NO response obtained in non-humanised subjects following physiological stimulation. However, it was important to note that NO levels recorded in humanised WT mice following saline administration and a 2-minute restraint test were slightly higher. Although, a significant difference was not determined between the NO amperometric response recorded in humanised WT mice to levels recorded in humanised PINK1 and SHAM mice, this can be attributed to the low concentrations of NO that exists *in vivo*. Additionally, for a significant difference to be detected the sample size of the experimental study would have to be expanded greatly which is outside the scope of this thesis.

Moreover, the ability of the NO sensor to detect endogenous fluctuations of NO was confirmed following L-NAME administration whereby a decrease in NO concentrations was measured in each of the cohorts. Thus, demonstrating the ability of the NO sensor to respond to deviations in NO concentrations *in vivo*. Similarly, a comparable amperometric NO signal was recorded in each of the animal groups following the administration of sodium ascorbate. Therefore, confirming that the NO sensor has retained selectivity towards the analyte of interest following implantation. Equally, 24-hour recordings of NO were similar in all three cohorts. However, although no significant differences existed between each of the three animal groups over the course of 24-hours, a reduced level of NO seemed to exist in PINK1 PD mice in response to neuronal activation during the night cycle.

O_2 amperometric measurements carried out in humanised animals reported a disparity in the temporal response when compared to non-humanised mice, following physiological stimulation. The O_2 amperometric response was noted to remain increased over a much longer period. In particular, O_2 levels were seen to remain elevated for the longest timeframe in humanised WT animals. As similarities appeared to exist between the amperometric responses obtained in PINK1 and SHAM animals, it was postulated that a reduced rate of O_2 utilisation exists in PD cell lines when

compared to the response obtained in the WT cohort. Following restraint tests, no significant difference was reported between each of these aforementioned cohorts. Therefore, it can be suggested that restraint tests elicit a larger overall change in O_2 both in the host brain tissue and in the transplanted graft masking any changes in tissue O_2 from being measured in the transplanted graft. As saline administration showed that tissue O_2 exhibited a reduced temporal response in humanised PINK1 mice, it may indicate a change in O_2 utilisation by these cells as the response resembled that obtained from SHAM mice. Previously, PINK1 mice have been demonstrated to favour glycolytic mechanisms during cellular respiration which may serve as a reason for the reduced temporal response measured in humanised PINK1 mice. However, more discussion around this hypothesis will be conducted in Chapter 8.

Again, similar O_2 responses were observed between humanised, SHAM and NOD SCID mice following the administration of the characterisation compounds, L-NAME and Diamox. Therefore, confirming successful functioning of the sensor to changes in O_2 in the xenotransplanted striatum of NOD SCID mice. However, as was discussed for measured NO responses, the comparable O_2 measurements in all three cohorts may result from the overall change in tissue O_2 in the host mouse brain as the graft lacks vasculature. This overall alteration in O_2 in the mouse brain may be so large that it masks any changes in utilisation that may be present in the transplanted graft. Hence, leading to a comparable O_2 response being detected in each of the cohorts.

Overall, the amperometric recordings carried out in humanised PINK1 and WT over the course of 24-hours indicated comparable O_2 levels when compared to recordings collected from NOD SCID mice. Additionally, similar trends in the O_2 response appeared to exist in between humanised and SHAM mice. It may be difficult to attribute any significant differences in the xenotransplanted grafts over the course of 24-hours due to the overall O_2 fluctuations in the mouse brain in response to neuronal activation.

Comparably, following the administration of an i.p. injection of saline, H_2O_2 amperometric responses were similar in PINK1 and WT cohorts. However, it is important to note that there was a tendency towards an increase in H_2O_2 levels in PINK1 cell lines following neuronal activation. In addition, restraint tests conducted on both cohorts reported no significant differences between the recorded responses. Although, it was clear that H_2O_2 levels appeared to be reduced in WT animals. Moreover, selectivity investigations involving sodium ascorbate confirmed that the

selectivity of the biosensor had been retained in each of the cohorts due to the comparable responses obtained. The levels of H_2O_2 measured over 24-hours were similar in both humanised animal groups. However, it was noticed that H_2O_2 levels illustrated a tendency towards increased H_2O_2 levels measured in PINK1 mice but a larger sample size would be need to confirm significance.

Following on from the successful integration of the humanised PINK1 and WT cells into the mouse striatum and the application of amperometric technology, it is now possible to apply complementary analytical techniques to the mouse model to aid in obtaining an overall signature in patient specific progression of PD. Microdialysis is a sampling technique widely used to assess levels of neurotransmitters, amines and amino acids in the extracellular fluid. Chapter 7 will further discuss the application of microdialysis in the humanised mouse model.

6.5 References

1. Reinhardt, P., Glatza, M., Hemmer, K., Tsytsyura, Y., Thiel, C. S., Höing, S., Moritz, S., Parga, J. A., Wagner, L., Bruder, J. M. & Wu, G. Derivation and Expansion Using Only Small Molecules of Human Neural Progenitors for Neurodegenerative Disease Modeling. *PLoS One* **8,** (2013).
2. Attwell, D., Buchan, A. M., Charpak, S., Lauritzen, M., MacVicar, B. A. & Newman, E. A. Glial and neuronal control of brain blood flow. *Nature* **468,** 232–243 (2010).
3. Hemmer, K., Zhang, M., van Wüllen, T., Sakalem, M., Tapia, N., Baumuratov, A., Kaltschmidt, C., Kaltschmidt, B., Schöler, H. R., Zhang, W. & Schwamborn, J. C. Induced neural stem cells achieve long-term survival and functional integration in the adult mouse brain. *Stem Cell Reports* **3,** 423–431 (2014).
4. Fellows, L. K., Boutelle, M. G. & Fillenz, M. Physiological Stimulation Increases Nonoxidative Glucose Metabolism in the Brain of the Freely Moving Rat. *J. Neurochem.* **60,** 1258–1263 (1993).
5. Cloutier, M., Bolger, F. B., Lowry, J. P. & Wellstead, P. An integrative dynamic model of brain energy metabolism using in vivo neurochemical measurements. *J. Comput. Neurosci.* **27,** 391–414 (2009).
6. Finnerty, N. J., O'Riordan, S. L., Brown, F. O., Serra, P. A., O'Neill, R. D., Lowry, J. P. In vivo characterisation of a Nafion®-modified Pt electrode for real-time nitric oxide monitoring in brain extracellular fluid. *Anal. Methods* **4,** 550 (2012).
7. Finnerty, N. J., O'Riordan, S. L., Pålsson, E. & Lowry, J. P. Brain nitric oxide: Regional characterisation of a real-time microelectrochemical sensor. *J. Neurosci. Methods* **209,** 13–21 (2012).

Chapter 7

Microdialysis Sampling with Metabolomic Analysis of Humanised PINK1 and WT Mice

7.1 Introduction

The overall aim of this project was to elucidate a neurochemical signature of PD. In order to achieve this goal, it was imperative to couple a variety of different analytical techniques to allow for an overall neurochemical signature of PD progression to be obtained. Previously, Chapters 5 & 6 has detailed the application of amperometric sensors in the striatum of non-humanised and humanised NOD SCID mice to allow for neurochemical events to be monitored. However, PD is a very complex and heterogenous disease which is difficult to diagnose. Diagnosis usually follows the appearance of clinical symptoms coupled with the patients' history and response to dopaminergic drugs. However, by the time diagnosis occurs the patient has already lost approximately 50 % - 80 % of the dopaminergic neurons in the substantia nigra which extend into the striatum[1–3]. At present, no biomarkers of PD exist as dopaminergic metabolite measurement does not allow for detection of prodromal PD or for continuous monitoring of disease progression. Therefore, interdisciplinary methods of assessing molecular and cellular pathways of disease progression must be assessed that will help in obtaining possible biomarkers of PD, potentially leading to earlier diagnosis and new pharmaceutical therapies[4].

PINK1 mutations are known to be associated with autosomal, recessive forms of PD[5]. PINK1 is a serine/threonine kinase located primarily in the mitochondrial membrane which highlights an important role for PINK1 in mitochondrial function[6]. PINK1 has been reported to have a neuroprotective function against apoptosis induced by oxidative stress whilst also regulating mitochondrial fission and fusion[7,8]. However, the aforementioned functions are lost in PINK1-associated PD signifying the need to investigate potential biomarkers associated with this monogenic form of the neurodegenerative disease.

Within this project, it was crucial to implement microdialysis sampling to allow for metabolomic analysis to be undertaken. Metabolomics involves the detailed measurement of small molecule metabolites (< 1800 Da) implemented in metabolic reactions and the products of these reactions which represent the phenotype of the organism[4,9]. Due to metabolites being extremely sensitive to cellular changes, they exist as one of the best indicators of the cell environment[10]. Metabolites are influenced by environmental and genetic interactions allowing for information to be obtained relating to the biological response of the disease state.

By investigation of the metabolites collected by microdialysis sampling (Section 3.9), metabolic changes accompanying disease development can be identified leading to an improvement in disease diagnosis and progression.

Identification of metabolites was undertaken by colleagues at Leiden University using liquid chromatography with tandem mass spectrometry (LC-MS/MS). Quantitative metabolite analysis by MS is highly selective and sensitive due to the variety of atmospheric pressure ionisation (API) methods available in both positive and negative modes which enables a wide variety of metabolites to be identified[11]. However, the identification of metabolites can be challenging due to the chemical and physical diversity that they possess. Therefore, making them difficult to identify by MS alone. Hence, LC-MS/MS was utilised within this study to ensure accurate identification of a wide array of metabolites that may be present in the samples collected from non-humanised and humanised subjects. LC-MS/MS works in a similar manner to LC-MS but LC-MS/MS includes the use of two mass analysers in the one mass spectrometry instrument allowing for more accurate identification of the contained metabolites to result. A high resolution MS/MS spectra can be obtained following ion fragmentation by collision-induced dissociation which allows for increased sensitivity of metabolite detection based on their obtained fragmentation pattern[9].

Therefore, by inclusion of interdisciplinary analysis techniques, such as microdialysis and metabolomic analysis by LC-MS/MS, a greater knowledge of the neurochemical events and the associated cellular and molecular pathways can be gained.

7.2 Experimental

Microdialysis experimentation was conducted in non-humanised NOD SCID and humanised PINK1 and WT mice. Microdialysis probes were implanted in non-humanised and, following a 6-week *in vivo* integration period, in humanised animals, as stated in Section 3.8.5. The experimental set-up for microdialysis sampling conducted in non-humanised and humanised NOD SCID mice is described in Section 3.9. All of the solutions and chemicals used during microdialysis sampling are included in Section 3.3. Firstly, microdialysis sampling was conducted in non-humanised NOD SCID mice using a microdialysis probe consisting of a 0.5 mm sampling membrane. All samples collected were stored at -40 ºC before being transported to Leiden University for metabolomic analysis. A full characterisation study was conducted on samples to allow for flow rate, collection, storage and transport conditions to be optimised prior to commencing further microdialysis sampling in humanised mice.

For efficient temporal profiling of metabolites, the microdialysis protocol was altered accordingly for microdialysis sampling to be conducted in humanised NOD SCID mice. A tether and swivel system (Figure 3.9.1) was incorporated for investigations in humanised animals which allowed for free movement of the animal during sampling. In addition, the size of the sampling membrane was increased to 1.0 mm to allow for an improved recovery of metabolites. Additionally, the length of the grafts were identified to be approximately 1 mm in length following immunohistochemical staining conducted by colleagues at the University of Luxembourg. Therefore, it was decided to implant microdialysis probes with a larger sampling membrane to ensure more of the graft was being sampled. Microdialysis sampling conducted in the striatum of humanised NOD SCID mice included four different experimental perturbations (Section 3.9). These perturbations included administration of an i.p. saline injection, 2-minute restraint test and 20-minute retroperfusions of 100 mM K^+ and 100 µM Paraquat solutions. Microdialysis sampling was conducted over 180-minutes with dialysate collected every 10-minutes. Each of the perturbations were carried out 50-minutes after the initiation of microdialysis sampling, to ensure a stable metabolite basal level had been reached. Within this 50-minute period, the final 20-minutes were averaged and set as a 100 % baseline level from which all the relative changes could be

calculated. Samples were then shipped to Leiden University for metabolomic analysis.

7.3 Results and Discussion

7.3.1 Characterisation of Microdialysis Sampling in the Striatum of NOD SCID Mice

Prior to conductance of microdialysis sampling in the striatum of humanised NOD SCID mice, it was vital to refine the microdialysis protocol between Maynooth and Leiden University where all samples would be analysed by LC-MS/MS following collection in Maynooth. Optimisation of microdialysis sampling techniques, sample storage and transport conditions were achieved during this study. Dialysate was collected from the striatum of 5 NOD SCID mice, four of which were freely-moving and one was anaesthetised. From the acceptance criteria of Relative Standard Deviation quality control (RSDqc) < 15 % stated by Leiden University, 54 compounds, out of the 73 amines collected, were identified as being present at an accepted standard. The 54 metabolites are stated below in Table 7.3.1.1. Following confirmation of the protocols associated with microdialysis sampling and metabolomic analysis, further investigations involving humanised mice were now ready to be investigated.

Table 7.3.1.1: Table of amines collected from the striatum of non-humanised NOD SCID mice during the characterisation study. The amines included below comply with the Leiden University acceptance criteria of RSDqc < 15 %.

Metabolites Detected by the Amine Platform					
3-Methoxytyramine	β-Alanine	Homocitrulline	L-Histidine	L-Threonine	Ornithine
3-Methoxytyrosine	γ- Aminobutyric acid	L-2-Aminoadipic Acid	L-Homoserine	L-Tryptophan	Putrescine
Anserine	γ- Glutamylglutamine	L-4-Hydroxy-Proline	L-Isoleucine	L-Tyrosine	S-Methylcysteine
Asymmetric Dimethylarginine	γ- L- Glutamyl-L-Alanine	L-Alanine	L-Kynurenine	L-Valine	Taurine
Citrulline	Glutathione	L-α- Aminobutyric Acid	L-Lysine	Methionine Sulfone	Symmetric Dimethylarginine
Cysteine	Glycine	L-Arginine	L-Methionine	Methyldopa	Sarcosine
DL-3-Aminoisobutyric Acid	Glycylglycine	L-Aspartic Acid	L-Phenylalanine	N6N6N6- Trimethyl-L-Lysine	L-Asparagine
Dopamine	Glycylproline	L-Glutamic Acid	L-Proline	O-Phosphoethanolamine	Homocysteine
Ethanolamine	Histamine	L-Glutamine	L-Serine	O-Phosphoserine	L-Leucine

7.3.2 Metabolomic Analysis of Microdialysis Sampling in the Striatum of Humanised Mice

Following completion of a full characterisation study detailed in Section 7.3.1, microdialysis sampling was conducted in the striatum of humanised WT and PINK1 mice. Thereafter, LC-MS/MS was utilised to analyse the dialysate collected from 5 humanised WT mice and 3 humanised PINK1 mice. Samples have also been collected from 2 additional humanised PINK1 mice but they unfortunately will not be analysed in time for the purpose of this thesis. However, all further data will be included in future publications. Characterisation investigations identified 54 metabolites, however, the number of analytes detected during temporal profiling was reduced. This can be attributed to the collection of a smaller volume of dialysate, in turn, resulting in a lower concentration of contained analytes (Section 2.7). A comprehensive metabolic profile was compiled following metabolomic analysis which is detailed in Table 7.3.2.1. It was found that 32 metabolites out of the 44 sampled were observed to be present at altered levels in humanised PD mice when compared to levels reported in humanised WT mice. Metabolites that were observed to be significantly, or close to significantly altered, are discussed in detail in this chapter. It must be stated that changes in metabolite levels were mainly associated with physiological stimulation associated with saline administration and restraint tests. A similar phenomenon was reported in Chapter 6 whereby the greatest change in the recorded amperometric response was associated with neuronal activation resulting from saline administration and restraint tests. Thus, for this reason, figures associated with 100 mM K^+ and 100 µM Paraquat retroperfusions were not included as no obvious differences were observed.

Relative response-time figures included in this Section are representative of (A) saline i.p. injections which were administered between t = 20/30 minutes and (B) restraint tests which were conducted between t = 20/30 minutes. Although relative response-time figures are not included, it is important to note that retroperfusions of 100 mM K^+ and 100 µM Paraquat were conducted during t = 20 and 30 minutes.

Table 7.3.2.1: Table of amines collected from the striatum of humanised NOD SCID mice during microdialysis sampling. The amines included below comply with the Leiden University acceptance criteria of RSDqc < 25 %. The arrows are indicative of metabolite changes in humanised PINK1 mice when compared to humanised WT mice. 'Y' signifies a change in metabolite levels observed between PINK1 and WT mice. 'N' indicates that no change was observed between PINK1 and WT mice.

Metabolite	Saline PD vs. WT	Restraint PD vs. WT	100 mM K^+ PD vs. WT	100 µM PQ PD vs. WT	Associated Pathways
3-Methoxytyramine	Y↓	N	N	Y↓	Dopamine metabolism
3-Methylhistidine	Y↑	N	N	N	Marker of skeletal muscle degradation
Anserine	N	Y↓	N	Y↓	β-Analine, Histidine metabolism
Citrulline	Y↑	Y↑	N	N	Urea cycle, Arginine/Proline Metabolism, Aspartate metabolism
DL-3-Aminoisobutyric acid	Y↓	N	N	Y↓	Pyrimidine metabolism, Mitochondrial Neurogastrointestinal Encephalopathy
Ethanolamine	N	N	Y↑	N	Phospholipid biosynthesis
GABA	Y↑	N	N	N	Inhibitory neurotransmitter, glutamate metabolism
γ-GlutamylGlutamine	N	N	N	N	Glutathione metabolism
Glycine	N	Y↑	N	N	Neurotransmission, Purine metabolism
GlycylGlycine	N	Y↑	N	N	Peptide biosynthesis

- Metabolites that demonstrated no difference between PINK1 and controls
- Metabolites that demonstrated no difference during physiological stimulation (saline and restraint)
- Metabolites that demonstrated differences during restraint only (*vs.* saline)
- Metabolites that demonstrated differences during saline only (vs. restraint)
- Metabolites that demonstrated differences during both saline and restraint

Homocitrulline	N	Y↓	N	N	
Homoserine	Y↑	Y↓	N	N	Methionine metabolism
Isoleucine	Y↓	Y↑	N	N	TCA cycle, Valine, Leucine and Isoleucine degradation
Kynurenine	N	Y↑	Y↓	N	Tryptophan metabolism
L-2-Aminoadipic Acid	Y↑	N	N	N	Lysine degradation, Antagonises neuroexcitatory activity
L-4-HydroxyProline	Y↓	Y↓	N	N	Proline metabolism, Collagen biosynthesis
L-Alanine	N	Y↑	N	N	Pyruvate, DNA, Carnosine, Anserine metabolism
L-AlphaAminoButyric Acid	N	N	N	N	Isoleucine biosynthesis
L-Arginine	Y↓	Y↑	N	N	Urea cycle, NO, L-glutamate, L-proline, creatine biosynthesis
L-Asparagine	N	Y↑	N	N	Glycoprotein biosynthesis
L-Aspartic acid	Y↑	Y↑	N	N	Excitatory neurotransmitter, arginine/proline/aspartate/glutamamte metabolism, urea cycle, purine metabolism
L-Carnosine	N	N	N	N	Beta-Alanine metabolism, Histidine metabolism
L-Glutamic Acid	Y↑	Y↑	N	N	Neurotransmission, Purine, gluthathione metabolism, TCA cycle
L-Glutamine	Y↓	Y↓	N	N	Glutamate, Purine metabolism, urea cycle

- Metabolites that demonstrated no difference between PINK1 and controls
- Metabolites that demonstrated no difference during physiological stimulation (saline and restraint)
- Metabolites that demonstrated differences during restraint only (*vs.* saline)
- Metabolites that demonstrated differences during saline only (vs. restraint)
- Metabolites that demonstrated differences during both saline and restraint

L-Histidine	N	Y↑	N	N	Neurontransmission, Histamine precursor, metallothionein biosynthesis
L-Leucine	Y↓	Y↑	N	N	Protein synthesis
L-Lysine	Y↓	Y↑	N	N	Lysine degradation, Biotin metabolism, Carnitine synthesis
L-Proline	N	Y↑	N	N	Protein biosynthesis
L-Serine	N	Y↑	N	Y↓	Methionine metabolism, Ammonia recycling, Purine/Pyrimidine biosynthesis, neuromodulator
L-Threonine	Y↓	Y↑	N	N	Immunostimulant, Glycine/Serine metabolism, TCA cycle
L-Tryptophan	N	Y↑	N	N	Serotonin/Melatonin biosynthesis, Tryptophan metabolism
L-Tyrosine	Y↓	Y↑	N	N	Catecholamine Biosynthesis, Thyroid hormone synthesis, Phenylalanine/Tyrosine metabolism
L-Valine	Y↓	Y↑	N	N	Protein Biosynthesis
Methionine	N	Y↑	N	N	Phospholipid biosynthesis, Transmethylation reactions, cysteine precursor
Methionine Sulfone	N	N	N	N	
Methionine Sulfoxide	Y↓	N	N	N	Methionine metabolism, Biological aging
N6N6N6 Trimethyl L-Lysine	N	N	N	N	Carnitine biosynthesis
O-Phosphoethanolamine	Y↓	Y↓	N	N	Phospholipid synthesis, neuritic proliferation

- Metabolites that demonstrated no difference between PINK1 and controls
- Metabolites that demonstrated no difference during physiological stimulation (saline and restraint)
- Metabolites that demonstrated differences during restraint only (*vs.* saline)
- Metabolites that demonstrated differences during saline only (vs. restraint)
- Metabolites that demonstrated differences during both saline and restraint

Ornithine	N	Y↑	N	Y↓	Urea cycle, ammonia detoxification
Phenylalanine	Y↓	Y↑	N	N	Phenylalanine, Tyrosine metabolism
Putrescine	Y↑	N	N	Y↓	Methionine metabolism
Sarcosine	N	N	N	N	Glycine/Serine metabolism, Methionine metabolism
S-Methylcysteine	N	N	N	N	Intracellular protein breakdown
Taurine	N	N	Y↑	N	Neurotransmitter, Bile acid biosynthesis

- Metabolites that demonstrated no difference between PINK1 and controls
- Metabolites that demonstrated no difference during physiological stimulation (saline and restraint)
- Metabolites that demonstrated differences during restraint only (*vs.* saline)
- Metabolites that demonstrated differences during saline only (vs. restraint)
- Metabolites that demonstrated differences during both saline and restraint

7.3.3 Identification of Metabolomic Changes in Humanised PINK1 *vs.* WT Mice

7.3.3.1 Tryptophan Metabolism

L-tryptophan is an important amino acid with a critical role in numerous metabolic functions. Primarily, L-tryptophan plays an important part in protein synthesis[12], whilst also being an important pre-cursor of three metabolic pathways. These pathways include the synthesis of kynurenine, serotonin and melatonin. Serotonin elicits an important function in the brain by acting as a neurotransmitter and neuromodulator which has been implicated in many functions of the central nervous system including mood, sleep and memory. Additionally, the hormone melatonin is synthesised through the tryptophan/serotonin pathway. Melatonin has an important role in the regulation of circadian rhythms in humans whilst having an influence on other systems such as the immune system[13].

Degradation of L-tryptophan by the kynurenine pathway is the most important route for L-tryptophan catabolism in humans[14]. Kynurenine can be degraded into a number of different intermediates before ultimately resulting in the production of nicotinamide adenosine dinucleotide (NAD^+)[15]. However, further degradation of kynurenine results in the formation of other neuroactive intermediates, such as KYNA, 3-HK and quinolinic acid. Firstly, KYNA exhibits neuroprotective functions by functioning as an antagonist of the glycine site of the NMDA receptor. KYNA is synthesised primarily in astrocytes[16]. The synthesis of KYNA along with its subsequent release is influenced by numerous factors including K^+ and glucose concentrations and agonist levels of glutamate receptors[17]. It has also been hypothesised that dopamine may attribute to the regulatory role of KYNA release due to the dopamine reuptake-inhibitor, D-amphetamine, reducing brain concentrations of KYNA[18].

Conversely, both 3-HK and quinolinic acid are neurotoxic due to the generation of free radicals by 3-HK whilst quinolinic acid acts as an agonist of the NMDA receptor[19]. Studies conducted in rodent brains involved administration of striatal injections of quinolinic acid which was reported to be excitotoxic causing axon-sparing lesions of a dose-dependent size proximal to the injection site[20]. The neurotoxic nature of this intermediate is amplified due to the numerous mechanisms

through which it can cause neuronal damage including the ability of quinolinic acid to stimulate the release of glutamate whilst simultaneously inhibiting its astroglial uptake[21]. Additionally, quinolinic acid acts to reduce the enzymatic activity of glutamine synthetase which works to produce glutamine from glutamate and ammonia[22]. Therefore, sustained increased concentrations of glutamate coupled with continual activation of excitatory neurons resulted in prolonged Ca^{2+} influx through ion channels ensuing in mitochondrial dysfunction, cytochrome C release and dysregulated activation of proteases and caspases[23]. Moreover, investigations conducted in cultured human neurons and astrocytes reported a dose-dependent increase in the activity of iNOS and nNOS following treatment with quinolinic acid leading to increased cellular toxicity and decreased NAD^{+}[24].

Metabolites commonly associated with tryptophan metabolism were seen to be altered in this study involving humanised PINK1 and WT mice. Firstly, L-tryptophan levels were seen to be significantly increased in humanised PINK1 mice during restraint tests (Figure 7.3.3.1.1, Table 7.3.3.1.1). The significantly increased levels of L-tryptophan that were observed during restraint tests may be attributed to increased neuronal activation. It must also be stated that following administration of saline, decreased levels of L-tryptophan measured in humanised PINK1 mice are close to significance (t = 20, 108.6 ± 5.6 (n = 5) *vs.* 80.5 ± 10.5 (n = 3), p = 0.05). This may indicate that levels of L-tryptophan are disrupted in humanised PINK1 mice, however, neuronal activation may need to be stimulated for a longer period in which to elicit a significant difference. Comparatively, levels of the L-tryptophan catabolite, Kynurenine, were also seen to be significantly increased during restraint tests when compared to levels measured in humanised WT mice (Figure 7.3.3.1.2, Table 7.3.3.1.2). Therefore, these results indicate that both metabolites are altered in humanised PINK1 mice following neuronal activation, suggesting that alterations in energy metabolic pathways and, in the production of neuroprotective metabolites and neurotransmitters, may be disrupted in the humanised mouse model of PINK1.

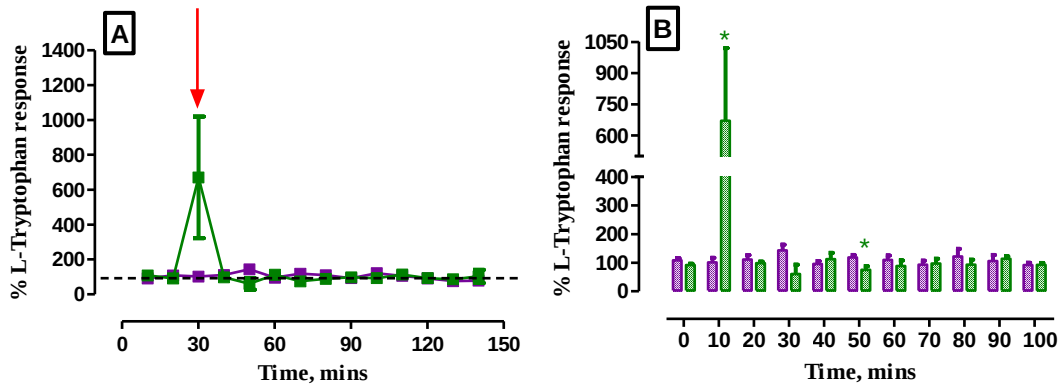

Figure 7.3.3.1.1: (A) Percentage relative response-time profile of L-tryptophan obtained following a 2-minute restraint test. Baseline levels were taken 20-minutes prior to the restraint test. (B) Bar graph comparing 10-min microdialysis samples of percentage L-tryptophan responses. Baseline levels are representative of 10-minutes before the restraint test. The relative response obtained from WT mice is represented in purple while PINK1 animals are highlighted in green. Red arrow indicates the point of neuronal perturbation.

Table 7.3.3.1.1: Statistical analysis of L-tryptophan obtained using unpaired *t*-test for 2-minute restraint tests conducted on humanised PINK1 (*n* = 3) and WT mice (*n* = 5).

L-tryptophan					
	Restraint WT		Restraint PINK1		
Time, mins	Mean	SEM	Mean	SEM	*p*
0	108.7	7.4	91.7	4.8	0.15
10	101.2	15.8	670.8	348.5	0.03
20	111.4	14.9	97.9	6.2	0.50
30	143.2	19.8	60.3	33.4	0.08
40	95.8	9.7	112.5	22.2	0.45
50	118.4	8.8	74.6	12.7	0.03
60	109.6	15.6	88.6	19.2	0.44
70	93.3	14.0	97.7	15.9	0.84
80	121.4	27.3	93.3	16.6	0.49
90	105.1	22.0	113.2	9.0	0.80
100	91.4	8.2	92.1	6.8	0.95

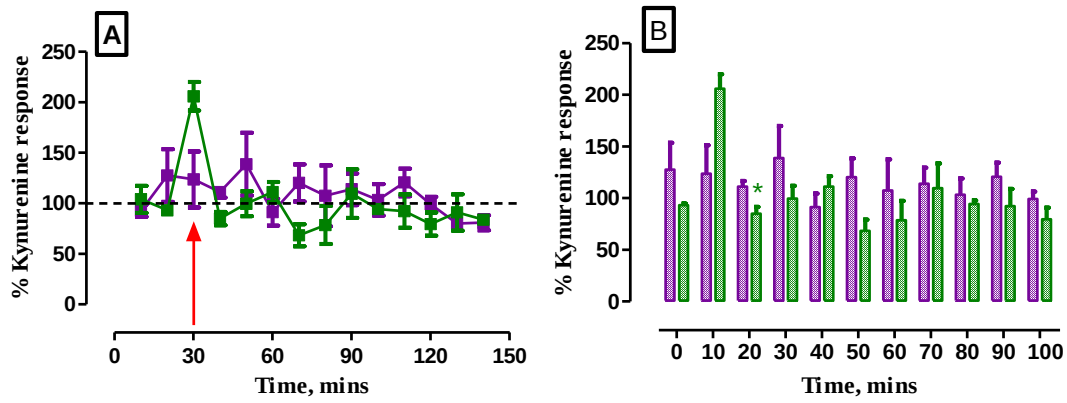

Figure 7.3.3.1.2: (A) Percentage relative response-time profile of Kynurenine obtained following a 2-minute restraint test. Baseline levels were taken 20-minutes prior to the restraint test. (B) Bar graph comparing 10-min microdialysis samples of percentage Kynurenine responses. Baseline levels are representative of 10-minutes before the restraint test. The relative response obtained from WT mice is represented in purple while PINK1 animals are highlighted in green. Red arrow indicates the point of neuronal perturbation.

Table 7.3.3.1.2: Statistical analysis of Kynurenine obtained using unpaired *t*-test for 2-minute restraint tests conducted on humanised PINK1 (*n* = 3) and WT mice (*n* = 5).

Kynurenine					
	Restraint WT		Restraint PINK1		
Time, mins	Mean	SEM	Mean	SEM	*p*
0	127.6	26.1	93.1	1.6	0.46
10	123.6	27.6	206.0	14.1	0.14
20	111.1	5.5	85.0	6.7	0.03
30	138.8	30.9	99.6	12.2	0.45
40	91.2	13.4	111.1	10.1	0.40
50	120.2	18.4	68.5	10.8	0.08
60	107.6	30.1	78.6	18.8	0.52
70	113.9	15.6	109.6	24.0	0.88
80	103.5	15.6	94.3	3.5	0.68
90	120.8	13.7	92.3	16.6	0.24
100	99.2	7.3	79.4	11.4	0.17

7.3.3.2 Branched-Chain Amino Acid (BCAA) Metabolism

BCAAs refers to the essential amino acids, leucine, isoleucine and valine due to the aliphatic side chain that they possess. BCAAs are implicated in a variety of metabolic pathways including protein synthesis, glutamate compartmentalisation and neurotransmitter and catecholamine synthesis from tryptophan, phenylalanine and tyrosine[25]. Additionally, when present in excess concentrations, metabolic products of BCAAs can be cytotoxic[26]. Localisation of the catabolic BCAA pathways are located in the mitochondria of cells with the first two steps of the process being common to all BCAAs[27]. A clear link exists between plasma concentrations of BCAAs and the production of neurotransmitters. BCAAs are transported into the brain by a transporter located on the blood brain barrier. However, this transporter is shared by numerous other amino acids such as tryptophan, tyrosine and phenylalanine making it almost fully saturated at normal plasma amino acid concentrations[25,28]. Elevations of plasma concentrations of BCAAs lead to an increased uptake into the brain whilst decreasing the uptake of tryptophan, tyrosine and phenylalanine simultaneously. Due to the involvement of tryptophan, tyrosine and phenylalanine in the synthesis of dopamine and serotonin, reductions in their uptake across the blood brain barrier results in the reduced synthesis of these neurotransmitters[29].

BCAAs have an important role in the regulation of protein synthesis which is achieved by enhanced translation of mRNA by rapamycin complex 1 (mTORC1) signalling stimulation ultimately leading to increased protein synthesis and tissue growth[30]. Additionally, metabolism of BCAAs results in the formation of coenzyme A derivatives, acetyl-CoA and succinyl-CoA, that consequently enter the TCA cycle in mitochondria[28,31] highlighting the importance of BCAAs in cellular respiration.

One of the most important excitatory neurotransmitters is glutamate which acts post-synaptically on three families of ionotropic receptors including the NMDA, AMPA and kainite receptor[32]. Glutamate is synthesised by BCAAs in astrocytes, with leucine exhibiting the greatest involvement in glutamate synthesis due to leucine entering the brain much more quickly than the other BCAAs[33]. As a result, it can be suggested that an increase in BCAA concentration may lead to altered glutamate metabolism leading to increased excitotoxicity and neuronal degradation as shown in neuronal cultures from the embryonic rat brain[34].

Tables 7.3.2.2.2 & 7.3.2.2.3 highlights a significant decrease in the concentration of L-leucine and L-valine secreted during saline administration measured in humanised PINK1 mice when compared to humanised WT mice. In contrast, a significant increase in BCAA levels was observed in humanised PINK1 mice following restraint tests suggesting a dysregulation of BCAA associated metabolite pathways (Figures 7.3.3.2.1 - 7.3.3.2.3). This significant increase exhibited by leucine, valine and isoleucine during restraint tests corroborate with results obtained by Luan *et al.* whereby elevated levels of BCAAs were detected during early stage, mid stage and late stage PD correlating to PD progression[35]. This suggests that significant increases in BCAAs exhibited during a 2-minute restraint test may be attributed to increased physiological stimulation over a longer period when compared with saline administration which only resulted in a transient increase in neuronal activation (Tables 7.3.3.2.1 - 7.3.3.2.3). This phenomenon is similar to results obtained in Chapter 5 & 6 whereby a greater elevation in amperometric responses were attained following restraint tests when compared with saline administrations.

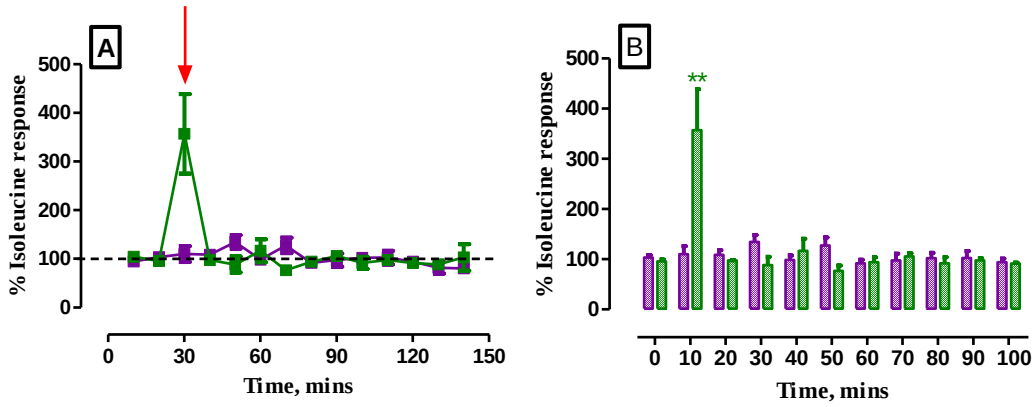

Figure 7.3.3.2.1: (A) Percentage relative response-time profile of Isoleucine obtained following a 2-minute restraint test. Baseline levels were taken 20-minutes prior to the restraint test. (B) Bar graph comparing 10-min microdialysis samples of percentage Isoleucine responses. Baseline levels are representative of 10-minutes before the restraint test. The relative response obtained from WT mice is represented in purple while PINK1 animals are highlighted in green. Red arrow indicates the point of neuronal perturbation.

Table 7.3.3.2.1: Statistical analysis of Isoleucine obtained using unpaired *t*-test for saline administrations and 2-minute restraint tests conducted on humanised PINK1 (*n* = 3) and WT mice (*n* = 5).

Isoleucine					
	Restraint WT		Restraint PINK1		
Time, mins	Mean	SEM	Mean	SEM	*p*
0	103.4	4.6	95.8	3.7	0.30
10	110.0	16.4	357.0	81.7	0.005
20	108.6	9.1	97.3	0.6	0.34
30	134.7	13.5	88.4	16.3	0.11
40	98.4	8.7	116.9	23.6	0.41
50	127.6	15.6	76.8	10.5	0.06
60	91.7	7.1	94.3	9.7	0.83
70	97.4	13.5	105.9	5.8	0.66
80	102.1	10.6	91.9	12.3	0.56
90	102.6	13.8	97.7	4.2	0.80
100	6.7	6.7	91.4	1.9	0.76

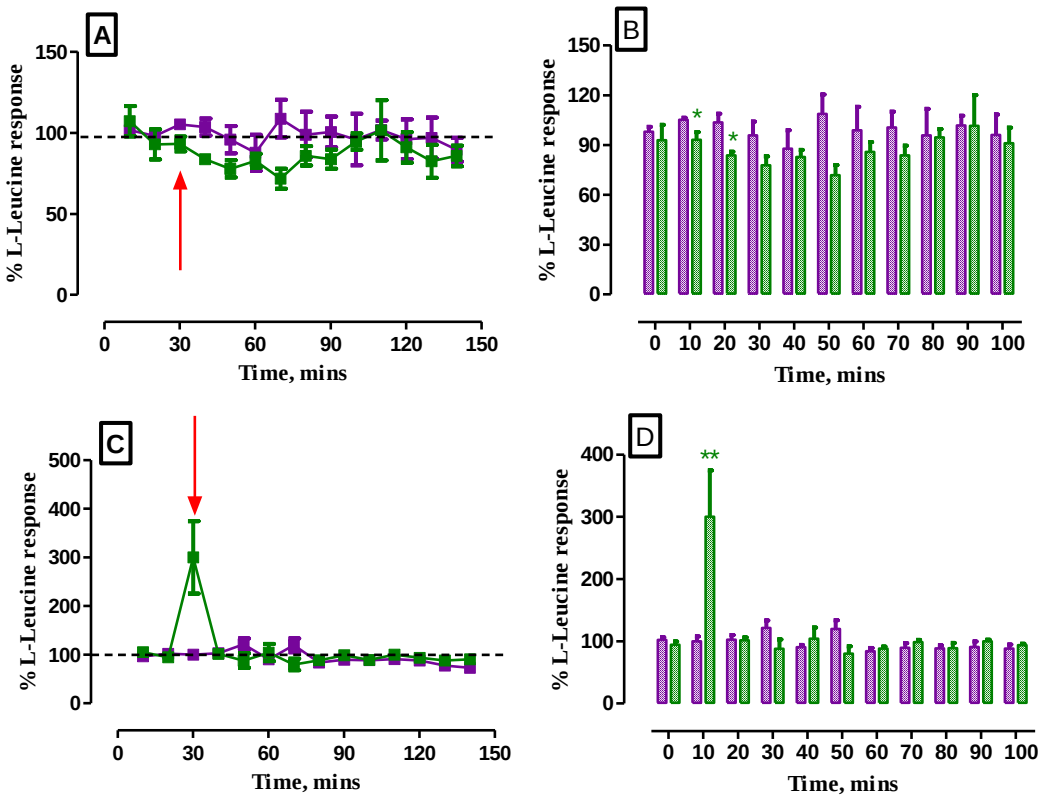

Figure 7.3.3.2.2: (A) Percentage relative response-time profile of L-leucine and (B) Bar graph comparing 10-min microdialysis samples of percentage L-leucine responses obtained following a 1 mL/kg saline i.p. administration (C) Percentage relative response-time profile of L-leucine and (D) Bar graph comparing 10-min microdialysis samples of percentage L-leucine responses obtained following a 2-minute restraint test. The relative response obtained from WT mice is represented in purple while PINK1 animals are highlighted in green. For graphs (A & C) baseline levels were taken 20-minutes prior to the perturbation. Baseline levels are representative of 10-minutes before the perturbation in graphs (B & D). Red arrows indicate the point of neuronal perturbation.

Table 7.3.3.2.2: Statistical analysis of L-leucine obtained using unpaired *t*-test for saline i.p. administrations and 2-minute restraint tests conducted on humanised PINK1 (*n* = 3) and WT mice (*n* = 5).

L-leucine										
	Saline WT		Saline PINK1			Restraint WT		Restraint PINK1		
Time, mins	Mean	SEM	Mean	SEM	*p*	Mean	SEM	Mean	SEM	*p*
0	98.0	2.9	92.8	9.3	0.53	102.3	4.4	94.5	5.4	0.31
10	105.2	1.1	93.1	4.6	0.02	100.3	7.7	300.3	74.4	0.005
20	103.6	5.3	83.7	2.3	0.03	102.9	7.5	101.5	4.5	0.89
30	95.7	8.4	77.8	5.3	0.18	121.7	11.8	88.0	15.1	0.17
40	87.7	11.1	82.8	4.3	0.73	90.7	3.7	104.4	17.5	0.36
50	108.7	11.6	71.7	6.2	0.06	119.6	14.1	80.1	11.9	0.10
60	98.8	14.1	85.8	5.9	0.52	84.2	5.1	88.5	3.0	0.57
70	100.5	9.5	83.7	5.8	0.25	90.0	7.5	98.8	3.5	0.41
80	95.8	15.9	94.5	5.0	0.95	88.9	4.6	89.1	8.5	0.98
90	101.7	5.8	101.5	18.5	0.99	90.8	9.1	100.1	2.7	0.48
100	96.0	12.2	91.0	9.4	0.79	88.2	6.8	93.8	2.2	0.57

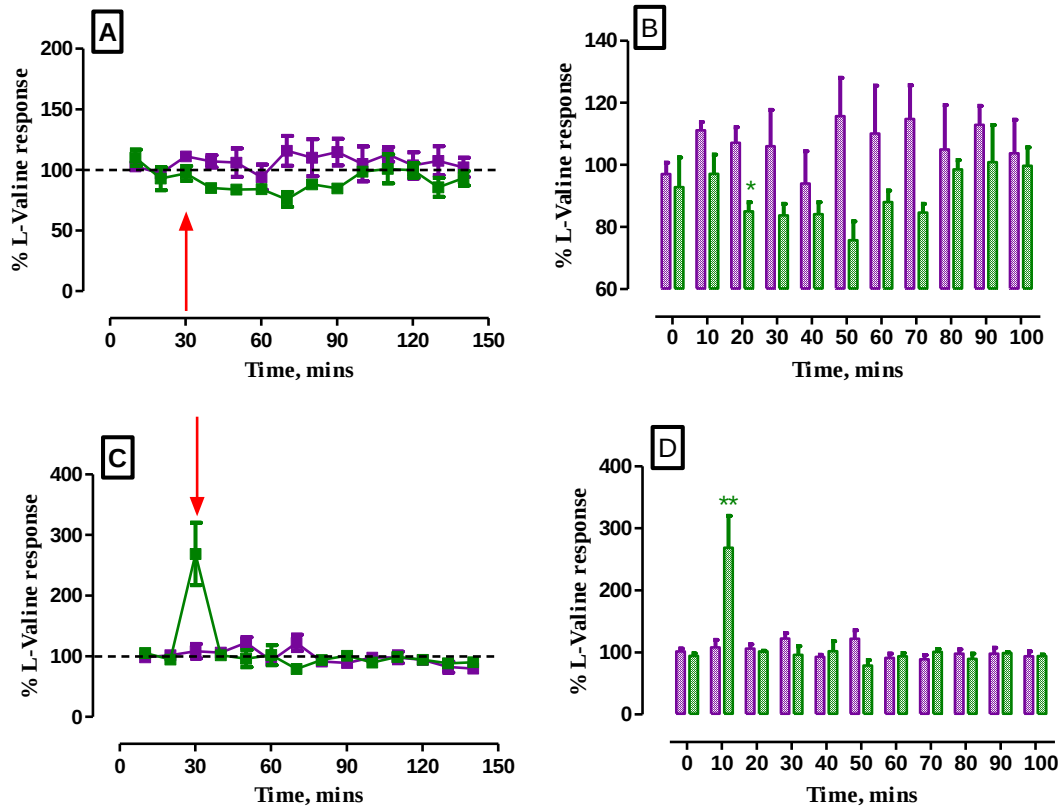

Figure 7.3.3.2.3: (A) Percentage relative response-time profile of L-valine and (B) Bar graph comparing 10-min microdialysis samples of percentage L-valine responses obtained following a 1 mL/kg saline i.p. administration (C) Percentage relative response-time profile of L-valine and (D) Bar graph comparing 10-min microdialysis samples of percentage L-valine responses obtained following a 2-minute restraint test. The relative response obtained from WT mice is represented in purple while PINK1 animals are highlighted in green. For graphs (A & C) baseline levels were taken 20-minutes prior to the perturbation. Baseline levels are representative of 10-minutes before the perturbation in graphs (B & D). Red arrows indicate the point of neuronal perturbation.

Table 7.3.3.2.3: Statistical analysis of L-valine obtained using unpaired *t*-test for saline i.p. administrations and 2-minute restraint tests conducted on humanised PINK1 (*n* = 3) and WT mice (*n* = 5).

L-valine										
	Saline WT		Saline PINK1			Restraint WT		Restraint PINK1		
Time, mins	Mean	SEM	Mean	SEM	*p*	Mean	SEM	Mean	SEM	*p*
0	97.1	3.6	92.8	9.5	0.64	101.7	4.4	64.7	3.6	0.32
10	111.1	2.7	97.2	6.1	0.05	108.4	11.9	268.8	51.4	0.005
20	107.1	5.0	85.0	2.9	0.02	106.1	7.2	101.5	1.2	0.61
30	106.0	11.7	83.7	3.7	0.21	122.3	9.1	96.0	14.1	0.18
40	94.0	10.4	84.1	3.9	0.47	92.7	3.6	101.9	16.3	0.50
50	115.7	12.3	75.7	6.1	0.06	122.1	13.5	79.1	8.4	0.06
60	110.1	15.4	88.0	3.7	0.33	91.1	7.0	94.0	5.2	0.79
70	114.8	10.9	84.6	2.8	0.09	89.0	6.9	100.8	4.9	0.28
80	105.0	14.3	98.5	3.0	0.72	97.9	7.0	89.8	8.0	0.49
90	112.9	6.1	100.9	12.0	0.37	98.0	9.5	99.2	1.5	0.93
100	103.7	10.8	99.7	6.0	0.80	93.9	7.7	94.3	2.4	0.98

7.3.3.3 Glutamate Metabolism

Glutamate is the major excitatory neurotransmitter that is observed to be involved in numerous biological processes[36]. Primarily, L-glutamate is associated with glutamatergic neurotransmission whereby it is released in a Ca^{2+} manner by vesicular glutamate transporter vesicles located in the presynaptic nerve terminals into the synaptic cleft, before binding to glutamate receptors located on the postsynaptic membrane[32,36]. However, it is imperative that neuronal glutamate is replaced to ensure glutamate pools in the neuron do not become depleted. Due to the incapability to synthesise glutamate in the neuronal compartment, glutamate must be produced by the astrocytes to compensate for the reduction in the glutamate precursor, glutamine. The glutamate/glutamine cycle involves uptake of released glutamate by the surrounding astrocytes. Glutamate is thereafter transformed into glutamine by glutamine synthetase before its subsequent release into the extracellular space ready for uptake by adjacent neurons. Glutamine is thereafter converted back to glutamate by phosphase-activated glutaminase allowing for depleted glutamate pools to be replenished[37]. Additionally,

L-aspartic acid is thought to contribute to the production of L-glutamate contained in vesicles by acting as an amino group donor to enable generation of L-glutamate by vesicle-associated aspartate amino transferase from 2-oxoglutarate[38].

Moreover, ammonia is known to be generated following the reaction involving the synthesis of glutamate from glutamine. As elevated levels of ammonia can have detrimental effects on a variety of cellular functions[39], it must be disposed of accordingly. Thus, it has been proposed that the disposal of ammonia occurs via two amino acid shuttles between the glutamatergic neurons and astrocytes. The first of which is facilitated by leucine while the other is based on the action of alanine. Ammonia is thought to incorporate itself into the amino acids allowing for it to be transported across the extracellular space[37]. Referring to Table 7.3.2.1, both L-leucine and L-alanine levels were increased in humanised PINK1 mice following a restraint test. Therefore, it could be postulated that an increase in ammonia is experienced in humanised PINK1 animals leading to an increased detection in metabolic levels of L-leucine and L-alanine.

Figure 7.3.3.3.1 illustrates an increase in levels of L-aspartic acid, which were close to significant, during 2-minute restraint tests at t = 10 mins. Additionally, a significant decrease was noted at t = 50 mins. It is important to remember that microdialysis is a sampling technique which does not occur in real-time. However, it allows for trends in the levels of particular metabolites to be measured in the ECF. As measurements are conducted in the ECF, the metabolite concentration that is present is a balance between its source of production and its region of uptake/metabolism. Therefore, even though a significant decrease is measured at t = 50 mins, it may not necessarily mean that there is a decrease in its production as it may also suggest an increase in the rate of uptake/metabolism of this metabolite. In addition, a significant increase was observed in L-glutamic acid (Figure 7.3.3.3.2) measured in humanised PINK1 mice during restraint tests at t = 10 mins and again at t = 60 mins and t = 80 mins which may be further associated with alterations of metabolite production and uptake following neuronal pertubrtaion. It can postulated following further analysis on the 2 additional humanised PINK1 mice that have been sampled, a significant difference in L-aspartic acid will result. Statistical analysis of these metabolites is included in Tables 7.3.3.3.1 & 7.3.3.3.2. Increased glutamate concentrations can cause neurotoxicity due to the excessive activation of glutamate receptors resulting in a loss

of post-synaptic structures such as dendrites and cell bodies[36]. Studies conducted by Rothstein *et al.*[40] also suggested that even a moderate increase in levels of glutamate was enough to induce toxicity. Conversely, a significant decrease in L-glutamine levels was observed (Figures 7.3.3.3.3) following restraint tests, measured from the striatum of humanised PINK1 subjects. Comparison of the metabolite response measured in humanised PINK1 and WT mice is contained in Table 7.3.3.3.3. It has been reported that for the glutamine-glutamate cycle to work efficiently, neurons must receive equal amounts of carbon from that that has been lost through the production of glutamate. Therefore, indicating that the transfer of glutamine from surrounding astrocytes must be equal to the quantity of glutamate lost from neurons[37]. However, a decrease in L-glutamine was measured in humanised PINK1 mice whereas L-glutamic acid levels were increased. Attainment of these results suggest no synchronicity between L-glutamine and L-glutamic acid levels in the humanised PD graft. Hence, it can be hypothesised that the glutamine-glutamate cycle has become dysregulated in the humanised PINK1 mouse model.

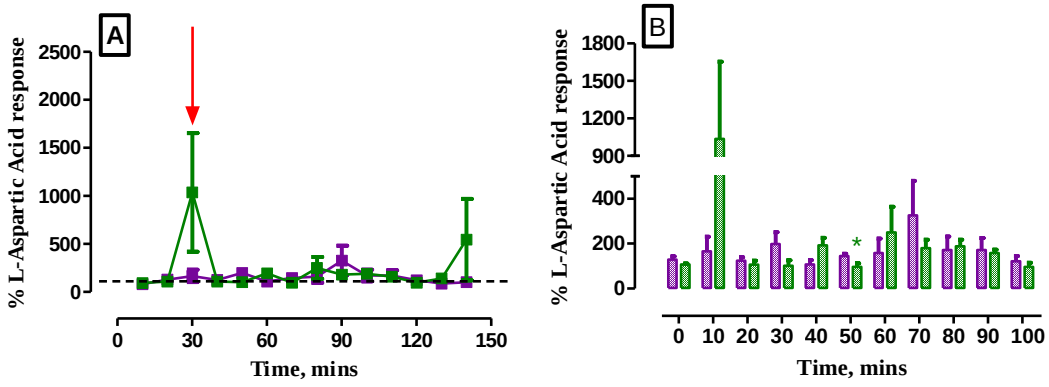

Figure 7.3.3.3.1: (A) Percentage relative response-time profile of L-aspartic acid obtained following a 2-minute restraint test. Baseline levels were taken 20-minutes prior to the restraint test. (B) Bar graph comparing 10-min microdialysis samples of percentage L-aspartic acid responses. Baseline levels are representative of 10-minutes before the restraint test. The relative response obtained from WT mice is represented in purple while PINK1 animals are highlighted in green. Red arrow indicates the point of neuronal perturbation.

Table 7.3.3.3.1: Statistical analysis of L-aspartic acid obtained using unpaired *t*-test for 2-minute restraint tests conducted on humanised PINK1 (*n* = 3) and WT mice (*n* = 5).

L-Aspartic Acid					
	Restraint WT		Restraint PINK1		
Time, mins	Mean	SEM	Mean	SEM	*p*
0	129.0	13.5	107.7	4.2	0.29
10	166.5	64.5	1035.8	617.6	0.05
20	123.7	16.6	106.6	16.8	0.51
30	198.7	52.6	101.8	23.7	0.29
40	107.7	18.8	192.4	33.0	0.05
50	145.0	10.2	96.3	16.6	0.04
60	157.6	65.0	250.0	113.8	0.47
70	326.0	153.2	180.1	37.8	0.51
80	171.1	60.3	188.0	29.4	0.85
90	171.2	53.8	158.3	14.9	0.87
100	121.6	23.1	96.6	18.1	0.49

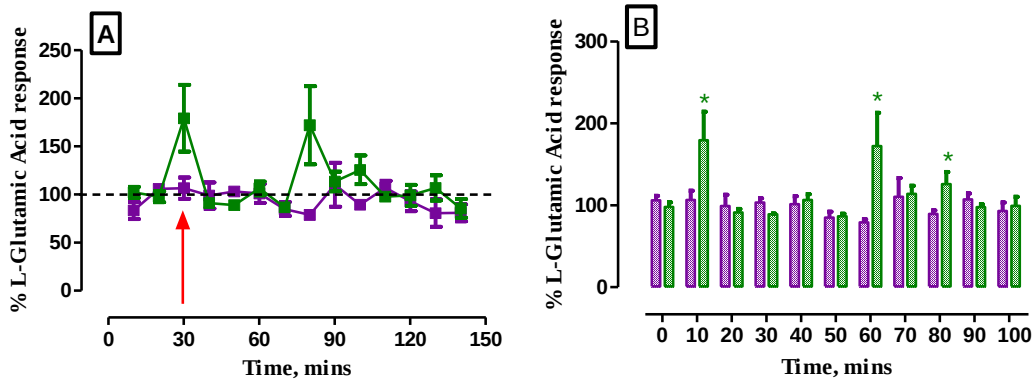

Figure 7.3.3.3.2: (A) Percentage relative response-time profile of L-glutamic acid obtained following a 2-minute restraint test. Baseline levels were taken 20-minutes prior to the restraint test. (B) Bar graph comparing 10-min microdialysis samples of percentage L-glutamic acid responses. Baseline levels are representative of 10-minutes before the restraint test. The relative response obtained from WT mice is represented in purple while PINK1 animals are highlighted in green. Red arrow indicates the point of neuronal perturbation.

Table 7.3.3.3.2: Statistical analysis of L-glutamic acid obtained using unpaired *t*-test for 2-minute restraint tests conducted on humanised PINK1 (*n* = 3) and WT mice (*n* = 5).

L-Glutamic Acid					
	Restraint WT		Restraint PINK1		
Time, mins	Mean	SEM	Mean	SEM	*p*
0	106.0	5.4	97.8	5.7	0.37
10	106.6	11.1	179.3	34.6	0.04
20	98.9	13.7	31.1	4.2	0.66
30	103.2	5.4	89.1	0.9	0.16
40	101.1	9.9	106.4	7.2	0.72
50	84.9	7.3	86.6	3.0	0.87
60	78.9	4.0	172.0	40.6	0.02
70	110.2	22.9	113.6	10.2	0.92
80	89.4	4.2	125.7	14.8	0.02
90	107.1	7.1	97.7	3.2	0.37
100	93.0	10.3	99.2	10.9	0.71

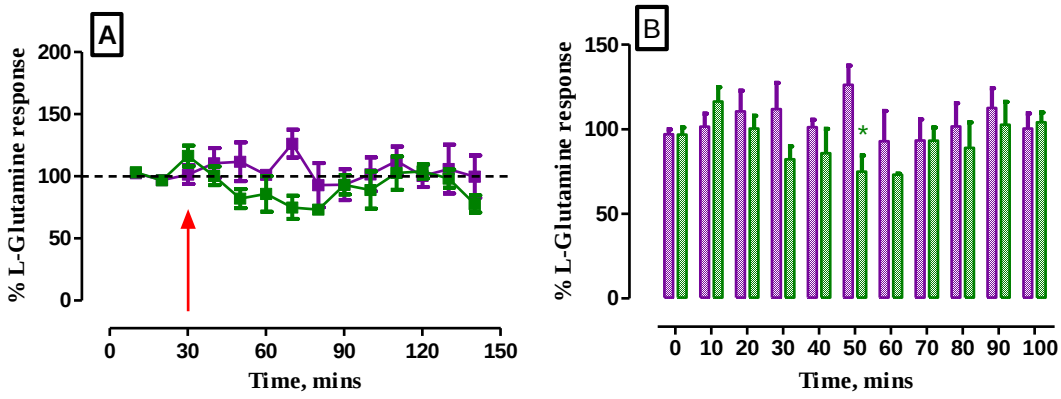

Figure 7.3.3.3.3: (A) Percentage relative response-time profile of L-glutamine obtained following a 2-minute restraint test. Baseline levels were taken 20-minutes prior to the restraint test. (B) Bar graph comparing 10-min microdialysis samples of percentage L-glutamine responses. Baseline levels are representative of 10-minutes before the restraint test. The relative response obtained from WT mice is represented in purple while PINK1 animals are highlighted in green. Red arrow indicates the point of neuronal perturbation.

Table 7.3.3.3.3: Statistical analysis of L-glutamine obtained using unpaired *t*-test for 2-minute restraint tests conducted on humanised PINK1 (*n* = 3) and WT mice (*n* = 5).

L-Glutamine					
	Restraint WT		Restraint PINK1		
Time, mins	Mean	SEM	Mean	SEM	*p*
0	97.0	2.8	96.8	4.2	0.97
10	101.5	7.6	116.3	8.4	0.32
20	110.5	12.2	100.4	7.5	0.54
30	111.8	15.5	82.1	7.7	0.28
40	101.2	4.3	85.8	14.2	0.24
50	126.2	11.2	75.0	9.4	0.02
60	92.9	17.8	73.2	0.5	0.44
70	93.3	12.5	93.1	7.7	0.99
80	101.6	13.6	88.9	15.0	0.57
90	112.4	11.7	102.6	13.4	0.62
100	100.4	8.9	104.0	5.8	0.78

7.3.3.4 Ornithine & Proline Metabolism

L-ornithine is produced by the enzymatic action of arginase on L-arginine resulting in the formation of urea[41]. Therefore, L-ornithine remains an integral part of the urea cycle in the disposal of excess nitrogen. Furthermore, L-ornithine is thought to inhibit increases in ammonia by promoting detoxification while allowing for increased efficiency in energy production[42]. Moreover, L-proline can be synthesised by arginine or ornithine by arginase or ornithine aminotransferase in all mammals[43]. L-proline is thought to play a vital role in protein synthesis and structure, as well as, functioning as a weak agonist of the glycine and NMDA receptors suggesting that it may function as potential endogenous excitotoxin[44,45]. Additionally, L-proline is involved in the scavenging of free radicals[46] suggesting that increases in L-proline may be attributed to an increase in cellular oxidative stress[47]. Furthermore, the L-proline metabolite, L-4-hydroxyproline, has been recently recognised to be a substrate in the synthesis of glycine while working as a scavenger of free radicals[44].

Concentrations of both L-ornithine and L-proline were significantly increased (Figures 7.3.3.4.1C & D & 7.3.3.4.4) during restraint tests. In addition, levels of L-

proline were observed to be significantly decreased following the systemic i.p administration of saline (Figure 7.3.3.4.1A & B). Therefore, indicating that levels of L-ornithine and L-proline are disrupted in humanised PINK1 mice following physiological stimulation. All statistical analysis is included in Tables 7.3.3.4.1 - 7.3.3.4.3. Moreover, it is important to state that L-4-hydroxyproline was decreased following saline administrations and during restraint tests (Figure 7.3.3.4.2). Similarly, L-arginine was decreased following systemic saline administration and increased during restraint tests (Figure 7.3.3.4.3). Although a significant difference was not noted, these results obtained were close to significance. Following conductance of metabolomic analysis on the additional 2 sets of microdialysis samples obtained from humanised PINK1 mice, it can be postulated that a significant difference in L-4-Hydroxyproline and L-arginine levels will be seen. Thus, L-4-Hydroxyproline results have been included in Section 7.3.3.4.

In addition, as L-ornithine is produced from L-arginine, the increased levels of L-ornithine may result from the increased concentration of L-arginine (Figure 7.3.3.4.3C & D). In addition, as discussed in Section 7.3.3.3, ammonia is produced from the glutamate/glutamine cycle. Thus, it was suggested that this cycle was dysregulated in humanised PINK1 mice. Therefore, it could be postulated that an increase in ammonia results leading to an increased need for L-ornithine to promote ammonia detoxification. Similarly, increased levels of L-proline may be due to the presence of an increased concentration of its precursor, L-glutamate being present in humanised PINK1 mice (Section 7.3.3.3) resulting in increased excitotoxicity in these subjects.

Disruption to L-ornithine metabolism is further supported by examining the levels of L-ornithine metabolites, citrulline and homocitrulline measured in humanised PINK1 mice. Figure 7.3.3.4.4 indicates that a close to significant increase in citrulline was measured in humanised PINK1 mice following a 2-minute restraint test. In contrast, a significant decrease in homocitrulline levels was observed as a result of physiological simulation which was induced by restraint tests (Figure 7.3.3.4.5). All statistical analysis is contained in Tables 7.3.3.4.4 & 7.3.3.4.5.

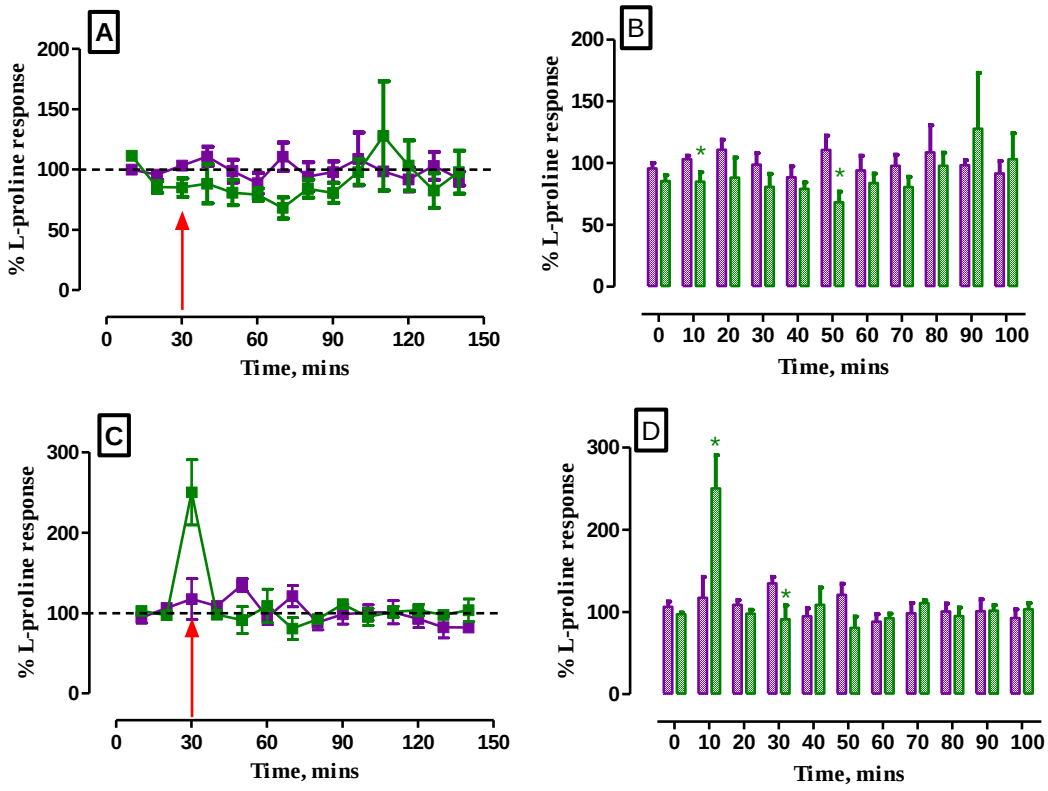

Figure 7.3.3.4.1: (A) Percentage relative response-time figure of L-proline and (B) Bar graph comparing 10-min microdialysis samples of percentage L-proline responses obtained following a 1 mL/kg saline i.p. administration (C) Percentage relative response-time profile of L-proline and (D) Bar graph comparing 10-min microdialysis samples of percentage L-proline responses obtained following a 2-minute restraint test. The relative response obtained from WT mice is represented in purple while PINK1 animals are highlighted in green. For graphs (A & C) baseline levels were taken 20-minutes prior to the perturbation. Baseline levels are representative of 10-minutes before the perturbation in graphs (B & D). Red arrows indicate the point of neuronal perturbation.

Table 7.3.3.4.1: Statistical analysis of L-proline obtained using unpaired *t*-test for saline i.p. administrations and 2-minute restraint tests conducted on humanised PINK1 (*n* = 3) and WT mice (*n* = 5).

L-Proline										
	Saline WT		Saline PINK1			Restraint WT		Restraint PINK1		
Time, mins	Mean	SEM	Mean	SEM	*p*	Mean	SEM	Mean	SEM	*p*
0	95.8	4.4	85.5	4.8	0.18	106.1	6.4	97.4	1.8	0.26
10	103.2	2.9	85.0	7.7	0.04	117.2	25.3	250.1	40.5	0.04
20	110.9	8.0	88.2	16.3	0.23	108.8	5.5	98.0	4.5	0.21
30	98.7	9.3	80.9	10.5	0.27	134.7	7.8	91.2	16.7	0.04
40	88.6	8.8	79.3	5.1	0.44	94.8	9.5	108.8	20.9	0.51
50	110.6	11.7	68.1	8.8	0.04	120.9	13.3	80.6	13.6	0.10
60	94.1	11.9	84.0	7.5	0.57	88.2	9.2	92.3	5.7	0.76
70	97.8	8.9	80.7	8.3	0.25	98.6	12.3	110.9	3.3	0.49
80	108.8	21.9	97.8	10.6	0.70	100.6	9.6	95.1	10.4	0.72
90	98.4	4.1	127.8	45.2	0.47	101.0	14.5	101.5	6.7	0.98
100	91.8	9.9	103.3	20.8	0.59	92.5	10.6	103.5	7.1	0.49

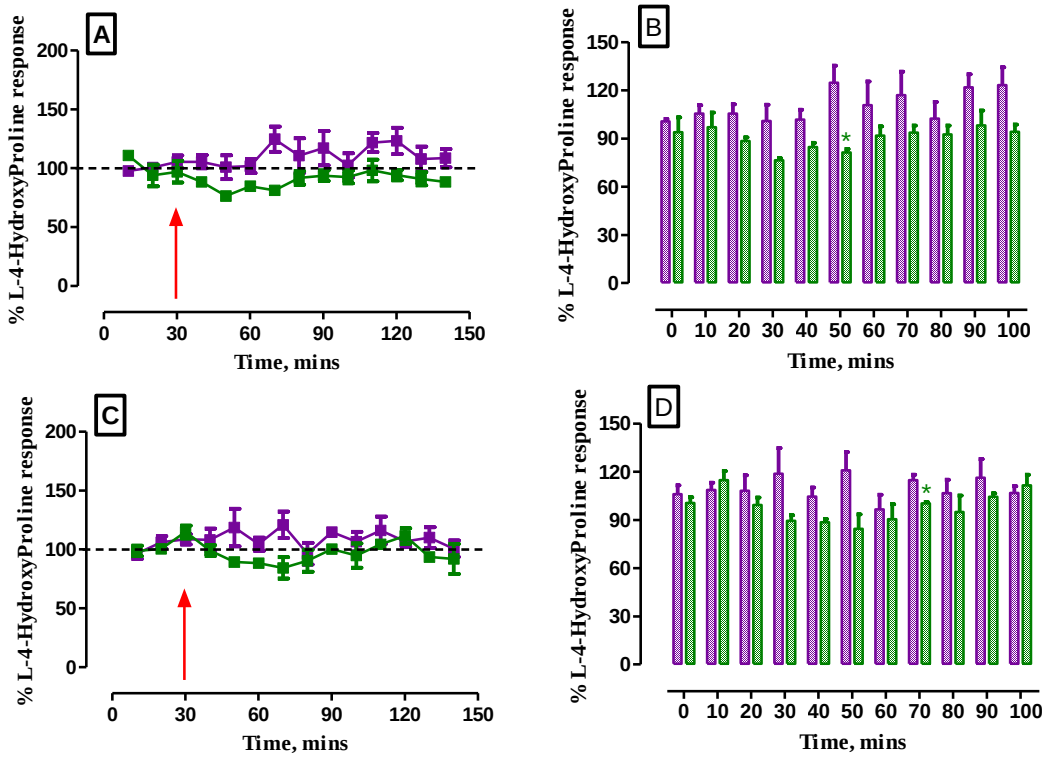

Figure 7.3.3.4.2: (A) Percentage relative response-time profile of L-4-hydroxyproline and (B) Bar graph comparing 10-min microdialysis samples of percentage L-4-hydroxyproline responses obtained following a 1 mL/kg saline i.p. administration (C) Percentage relative response-time profile of L-4-hydroxyproline and (D) Bar graph comparing 10-min microdialysis samples of percentage L-4-hydroxyproline responses obtained following a 2-minute restraint test. The relative response obtained from WT mice is represented in purple while PINK1 animals are highlighted in green. For graphs (A & C) baseline levels were taken 20-minutes prior to the perturbation. Baseline levels are representative of 10-minutes before the perturbation in graphs (B & D). Red arrows indicate the point of neuronal perturbation.

Table 7.3.3.4.2: Statistical analysis of L-4-hydroxyproline obtained using unpaired *t*-test for saline i.p. administrations and 2-minute restraint tests conducted on humanised PINK1 (*n* = 3) and WT mice (*n* = 5).

L-4-Hydroxyproline										
	Saline WT		Saline PINK1			Restraint WT		Restraint PINK1		
Time, mins	Mean	SEM	Mean	SEM	*p*	Mean	SEM	Mean	SEM	*p*
0	100.6	1.6	93.9	9.2	0.38	106.0	5.4	100.5	3.6	0.50
10	105.5	5.4	97.0	9.1	0.42	108.6	4.5	114.8	5.5	0.47
20	105.5	5.7	88.4	2.3	0.06	108.1	9.7	99.2	4.6	0.50
30	100.9	10.0	76.5	1.3	0.12	118.7	15.9	89.3	3.6	0.29
40	101.8	6.0	84.7	2.5	0.07	104.6	5.5	88.5	2.0	0.08
50	124.7	10.7	81.3	2.2	0.02	120.9	11.3	84.4	9.1	0.07
60	110.7	14.7	91.8	5.8	0.38	96.4	9.2	90.4	9.4	0.69
70	117.1	14.6	93.6	4.4	0.28	114.8	3.3	100.3	0.9	0.02
80	102.4	10.2	92.5	5.5	0.48	106.6	8.3	94.9	10.3	0.41
90	121.8	8.1	98.2	9.2	0.11	116.2	11.7	104.4	2.0	0.48
100	123.3	11.1	94.1	4.5	0.10	106.7	4.4	111.5	6.6	0.55

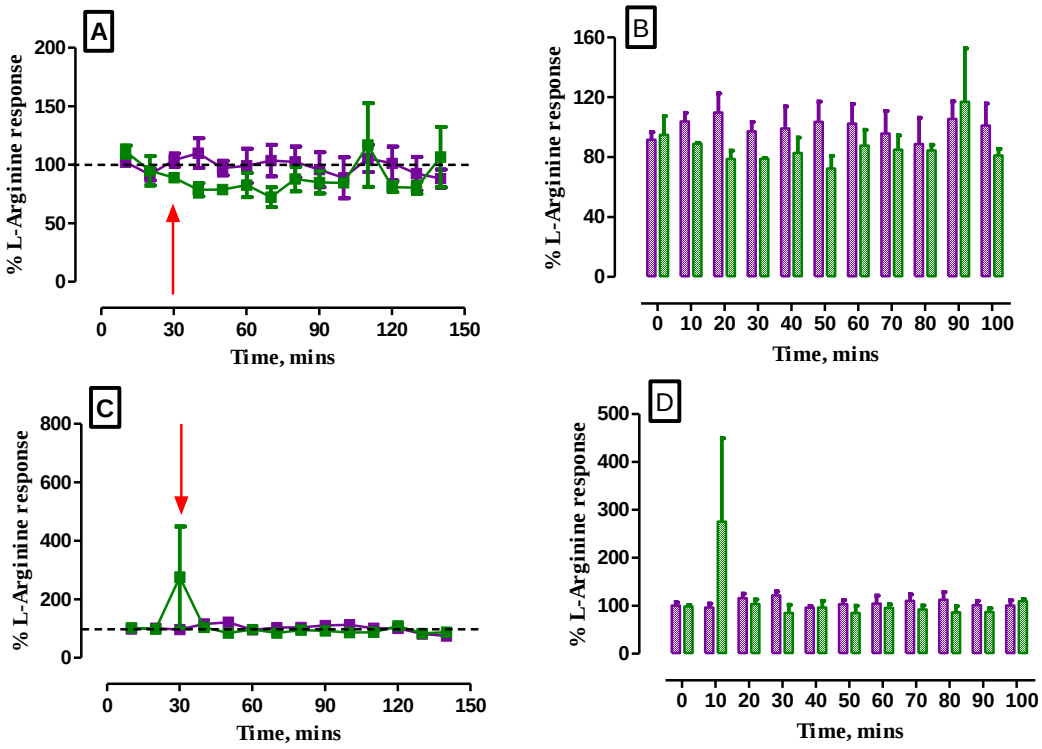

Figure 7.3.3.4.3: (A) Percentage relative response-time profile of L-arginine and (B) Bar graph comparing 10-min microdialysis samples of percentage L-arginine responses obtained following a 1 mL/kg saline i.p administration (C) Percentage relative response-time profile of L-arginine and (D) Bar graph comparing 10-min microdialysis samples of percentage L-arginine responses obtained following a 2-minute restraint test. The relative response obtained from WT mice is represented in purple while PINK1 animals are highlighted in green. For graphs (A & C) baseline levels were taken 20-minutes prior to the perturbation. Baseline levels are representative of 10-minutes before the perturbation in graphs (B & D). Red arrows indicate the point of neuronal perturbation.

Table 7.3.3.4.3: Statistical analysis of L-arginine obtained using unpaired *t*-test for saline i.p. administrations and 2-minute restraint tests conducted on humanised PINK1 (*n* = 3) and WT mice (*n* = 5).

L-Arginine										
	Saline WT		Saline PINK1			Restraint WT		Restraint PINK1		
Time, mins	Mean	SEM	Mean	SEM	*p*	Mean	SEM	Mean	SEM	*p*
0	91.6	5.1	94.9	12.6	0.78	100.9	6.5	98.5	3.2	0.80
10	103.9	5.6	89.0	0.61	0.09	96.3	7.9	275.9	173.2	0.11
20	109.9	12.7	78.7	5.7	0.10	116.2	8.9	104.0	9.3	0.40
30	97.2	6.3	78.8	0.6	0.07	121.5	8.6	84.8	17.1	0.09
40	99.2	14.7	82.7	10.4	0.43	95.8	3.9	96.3	14.2	0.97
50	103.6	13.6	72.4	8.5	0.15	103.5	8.5	85.0	15.2	0.29
60	102.5	13.2	87.8	10.5	0.47	104.4	16.9	95.4	7.8	0.69
70	95.8	15.1	85.0	9.5	0.63	110.5	13.4	92.2	8.4	0.37
80	88.8	17.5	84.5	3.7	0.85	112.6	16.2	86.6	12.5	0.31
90	105.5	11.7	116.9	35.8	0.74	101.1	9.2	87.4	7.0	0.35
100	101.2	14.6	81.1	4.5	0.35	100.9	10.6	109.4	4.0	0.58

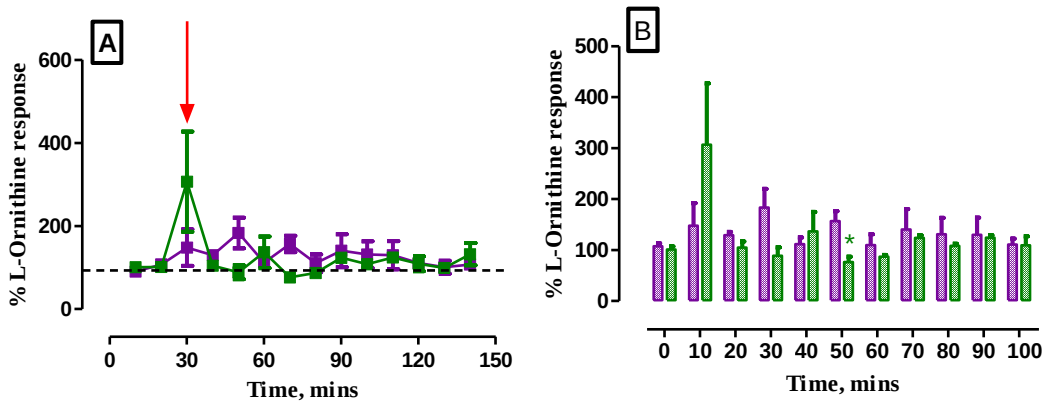

Figure 7.3.3.4.4: (A) Percentage relative response-time profile of L-ornithine obtained following a 2-minute restraint test. Baseline levels were taken 20-minutes prior to the restraint test. (B) Bar graph comparing 10-min microdialysis samples of percentage L-ornithine responses. Baseline levels are representative of 10-minutes before the restraint test. The relative response obtained from WT mice is represented in purple while PINK1 animals are highlighted in green. Red arrow indicates the point of neuronal perturbation.

Table 7.3.3.4.4: Statistical analysis of L-ornithine obtained using unpaired *t*-test for 2-minute restraint tests conducted on humanised PINK1 (*n* = 3) and WT mice (*n* = 5).

L-Ornithine					
	Restraint WT		Restraint PINK1		
Time, mins	Mean	SEM	Mean	SEM	*p*
0	107.7	5.8	101.3	5.9	0.50
10	148.0	43.9	306.8	120.4	0.16
20	129.6	5.6	104.7	12.2	0.10
30	183.4	36.8	88.6	16.6	0.17
40	111.9	12.8	136.7	38.0	0.47
50	156.7	19.6	76.5	10.0	0.03
60	110.2	21.3	86.9	3.8	0.45
70	140.7	39.8	123.7	5.1	0.76
80	131.2	31.9	108.0	4.4	0.61
90	129.7	34.0	124.2	5.3	0.91
100	110.9	11.5	109.4	17.8	0.94

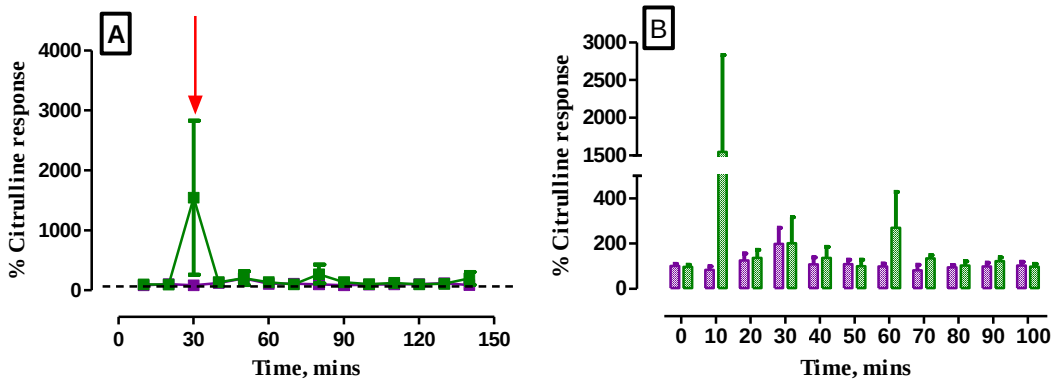

Figure 7.3.3.4.5: (A) Percentage relative response-time profile of Citrulline obtained following a 2-minute restraint test. Baseline levels were taken 20-minutes prior to the restraint test. (B) Bar graph comparing 10-min microdialysis samples of percentage Citrulline responses. Baseline levels are representative of 10-minutes before the restraint test. The relative response obtained from WT mice is represented in purple while PINK1 animals are highlighted in green. Red arrow indicates the point of neuronal perturbation.

Table 7.3.3.4.5: Statistical analysis of Citrulline obtained using unpaired *t*-test for 2-minute restraint tests conducted on humanised PINK1 (*n* = 3) and WT mice (*n* = 5).

Citrulline					
	Restraint WT		Restraint PINK1		
Time, mins	Mean	SEM	Mean	SEM	*p*
0	100.9	9.8	96.3	8.9	0.76
10	83.6	15.4	1547.0	1285.0	0.08
20	125.3	30.8	136.7	35.8	0.82
30	198.0	72.0	201.1	115.8	0.98
40	108.8	30.4	137.0	48.5	0.62
50	109.6	18.8	99.7	29.3	0.77
60	98.3	13.0	269.8	158.7	0.19
70	81.7	24.0	134.6	14.0	0.15
80	95.5	10.0	102.5	18.7	0.70
90	98.1	17.1	122.6	16.3	0.38
100	102.8	17.0	97.6	12.8	0.84

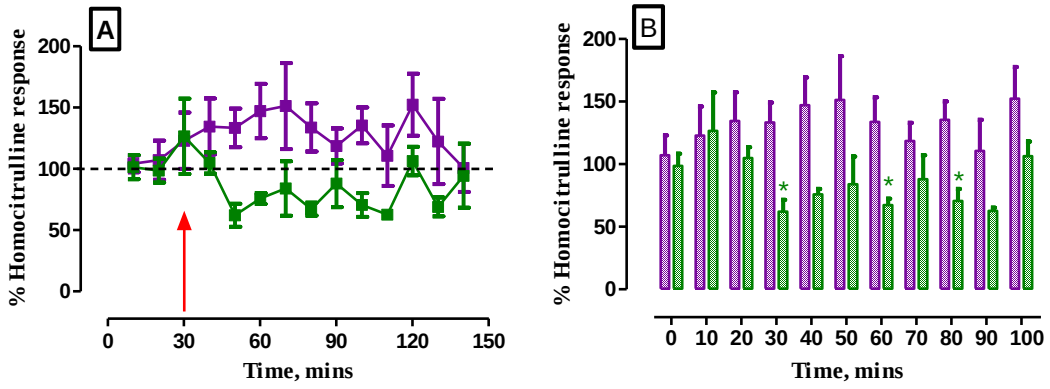

Figure 7.3.3.4.6: (A) Percentage relative response-time profile of Homocitrulline obtained following a 2-minute restraint test. Baseline levels were taken 20-minutes prior to the restraint test. (B) Bar graph comparing 10-min microdialysis samples of percentage Homocitrulline responses. Baseline levels are representative of 10-minutes before the restraint test. The relative response obtained from WT mice is represented in purple while PINK1 animals are highlighted in green. Red arrow indicates the point of neuronal perturbation.

Table 7.3.3.4.6: Statistical analysis of Homocitrulline obtained using unpaired *t*-test for 2-minute restraint tests conducted on humanised PINK1 (*n* = 3) and WT mice (*n* = 5).

Homocitrulline					
	Restraint WT		Restraint PINK1		
Time, mins	Mean	SEM	Mean	SEM	*p*
0	107.1	16.0	98.7	9.8	0.72
10	122.9	23.1	126.6	30.8	0.93
20	134.6	22.8	105.0	8.7	0.34
30	133.4	15.8	62.2	9.4	0.04
40	147.2	22.1	75.8	4.4	0.05
50	151.3	35.1	84.0	22.2	0.22
60	133.8	19.6	67.2	5.3	0.04
70	118.7	14.4	88.0	19.2	0.24
80	135.5	14.7	70.6	9.8	0.02
90	110.7	24.8	62.7	2.6	0.20
100	152.3	25.4	106.4	11.7	0.24

7.3.3.5 Phenylalanine & Tyrosine Metabolism

One of the most important functions of aromatic amino acids is the ability to act as pre-cursors for the production of neurotransmitters such as serotonin and catecholamines. For this reason, brain concentrations of relevant amino acids are directly correlated to the rate of neurotransmitters production and its subsequent release. Catecholamine production is stimulated by increasing brain concentrations of tyrosine. However, tyrosine is only produced following elevation of brain phenylalanine concentrations as phenylalanine is a known pre-cursor of tyrosine production. Subsequently, increased tyrosine concentrations stimulates catecholamine production leading to an increase in actively firing neurons[48]. However, the concentration of phenylalanine in the brain is directly influenced by the availability of the phenylalanine from the blood. As seen with BCAA and tryptophan transport into the brain (Sections 7.3.3.1 & 7.3.3.2), transport of specific amino acids is dependent on the common transporter across the blood brain barrier. Therefore, phenylalanine must be able to actively compete against other larger neural amino acids for transport into the brain to allow for the synthesis of monoamine neurotransmitters[49]. Previous

investigations have shown that catecholamine synthesis increased in the striatum of rats following administration of L-tyrosine[50]. Synthesis of catecholamines, such as dopamine, from tyrosine occurs following hydroxylation of tyrosine by tyrosine hydroxylase to dihydroxyphenylalanine (DOPA). This step is considered to be rate limiting in the overall synthesis of catecholamines[51]. Following DOPA synthesis, DOPA is rapidly decarboxylated to DA which can then be used by surrounding neurons as a neurotransmitter[48]. Moreover, 3-methoxytyramine (3-MT) is a known metabolite of dopamine. Until recently, 3-MT has been considered to be largely biologically inactive. However, studies have indicated that 3-MT works as a neuromodulator by acting on the G protein-coupled trace amine receptor 1 (TAAR1)[52] to induce disorganised abnormal movements including tremor and head bobbing in mice. Additionally, it has been estimated that concentrations of 3-MT should be 500 nM or greater in which to induce these neuromodulatory effects. Presently, it remains unclear if the normal 3-MT concentrations are sufficient to achieve activation of TAAR1 but it is postulated that in pathological conditions whereby DA release is significantly higher or a monoamine oxidase (MAO) deficiency exists that accumulations of 3-MT may reach concentrations required to activate TAAR1[53].

Similar to metabolites associated with BCAA metabolism discussed in Section 7.3.3.2, levels of 3-MT, phenylalanine and L-tyrosine were noted to significantly decrease during saline administration (Figures 7.3.3.5.1 - 7.3.3.5.3) while phenylalanine and L-tyrosine increased significantly during restraint stress tests in humanised PINK1 mice when compared to non-humanised WT mice (Figures 7.3.3.5.2 & 7.3.3.5.3). Previous reports have highlighted that an altered level of phenylalanine can be indicative of disrupted phenylalanine metabolism in early-stage PD[35]. Furthermore, altered levels of 3-MT may act to induce involuntary movements in humanised PINK1 mice by acting on TAAR1. The results obtained following statistical analysis are contained in Tables 7.3.3.5.1 - 7.3.3.5.3. Additionally, as discussed in Section 7.3.3.2, restraint tests may cause a greater effect on neuronal activation when compared to saline administration leading to an increase in metabolite levels being observed.

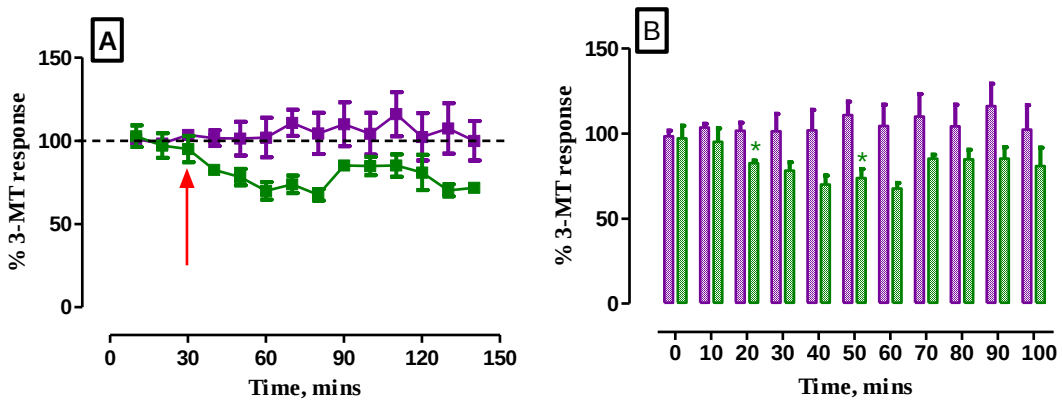

Figure 7.3.3.5.1: (A) Percentage relative response-time profile of 3-methoxytyramine obtained following a 1 mL/kg saline i.p. administration. Baseline levels were taken 20-minutes prior to the restraint test. (B) Bar graph comparing 10-min microdialysis samples of percentage 3-methoxytyramine responses. Baseline levels are representative of 10-minutes before the restraint test. The relative response obtained from WT mice is represented in purple while PINK1 animals are highlighted in green. Red arrow indicates the point of neuronal perturbation.

Table 7.3.3.5.1: Statistical analysis of 3-methoxytyramine obtained using unpaired *t*-test for saline i.p. administrations conducted on humanised PINK1 (*n* = 3) and WT mice (*n* = 5).

3-Methoxytyramine					
	Saline WT		Saline PINK1		
Time, mins	Mean	SEM	Mean	SEM	*p*
0	98.5	3.1	97.2	7.4	0.86
10	103.6	2.0	95.1	8.0	0.23
20	101.6	4.7	82.6	1.4	0.02
30	101.3	10.1	78.1	4.9	0.15
40	101.9	11.9	69.9	5.2	0.08
50	110.8	7.8	73.8	5.2	0.01
60	104.4	12.5	67.5	3.4	0.07
70	109.9	13.2	85.2	2.2	0.21
80	104.3	12.5	84.9	5.4	0.27
90	116.0	13.3	85.1	6.7	0.12
100	102.3	14.3	81.0	10.6	0.34

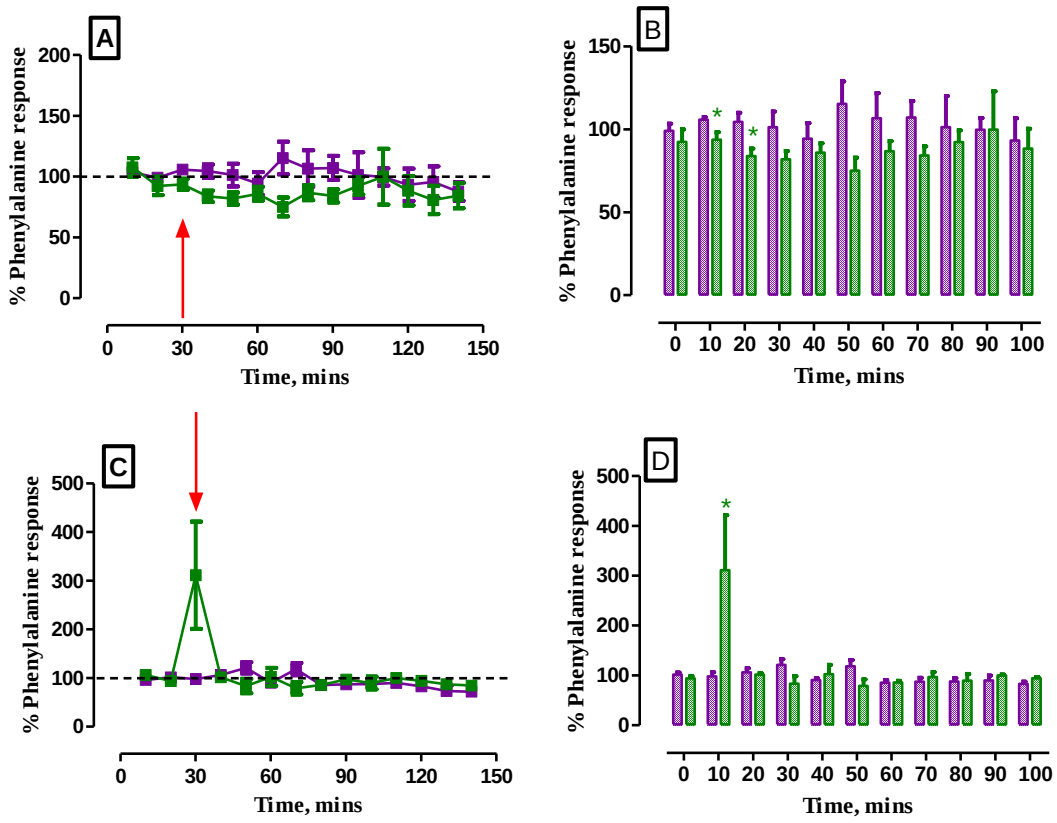

Figure 7.3.3.5.2: (A) Percentage relative response-time profile of Phenylalanine and (B) Bar graph comparing 10-min microdialysis samples of percentage Phenylalanine responses obtained following a 1 mL/kg saline i.p. administration (C) Percentage relative response-time profile of Phenylalanine and (D) Bar graph comparing 10-min microdialysis samples of percentage Phenylalanine responses obtained following a 2-minute restraint test. The relative response obtained from WT mice is represented in purple while PINK1 animals are highlighted in green. For graphs (A & C) baseline levels were taken 20-minutes prior to the perturbation. Baseline levels are representative of 10-minutes before the perturbation in graphs (B & D). Red arrows indicate the point of neuronal perturbation.

Table 7.3.3.5.2: Statistical analysis of Phenylalanine obtained using unpaired *t*-test for saline i.p. administrations and 2-minute restraint tests conducted on humanised PINK1 (*n* = 3) and WT mice (*n* = 5).

Phenylalanine										
	Saline WT		Saline PINK1			Restraint WT		Restraint PINK1		
Time, mins	Mean	SEM	Mean	SEM	*p*	Mean	SEM	Mean	SEM	*p*
0	99.2	4.2	92.4	7.6	0.42	101.8	4.1	93.8	4.5	0.26
10	105.7	1.7	93.6	4.6	0.02	98.1	8.6	311.4	110.2	0.02
20	104.5	5.5	83.8	4.6	0.04	106.2	8.0	101.5	2.6	0.64
30	101.3	9.3	81.9	4.9	0.18	120.9	11.7	83.5	14.8	0.13
40	94.3	9.4	85.9	5.7	0.52	90.7	3.6	102.5	18.7	0.45
50	115.3	13.5	75.1	7.7	0.08	118.4	12.6	79.1	12.6	0.09
60	106.6	15.1	86.7	6.1	0.37	85.2	5.5	86.1	3.2	0.92
70	107.2	9.8	84.2	5.4	0.14	87.4	7.8	96.9	9.8	0.48
80	101.4	18.7	92.3	7.1	0.71	87.6	6.7	89.7	13.1	0.88
90	99.7	7.0	99.8	23.0	0.99	90.1	9.5	100.0	1.5	0.46
100	93.3	13.3	88.4	12.0	0.81	83.3	4.0	94.1	2.3	0.10

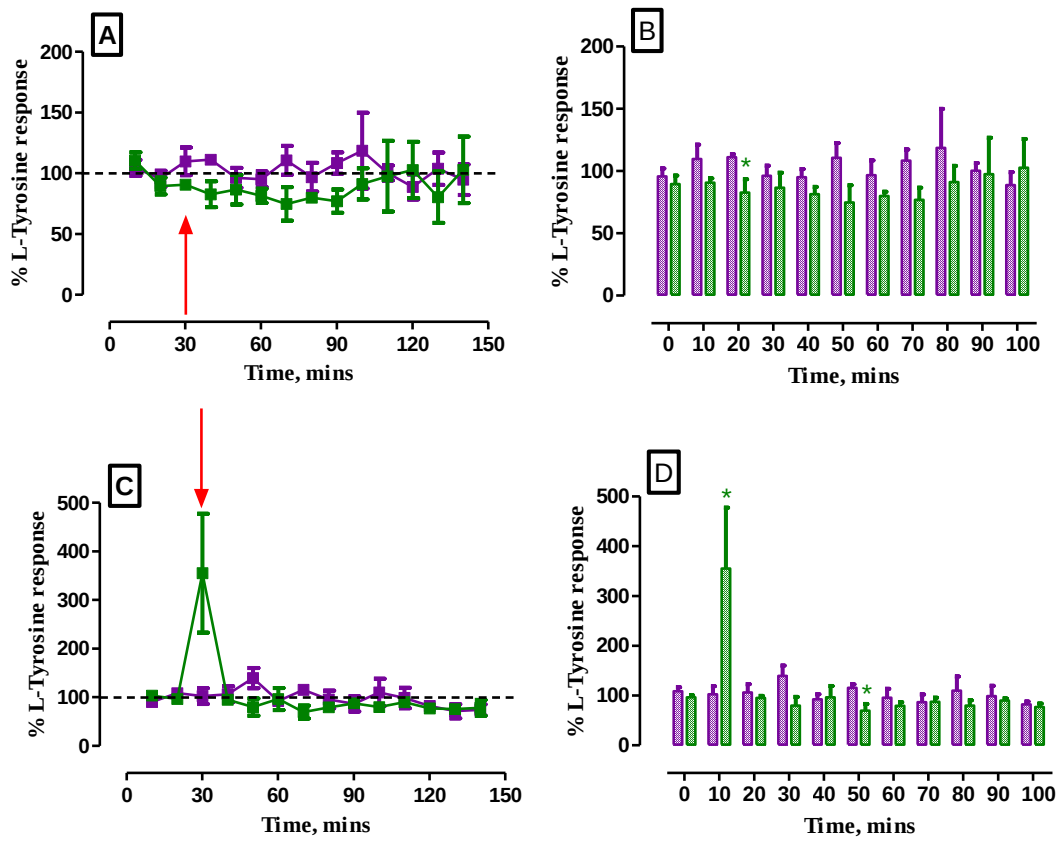

Figure 7.3.3.5.3: (A) Percentage relative response-time profile of L-tyrosine and (B) Bar graph comparing 10-min microdialysis samples of percentage L-tyrosine responses obtained following a 1 mL/kg saline i.p. administration (C) Percentage relative response-time profile of L-tyrosine and (D) Bar graph comparing 10-min microdialysis samples of percentage L-tyrosine responses obtained following a 2-minute restraint test. The relative response obtained from WT mice is represented in purple while PINK1 animals are highlighted in green. For graphs (A & C) baseline levels were taken 20-minutes prior to the perturbation. Baseline levels are representative of 10-minutes before the perturbation in graphs (B & D). Red arrows indicate the point of neuronal perturbation.

Table 7.3.3.5.3: Statistical analysis of L-tyrosine obtained using unpaired *t*-test for saline i.p. administrations and 2-minute restraint tests conducted on humanised PINK1 (*n* = 3) and WT mice (*n* = 5).

L-tyrosine										
	Saline WT		Saline PINK1			Restraint WT		Restraint PINK1		
Time, mins	Mean	SEM	Mean	SEM	*p*	Mean	SEM	Mean	SEM	*p*
0	95.6	6.6	89.6	6.9	0.57	108.8	7.9	96.3	4.5	0.30
10	109.8	11.4	90.7	3.5	0.26	102.5	16.3	355.4	122.4	0.02
20	111.2	2.4	82.7	10.7	0.03	106.4	16.4	95.4	3.8	0.60
30	96.2	8.2	86.5	12.1	0.52	139.7	20.9	79.7	17.5	0.15
40	95.1	6.4	81.5	5.8	0.19	92.4	10.0	96.6	22.6	0.85
50	110.6	11.8	74.8	13.9	0.10	115.5	7.2	69.7	13.3	0.02
60	96.8	11.8	79.9	3.5	0.33	95.4	18.2	79.3	7.5	0.54
70	108.4	8.9	77.0	9.5	0.06	86.6	15.4	87.9	7.7	0.95
80	118.7	31.2	91.3	12.9	0.51	110.0	28.3	80.0	10.7	0.47
90	100.2	6.1	97.6	29.1	0.92	98.7	21.0	89.9	4.4	0.76
100	88.8	10.4	102.8	23.1	0.55	82.1	5.9	76.9	7.1	0.60

7.3.3.6 Glycine Synthesis & Metabolism

Glycine is synthesised in the central nervous system by the catalysis of serine by the enzymatic activity of serine-hydroxymethyltransferase[54]. Glycine is observed to exhibit a dual role by functioning as an inhibitory neurotransmitter at many strychnine-sensitive glycine receptor (GlyR)-chloride channels[55] while also acting as a co-agonist of the NMDA receptor[56]. Important brain functions such as learning and memory rely on a balanced regulation between the excitation and inhibition of neurons. Thus, it can be postulated that glycine plays an important role in this regulation. Zhang *et al.* have previously shown that hippocampal glycine increases GlyR-mediated inhibition while simultaneously facilitating increases in NMDAR-dependent excitation[57]. Hence, this evidence supports the hypothesis for the involvement of glycine in the balanced regulation of inhibitory and excitatory processes in the neuronal network. Additionally, uptake of glycine from the extracellular space is mediated through various sodium/chloride transporters, GlyT1 and GlyT2[58], which are found to be highly expressed in the brain stem, brain

hemispheres and the cerebellum[59]. In particular, GlyT1 transporters are known to be widely expressed in astrocytic glial cells where it is thought that GlyT1 is involved in the regulation of extracellular glycine concentrations and glycine binding to NMDA receptors leading to excitatory neuronal signalling[56]. Previous studies have observed that following administration of glycine into the striatum of conscious rats, dopamine is released into the ECF highlighting the action of glycine as an excitatory neurotransmitter[60].

During restraint tests, levels of L-serine, homoserine, glycine and its derivative, glycylglycine, were seen to be significantly increased in humanised PINK1 mice following physiological stimulation (Figures 7.3.3.6.1 - 7.3.3.6.4). Moreover, L-serine was seen to be significantly decreased following saline administration which is known to cause transient changes in neuronal activation (Figure 7.3.3.6.1A & B). Statistical analysis was conducted on the aforementioned metabolites measured in the dialysate collected from humanised animals which are contained in Tables 7.3.3.6.1 - 7.3.3.6.4. These altered levels of L-serine, homoserine, glycine and glycylglycine observed may be due to alterations in glycine synthesis and metabolism which may be associated with PINK1 mutations. Previous studies have reported that both glycine and its derivatives are altered significantly in the urine of PD patients[35].

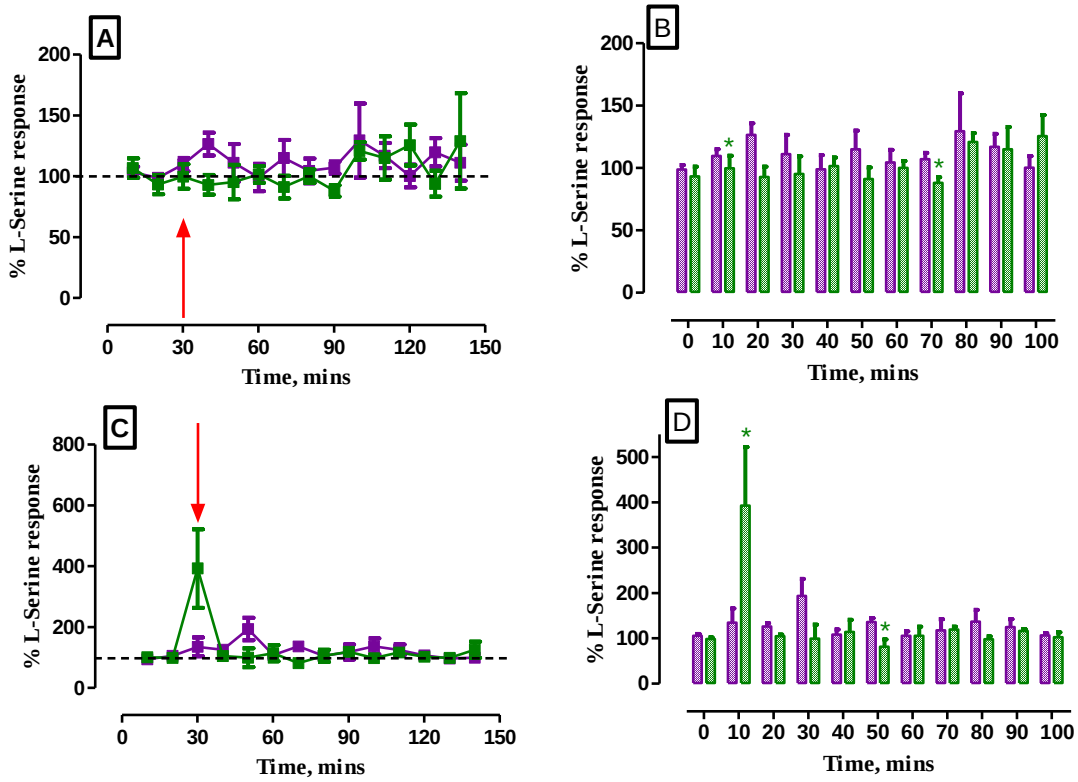

Figure 7.3.3.6.1: (A) Percentage relative response-time profile of L-serine and (B) Bar graph comparing 10-min microdialysis samples of percentage L-serine responses obtained following a 1 mL/kg saline i.p. administration (C) Percentage relative response-time profile of L-serine and (D) Bar graph comparing 10-min microdialysis samples of percentage L-serine responses obtained following a 2-minute restraint test. The relative response obtained from WT mice is represented in purple while PINK1 animals are highlighted in green. For graphs (A & C) baseline levels were taken 20-minutes prior to the perturbation. Baseline levels are representative of 10-minutes before the perturbation in graphs (B & D). Red arrows indicate the point of neuronal perturbation.

Table 7.3.3.6.1: Statistical analysis of L-serine obtained using unpaired *t*-test for saline i.p. administrations and 2-minute restraint tests conducted on humanised PINK1 (*n* = 3) and WT mice (*n* = 5).

L-serine										
	Saline WT		Saline PINK1			Restraint WT		Restraint PINK1		
Time, mins	Mean	SEM	Mean	SEM	*p*	Mean	SEM	Mean	SEM	*p*
0	98.9	3.5	93.2	7.9	0.47	105.8	4.1	98.7	3.6	0.28
10	109.7	5.4	99.8	10.0	0.37	134.9	31.0	392.8	129.2	0.03
20	126.5	9.3	92.9	8.0	0.04	125.9	7.8	104.8	3.6	0.08
30	111.1	15.5	95.3	14.0	0.52	193.9	37.2	99.4	30.8	0.18
40	99.1	11.2	101.6	6.9	0.87	108.3	11.0	114.2	26.7	0.82
50	115.1	14.8	91.2	9.3	0.29	136.4	8.0	81.5	15.8	0.01
60	104.5	10.1	100.1	5.5	0.77	105.8	9.8	105.8	20.0	1.00
70	107.1	5.0	88.0	4.7	0.04	118.1	24.2	119.2	6.5	0.97
80	129.5	30.5	120.9	7.2	0.82	136.5	26.1	97.9	6.1	0.31
90	117.0	10.3	115.1	17.7	0.93	124.8	17.5	116.4	4.1	0.73
100	100.3	9.2	125.7	16.8	0.19	106.7	4.5	102.6	10.6	0.69

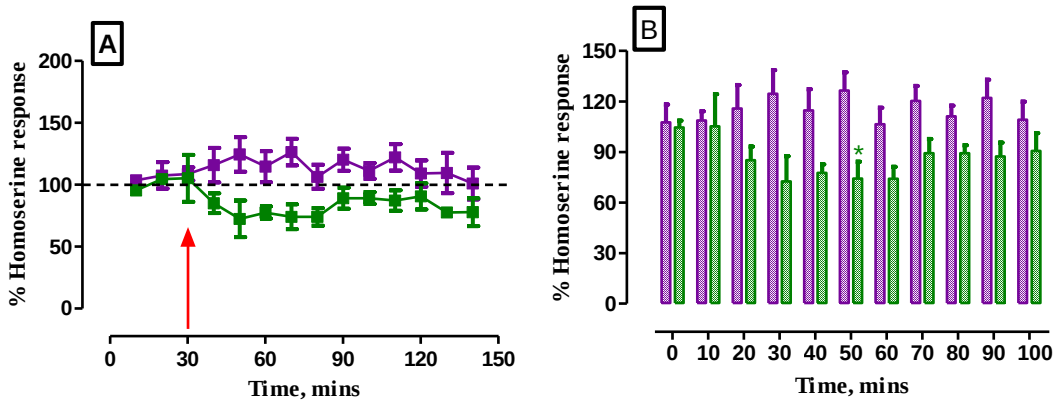

Figure 7.3.3.6.2: (A) Percentage relative response-time profile of Homoserine obtained following a 2-minute restraint test. Baseline levels were taken 20-minutes prior to the restraint test. (B) Bar graph comparing 10-min microdialysis samples of percentage Homoserine responses. Baseline levels are representative of 10-minutes before the restraint test. The relative response obtained from WT mice is represented in purple while PINK1 animals are highlighted in green. Red arrow indicates the point of neuronal perturbation.

Table 7.3.3.6.2: Statistical analysis of Homoserine obtained using unpaired *t*-test for 2-minute restraint tests conducted on humanised PINK1 (*n* = 3) and WT mice (*n* = 5).

Homoserine					
	Restraint WT		Restraint PINK1		
Time, mins	Mean	SEM	Mean	SEM	*p*
0	107.5	10.6	104.6	3.9	0.84
10	108.7	5.3	105.3	19.0	0.81
20	115.8	13.9	85.1	8.0	0.14
30	124.5	14.0	72.5	14.9	0.09
40	114.7	12.5	77.6	5.0	0.07
50	126.4	10.7	74.2	10.0	0.02
60	106.5	9.7	74.1	7.1	0.06
70	120.2	8.9	89.2	8.5	0.06
80	111.2	6.3	89.2	4.8	0.05
90	122.1	10.8	87.3	8.2	0.07
100	109.1	10.7	90.6	10.7	0.30

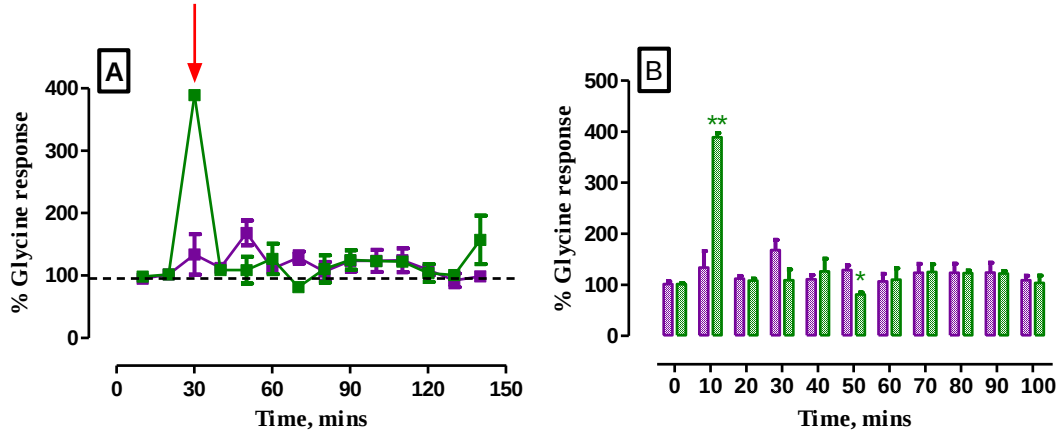

Figure 7.3.3.6.3: (A) Percentage relative response-time profile of Glycine obtained following a 2-minute restraint test. Baseline levels were taken 20-minutes prior to the restraint test. (B) Bar graph comparing 10-min microdialysis samples of percentage Glycine responses. Baseline levels are representative of 10-minutes before the restraint test. The relative response obtained from WT mice is represented in purple while PINK1 animals are highlighted in green. Red arrow indicates the point of neuronal perturbation.

Table 7.3.3.6.3: Statistical analysis of Glycine obtained using unpaired *t*-test for 2-minute restraint tests conducted on humanised PINK1 (*n* = 3) and WT mice (*n* = 5).

Glycine					
	Restraint WT		Restraint PINK1		
Time, mins	Mean	SEM	Mean	SEM	*p*
0	101.8	4.8	101.7	1.7	0.99
10	133.8	32.6	389.3	8.1	0.006
20	112.5	4.8	108.7	3.4	0.58
30	168.3	19.8	108.8	21.5	0.14
40	110.9	8.4	126.8	24.3	0.48
50	128.8	9.5	81.3	3.6	0.01
60	106.7	14.9	110.6	22.0	0.88
70	123.6	17.3	125.1	15.5	0.96
80	123.6	17.8	123.1	4.8	0.98
90	124.5	19.0	122.3	4.7	0.93
100	109.1	8.7	104.0	14.3	0.75

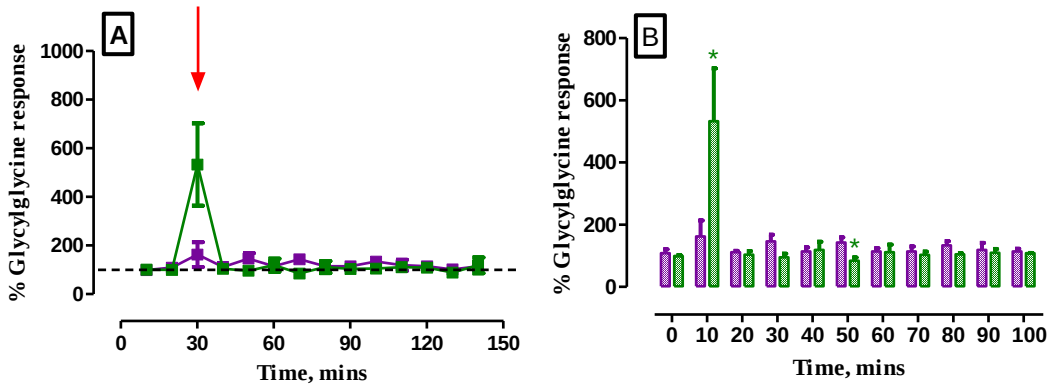

Figure 7.3.3.6.4: (A) Percentage relative response-time profile of Glycylglycine obtained following a 2-minute restraint test. Baseline levels were taken 20-minutes prior to the restraint test. (B) Bar graph comparing 10-min microdialysis samples of percentage Glycylglycine responses. Baseline levels are representative of 10-minutes before the restraint test. The relative response obtained from WT mice is represented in purple while PINK1 animals are highlighted in green. Red arrow indicates the point of neuronal perturbation.

Table 7.3.3.6.4: Statistical analysis of Glycylglycine obtained using unpaired *t*-test for 2-minute restraint tests conducted on humanised PINK1 (*n* = 3) and WT mice (*n* = 5).

Glycylglycine					
	Restraint WT		Restraint PINK1		
Time, mins	Mean	SEM	Mean	SEM	*p*
0	108.6	12.3	99.4	2.2	0.60
10	162.8	51.1	533.0	169.6	0.03
20	111.7	4.2	104.2	11.3	0.52
30	146.0	21.9	95.5	11.6	0.21
40	114.7	12.0	118.9	27.0	0.87
50	142.9	16.6	84.3	10.3	0.04
60	114.4	10.3	111.3	24.8	0.89
70	114.4	15.8	103.5	10.0	0.64
80	133.4	14.0	105.0	3.7	0.18
90	118.6	23.0	110.2	11.8	0.80
100	114.4	8.4	108.9	0.6	0.64

7.4 Conclusion

The focus of this chapter was to elucidate a neurochemical signature of PD. Due to the heterogeneous nature of PD, it was vital to combine a variety of neurochemical analytic techniques to enable an overall signature of PD to be obtained. Therefore, microdialysis sampling and metabolomic analysis were included to attempt to correlate any metabolic changes that may be associated with fluctuations in neurochemical events which were observed in Chapter 6. Hence, by association of changes in metabolite concentration with specific neurochemical transitions, it may be possible to identify potential biomarkers of PD which may lead to an earlier diagnosis.

It was of crucial importance to firstly characterise the performance of microdialysis sampling in NOD SCID mice to enable optimal sample collection, storage and transport of samples to Leiden University for subsequent analysis. Throughout this characterisation, 60-minute samples were collected over 180-minutes using a variety of different flow rates. Following metabolomic analysis, 73 metabolites were identified, with 54 metabolites being observed to meet the acceptance criteria of RSDqc < 15 % set by Leiden. Following on from characterisation studies, it was decided to reduce sampling intervals to 10-minutes over 180-minutes for microdialysis sampling conducted in humanised PINK1 and WT mice. Although, the absolute concentration of metabolites in the samples was reduced, the frequency of sampling was increased leading to a dynamic temporal profile to be achieved. Samples identified 44 metabolites in the collected samples of which 32 met Leidens acceptance criteria of RSDqc < 25 %.

Saline and restraint stress perturbations were seen to result in interesting alterations in a variety of metabolites collected from humanised PINK1 and WT mice. However, retroperfusions of 100 mM K^+ and 100 µM paraquat did not produce any significant changes in metabolite concentrations, thus, they were not discussed in detail in this chapter. Metabolic changes associated with the performance of saline i.p. injections and restraint tests were correlated with deviations in cellular pathways that are observed to be altered in PD. With reference to Table 7.3.2.1, alterations in tryptophan and kynurenine metabolism, branched chain amino acids, phenylalanine and tyrosine metabolism, glutamate/glutamine cycle, urea cycle and glycine metabolism were identified in humanised PINK1 mice when compared to humanised WT mice. Dysfunction of the aforementioned processes can be attributed to

mitochondrial dysfunction, altered catecholamine and hormone synthesis, changes in protein synthesis and dysregulated macrophagy and mitophagy. Each of these processes have important implications in the progression of PD. In addition, altered levels of L-histidine, L-lysine, Methoinine, L-threonine, O-phosphoethanolamine and L-asparagine were also noted. However, alterations in levels of these metabolites in humanised PINK1 mice will be further discussed in Chapter 8. Moreover, the production of a variety of these measured metabolites result from the formation of intermediates that are produced as a result of glycolysis. Thus, due to the increase in a number of metabolites sampled from humanised PINK1 mice, it can be hypothesised that an increase in the production of the glycolytic intermediates also exists which suggests a surge in glycolytic activity in humanised PINK1 mice. This hypothesis will be further discussed in Chapter 8. Moreover, alterations in metabolite concentrations were mainly associated with restraint tests suggesting that when neuronal activation is active for a longer period, an alteration in metabolite levels was observed. Interestingly, differences in amperometric analyte responses detailed in Chapter 6 were closely associated with physiological stimulation resulting from saline administration and restraint tests. Thus, a correlation between neuronal activation, altered metabolite levels and neurochemical dynamics may exist.

By correlation of alterations recorded in the metabolites sampled from humanised PINK1 mice with deviations in amperometric recordings recorded in Chapter 6, differences in cellular pathways can be deduced leading to an overall signature of PD to be achieved. Chapter 8 will detail this further discussion whereby cellular dysfunction in certain biological pathways will be correlated to existing hypothesis obtained from literature, hence, allowing for new hypothesis into PD progression and its associated biomarkers to be made.

7.5 References

1. Dauer, W. & Przedborski, S. Parkinson's Disease. *Neuron* **39,** 889–909 (2003).
2. Ross, G. W., Petrovitch, H., Abbott, R. D., Nelson, J., Markesbery, W., Davis, D., Hardman, J., Launer, L., Masaki, K., Tanner, C. M. & White, L. R. Parkinsonian signs and substantia nigra neuron density in decendents elders without PD. *Ann. Neurol.* **56,** 532–539 (2004).
3. Lang, A., E., Lozano, A., M. Parkinson's Disease. First of two parts. *N Engl J Med* **339,** 1044–1053 (1998).
4. Gill, E. L., Koelmel, J. P., Yost, R. A., Okun, M. S., Vedam-Mai, V. & Garrett, T. J. Mass Spectrometric Methodologies for Investigating the Metabolic Signatures of Parkinson's Disease: Current Progress and Future Perspectives. *Anal. Chem.* **90,** 2979–2986 (2018).
5. Valente, E. M., Abou-Sleiman, P. M., Caputo, V., Muqit, M. M., Harvey, K., Gispert, S., Ali, Z., Del Turco, D., Bentivoglio, A. R., Healy, D. G. & Albanese, A. Hereditary Early-Onset Parkinson 's Disease Caused by Mutations in PINK1. *Science.* **304,** 1158–1161 (2004).
6. Heeman, B., Van den Haute, C., Aelvoet, S. A., Valsecchi, F., Rodenburg, R. J., Reumers, V., Debyser, Z., Callewaert, G., Koopman, W. J., Willems, P. H. & Baekelandt, V. Depletion of PINK1 affects mitochondrial metabolism, calcium homeostasis and energy maintenance. *J. Cell Sci.* **124,** 1115–1125 (2011).
7. Henchcliffe, C. & Beal, M. F. Mitochondrial biology and oxidative stress in Parkinson disease pathogenesis. *Nat. Clin. Pract. Neurol.* **4,** 600–609 (2008).
8. Yu, W., Sun, Y., Guo, S. & Lu, B. The PINK1/Parkin pathway regulates mitochondrial dynamics and function in mammalian hippocampal and dopaminergic neurons. *Hum. Mol. Genet.* **20,** 3227–3240 (2011).
9. Zhou, B., Xiao, J. F., Tuli, L. & Ressom, H. W. LC-MS-based metabolomics. *Mol. Biosyst.* **8,** 470–481 (2012).
10. Chen, X., Xie, C., Sun, L., Ding, J. & Cai, H. Longitudinal metabolomics profiling of Parkinson's disease-related α-synuclein A53T transgenic mice. *PLoS ONE* **10,** (2015).
11. Xiao, J. F., Zhou, B. & Ressom, H. W. Metabolite identification and quantitation in LC-MS/MS-based metabolomics. *TrAC - Trends Anal. Chem.*

32, 1–14 (2012).

12. Sainio, E., L., Pulkki, K. & Young, S., N. L-Tryptophan: Biochemical, nutritional and pharmacological aspects. *Amino Acids* **10,** 21–47 (1996).
13. Singh, M. & Jadhav, H. R. Melatonin : functions and ligands. *Drug Discov. Today* **19,** 1410–1418 (2014).
14. Havelund, J.F., Andersen, A.D., Binzer, M., Blaabjerg, M., Heegaard, N.H., Stenager, E., Færgeman, N.J. and Gramsbergen, J. . Changes in kynurenine pathway metabolism in Parkinson patients with L-DOPA-induced dyskinesia. *J. Neurochem.* **142,** 756–766 (2017).
15. Maddison, D. C. & Giorgini, F. The kynurenine pathway and neurodegenerative disease. *Semin. Cell Dev. Biol.* **40,** 134–141 (2015).
16. Guillemin, G. J., Kerr, S. J., Smythe, G. A., Smith, D. G., Kapoor, V., Armati, P. J., Croitoru, J. & Brew, B. J. Kynurenine pathway metabolism in human astrocytes: A paradox for neuronal protection. *J. Neurochem.* **78,** 842–853 (2001).
17. Gramsbergen, J. B., Hodgkins, P. S., Rassoulpour, A., Turski, W. A., Guidetti, P. & Schwarcz, R. Brain-specific modulation of kynurenic acid synthesis in the rat. *J. Neurochem.* **69,** 290–298 (1997).
18. Rassoulpour, A., Wu, H. Q., Poeggeler, B. & Schwarcz, R. Systemic d-amphetamine administration causes a reduction of kynurenic acid levels in rat brain. *Brain Res.* **802,** 111–118 (1998).
19. Schwarcz, R., Bruno, J., P., Muchowski, P. & Wu, H. Kynurenines in the Mammalian Brain: When Physiology Meets Pathology. *Nat. Rev. Neurosci.* **13,** 465–477 (2013).
20. Schwarcz, R., Whetsell, W. O. & Mangano, R. M. Quinolinic Acid : An Endogenous Metabolite that Produces Axon-Sparing Lesions in Rat Brain Published by : American Association for the Advancement of Science Stable. *Science.* **219,** 316–318 (1983).
21. Tavares, R. G., Tasca, C. I., Santos, C. E., Alves, L. B., Porciúncula, L. O., Emanuelli, T. & Souza, D. O. Quinolinic acid stimulates synaptosomal glutamate release and inhibits glutamate uptake into astrocytes. *Neurochem. Int.* **40,** 621–627 (2002).
22. Ting, K., Brew, B. J. & Guillemin, G. J. Effect of quinolinic acid on human

astrocytes morphology and functions: implications in Alzheimer's disease. *J. Neuroinflammation* **6,** 36 (2009).

23. Cruz, V. P. D. La, Carrillo-Mora, P. & Santamaría, A. Quinolinic acid, an endogenous molecule combining excitotoxicity, oxidative stress and other toxic mechanisms. *Int. J. Tryptophan Res.* **5,** 1–8 (2013).
24. Braidy, N., Grant, R., Adams, S., Brew, B. J. & Guillemin, G. J. Mechanism for quinolinic acid cytotoxicity in human astrocytes and neurons. *Neurotox. Res.* **16,** 77–86 (2009).
25. Fernstrom, J., D. Branched-Chain Amino Acids and Brain Function. *J. Nutr.* **135,** 1539–1546 (2005).
26. Huang, Y., Zhou, M., Sun, H. & Wang, Y. Branched-chain amino acid metabolism in heart disease: An epiphenomenon or a real culprit? *Cardiovasc. Res.* **90,** 220–223 (2011).
27. Shimomura, Y. & Kitaura, Y. Physiological and pathological roles of branched-chain amino acids in the regulation of protein and energy metabolism and neurological functions. *Pharmacol. Res.* **133,** 215–217 (2018).
28. Rohini, A., Agrawal, N., Kumar, H. & Kumar, V. Emerging role of branched chain amino acids in metabolic disorders: A mechanistic review. *PharmaNutrition* **6,** 47–54 (2018).
29. Corkey, B. E., Martin-Requero, A., Walajtys-Rode, E., Williams, R. J. & Williamson, J. R. Regulation of the branched chain alpha-ketoacid pathway in liver. *J. Biol. Chem.* **257,** 9668–9676 (1982).
30. Yoon, M. S., Du, G., Backer, J. M., Frohman, M. A. & Chen, J. Class III PI-3-kinase activates phospholipase D in an amino acid-sensing mTORC1 pathway. *J. Cell Biol.* **195,** 435–447 (2011).
31. Harris, R. a, Joshi, M., Jeoung, N. H. & Obayashi, M. Overview of the Molecular and Biochemical Basis of Branched-Chain Amino Acid Catabolism. *J. Nutr.* **135,** 1527S–30S (2005).
32. Meldrum, B. S. Glutamate as a neurotransmitter in the brain: review of physiology and pathology. *J. Nutr.* **130,** 1007S–15S (2000).
33. Yudkoff, M. Interactions in the Metabolism of Glutamate and the Branched-Chain Amino Acids and Ketoacids in the CNS. *Neurochem. Res.* **42,** 10–18 (2017).

34. Contrusciere, V., Paradisi, S., Matteucci, A. & Malchiodi-Albedi, F. Branched-chain amino acids induce neurotoxicity in rat cortical cultures. *Neurotox. Res.* **17,** 392–398 (2010).
35. Luan, H., Liu, L. F., Tang, Z., Zhang, M., Chua, K. K., Song, J. X., Mok, V. C., Li, M. & Cai, Z. Comprehensive urinary metabolomic profiling and identification of potential noninvasive marker for idiopathic Parkinson's disease. *Sci. Rep.* **5,** 1–11 (2015).
36. Lewerenz, J. & Maher, P. Chronic glutamate toxicity in neurodegenerative diseases-What is the evidence? *Front. Neurosci.* **9,** 1–20 (2015).
37. Bak, L. K., Schousboe, A. & Waagepetersen, H. S. The glutamate/GABA-glutamine cycle: Aspects of transport, neurotransmitter homeostasis and ammonia transfer. *J. Neurochem.* **98,** 641–653 (2006).
38. Takeda, K., Ishida, A., Takahashi, K. & Ueda, T. Synaptic vesicles are capable of synthesizing the VGLUT substrate glutamate from α-ketoglutarate for vesicular loading. *Journal of Neurochemistry* **121,** 184–196 (2012).
39. Felipo, V. & Butterworth, R. F. Neurobiology of ammonia. *Prog. Neurobiol.* **67,** 259–279 (2002).
40. Rothstein, J. D., Jin, L., Dykes-Hoberg, M. & Kuncl, R. W. Chronic inhibition of glutamate uptake produces a model of slow neurotoxicity. *Proc. Natl. Acad. Sci.* **90,** 6591–6595 (1993).
41. F. Blachier, M. Selamnia, V. Robert, H. M'Rabet-Touil, P. H. D. Metabolism of L-arginine through polyamine and nitric oxide synthase pathways in proliferative or differentiated human colon carcinoma cells. *Biochim. Biophys. Acta.* **1268,** 255–262 (1995).
42. Sugino, T., Shirai, T., Kajimoto, Y. & Kajimoto, O. l-Ornithine supplementation attenuates physical fatigue in healthy volunteers by modulating lipid and amino acid metabolism. *Nutr. Res.* **28,** 738–743 (2008).
43. Wu, G., Bazer, F. W., Datta, S., Johnson, G. A., Li, P., Satterfield, M. C. & Spencer, T. E. Proline metabolism in the conceptus: Implications for fetal growth and development. *Amino Acids* **35,** 691–702 (2008).
44. Burghardt, R. C. & Johnson, G. A. Proline and hydroxyproline metabolism: implications for animal and human nutrition. *Amino Acids* **40,** 1053–1063 (2013).

45. Henzi, V., Reichling, D.B., Helm, S., W. & MacDermott, A. B. L-proline activates glutamate and glycine receptors in cultured rat dorsal horn neurons. *Mol. Pharmacol.* **41,** 793–801 (1992).
46. Kaul, S., Sharma, S. S. & Mehta, I. K. Free radical scavenging potential of L-proline: Evidence from in vitro assays. *Amino Acids* **34,** 315–320 (2008).
47. Verbruggen, N. & Hermans, C. Proline accumulation in plants: A review. *Amino Acids* **35,** 753–759 (2008).
48. Fernstrom, J. D. & Fernstrom, M. H. Tyrosine, phenylalanine, and catecholamine synthesis and function in the brain. *J. Nutr.* **137,** 1539S–1548S (2007).
49. Fernstrom, J. D. Role of precursor availability in control of monoamine biosynthesis in brain. *Physiol. Rev.* **63,** 484–546 (1983).
50. Brodnik, Z., Bongiovanni, R., Double, M. & Jaskiw, G. E. Increased tyrosine availability increases brain regional DOPA levels in vivo. *Neurochem. Int.* **61,** 1001–1006 (2012).
51. Daubner, S. C., Le, T. & Wang, S. Tyrosine Hydroxylase and Regulation of Dopamine Synthesis. *Arch Biochem Biophys* **508,** 1–12 (2012).
52. Hu, L. A., Zhou, T., Ahn, J., Wang, S., Zhou, J., Yi, H. U. & Liu, Q. Human and mouse trace amine-associated receptor 1 have distinct pharmacology towards endogenous monoamines and imidazoline receptor ligands. *Biochem. J* **424,** 39–45 (2009).
53. Sotnikova, T. D., Beaulieu, J. M., Espinoza, S., Masri, B., Zhang, X., Salahpour, A., Barak, L. S., Caron, M. G. & Gainetdinov, R. R. The dopamine metabolite 3-methoxytyramine is a neuromodulator. *PLoS One* **5,** (2010).
54. Meléndez-Hevia, E. & De Paz-Lugo, P. Branch-point stoichiometry can generate weak links in metabolism: The case of glycine biosynthesis. *J. Biosci.* **33,** 771–780 (2008).
55. Legendre, P. The glycinergic inhibitory synapse. *Cell. Mol. Life Sci.* **58,** 760–793 (2001).
56. Xu, T. Le & Gong, N. Glycine and glycine receptor signaling in hippocampal neurons: Diversity, function and regulation. *Prog. Neurobiol.* **91,** 349–361 (2010).
57. Zhang, L. H., Gong, N., Fei, D., Xu, L. & Xu, T. Le. Glycine uptake regulates

hippocampal network activity via glycine receptor-mediated tonic inhibition. *Neuropsychopharmacology* **33,** 701–711 (2008).

58. Guastella, J., Brecha, N., Weigmann, C., Lester, H. A. & Davidson, N. Cloning, expression, and localization of a rat brain high-affinity glycine transporter. *Proc. Natl. Acad. Sci. U. S. A.* **89,** 7189–93 (1992).
59. Zafra, F., Aragon, C., Olivares, L., Danbolt, N. C., Gimenez, C. & Storm-Mathisen, J. Glycine Transporters Are Differentially Expressed among CNS Cells. *J. Neurosci.* **15,** 3952–3969 (1995).
60. Yadid, G., Pacak, K., Golomb, E., Harvey-White, J. D., Lieberman, D. M., Kopin, I. J. & Goldstein, D. S. Glycine stimulates striatal dopamine release in conscious rats. *Br. J. Pharmacol.* **110,** 50–53 (1993).

Chapter 8

General Discussions

In recent times, there has been a clear demographic shift towards a greater proportion of elderly individuals in populations. Certain neurological disorders, such as PD, tend to be more prevalent within this age group. Hence, this creates a greater need to develop neurotherapeutic agents to help slow the progression of PD. Although knowledge of the aetiopathogenesis of PD has improved significantly in recent times, translation of pharmacokinetic agents from preclinical models to their human counterparts has proved difficult due to the aetiopathogenic diversity of this disease. Thus, it is crucial that the underlying mechanisms of this disease are investigated, which at present poses the most challenging objective of all.

Previous reports have indicated that mitochondrial dysfunction can be associated with the onset of PD. As a result of this dysfunction, numerous neurochemical analytes and other endogenous metabolites may be altered in the PD brain. The brain is a complex network made up of numerous neurons and glial cells. It is through this network that cell-to-cell communication can be facilitated by means of electrical and chemical processes. This communication network comprises of sites of chemical release and chemical uptake. Following analyte release, it must diffuse away from the release site into the ECF[1]. As these neurochemicals are present in the ECF, the measurement of these substrates can provide a valuable insight into various neurochemical processes that occur in the brain. The implantation of an electrochemical sensor into the ECF allows for real-time *in vivo* amperometric measurements to be made. Amperometric techniques are important for the measurement of transient *in vivo* processes due to the excellent temporal and spatial resolution they exhibit. Additionally, the inclusion of microdialysis sampling can provide important information into varying metabolite concentrations found at particular time points. It is important to reiterate that microdialysis sampling does not occur in real-time. However, an overall trend into the changes in metabolite concentration occurring in the brain can be obtained.

The principal objective of this thesis is to attempt to elucidate a neurochemical signature of patient-specific PD. By neurochemical monitoring of target analytes, using amperometric sensors and microdialysis sampling, the progression of patient-derived PD can be assessed. Additionally, the development of a humanised mouse model of PD by colleagues in University of Luxembourg has allowed for patient-

derived PD cells to be neurochemically monitored in a physiological environment for the first time[2].

Chapter 4 details the *in vitro* validation of the previously characterised NO sensor[3,4], O_2 sensor[5,6] and the H_2O_2 biosensor[7,8] which confirmed the replication of previously reported performance parameters before their ultimate deployment in the striatum of NOD SCID mice. This chapter was primarily concerned with validating the sensitivity, selectivity and stability of each of the aforementioned sensors. Additionally, *ex vivo* sensocompatibility studies confirmed that the selective properties of each of the sensors would be retained following contact with biological tissue.

Following validation of the performance parameters *in vitro*, characterisation of each of the aforementioned sensors was undertaken in the striatum of NOD SCID mice (Chapter 5). The purpose of this characterisation study was to investigate the sensor response to neuronal perturbation and a range of characterisation compounds, as the sensors had previously been characterised in freely-moving rats. As all the characterisation compounds were formulated in saline, saline administrations were used to characterise the amperometric response following i.p. administration. Chapter 5 highlighted a decrease in the amperometric NO signal following the i.p administration of saline (see Section 5.3.1.1). Previous studies conducted in wistar rats[9,10] showed an increase in the amperometric signal which is different to the response obtained in NOD SCID mice. Additionally, an initial decrease in the NO signal was observed following administration of L-NAME (Figure 5.3.1.2.1) and the performance of a 2-minute restraint (Figure 5.3.1.5.1). It could therefore be hypothesised that this initial decrease in NO may result from increased neuronal activation resulting from physiological stimulation. As the NO sensor has previously not been implanted in immunocompromised NOD SCID mice, this decrease may be due to *in vivo* recordings being conducted in this rodent species. In contrast, the O_2 sensor exhibited an increase in the amperometric current following the i.p. administration of saline which is similar to responses recorded in wistar rats[11,12]. Additionally, H_2O_2 levels were not altered following saline administration indicating that saline may not elicit a response in immunocompromised mice.

Sodium ascorbate was administered to confirm that the permselective membranes of the NO sensor and the H_2O_2 biosensor had been maintained *in vivo*.

The NO response demonstrated a decrease in current which once more may be attributed to the effect of sodium ascorbate in NOD SCID mice. Previous studies conducted in wistar rats[9,10] reported no decrease following an i.p. administration of sodium ascorbate. Therefore, this decrease in NOD SCID mice may be attributed to investigations being undertaken in a different rodent strain. However, as no increase was observed, it was concluded that the NO sensor had retained its selective properties. Additionally, no change in the H_2O_2 response was reported which confirmed that the interference rejection layer of the H_2O_2 biosensor had been maintained. Furthermore, the NO and O_2 sensors were found to exhibit excellent stability over an 8-day period. These results are in good agreement with *ex vivo* investigations carried out in Chapter 4 whereby each sensor was found to retain selectivity for up to 14-days allowing for accurate real-time recordings to be performed *in vivo*. Similarly, the H_2O_2 biosensor demonstrated excellent selectivity for 5-days which is in accordance with *ex vivo* studies conducted in Chapter 4 which reported that the H_2O_2 biosensor retained selectivity for 7-days. Following validation of the performance parameters of each of the aforementioned sensors, they were ready to deployed in the humanised mouse model of PD.

Many of the major findings in this thesis are contained in Chapter 6 & 7 which detail *in vivo* amperometry investigations and microdialysis sampling undertaken in humanised mice. The humanised mouse model of PD gave an exciting opportunity from which to investigate the neurochemical dynamics in human-derived PD cells within a physiological setting for the first time. It is important to understand that both amperometric recordings and microdialysis samples measured from the ECF are influenced by a number of factors. By referring back to Section 2.3.2, the amperometric measurement of target analytes and metabolite collection are dependent on the process of diffusion between the supply of the analyte (source) and utilisation of the analyte (sink). When an increase is detected in either amperometric investigations or metabolite concentration, it does not necessarily mean that there is an increased rate of said species produced. It may indicate that there is a disrupted uptake or removal mechanism for a particular analyte. Thus, leading to the presence of an increased concentration of the target species in the ECF. Therefore, it is important to consider that any alterations in analyte levels reported in Chapter 6 & 7

may have resulted from a disruption in the metabolic pathways associated with that species.

Firstly, by examining the data collected from amperometric investigations, it was concluded that a number of alterations in NO, O_2 and H_2O_2 were affected in the PINK1 cohort when compared to each of the other animal cohorts. Firstly, the NO response to saline administrations was examined. There appeared to be a tendency in WT cells to exhibit a higher NO response to neuronal activation when compared to measurements obtained from PINK1, SHAM and NOD SCID animals. The NO response recorded in PINK1 mice shared similarities to the responses obtained in the SHAM and NOD SCID cohorts which suggests influences on NO levels from the surgical procedures. Therefore, it could be suggested that reduced NO changes occur in PINK1 PD cell lines when subjected to increased neuronal activation.

Similarly, a 2-minute restraint test carried out on each of the animal groups highlighted a comparable NO response. However, there appeared to be a clear tendency towards reduced NO levels in response to neuronal activation in PINK1 mice. Although comparable responses were observed between each of the animal groups, a small increase in NO levels was observed in WT animals when compared to PINK1 mice which suggests that elevated NO activity exists in the WT cohort. It was interesting to note that a near identical response was obtained between WT and NOD SCID animals in contrast to the reduced NO response recorded in PINK1 mice. Therefore, this further supports that a reduced NO activity may exist in PINK1 grafts. Additionally, it is worth noting that a similar trend in the NO response was obtained following saline administration and restraint tests in each cohort which highlighted that similar levels of neuronal activation was initiated following both perturbations. This finding was confirmed by time bin analysis which reported no significant differences between the recorded responses (Figure 8.1B & D). Figure 8.1A & B illustrates a short-lived NO response of much lower magnitude in the PINK1 cohort, when compared to the larger NO response observed in WT animals (Figure 8.1C & D), following neuronal activation. Additionally, the NO current appears to remain elevated for a longer timeframe in the WT cohorts. Ultimately, these findings may suggest that altered NO dynamics exist in PD cell lines which may have a negative influence on additional biological processes, thus, contributing to the overall pathology of the disease.

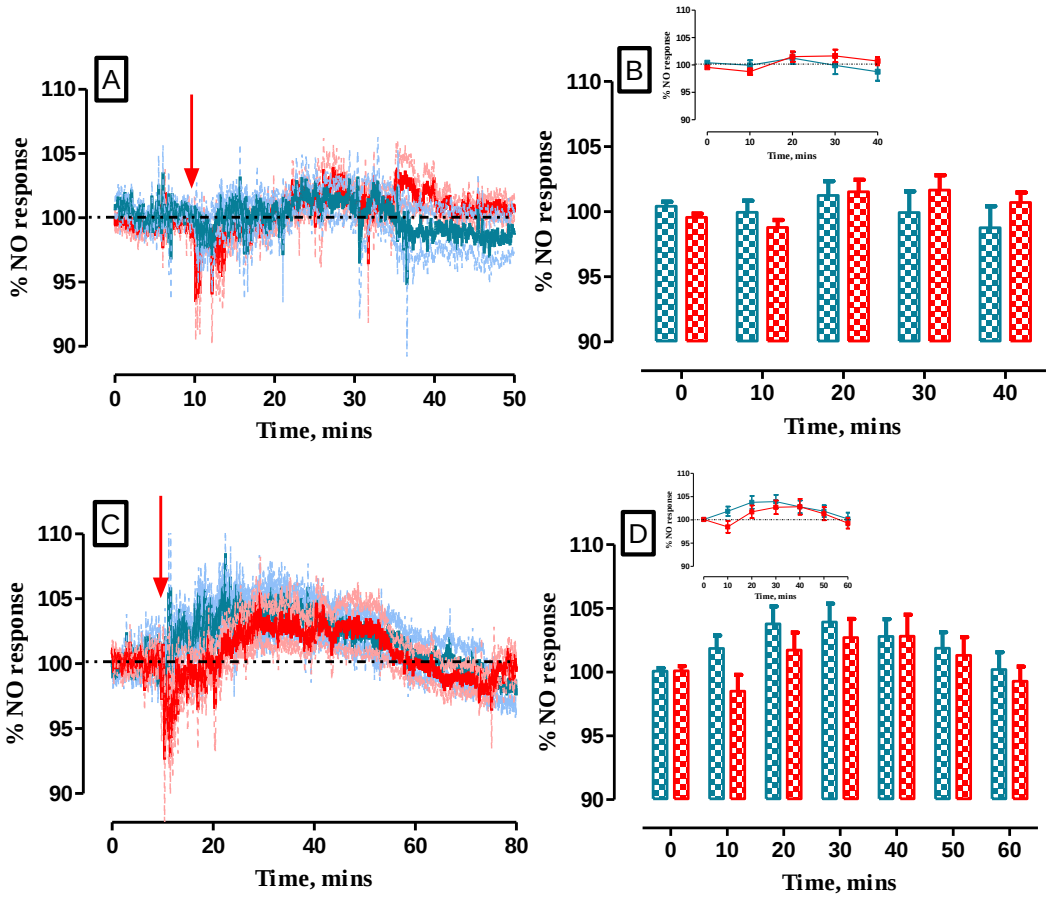

Figure 8.1: Overlay of the averaged percentage raw data current response recorded using NO sensors implanted in the striatum of (A) humanised PINK1 (*n* = 8) and (C) WT (*n* = 10) mice following a 1 mL/kg saline i.p. injection (blue trace) and 2-minute restraint (red trace). Red arrow indicates the point of perturbation. Bar graph comparing 10-minute time bin analysis of raw percentage data current responses in (B) PINK1 and (D) WT mice following 1 mL/kg saline i.p. injection and 2-minute restraint. Data represented as mean percentage current ± SEM.

Figure 8.2A & C displays the O_2 response measured in PINK1 and WT cohorts following neuronal activation. Amperometric recordings obtained in Chapter 5 & 6 highlight large disparities in the recorded O_2 response amongst each of the experimental cohorts following saline administration. By referring back to Section 5.3.2.1, it was observed that a transient increase in tissue O_2 levels resulted from i.p. administration. This transient increase resulted from increased O_2 supply from the CBF to facilitate the increased O_2 utilisation by the surrounding cells[13]. Following a reduction in neuronal activation, the brain signals to reduce the rate of supply due to

the tight regulation of O_2 in the brain. Concurrently, utilisation continues resulting in a return of the amperometric current to baseline levels.

However, very different O_2 responses were illustrated in PINK1, WT and SHAM animals. It was previously discussed in Chapter 6 that the humanised grafts lack vasculature. As a result, O_2 delivery must be maintained from the surrounding murine tissue to allow graft survival. It was noted that the initial O_2 current response in PINK1, WT and SHAM cohorts appeared to share similar increases at t = 10 mins and t = 20 mins following i.p. administration as was previously seen in NOD SCID mice. It can therefore be hypothesised that this increase can be attributed to the graft signalling to the adjacent areas to increase CBF. Following this initial similarity in the recorded responses, a comparable response was observed between PINK1 and SHAM cohorts. It appears that the surgical procedure may be having some effect on tissue O_2 levels which may be attributed to the formation of a glial scar. As the O_2 amperometric responses obtained in PINK1 and SHAM mice are noticeably higher than what was obtained in NOD SCID mice, it may be postulated that there is an increased demand for O_2 in these animal groups. Additionally, these elevated O_2 measurements may also be attributed to a reduced rate of O_2 utilisation in PINK1 cells. It is apparent that these higher O_2 levels are not sustained as a return to baseline is observed. This further supports the theory that a reduced rate of O_2 utilisation exists in the PINK1 cohort when compared to the WT animal group as O_2 levels return quicker due to a lesser requirement for O_2 by the PINK1 graft. In addition, the WT O_2 response remains elevated over a longer period which may suggest an increased rate in O_2 supply and utilisation. This theory can be further supported by referring back to Section 5.3.2.4 whereby a similar O_2 response was obtained following Diamox administration. However, the amperometric current returned to baseline over a shorter period following a reduction in O_2 delivery in NOD SCID animals. As utilisation remained constant, the signal returned to basal levels. This trend in the Diamox signal is comparable to the WT O_2 response further supporting that a reduction in utilisation exists in PINK1 cells.

Furthermore, restraint tests were conducted in all 4 animal cohorts. As restraint tests were performed over a 2-minute period, a much greater level of neuronal activation was achieved. Section 5.3.2.5 discusses restraint tests carried out in NOD SCID mice. The O_2 response recorded was reported to last over a 60-minute period

which is considerably longer in duration than what was previously noted in wistar rats[14]. In comparison, a similar trend in the O_2 response was recorded in PINK1, WT and SHAM mice. Restraint tests initiate a greater level of neuronal activation than saline administrations resulting in an increase in the rate of supply from CBF. As humanised grafts contain no vasculature, the rate of O_2 supply must work to maintain the additional cellular O_2 demand. In Figure 8.2, this increase can be observed in the humanised cohorts. Following this increase in O_2 supply, a comparable O_2 amperometric current is observed between the PINK1 and WT cohorts. It can be postulated that the reason why comparable responses are obtained in each cohort is due to the larger cellular O_2 demand by the transplanted graft. With this comes an increase in the rate of CBF, however, any alterations in the rate of utilisation by the grafted tissue may be masked by the overall O_2 increase in the host tissue and graft in response to a restraint test. The O_2 amperometric response in WT animals returns to baseline gradually following a 2-minute restraint which suggests a normal balance between supply and utilisation, in both graft and murine tissue. Additionally, the response observed in the WT cohort bares similarities to the restraint response recorded in NOD SCID mice (Figure 5.3.2.5) which lends support to this theory.

However, it is important to note that between t = 20 mins and t = 50 mins (Figure 8.2A & C), the O_2 PINK1 current appears to be higher when compared to each of the other recorded responses. This increase in the recorded response may result from an increase in CBF coupled with a decrease in cellular O_2 utilisation by the graft. As these processes occur simultaneously, an increase in tissue O_2 levels would result. This hypothesis is supported by observations obtained in Section 5.3.2.3. Following the administration of the anaesthetic, chloral hydrate, neuronal activation and O_2 utilisation decreases while the rate of CBF remains constant. This resulted in an increase in tissue O_2 levels being reported.

Additionally, this theory is further supported by the observed trend in O_2 obtained in SHAM animals. A comparable trend was noted in SHAM and PINK1 mice, however, SHAM mice do not contain any transplanted cells. Thus, the increase in the SHAM response could be attributed to an increase in O_2 supply by the murine brain in response to the restraint test. However, due to the absence of transplanted cells, there is a reduced demand for O_2 delivery which is indicated by the absence of any increase at t = 40 mins (see Figure 6.3.6.2.1). Therefore, this lends to support to

the theory that a reduced rate of O_2 utilisation exists in PD patient-derived cells. If a reduced rate of O_2 utilisation is prevalent in PINK1 PD, it could be postulated that production of ATP through oxidative processes may switch to glycolytic pathways which do not require the same levels of oxygen to produce cellular energy. Previous studies conducted involving PINK knock-out embryonic fibroblasts reported that in the absence of PINK1, glycolysis is stimulated to maintain cell proliferation[15].

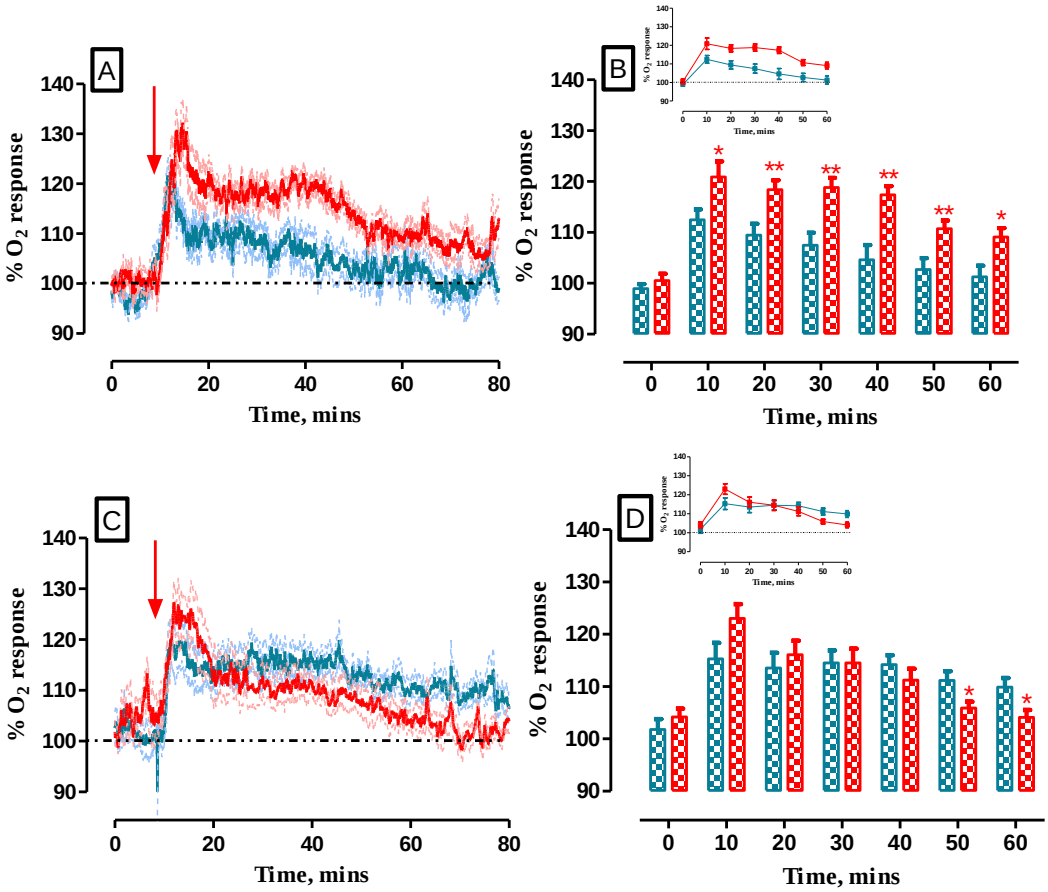

Figure 8.2: Overlay of the average averaged percentage raw data current response recorded using O_2 sensors implanted in the striatum of (A) humanised PINK1 (*n* = 8) and (C) WT (*n* = 8) mice following a 1 mL/kg saline i.p. injection (blue trace) and 2-minute restraint (red trace). Red arrow indicates the point of perturbation. Bar graph comparing 10-minute time bin analysis of raw percentage data current responses in (B) PINK1 and (D) WT mice following 1 mL/kg saline i.p injection and 2-minute restraint. Data represented as mean percentage current ± SEM.

Collectively, these results imply that reduced NO activity exists in PD cell lines coupled with a decreased rate of O_2 utilisation. Similarly, there was a tendency for increased levels of H_2O_2 to occur in the PINK1 cells following neuronal

perturbation. However, it is much more difficult to definitively attribute differences in H_2O_2 levels to PINK1 associated processes. Nevertheless, it appears that clear alterations in the production and utilisation of these target analytes exist in humanised PINK1 cohorts which may attribute the pathology of PD.

Findings obtained from microdialysis sampling performed in humanised animals are contained in Chapter 7. One of the most striking features of this chapter was that many of the metabolites sampled were seen to be increased in the PINK1 cohort which were usually observed at t = 10 mins. It is important to consider that any alterations in metabolite levels that are reported in Chapter 7 may have resulted from a disruption in the metabolic pathways associated with that metabolite. Additionally, microdialysis sampling involved collecting a vial of dialysate every 10-minutes. Neuronal perturbations were performed at t = 10 mins. Subsequent vials that were collected at 10-minute timeframes thereafter did not incur any neuronal perturbations. It is important to remember that microdialysis sampling is not conducted in real-time. Thus, it only allows for a trend in analyte levels to be obtained. Sampling occurred in the ECF where metabolites are in constant flux between their source of production and uptake/metabolism by surrounding cells. Therefore, microdialysis only allows for a small fraction of these analytes to be sampled. This may explain why very little change in analyte levels were observed following t = 10 mins.

Observed alterations in metabolite concentrations were closely associated with an increase in neuronal activation. In particular, many of the metabolic changes were noted to result from a 2-minute restraint and saline administrations. As seen in Chapter 5 & 6, restraint tests were noted to result in neuronal activation in both the mouse tissue and the graft over a sustained period when compared to saline administrations. Additionally, changes in metabolite levels were reported to be altered following restraint test in most cases due to the greater level of neuronal activation that results. By referring back to Section 7.4, alterations in a number of metabolic pathways were observed. Dysfunction of these pathways could be attributed to mitochondrial dysfunction, altered catecholamine and hormone synthesis, changes in protein synthesis and dysregulation of macrophagy and mitophagy processes. Additionally, a number of these metabolites are known to be produced from intermediates formed through glycolytic and oxidative processes (Figure 8.3).

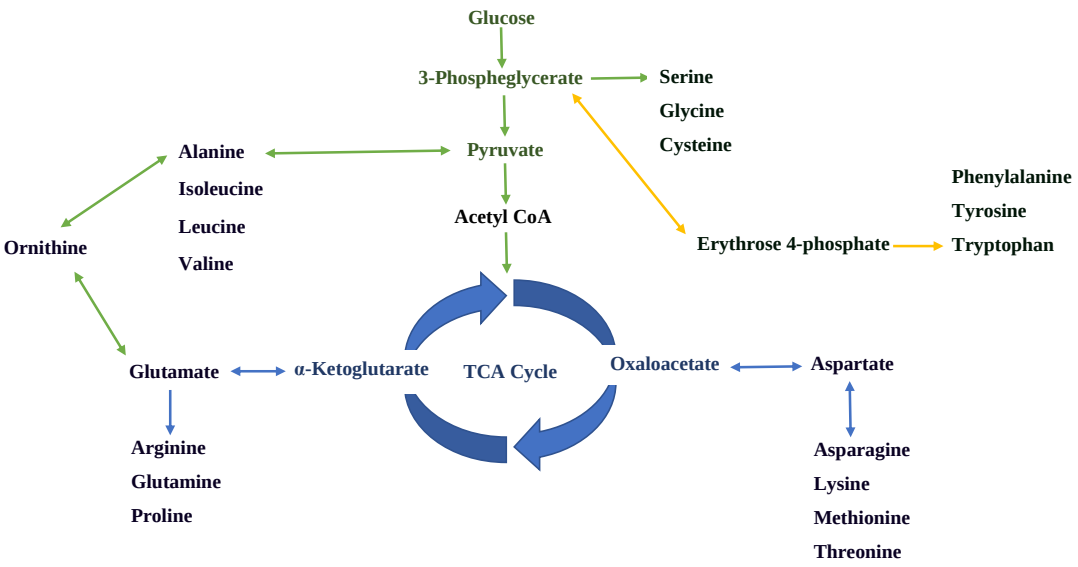

Figure 8.3: The hypothesised amino acid synthesis in PINK1 mice. (Adapted from: https://www.diapedia.org/metabolism-and-hormones/5105758814/amino-acid-metabolism). Green arrows illustrate the glycolytic pathway. Blue arrows represent oxidative pathways and yellow arrows are indicative of the pentose phosphate pathway.

Chapter 7 highlighted alterations in a variety of metabolites sampled from PINK1 mice. It was reported that alanine and BCAAs are present in the ECF at altered levels in response to neuronal activation, in particular, each one of these analytes are increased following a 2-minute restraint test. The synthesis of the aforementioned amino acids is known to occur through glycolysis. While the production of these metabolites further contributes to the production of ornithine, glutamate, glutamine, arginine and proline which were all seen to exist at altered levels following neuronal perturbation. Therefore, it could be hypothesised that an increase in glycolytic intermediates may occur due to a surge in glycolytic activity in PINK1 PD cells. Additionally, NO production bares a close relationship with glutamate, glutamine and arginine. Therefore, due to alterations in each of the aforementioned metabolites it may suggest a reason for the altered NO dynamics observed in NO amperometric recordings in the PINK1 cohort in Chapter 6. Furthermore, if altered levels of pyruvate exist as a result of increased glycolytic processes in PD cell lines, this could attribute to the formation of altered levels of metabolites through the TCA cycle which may have a knock-on effect on oxidative cellular respiratory processes. Likewise, if a switch to glycolysis does exist in PINK1 animals, it could be postulated that an

increase in tissue O_2 levels may result. Glycolysis is an anaerobic process, therefore, this theory would support why a decrease in O_2 utilisation was observed in PINK1 PD mice in Chapter 6.

It was reported that PINK1 patient cells do not respond efficiently to cellular demands as a result of altered cellular metabolism[16]. Additionally, a significant reduction in mitochondrial respiration powered by the ETC was described in PINK1-knockout drosophila flies. Such impairment is known to be associated with the respiratory chain, in particular, the decreased enzymatic activity of complex I and complex IV[17]. As it appears that ATP production is significant reduced in PD cell lines. It is further inferred that a higher dependency on glycolytic processes exists to ensure cell survival[16]. This hypothesis is supported by previous observations which reported that loss of PINK1 in neurons triggered a two-fold increase in the rate of glucose uptake and glycolysis than what was observed in the WT cohort[15]. Therefore, it can be suggested that an increase in glycolysis results in the increased production of ATP to meet cellular demand. However, literature has also outlined that even when oxidative phosphorylation is impaired under cellular stress, neurons may not elicit the ability to switch to glycolysis to enable ATP production[18]. Therefore, further highlighting the sensitivity of PINK1 PD cells to stress. Further studies conducted by Yao *et al.*, demonstrated that a high rate of glycolysis did exist in PINK1 cells following the prolonged impairment of oxidative phosphorylation. However, this heightened rate of glycolysis may provide additional energy to the surrounding neurons which may act to increase oxidative stress and apoptotic processes[19].

Additionally, alterations in metabolites produced from the pentose-phosphate pathway was noted in Chapter 7. Previously, Dias et al.[20] describe how alterations in this pathway results in decreased regeneration of GSH which contributes to an increase in the glycolytic rate. GSH is tripeptide composed of glutamate, cysteine and glycine and each one of these metabolites were reported to be altered following neuronal activation (Table 7.3.2.1). Therefore, it could be suggested alterations in the pentose-phosphate pathway further contributes to the glycolytic tendencies of PINK1 cells. Moreover, gene correction of patient PINK1 cells was undertaken[16]. It was observed that following correction of the point mutation, increased ATP production resulted due to a greater tendency to rely on the mitochondrial ETC rather than on glycolytic processes.

Furthermore, reports by Jarazo detail how larger mitophagy events occur in patient cell lines[16]. These investigations describe the accumulation of larger mitochondrial structures prior to their degradation resulting in a larger mitophagy event being required. In particular, BCAAs are known to regulate mitophagy through activation of mTORC1[21]. However, in Section 7.3.3.2, many of the BCAAs measured were observed to be present at altered levels in the ECF following neuronal activation. Therefore, suggesting that this dysregulation in mitophagy processes may contribute to the accumulation of mitochondrial damage and the overall death of the surrounding cells. Moreover, cellular phenotyping conducted by colleagues in the University of Luxembourg reported tendencies for increased cell death and reduced neurite complexity in PINK1 grafts when compared to healthy controls. This findings further supports that PINK1 cells tend to exhibit an increased tendency towards cell death when compared to healthy cohorts.

A host of neuromodulatory amino acids were reported to exist at varying levels following neuronal perturbation. Altered levels of BCAAs, kynurenine, L-proline and glycine were measured in PINK1 cell lines. Each of the aforementioned substances can act on voltage-gated calcium channels, G protein coupled receptors, receptor ion channels and glycine transporters. Therefore, alterations of the metabolic pathways associated with each of the aforementioned amino acids may contribute to prolonged activation of receptors and transporters. Ultimately, this may lead to a loss of post-synaptic structures and so, attributing to the overall pathology of PD.

To conclude, this project has highlighted clear alterations in the neurochemical monitoring of NO, O_2 and H_2O_2 in PINK1 PD cells. The changes observed in the recorded amperometric responses highlighted alterations in the aforementioned analytes which may be associated with cellular metabolism dysfunction. Additionally, the identification of differing levels of sampled metabolites from the ECF infers dyregulation of many metabolic pathways in patient-derived PINK1 cells. Collectively, these findings suggest a clear shift in cellular metabolism coupled with mitochondrial dysfunction. This thesis project has helped to elucidate a potential neurochemical signature of PD by identification of these alterations which proves crucial in the potential development of new pharmacokinetic drugs in the treatment of PD.

8.1 References

1. Paul, D.W., Stenken, J. A. A review of flux considerations for in vivo neurochemical measurements. *Analyst* **140,** 3709 (2015).
2. Hemmer, K., Smits, L. M., Bolognin, S. & Schwamborn, J. C. In vivo phenotyping of Parkinson-specific stem cells reveals increased a-Synuclein levels but no spreading. *bioRxiv*, 140178 (2017).
3. Brown, F. O., Finnerty, N. J. & Lowry, J. P. Nitric oxide monitoring in brain extracellular fluid: characterisation of Nafion®-modified Pt electrodes in vitro and in vivo. *Analyst* **134,** 2012–20 (2009).
4. Wynne, A. M., Reid, C. H. & Finnerty, N. J. In vitro characterisation of ortho phenylenediamine and Nafion®-modified Pt electrodes for measuring brain nitric oxide. *J. Electroanal. Chem.* **732,** 110–116 (2014).
5. Bolger, F., Bennett, R. & Lowry, J. An in vitro characterisation comparing carbon paste and Pt microelectrodes for real-time detection of brain tissue oxygen. *Analyst* **136,** 4028–35 (2011).
6. Bolger, F. B., McHugh, S. B., Bennett, R., Li, J., Ishiwari, K., Francois, J., Conway, M. W., Gilmour, G., Bannerman, D. M., Fillenz, M. & Tricklebank, M. Characterisation of carbon paste electrodes for real-time amperometric monitoring of brain tissue oxygen. *J. Neurosci. Methods* **195,** 135–42 (2011).
7. O'Brien, K. B., Killoran, S. J., O'Neill, R. D. & Lowry, J. P. Development and characterization in vitro of a catalase-based biosensor for hydrogen peroxide monitoring. *Biosens. Bioelectron.* **22,** 2994–3000 (2007).
8. O'Riordan, S. L., McLaughlin, K., Lowry, J. P. In vitro physiological performance factors of a catalase-based biosensor for real-time electrochemical detection of brain hydrogen peroxide in freely-moving animals. *Anal. Methods* **8,** 7614–7622 (2016).
9. Finnerty, N. J., O'Riordan, S. L., Pålsson, E. & Lowry, J. P. Brain nitric oxide: Regional characterisation of a real-time microelectrochemical sensor. *J. Neurosci. Methods* **209,** 13–21 (2012).
10. Finnerty, N. J., O'Riordan, S. L., Brown, F. O., Serra, P. A., O'Neill, R. D., Lowry, J. P. In vivo characterisation of a Nafion®-modified Pt electrode for real-time nitric oxide monitoring in brain extracellular fluid. *Anal. Methods* **4,**

550 (2012).

11. Bolger, F. B. & Lowry, J. P. Brain tissue oxygen: In vivo monitoring with carbon paste electrodes. *Sensors* **5,** 473–487 (2005).
12. O'Riordan, S. L., Lowry, J. P. In vivo characterisation of a catalase-based biosensor for real-time electrochemical monitoring of brain hydrogen peroxide in freely-moving animals. *Anal. Methods* **9,** 1253–1264 (2017).
13. Leithner, C. & Royl, G. The oxygen paradox of neurovascular coupling. *J. Cereb. Blood Flow Metab.* **34,** 19–29 (2014).
14. Kealy, J., Bennett, R. & Lowry, J. P. Simultaneous recording of hippocampal oxygen and glucose in real time using constant potential amperometry in the freely-moving rat. *J. Neurosci. Methods* **215,** 110–120 (2013).
15. Requejo-Aguilar, R., Lopez-Fabuel, I., Fernandez, E., Martins, L. M., Almeida, A. & Bolaños, J. P. PINK1 deficiency sustains cell proliferation by reprogramming glucose metabolism through HIF1. *Nat. Commun.* **5,** 4514 (2014).
16. Jarazo, J. The Parkinson's Disease Associated PINK1-Parkin Pathway in Pathology and Development. PhD Thesis (University of Luxembourg, Luxembourg, 2018).
17. Liu, W., Acín-Peréz, R., Geghman, K. D., Manfredi, G., Lu, B. & Li, C. Pink1 regulates the oxidative phosphorylation machinery via mitochondrial fission. *Proceedings of the National Academy of Sciences* **108,** 12920–12924 (2011).
18. Herrero-Mendez, A., Almeida, A., Fernández, E., Maestre, C., Moncada, S. & Bolaños, J. P. The bioenergetic and antioxidant status of neurons is controlled by continuous degradation of a key glycolytic enzyme by APC/C-Cdh1. *Nat. Cell Biol.* **11,** 747–752 (2009).
19. Yao, Z., Gandhi, S., Burchell, V. S., Plun-Favreau, H., Wood, N. W. & Abramov, A. Y. Cell metabolism affects selective vulnerability in PINK1-associated Parkinson's disease. *J. Cell Sci.* **124,** 4194–4202 (2011).
20. Dias, V., Junn, E. & Mouradian, M. M. The role of oxidative stress in parkinson's disease. *J. Parkinsons. Dis.* **3,** 461–491 (2013).
21. Valerio, A., D'Antona, G. & Nisoli, E. Branched-chain amino acids, mitochondrial biogenesis, and healthspan: An evolutionary perspective. *Aging* **3,** 464–478 (2011).

8.2 Conference Presentations

Reid, C.H., Finnerty, N.J. "Continuous Long-Term Recordings Using Microamperometric Sensors in the Extracellular Fluid of Immunocompromised NOD SCID Mice". 69th Irish Universities Chemistry Research Colloquium, Dublin City University, Dublin. June 22nd & 23rd 2017. [Oral Presentation].

Reid, C.H., Finnerty, N.J. "In Vivo Characterisation of Microamperometric Sensors in the Brain Extracellular Fluid of Immunocompromised Mice". 2nd International Conference on Neurology and Brain Disorders, Valencia, Spain. June 26th – 28th 2017. [Poster Presentation].

8.3 Publications

Reid, C.H., Finnerty, N.J. Long Term Amperometric Recordings in the Brain Extracellular Fluid of Freely Moving Immunocompromised NOD SCID Mice. *Sensors* **2017**, *17*, 419.

Reid, C.H., Finnerty, N.J. Real-Time Amperometric Recording of Extracellular H_2O_2 in the Brain of Immunocompromised Mice: An *In Vitro*, *Ex Vivo* and *In Vivo* Characterisation Study. *Sensors*. **2017**,17, 1596.